Heat Transfer in High Current Density Electrical Machines

Robert Camilleri

Department of Engineering Science
University of Oxford

Dissertation submitted for the degree of
Doctor of Philosophy

Hilary, 2016

Declaration

The work presented in this dissertation was carried out between January 2012 and April 2016 under the supervision of Prof Malcolm McCulloch and Prof David Howey.

The author wishes to declare that, except for commonly understood and accepted ideas or where reference is made to the work of others, the work in this dissertation is his own, and includes nothing which is the outcome of work done in collaboration. It has not been submitted in part, or in whole, to any other university for a degree, diploma or other qualification.

Robert Camilleri
Hilary 2016

To my wife Charmaine, in gratitude of your love

To my parents, in humble appreciation of your devotion

Acknowledgements

I thank my supervisor Prof Malcolm McCulloch for providing me with the opportunity to pursue my studies within the Energy and Power Group. His guidance, wit and eloquence are appreciated. The academic freedom I enjoyed throughout this research is greatly valued. My thanks also go to Prof David Howey for his expert advice and attention to detail. I would also like to express my thanks to Mr Michael Seifert for funding my studies.

My thanks also go to the numerous people who were involved with my experimental work: Mr Tony Hickman from the Physics department for always being available to wind pole pieces; Trevor Godfrey from the Osney Labs for manufacturing the thin film gauges and Dr Paul Beard for his enthusiasm and help with calibration and processing thin film gauges; Dr Igor Dyson and Dr Kalin Dragnevski for their help with measuring material properties; Mr Morris Keble Smith, Mr Cleveland Williams for the assistance in the tool shop, and Mr Robin Vincent for the many things I borrowed while setting up my experimental test rigs. I also thank Dr Budimir Rosic and Dr Salvador Luque Martinez for their friendship and valuable discussions on the topics of heat transfer.

I would like to show my appreciation to my colleagues and friends within the Energy and Power Group, both at Begbroke and Holder building. In particular: Johannes, Kostas, Fran, Pete, Ren, Richard, Nicole and Nathan. The numerous coffee breaks; the work we have put into PEGGIE and the endless discussions over lunch and in pubs will be treasured dearly.

I thank my parents for their sacrifice to provide my brothers and I with a good education, and my in-laws for their support and prayers. Finally, I wish to thank my loving wife, Charmaine for the sacrifice, patience and support throughout these challenging few years.

Heat Transfer in High Current Density Electrical Machines

Robert Camilleri
Energy and Power Group, Dept. of Eng. Sc., University of Oxford

Dissertation submitted for the degree of Doctor of Philosophy

Abstract

The aim of this research is to increase the current density of electrical machines by improving the heat transfer from the stator. Hence, this research investigates key heat transfer parameters that limit convective and conductive heat transfer. The current density is interdependent on temperature and parameters governing heat transfer. Therefore, thermal analysis of electrical machines is important to design high current density electrical machines.

This research starts by investigating the role air-cooled axial flux machines in the context of electric transportation. These are found to suffer from thermal limitations, forcing the propulsive power to be distributed among several wheels. The machine topology is found to play an important role in the heat transfer limits. The internal rotor topology suffers from heat transfer limits from the casing while the internal stator topology suffers from heat transfer in the rotor-stator gap. Addressing the latter is more challenging. This research does this by investigating a novel evaporative cooling mechanism to transport heat from the machine's internal stator to the outer rotor. A proof of concept was experimentally established and the challenges for adopting this mechanism to an electrical machine are investigated.

The research focus is turned to direct oil-cooled machines. These do not suffer from the same thermal limits as they use an external radiator to expel heat. However, direct liquid cooled machines suffer from a non-uniform flow distribution, which affects the stator temperature distribution. To investigate this problem, an efficient thermo-fluid model was developed to predict the flow and temperature distribution in an oil-cooled stator. This was compared to CFD models and validated to within 6% of experimental results. The stator temperature distribution is improved by carefully controlling the flow distribution. The hot spot temperature is reduced by 13 K, doubling the insulation lifetime, or for the same hot spot temperature increasing the current density by 7%. The heat transfer coefficient an oil-cooled machine was measured by adapting the double layer thin film heat flux gauge technique. Correlations for the heat transfer coefficient on the pole piece surfaces are established and compared with analytical and CFD predictions.

Finally the focus is turned to conductive heat transfer in concentrated windings. These are shown to suffer from a severe temperature gradient. Heat is transferred from one winding layer to the next and a hotspot is formed on the layer with the longest thermal path. The hotspot limits the current density of the machine. A lumped parameter thermal model was developed to predict the value and location of the hotspot in concentrated windings. To shorten the thermal path of the windings, a heat sink was interleaved between the windings. The new construction offers a reduction in hotspot temperature by up to 70 K. For the same maximum temperature the current density is increased by 30%. This thesis revisits flat windings and addresses their manufacturing challenges. Lastly, the relevance of thermal contact resistances is broadened to the general thermal design of electrical machines. This research shows that modeling the thermal resistance at the interface of concentric geometry by a constant parameter is an oversimplification. This was experimentally demonstrates to change with heat flux, contact pressure and material properties.

Nomenclature

Roman Symbols

a	machine thermal constant	
a′	Arrhenius equation constant	
A	cross sectional area	m^2
A’	filler constant for open pack coils in the Kanzaki eqn. $A' = 2\sqrt{\frac{\upsilon_c+\upsilon_i}{\pi}}$	
b	machine thermal constant	
B	filler constant for open pack coils in the Kanzaki eqn. $B = \frac{1}{1-2s\prime s}$	
Bi	Biot number	
c	specific heat capacity	J/kgK
c’	material hardness constant	
C	conductivity constant for open pack coils in the Kanzaki eqn. $C = k_e(k_i - k_c)$	
C_{th}	thermal capacitance	J/K
C_m	coefficient of moment	
dQ	incremental correction in flow	m^3
D	diameter	m^2
D’	conductivity constant for the Ott eqn. $D' = 2\sqrt{\left(\frac{\pi}{PF}\right)}.k_c[2(k_e - k_c)]$	
D_h	hydraulic diameter	m
E	Young’s modulus	Pa
E’	conductivity constant for open pack coils in the Kanzaki eqn. $E' = k_c(k_e - k_i)$	
E_a	activation Energy	J
$\dot{E}$	rate of energy exchange	W
f	friction factor	
f_{app}	apparent friction factor	
F	filler constant for closed pack coils in the Kanzaki eqn. $F = \sqrt{\frac{2\sqrt{3}\upsilon_c}{\pi}}$	
F_R	radiation function of view factor and emissivity	
g	gravitational constant	m/s^2
G	radius to gap ratio	
h	heat transfer coefficient	W/m^2K
h_f	pressure head loss	m
h_o	average film thickness	m
H	height	m
H_c	micro contact hardness	MPa
I	electric current	A
J	current density	A/mm^2

k	thermal conductivity	W/mK
k_b	Boltzmann constant	m^2kg/s^2K
K	pressure loss coefficient	
K_μ	viscosity correction factor	
l	length	m
L	lifetime	years
L_o	material constant	
L_c	characteristic length	m
L_e	entrance length	m
L_v	latent heat of vaporization	J/kgK
m	vehicle mass	kg
m’	heat sink parameter	
ms	mean asperity slopes, $ms = \sqrt{{ms_1}^2 + {ms_2}^2}$	
$\dot{m}$	mass flow rate	kg/s
n	rotational speed	rpm
$\tilde{n}$	number of flux tubes	
N	number of measured quantity	
Nu	Nusselt number	
P	machine power	W
P_{app}	apparent pressure	N/m^2
P_r	perimeter	m
P_{sh}	shrink pressure	N/m^2
P_t	traction power	W
PF	packing factor	
Pr	Prandtl number	
$\dot{q}$	heat flux	W/m^2
Q	heat losses	W
$\dot{Q}$	volume flow rate	m^3/s
r	radius	m
R	electrical resistance	Ω
R_{th}	thermal resistance	K/W
Re	Reynolds number	
s	ratio of insulation thickness to wire diameter	
s’	ratio of wire deformation to insulation thickness	
t	time	s
T	temperature	K
ΔT	change in temperature	K
U	overall heat transfer coefficient	W/K
U_o	material constant	
$u( )$	uncertainty	

u	velocity vector in the x direction	m/s
v_f	velocity of the flow	m/s
v	velocity vector in the y direction	m/s
V	electrical voltage	V
V	velocity vector in the three dimensions	m/s
V_b	body volume	m^3
w	velocity vector in the z direction	m/s
x	thickness	m
x	orientation along the x axis	
y	orientation along the y axis	
Y	mean plane separation	
z	orientation along the z axis	
Z	measured quantity	

Greek Symbols

α	temperature coefficient of resistivity	1/K
β	flow ratio	
γ	ratio of specific heats	
γ'	material constant	
δ	difference in cylinder radius	m
Δ_j	head-flow ratio for a loop	
ΔT	change in temperature	K
ε	surface roughness	μm
η	efficiency	
λ	relative mean plane separation, $\lambda = {Y}/{\sigma}$	
Λ	molecular mean free path	
μ	dynamic viscosity	Pa.s
ν	kinematic viscosity	m^2/s
ρ	density	kg/m^3
ρ_r	electrical resistivity	Ωm
σ	mechanical stress	Pa
σ_{sr}	RMS surface roughness, $\sigma = \sqrt{{\sigma_1}^2 + {\sigma_2}^2}$	
$\sigma_{\bar{x}}$	standard deviation of the mean	
σ_x	standard deviation	
ζ	relative contact spot radius, $\zeta = \sqrt{{A_r}/{A_a}}$	
τ	thermal time constant	
υ	Poisson's ratio	
Υ	volume ratio	

ϕ	non uniformity factor	
$\psi(\epsilon)$	spreading resistance	
ω	angular velocity	rad/s

Subscripts and Superscripts

a	amalgam
app	apparent
amb	ambient
b	bulk
ct	contact
c	conductor
cc	contact conductance
calib	calibration
csa	cross sectional area
dev	developing flow
e	epoxy
eq	equivalent
f	fluid
fd	fully developed flow
fin	heat sink fin
F	flow
g	generated
gc	air gap across bodies in contact
gap	gap of the fin channel
H	housing
i	insulation
i	pipe number
in	into component
imp	impregnation
iso	isothermal
j	loop number
jc	joint conductance
m	closed loop
n	machine constant
o	at a reference temperature of 0 ^{o}C
out	out of component
over	over all uncertainty
r	real
R	rotor
rad	radiation

rand	random uncertainty
Ri	internal rotor
Ro	outer rotor
s	solid
S	stator
slot	slot of an induction machine
st	stored
subs_b	bottom of the substrate
subs_t	top of the substrate
sys	systematic uncertainty
T	at a current temperature
u	planar
w	wall
ϕ	rotational
∞	ambient temperature

Abbreviations

AFIR	axial flux internal rotor
AFIS	axial flux internal stator
AFPM	axial flux permanent magnet
CFD	computational fluid dynamics
HTC	heat transfer coefficient
LPNA	lumped parameter network analysis
SMC	soft magnetic composite
TCR	thermal contact resistance

Table of Contents

1| INTRODUCTION 1

1.1 MOTIVATION FOR THIS RESEARCH 1
1.2 THERMAL ASPECTS OF ELECTRICAL MACHINES 2
1.3 THE PHYSICS OF HEAT TRANSFER 5
1.3.1. CONDUCTION 5
1.3.2. CONVECTION 6
1.3.3. RADIATION 8
1.4 HIGH CURRENT DENSITY ELECTRICAL MACHINES 8
1.4.1. THE MACHINE TYPE 9
1.4.2. THE MACHINE TOPOLOGY 10
1.4.3. THE WINDING CONFIGURATION 13
1.4.4. THE COOLING CONFIGURATION 13
1.5 THE YASA MACHINE: A TEST CASE STUDY 18
1.6 SCOPE OF THIS RESEARCH AND OUTLINE OF THIS THESIS 20
1.7 SCIENTIFIC CONTRIBUTION 24
1.8 LIST OF PUBLICATIONS 25

2| LITERATURE REVIEW 27

2.1 THE THERMAL BEHAVIOUR OF ELECTRICAL MACHINES 27
2.2 THERMAL ANALYSIS OF ELECTRICAL MACHINES 30
2.3 THE HEAT TRANSFER COEFFICIENT IN ELECTRICAL MACHINES 33
2.3.1. THE RELATIONSHIP OF HEAT TRANSFER WITH AIRFLOW 33
2.3.2. CFD PREDICTION AND HEAT FLUX MEASUREMENTS 35
2.4 THERMAL MODELLING OF THE STATOR WINDINGS 40
2.5 THERMAL CONTACT RESISTANCE IN ELECTRICAL MACHINES 48

3| AIR COOLED ELECTRICAL MACHINES 50

3.1. CONTEXT TO THIS CHAPTER 50
3.2. VEHICLE DIMENSIONS AND POWERTRAIN SIZING 51
3.3. TOTALLY ENCLOSED AIR-COOLED MACHINES 54
3.3.1. THERMAL MODELLING OF AN AFIR MACHINE 55
3.3.2. THERMAL MODELLING OF AN AFIS MACHINE 57
3.4. RESULTS AND DISCUSSION 61
3.5. IMPROVING THE HEAT TRANSFER FROM THE CASING 64
3.5.1. A HEAT SINK FOR THE CASING OF AFIR MACHINES. 66
3.5.2. A HEAT SINK FOR AFIS MACHINES. 70

3.6. CONCLUSION **72**

4| EVAPORATIVE COOLED ELECTRICAL MACHINES **74**

4.1 CONTEXT TO THIS CHAPTER **74**

4.2 DESIGN CONSIDERATIONS AND OPERATING LIMITS **75**

4.2.1. THE WORKING FLUID 75

4.2.2. CLASSICAL HEAT PIPE LIMITS 77

4.2.3. THE WICKING MATERIAL AND CAPILLARY LIMIT 79

4.3 EVALUATION OF THE HEAT TRANSPORT MECHANISM **81**

4.3.1. EXPERIMENTAL WORK 81

4.3.2. THERMAL TEST RESULTS AND IMPLICATIONS 82

4.4 EXPERIMENTAL OBSERVATION ON THE FLUID DYNAMICS **84**

4.4.1. INVESTIGATION OF RIMMING FLOWS IN LOW ASPECT RATIO CYLINDERS 84

4.4.2. THE EFFECTS OF REAL MACHINE GEOMETRY 86

4.5 SYSTEMS INTEGRATION **88**

4.5.1 THE DESIGN OF THE WICK 88

4.5.2 THE IMPLICATIONS OF WORKING FLUID ON THE MACHINE RATING 89

4.6 DISCUSSION AND CONCLUSION **91**

5| DIRECT LIQUID COOLED ELECTRICAL MACHINES **92**

5.1. CONTEXT TO THIS CHAPTER **93**

5.2. A DIRECT LIQUID COOLING CONFIGURATION **94**

5.3. THERMO-FLUID MODELLING **95**

5.3.1 PRINCIPLES OF FLUID MECHANICS 95

5.3.2. THE ITERATIVE FLOW NETWORK MODEL 99

5.3.3. THE LUMPED PARAMETER THERMAL MODEL 103

5.4. COMPUTATIONAL FLUID DYNAMICS **107**

5.4.1. THE GOVERNING EQUATIONS FOR FLUID FLOW AND HEAT TRANSFER 108

5.4.2. SOLVING THE GOVERNING EQUATIONS NUMERICALLY 109

5.4.3. CFD OF THE STATOR GEOMETRY 110

5.5. EXPERIMENTAL WORK **117**

5.5.1. MANUFACTURING THE TEST PIECE 117

5.5.2. MEASURING THE TEMPERATURE DISTRIBUTION IN THE STATOR 118

5.6. TEST RESULTS AND MODEL VALIDATION **120**

5.7. SIMULATION OF THE MACHINE STATOR **124**

5.8. IMPROVEMENTS TO THE STATOR TEMPERATURE DISTRIBUTION **125**

5.9. DISCUSSION AND CONCLUSION **129**

6| THE HEAT TRANSFER COEFFICIENT IN DIRECT LIQUID COOLED STATORS **131**

6.1. THE HEAT TRANSFER COEFFICIENT: A DEFINITION 131
6.2. PREDICTING THE HTC IN AN OIL COOLED STATOR 132
6.2.1. EMPIRICAL CORRELATIONS FOR A LAMINAR FLOW REGIME 132
6.2.2. CFD PREDICTION OF THE HTC IN AN OIL COOLED STATOR 133
6.3. EXPERIMENTAL WORK 135
6.3.1. A BRIEF DESCRIPTION OF THE MEASUREMENT TECHNIQUES 135
6.3.2. A STEADY STATE HTC MEASUREMENT USING THIN FILM GAUGES 138
6.3.3. MANUFACTURING AND CALIBRATION OF THE INSTRUMENTED TEST PIECE 140
6.3.4. ASSESSMENT OF THE POLE PIECE HEATING SYSTEM 142
6.3.5. THE EXPERIMENTAL SETUP 143
6.4. RESULTS AND DISCUSSION 145
6.4.1. POST PROCESSING THE GAUGE MEASUREMENTS 145
6.4.2. PREDICTED AND MEASURED HTC VALUES 146
6.5. CONCLUSION 152

7| CONDUCTIVE HEAT TRANSFER IN CONCENTRATED WINDINGS 153

7.1. CONTEXT TO THIS CHAPTER 153
7.2. A NEW LP BASED MODEL FOR THE WINDINGS 155
7.2.1. DESCRIPTION OF THE MODEL 155
7.2.2. DEFINING THE MATERIAL AND THERMAL PROPERTIES 158
7.2.3. THE ELECTRICAL PROPERTIES OF COPPER WINDINGS AND SMC IRON BOBBIN 159
7.2.4. PARAMETRIC MODELLING AND VISUALISATION 161
7.3. EXPERIMENTAL INVESTIGATION 162
7.3.1. MANUFACTURING CONCENTRATED WOUND POLE PIECES 163
7.3.2. MANUFACTURING THE FLOW GEOMETRY 165
7.3.3. MEASURING THE TEMPERATURE PROFILE ACROSS THE POLE PIECE 166
7.4. TEST RESULTS AND MODEL VALIDATION 168
7.4.1. EPOXY-INFILTRATED WINDINGS 168
7.4.2. NON-INFILTRATED WINDINGS 170
7.5. DISCUSSION 172
7.5.1. THE TEMPERATURE GRADIENT 172
7.5.2. THE THERMAL RESISTANCES 172
7.5.3. THE THERMAL CAPACITY 174
7.5.4. THE EFFECT OF EPOXY-INFILTRATION ON THE TEMPERATURE PROFILE 175
7.5.5. THE IMPLICATION ON LIFETIME ESTIMATIONS OF THE WINDINGS 179
7.6. DEMONSTRATION OF THE MODEL AND FURTHER DEVELOPMENT 180
7.6.1. THE EFFECT OF COOLING THE IRON BOBBIN 180
7.6.2. THE TEMPERATURE PROFILE OF INDIRECTLY COOLED CONCENTRATED WINDINGS 181
7.6.3. THE EFFECT OF AXIAL HEAT FLUX 183
7.7. CONCLUSION 183

8| IMPROVING THE CURRENT DENSITY IN CONCENTRATED WINDINGS 185

8.1. MOTIVATION AND INTRODUCTION TO THIS CHAPTER 185

8.2. INTEGRATING A HEAT SINK INTO CONCENTRATED WINDINGS 186

8.2.1. DESIGN AND CONCEPT FORMULATION 186

8.2.2. CFD MODELLING OF THE NEW CONSTRUCTION WITH INTEGRATED HEAT SINK 187

8.2.3. LP MODELLING OF THE NEW CONSTRUCTION WITH INTEGRATED HEAT SINK 193

8.2.4. EXPERIMENTAL INVESTIGATION OF THE CONCEPT 194

8.2.5. TEST RESULTS AND DISCUSSION 197

8.3. RETHINKING FLAT COPPER WINDINGS 199

8.3.1. DESIGN AND CONCEPT FORMULATION 199

8.3.2. LP MODELLING OF FLAT WINDINGS 202

8.4. THE CURRENT DENSITY OF THE NEW CONSTRUCTIONS 204

8.5. DISCUSSION AND CONCLUSION 206

9| THE RELEVANCE OF THERMAL CONTACT RESISTANCE IN ELECTRICAL MACHINES 208

9.1. MOTIVATION BEHIND THIS CHAPTER 208

9.2. DESIGN OF THE EXPERIMENT 210

9.4. EXPERIMENTAL WORK 212

9.4.1. MANUFACTURING THE TEST SAMPLES 212

9.4.2. THE SURFACE ROUGHNESS 212

9.4.3. MATERIAL BULK AND MICRO HARDNESS 213

9.4.4. SHRINK FIT ASSEMBLIES 214

9.4.5. MEASURING THE THERMAL CONTACT RESISTANCE 215

9.5. TEST RESULTS 216

9.6. DISCUSSION AND CONCLUSION 217

10| CONCLUSIONS AND FURTHER WORK 221

List of Figures

Figure 1.1. Relationship of copper electrical resistivity with temperature and residual-resistance ratio (RRR). Data from Cryogenic properties of Copper, (2015) 3
Figure 1.2. NdFeB polarization and induction demagnetization curves with increasing temperatures, reproduced from Calin and Helerea, (2011) 4
Figure 1.3. A comparison of the heat transfer coefficient in different flow conditions and media. Data from Engineersedge.com: Convective heat transfer coefficients tables, retrieved online on 21/09/2015. 8
Figure 1.4. Comparison of the current density between in electrical machines with different cooling technology. Data from Yeadon and Frustaglio, (2010) 9
Figure 1.5. Example of two direct drive YASA-750 axial flux machines installed in a Formula student 12
Figure 1.6. An example of a radial flux permanent magnet machine with short axial length and concentrated wound stator teeth for a for a Honda Insight hybrid. (Figure from ABG First Drive: 2010 Honda Insight, retrieved on July 2014) 12
Figure 1.7. Categories of cooling mechanisms in electrical machines 13
Figure 1.8. Comparison of the Continuous Power density and Torque density for axial flux machines with air and liquid cooling configurations 14
Figure 1.9. Demonstration of the interdependencies of the terms in eqn. 1.16 16
Figure 1.10. Current density for a maximum winding temperature of 120 °C (Right: Enlarged window) 17
Figure 1.11. Current density for a maximum winding temperature of 250 °C (Right: Enlarged window) 17
Figure 1.12. Schematic of the YASA topology, reproduced from Woolmer and McCulloch, (2007) 19
Figure 1.13. Efficiency chart of the YASA 750 Machine, reproduced from YASA, (2010) 20
Figure 1.14. Geometrical dimensions of the YASA 750 Machine, reproduced from YASA, (2010) 20
Figure 2.1. An example of a LP thermal model reproduced from Sahin, (2001) 31
Figure 2.2. Schematic showing how an electrical machine in a) is converted into a resistance network shown in b). Figures extracted from MotorCAD, (2015) and Boglietti et al., (2009) 33
Figure 2.3. Heat flux gauge mounted on the end windings, reproduced from Hettenger, (2012) 36
Figure 2.4. (left) Thin film electric heater fixed to the stator, (right) Schematic of the rotor-stator test rig. Figures extracted from Howey, (2010, 2011) 38
Figure 2.5. An example of Closed Pack and Open Pack windings investigated in Kanzaki et al., (1992) 42
Figure 2.6. Layered winding model for the slot geometry of induction machines reproduced from Staton et al., (2005) 46
Figure 2.7. Elliptical layered winding model for the slot geometry of induction machines, reproduced from Nategh et al., (2012) 47
Figure 2.8. Interference gap values for induction machines. Data from Boglietti et al., (2008) 49
Figure 3.1. Survey of EV continuous power for vehicles the market at 2013 52
Figure 3.2. Motor losses for 20kW motor designs with various gear ratios 53
Figure 3.3. Chart showing motor losses for various motor, power distribution and gear ratios 54
Figure 3.4. Schematic of an Axial Flux Internal Rotor (AFIR) electrical machine (Left), an Axial Flux Internal Stator (AFIS) electrical machine (Right) 54
Figure 3.5. A thermal resistance network for an Axial Flux Internal Rotor (AFIR) electrical machine 56
Figure 3.6. A thermal resistance network for an Axial Flux Internal Stator (AFIS) electrical machine 58

Figure 3.7. Chart Showing the four flow regimes. Data from Daily and Nece, (1960). 60
Figure 3.8. Example of the thermal resistance components for an AFIS topology fitted to a 15" wheel 63
Figure 3.9. Plot of the continuous heat generation and continuous cooling capacity for AFIR machine 63
Figure 3.10. Plot of the continuous heat generation and continuous cooling capacity for AFIS machine 64
Figure 3.11. CAD of AFIR type machine with extended surfaces. Insert: example of the fin geometry 65
Figure 3.12. CAD model of a shrouded disc brake heat type sink (left) and an unshrouded radial vane heat sink for an AFIS machine 66
Figure 3.13.Variation of heat sink thermal resistance with fin thickness and number of fins 69
Figure 3.14. Variation of heat sink mass with fin thickness and channel spacing 69
Figure 3.15. The cooling performance of a motor fitted to a 15" wheel with an ideal scenario (no external surfaces), and with an installed heat sink 70
Figure 3.16. Comparison between the thermal resistance of a rotating disc and rotating heat sink 71
Figure 3.17. The heat transfer from a motor fitted to a 15" wheel with an ideal scenario (no external surfaces), and with an installed heat sink 72
Figure 4.1. Similarities in operating principles between a) heat pipe, and b) evaporative cooled machine 75
Figure 4.2. Properties of working fluid candidates, data from Boiling Points, Fluids and Gasses, (2013), Fluids – Latent Heat of Evaporation, (2013) and Dielectric Constants for some common Liquids, (2013) 77
Figure 4.3. Schematic of the classical heat pipe limits with as the evaporator temperature increases, reproduced from Dunn and Reay, (1994) 78
Figure 4.4. Setup to measure the wicking rates for various fabrics with 1) ruler, 2) wicking material under test, 3) liquid pool. 4) video camera 80
Figure 4.5. Example of wicking performance of different materials with methanol 80
Figure 4.6. Experimental setup for a) wick assisted setup, b) immersion setup, with 1) fan, 2) heat sink, 3) test box, 4) working fluid, 5) copper windings, 6) pole piece iron, 7) insulating material, 8) wicking material. Inserts: Photographs of the wick assisted and immersion cooling test boxes. 82
Figure 4.7. Wick assisted cooling with methanol comparing (Top) immersion cooling, (Bottom) wick assisted cooling concept 83
Figure 4.8. Wick assisted cooling with propanol comparing (Top) immersion cooling, (Bottom) wick assisted cooling concept 83
Figure 4.9. Experimental setup investigating fluid behaviour in rotating cylinders with 1) dc motor, 2) connecting shaft, 3) filled cylinder under test, 4) speed sensor, 5) high speed camera 85
Figure 4.10. Observation of fluid behaviour with rotational speed 86
Figure 4.11. Motor replica with 1) Outer rotor housing, 2) stator, 3) rotor iron 4) permanent magnets, 5) bearing, 6) connecting shaft 87
Figure 4.12. Observations of rimming flow in motor replica 87
Figure 4.13. Schematic showing the concept of the wick with 1) motor casing, 2) rimming flow, 3) wick design with a "finger" reaching into the fluid, 4) concentrated windings, 5) pole piece iron 88
Figure 4.14. Comparison of the stator heat losses with the heat transfer from the casing for methanol 90
Figure 4.15. Comparison of the stator heat losses with the heat transfer from the casing for propanol 90
Figure 5.1. Schematic of a direct liquid cooled stator for an axial flux machine. Highlighted: quarter of the stator used for reference at a later section within this chapter 95
Figure 5.2. Schematic of a direct liquid cooled stator for a radial flux machine 95
Figure 5.3. Schematic showing the development of the boundary layer 97

Figure 5.4. Comparison of the theoretical head loss in laminar entry region for a developing and developed flow. Data of the developing flow reproduced from Langhaar, (1942) ____ 98
Figure 5.5. Definition of the flow directions in a) a dividing T-junction, b) a combining T-junction ____ 99
Figure 5.6. Schematic of a simplified flow network for the YASA machine ____ 100
Figure 5.7. Flow chart showing the process to solve the iterative 1D flow model for each stator ____ 102
Figure 5.8. Variation of Opticool properties with temperature. Data points from DSI, (2015). ____ 105
Figure 5.9. Flow chart showing the process to solve the iterative LP thermal model ____ 107
Figure 5.10. Schematic showing the process of CFD ____ 108
Figure 5.11. Details of the 2D CAD geometry ____ 111
Figure 5.12. Details of the 3D CAD geometry. ____ 112
Figure 5.13. Details of the boundary conditions applied to the 2D model ____ 113
Figure 5.14. Details of the boundary conditions applied to the 3D model ____ 113
Figure 5.15. Mesh setup for the 2D model with inserts of the uniform mesh in the fluid channels and details of the gradation boundary layer mesh at the solid-fluid boundary ____ 115
Figure 5.16. Schematic of the machine pole piece with installed heater ____ 118
Figure 5.17. Test rig representing the first quarter of the machine stator ____ 118
Figure 5.18. Test setup with 1) oil reservoir, 2) temperature sensors, 3) test box, 4) pump, 5) heat exchanger, 6) variable area flow meter, 7) globe valve, 8) ac power supply, 9) variable transformer to power fluid heater, 10) variable transformer to power pole piece heaters ____ 119
Figure 5.19. Comparison of the measured pole piece temperature with LP model and CFD model for the test conditions 1-4 ____ 122
Figure 5.20. Comparison of the measured pole piece temperature with LP model and CFD model for the test conditions 5-8 ____ 122
Figure 5.21. Comparison of the flow distribution from the LP model and CFD model for the test conditions 1-4 ____ 123
Figure 5.22. Comparison of the flow distribution from the LP model and CFD model for the test conditions 5-10 ____ 123
Figure 5.23. a) Example of the fluid velocity map and b) the resulting pressure distribution through the stator flow domain for Test condition 5 from the 2D CFD simulations ____ 123
Figure 5.24. a) Example of the Temperature map of the stator and b) the resulting viscosity map in the stator fluid domain for Test condition 5 from the 2D CFD simulations ____ 123
Figure 5.25. Simulation of the machine stator temperature distribution with pole piece heat loads of 250 W, 200 W and 150 W. Insert: schematic of the stator with numbered pole pieces ____ 124
Figure 5.26. Simulation of the machine stator temperatures for a fixed flow rate and constant heat load and distribution rings of 10 mm, 8 mm and 6 mm width. Insert: schematic of the modified dimension ____ 125
Figure 5.27. Comparison of the flow ratio for the four motor sectors before and after the changes to the stator flow geometry. Simulation with a coolant flow rate of 6 lpm, coolant inlet temperature of 80 °C, and pole piece losses of 250 W ____ 127
Figure 5.28. Comparison of the predicted stator pole piece temperatures for the original and improved stator flow geometry. Simulation with a coolant flow rate of 6 lpm, coolant inlet temperature of 80 °C, and pole piece losses of 250 W ____ 128
Figure 5.29. The resulting stator flow geometry achieving an improved temperature distribution ____ 129
Figure 6.1. (Left) direct liquid cooled stator with highlighted portion of liquid channel ____ 133

Figure 6.2. Details of the boundary conditions applied to the single channel model ____ 134
Figure 6.3. Mesh setup for the single channel model ____ 134
Figure 6.4. Schematic showing a Double sided Direct Heat Flux Gauge ____ 138
Figure 6.5. Instrumented aluminium pole piece replica (Numbers 1-8 referenced in local HTC results) __ 140
Figure 6.6. Example of a calibration chart for a thin film gauge, from which the values of temperature coefficient α and reference resistance Ro (y-intersect at T=0 °C) for each gauge is determined 141
Figure 6.7. Material and boundary conditions to assess the heating system on the aluminium block ____ 143
Figure 6.8. Simulation results of the temperature distribution on the aluminium block ____ 143
Figure 6.9. Test box showing a section of the stator machine and instrumented pole piece ____ 144
Figure 6.10. Test rig for measuring the HTC ____ 144
Figure 6.11. Change in gauge resistance with block temperature ____ 146
Figure 6.12. Charts mapping (top) The gauge's temperature, (middle) Temperature difference across the insulation substrate, (bottom) Estimated heat flux across the gauges for a specific location instrumented with a set of gauges. The discarded point is shown in red. ____ 147
Figure 6.13. Example of the local heat transfer coefficient along the length of the pole piece sides for an inlet flow rate of 2.2 lpm and inlet temperature of 26 °C ____ 147
Figure 6.14. Measurement of the average HTC along the length of the pole piece surfaces marked A and B, with superposition of the predicted HTC ____ 149
Figure 6.15. Heat flux on the pole piece surfaces (Left) Side 1 (Right) Side 2, at a Re = 150 ____ 151
Figure 6.16. Plot of the non-dimensional Nusselt numbers with channel Reynolds numbers ____ 151
Figure 7.1. Cross section of the windings cross section and fill factor with a) square wire cross section and open pack windings configuration, b) circular wire cross section and open pack winding configuration, and c) circular wire cross section and closed pack winding configuration. ____ 154
Figure 7.2. Simplification of the winding geometry. Figure showing a cross section of the pole piece for better demonstration purposes ____ 155
Figure 7.3. LP thermal model with node on each winding layer. (Insert) Thermal resistance network with thermal capacitance and heat generation at each node and thermal resistances between the nodes ____ 156
Figure 7.4. LP thermal model with nodes on either sides of the pole piece ____ 156
Figure 7.5. Thermal resistance network of the pole piece with left and right temperature resolution ____ 156
Figure 7.6. The electrical resistivity of copper windings with temperature ____ 160
Figure 7.7. Electrical resistance of SMC iron with temperature ____ 161
Figure 7.8. Cross sectional area along the XZ plane for half the YASA pole piece ____ 161
Figure 7.9. Visualisation of the pole piece cross sectional area along the XY plane ____ 162
Figure 7.10. Schematic of a directly oil cooled segmented stator. (Highlighted) test Section with one pole piece and respective flow channels ____ 162
Figure 7.11. Details of the winding machine. (Insert) Details of the clamped part ____ 163
Figure 7.12. Details of the winding process with a) thermocouples mounted on the iron pole, b) thermocouples mount between the winding layers ____ 164
Figure 7.13. a) Concentrated wound pole pieces with no epoxy filler b) Concentrated wound pole piece with Stycast epoxy infiltration ____ 165
Figure 7.14. Test Section with recreated flow geometry and marked locations of temperature sensors ____ 165
Figure 7.15. Thermal characterisation of the model with three winding layers for a pole piece with epoxy-infiltrated and experiment conditions as shown in Table 7.3, Test No. 1 ____ 168

Figure 7.16. The temperature profile for the pole piece with epoxy infiltration under steady state conditions _____ 169
Figure 7.17. Correlation of the thermal resistances across the layers with convective thermal resistance 170
Figure 7.18. Thermal characterisation of non-infiltrated windings for experiment conditions in Test 1 __ 171
Figure 7.19. Comparison of the temperature profile across the pole piece with no epoxy infiltration _____ 171
Figure 7.20. Description of the break down of the thermal resistance across non-infiltrated winding layers _____ 172
Figure 7.21. Comparison of the temperature profile of: (a) non-infiltrated concentrated windings and (b) epoxy-infiltrated concentrated windings _____ 175
Figure 7.22. Representation of a) non-infiltrated windings, b) perfectly infiltrated in the gaps, c) partial infiltration and d) a thick layer of infiltration material applied between the windings _____ 176
Figure 7.23. Comparison of the joint conductance with different infiltration methods. (Material thickness x for painting assumed at 0.1mm) _____ 178
Figure 7.24. Examples of cooling geometries (Left) Traditional direct liquid cooled bobbin, (Centre) Pole piece with cooling channels on the shoe, (Right) Pole piece with cooling channels within the iron and shoe _____ 180
Figure 7.25. Modified LP model to investigate the effect of improving the cooling on the iron bobbin_____ 180
Figure 7.26. Example of how the software captures the temperature profile for a pole piece with: _____ 181
Figure 7.27. Example of an indirect cooled electrical machine using a water cooling jacket._____ 181
Figure 7.28. LP model to investigate the temperature profile of indirect cooled stator windings _____ 182
Figure 7.29. Temperature profile for an indirect cooled pole piece _____ 182
Figure 7.30. (Left) LP thermal model with an individual node on each winding with radial and axial heat flux. (Right) Visualisation of the winding temperature distribution in a pole piece experiencing axial and radial heat flux_____ 183
Figure 8.1. CAD model of the heat sink concept _____ 187
Figure 8.2. CAD model showing cross section of the pole piece with integrated heat sink _____ 187
Figure 8.3. Details of the CAD geometry. a) A traditional pole piece with windings modelled as layers, b) The new construction with windings modelled as layers and integrated heat sink _____ 188
Figure 8.4. Schematic showing material and boundary conditions _____ 189
Figure 8.5. Mesh setup with insert showing the details at the solid-fluid boundary._____ 190
Figure 8.6. Temperature profile of the windings for a) conventional construction, b) new construction with heat sink mounted on the SMC, c) new construction with heat sink mounted between the 1st and 2nd layers_____ 191
Figure 8.7. Velocity profiles on plane AA' for a) traditional construction, and b) new construction _____ 192
Figure 8.8. Schematic showing velocity traces a) windings with no heat sink, b) windings with heat sink 192
Figure 8.9. Schematic of the LP model of the new pole piece construction with integrated heat sink between the windings _____ 193
Figure 8.10. Schematic of the LP model broken down into the left and right components _____ 193
Figure 8.11. Manufacturing of the pole piece with integrated heat sink and epoxy resin infiltration_____ 194
Figure 8.12. Prototype of a concentrated wound pole piece with integrated heat sink and epoxy on the windings, instrumented with temperature sensors _____ 195
Figure 8.13. Thermal characterisation of the model for the new construction with infiltrated pole piece and experiment conditions shown in Test 1 _____ 197
Figure 8.14. The temperature profile for the new construction under steady state conditions _____ 198

Figure 8.15. Concept of stacking flat windings _____ 199
Figure 8.16. Manufacturing a prototype of the winding with: a) flat windings from a single sheet and, b) folded sample of the windings _____ 200
Figure 8.17. Side view (left) and Top view (right) of a flat winding assembled on half a bobbin _____ 200
Figure 8.18. Example of the folds outside the winding area to act as heat exchangers _____ 201
Figure 8.19. Schematic of the flat winding showing (Left) the overlapping area at the fold, (Middle) the introduction of the slit at the fold and (Right) the folded slit_____ 202
Figure 8.20. Intermesh of the windings to reduce wastage _____ 202
Figure 8.21. Schematic of the LP model of the new pole piece construction with flat windings _____ 203
Figure 8.22. Sensitivity analysis of the model with variation in thermal resistance R_1 and a constant value of convective resistance R_2_____ 203
Figure 8.23. Comparison of the steady state temperature profile for (left) conventional construction with epoxy-infiltrated concentrated windings used as a reference, (middle) new construction with integrated heat sink and epoxy infiltration, and (right) flat windings. Note that the non-linear temperature scale_____ 204
Figure 8.24. Comparison of the transient temperature profile for a) conventional construction with epoxy-infiltrated concentrated windings, b) new construction with integrated heat sink and epoxy infiltration, and c) flat windings _____ 205
Figure 8.25. Temperature profile for the new construction with integrated heat sink (left) and new construction with flat windings (right) _____ 205
Figure 9.1. Highlights of TCR within (left) an induction machines and (right) a permanent magnet machines _____ 208
Figure 9.2. Variation of thermal conductivity with Silicon content. Data from (Gotter, 1954, Roberts, 1969, Banks, 1961, Schumichen, 1966) _____ 210
Figure 9.3. Test setup with 1) temperature sensors (locations marked with a red dot), 2) concentric assembly with 3) internal cartridge heater, 4) variable transformer, 5) ac power supply_____ 211
Figure 9.4. Micro hardnessp for (Left) Aluminium outer cylinder (Right) inner Carbon Steel cylinder ___ 213
Figure 9.5. Example of a shrink fit assembly_____ 215
Figure 9.6. Variation of thermal contact conductance with heat flux and shrink fit pressure _____ 216
Figure 9.7. Variation of temperature with heat flux for all shrink fit assemblies _____ 219
Figure A.1. Schematic showing flow meter calibration by mass using 1) gate valve, 2) pump, 3) heat exchanger, 4) thermometer, 5) flow meter, 6) 3-way valve, 7) reservoir, 8) collecting beaker, 9) scales, 10) video camera_____ ii
Figure A.2. Calibration chart for flow meter A (originally calibrated for a water flow rate range between 0.2-2 lpm at 20 ^{o}C). _____iii
Figure A.3. Calibration chart for flow meter B (originally calibrated for a water flow rate range between 2-22 lpm at 20 ^{o}C).._____iii
Figure A.4. Calibration charts for a thin film gauges 1-6_____ v
Figure A.5. Calibration charts for a thin film gauges 7-14 _____vi
Figure A.6. Calibration charts for a thin film gauges 15-22_____vii
Figure A.7. Calibration charts for a thin film gauges 24-27, 29-32 _____ viii
Figure A.8. Resistance with temperature for a flow rate of 2.2 lpm and inlet temperature of 26 ^{o}C _____ x
Figure A.9. Resistance with temperature for a flow rate of 2.6 lpm and inlet temperature of 38 ^{o}C _____ x
Figure A.10. Resistance with temperature for a flow rate of 2.4 lpm and inlet temperature of 41.1 ^{o}C_____xi

Figure A.11. Resistance with temperature for a flow rate of 3.5 lpm and inlet temperature of 26.5 °C_____xi
Figure A.12. Resistance with temperature for a flow rate of 3.8 lpm and inlet temperature of 37.7 °C_____ xii
Figure A.13. Resistance with temperature for a flow rate of 3.6 lpm and inlet temperature of 42.6 °C_____ xii
Figure A.14. Resistance with temperature for a flow rate of 4.7 lpm and inlet temperature of 28.3 °C_____ xiii
Figure A.15. Resistance with temperature for a flow rate of 5 lpm and inlet temperature of 35.5 °C_____ xiii
Figure A.16. Resistance with temperature for a flow rate of 6.6 lpm and inlet temperature of 45 °C_____ xiv
Figure A.17. Temperature difference and heat flux across the sensors mounted on side A for a flow rate of 2.2 lpm and inlet temperature of 26 °C_____ xv
Figure A.18. Temperature difference and heat flux across the sensors mounted on side B for a flow rate of 2.2 lpm and inlet temperature of 26 °C_____ xvi
Figure A.19. Temperature difference and heat flux across the sensors mounted on side A for a flow rate of 2.6 lpm and inlet temperature of 38 °C_____xvii
Figure A.20. Temperature difference and heat flux across the sensors mounted on side B for a flow rate of 2.6 lpm and inlet temperature of 38 °C_____xviii
Figure A.21. Temperature difference and heat flux across the sensors mounted on side A for a flow rate of 2.4 lpm and inlet temperature of 41.1 °C_____ xix
Figure A.22. Temperature difference and heat flux across the sensors mounted on side B for a flow rate of 2.4 lpm and inlet temperature of 41.1 °C_____ xx
Figure A.23. Temperature difference and heat flux across the sensors mounted on side A for a flow rate of 3.5 lpm and inlet temperature of 26.5 °C_____ xxi
Figure A.24. Temperature difference and heat flux across the sensors mounted on side B for a flow rate of 3.5 lpm and inlet temperature of 26.5 °C_____xxii
Figure A.25. Temperature difference and heat flux across the sensors mounted on side A for a flow rate of 3.8 lpm and inlet temperature of 37.7 °C_____xxiii
Figure A.26. Temperature difference and heat flux across the sensors mounted on side B for a flow rate of 3.8 lpm and inlet temperature of 37.7 °C_____ xxiv
Figure A.27. Temperature difference and heat flux across the sensors mounted on side A for a flow rate of 3.6 lpm and inlet temperature of 42.6 °C_____xxv
Figure A.28. Temperature difference and heat flux across the sensors mounted on side B for a flow rate of 3.6 lpm and inlet temperature of 42.6 °C_____ xxvi
Figure A.29. Temperature difference and heat flux across the sensors mounted on side A for a flow rate of 4.7 lpm and inlet temperature of 28.3 °C_____ xxvii
Figure A.30. Temperature difference and heat flux across the sensors mounted on side B for a flow rate of 4.7 lpm and inlet temperature of 28.3 °C_____xxviii
Figure A.31. Temperature difference and heat flux across the sensors mounted on side A for a flow rate of 5 lpm and inlet temperature of 35.5 °C_____ xxix
Figure A.32. Temperature difference and heat flux across the sensors mounted on side B for a flow rate of 5 lpm and inlet temperature of 35.5 °C_____xxx
Figure A.33. Temperature difference and heat flux across the sensors mounted on side A for a flow rate of 6.6 lpm and inlet temperature of 45 °C_____ xxxi
Figure A.34. Temperature difference and heat flux across the sensors mounted on side B for a flow rate of 6.6 lpm and inlet temperature of 45 °C_____ xxxii
Figure A.35. Local heat transfer coefficients for a flow rate of 2.2 lpm and inlet temperature of 26 °C____xxxiii
Figure A.36. Local heat transfer coefficients for a flow rate of 2.6 lpm and inlet temperature of 38 °C____xxxiii

Figure A.37. Local heat transfer coefficients for a flow rate of 2.4 lpm and inlet temperature of 41.1 °C _xxxiii
Figure A.38. Local heat transfer coefficients for a flow rate of 3.5 lpm and inlet temperature of 26.5 °C _xxxiii
Figure A.39. Local heat transfer coefficients for a flow rate of 3.8 lpm and inlet temperature of 37.7 °C _xxxiii
Figure A.40. Local heat transfer coefficients for a flow rate of 3.6 lpm and inlet temperature of 42.6 °C _xxxiii
Figure A.41. Local heat transfer coefficients for a flow rate of 4.7 lpm and inlet temperature of 28.3 °C _xxxiv
Figure A.42. Local heat transfer coefficients for a flow rate of 5 lpm and inlet temperature of 35.5 °C____xxxiv
Figure A.43. Local heat transfer coefficients for a flow rate of 6.6 lpm and inlet temperature of 45 °C____xxxiv
Figure A.44. Comparison of modelled and measured transient thermal behaviour for a pole piece infiltrated with epoxy resin and experiment conditions shown in Test 2._____ xxxv
Figure A.45. Comparison of modelled and measured transient thermal behaviour for a pole piece infiltrated with epoxy resin and experimental details of Test 3. _____ xxxv
Figure A.46. Comparison of modelled and measured transient thermal behaviour for a pole piece infiltrated with epoxy resin and experimental details of Test 4. _____ xxxv
Figure A.47. Comparison of modelled and measured transient thermal behaviour of a non-infiltrated windings for experimental details of Test 2 _____xxxvi
Figure A.48. Comparison of modelled and measured transient thermal behaviour of a non-infiltrated windings for experimental details of Test 3 _____xxxvi
Figure A.49. Comparison of modelled and measured transient thermal behaviour of a non-infiltrated windings for experimental details of Test 4 _____xxxvi
Figure A.50. Comparison between modelled and measured transient thermal behaviour for the new construction with infiltrated pole piece and experiment conditions shown in Test 2. _____ xxxvii
Figure A.51. Comparison between modelled and measured transient thermal behaviour for the new construction with infiltrated pole piece and experiment conditions shown in Test 5. _____ xxxvii
Figure A.52. Comparison between modelled and measured transient thermal behaviour for the new construction with infiltrated pole piece and experiment conditions shown in Test 6. _____ xxxvii
Figure A.53. Schematic of the conductive heat transfer across a joint. σ is the RMS surface roughness of the surface, m is the asperity slope and Y the mean plane separation._____ xxxviii
Figure A.54. The micro hardness relationship for AWG 14 copper winding. _____ xlii

List of Tables

Table 1.1 Specifications of the YASA Liquid Cooled Machine 19
Table 3.1 Distribution of traction power 52
Table 3.2 Definition of Symbols used in the 1D thermal resistance network 56
Table 3.3 Definition of Flow Regimes and correlations 60
Table 3.4 Typical values for estimating the machine thermal resistance 62
Table 3.5 Table of thermal resistances for AFIR topology 62
Table 3.6 Heat sink solutions for the motor casing of an AFIR machine 65
Table 3.7 Heat sink solutions for the motor casing of an AFIS machine 66
Table 3.8 Empirical correlations heat transfer correlations from rotor passages 71
Table 4.1 Technical Specifications for an in-wheel motor with YASA topology 81
Table 4.2 List of wetting mechanisms explored 89
Table 5.1 Variation of Coolant Properties with Temperature T [^{o}C] 105
Table 5.2 Description and Application of Advection Schemes as from Autodesk, (2016) 116
Table 5.3. Experiment Details 119
Table 5.4 Comparison of the Flow non-uniformity for the Original and Improved stator geometry 128
Table 5.5 Comparison of the Temperature Variance for the Original and Improved stator geometry 128
Table 6.1. Substrate thermal properties 139
Table 6.2. Test matrix for three oil flow rates of between 1 and 6 lpm 145
Table 7.1. List of thermal and material properties for SMC iron and Copper windings 158
Table 7.2. Technical specifications of Stycast Epoxy 164
Table 7.3. Experiment details for the transient characterisation of epoxy-infiltrated windings 167
Table 7.4. Experiment details for the transient characterisation of non infiltrated windings 167
Table 7.5. Steady state experiment details for epoxy-infiltrated windings 167
Table 7.6. Steady state experiment details for non-infiltrated windings 167
Table 7.7. Experimental fit of the thermal resistances for epoxy infiltrated windings 169
Table 8.1. Experiment details for the transient characterisation of the new construction 196
Table 8.2. Experiment details for the steady state temperature profile of the new construction 196
Table 8.3. Calibrated thermal parameters for the new construction 197
Table 9.1. Comparison between measured and reference surface properties 212
Table 9.2. Bulk Hardness values for the inner and outer cylinders and comparison of the micro hardness coefficients c_1' and c_2' 214
Table 9.3. Dimensions of test geometry 215
Table 9.4. correlations of conductance with heat flux 217
Table 9.5. Details of the machines used to compare the thermal contact conductances. Data from Boglietti et al., (2008), Staton et al., (2005) and Mellor, (1995). 218

Table A.1 Approximations of the mean plane separation xxxix
Table A.2 Variation of air parameters with temperature T [K] xli

1 | Introduction

This research investigates heat transfer in high current density electrical machines, particularly in the context of electric and hybrid vehicles. While it is known that the current density of electrical machines is thermally limited, the inter-relationship between current and temperature has not been thoroughly investigated. This is therefore the topic of this thesis, which seeks to understand the mechanics and causes of high temperature in electrical machine components. This research develops thermal models that aid in the investigation of the thermal behaviour of electrical machines. Following experimental validation, the models are used to identify the limiting thermal factors and identify novel heat transfer solutions that stretch the thermal envelope of electrical machines. These solutions address the convective heat transfer and the conductive path within the windings to improve the current density and/or the lifetime of electrical machines.

1.1 Motivation for this research

The ever-increasing pressure on cities and the global environment are pushing electrical machines into new domains of electrical and hybrid transportation. Electrical machines generate approximately 80% of electrical energy and consume over 60% of all electricity generated. The introduction of electrical machines to the transport sector increases their impact on the world energy consumption. Despite that the importance of electrical machines is often overlooked by the focus on energy storage (Lamperth, Beaudet and Jaensch, 2007), slight improvements in the current density of electrical machines have wide global implications. This is therefore the motivation for this research.

Electrical and hybrid powertrains require electrical machines with high current density, high efficiency and have a long life. While a significant amount of papers on

the electromagnetic design of the machine are published yearly, the current density of traction machines seem to have reached a saturation point of approximately 13-16 A/mm^2. It is the author's belief that advances in machine cooling technology has an important role in furthering improvements in the machine's current density.

Following an introductory overview of the thermal aspects in electrical machines, this chapter describes the physics behind the main modes of heat transfer. The focus is then turned onto the main characteristics of high current density electrical machines, setting the geometrical boundary for this investigation. Finally, this chapter describes the scope of this dissertation, its organization and scientific contribution.

1.2 Thermal Aspects of Electrical Machines

Electrical machines are not 100% efficient. During operation, losses generate heat in different components of the machine. If not extracted, this raises the temperature of the machine components and presents a number of implications that affect the performance and the lifetime of electrical machines.

In the stator, the copper I^2R losses increase the temperature of the windings. If not cooled, this has two main effects:

1. It increases the copper electrical resistivity. This quantifies how strongly a material opposes a flow of electric current and is proportional to the electrical resistance. An increase in copper resistance with temperature decreases the machine efficiency. This in turn increases the losses and the component temperature causing thermal runaway.

The relationship of the resistivity of copper with temperature and residual resistance ratio (RRR) is shown in Figure 1.1 The RRR is a measure of the material impurities and crystallographic defects. In the operating temperature range of electrical machines the electrical resistivity is approximated by a linear law:

$$\rho_{rT} = \rho_{ro}[1 + \alpha(T_T - T_o)] \qquad \text{eqn. 1.1}$$

where ρ_r is the resistivity, T is the temperature and α the temperature coefficient. The subscripts $_T$ and $_o$ refer to the operating condition and reference condition respectively. The electrical resistance R is directly proportional to the resistivity and defined as:

$$R = \frac{\rho_{rT} l}{A_{csa}} \qquad \text{eqn. 1.2}$$

where l is the winding length and A_{csa} its cross sectional area of copper.

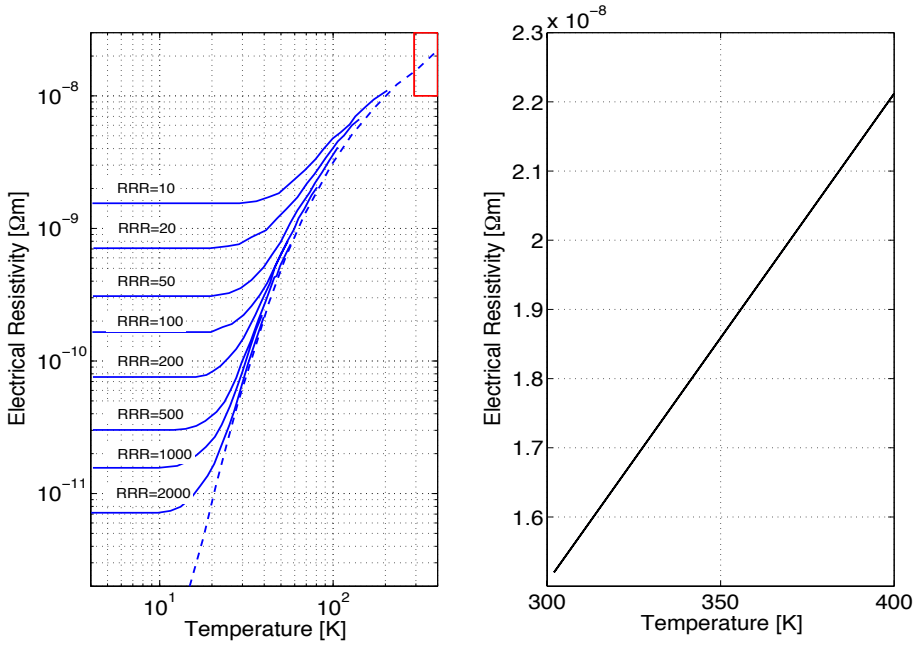


Figure 1.1. Relationship of copper electrical resistivity with temperature and residual-resistance ratio (RRR). Data from Cryogenic properties of Copper, (2015)

It can be seen how increasing the winding temperature between 30 ^{o}C and 130 ^{o}C increases the copper resistivity by approximately 45%.

2. It reduces the lifetime of the windings in electrical machines. The copper windings are coated by an electrical insulation, typically polyimide or polyamide-imide. Montsinger, (1930) introduced the rule of thumb that the insulation life halves for every 10 K increase in temperature. This rule is still observed by machine designers (Brancato, 1992; Oraee, 2000). Dakin, (1948) postulated that the insulation life L could be modelled by the Arrhenius chemical equation as:

$$L = a'.e^{\left(\frac{-E_a}{k_b T}\right)} \qquad \text{eqn. 1.3}$$

where a' is the Arrhenius equation constant, k_b is the Boltzmann constant, E_a is the activation energy and T is the temperature.

In a study performed on large induction machines, (Bruetsch, et al. 2008), report that 22% of failures were due to thermal damages or ageing in polymer based insulation. A further 17% of machine failures were due to thermal induced damage on other components of the machine.

In the rotor, permanent magnets can be employed to increase the power density of electrical machines. These have a curie point of between 80 ^{o}C - 190 ^{o}C (Polikarpova, 2014), beyond which their permanent magnetism becomes an induced magnetism. Neodium-iron-boron (NdFeB) magnets are generally the preferred type due to their mechanical properties, energy density and lower cost (compared to other rare earth metals). Calin and Helerea, (2011) experimentally measure the strong temperature influence on $Nd_2Fe_{14}B$ permanent magnet performance and show how their magnetic properties deteriorate with increasing operating temperature. An example of the experimental results are replicated in Figure 1.2. Similar observations were made by Gieras et al., (2008).

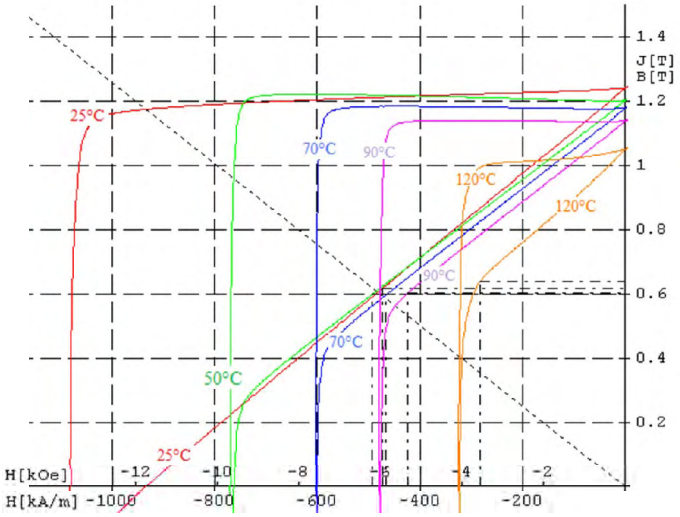


Figure 1.2. NdFeB polarization and induction demagnetization curves with increasing temperatures, reproduced from Calin and Helerea, (2011)

Materials used for the construction of the machine such as polymer adhesives are also limited to approximately 120 ^{o}C. While high torque machines are associated with higher current density machines, high speed machines are associated with high voltage and current frequencies. This increases the iron losses in the stator and rotor steel laminations and the permanent magnets. Interestingly, Schutzhold and Hofmann, (2013) show that with rising temperature, the iron losses in electrical machines

decrease. With increase in temperature, the atomic energy increases and therefore less polarization energy is needed to produce hysteresis losses. As a result the remanence and coercivity decreases in magnetically soft iron cores. Likewise the eddy current losses resulting from induced voltages depend on the electric resistance of iron and decrease with increasing temperature. Therefore an optimal temperature for the motor is likely to exist. The overall behaviour of a permanent magnet electrical machines was described by Ruoho, Kolehmainen et al., (2010) as "*a coupled thermo-electro-magnetic behaviour*". When loaded with a constant torque requirement, the permanent magnets of a machine that is not well cooled suffers from partial demagnetization. To maintain the torque requirement, more current is drawn which causes more Joule losses in the stator. This further decreases the efficiency, generating higher losses and increases the machine temperature further. In turn this makes the permanent magnets more prone to demagnetzation causing a vicious circle.

As the current density increases, the thermal capacity of the electrical machine decreases, the machine temperature increases at a faster rate reaching the temperature limits earlier. An improvement in heat transfer is therefore important to prevent this from happening. The following section provides a brief overview into the physical principles of heat transfer.

1.3 The Physics of Heat Transfer

Heat is a form of energy, transferred from hot to cold by three main mechanisms: Conduction, Convection and Radiation.

1.3.1. Conduction

Conduction is the mechanism of transferring heat from one part of a material at a high temperature to another part at lower temperature. When high-energy vibrating atoms in the high temperature region collide with their slower neighbours, they exchange energy and momentum. Therefore there is a continuous transport of energy from the high temperature region to the low temperature region, without having an appreciable displacement of molecules (Eastop and McConkey, 1993). In solids, the steady state

rate of heat flow through a single homogeneous material is dictated by Fourier's empirical law of conduction:

$$\mathrm{Q} = -k.A.\frac{dT}{dx} \qquad \text{eqn. 1.4}$$

where k is the thermal conductivity of the material, A is the cross sectional area perpendicular to the direction of the flow of heat, $-{}^{\mathrm{dT}}/_{\mathrm{d}x}$ is the negative temperature gradient along the thickness of the body. For the vast majority of solids, the thermal conductivity is constant across a wide range of temperatures. Electrical machines are complex devices made of more than one material. Therefore heat is sometimes transferred from one solid interface to another. At the interface where the two solids are in contact, a thermal contact resistance exists making the conduction process more complex to analyse. The thermal contact resistance is a function of the surface roughness and contact pressure amongst others and is sometimes modelled by introducing an effective air gap between the two solid interfaces (Staton, 2005). The thickness of the air gap is often obtained following an initial experiment to calibrate the model. This topic will be dealt with in more detail in Chapter 7.

1.3.2. Convection

Convection is the mechanism of transferring heat from a surface to a fluid in motion. Kays (2005) describes the mechanism as "energy and mass are transported both by potential gradients and by the movement of the fluid itself". When the flow is caused by an external means such as a pump or a fan, the heat transfer mechanisms is termed 'forced convection'. Otherwise, if the movement of the fluid is "induced by gravitational forces acting on density gradients occurring due to temperature gradients produced by heat transfer itself", the mechanism is termed 'natural convection'. The heat flux $\dot{q}$ transported from the surface of a solid is determined by a heat transfer coefficient (HTC), h and the temperature gradient between the solid T_s and fluid T_f and is defined as:

$$\dot{q} = h(T_s - T_f) \qquad \text{eqn. 1.5}$$

The HTC is often defined within a non-dimensional parameter termed the Nusselt number. The Nusselt number Nu is defined as:

$$Nu = \frac{hD}{k} \qquad \text{eqn. 1.6}$$

where h is the heat transfer coefficient, D is a characteristic length or diameter and k is the conductivity of the fluid.

The Nusselt number provides a ratio of heat convected away by the fluid to the heat conducted at the solid-fluid boundary where the velocity of the fluid is zero. The Nusselt number is often described as a function of the fluid flow characteristics and the fluid thermal properties such that:

$$Nu = f(Re, Pr) \qquad \text{eqn. 1.7}$$

where Re is the Reynolds number and Pr the Prandtl number. The Reynolds number provides a ratio of the inertial forces to the viscous forces acting on the fluid. This is defined by:

$$Re = \frac{v_f D}{\upsilon} \qquad \text{eqn. 1.8}$$

where v_f is the fluid velocity, D is a characteristic length such as the diameter for a flow in a tube or the length of the plate for a flow over a flat plate. υ is the kinematic viscosity of the fluid. The Prandtl number provides a ratio of the momentum diffusivity to the thermal diffusivity and is defined as:

$$Pr = \frac{\mu c}{k} \qquad \text{eqn. 1.9}$$

where μ is the dynamic viscosity, c is the specific heat capacity and k the thermal conductivity of the fluid. It can be seen how the heat transfer coefficient is influenced by the fluid properties and flow characteristics and heat transfer mechanism itself. The heat transfer can vary by several orders of magnitude as shown in Figure 1.3.

While there are many cases in which eqn. 1.5 is almost directly proportional to the temperature gradient, there are numerous cases in which the heat transfer coefficient h is also a function of temperature. In such cases the conductive and convective heat transfer mechanisms across the solid – fluid boundary are closely coupled together and are termed ‘conjugate heat transfer’. Throughout the course of this thesis it is shown how this is the case in some cooling mechanisms within electrical machines.

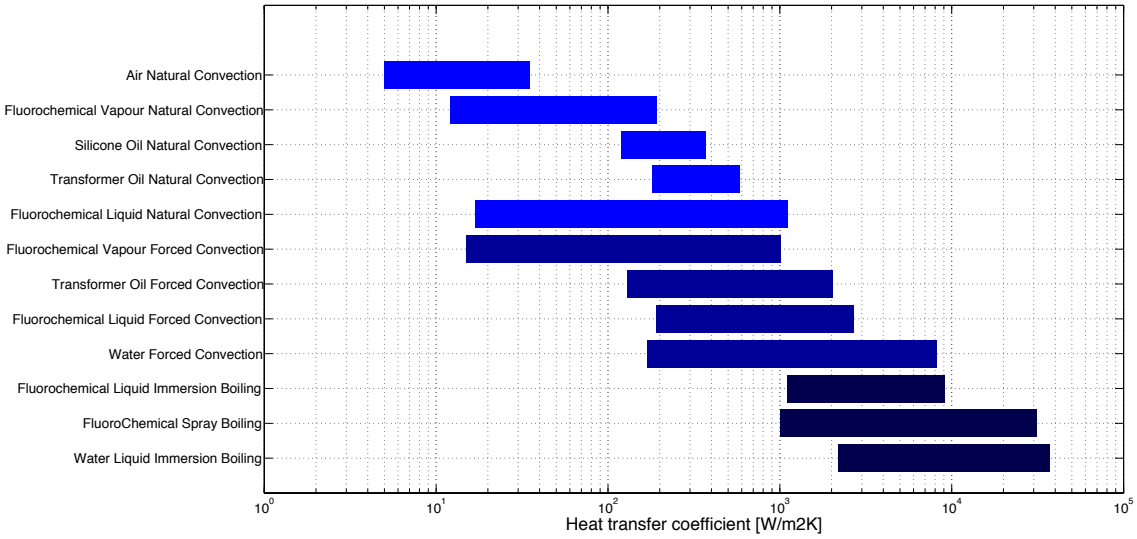


Figure 1.3. A comparison of the heat transfer coefficient in different flow conditions and media. Data from Engineersedge.com: Convective heat transfer coefficients tables, retrieved on 21/09/2015.

1.3.3. Radiation

Radiation heat transfer is the process of transmitting heat in the form of waves or particles through space or a medium. The heat exchanged between two neighbouring bodies 1 and 2 in the line of sight of each other is expressed as:

$$Q = F_R A k_b \left(T_1{}^4 - T_2{}^4\right) \qquad \text{eqn. 1.10}$$

where F_R is a function of the view factor and emissivity of the body, A is the surface area of a body and k_b is the Boltzmann constant. Boglietti, (2009) states that radiation is almost always neglected in electrical machines. The difference in temperature of internal components is small and hence radiation may not be an effective mode of heat transfer. Thermal radiation may however be significant when considering the heat transfer from the casing to ambient. The relative importance of each heat transfer mode should hence be based on the design of the machine.

1.4 High Current Density Electrical Machines

Following an overview of the thermal aspects of electrical machines and heat transfer mechanisms the attention of this chapter is now turned to the main characteristics of high current density machines. This section poses the question: "What is considered as a high current density electrical machine?" Yeadon and Frustaglio, (2010) discuss their experience in developing induction machines and show how current density is not only linked with machine design, but also with the cooling mechanism employed

in the machine. The authors show how liquid cooled induction machines achieve a current density between 16-18 A/mm^2, as shown in Figure 1.4. However, they caution against exceeding 16 A/mm^2 due to the rapid thermal degradation on the windings. Nevertheless, this is only likely to happen when conventional cooling techniques are adopted to electrical machines. The authors explain how some manufacturers determine the winding conductor size experimentally until the insulation on the winding smokes and then opt for one conductor gauge larger. This highlights the requirement for a wider dissemination of thermal modelling within the industry in an effort to improve the performance of electrical machines.

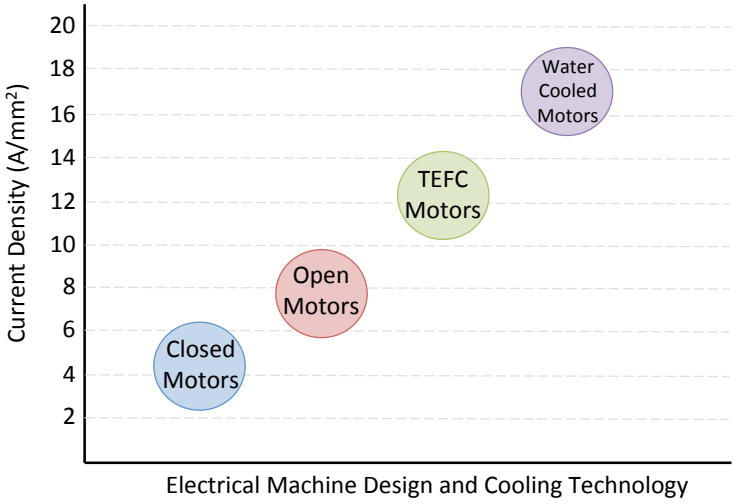


Figure 1.4. Comparison of the current density between in electrical machines with different cooling technology. Data from Yeadon and Frustaglio, (2010)

The key drivers in developing electrical machines are often not only dictated by power density, but also by the market requirements. In the context of electric and hybrid vehicles the market is very sensitive to cost and machine reliability, and therefore the power density often becomes secondary to these issues. In an attempt to establish the main trends in high current density electrical machine for electric and hybrid vehicles, the following section presents a brief overview of the machine type, topology, winding configuration and cooling method.

1.4.1. The Machine Type

Xu et al., (2009) reviewed the characteristics of four traditional machine types – permanent magnet, induction, DC and switch reluctance machines, for electric vehicles (EVs). The author adopted a subjective point grading system for six major

characteristics. While high current density electrical machines come in various types, the authors conclude that permanent magnet electrical machines and induction machines are the preferred drives for electric propulsion.

Dajaku and Gerling, (2012) showed that in applications where high torque and power density machines are required, the use of permanent magnets (PM) with high-energy magnet material such as NdFeB or SmCo are preferable. PM machines offer higher torque densities and efficiencies because the field excitation losses are eliminated. These are however made of rare earth materials, which come at a cost disadvantage and price volatility. Zhang et al., (2012) reports that between 2010 and mid 2011, the price of Nd doped magnets increased by a factor of 5. For the same period the price of Dy doped magnets increased by a factor of 9.

Induction machines have also been applied to the EV market due to their robustness, low production cost and mature technology. However, they have a limited constant power range and their efficiency is lower than that of a similarly sized permanent magnet (PM) machine. Likewise, whilst DC machines also offer technology maturity and control simplicity, their need for commutators and brushes make them unsuitable for maintenance free and high-speed operation. Other non-permanent magnet machines such as switched reluctance (SR) machines are also of interest to automotive manufacturers. Despite that the power density of SR machines is lower than that of permanent magnet and induction machines (Gao and McCulloch, 2012), they are highly fault tolerant and cost effective.

1.4.2. The Machine Topology

Like with like comparison of different electrical machine topology is difficult, and therefore several researchers have attempted to impose constraints to force equality in comparison (Patterson, et al., 2007; Huang et al., 2002). Huang et al., (2002) presents general purpose sizing equations as a function of the machine outer diameter and axial length to compare radial and axial flux machines. The authors conclude that axial flux machines consistently produced higher torque densities than radial flux machines. TORUS type axial flux machines with an internal stator and two end rotors were found to offer the highest torque densities. Zhang et al., (1996) derived the specific

torque between permanent magnet radial and axial machines using well-known sizing equations. When compared to a radial flux machine, a single sided axial flux machine had higher torque density by a factor of 1.8, a single stator - twin rotor axial flux machine by a factor of 2.1 and a two stator – single rotor Torus NN by a factor of 2.4. Sitapiti and Krishnan, (2001) compared radial flux machines to 4 different axial flux machines at different power levels and conclude that the axial flux machines always have higher torque densities than the radial equivalent. However, these will need more active material increasing the cost. Parviainen et al., (2005) concludes that the cost is a function of the number of poles. At 8 poles or more the axial flux geometry has a lower cost than the radial flux counterpart. Lamperth et al., (2008) attribute the advantages of axial flux machines purely to geometry. In a simplified analysis the authors demonstrate how the torque for a radial machine is proportional to the square of the machine radius while for an axial machine this is proportional to the cube of the machine radius.

An extensive review of permanent magnet machine topologies is given in Aydin, (2004) and Woolmer, (2009). The authors describe the structure, advantages and features of various axial flux permanent magnet topologies. Woolmer, (2009) discusses that despite having high torque densities, Axial Flux Internal Rotor (AFIR) machines suffer from higher iron and copper losses when compared to axial flux internal stator (TORUS) machines. The author concludes that the NS TORUS-S topology achieves the highest torque density and efficiency and is therefore the most adequate topology for high current density machines. The author developed a derivative of this topology with a segmented stator and concentrated windings, called a Yokeless And Segmented Armature (YASA) machine. The machine was applied as a direct drive to high performance sports cars as shown in Figure 1.5. More details on this machine are provided in Section 1.5.

Despite their reported advantages, axial flux machines have for long remained an academic exercise and have not managed to gain the necessary momentum to infiltrate the markets. Their uptake was largely hindered by mechanical challenges in maintaining a small air gap in a large disk shaped machine subjected to large magnetic forces, (Patterson et al., 2007; Lamperth et al., 2008). Moreover, the recent developments of permanent magnet radial flux topologies having a low axial length,

as shown in Figure 1.6, still continue to provide a major obstacle. The large radius of this machine offers torque densities comparable to axial flux topology. Moreover, the body of existing manufacturing knowhow on radial flux machines, and their ease to control the air gap during manufacturing has enabled them a fast uptake in electric and hybrid vehicles.

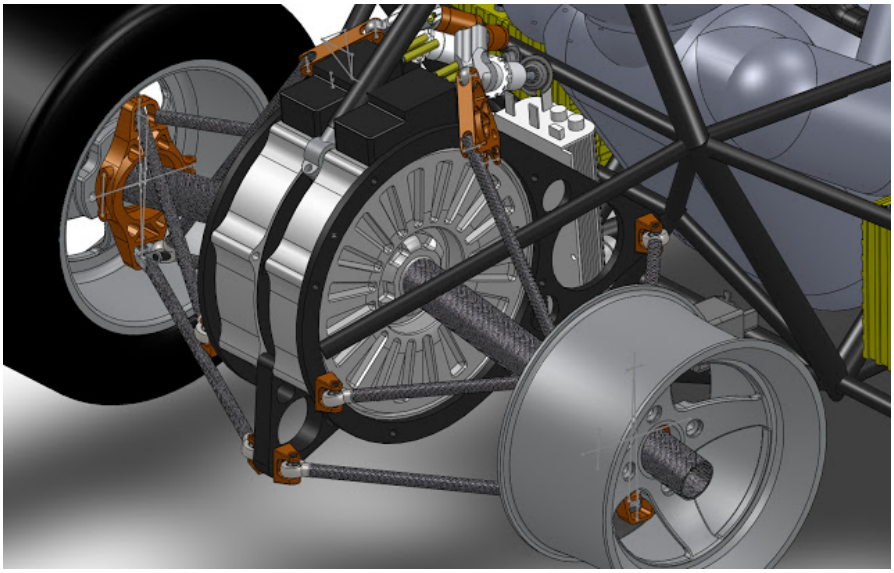


Figure 1.5. Example of two direct drive YASA-750 axial flux machines installed in a Formula student all-electric vehicle from NGRN, retrieved on Mar. 2015

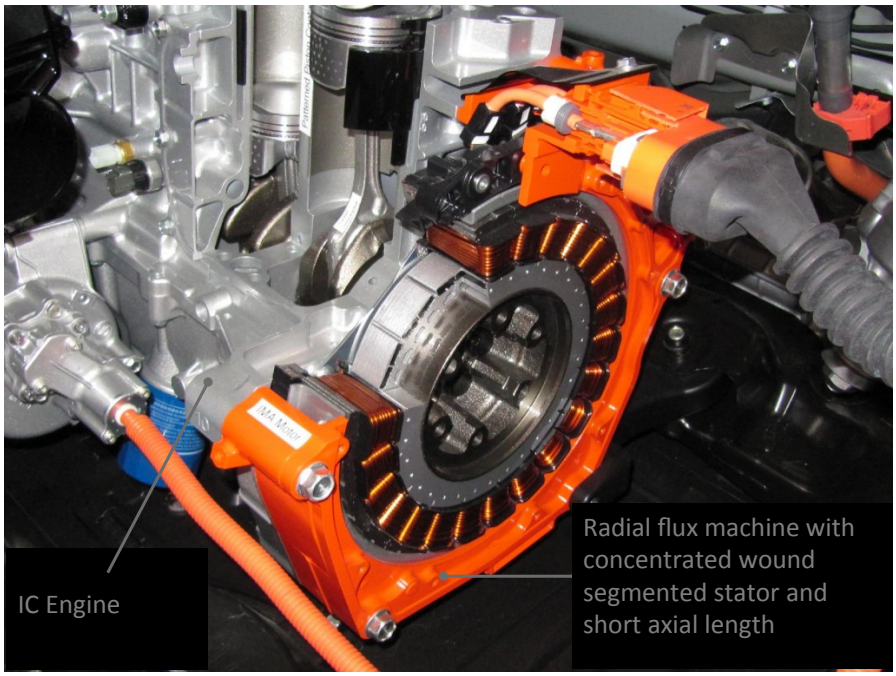


Figure 1.6. An example of a radial flux permanent magnet machine with short axial length and concentrated wound stator teeth for a for a Honda Insight hybrid. (Figure from ABG First Drive: 2010 Honda Insight, retrieved on July 2014)

1.4.3. The Winding Configuration

Electrical machines with high current and torque densities require the active material to be as small as possible. Potgieter, (2014) compared the active winding and magnet material for a double rotor toroidal winding PM machine with distributed and concentrated windings across a wide range of power levels. The author shows how concentrated windings offer significantly reduced active materials over distributed windings for machine sizes under 300 kW. As the machine geometry gets smaller, space becomes at a premium and the manufacturing of small stator windings becomes more challenging. Therefore with concentrated windings, the volume of copper used for end windings is reduced significantly. This is particularly useful if the axial length of the machine is small, (Cros and Viarouge, 2002). When compared to more traditional structures with one slot per pole and per phase, concentrated windings achieve reduced Joule losses therefore improving the efficiency of the machine. Concentrated windings also offer high slot fill factor, low cogging torque and greater fault tolerance. Their simple manufacturing process offers lower manufacturing costs (Dajaku and Gerling, 2012), often making concentrated windings the preferred type of windings in high current densities electrical machines.

1.4.4. The Cooling Configuration

The quest to improve the current density in electrical machines requires both the electromagnetic and thermal aspects of the machine to be optimized. While there are numerous papers demonstrating improvement in electromagnetics, studies demonstrating improvements in the thermo-fluids aspects of electrical machines are fewer (Boglietti, 2008). While cooling of electrical machines can be broadly categorised into air-cooling or liquid cooling as shown in Figure 1.7, higher current and torques densities have long been associated with liquid cooled machines

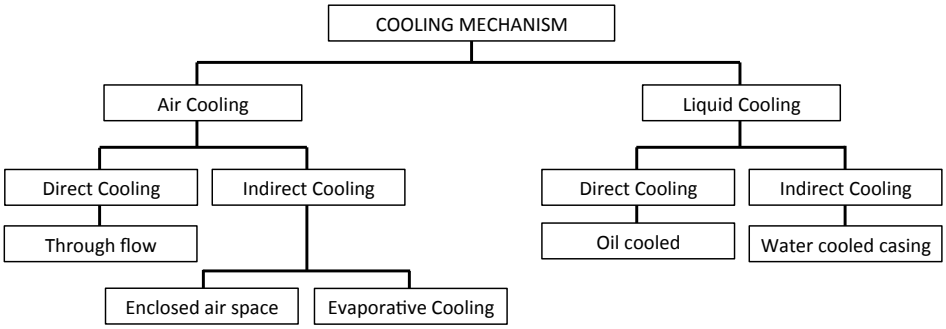


Figure 1.7. Categories of cooling mechanisms in electrical machines

This can be also seen in Figure 1.8, which presents the results of a survey on the torque and power densities of axial flux machines and their cooling mechanism, as published in the literature. This section therefore investigates the effect of convective and conductive heat transfer on the current density of the machine.

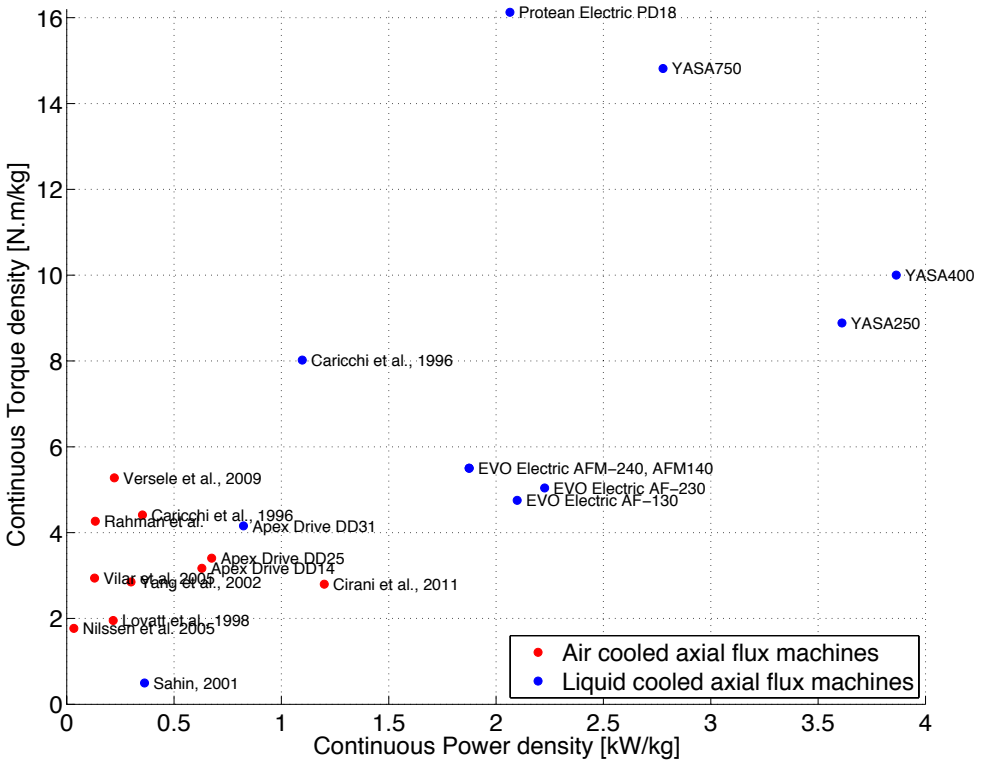


Figure 1.8. Comparison of the Continuous Power density and Torque density for axial flux machines with air and liquid cooling configurations

Assuming that the losses of electrical machines are concentrated in the stator windings, the heat transfer from the stator Q can be expressed as:

$$Q = \frac{(T_s - T_f)}{R_{th}} \qquad \text{eqn. 1.11}$$

where T_s is the stator temperature and is the T_f fluid temperature, and R_{th} is the thermal resistance. This is made from all the thermal conductive and convective terms. This can be simplified by assuming that stator as a block. Therefore the thermal resistance can be modelled as:

$$R_{th} = \sum \frac{1}{hA} + \frac{x}{k_{eq}A} \qquad \text{eqn. 1.12}$$

where the summation $\sum \frac{1}{hA}$ represent the heat transfer coefficients acting on the stator, through various cooling mechanisms. x is the stator thickness and k_{eq} is the equivalent stator conductivity and A is the heat transfer area. Since the stator is generally made

from a composite of copper windings an equivalent conductivity can be used. Simpson, (2013) found that this is generally of the order of 1-2 W/mK. The topic of establishing an equivalent thermal conductivity for stator windings is discussed further in Section 2.5 of The Literature Review. The following analysis investigates the effects of the thermal resistance on the current density.

The heat generation in the copper windings is defined as:

$$Q = I^2 R \qquad \text{eqn. 1.13}$$

where I is the current through the windings and R the electrical resistance. Replacing the electrical resistance as a function of resistivity leads to:

$$Q = I^2 \left(\frac{\rho_T l}{A_c}\right) \qquad \text{eqn. 1.14}$$

where ρ_T is the copper resistivity at a given temperature, l is the copper length and A_c is the copper cross sectional area. As the current density of the windings can be defined in terms of the current through the windings, $J=I/A_c$, by making I subject the heat generated is defined by:

$$Q = J^2 \rho_T l A_c \qquad \text{eqn. 1.15}$$

Or in terms of the copper volume V_c:

$$Q = J^2 \rho_T V_c \qquad \text{eqn. 1.16}$$

Assuming that the heat generated in the copper windings is equal to the heat transferred from the machine eqn. 1.11 can be equated to eqn. 1.16 such that:

$$J = \left[\left(\frac{(T_s - T_f)}{\sum \frac{1}{hA} + \frac{x}{k_{eq}A}}\right) \cdot \left(\frac{1}{\rho_T V_c}\right)\right]^{0.5} \qquad \text{eqn. 1.17}$$

While the current density is influenced by the convective and conductive terms, these terms are also dependent on the temperature. The temperature is in turn dependent on the rate of heat exchanged and heat stored. Figure 1.9 describes the interdependencies of each component.

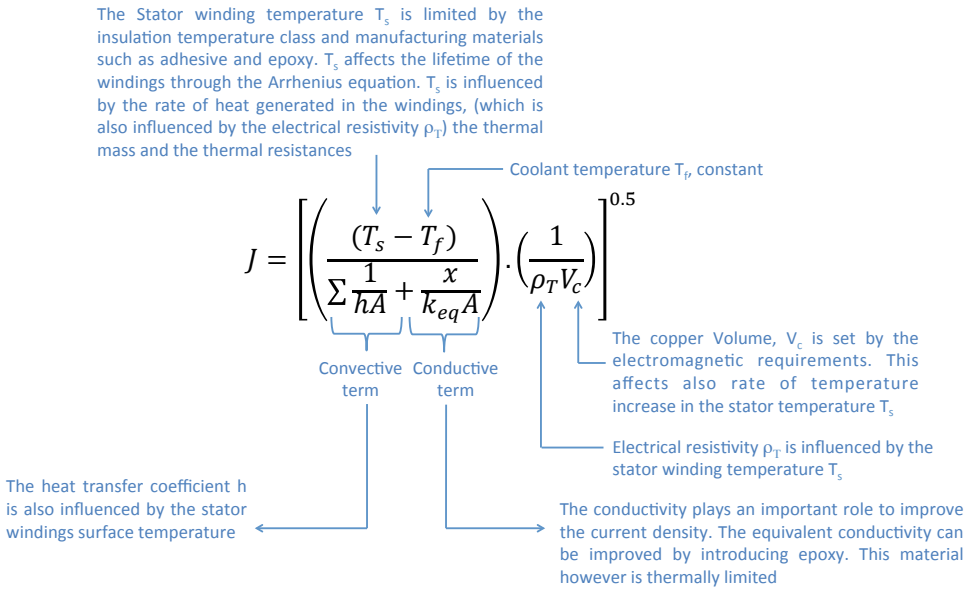


Figure 1.9. Demonstration of the interdependencies of the terms in eqn. 1.16

In a similar analysis Howey, (2010) assumes that the heat transfer area is equivalent to the area of the copper windings for conduction, leading to an expression of:

$$J = \left[\frac{\Delta T_{max}}{\rho_T L_A \left(\frac{x_A}{2k_A} + \frac{x_B}{k_B} + \frac{1}{h}\right)}\right]^{0.5} \qquad \text{eqn. 1.18}$$

where x_A is the axial thickness of the copper, x_B is the axial thickness of the epoxy resin, k_A and k_B are the thermal conductivity of the copper and resin respectively. Howey, (2010) furthers the analysis by ignoring the conduction terms to derive an expression of current density with heat transfer coefficient. However, throughout the course of this research the conductive term was identified as an important variable and therefore the author disagrees with this simplification.

To test the sensitivity of the current density to the convective and conductive thermal resistance a worked example is used by which the machine radius is fixed at 300 mm and the half stator thickness is set at 15 mm. Figure 1.10 shows the current density for a winding stator temperature to 120 ^{o}C. The temperature was chosen as this is regarded as a low-end winding with polyethylene insulation as defined by the IEC thermal classification. The process was repeated for a winding temperature of 250 ^{o}C as a high-end winding with polyamide-imide insulation. The results are shown in Figure 1.11. From this investigation it can be seen that the current density improves dramatically with an increase in the heat transfer coefficient *h*.

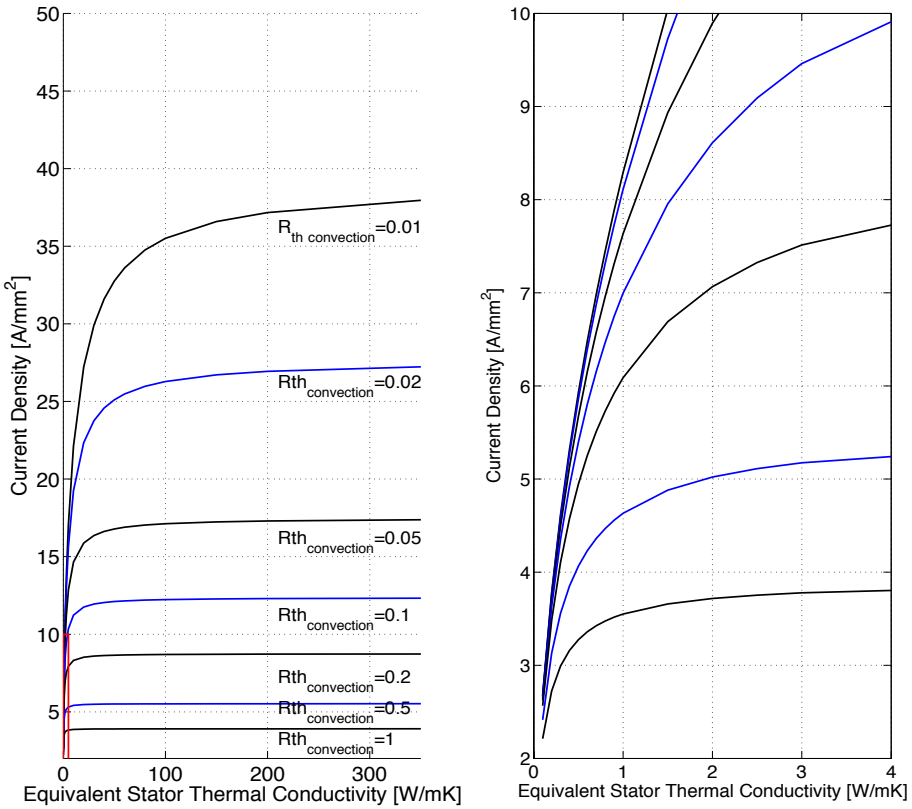


Figure 1.10. Current density for a maximum winding temperature of 120 °C (Right: Enlarged window)

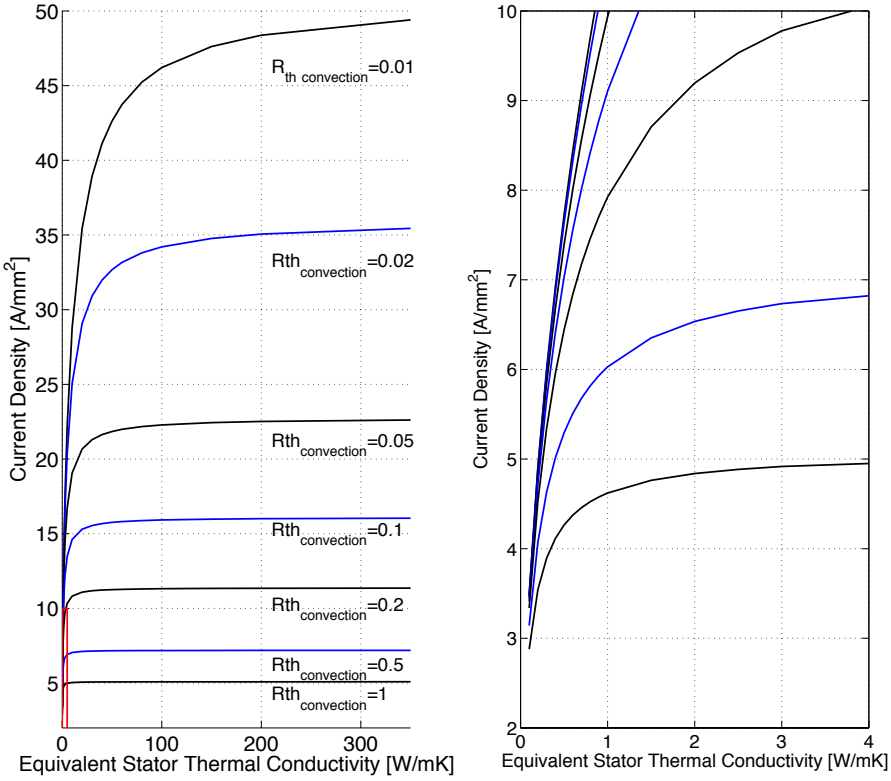


Figure 1.11. Current density for a maximum winding temperature of 250 °C (Right: Enlarged window)

In Figure 1.3, the heat transfer coefficient in forced liquid cooling was shown to be higher than forced air-cooling, thus explaining why liquid cooled machines are likely to achieve higher current densities. However, as current equivalent conductivity of anisotropic windings is between 1-2 W/mK, small improvements in the conductive path may be very effective to increase the current density. The impact increases as the convective thermal resistance decreases. The temperature difference between the winding is also noted to make an important contribution to increasing the current density. Hence the development of materials such as winding insulation and adhesives that can withstand high temperature plays an important role. However, even with winding insulation in the low end of the spectrum, current densities that are much higher than those achieved to date (15-18 A/mm^2) can be reached.

So far this chapter has discussed how while high current density electrical machines generally have a few features in common such as concentrated windings, they vary in geometry extensively. It was also shown that direct liquid cooling has the potential to achieve high current density machines. One of the machine architectures to make use of concentrated windings and direct liquid cooling is the Yokeless and Segmented Armature (YASA) machine. Its performance characteristics were compared to other machines in Figure 1.8. This high current density architecture has attracted increasing attention in recent years. Several variants can now be found in the literature (Vun, McCulloch and Leong, 2011; Vun and McCulloch, 2015; Du-Bar, 2011; Vansompel et al., 2012; Fei, Luk and Jinupun, 2008; Zhang and Doppelbauer, 2014). This thesis narrows down the machine architecture to this machine and uses it as a test case study. The following section gives a brief overview of the machine.

1.5 The YASA Machine: A test case study

The YASA machine shown in Figure 1.12 is an axial flux permanent magnet type machine. Its topology is derived from the NS TORUS-S but has its stator yoke removed leaving a segmented stator with an enlarged pitch of the teeth. Each segmented stator pole piece of the YASA machine is made from concentrated windings of square cross section wire. This ensures a high fill factor and short end windings, therefore maximising the active copper used.

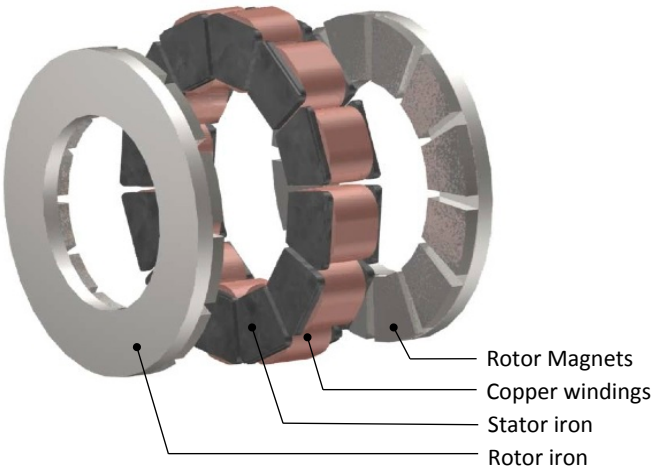


Figure 1.12. Schematic of the YASA topology, reproduced from Woolmer and McCulloch, (2007)

This design reduces the iron in the stator by around 50%, increasing the torque density by around 20% when compared to other axial flux machines. Moreover the peak efficiency can be maintained at over 95% (Woolmer and McCulloch, 2007). The machine has an internal segmented stator with a rotor on each side that are mechanically coupled together. The stator is enclosed in a glass fibre casing, allowing liquid coolant to be injected into the stator in direct contact with the windings. The liquid coolant has dielectric properties to avoid dielectric breakdown of the insulation. The coolant is also desired to have low viscosity enabling higher flow rates for a fixed pump. Hence a synthetic Opticool Fluid (DSI, 2015) is used as the coolant for this machine and throughout parts of this research. The specifications of the direct liquid cooled motor are listed in Table 1.1. The experimentally derived efficiency chart is shown in Figure 1.13 and the geometrical dimensions of the machine are shown in Figure 1.14.

Table 1.1 Specifications of the YASA Liquid Cooled Machine

Machine name	YASA750
Peak power	100 kW
Peak torque	750 N·m
Continuous power	55 kW
Continuous torque	400 N·m
Peak efficiency	94%

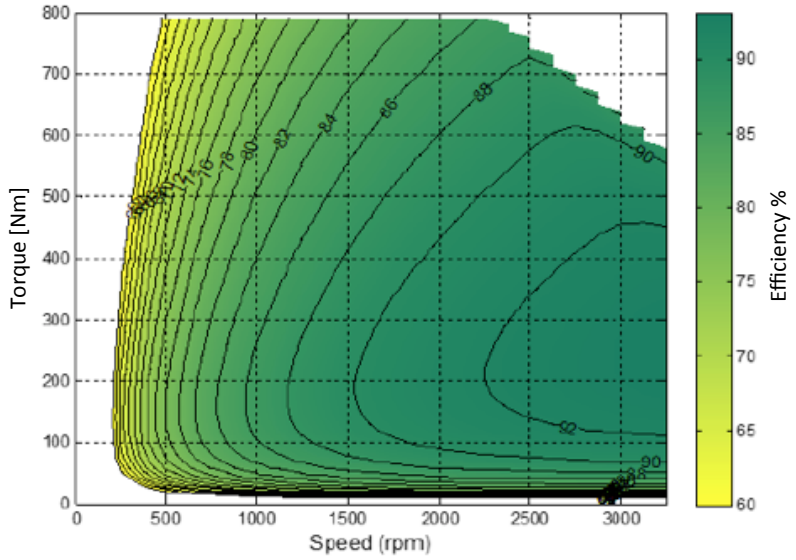


Figure 1.13. Efficiency chart of the YASA 750 Machine, reproduced from YASA, (2010)

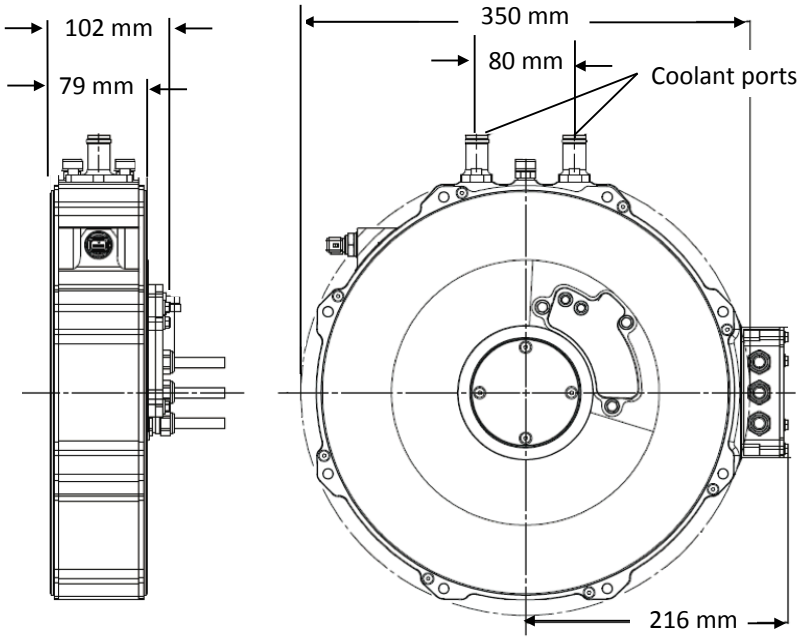


Figure 1.14. Geometrical dimensions of the YASA 750 Machine, reproduced from YASA, (2010)

1.6 Scope of this research and Outline of this thesis

After having discussed the thermal aspects of electrical machines and set the geometrical boundary condition to which heat transfer principles will be applied, this section sets the scope and the outline of this research.

The research aims to increase the current density of an existing machine topology by addresses the key parameters limiting convective and conductive heat transfer. On the topic of convective heat transfer, this thesis poses the following research questions:

- What is the thermal limit of air-cooled electrical machines and what role will they play in electric or hybrid vehicles?
- Can the thermal limits of air-cooled electrical machines be improved by introducing novel cooling mechanisms such as evaporative cooling? What are the main challenges that need to be addressed to make this cooling mechanism feasible?
- What role does direct liquid cooling play within the context of a high current density electrical machine for application in hybrid and electrical transportation? What challenges are still linked with direct oil cooling and how can they be addressed?
- How can the thermal behaviour of direct liquid cooled machines be modelled? How can we establish missing parameters such as the heat transfer coefficient to model direct oil cooled machines?

On the topic of conductive heat transfer, this dissertation seeks to address the following research questions:

- How do we model the temperature profile of concentrated windings with a high degree of accuracy? What is the thermal path in concentrated windings? How does this affect the current limit? How do processes like impregnation play a role in improving the current density?
- How do we manufacture windings so that the thermal path is improved thereby improving their current density?
- What is the role of thermal contact resistance and its relevance to the design, manufacturing and operation of electrical machines?

Following a literature review in **Chapter 2,** which investigates current thermal modelling and experimental research applied to electrical machines, the above research questions are addressed in separate chapters. While Chapters 3-6 investigates the convective heat transfer limitations in various cooling mechanisms, Chapters 7-9 focus on the conductive heat transfer in electrical machines.

In **Chapter 3: Air Cooled Electrical Machines,** the application of air-cooled electrical machines for traction machines is investigated. The chapter makes use of existing correlations to establish the continuous rate of heat transfer from the machines. The chapter demonstrates that air cooled machines are thermally limited by the convective heat transfer in the rotor-stator air gap and the thermal path from the machine casing. This causes traction power to be distributed amongst many wheels. The machine topology is found to play an important role with internal stator topologies suffering from low convective heat transfer in the rotor-stator gap. This problem is addressed in **Chapter 4: Evaporative Cooled Electrical Machines**, which investigates a novel evaporative cooling mechanism to transport heat from the machine stator to the casing of an outer rotor electrical machines. This chapter experimentally investigates this technique highlighting and the challenges that need to be address to make this mechanism a feasible one.

Unlike air-cooling, thermal limitations associated with heat transfer from the machine casing do not exist in liquid cooled machines because the heat transfer is augmented by the extended surfaces of an external radiator. While indirect water-cooling provides an effective heat transfer on the active winding, it was shown to be ineffective on the stator end windings (Nategh, 2013). The hotspot formed on the end windings still limit the current density of the machine. To solve this problem, direct liquid cooling has therefore been employed. Despite its advantages, direct liquid cooling is affected by the flow distribution within the stator. This is the subject of **Chapter 5: Direct Liquid Cooled Electrical Machines,** which presents a fast and accurate thermo-fluid model to determine the flow and temperature distribution of the machine. The model is compared to computational fluid dynamics and validated with experiments.

Empirical heat transfer correlations have been used to establish the heat transfer coefficient in the direct liquid cooled model presented in Chapter 5. While many experimental works have been dedicated to the heat transfer coefficient of air-cooled electrical machines, to the author's knowledge no such research on direct liquid cooling exists. This is therefore the focus of **Chapter 6: The Heat Transfer Coefficient.** In this chapter, an experimental technique often applied to gas turbine

blade cooling research was adapted for the flow conditions presented by direct oil cooling.

Having identified the convective parameters within the surface of the pole piece geometries, in the following chapters the attention is turned to the conduction process. The focus is placed on the stator windings. While the literature review shows several efforts to model the windings using an equivalent conductivity, these techniques do not identify the hotspot value within the windings. In **Chapter 7: Conductive Heat Transfer in Concentrated Windings,** the temperature distribution across a single concentrated wound pole piece is investigated. The chapter develops a lumped parameter thermal model by which the current carrying conductors are simplified into winding layers from which heat is transferred radially. The model is validated with experiments. This chapter also investigates the effect of epoxy resin impregnation on the windings and identifies the thermal resistance between the winding layers as a major limitation in the thermal path. This leads to hot spots forming on the winding layer with the longest thermal path, limiting the current density of concentrated wound machines. The results from this chapter are discussed in light of thermal contact resistance (TCR) models, which provide insight into the behaviour of the windings.

The insight developed in the previous chapter inspires new windings constructions. These are proposed in **Chapter 8: Improving the Current Density in Concentrated Windings,** in which the thermal resistance across the winding layers is significantly reduced to lower the hot spot temperature. Provided that the electromagnetic flux is not saturated, the current density of the machine can be increased until the same temperature is achieved. Alternatively the machine can be run at a lower operating temperature increasing its lifetime. The discussion about thermal contact resistance is broadened to general machine design in **Chapter 9: The Relevance of Thermal Contact Resistance in Electrical Machines.** This chapter takes an experimental approach to establish empirical correlations for the TCR at the stator-housing interface. The aim is to bring some of the complexities governing thermal contact resistance to the attention of thermal designers and draws conclusions on the construction procedure of electrical machines.

Finally **Chapter 10: Conclusion and Further Work**, discusses the results of this thesis and presents topics that the author feels can be furthered within the domain of heat transfer in electrical machines.

1.7 Scientific Contribution

Having described the structure of this thesis, this section lists the main scientific contributions. Their order is related to their location within the chapters throughout this thesis. The contributions of this thesis are as follows:

- Establishing the thermal limitations of air-cooled axial flux machines and evaluating their application to road transportation. This research is demonstrated in Chapter 3.
- Developing a novel evaporative cooling system for axial flux electrical machines. The concept was tested in Chapter 4. A mechanism to wet the surface of the winding has been identified and the key challenges linked with this cooling mechanism studied.
- Identifying the link between flow and temperature distribution in a direct oil cooled electrical machine. Developing a fast and accurate thermal model of the flow and produce on the overall temperature map of the machine. Developing a method to improve the flow and temperature distribution. This research is demonstrated in Chapter 5.
- Developing an experimental correlation of the heat transfer coefficient in direct liquid cooled electrical machines. The experimental technique is an adaptation of the double-sided thin film heat flux gauges technique, making use of steady state measurements. This research is found in Chapter 6.
- Identifying the existence of a temperature gradient in concentrated windings and developing a thermal model to capture the location and value of the hot spot. This research is found in Chapter 7.
- Developing a new winding construction for concentrated pole pieces to achieving higher current densities in Chapter 8.
- Demonstrating the relevance of thermal contact resistance to electrical machines. This research produces experimental correlations of the variation in TCR with heat flux, contact pressure, surface and material properties. This research is found in Chapter 9.

1.8 List of Publications

This section lists peer reviewed conference and journal publications related to the work presented in this thesis. The order of the list is related to the order they appear in the chapters throughout this thesis:

1. Camilleri, R., Howey, D.A., McCulloch, M.D., *Thermal Limitations in Air-Cooled In-Wheel Motors for Urban Mobility Vehicles*, The IEEE International Conference on Electrical Systems for Aircraft, Railway and Ship Propulsion ESARS2012 - Special Session on Innovative Electric Propulsion Systems For Urban Mobility, 16-18th October, Bologna, Italy.
2. Camilleri, R., McCulloch, M.D., *Investigating Mechanisms for an Evaporative Cooled AFPM Machine*, The 13th UK Heat Transfer Conference, UKHTC2013, 2-3 September, Imperial College, London, UK.
3. Camilleri, R., McCulloch, M.D., *Investigation of an Integrated Evaporative Cooling Mechanism for an Outer-Rotor Permanent Magnet Machine,* Heat Transfer Engineering, 2015, Vol. 36, Iss. 14-15, pp. 1192-1202.
4. Camilleri, R., Howey, D.A., McCulloch, M.D., *Predicting the temperature and flow distribution in a direct oil cooled electrical machine with segmented stator*, IEEE Trans. Ind. Electron., 2016, Vol. 63. Iss. 1, pp. 82-91.
5. Camilleri, R., Howey, D.A., McCulloch, M.D., *Predicting the flow distribution in compact parallel flow heat exchangers*, Applied Thermal Engineering, Nov. 2015, Vol. 90, pp. 551-558.
6. Camilleri, R., Beard, P., Howey, D.A., McCulloch, M.D., *Measuring the Heat transfer Coefficient in a Direct Oil-Cooled Electrical Machine with Segmented Stator*, The 14th UK Heat Transfer Conference (UKHTC2015), 7-8 Sept., 2015, Edinburgh, Scotland.
7. Camilleri, R., Woolmer, T., Court, A., McCulloch, M.D., *Investigation into the temperature profile of a liquid cooled YASA AFPM Machine*, The 6th IET International Conference on Power Electronics, Machines and Drives PEMD2012, 27-29th March, Bristol, UK.

8. Camilleri, R., Howey, D.A., McCulloch, M.D., *Experimental investigation of the thermal contact resistance in shrink fit assemblies with relevance to electrical machines*, The 7th IET International Conference on Power Electronics, Machines and Drives PEMD2014, Manchester, UK, 8-10th April 2014.

Patent Applications:

1. Camilleri, R., McCulloch, M.D., Winding Construction for an Electric Machine, Patent Application No. 1505756.5, filed April 2nd, 2015.
2. Camilleri, R., McCulloch, M.D., Winding Construction for an Electric Machine, Patent Application No. 1505759.9, filed April 2nd, 2015.

The author was also involved in the following publications, which do not feature in this thesis:

1. Camilleri, R., Armstrong, P., Ewin, N., Richardson, R., Howey, D.A., McCulloch, M.D., *The Value of a Clutch Mechanism in Electric Vehicles*, The 27th Electric Vehicle Symposium, EVS27, Barcelona, Spain, 17-20th November, 2013.
2. Armstrong, P., Wong, R., Kang, R., Camilleri, R., Howey, D.A., McCulloch, M.D., *A Reconfigurable PV Array Scheme Integrated into an Electric Vehicle*, The 4th Hybrid and Electric Vehicles Conference HEVC2013, London, UK, 6-7th November 2013.

2| Literature Review

In the introductory chapter, the construction of high current density electrical machines and the thermal aspects of electrical machines were examined. The chapter identified the convective heat transfer coefficient and the conductive process as the limiting factors for higher current densities. The literature review focuses on various topics that are important for the accurate thermal modelling of electrical machines. These include the heat transfer coefficient in electrical machines, thermal modelling of the windings, and the thermal contact resistance. Within each aspect, this chapter explores the modelling techniques and the experimental procedures that have been applied so far and discusses their strong points and weaknesses.

2.1 The Thermal Behaviour of Electrical Machines

The concerns related to the temperature limits on the winding insulation and its effect on the continuous rated load of electrical machines has been documented since the early days of machine design (Steven, 1983, Karapetoff, 1906). At the time, "thermal management" relied on the large thermal mass of the machine and natural convection from the casing. The time required for the machine to reach critical temperatures was important and the temperature rise in electrical machines ΔT was often correlated to the machine power P as:

$$\Delta T = aP^b \qquad \text{eqn. 2.1}$$

where a and b are machine dependent and experimentally derived constants. The value of b is often between 1.4 and 2. Kennelly (1925) recognised the requirement to predict the thermal behaviour of electrical machines with time and produces a definition of the thermal time constant as follows:

> *"The thermal time constant of a machine, assumed as conforming strictly to an exponential law of temperature rise above a constant ambient temperature, after being transferred suddenly from one steady load to another, is taken as the time required to attain* $1 - e^{-1}$ *or 63.2 per cent of the final temperature change. This may be called the exponential thermal time constant. This is a fundamentally scientific quantity; but is very awkward to remember or to explain to a person not well versed in the mathematical theory of the subject"*

It is interesting to note that while the paper was published, it got mixed reviews. In the discussion section, Karapetoff – a reviewer, comes to the conclusion that the exponential theory is inadequate! Today this same technique forms the basis of analytical temperature prediction in electrical machines.

The thermal behaviour of electrical machines is still very relevant, and is also the topic of this thesis. To investigate the effects of increasing the power density on the thermal time constant, consider a simplified solid body exchanging heat $\dot{E}$ with its surroundings, and generating its own internal heat $\dot{E}_g$. From the first law of thermodynamics, the rate of energy stored in the body ${}^{dE_{st}}/_{dt}$ can be computed using:

$$\frac{dE_{st}}{dt} = \dot{E}_{in} - \dot{E}_{out} + \dot{E}_g \qquad \text{eqn. 2.2}$$

where Subscripts *in*, and *out* define the direction of the energy into or out of the body. Considering that the body has a uniform spatial temperature distribution, its temperature response with time can be predicted using:

$$T = T_\infty + (T_{t=0} - T_\infty)e^{\frac{-t}{\tau}} + \dot{E}_g R_{th}\left[1 - e^{\frac{-t}{\tau}}\right] \qquad \text{eqn. 2.3}$$

where T is the temperature and t is the time. Subscripts t=0 denotes the initial temperature and ∞ denotes ambient. τ is the thermal time constant defined as the product of the thermal capacitance C_{th} and the thermal resistance R_{th}.

$$\tau = C_{th}R_{th} \qquad \text{eqn. 2.4}$$

The thermal capacitance is a function of the material density ρ and volume Vc, and is defined as:

$$C_{th} = \rho V c \qquad \text{eqn. 2.5}$$

The thermal resistance is a function of the heat transfer mechanisms. These will be explored further in the next section. However, the thermal resistance is often also defined in terms of its electrical analogy such that:

$$R_{th} = \frac{1}{hA} = \frac{\Delta T}{Q} \qquad \text{eqn. 2.6}$$

where h is the heat transfer coefficient, A the surface area, Q is the heat transfer from the body and ΔT is the temperature difference from the body to ambient. Consider now an electrical machine with total heat generated Q_g, such that:

$$Q_g = P(1 - \eta) \qquad \text{eqn. 2.7}$$

where P is the total machine power and η is the machine efficiency. For the machine to reach a thermal steady state, the heat generated should equal the heat transferred:

$$Q = Q_g \qquad \text{eqn. 2.8}$$

For the power density of the machine to increase, either the power of the machine increases or the mass of the active materials of the machine is reduced. Assuming same machine efficiency and temperature ratings, increasing the power of the machine increases the heat generated. From eqn. 2.6, this results in a reduced thermal resistance, which in turn reduces the thermal time constant. Likewise decreasing the mass of the machine reduces the thermal capacitance of the machine, which also reduces the thermal time constant. Therefore as the power density of a machine increases, the rated temperature of the machine is reached quicker and therefore the safety factor of the machine is reduced. Kennelly (1925) comments that the time for a machine to reach a new steady state temperature following a transient operation "*may require many hours to complete*". With high current density electrical machines, this is no longer the case. Therefore the ability to accurately predict the temperature of electrical machines is important.

It is also interesting to note how Kennelly (1925) attributes the discrepancy between the model predicted temperature and the measured temperatures to the fact that the windings and the steel in the stator form independent thermal systems, each with their own heat generation and thermal time constants. A single thermal time constant for the machine leads to inaccuracies because they are not united by perfect thermal conduction. The authors note how the stator components are "*semi-detached, being in*

mutual communication through thermal resistances; so that each tends to modify the behaviour of the other". This statement is still relevant to the research presented in this research as is shown by the results presented in Chapter 7: Conductive Heat Transfer in Concentrated Windings.

2.2 Thermal Analysis of Electrical Machines

Accurate thermal modelling of electrical machines provides the machine designer with invaluable insights into the component temperatures. This allows the designer to take informed decisions such as the electrical and magnetic loading (Simpson et al., 2013), and permits proper choice of materials, avoids unnecessary de-rating and reduces safety factors thus achieving higher torque density machines. The early correlations to predict the temperature rise in electrical machines provide no insight of where the design may be compromised (Staton et al. 2001). Consequently no knowhow for improving the thermal design is developed (Boglietti et al., 2009). Thermal modelling has nowadays come a long way and is performed either through analytical techniques such as Lumped Parameter (LP) Networks or numerical techniques such as Finite Element Analysis (FEA) or Computational Fluid Dynamics (CFD).

Each modelling technique offers a trade-off between spatial thermal resolutions, accuracy, and time to solve the problem. The qualities and defects of each technique is discussed in Boglietti et al., (2009). LP thermal models require time and effort defining a circuit that accurately models the main heat transfer paths (Mellor et al., 1991, Boglietti et al., 2008, Qi et al., 2014). These however are fast to solve and allows the investigation of machine temperatures at various operating conditions in a short time. LP models simplify spatial temperature distribution in solids, providing limited information unless the number of thermal nodes is increased. Moreover LP models require unknown input parameters such as the heat transfer coefficient (HTC) at a solid fluid-boundary and the thermal contact resistances between two solid components. These are difficult to obtain (Staton et al., 2005, Boglietti et al., 2008) and therefore LP models often undergo an initial experimental calibration stage in order to determine the correct value of the missing parameters.

FEA and CFD models provide very detailed information but require an excessive time to solve the problem (Wrobel et al., 2011). These models also require extensive validation tests. It is often found that numerical techniques are applied to machine components to extract valuable data. These are then input into an LP model that is used to investigate the overall temperature profile of the machine.

The application of LP models for an overall temperature prediction of electrical machines during steady state operation was first proposed by Perez and Kassakian, (1979). The model was in its most basic form and analogous to an electrical network in which a node is used to represent the component temperature. Each node was connected to another through a thermal resistance. Mellor et al., (1991), introduced the thermal capacitance to each node in the network therefore giving the solid a thermal mass and enabling the model to predict the temperature in transient operation of the machine. During a transient state in which the body is heated, the temperature of the component modelled is found to follow the exponential theory referred to in eqn 2.2. The thermal time constant replaces the electrical time constant. The simplicity of LP models encouraged their adaptation to various machine topologies. The complete machine is often represented by 10-30 thermal nodes (Mellor et al., 1991, Boglietti et al., 2002). Many research papers dividing the electrical machine into a small number of components typically consisting of the copper windings, the stator iron, the motor housing, bearings and the rotor. An example is reproduced from Sahin, (2001) and shown in Figure 2.1.

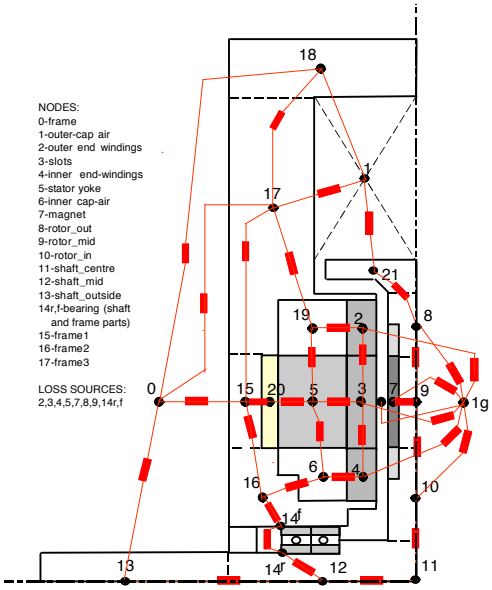


Figure 2.1. An example of a LP thermal model reproduced from Sahin, (2001)

Indeed, Mellor et al., (1991) recommend that the thermal model *"should be sufficiently detailed to distinguish between the stator and rotor components"*. However, as the current density of electrical machines increase, the requirement for an improved temperature resolution increases. Qi et al, (2014), Simpson et al, (2014) and Wrobel and Mellor, (2010), discuss the introduction of a 'T' type cuboidal element for a more accurate average temperature prediction in anisotropic materials with internal heat generation. The authors argue that when classical LP networks are applied to components with internal heat generation, the predicted temperature contains inaccuracies. Therefore the 'T' type element which includes a third negative resistor was proposed. The negative resistor was defined as:

$$R_{th_3} = \frac{T}{q\dot{A}l} - \frac{R_{th_1}R_{th_2}}{R_{th_1} + R_{th_2}} = -\frac{l}{6kA} \qquad \text{eqn. 2.9}$$

The negative resistance caters for the overestimation in the average temperature but this element introduces new complexities.

This thesis adopts the classical element but introduces more nodes in the windings to capture the hotspot temperature where it matters most. This topic was discussed in Paper 7: *Investigation into the temperature profile of a liquid cooled YASA AFPM Machine,* and is the subject of Chapter 7 in this thesis. Qi et al., (2014) also discusses the benefits of larger discretisation. Apart from a higher temperature resolution and a more accurate component temperature prediction, increasing the number of nodes would also benefit the model from a more accurate inhomogeneous assignment of the component losses. This in return also affects the component temperature distribution. Increasing the number of nodes increases the number of thermal resistances and unknown input parameters. The authors develop an automated build up for a switched reluctance stator to reduce the initial effort and compare their LP model to FE models.

Since their inception, LP Models have been used extensively and validated in a large number of machines. This has increased the confidence of thermal designers in LP models. Software Packages such as MotorCAD have been developed. This is nowadays one of the most widely used tools for thermal modelling of electrical machines. The software package requires only the motor geometry, the winding configuration and a definition of the materials for it to automatically set up the

thermal network, (Boglietti et al., 2009). An example of the thermal network set up by MotorCAD is shown in Figure 2.2.

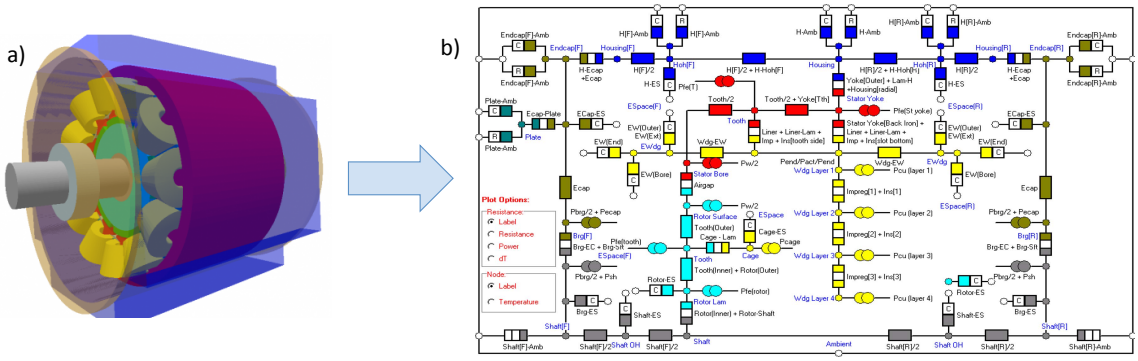


Figure 2.2. Schematic showing how an electrical machine in a) is converted into a resistance network shown in b). Figures extracted from MotorCAD, (2015) and Boglietti et al., (2009)

Some of the models or parameters presented in this literature review have been incorporated in MotorCAD. These are generally gauged against experimental investigations and customer feedback. This setup gives the industry the freedom to compare different modelling techniques and parameters. For example, the model proposed in Wrobel and Mellor, (2010), was initially set as a default model for MotorCAD. However, this was later reported to under-predict temperature values, and the general resistive network is now set as default. Despite the widespread use of LP models, their dependence on critical unknown parameters such as the heat transfer coefficient (HTC) at the solid-fluid boundary and the thermal contact resistances at solid-solid boundaries still remain a challenge, (Staton et al., 2005). Furthermore the accurate temperature prediction of the stator windings is becoming increasingly important due to higher current density electrical machines and the need to reduce excessive safety factors. These topics are the critical parts in thermal analysis of electrical machines, (Nategh et al., 2013). They are also the focus of Chapters 5-7 within this thesis. Therefore the remaining sections of this literature review focus on these topics.

2.3 The Heat Transfer Coefficient in Electrical Machines

2.3.1. The Relationship of Heat Transfer with Airflow

In the previous section it was shown that the energy stored in a component, (and therefore its temperature behaviour with time), depends on the heat generated and the net heat transfer from the component. The heat rejected is dictated by the heat transfer

coefficient on the surface of the solid. Luke, (1923) recognizes that the development of high-speed generators and forced ventilation prevented electrical machines from overheating, resulting in greater machine ratings. The author was the first to introduce the term "coefficient of heat transfer" in a field that was dominated by electrical engineers. The author investigated the variation of the heat transfer coefficient with different simple geometries and air velocities for application in high-speed generators.

The adoption of heat transfer correlations for ideal geometries to electrical machine geometry is still very much in use, (Staton and Cavagnino, 2008, Howey et al., 2012). Such correlations require an accurate prediction of the Reynolds number, and therefore the flow rate and velocity are required. The operating flow rate of an air-cooled machine is determined by superimposing the fan curve on the impedance curve. Taylor, (1960), Bone, (1978), and Staton and Cavagnino, (2008) show how by applying pipe loss correlations a pressure loss curve is derived. The head loss h_f takes the form of:

$$h_f = K\dot{Q}^2 \qquad \text{eqn. 2.10}$$

where K is a loss coefficient and $\dot{Q}$ the flow rate. This calculation becomes more complex when a closed circuit exists and the flow is distributed within the machine. The solution for the closed circuit flow distribution can be found iteratively. One example of a closed circuit flow is a direct liquid cooled stator in which the flow is distributed among a number of segmented stator pole pieces. This is the subject of Chapter 5, which couples a flow network model to a lumped parameter model.

Connor et al, (2012), investigated the airflow distribution in a full CFD model of a mid-sized four pole synchronous generator. CFD provides additional benefits insights into the behaviour of the flow. CFD modelling of the airflow domain of an entire electrical machine is a challenging to mesh efficiently due to the variation in the geometry scales of <1mm in the air gap to region >100mm. The authors used a hybrid mesh with hexahedral and tetrahedral elements consisting of 8M cells. The authors developed a wind tunnel experiment to measure the airflow through the machine and pressure drops along the various machine components. The predicted airflow in the CFD model was validated to within 4% of experimental measurements.

CFD models for a whole machine is generally beyond the resources of most companies and many researchers make use of CFD and analytical techniques in parallel. In design procedures where many machine iterations are required, CFD analysis may consume up to months of simulation time (Lim, Airoldi et al. 2010). Hence CFD models are often limited to extract parameters such as the heat transfer coefficient from components of the machine. These parameters are input in LP models, (Staton, et al., 2001, Boglietti, Cavagnino and Staton, 2009).

One major limitation with adopting heat transfer correlations is that these are geometry specific. Variations of the machine geometry from the ideal geometry lead to inaccuracies when using ideal correlations. Romanazzi and Howey, (2015), demonstrate this when investigating the air gap convection in a switched reluctance (SR) machine. The authors use CFD simulations to show how salient pole geometry of SR machines changes the airflow pattern within the air gap from the traditional Taylor vortices found in an ideal cylindrical gap. A new correlation of the Nusselt number specific to SR machines was proposed.

To avoid the inaccuracies associated with empirical correlations for ideal geometry, researchers often resort to prediction and complex experimental techniques. HTC measurement techniques require a means of measuring the wall temperature and the heat flux perpendicular to the wall. The following section presents a description of existing techniques and their application to electrical machines.

2.3.2. CFD Prediction and Heat Flux Measurements

Micallef et al., (2008) investigate the heat transfer on the end region of a 200 kW two pole strip wound, totally enclosed Fan Cooled Induction Electric Machine. A CFD simulation of a 45^{o} sector of the end region was developed. A rotating reference frame technique was applied to account for the rotor effects. An unstructured mesh using tetrahedral cells was constructed and the $k - \varepsilon$ turbulence model applied to determine the velocity flow field and the heat transfer coefficient on the end windings. The author used micro foil heat-flux gauges consisting of a thermopile and a T-type thermocouple to measure the heat flux and wall temperature at 30 locations on the heated end-winding coil and frame. Experimental measurements of the mean velocity

in key locations of the machine using a five-hole airflow probe were produced. Wool tufts were attached to the end of a rod and positioned at various places to gain an insight of the overall flow field direction. Simulated HTC values were within 7% of measurements. The CFD model was used to investigate changes to the machine design so that the HTC is improved. It was shown that the temperature of end windings decrease if mechanisms which direct air onto critical surfaces can be included, or if higher air velocities are produced.

Hettegger et al., (2012) also investigate the heat transfer from the end windings of a strip wound 120kW air-cooled induction machine. The authors experimented with various CFD turbulence models to capture the turbulent flow on the end windings. The turbulence models were first compared to well-documented empirical correlations of the HTC for a cylinder in a cross flow at varying flow angles. The scale adaptive simulation (SAS) model was deemed to fit best up to a flow angle of approximately 80^{o}. Beyond this point the authors found that the flow stalls. This was found difficult to capture by CFD resulting in an over-prediction of about 7%. The SAS model was subsequently applied to the complex end windings of the electrical machine and validated with measurements. The CFD model was validated against experimental measurements using a ceramic heat flux sensor stuck to the end windings. PT100 temperature sensors were used to measure the bulk air temperature next to the surface of the end windings, while the wall temperature was measured using a thermocouple inside the heat flux sensor. A picture of the test rig has been reproduced in Figure 2.3.

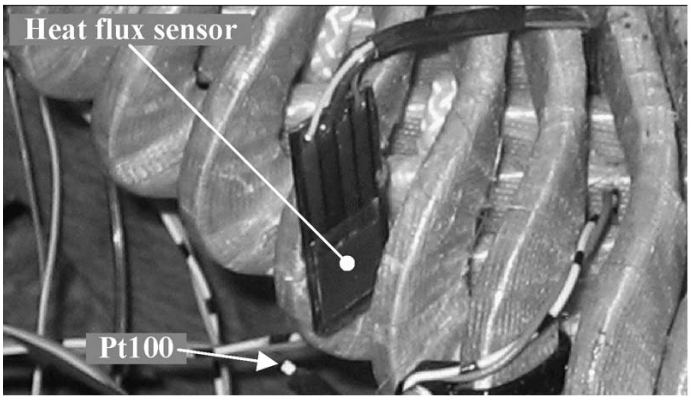


Figure 2.3. Heat flux gauge mounted on the end windings, reproduced from Hettenger, (2012)

It was found that turbulence models such as the $k-\omega$ and the $k-\varepsilon$ model underestimated results by over 35% while the SAS model still under predicts the model by about 20%. However, the accuracy of the measurements presented are questionable because of the scale (100 mm x 100 mm x 3 mm) of the sensor relative to the windings. The sensor may cause disturbances to the flow and influence the measurements. The authors conclude that separation and reattachment cannot always be simulated accurately, and that the choice of the turbulence model is essential. The importance of the choice of turbulence model has been found to vary with different machine designs. For example, Howey, (2011) found that the accuracy in the geometry of an axial flux permanent magnet (AFPM) machine is more important.

Airoldi et al., (2008) investigated the HTC on the stator surfaces in the air gap of a through flow AFPM machine. In this machine, cooling is provided by forced convection in which air is sucked through an opening in the shaft and leaves the machine radially. The authors develop a CFD model of the flow domain to establish a basic flow pattern and the HTC along the radius of the stator. A hot wire anemometer was calibrated with an orifice plate and used to establish the mass flow through the machine. Three heat flux sensors were fixed along the machine stator radius to measure the HTC. Heat mats were fixed to the back of the stator plate to provide the stator heat load. The authors found the predicted mass flow rate through the machine to be within 9% of the measured value. While the simulated HTC matches well with the measured values, the experimental setup does not provide a sufficiently high resolution to validate radial predictions across the machine.

Howey et al., (2011) produced a higher measurement resolution by adopting thin foil heaters to measure the HTC on the rotor and stator surfaces of a through flow, air-cooled axial flux machine. These comprised of 14 spiral shaped copper heater elements with a very small pitch. The sensor was based on a printed circuit board and installed on the stator as shown in Figure 2.4 (left). Its application in a rotor-stator disc system with an adjustable air gap is shown in Figure 2.4 (right). During the test an accurately measured DC voltage is supplied to the individual heaters. Therefore the heat flux could be determined from the power supplied to the heaters. The change in resistance of the copper thin film heaters with temperature allows them to be simultaneously used to infer the surface temperature. The authors compare the measured average Nusselt number along the disk to classical free rotor empirical

correlations for laminar flows by Dorfman, (1963) and correlations for turbulent flows by Owen et al., (1974).

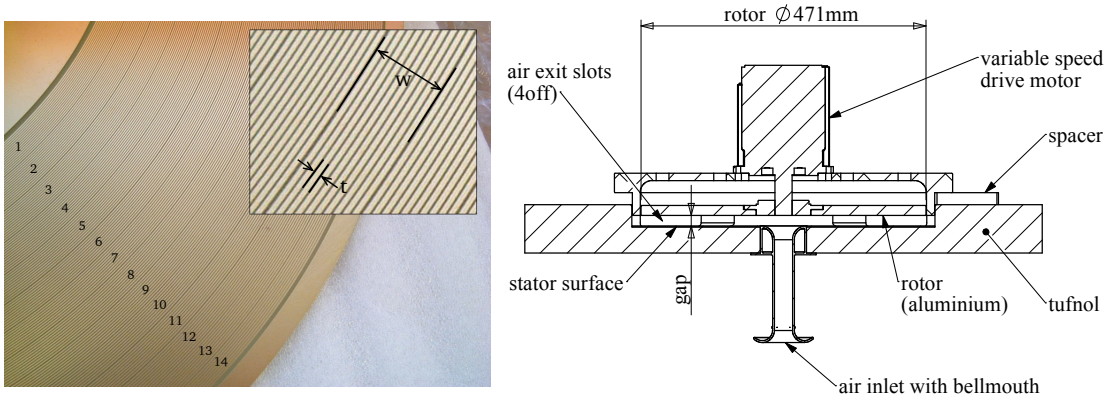


Figure 2.4. (left) Thin film electric heater fixed to the stator, (right) Schematic of the rotor-stator test rig. Figures extracted from Howey, (2010, 2011)

Two CFD for a simple rotor and a rotor with 16 protrusions designed to mimic the magnets in an AFPM machine were also produced. The flat rotor simulations showed a Stewartson flow profile in the laminar regime and a Batchelor flow in the fully turbulent regime. It was noted that the average Nusselt number increases with Reynolds number. The flow pattern in the rotor with protrusions was found to be very different with most of the fluid entrained in the channel between the magnet protrusions and flung outwards. This is in good agreement with the observations made in Airoldi, (2010).

The CFD approach was also applied to investigate the flow in liquid cooled electrical machines. Borges et al., (2008) adopt a CFD approach to optimize the flow inside a water-cooled jacket and increase to maximize the power/frame ratio. The authors simulated flow path geometries in which the water is unrestricted or guided in a serpentine configuration. While unrestricted water showed regions of recirculation that would present hotspots, a serpentine configuration was found to slow the water velocity, limiting the heat transfer coefficient. The authors opted for a compromise with minimal guides to prevent recirculation. The authors apply an Infra-red (IR) Thermography to establish the location of hot spots on the outer casing of an indirect water-cooled electrical machine. These results are difficult to correlate with CFD predictions.

The design of a water-cooling jacket for an electrical machine is also treated in Huang et al, 2012 and Pechanel and Bouzek, (2012). Both studies adopt a CFD approach. While Huang et al, (2012) investigate the effect of the channel geometry in the machine housing, Pechanel and Bouzek, (2012) investigate the differences between serpentine and a spiral flows along the machine housing. The former was found to produce a lower casing temperature but produces higher pressure drops across the water channels. Neither of the two research papers presents experimental validation.

Ponomarev et al., (2012), presents a conjugate heat transfer analysis of an oil cooled permanent magnet machine using CFD. The authors compare the solution to a LP and FEA models. While the CFD model present a higher degree of illustrative results, the author comments that even though a powerful PC with 24GB RAM and several computational cores was used, the solution process took several days. The hotspot temperature in the LP model is 18% lower than that predicted by CFD while the FE predicted hotspot is 22% lower than the CFD predicted one. However, the models are still to be compared to experimental measurements.

To shorten the simulation time, Nategh et al., (2013), adopts a partial CFD approach to estimate the flow distribution and the velocity of the coolant on the end windings of a directly oil cooled electrical machine. In this paper, the authors simulate the flow domain. The values of velocity are used to establish non-dimensional parameters such as the Reynolds number, which is used in appropriate heat transfer correlations. These are then fed into a LP model. The predicted temperatures of the machine components were validated to experimental measurements to within 5.5%.

The topic of flow distribution in a direct oil cooled electrical machine is investigated in Chapter 5 of this dissertation. Furthermore the investigation of the HTC in a direct oil cooled stator is the subject of Chapter 6. Following an overview of the research performed in determining the HTC, the focus is now turned to the literature review on modelling stator windings.

2.4 Thermal Modelling of the Stator Windings

Heat generation in the windings offers one of the major limitations in designing and exploiting high current density electromagnetic machinery. While the application of LP models to strip wound induction machines (example Figure 2.3) may produce an accurate result, the evolution towards stator windings made from litz wire or concentrated windings introduces a larger degree of manufacturing parameters that need to be reflected in the thermal model.

Windings are a composite of materials and typically consist of multiple copper conductors wound around (or onto) a stator iron tooth or an iron bobbin. Each copper conductor is coated with a two-part insulation consisting of a modified polyester basecoat with a superimposed amide-imide outer coating of approximately two microns thickness. The wire cross sectional geometry (square or circular) and the winding configuration (open pack or closed pack) influences the fill factor in the pole piece and the parameters used in modelling the thermal behaviour of the winding accurately. Furthermore during the winding process of concentrated wound pole pieces, a tension is applied to the wire resulting in a contact pressure between winding layers. The windings may be sometimes treated with epoxy resin or a process of Vapour Pressure Impregnation (VPI) to increase mechanical rigidity. This makes thermal modelling of these windings complex and challenging (Jack et al., 1999, Wrobel, Mellor and Holliday, 2011).

While low resolution LP models do not provide enough information on the temperature of the windings, representing the individual insulated conductors in an FEA based thermal model requires an inefficient fine-meshing process (Kanzaki et al., 1992). This adds significant complexity that will lead to long solution times, (Simpson et al., 2013). To simplify the problem of modelling windings, most researchers have treated the heterogeneous windings as a homogeneous material by using equivalent thermal properties. This modelling technique requires initial experiments to establish the equivalent material properties. Most of the heat transfer research of stator windings has adopted this direction and focuses on theoretical, numerical or experimental techniques for determining equivalent properties. The following is a brief collection of this research.

Hashin, (1972) derived an expression for the equivalent thermal conductivity k_{eq} for a composite material made of a cylindrical fibres embedded in an epoxy matrix:

$$k_{eq} = k_e \frac{(1+\Upsilon_c)k_c + (1-\Upsilon_c)k_e}{(1-\Upsilon_c)k_c + (1+\Upsilon_c)k_e} \qquad \text{eqn. 2.11}$$

where Υ_c is the volume ratio of the conductor. k_c is the conductivity of the conductor, k_e the conductivity of epoxy. While the H&S equation only considers two components, it has been adopted for electrical windings by assuming that the properties of the polyamide-imide insulation coating are similar to the embedding epoxy material. The H&S equation is solely applicable to cylindrical wires. Similarly, Ott, (1981) presented an equation to determine the equivalent thermal conductivity of reinforced glass fibre strands within it's epoxy matrix such that:

$$k_{eq} = k_e \left(1 - 2\sqrt{\frac{PF}{\pi}}\right) + \frac{k_c k_e}{2(k_c - k_e)}\left[\pi - \frac{4D'}{\sqrt{D'^2 - 1}}\arctan\left(\frac{D'-1}{\sqrt{D'^2-1}}\right)\right] \qquad \text{eqn. 2.12}$$

Where the subscripts of the thermal conductivity *k* have the same meaning as above, PF the packing factor and D' a conductivity constant defined by:

$$D' = 2\sqrt{\left(\frac{\pi}{PF}\right)}.k_c.(k_e - k_c) \qquad \text{eqn. 2.13}$$

The applicability of this equation is not limited by the geometry of the materials but to the author's knowledge, this equation was never applied to electrical windings.

Kanzaki et al., (1992), argue that these equation are only applicable for a two-component composite and are therefore not effective for a three-component composite such as electrical machine windings. The authors investigate a method to predict equivalent thermal conductivity of an open pack and closed pack electric coils reproduced in Figure 2.5, with a filling of resin or air.

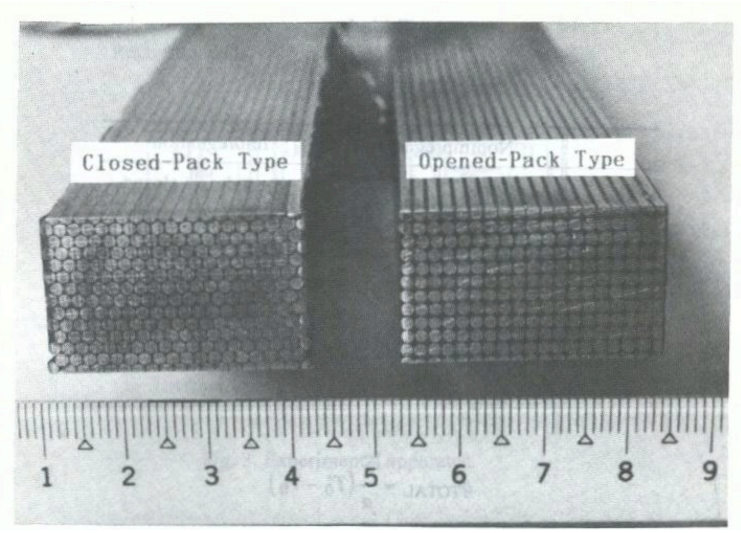


Figure 2.5. An example of Closed Pack and Open Pack windings investigated in Kanzaki et al., (1992)

For an open pack with windings not in contact, the equivalent conductivity k_{eq} is determined as:

$$k_{eq} = \int_0^{(1-2s\prime)A} \frac{k_c k_i k_e}{B\sqrt{A'^2 - x^2} + C\sqrt{(1-2s')^2 A'^2 - x^2} + k_c k_i} dx + \int_{(1-2s\prime)A}^{A} \frac{k_i k_e}{(k_e - k_i)\sqrt{A'^2 - x^2} + k_i} dx + \int_A^1 k_e dx \quad \text{eqn. 2.14}$$

where *A'*, *B* and *C* are constants defined as:

$$A' = 2\sqrt{\frac{\Upsilon_c + \Upsilon_i}{\pi}} \quad \text{eqn. 2.15}$$

$$B = \frac{1}{1 - 2s's} \quad \text{eqn. 2.16}$$

$$C = k_e.(k_i - k_c) \quad \text{eqn. 2.17}$$

where Υ_c and Υ_i are volume ratios of the conductor and insulator respectively. s' is the ratio of insulation thickness to wire and s is the wire deformation ratio to insulation thickness. For an open pack with windings in contact the equivalent conductivity k_{eq} is determined as:

$$k_{eq} = \int_0^{2B\sqrt{ss'(1-ss')}} \frac{k_c k_i}{(k_i - k_c)\sqrt{(1-2s')^2 B^2 - x^2} + k_c} dx + \int_{2B\sqrt{ss'(1-ss')}}^{(1-2s')B} \frac{k_c k_i k_e}{E'\sqrt{B^2 - x^2} + C\sqrt{(1-2s')^2 B^2 - x^2} + k_c k_i} dx + \int_{(1-2s')B}^{1} \frac{k_i k_e}{(k_e - k_i)\sqrt{B^2 - x^2} + k_i} dx \quad \text{eqn. 2.18}$$

where

$$E' = k_c.(k_e - k_i) \quad \text{eqn. 2.19}$$

For a closed pack the equivalent conductivity in the x direction. k_x is determined by:

$$k_x = 2\sqrt{3}\left\{\int_0^{1-F} \frac{k_c k_a}{(k_a - k_c)\sqrt{F^2 - y^2} + \sqrt{3}k_c} dy + \int_{1-F}^{0.5} \frac{k_c k_a}{(k_c - k_a)\left[\sqrt{3} - \sqrt{F^2 - y^2} - \sqrt{F^2 - (y-1)^2}\right] + \sqrt{3}k_a} dy\right\} \quad \text{eqn. 2.20}$$

where k_a is an amalgam thermal conductivity of the insulation thermal conductivity k_i and thermal conductivity of the epoxy resin filler k_e. k_a is described as:

$$k_a = \frac{\Upsilon_i k_i + \Upsilon_e k_e}{\Upsilon_i + \Upsilon_e} \quad \text{eqn. 2.21}$$

And F is a filler constant defined as:

$$F = \sqrt{\frac{2\sqrt{3}\Upsilon_c}{\pi}} \quad \text{eqn. 2.22}$$

The equivalent conductivity in the y direction is determined by:

$$k_y = \frac{2}{\sqrt{3}}\left\{\int_0^{\sqrt{3}-F} \frac{k_c k_a}{(k_a - k_c)\sqrt{F^2 - x^2} + k_c} dx + \int_{\sqrt{3}-F}^{\frac{\sqrt{3}}{2}} \frac{k_c k_a}{(k_c - k_a)\left[\sqrt{F^2 - x^2} - \sqrt{F^2 - \left(x - \sqrt{3}\right)^2}\right] + k_a} dx\right\} \quad \text{eqn. 2.23}$$

The average equivalent thermal conductivity was compared to experimental measurements. These were found to be within the experimental error of the measurements. However, this technique is very complex to apply and has not been adopted by many thermal designers.

Boglietti et al., (2002), provided a simplified empirical equivalent conductivity for windings within the stator slot of an induction machine. The equivalent conductivity was defined as:

$$k_{eq} = 0.1076.PF + 0.029967 \quad \text{eqn. 2.24}$$

where PF is the packing factor of the windings. This equation shows a very low R^2 fit factor and a more accurate definition is later proposed in (Boglietti et al., 2008), to:

$$k_{eq} = 0.2425[(1 - PF)A_{slot}l_{core}]^{-0.4269} \quad \text{eqn. 2.25}$$

Where A_{slot} is the slot area and l_{core} is the axial length of the core of an induction machine.

Simpson et al., (2013) uses a detailed FE model of windings to determine the equivalent thermal conductivity of windings and compare it to a modified H&S equation to include three components. The authors present an additional step in which the value of the conductivity of the epoxy k_e in the H&S eqn 2.10 is replaced the equivalent conductivity of the insulation amalgam:

$$k_{eq} = k_a \frac{(1 + \Upsilon_c)k_c + (1 - \Upsilon_c)k_a}{(1 - \Upsilon_c)k_c + (1 + \Upsilon_c)k_a} \quad \text{eqn. 2.26}$$

The insulation amalgam $k_a$is defined as:

$$k_a = k_e\left(\frac{\Upsilon_e}{\Upsilon_e + \Upsilon_i}\right) + k_i\left(\frac{\Upsilon_i}{\Upsilon_e + \Upsilon_i}\right) \quad \text{eqn. 2.27}$$

where Υ_c, Υ_e and Υ_i are the volume ratios of the conductor, epoxy and insulation respectively, and

$$\Upsilon_c + \Upsilon_i + \Upsilon_e = 1 \quad \text{eqn. 2.28}$$

The volume ratio of the conductor Υ_c, epoxy Υ_e, and insulation Υ_i are estimated from the wire dimensions using:

$$\Upsilon_c + \Upsilon_i = PF \quad \text{eqn. 2.29}$$

$$\Upsilon_c = PF\left(\frac{{r_c}^2}{(r_c + x_i)^2}\right) \quad \text{eqn. 2.30}$$

$$\Upsilon_e = 1 - PF \quad \text{eqn. 2.31}$$

$$\Upsilon_i = PF\left(\frac{2r_c x_i + {x_i}^2}{(r_c + x_i)^2}\right) \quad \text{eqn. 2.32}$$

where r_c is the radius of the conductor and the x_i insulation thickness.

However, when compared to experimental results this procedure presents an over estimation of 21-29%. The H&S equation presents an overestimation between 11-34% and the FEM was found to be the most accurate with an overestimation between 4-11%. Interestingly, the experimental results show that very little difference between the equivalent thermal conductivity of closed pack and open pack systems exist.

Wrobel and Mellor, (2011), take an experimental approach to determine the equivalent properties of the windings. The authors design a set of experiments to determine the equivalent thermal conductivity of the windings. In their research paper, the authors adopt the idea to treat an FEA model of a high energy density wound component in lumps of homogeneous material and apply equivalent thermal properties to the model. The predicted temperature results from the FE model compares well to experimental measurements. The process was repeated by Wrobel, et al., (2011) who perform a thermal analysis on a segmented stator winding of an electrical machine following a characterization of a single tooth winding. The author compares the simulated temperature of various parts of a machine with measurements from an instrumented prototype. While the comparison shows that the predicted temperature was found to be within 9% of the measured temperature, the paper does not specify clearly the location of the temperature sensors within the machine.

Siesing et al., (2014), make used of FE models to determine the equivalent thermal conductivity of windings with different wire diameters, fill factors and infiltration with epoxy resin. The FE model consists of detailed quarter of a wire in touch with another. The heat flux patterns through the wires are investigated. A temperature difference was applied across their boundaries and the equivalent thermal conductivity was determined from the resulting heat flux. The FE model was compared to the H&S analytical solution and experimental measurements. The equivalent thermal conductivity of infiltrated and non-infiltrated sample windings was determined using a transient plane source heat flux sensor. The authors note that wire diameters play no role in the equivalent thermal conductivity. This however can be increased either by increasing the fill factor or infiltrating the windings with epoxy resin. The authors note that the fill factor cannot be increased indefinitely as the high forces are required which risk causing deformation and damage to the wires. Both FE models are seen to match experiments with infiltrated windings matching better than

non-infiltrated windings. Conversely, the H&S analytical model matches both infiltrated and non-infiltrated windings.

Staton et al., (2005) broke away from the trend in researching an equivalent conductivity and proposed that the windings in the slot geometry are grouped together according to their expected temperature distribution and modelled in a series of layers of impregnation epoxy, winding insulation and winding conductor. A figure showing the winding model is reproduced in Figure 2.6.

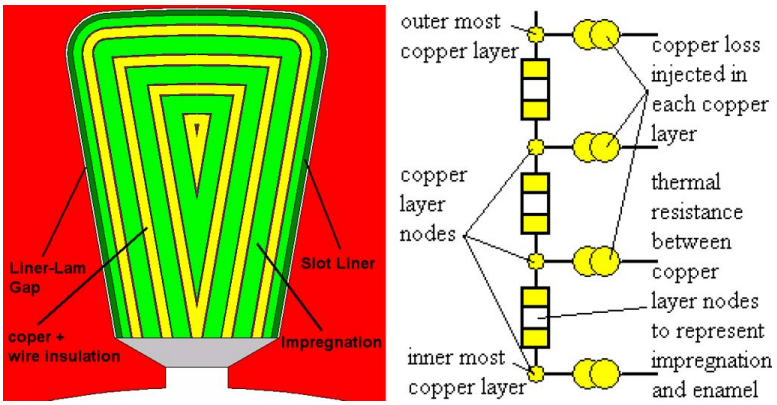


Figure 2.6. Layered winding model for the slot geometry of induction machines reproduced from Staton et al., (2005)

However, this technique is found to underestimate the temperature of the windings. The authors attribute this due to the imperfections in the impregnation and introduce an impregnation goodness factor to calibrate the conductivity of the epoxy used in the model with an initial calibration experiment. Despite that the model provides a temperature distribution in the stator slot, it does not fully represent the physical windings within the slot. This technique is adopted by MotorCAD and is probably one of the most used in industry due to the popularity of the software. Nategh et al., (2012), develops the idea of layered windings further and identifies a mathematical solution to the number of layers. The authors propose that the winding in the stator slot is modelled as a series of elliptical copper and impregnation layers. A schematic of the winding layers is reproduced in Figure 2.7. A procedure to determine the equivalent radii of the ellipse from the slot height and width is developed. The thermal resistance due to conduction across the conduction layers is deemed negligible and only the thermal resistance across the conduction through the impregnation layers is considered.

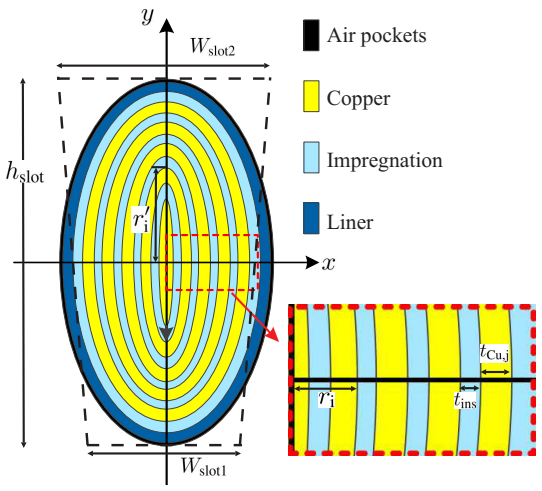


Figure 2.7. Elliptical layered winding model for the slot geometry of induction machines, reproduced from Nategh et al., (2012)

An expression of the thermal resistance across the insulation of each layer is derived as a function of the geometry parameters such that:

$$R_{th} = \frac{1}{2\pi l k_e N_{slot}} \left\{ ln\left[4(r_i + x_e) + 2\Delta r + 4\sqrt{(r_i + x_e)^2 + \Delta r(r_i + x_e) + \frac{\Delta r^2}{2}} \right] - ln\left[4r_i + 2\Delta r + 4\sqrt{{r_i}^2 + \Delta r r_i + \frac{\Delta r^2}{2}} \right] \right\} \quad \text{eqn. 2.33}$$

where l is the length of the stator, k_e the conductivity of the epoxy, N_{slot} the number of slots of the machine, r_i the major radius of the elipse, x_e the thickness of the epoxy and Δr the difference in major and minor elipse radii. The results from the LP model were compared to an FEA model making use of an equivalent thermal conductivity and experimental measurements. PT100 temperature sensors were placed on the outer edge of the slot. The authors note that the accurate temperature distribution in the windings could not be measured or compared. The authors noted that while the temperature of the end windings was accurately predicted (<1%), other aspects of the active winding had an overestimation between 13-22%. The error was found to increase as the machine loading increases.

This thesis furthers the concept of layered winding models and adopts the technique for concentrated windings. The new LP thermal model developed has key differences in the definition and placement of the thermal resistances. Rather than attributing the thermal resistance to the conductivity in the epoxy, this thesis attributes the thermal resistance to the contact between the winding layers. When discussed in light of the

thermal contact resistance models, the developed LP model provides more insights into the thermal behaviour of the windings than existing techniques. This research is presented in Chapter 7. Having investigated the existing body of knowledge for modelling the conductive heat transfer in the windings, the focus of this literature review turned to modelling the conduction processes at the interface of two solid electrical machine components.

2.5 Thermal Contact Resistance in Electrical Machines

While convective heat transfer in the solid-fluid interface of electrical machine components has been extensively researched, the same cannot be said to heat transfer in solid-solid interfaces. Heat transfer at a solid-solid interface is limited by thermal contact resistance (TCR). In electrical machines, TCR is important as it is often on the main thermal path of the machine and affects the accuracy of the predicted stator temperatures and temperature distribution (Boglietti et al., 2008). This section discusses research of this parameter as applied to electrical machines.

Holman, (1997) and Mills, (1999), suggest that TCR between solid boundaries can be modelled by introducing a small effective interface air gap and provide some values. In their experience modelling electrical machines, Staton et al., (2005), comment that real machines often require an effective air gap thicknesses that is an order of magnitude larger than those suggested. Therefore the thermal resistances are often guessed and validated using an initial experimental calibration process to determine the correct size of the effective gap. This practice was found in various thermal analysis of electrical machines, (Staton et al., 2005, Nategh et al., 2012). Boglietti et al., (2008) provides a table of effective interface air gaps used in modelling induction machines of different sizes. The authors claim that the values do not follow a logical correlation, and are mostly dependent on the manufacturing process. However, when grouped according to the material interface, this research shows that a weak correlation can be produced and is shown in Figure 2.8. This provides a hint that TCR values go beyond the dependence on the machine manufacturing process.

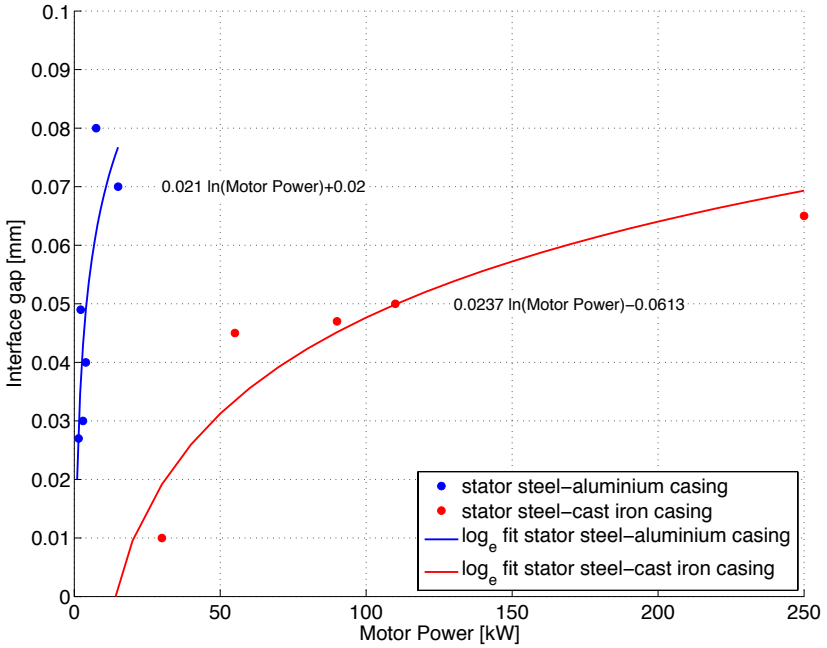


Figure 2.8. Interference gap values for induction machines. Data from Boglietti et al., (2008)

Kulkarni et al, (2012), performed an experimental investigation to determine the thermal resistance at the interface of a silicon steel stator and a shrink fit mild steel housing used in a liquid cooled generator applied in a wind turbines. The authors investigate a total of 6 assemblies with shrink fit pressures of 10 MPa, 14 MPa, 17 MPa, 21 MPa and 39 MPa. In these experiments the heat load in the stator is simulated using cartridge heaters. The temperature in the stator and housing are measured and the thermal contact resistance is found using eqn. 2.6. The paper presents general observations such as the reduction in thermal contact resistances with increasing contact pressure, improved surface finish and with the application of thermal interface material. However, the paper does not provide sufficient information on the simulated heat loads, motor geometry, material properties and surface finish. Hence results cannot be replicated or compared to. The paper fails to provide a correlation that can be used for thermal modelling and assumes that thermal contact resistances only depend on the initial shrink fit pressure and surface conditions. Chapter 9 of this thesis shows that this is an oversimplification.

Following the review on important aspects in the thermal modelling of electrical machines, this thesis proceeds to investigate the convective heat transfer challenges associated with air-cooled electrical machines, liquid cooled machines and the conductive mechanism, particularly within the windings.

3 | Air Cooled Electrical Machines

In the introductory chapter, the convective heat transfer was highlighted as one of the key parameters for increasing the current density in electrical machines. Fig. 1.3 shows that this parameter is dependent on the cooling mechanism. This chapter focuses on the heat transfer from air-cooled electrical machines and investigates the role that this cooling mechanism can play in the context of electric vehicles. This chapter is based on the publication of paper 1.

3.1. Context to this chapter

The idea of having electric personal urban mobility vehicles that can provide a cleaner, more efficient means of transport, better supported within an urban infrastructure has now been suggested for some time, (Lark, 2005, Mitchell at al., 2010, Borroni-Bird, 2012, General Motors, 2012, Toyota, 2012, Renault, 2012). Modern vehicles typically have around one third of the vehicle dedicated for the combustion engine and its cooling bay. If electric vehicle designers were to swap the ICE with the electric motor, it will be rather difficult to design compact city EV's. As it is important to maximize the passenger space, in-wheel motors have been proposed for such applications, (Borroni-Bird, 2012). The use of in-wheel motors for automotive applications has been demonstrated by Porsche in 1898, (Lohner-Porsche-Mixte-Voiturette, 2011). Their use has been exclusive to trains and heavy machinery, and only through the last decade they have been reconsidered for EV's (Jain and Williamson, 2009, Rahman, 2004, Lovatt et al, 1998).

In the introductory chapter it was shown how electrical machine cooling is categorized into liquid cooling and air-cooling. Whereas high power on-board electrical motors typically rely on liquid cooling and utilize a heat exchanger to expel

the heat to ambient air, applying this technique for in-wheel motors will increase the plumbing complexity and the fragility of the vehicle. Air-cooled motors are hence preferred. Since motors used in-wheel operate at a harsher work environment than onboard motors, a high level of ingress protection is required. Therefore through flow air-cooled machines are less attractive and this study focuses on enclosed motor geometry. Several studies on the electromagnetic design for in-wheel applications exist (Caricchi et al., 1996, Jain and Williamson, 2009, Rahman, 2004, Lovatt et al, 1998). Yet a number of questions on the thermal aspects and the limitations that the cooling mechanism may impose on the design of the machine still exist. This is the topic of this chapter, which investigates the heat transfer from totally enclosed air-cooled axial flux machines and assess their application to electrical transportation.

The chapter is hence organised in the following manner: Section 3.2 establishes a target vehicle dimension, the powertrain configuration and the associated heat loads. Section 3.3 establishes the machine topology and identifies the thermal path from the stator windings. The chapter adopts established empirical correlations to estimate the heat transfer from electrical machines with ideal flat surfaces. The continuous heat load is compared against the heat transfer from the machine in section 3.4. Thus the thermal implications on each machine topology are discussed. Finally, Section 3.5 investigates the machine performance with the introduction of extended surfaces.

3.2. Vehicle Dimensions and Powertrain Sizing

To determine the suitability of air-cooling for in-wheel motors, the continuous heat losses generated by the machine have to be sustained without over heating. This section estimates a typical heat load for in-wheel motors. The power required to push the vehicle forward at a steady speed needs to overcome the rolling resistance, aerodynamic drag and road inclination. The continuous motor power for a number of electric vehicles in the market by 2013, have been surveyed and are presented in Figure 3.1. The vehicle traction power P_t has been correlated with the vehicle mass m by the power law:

$$P_t = 6.79e^{-5}m^{1.95} \qquad \text{eqn. 3.1}$$

The data has an R^2 value of 0.6065. The spread is attributed to the fact that vehicles surveyed vary from small city cars to light trucks and sports cars. It can be seen that

very few vehicles sub 500 kg. Current city cars such as the Reva or the Smart have a mass between 800 – 1000 kg. An estimation of the aerodynamic forces acting on a vehicle, and the rolling resistances show that a traction power of 20 kW should be enough to get the vehicle up to an average speed of 62km/hr, as defined by the Extra Urban Drive Cycle (EUDC).

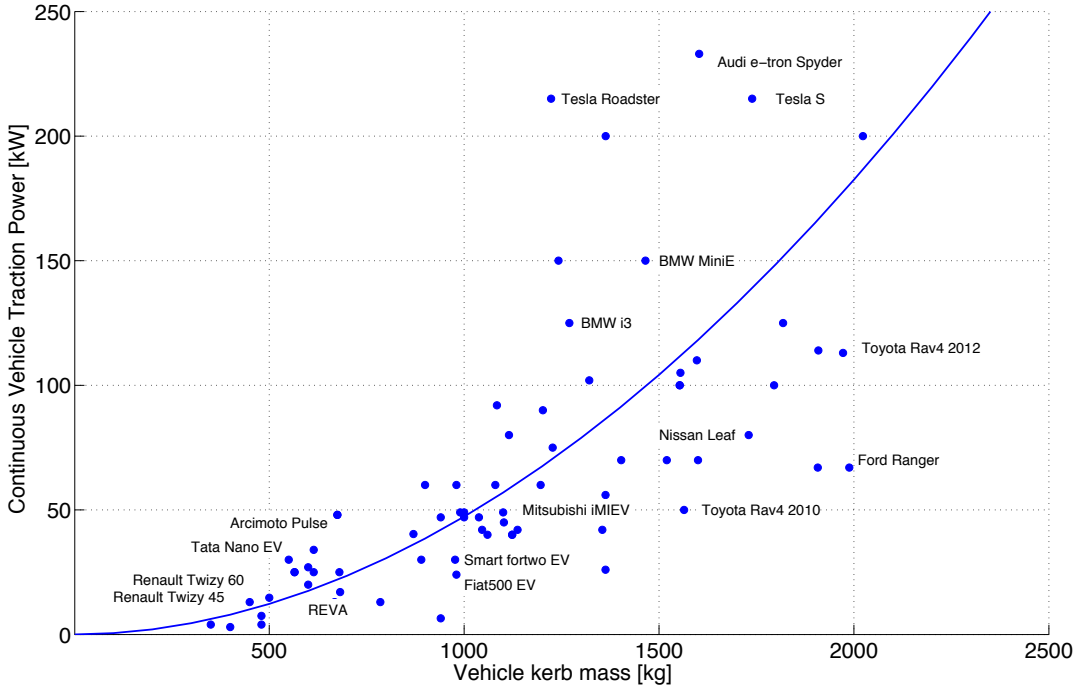


Figure 3.1. Survey of EV continuous power for vehicles the market at 2013

As the traction power required by the electrical machine can be distributed amongst a number of wheels, the size of the in-wheel motor is determined by dividing the total required power by the number of wheels powered, as shown in Table 3.1.

Table 3.1 Distribution of traction power

Scenario	No. of Powered Wheels	Wheel Traction Power P_t [kW]
1	1	20
2	2	10
3	3	6.6
4	4	5

Furthermore, the wheel traction power can be delivered through a direct drive machine or a geared drive. Different gear ratios would require different machine designs. In this thesis, five fixed gear ratios between 1-10 were analysed, therefore investigating 5 motors for each scenario. By scaling the efficiency charts from the

YASA topology, (Yasa Motors, 2010), the heat load over the range of motor speeds for a constant torque is achieved. Figure 3.2 shows an example of the exercise for scenario 1, in which a 20kW traction power can be delivered to a single wheel through a single gear ratio of 1, 1.3, 2, 4 and 10.

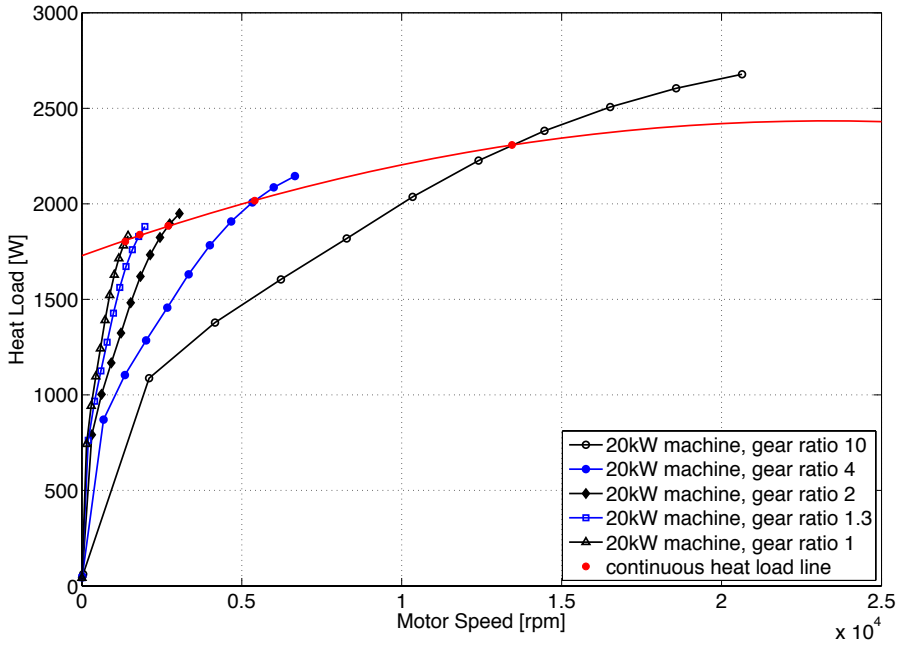


Figure 3.2. Motor losses for 20kW motor designs with various gear ratios

For each scenario the heat load at the continuous operation point is also marked. The continuous operation is the point at which the vehicle reaches its design speed. By joining the heat loads from the continuous operating points a continuous operating heat load line for each scenario is formed. The process has been repeated for scenarios 2-4 to determine the continuous operating line for multiple in-wheel motor power. The result is shown in Figure 3.3.

Having established the heat load for various machine topologies, the following section sets the geometrical boundary conditions of the machines investigated and defines the main thermal resistances from the machine. Using empirical correlations the heat rejected from the machine is calculated. By comparing the continuous heat loss generated and the heat transfer from the machine, the ability to sustain a continuous machine operation is determined.

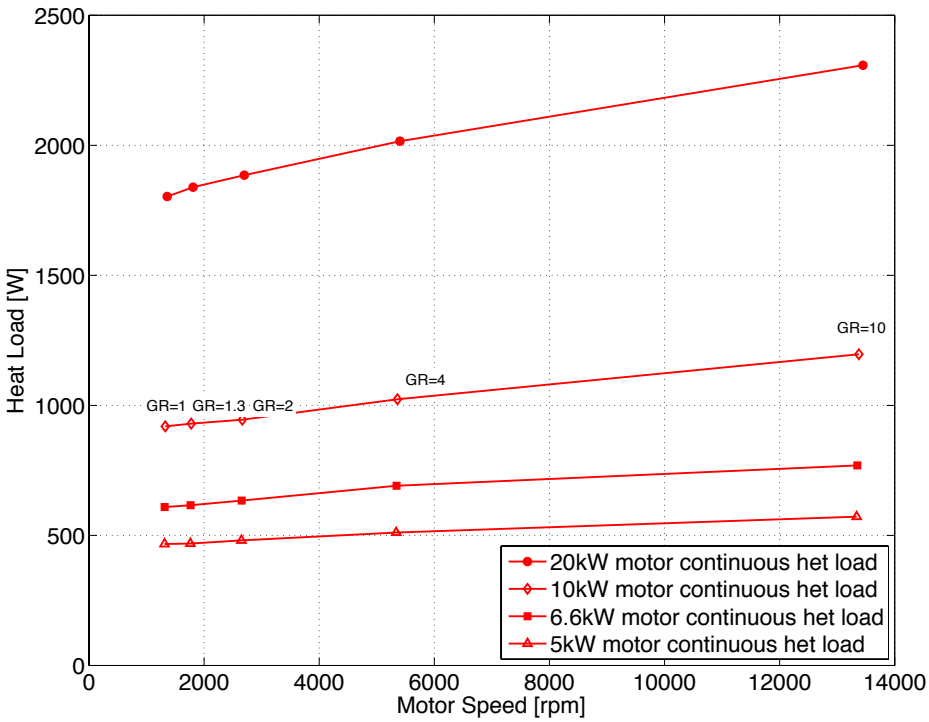


Figure 3.3. Chart showing motor losses for various motor, power distribution and gear ratios

3.3. Totally Enclosed Air-Cooled Machines

Section 1.4.2 of the introductory chapter shows that double sided axial flux machines provide higher torque densities and are better suited for electric vehicle applications, (Caricchi et al., 1996, Lamperth et al., 2008, Aydin et al., 2004, Woolmer and McCulloch, 2007), with the axial flux internal rotor (AFIR) topology and the axial flux internal stator (AFIS) topology being the most promising. These machine geometries, shown in Figure 3.4 will hence be used as the geometrical constraint for this chapter.

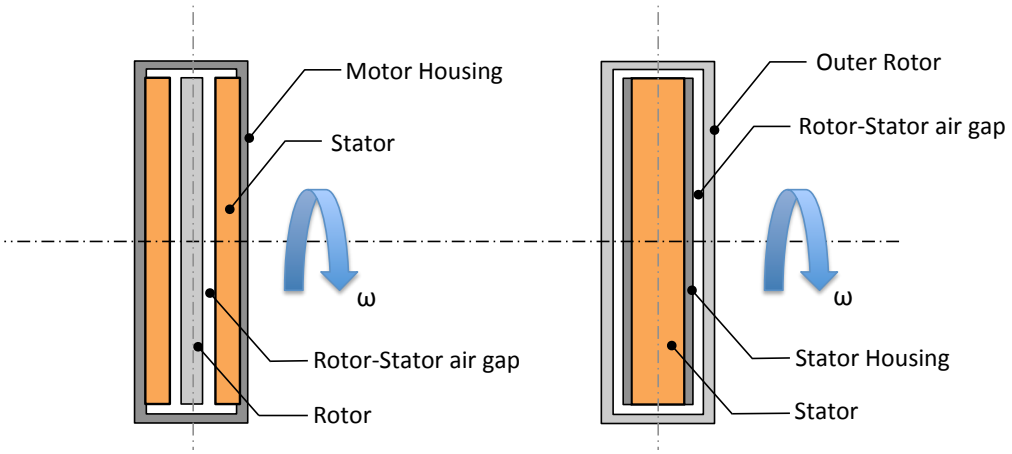


Figure 3.4. Schematic of an Axial Flux Internal Rotor (AFIR) electrical machine (Left), an Axial Flux Internal Stator (AFIS) electrical machine (Right)

The cooling mechanism of the motors must offer the potential of rejecting the heat generated during continuous operation. Assuming that the concentration of the heat load lies within the stator windings, for a steady state operation the heat transfer Q from the machine stator is calculated using:

$$Q = \frac{T_s - T_\infty}{R_{th}} \qquad \text{eqn. 3.2}$$

where T_s and T_∞ define the stator temperature and the ambient temperature respectively. R_{th} is the thermal resistance in the heat path between the stator and ambient. This can be broken down into a convective component and conductive component. Their make up depends on the geometry and construction of the machine. Howey, (2010) and Airoldi, (2010), showed that in air-cooled machines the convective terms are generally the limiting factors within the thermal path of a machine. In the following sections the focus is placed on the convective thermal resistances. The detailed analysis of the stator windings is ignored here as this will be the subject of Chapters 7 and 8. After defining the thermal path in AFIR and AFIS geometries, empirical correlations are used to determine the convective thermal resistances. The effect of the thermal limit on the applicability of the machine to urban transportation is then discussed.

3.3.1. Thermal modelling of an AFIR machine

Defining the thermal Path

In Section 2.2 of the literature review it was shown that the thermal network of electrical machines often include a thermal capacitance on the nodes to model the transient thermal effects on components. In the context of road transportation this is useful to model the transient thermal effects due to the variability of the drive cycle including the vehicle starting and stopping. However, this chapter focuses on estimating the heat transfer from the electrical machine when the vehicle is at a fixed velocity. Hence the machine is operating at a steady state and therefore the thermal network for the AFIR electrical machine is simplified to include only the thermal resistances as shown in Figure 3.5. The symbols used in the figure are described in Table 3.2.

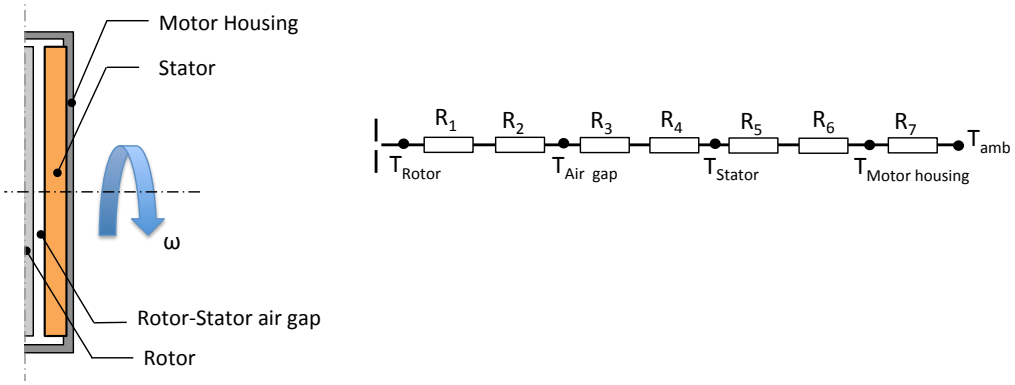


Figure 3.5. A thermal resistance network for an Axial Flux Internal Rotor (AFIR) electrical machine

Table 3.2 Definition of Symbols used in the 1D thermal resistance network

Symbol	AFIR		AFIS	
R1	Conductive thermal resistance through the rotor	$\left(\frac{x}{2k}\right)_R$	Conductive thermal resistance through half the stator	$\left(\frac{x}{2k}\right)_S$
R2	Convective thermal resistance for the rotor side – RS gap	$\left(\frac{1}{h}\right)_R$	Conductive thermal resistance through the stator housing	$\left(\frac{x}{k}\right)_H$
R3	Convective thermal resistance for the stator side – RS gap	$\left(\frac{1}{h}\right)_S$	Convective thermal resistance for the stator side – RS gap	$\left(\frac{1}{h}\right)_S$
R4	Conductive thermal resistance through half the stator	$\left(\frac{x}{2k}\right)_S$	Convective thermal resistance for the rotor side – RS gap	$\left(\frac{1}{h}\right)_{Ri}$
R5	Conductive thermal resistance through half the stator	$\left(\frac{x}{2k}\right)_S$	Conductive thermal resistance for half the rotor	$\left(\frac{x}{2k}\right)_R$
R6	Conductive thermal resistance for stator housing	$\left(\frac{x}{k}\right)_H$	Conductive thermal resistance for half the rotor	$\left(\frac{x}{2k}\right)_R$
R7	Convective thermal resistance stator out	$\left(\frac{1}{h}\right)_H$	Convective thermal resistance rotor out	$\left(\frac{1}{h}\right)_{Ro}$

By simplifying the stator and rotor to a homogeneous solid material with an equivalent thermal conductivity, the thermal resistances limiting the heat transfer from the stator in an AFIR type machine is defined as:

$$R_{th} = \frac{1}{A_s}\sum_{5}^{7} R \qquad \text{eqn. 3.3}$$

$$R_{th} = \left[\left(\frac{x}{2k}\right)_S + \left(\frac{x}{k}\right)_H + \left(\frac{1}{h}\right)_H\right] \qquad \text{eqn. 3.4}$$

where x is the axial thickness, k is the thermal conductivity and h is the heat transfer coefficient (HTC). The subscripts S and H denote the stator and housing respectively. The heat generated in the stator of an AFIR type motor will be conducted to the

machine casing and convected away by the oncoming flow as the vehicle velocity increases.

To assess the convective heat transfer from the casing of an AFIR machine, empirical correlations of a stationary disc subjected to parallel flow are used. The analysis shown in the next section is used to estimate the HTC and the value of R7 in the AFIR type machine.

Heat transfer from a stationary disc subjected to parallel flow

Aus der Wische, (2006) correlates the average Nusselt number Nu_{avg} with the planar Reynolds number Re_u as follows:

for $10^3 < Re_u \leq 5\text{x}10^4$, $\text{Nu}_{avg} = 0.417\text{Re}_u^{0.5}$ eqn. 3.5

for $Re_u > 10^5$ $\text{Nu}_{avg} = 0.0127Re_u^{0.8}$ eqn. 3.6

The planar Reynolds number has been defined as:

$$Re_u = \frac{\text{ur}}{v} \quad \text{eqn. 3.7}$$

where u is the planar velocity, r is the disc radius and v is the kinematic viscosity. The mean heat transfer coefficient is estimated using:

$$h_{avg} = \frac{Nu_{avg}k_\infty}{r} \quad \text{eqn. 3.8}$$

where k_∞ is the thermal conductivity of air. In this study, the Reynolds number is based on the Extra Urban Drive Cycle (EUDC) average speed of 62km/h and motors mounted on wheel dimensions of 15", 13" and 11" respectively. At this speed and wheel dimensions the planar Reynolds number ranges between $1.21\text{x}10^8$ and $1.65\ \text{x}10^8$. Having investigated the correlations applicable to a simplified AFIR machine, the procedure is repeated to assess the heat transfer from an AFIS machine.

3.3.2. Thermal modelling of an AFIS machine

Defining the thermal Path

The thermal network for an AFIS type machine shown in Figure 3.6. The symbols are described in Table 3.2.

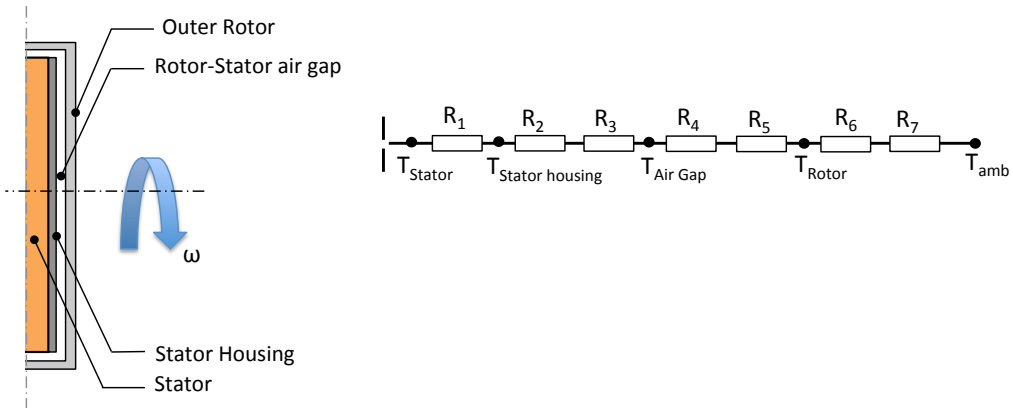


Figure 3.6. A thermal resistance network for an Axial Flux Internal Stator (AFIS) electrical machine

The heat generated in the stator of an AFIS type machine is convected through the rotor-stator gap, conducted through the machine rotor and convected to ambient from the rotation of the rotor and the oncoming flow due to the vehicle speed. The thermal resistance for an AFIS is defined as:

$$R_{th} = \frac{1}{A_s}\sum_{1}^{7} R \qquad \text{eqn. 3.9}$$

$$R_{th} = \frac{1}{A_S}\left[\left(\frac{x}{2k}\right)_S + \left(\frac{x}{k}\right)_H + \left(\frac{1}{h}\right)_S + \left(\frac{1}{h}\right)_{Ri} + \left(\frac{x}{k}\right)_R + \left(\frac{1}{h}\right)_{Ro}\right] \qquad \text{eqn. 3.10}$$

where x is the axial thickness, k is the thermal conductivity and h is the heat transfer coefficient. The subscripts S, H and R denote the stator and housing and the rotor respectively.

As the heat transfer coefficient varies between the inner and outer side of the rotor these are defined with subscripts R_i and R_o respectively. To assess the convective heat transfer from the rotors of an AFIS machine, (defined in the thermal resistance by R7), the empirical correlations of a rotating disc subjected to parallel flow are used. The following section defines the empirical correlations used to estimate the heat transfer coefficient.

Heat transfer from a rotating disc subjected to parallel flow

The subject of rotating discs in still air has been thoroughly studied, (Dorfman, 1963, Cobb and Saunders, 1956, Owen, 1974). Conversely studies of heat transfer from rotating discs subjected to a parallel flow are limited. Aus der Wische, (2006) shows how the problem is a combination of the two separate above-mentioned problems in

which the complex interactions between the planar and rotating flow generates vortices close to the surface. This augments the heat transfer from the disc. The heat transfer is hence a function of both the rotational Reynolds number $Re_{\emptyset}$ and planar Reynolds number Re_u as follows:

for $10^3 < Re_u \leq 5\text{x}10^4$ and $\mathrm{Re}_\phi / Re_u \leq 1.4$, $\quad \mathrm{Nu}_{avg} = 0.417\mathrm{Re}_u^{0.5}$ eqn. 3.11

for $10^3 < Re_u \leq 5\text{x}10^4$ and $\mathrm{Re}_\phi / Re_u > 1.4$, $\quad \mathrm{Nu}_{avg} = 0.33\mathrm{Re}_u^{0.5}$ eqn. 3.12

for $Re_u > 10^5$ and $\mathrm{Re}_\phi < 2\text{x}10^5$, $\quad \mathrm{Nu}_{avg} = \sqrt{(0.0127\mathrm{Re}_u^{0.8})^2 + \left(0.33\mathrm{Re}_\phi^{0.5}\right)^2}$ eqn. 3.13

for $Re_u > 10^5$ and $\mathrm{Re}_\phi > 2\text{x}10^5$, $\quad \mathrm{Nu}_{avg} = \sqrt{(0.0127\mathrm{Re}_u^{0.8})^2 + \left(0.015\mathrm{Re}_\phi^{0.8}\right)^2}$ eqn. 3.14

The rotational Reynolds number is defined as:

$$Re_{\emptyset} = \frac{\omega r^2}{v} \qquad \text{eqn. 3.15}$$

where ω is the rotational speed, r the radius of the disc and v the kinematic viscosity.

With the convective heat transfer from the outer rotors of the AFIS machine defined, the attention is now turned to the convective heat transfer in the rotor stator gap of the machine. These are defined in the thermal path by R3 and R4. In the literature review the investigation of this parameter by Airoldi, (2010), Howey, (2010) and Hey et al., (2010) were reported. The geometrical similarity in the air-gap of a Rotor-Stator (R-S) system have led researchers to adopt correlations from classical studies of R-S systems for axial flux machines (Gieras et al., 2008, Childs, 2011, Howey et al., 2012). These correlations are also adopted in this thesis, which assumes smooth surfaces for the rotor and stator to determine values of thermal resistances.

Heat transfer in rotor-stator gap of enclosed rotor-stator systems

The fundamental fluid mechanics associated with enclosed R-S systems has been established by Daily and Nece, (1960). The author describes four flow regimes for enclosed rotor-stator discs with no superimposed flows. The flow regimes were categorized by the air-gap ratio G and the rotational Reynolds number Re_ϕ. The flow was observed to move radially outward at the rotating disc and return radially inwards

at the stator disc. For a small gap ratio G, the boundary layers at the rotor and stator were observed to be merged, while for a large gap ratio, the boundary layers remain separate with a bulk fluid core between the discs being observed to rotate at approximately half the rotor speed. The moment coefficient on the disc for values of $10^3 < \mathrm{Re}_\phi < 10^7$was measured. The results were also replicated by Kreith, (1968), for which he proposed minor corrections. The flow regimes are defined in Table 3.3 and shown in Figure 3.7.

Table 3.3 Definition of Flow Regimes and correlations

Flow Regime	Description	Moment Coefficient	
		(Daily and Nece, 1960)	(Kreith, 1968)
I	Laminar flow, small R-S gap, Merged boundary layers	$C_m = \frac{\pi}{GRe_\emptyset}$	
II	Laminar flow, Large R-S gap, Separate boundary layers	$C_m = 1.85G^{0.1}Re_\emptyset^{-0.5}$	$C_m = 2G^{0.1}Re_\emptyset^{-0.5}$
III	Turbulent flow, Small R-S gap, Merged boundary layers	$C_m = 0.04G^{-0.2}Re_\emptyset^{-0.25}$	$C_m = 0.036G^{-0.166}Re_\emptyset^{-0.25}$
IV	Turbulent flow, Large R-S gap, Separate boundary layers	$C_m = 0.051G^{0.1}Re_\emptyset^{-0.2}$	$C_m = 0.054G^{0.1}Re_\emptyset^{-0.2}$

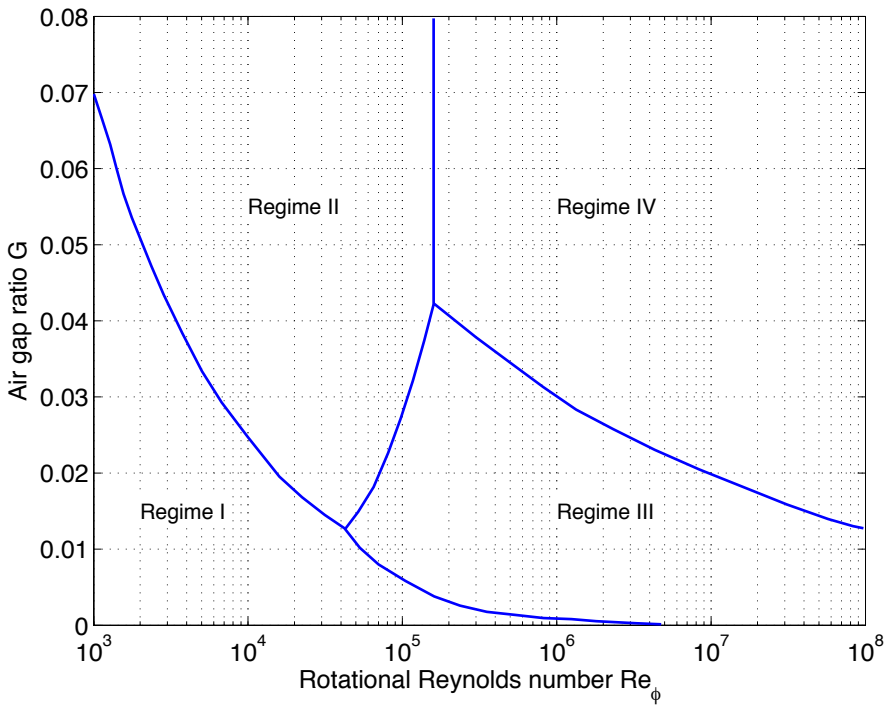


Figure 3.7. Chart Showing the four flow regimes. Data from Daily and Nece, (1960).

For torque equilibrium the moment created by the rotor is dissipated on the stator and the enclosing wall, hence:

$$C_{mR} = C_{mS} + C_{mW} \quad \text{eqn. 3.16}$$

However, for an axial flux machine in which the R-S gap is very small, it can be assumed that:

$$C_{mS} \gg C_{mW} \rightarrow C_{mR} \simeq C_{mS} \quad \text{eqn. 3.17}$$

Owen, (1971), shows that the Reynolds analogy can be extended to enclosed R-S systems. The author establishes a procedure to correlate the Nusselt number Nu with the moment coefficient C_m imposed on the fluid as:

$$Nu_{avg} = \frac{Re_{\phi} C_m}{\pi} \quad \text{eqn. 3.18}$$

The analogy is valid as long as the following conditions are observed:

1. The Prandtl number is close to 1
2. The disc temperature varies as a quadratic function of the radius and the total enthalpy of the free stream is constant
3. The radial and tangential viscosities are equal
4. The initial tangential velocity and enthalpy distributions are similar

Rasekh et al. (2015) applied these assumptions to electrical machine analysis and showed that at values of $G = 0.013, Re_{\emptyset} \approx 4x10^5$ the difference the Nu at rotor and stator was less than 5%. This increases as G and $Re_{\emptyset}$ increases. A detailed review of thermo-fluid research in enclosed R-S gaps with no inflows is found in Launder et al, (2010).
With the correlations governing the convective heat transfer established, the following section uses typical motor geometry values to establish the thermal resistances. The heat generated by the stator of each machine is compared to the heat rejected. The implications of the thermal results on the vehicle architecture are discussed

3.4. Results and Discussion

Using typical values for a motor design shown in

Table 3.4, the convective and conductive thermal resistances can be established. A breakdown of the thermal resistance for AFIR machines is shown in Table 3.5.

Table 3.4 Typical values for estimating the machine thermal resistance

	AFIR	**AFIS**
Stator Windings		
Half Thickness [mm]	15	15
Equivalent conductivity [W/mK]	3	3
Stator Housing		
Thickness [mm]	5	2
Conductivity [W/mK]	50	0.4
Rotor Stator Gap ratio G	0.01	0.01
Rotor		
Thickness [mm]	N/A	5
Conductivity [W/mK]	N/A	50

It can be seen that the thermal resistance for AFIR machines is dominated by the convective component at the casing. This is dictated by the ram air from the vehicle speed and the planar Reynolds numbers on the outer surfaces. In this analysis the ram air speed was assumed to be 17.2 m/s based on the average speed of 62 km/h in the EUDC.

Table 3.5 Table of thermal resistances for AFIR topology

Description	Symbol	15” wheel motor	13” wheel motor	11” wheel motor
Conduction through the stator windings	R5	0.0438	0.0584	0.0816
Conduction through the machine casing	R6	0.00088	0.00117	0.00163
Convection from the machine casing	R7	0.296	0.383	0.516

Figure 3.8 shows a breakdown of the thermal resistance for AFIS machines and the variation with motor speed. The thermal resistance of AFIS machines is dominated by the convective resistance at the rotor stator gap. This is followed by the convective thermal resistance from the rotor to ambient up to rotor speeds of approximately 6000 rpm, beyond which the conductive thermal resistances takes over. Similar calculations for motors fitted to 13” wheels and 11” wheels show the same trends although the resistances tend to shift upwards due to the smaller surface area.

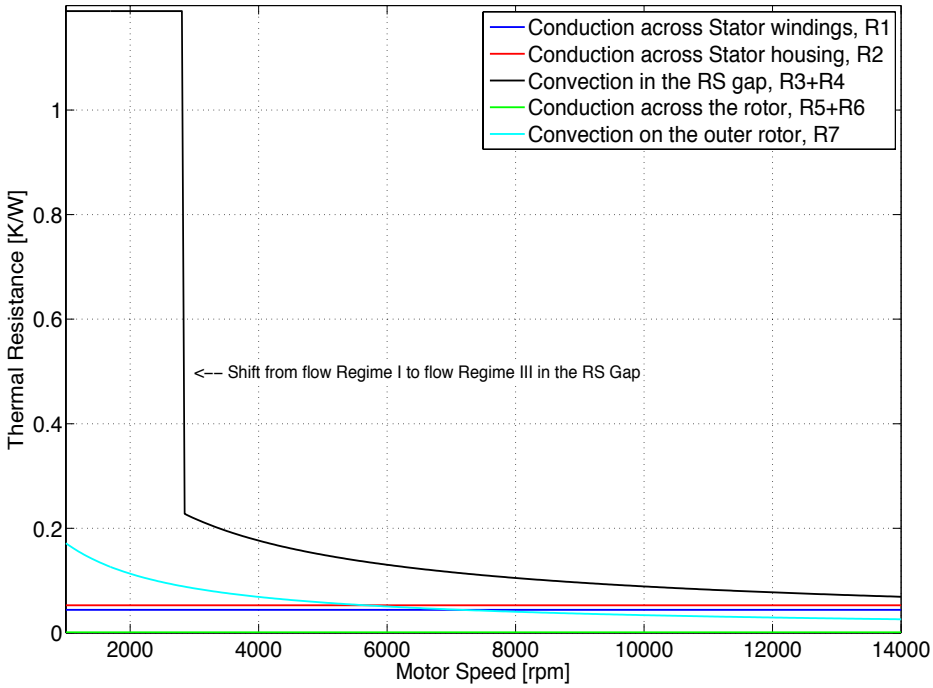


Figure 3.8. Example of the thermal resistance components for an AFIS topology fitted to a 15" wheel

To identify an air-cooled drivetrain topology that can support a constant heat loss without the motor overheating, the heat transfer from each machine topology is computed. This is then compared to the heat transfer curves for each machine topology. Figure 3.9 compares the heat load to the heat transfer for an AFIR topology while Figure 3.10 is for AFIS topology.

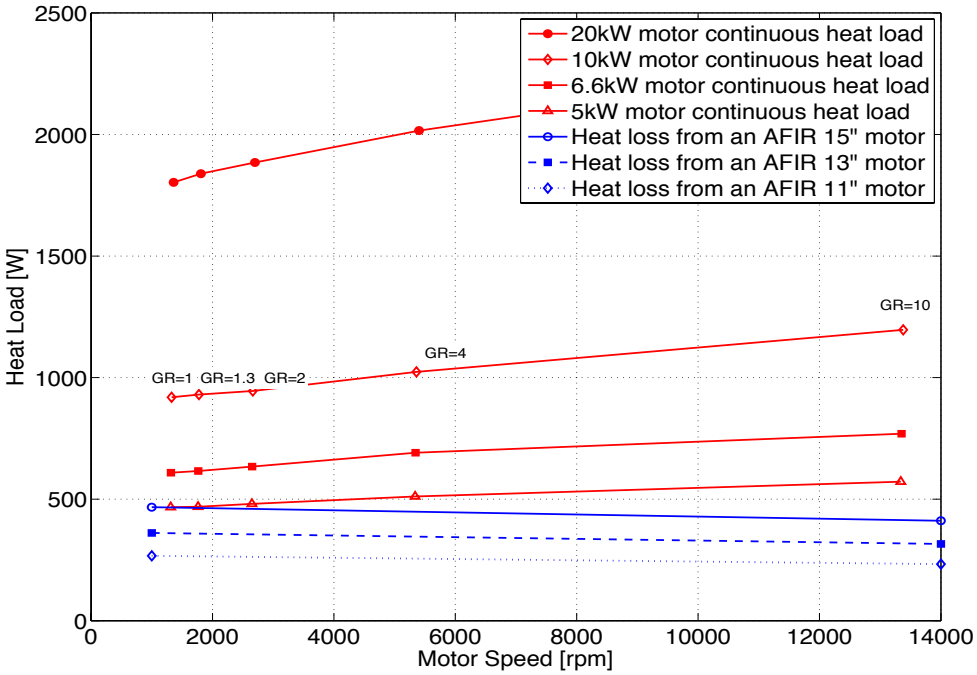


Figure 3.9. Plot of the continuous heat generation and continuous cooling capacity for AFIR machine

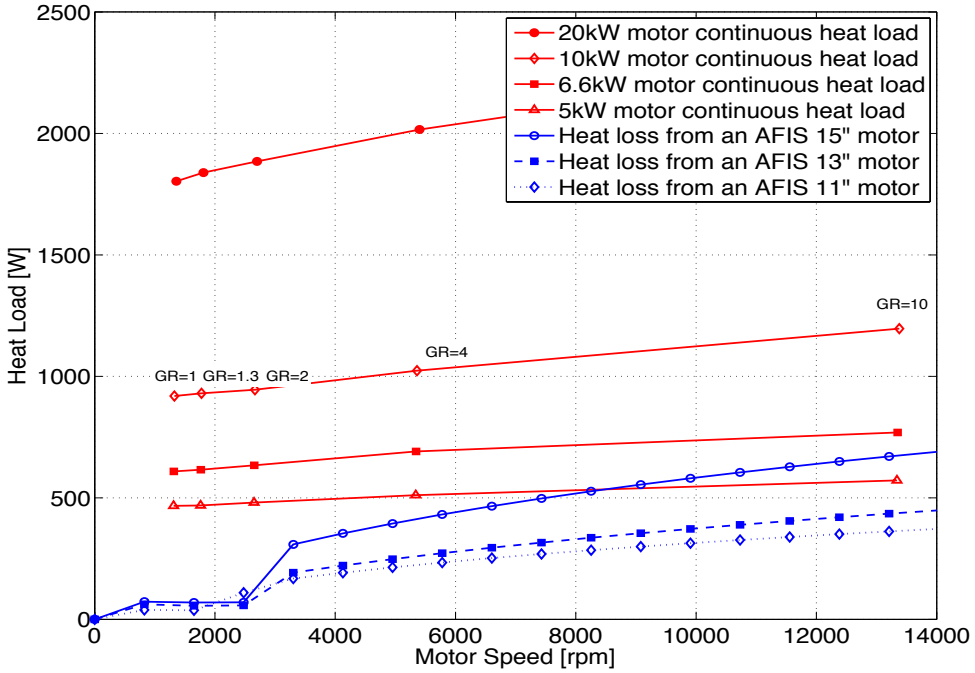


Figure 3.10. Plot of the continuous heat generation and continuous cooling capacity for AFIS machine

This study identifies convection to play a significant role in both machine topologies. It can be seen that if the machines are made from ideal surfaces, AFIR machines are subjected to constant thermal resistance dictated by the ram air. This allows it to support the continuous operation of machines with a power up to 5 kW at speeds and speed up to 2000 rpm. In the context of in wheel application the machine will be coupled to a gear ratio of up to 1.3. Conversely the thermal resistance of AFIS machines decreases with rotor speeds. This supports the continuous operation of a 5 kW machine at speeds beyond 8000 rpm. In the context of urban mobility and application to an in-wheel motor a drivetrain using an AFIS topology will require a gearing ratio greater than 6.

Having investigated the ideal scenario the last section of this chapter investigates the effect of extended surfaces on the machine housing.

3.5. Improving the heat transfer from the casing

In the analysis of Sections 3.3 and 3.4, the machines were considered to have ideal surfaces. However, electrical machines often employ extended surfaces to improve the thermal resistance from the casing. While the optimal design of heat sinks can be found in the literature (Lee, 1995, Teestra et al., 1999, Culham and Muzychka, 2001), this is not the scope of this section, but rather to give the reader and thermal designer

a sense of the impact of changing variables in the design process and the complexities in introducing a new component. While AFIR type machines may make use of traditional extended fins on the casing as shown in Figure 3.11, AFIS type machines requires a rotating heat sink geometry mounted on the rotor. Some examples of this include disc brakes or un-shrouded ribs are shown in Figure 3.12. Table 3.6 and Table 3.7 list the advantages and disadvantages from such heat sink geometries. Hence, this section identifies the trade off between the improvement in thermal performance and added weight that the thermal designer would be required to make during the design procedure of the drivetrain. To achieve this, established correlations for heat sink geometries are used and the thermal resistances of the heat sink is weighed against its additional mass.

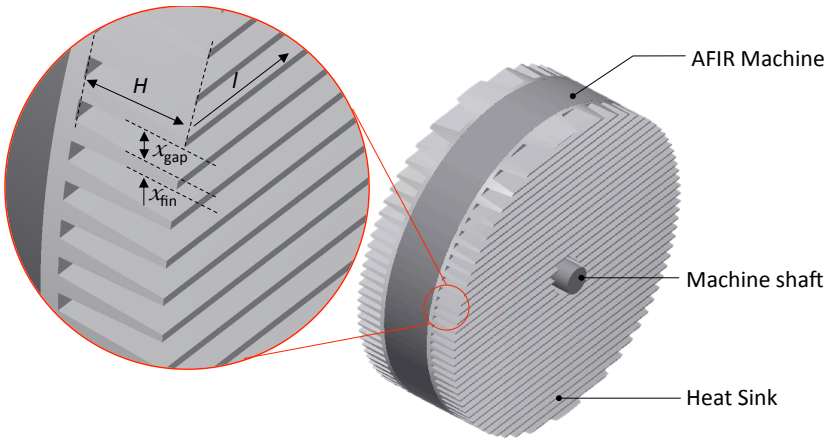


Figure 3.11. CAD of AFIR type machine with extended surfaces. Insert: example of the fin geometry

Table 3.6 Heat sink solutions for the motor casing of an AFIR machine

Solution	Advantages	Disadvantage
Ideal Motor housing	No added weight	Poor heat transfer capability
Fins on Casing	Improvement in heat transfer	Added weight (2-20 Kg)
	Simple bolt-on solution	Added noise

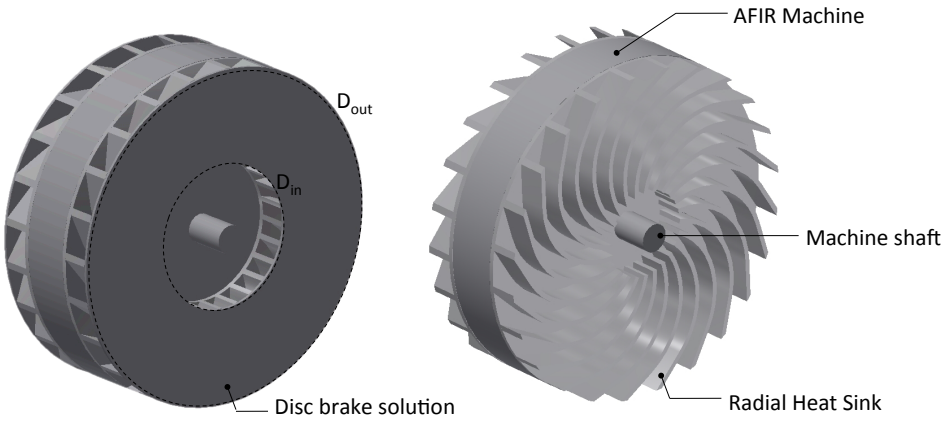


Figure 3.12. CAD model of a shrouded disc brake heat type sink (left) and an unshrouded radial vane heat sink for an AFIS machine

Table 3.7 Heat sink solutions for the motor casing of an AFIS machine

Solution	Advantages	Disadvantage
Ideal Motor housing	No added weight	Poor heat transfer capability
Shrouded radial fins (resembling disc brake geometry on rotor)	Improvement in heat transfer Bolt-on solution	Approximately 1.65 kg added weight (depending on the number of radial fins)
Unshrouded radial fins	Improvement in heat transfer Bolt-on solution or extrusion	Approximately 1 kg added weight

3.5.1. A Heat Sink for the casing of AFIR machines.

In Section 3.2.3 it was shown that a plain geometry of AFIR machine are only able to support machines up to around 5 kW at rotating speeds lower than 2000 rpm. The introduction of a heat sink reduces the thermal resistance from the casing, thereby improving the heat transfer from the machine casing. Heat sinks come in various geometries, (Lee, 1995). Developing an optimum geometry for the application requires a detailed calculation and a trade off between performance, dimensional constraints, airflows and cost, (Teetstra, et al., 1999). While the design of an optimum heat sink is beyond the scope of this chapter, the extent of the enhancement in machine performance of air-cooled electrical machines is an interesting topic. Therefore this section considers a plate fin heat sink as one of the most common configurations and makes use of empirical correlations to obtain an estimation of its performance and effect. The symbols used in this analysis are referred to the definition in Figure 3.11. Teetstra, et al., (1999) defines the thermal resistance of a parallel plate-fin heat sink R_{HS} as:

$$R_{HS} = R_{base} + R_{fin} \quad \text{eqn. 3.19}$$

where R_{base} is the conductive thermal resistance across the thickness of the heat sink base. R_{fin} is the overall thermal resistance across the fins as defined by Kraus and Bar-Cohen, (1995):

$$R_{fin} = \frac{1}{h\left(A_{base} + N_{fin}\eta_{fin}A_{fin}\right)} \quad \text{eqn. 3.20}$$

where A_{base} is the base area while $A_{fin}$is the surface area for one fin. N_{fin} is the number of fins while η_{fin} is the fin efficiency. Under optimum study the fin efficiency is a key parameter as to establish the fin thickness as it defines the ratio of heat convected from fin area to the heat conducted along the fin, (Incropera and DeWitt, 1996):

$$\eta_{fin} = \frac{\tanh\left(m'.H\right)}{m'.H} \quad \text{eqn. 3.21}$$

where H is the fin height and *m'* is a heat sink parameter defined by:

$$m' = \sqrt{\frac{\mathrm{h}P_{fin}}{k_{fin}A_{fin}}} = \sqrt{\frac{2\mathrm{h}(l + x_{fin})}{k_{fin}lx_{fin}}} \quad \text{eqn. 3.22}$$

where k_{fin} is the conductivity of the fin while $x_{fin}$is the thickness of the fin. h is the HTC for the fins defined in terms of the Nusselt number *Nu*, air conductivity k_{∞}, and average gap thickness between the fins x_{gap}:

$$h_{fin} = \frac{Nu.k_{\infty}}{x_{gap}} \quad \text{eqn. 3.23}$$

Teetstra, et al., (1999) presents an analytical correlation for the Nusselt number for shrouded heat sinks that includes the effects of fully developed and developing flows. The asymptotic effects of the fully developing and developed flows are combined using the inverse form solution by (Churchill and Usagi, 1972):

$$Nu = \left[\left(\frac{1}{Nu_{fd}}\right)^{n} + \left(\frac{1}{Nu_{dev}}\right)^{n}\right]^{\left(\frac{-1}{n}\right)} \quad \text{eqn. 3.24}$$

The index was found to have a value of 3 by comparing the solution to numerical models. Hence the Nusselt number for the fins is defined as:

$$Nu = \left[\frac{1}{(0.5Re^{*}.Pr)^{3}} + \frac{1}{\left(0.664\sqrt{Re^{*}}.Pr^{0.33}\sqrt{1 + \frac{3.65}{\sqrt{Re^{*}}}}\right)^{3}}\right]^{-0.33} \quad \text{eqn. 3.25}$$

where Pr is the Prandtl number and Re^* a variation of the Reynolds number in the fin gap defined as:

$$Re^* = \left(\frac{V.x_{gap}}{\nu}\right).\left(\frac{x_{gap}}{l}\right) \quad \text{eqn. 3.26}$$

The model is valid for $0.1 < Re^* < 100$. The optimal fin and gap spacing of a heat sink depends on the velocity of the airflow within the channels. In this research the heat sink analysis is simplified by assuming that the shrouded heat sink is mounted with a scoop that captures the ram air at an average vehicle speed of 62km/h. The velocity is based on the Extra Urban Drive Cycle (EUDC). However, Culham and Muzychka, (2001), show how the pressure drop in the heat sink channels vary with fin geometry and number of fins. This affects the operating airflow through the heat sink and the heat transfer coefficient. Furthermore, Simons and Schmidt, (2012) providing insight into the complexities of optimizing heat sinks for this application by investigate the effect of bypass air over un-shrouded heat sinks. This research also ignores secondary aerodynamic effects under the wheel arch. To provide an idea of the decision-making process in designing a heat sink for a machine casing, this thesis considers a case study on a motor fitted to a 15" wheel.

The variation of heat sink thermal resistance with fin thickness, fin length and number of fins is shown in Figure 3.13. Likewise, the effect of the heat sink design parameters on its weight is shown in Figure 3.14. This provides the thermal designer with the necessary information to weigh the benefits of reducing the thermal resistance against the added mass. The improvement in heat transfer for this case study is shown in Figure 3.15. The introduction of the heat sink allows the machine to sustain continuous loads from 10 kW machines at a wide range of rotor speeds and gear ratios. A similar exercise for motors installed onto 13" and 11" wheels found similar improvements albeit to a lesser degree. Following the investigation on the heat sink in AFIR machines, the attention is turned to heat transfer from the casing of AFIS machines.

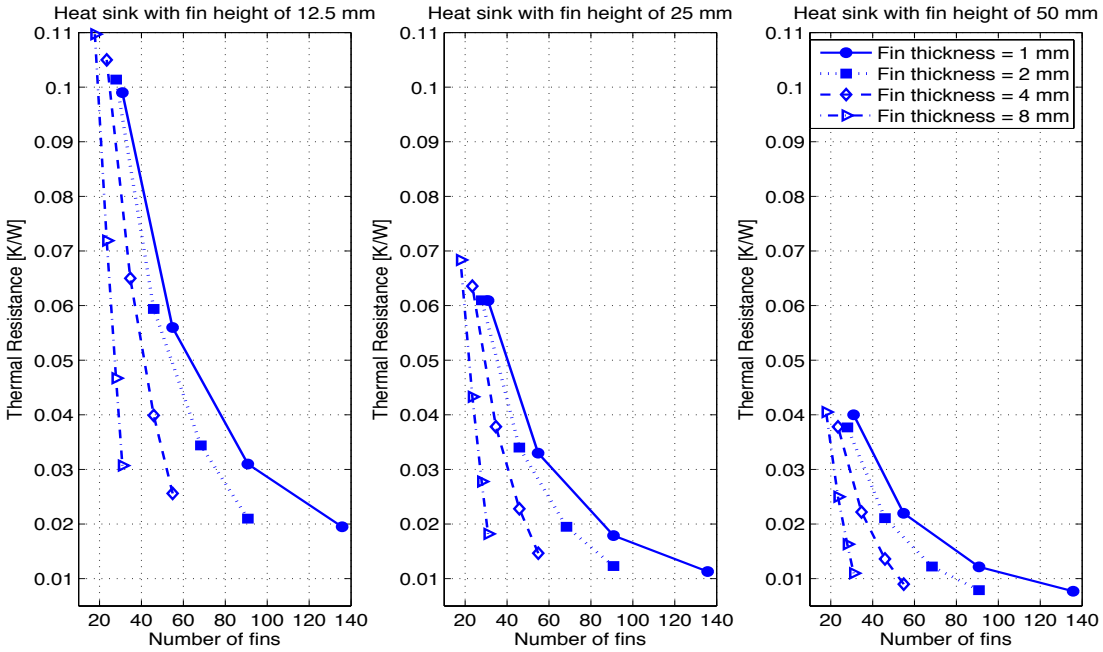


Figure 3.13.Variation of heat sink thermal resistance with fin thickness and number of fins

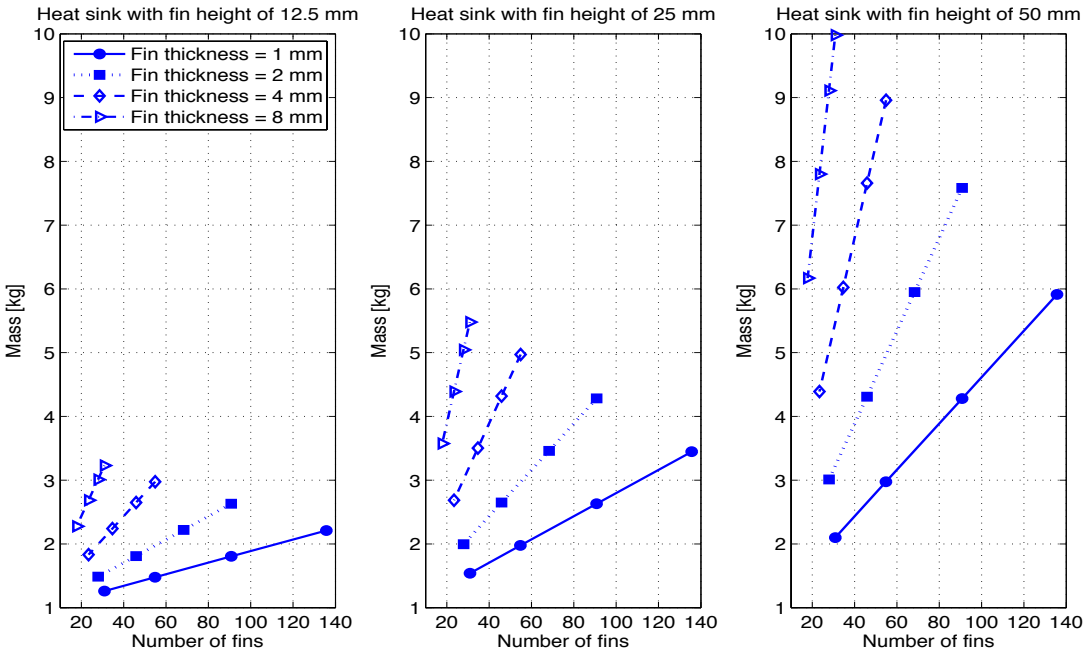


Figure 3.14. Variation of heat sink mass with fin thickness and channel spacing

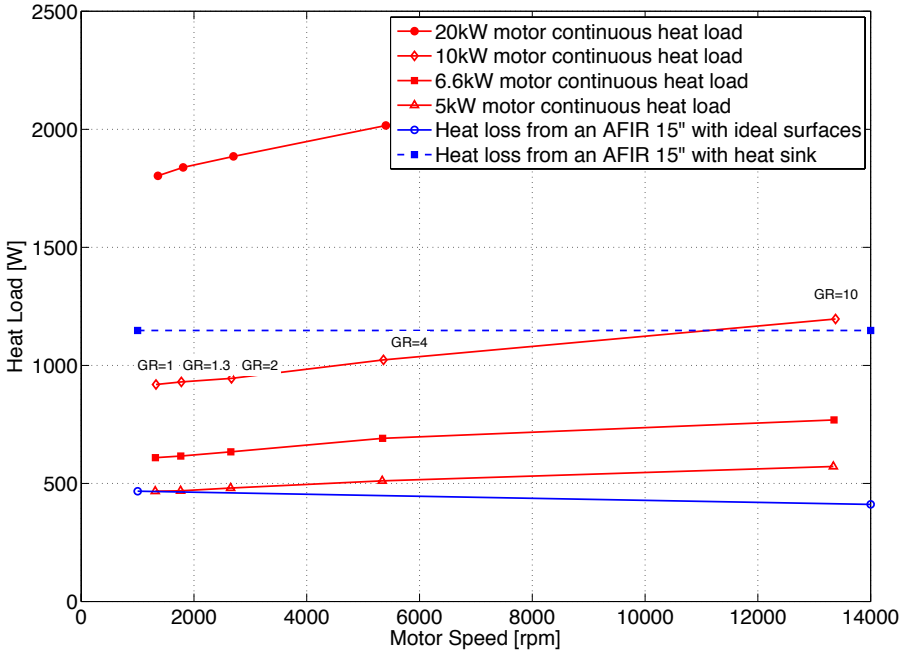


Figure 3.15. The cooling performance of a motor fitted to a 15" wheel with an ideal scenario (no external surfaces), and with an installed heat sink

3.5.2. A Heat Sink for AFIS machines.

In Section 3.3.2 it was shown that ideal geometry of AFIS machines are only able to support machines smaller than 5 kW at rotating speeds greater than 8000 rpm. This section examines the effect of reducing the thermal resistance from the machine casing by installing a rotating heat sink as shown in Figure 3.12. This analysis makes use of existing correlations applied to automotive disc brakes. While there have been many modern analysis using computational fluid dynamics (Gallindo Lopez, 2001, Wallis et al., 2002, McPhee and Johnson, 2007), these are often referenced to empirical heat transfer correlations by Limpert, (1975) for straight radial vanes, and Sisson, (1978) for straight radial vanes with rounded edges. The correlations are replicated in Table 3.8.

While many other more complex vane geometries such as tear drop designs have been explored, these are not found to offer a greater heat transfer advantage (Wallis, 2002). The straight radial vanes with rounded edges are found to enable a higher airflow through the disc. Therefore this research makes use of the correlations by Sisson. The author recognizes that these correlations have been validated for lower rotational speeds than that of AFIS machines and notes that this is a limitation of this research.

Table 3.8 Empirical correlations heat transfer correlations from rotor passages

Straight Radial Vanes, (Limpert, 1975)		Rounded Straight Radial Vanes, (Sisson, 1978)	
$Nu = 1.86\left(Re_{D_h}.Pr\right)^{0.33}\left(\frac{D_h}{l}\right)^{0.33}$ for $Re_{D_h} < 1x10^4$	eqn. 3.27	$Nu_{\left(D_{out}/2\right)} = 0.045Re_{\left(D_{out}/2\right)}^{0.8}\left(D_{out}/2\right)^{0.2}.\left[1+6.6\left(D_{out}/2\right)^{0.8}\right]$	eqn. 3.32
$Nu = 0.023{Re_{Dh}}^{0.8}Pr^{0.33}\left[1+\left(\frac{D_h}{l}\right)^{0.67}\right]$ for $Re_{D_h} > 1x10^4$	eqn. 3.28		
$Re_{D_h} = \frac{V_{avg}D_h}{\upsilon}$	eqn. 3.29	$Re_{\left(D_{out}/2\right)} = \frac{V_{avg}\left(D_{out}/2\right)}{\upsilon}$	eqn. 3.33
$V_{avg} = 0.5V_{in}\left(1+\frac{A_{in}}{A_{out}}\right)$	eqn. 3.30	$V_{avg} = \sqrt{\left(-0.02+-0.908D_{in}-0.202{D_{in}}^2\right)}.\omega\left(D_{out}/2\right)$	
$V_{in} = 0.0518\mathrm{n}\left({D_{out}}^2-{D_{in}}^2\right)^{0.5}$	eqn. 3.31		eqn. 3.34

where D_h is the hydraulic vane diameter and l is the vane length. Re is the Reynolds, V_{avg} is the average velocity through the vane and V_{in} is the inlet velocity. A_{in} and A_{out} are the flow area of the disc vanes and D_{in} and D_{out} are the disc inner and outer diameters respectively. n is the rotational speed in rpm.

Figure 3.16 shows that a rotating disc with vanes achieves a lower thermal resistance than an ideal rotating disc. Despite this, Figure 3.17 shows that this does not increase heat transfer from this machine topology, because the thermal path of this machine topology is dominated by the convective heat transfer in the rotor-stator air-gap.

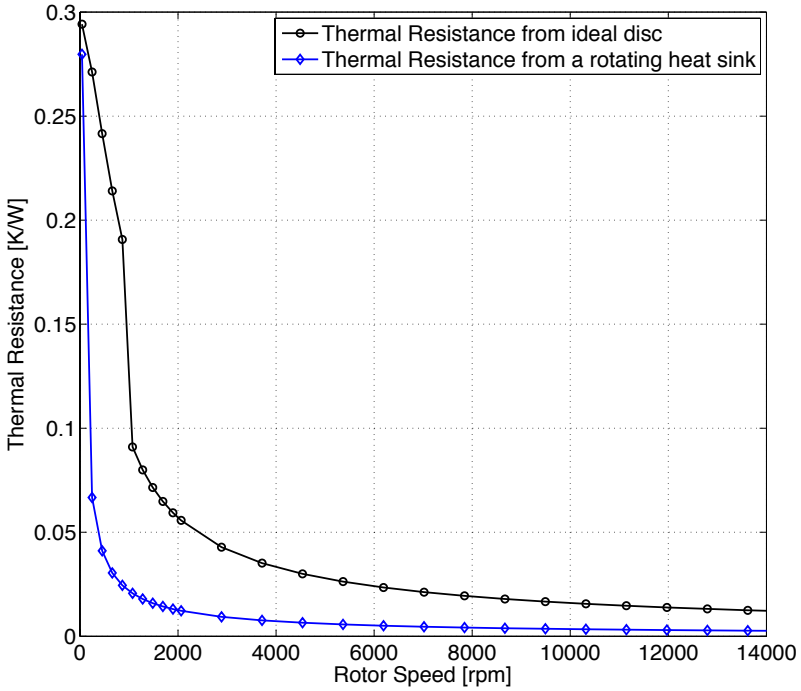


Figure 3.16. Comparison between the thermal resistance of a rotating disc and rotating heat sink

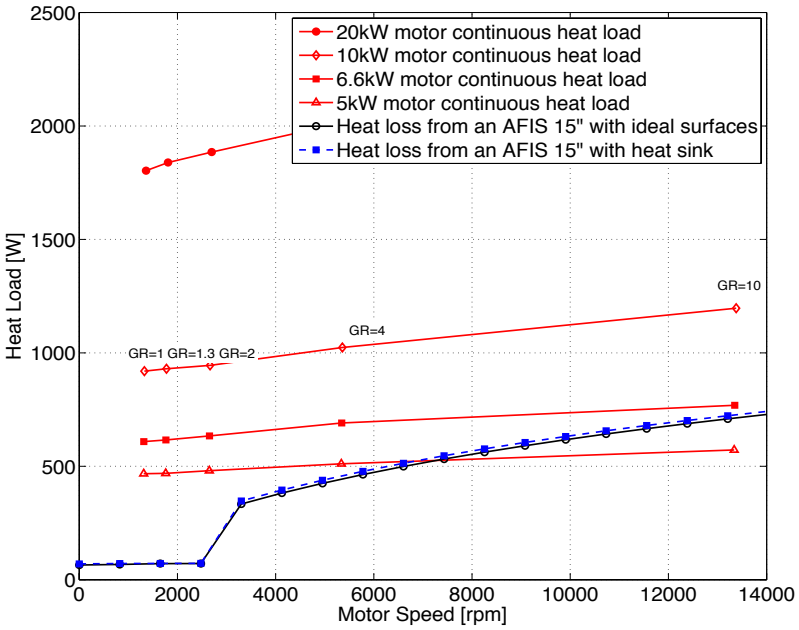


Figure 3.17. The heat transfer from a motor fitted to a 15" wheel with an ideal scenario (no external surfaces), and with an installed heat sink

3.6. Conclusion

While the literature presented several concepts of in-wheel motors applied to road transportation, the thermal analysis from such designs was lacking. This chapter addressed this gap and showed that air cooled axial flux machines suffer from thermal limitations. Generally, AFPM with enclosed R-S gaps and ideal surfaces lack the ability to support continuous operation of machine greater than 5 kW. However machine topology was found to play an important role. Heat transfer from AFIR machines depends solely on the ram air from the vehicle velocity and the thermal resistance from the machine casing was found to dominate the heat transfer. It was shown that this machine design favours low machine speeds. Introducing extended surfaces on the machine casing supports a continuous operation of machines up to 10 kW. Conversely, the heat transfer from AFIS is dependent on the rotor speed. The thermal resistance in AFIS machines is dominated by the convection in the rotor-stator gap and is reduced with increasing rotor speeds. This favours high machine speeds. Extended fins on the outer surfaces were shown to have very little impact on the heat transfer from the machine. In axial flux permanent magnet machines, the rotor-stator gap is often between 1 - 2 mm thick. Augmenting the heat transfer in the rotor-stator gap is challenging.

This thesis addresses this problem in the next chapter by proposing a novel evaporative cooling mechanism. While this chapter investigated the implications of the cooling mechanism on the application to urban mobility, choosing the right topology will require an in-depth feasibility study to assess the overall complexity, weight and cost issues associated with adapting AFIR and AFIS machines drive trains.

4 | Evaporative Cooled Electrical Machines

The previous chapter showed how totally enclosed air-cooled axial flux machines suffer from thermal limitations. The Axial Flux Internal Stator (AFIS) topology was found particularly susceptible to low convective heat transfer in the rotor-stator gap. This chapter addresses this problem by adopting evaporative cooling as a means for transporting heat from the machine's internal stator to the outer rotor. The chapter investigates the challenges linked with this mechanism within the boundaries of an electrical machine with a segmented stator and concentrated windings. The YASA topology is hence used as a test case study. This chapter is based on papers 2 and 3.

4.1 Context to this chapter

The ability of the latent heat to absorb large quantities of thermal energy during the phase change process has been well documented in Silverstein, (1992) and Reay, (2006) amongst others. The application of this mechanism to cool electrical machines, for example by integrating heat pipes has been suggested in the literature (Liang, 1974, Torok, 1976, Kostikov et al., 1980, Thoolen te Horn, 1996, Scowby et al., 2004) Similar designs have been recently applied by electric vehicle manufacturers such as Tesla, (Fedoseyev and Pearce, 2014). However, these designs make a clear distinction between the cooling device and the cooled component. Woolmer, (2010), proposes a derivative of the YASA machine with integrated evaporative cooling for a direct-drive in wheel motor. The machine makes use of a single inner stator between the two axial rotors. The rotors are linked together by the outer cylinder, thus forming an outer rotor machine.

This chapter adopts an experimental approach to prove the concept and develop an operating envelope of the machine. The concept makes use of a two-phase coolant in

direct contact with the stator windings. As heat is absorbed from the windings, the liquid coolant vaporizes and moves within the motor to the cooler rotor surfaces. Upon contact with the cooler surfaces it condenses back to liquid droplets, which trickle back to the liquid pool. This self-sustaining loop is maintained as long as a temperature gradient between the stator windings and ambient air is kept. The phase change material therefore acts as a heat transport mechanism between the stator and the rotor, solving the heat transfer limitation in the rotor-stator gap. This chapter presents the underlying study behind this patent.

The design of the cooling concept is in many aspects similar to a heat pipe with each individual stator pole piece acting as an evaporator while the outer rotor acts as a condenser. A comparison between the heat pipe and the proposed evaporative cooled electrical machine is shown in Figure 4.1. The effectiveness of this cooling concept depends on a number of limitations, most of which are common with heat pipes. The following section therefore investigates some of the design considerations and operating limits of heat pipes and their application to electrical machines.

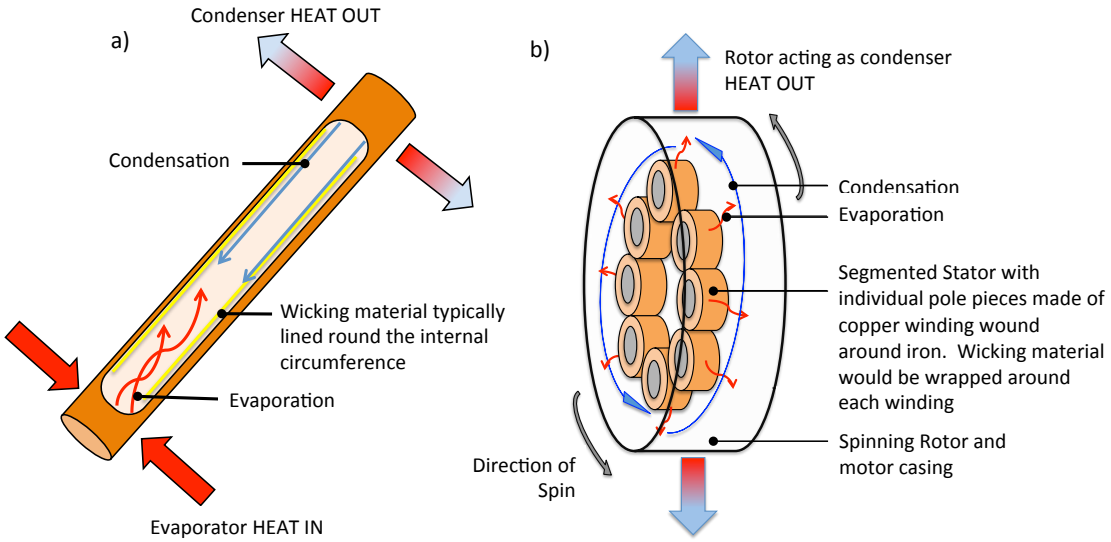


Figure 4.1. Similarities in operating principles between a) heat pipe, and b) evaporative cooled machine

4.2 Design Considerations and Operating Limits

4.2.1. The Working Fluid

The choice of the working fluid in heat pipes is influenced by thermodynamic properties such as the operating temperature, the latent heat of vaporization, and the vapour pressure, as well as chemical properties such as compatibility with the wick,

chemical stability, and toxicity (Peterson, 1994). In the application within the electrical machine, the working fluid is required to have dielectric properties and compatibility with the insulation on the windings. Bruetsch et al., (2008) suggest that at low winding temperatures (<50 ^{o}C), the copper windings are rigid and do not cope well with mechanical stresses. At this temperature range the authors note that mechanical failures are predominant. However at high temperatures the copper resistivity and associated losses increases and the insulation life decreases. The author suggests that winding temperatures between 90-100 ^{o}C offer a good compromise between electrical losses and mechanical malleability.

The author of this thesis is aware of the importance of low dielectric properties to avoid insulation breakdown when subjected to intense electrical fields, and compatibility of the working fluid with the winding insulation. However, the selection of the working fluid for this research was based solely on thermodynamic considerations, namely the boiling point and latent heat of vaporization. A robust test programme to assess the deterioration of the insulation life for the choice of working fluids will be required. In order to establish the working fluid for the evaporative cooled electrical machine, the boiling point, the latent heat of vaporisation and the dielectric constant of alcohols and refrigerants with a boiling point below 100 ^{o}C were surveyed and are shown in Figure 4.2.

In evaporative cooling, the latent heat absorbed Q by the working fluid is determined by the product of its mass flow rate $\dot{m}$ and latent heat of vaporization L_v:

$$Q = \dot{m}.L_v \qquad \text{eqn. 4.1}$$

Conversely the heat rejected from the machine casing is proportional to the temperature difference between the machine and ambient as shown in eqn. 1.5

Hence the heat transfer mechanism in the evaporative cooled machine requires achieving an important balance between the heat absorbed from the stator and that rejected by the motor casing. The design of the wick on the segmented stator and the choice of the respective latent heat of vaporisation of the working fluid; as well as the design of the heat sink on the machine casing and the respective boiling point of the working fluid play an important role in achieving this balance. If the wick pumping

capacity is small, a working fluid with a high latent heat of vaporization is preferred in order to maximise the heat absorbed. However, if the evaporated fluid is not condensed back to liquid quickly enough to replenish the liquid pool, a working fluid with a higher boiling point can be chosen. The higher boiling point raises the motor wall temperature, encouraging heat transfer to ambient and a higher rate of condensation. With this rationale, the choice of fluids was narrowed down to two fluids: (1) methanol, due to its high latent heat of vaporization and (2) propanol, for its high boiling point. Experiments with these working fluids were carried out in parallel. However, prior to the experimental investigation, the following section discusses the classical heat pipe limits and their application to the motor concept.

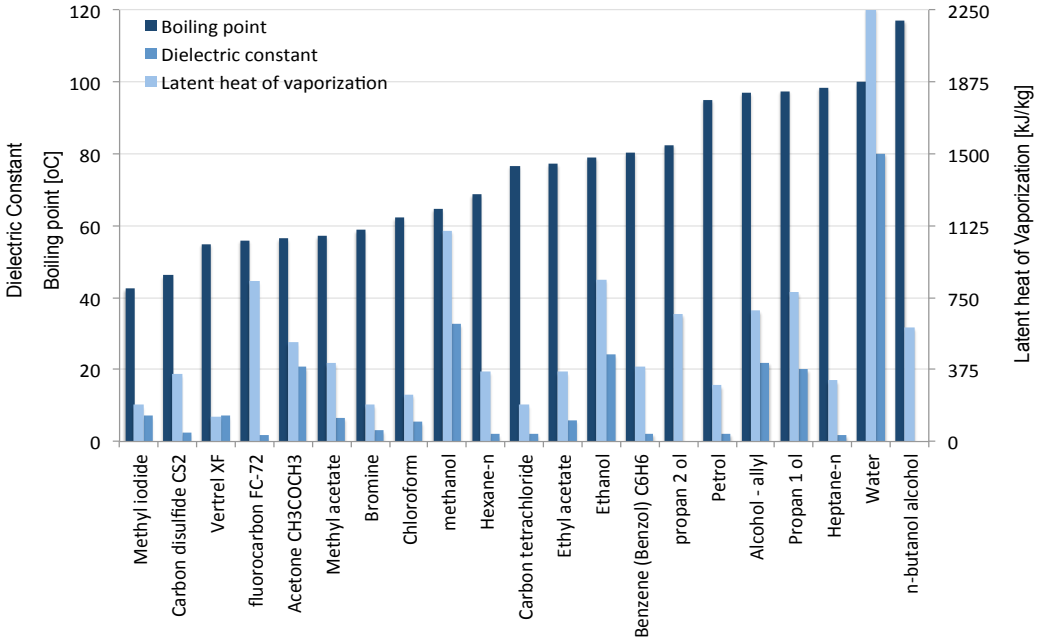


Figure 4.2. Properties of working fluid candidates, data from Boiling Points, Fluids and Gasses, (2013), Fluids – Latent Heat of Evaporation, (2013) and Dielectric Constants for some common Liquids, (2013)

4.2.2. Classical Heat Pipe Limits

Having identified potential candidates for the working fluids, this section discusses the classical heat pipe limits and discusses their influence on the design of the evaporative cooled electrical machine. The heat transfer in heat pipes is often limited by one or more processes, which are referred to as the classical heat pipe limits. These are often summarized as: the viscous limit, the sonic limit, the capillary limit, the entrainment limit, and the boiling limit. The heat transfer from the heat pipe is also limited by the ability of the heat pipe to reject heat – known as the condenser limit.

The analysis on the machines ability to reject heat from its rotors has already been explored in Chapter 3 and therefore this chapter focuses only on the classical heat pipe limits and the validation of the concept. A detailed explanation of the classical heat pipe theory can be found in Silverstein, (1992), and Dunn and Reay, (1994). The authors produced a map of these operating limits within the operating profile of a heat pipe, which is reproduced in Figure 4.3. A brief description of these limits, and how they apply to the design of an electrical machine is now produced:

- The Sonic Limit: As the mass flow rate of the vapour leaving the evaporator increases, the process reaches a point at which the flow gets choked. This limits further increase in mass flow rate and hence a further increase in heat transport of the heat pipe. However, this is a function of the pipe geometry. In this motor application the vapour will not be restricted by the pipe geometry and hence the sonic limit is less critical.

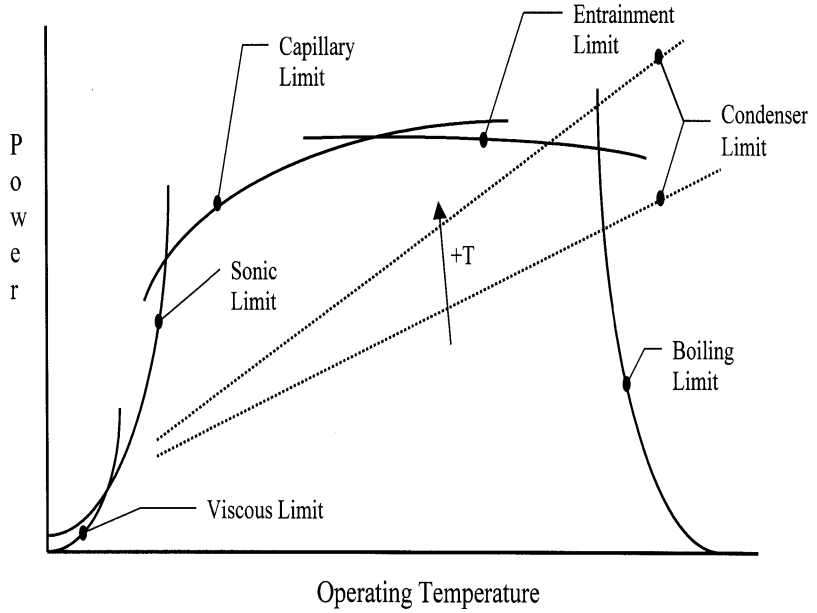


Figure 4.3. Schematic of the classical heat pipe limits with as the evaporator temperature increases, reproduced from Dunn and Reay, (1994)

- In heat pipe operation, the wick returns the liquid to the evaporator through its capillary pumping mechanism. If the wick fails to pump the fluid at an adequate flow rate, the evaporator dries out and the heat pipe operation fails. In electrical machines, this limit is critical as reaching the capillary limit would lead to the overheating of the stator windings. This limit is investigated further in Section 4.2.3 and Section 4.5.1.

- The Entrainment limit: The design of heat pipes is such that both the vapour flowing towards the condenser and the counter flowing condensate passes through the same volume. At sufficiently high vapour velocity, the shear stress causes the liquid droplets to get torn away from the bulk condensate and transported back to the condenser. This limits the return of the condensate and the rate of replenishing the evaporator. However, this phenomenon is observed in very restricted passages associated with thin heat pipes. As the motor design does not suffer from the same restrictions, this limit is very unlikely to be reached.
- The Boiling limit: If the heat flux from the evaporator is too high, nucleation boiling from within the wick may occur. The vapor bubbles that form may hinder transport of liquid and wetting the evaporator surface. In the context of the application to the machine, the boiling limit may cause dry out causing the windings to overheat. Various authors (Dunn and Reay, 1994, Reay and Kew, 2006) show that an optimum wicking thickness that enables maximum heat flux before reaching the boiling limit can be found.

4.2.3. The Wicking Material and Capillary Limit

Wicks used in heat pipes are classified into homogeneous, composites, and advanced designs (Peterson, 1994, Dunn and Reay, 1994, Silverstein, 1992). These are typically made of stainless steel, nickel, copper, aluminum, or metal foams (MetaFoam, 2013). The construction of the wick is dependent on its compatibility with the working fluid. Although the pumping ability of metal meshes is well understood (Peterson, 1994, Dunn and Reay, 1994, Silverstein, 1992), these are typically correlated with the pipe geometry. Therefore such correlations cannot be adopted for the electrical machine. Furthermore, assembling a metal wick onto the stator windings involves risks of damaging the winding insulation. In view of this, alternative fabric materials were investigated.

Burton Simile, (2004), and Sishoo, (2012), investigated wicking in fabrics typically used in cleaning or sports wear. Wicking in fabrics is not only dependent on the pore size but also on the yarn, which is difficult to measure. In order to compare the wicking capacity of several fabrics, Burton Simile, (2004) adopted a standard vertical test, which compares the rate of climb of the liquid along a vertical wicking material.

The test is defined by DIN53924. In order to obtain an overview of the material requirements for the evaporative cooled machine this standard was also adopted during this research. The set up, shown in Figure 4.4 was used to measure the performance of various fabrics. The fabric material was lined up against a ruler while having one end dipped into a pool of liquid. The vertical climb of the liquid against gravity was filmed on camera, from which the vertical climb of the fluid with time was then derived. Various materials are compared. An example of the comparison of wicking performance with methanol is shown in Figure 4.5.

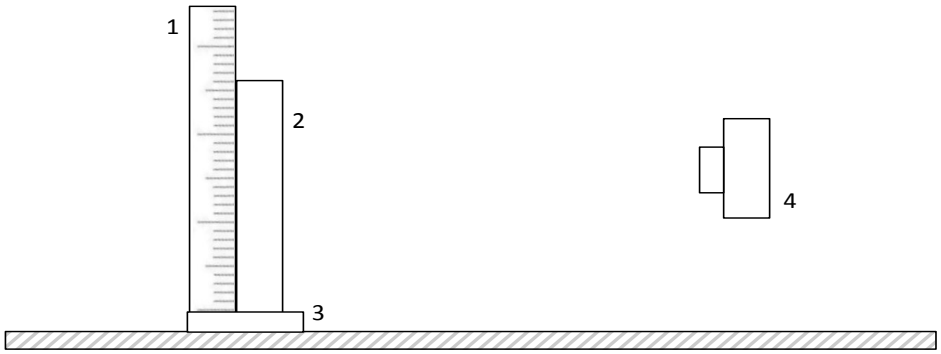


Figure 4.4. Setup to measure the wicking rates for various fabrics with 1) ruler, 2) wicking material under test, 3) liquid pool. 4) video camera

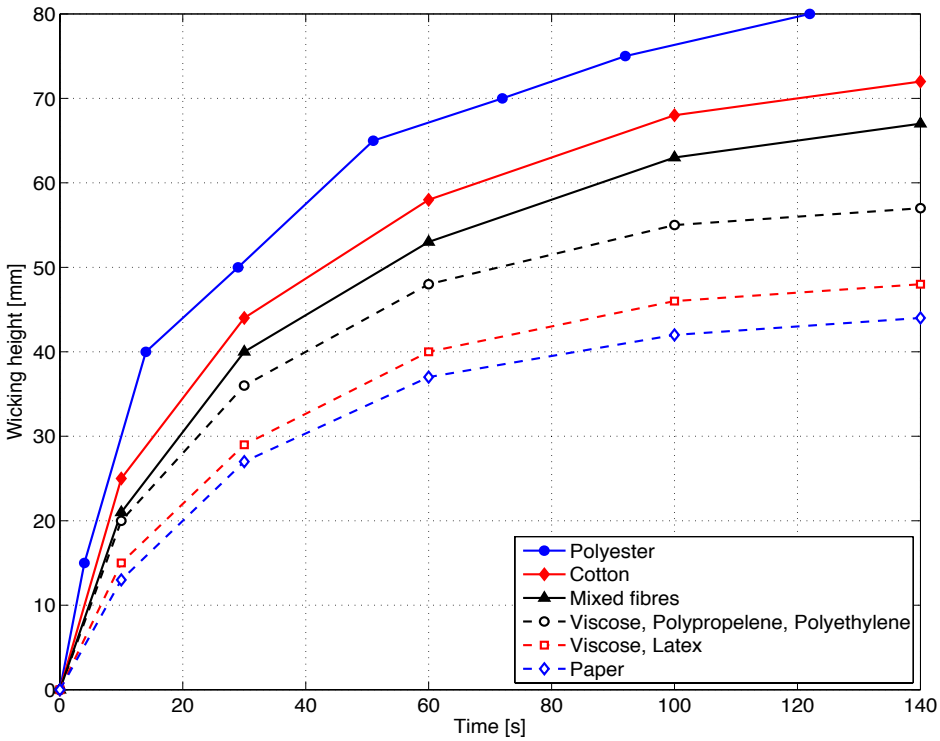


Figure 4.5. Example of wicking performance of different materials with methanol

Synthetic materials were found to perform best, followed by organic materials and different mixes. Burton Simile, (2004) shows how the performance in synthetic

material is due to their ordered capillary fibres. Conversely, organic materials have high absorbency rates but highly unstructured fibres, which do not promote capillary flow. It is believed that other materials with mixed compositions that have been optimized for absorbing water-based solutions perform worse for alcohols due to the different wicking angle of the fluid with the material. Very little comparison with literature can be made, as fabrics are typically developed for wicking water-based solutions. While it is possible to introduce nano-coatings to improve the wicking speed of materials, this option has not been explore during this research.

Having explored the working fluid and the classical heat pipe theory, the following section produces an experimental investigation for a single concentrated wound pole piece under evaporative cooling.

4.3 Evaluation of the Heat Transport Mechanism

To establish the heat loss from a wound pole piece, an in-wheel YASA motor with segmented stator was used as a test case study. The machine specifications are shown in Table 4.1.

Table 4.1 Technical Specifications for an in-wheel motor with YASA topology

Machine concept name	YASA-Evaporative Concept
Peak power	20 kW
Peak torque	200 N·m
Continuous power	10.5 kW
Peak efficiency	94%

4.3.1. Experimental Work

A pole piece was constructed by YASA Motors and mounted with T-type thermo couples on the winding surface and the iron core. The winding was wrapped in a synthetic wicking fabric and assembled onto an insulation block in a test box. The test box was sealed and mounted with a fan-heat sink system. A vacuum ejector was used to create a vacuum in the test box and filled with 5% of the working fluid. The experimental setup is shown in Figure 4.6a). The machine's efficiency chart was used to establish a heat loss of 120 W from the pole piece. These were divided between the iron and windings at a ratio of 20% and 80% respectively, as recommended by the manufacturer. The winding and iron were powered simultaneously using separate dc

power supplies. Voltage and current probes were connected to a Picoscope 3000 series oscilloscope to record the the voltage and current for iron and windings at 1 Hz. A Pico data logger TC-08 was used to record temperatures at 1 Hz. Tests were repeated for both methanol and propanol. To assess the limitations of the wick the experiment was repeated for a fully immersed pole piece as shown in Figure 4.6b).

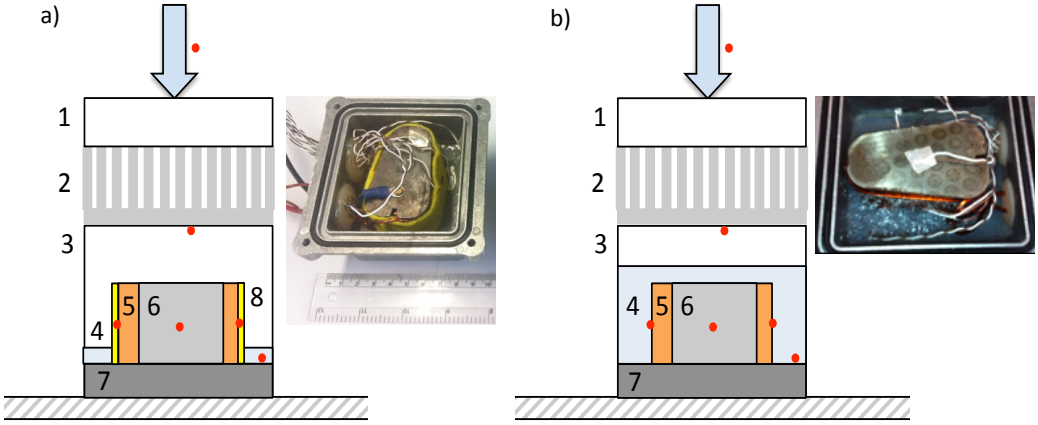


Figure 4.6. Experimental setup for a) wick assisted setup, b) immersion setup, with 1) fan, 2) heat sink, 3) test box, 4) working fluid, 5) copper windings, 6) pole piece iron, 7) insulating material, 8) wicking material. Inserts: Photographs of the wick assisted and immersion cooling test boxes.

4.3.2. Thermal Test Results and Implications

Test results discussed in the section are made with reference to the positions of the temperature sensors shown in Figure 4.6. The temperature profiles for wick-assisted and immersion cooling with methanol is shown in Figure 4.7. Those for propanol are shown in Figure 4.8. The following observations can be made:

- The wick-assisted concept reached a self-sustaining, steady state condition, thus proving that the wick pumping capacity and the condensation rates in the test box were enough to prevent the windings from drying out.
- Using eqn. 4.1 the mass flow rate through the wick for methanol was calculated at 0.118 kg/s while a mass flow rate for propanol was calculated at 0.165 kg/s. Although propanol puts the wick under a higher stress to pump the fluid this was still able to fulfil the requirement.
- No negative impacts from the wick on the cooling performance are observed. The wick is seen to keep the winding temperatures lower than immersion cooling by 5–10 ◦C. This is likely due to the prevention of film boiling, which would otherwise inhibit the liquid from replenishing vaporized fluid.

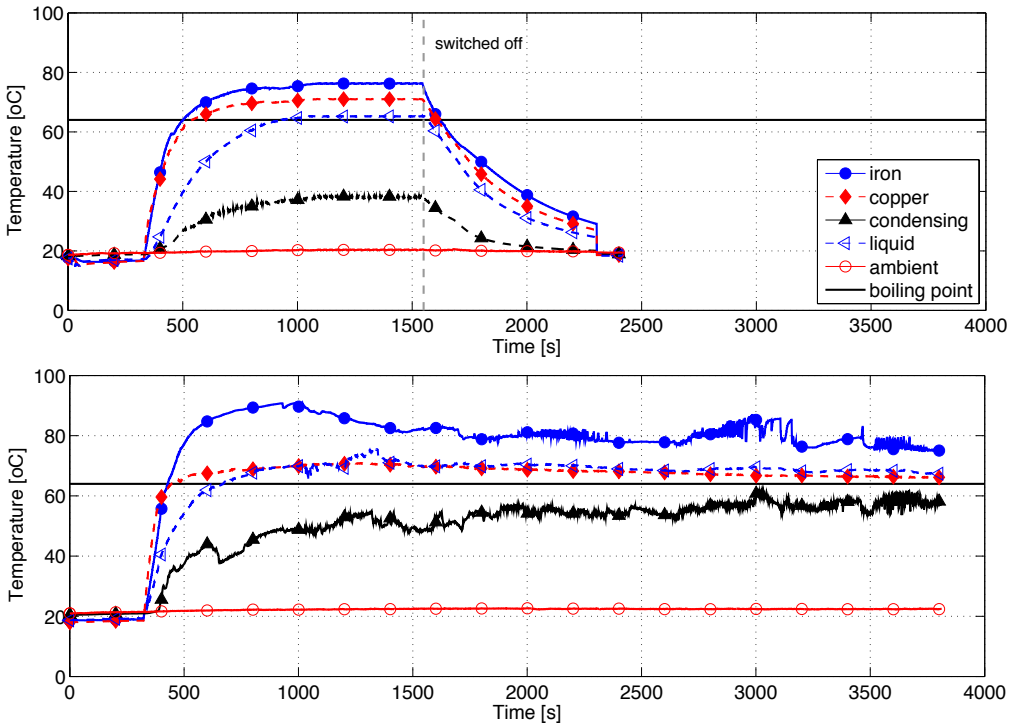


Figure 4.7. Wick assisted cooling with methanol comparing (Top) immersion cooling, (Bottom) wick assisted cooling concept

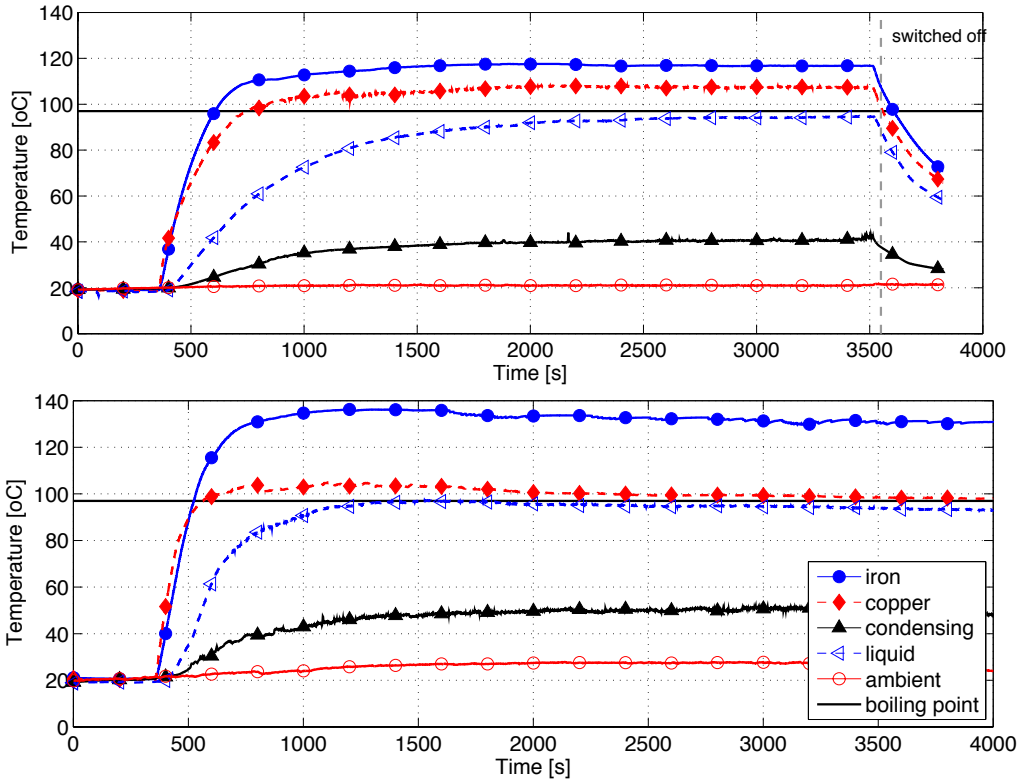


Figure 4.8. Wick assisted cooling with propanol comparing (Top) immersion cooling, (Bottom) wick assisted cooling concept

- The lower volume fill in wick-assisted cooling also results in a lower overall time constant because less heat is dissipated to raise the temperature of the volume of liquid as is done in immersion cooling.
- When propanol is used as the working fluid, a higher temperature difference between the winding and the iron exists compared to when methanol is used as the working fluid. The author attributes this to the condensate, which may drop back onto the iron. As the iron is at a higher temperature than the boiling point of the fluid, this immediately evaporates back absorbing heat. Methanol has a larger latent heat than propanol. Hence a droplet of methanol condensate absorbs more heat than propanol condensate. For a fixed heat load, a larger drop in iron temperature is hence experience with methanol as the working fluid. Thus the two experiments demonstrate a different temperature difference between the iron and the copper. The droplets of condensate on the iron would also explain the "random" fluctuations in iron temperature.

This chapter has so far established that in a stationary environment, the cooling effect through a wicking mechanism can be sustained as long as heat can be transferred from the casing to ambient air. However, this mechanism will be employed in an outer rotor machine. Therefore the working fluid will be sloshing within a confined compartment as the machine outer rotor speeds up. Investigating the behaviour of the working fluid within this context is important as this will have an impact on the design of the machine. The following section studies this problem by experimental observation of the fluid dynamics and identifies the challenges for enabling a mechanism to wet the stator windings.

4.4 Experimental observation on the fluid dynamics

4.4.1. Investigation of rimming flows in low aspect ratio cylinders

Thoroddsen et al., (1997), presented experimental observations of a viscous fluid partially filling long horizontal rotating cylinders. The experiments were applied for a range of Reynolds numbers, Re, defined as follows:

$$10 < \mathrm{Re} = \frac{\rho \omega r h_o}{\mu} < 20000 \qquad \text{eqn. 4.2}$$

where ρ and μ are the fluid density and viscosity, respectively, ω is the angular velocity, and r is the cylinder radius. h_o is the average film thickness, defined as:

$$h_o = \frac{V_f}{2\pi r l} \qquad \text{eqn. 4.3}$$

where V_f is the volume of fluid and l is the cylinder length. However these observations have been made on cylinders with aspect ratios in the range of:

$$6 < a = \frac{l}{r} < 16 \qquad \text{eqn. 4.4}$$

No reference to fluid behaviour in low-aspect-ratio cylinders is found in the literature. To investigate this, an experimental setup shown in Figure 4.9 was designed.

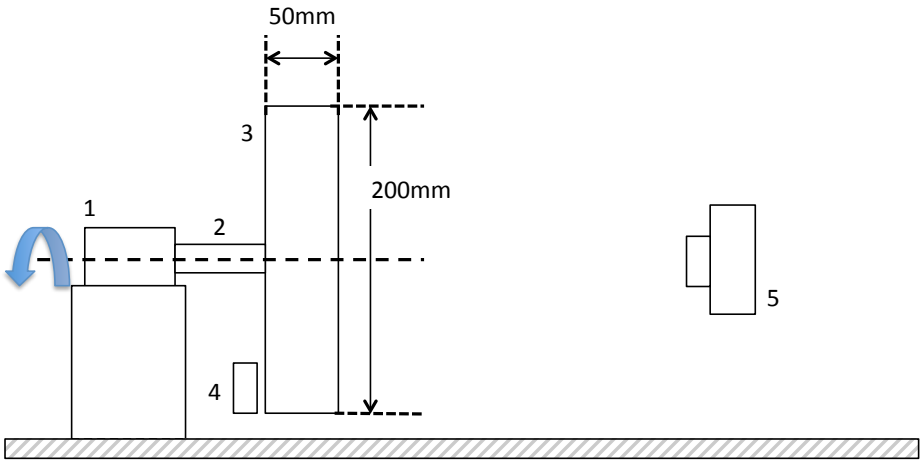


Figure 4.9. Experimental setup investigating fluid behaviour in rotating cylinders with 1) dc motor, 2) connecting shaft, 3) filled cylinder under test, 4) speed sensor, 5) high speed camera

A transparent cylinder with an aspect ratio of 0.16 was built and coupled to a DC motor. 10% of the cylinder's volume was filled with the working fluid and a dye was introduced to make the fluid behaviour more visible. A high-speed camera was used to record and observe the motion of the fluid through the various cylinder speeds and flow regimes. It was observed that at slow rotational speeds a thin film is pulled up, wetting the entire curved cylinder surface. Fluid end effects on the flat sides were also noted in which the fluid in contact with the flat surfaces appeared to be pulled up with the rotating sides. As the rotating speed increases, the front of the pool recedes back and the film thickness increases. This continues until a critical speed is reached, after which a fluid curtaining process rapidly occurs. The critical Reynolds number was found to be approximately 13,000. When the critical speed is passed, the centrifugal forces dominate the fluid behaviour causing the flow pattern to develop into a

homogeneous rimming flow. This coats the cylinder uniformly and rotates with the cylinder rigidly. On slowing down the cylinder, a hysteresis was observed. Once the fluid enters the rimming mode, the velocity of the cylinder could be reduced well below critical speed for the fluid to fall out of the rimming mode. The general behaviour agrees with the description given in Thoroddsen et al., (1997). However, unlike high-aspect ratio cylinders, curtaining was observed to develop only at the centre of the cylinder. This is likely due to the influence of the windage of the axial rotors in low-aspect ratio cylinders. The transition in fluid behaviour as the cylinder rotational speed is varied from stationary to full speed is shown in Figure 4.10.

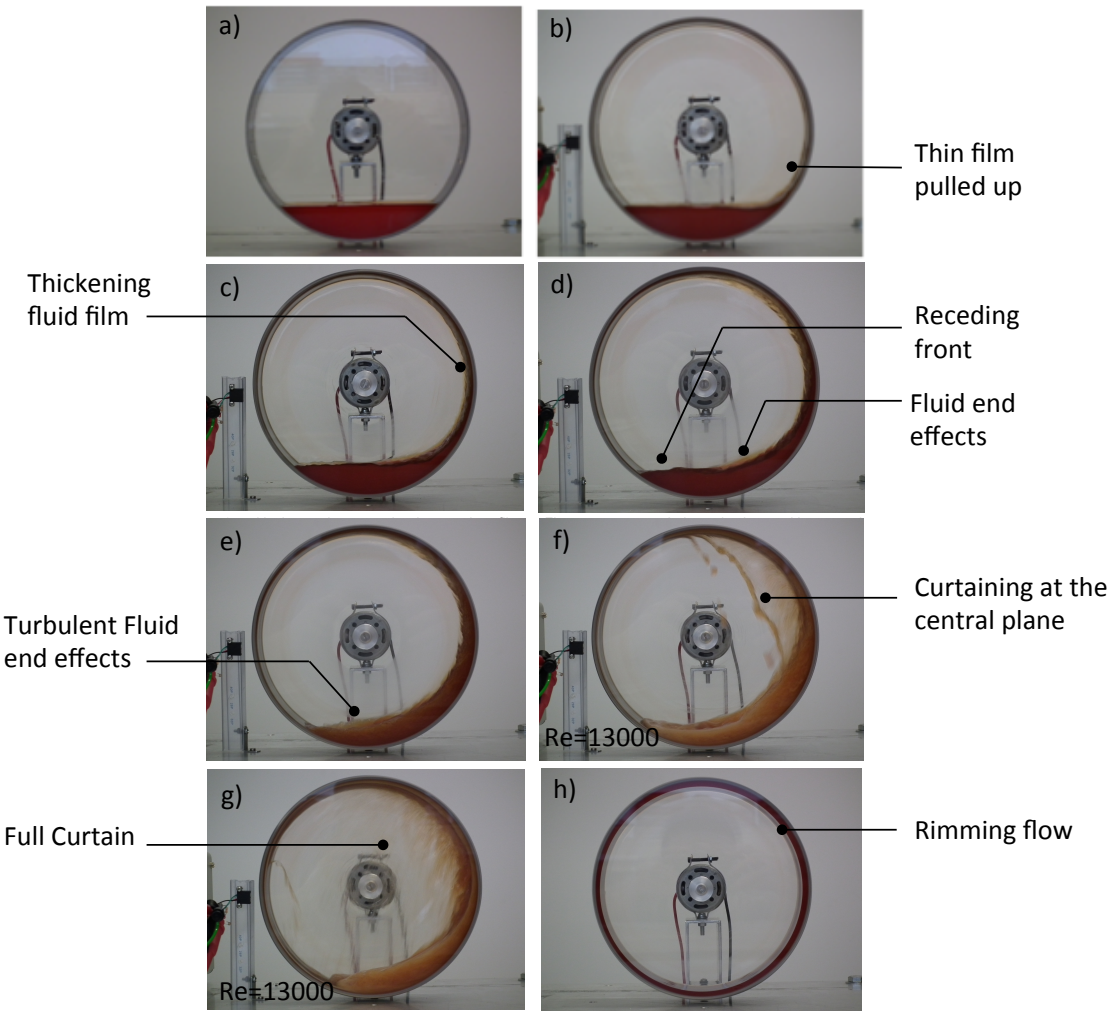


Figure 4.10. Observation of fluid behaviour with rotational speed

4.4.2. The Effects of real machine geometry

The experiment was repeated, this time introducing a stator and magnet-like geometries into the cylinder to resemble an axial flux machine. The construction of

the motor replica is shown in Figure 4.11. It was noted that while the front of the fluid still recedes back, the magnets act as paddles, picking up liquid each time they pass through the pool. In a real machine this would lead to torque losses. No curtaining was observed prior to transitioning to the rimming flow shown in Figure 4.12.

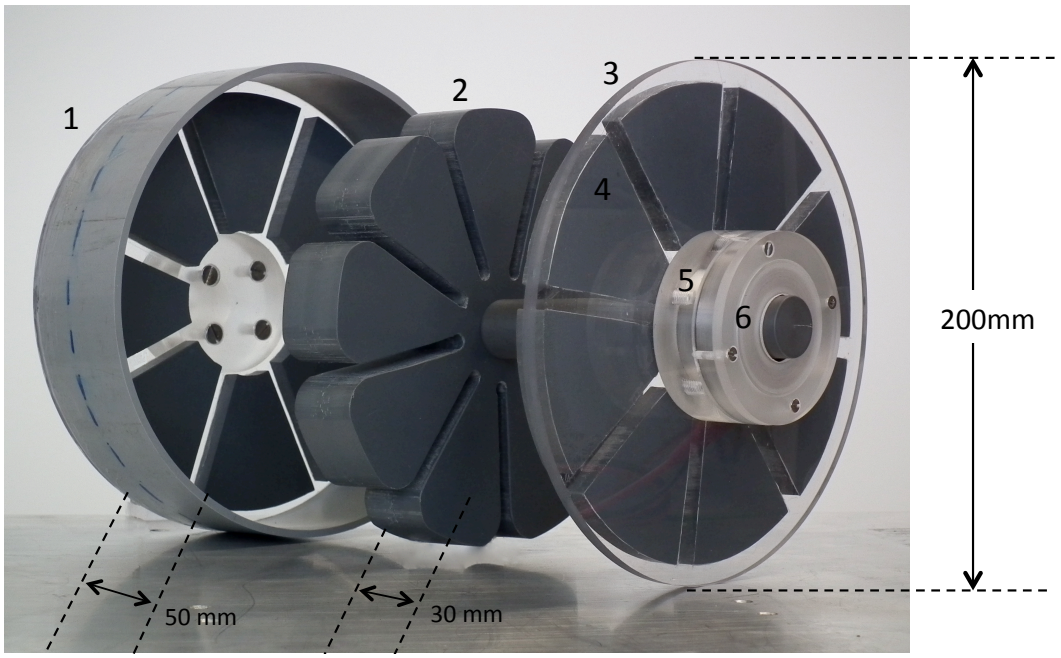


Figure 4.11. Motor replica with 1) Outer rotor housing, 2) stator, 3) rotor iron 4) permanent magnets, 5) bearing, 6) connecting shaft

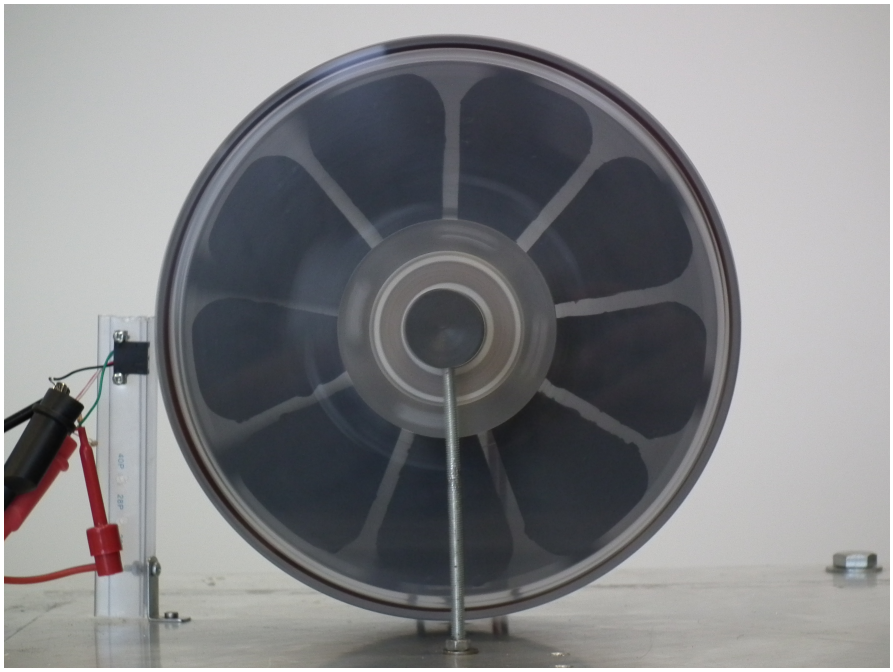


Figure 4.12. Observations of rimming flow in motor replica

4.5 Systems Integration

Having considered the individual mechanisms, this section examines how these components work together within the context of an electrical machine.

4.5.1 The design of the wick

The design of the wick is critical to the continuous cooling of the pole pieces. However, in Section 4.4.2 it was observed that at motor speeds below 100 rpm (with a critical rotational Reynolds number less than 13000) the wick needs to pick up fluid from the bottom of the motor while beyond the critical Reynolds number the wick needs to capture the rimming flow. Below the critical speeds, the machine losses are lower and thermal mass of the pole pieces is enough to withstand the temperature increase for a short period of time. However, as the speed of the machine increases and the internal flow develops into a rimming flow, the wicking problem becomes more challenging. A number of wetting and wicking mechanisms were investigated to determine their ability to wet the stator windings. Table 4.2 provides a list of these mechanisms together with their advantages and disadvantages. A wick that taps into the fluid film pulled up along the curved surface (and subsequently the rimming flow), and which provides the pole pieces with a continuous supply of fluid irrespective of the flow regime is required. One potential concept is shown in Figure 4.13. The manufacturing and assembly of the wick is however challenging as a very small tolerance between the wick and the rotor exists. More development on the integration of the wick within the machine geometry is required.

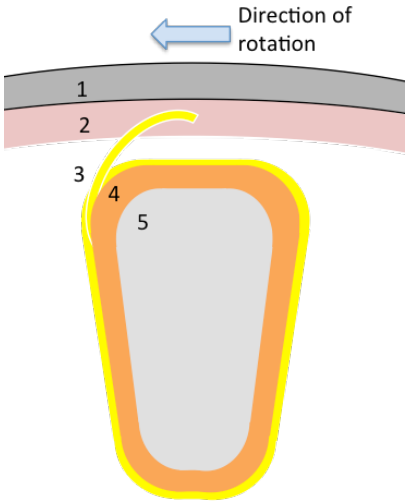


Figure 4.13. Schematic showing the concept of the wick with 1) motor casing, 2) rimming flow, 3) wick design with a “finger” reaching into the fluid, 4) concentrated windings, 5) pole piece iron

Table 4.2 List of wetting mechanisms explored

Name/Description	Advantages	Disadvantages
Stator void packed with absorbent material	Easy to manufacture	Poor wicking properties due to discontinuity in the wick A clearance between the rotor and stator is required to avoid torque losses. However, the wick needs to tap into rimming flow making the ideas incompatible
Stator void filled with a single sponge-like cut out	Easy to manufacture	A clearance between the rotor and stator is required to avoid torque losses. However, the wick needs to tap into rimming flow making the ideas incompatible
Introduce a bearing structure between the rotor and stator. The bearing will help to have liquid trickle over the pole pieces		Expensive Higher risks to damage winding insulation during assembly Difficulty in wetting pole pieces in the lower half during rimming flow. Difficulty to sufficiently wet pole pieces in the upper half during low speed operation.
Introducing a brush like mechanism on the rotor. This will wet each pole piece as the rotor turns	Simple	Potential creation of static Difficulty in wetting pole pieces in the lower half during rimming flow. Difficulty to sufficiently wet pole pieces in the upper half during low speed operation.
Introduce a Bi-metallic strip on the pole pieces to reach into the liquid layer when pole piece reaches a critical temperature. This allows liquid to drip onto the pole piece. The pole piece would still require a wicking fabric to distribute the liquid over the entire coil		Complex to manufacture and mount on the pole pieces
A plastic structure covered in wicking material could be designed to mount on the pole piece. The structure would have a part which extends into the liquid layer hence ensuring that one end of the wick is always kept wet	Simple Easy to manufacture Effective to distribute liquid around entire winding	

Having observed the flow behaviour within the machine, the following section estimates the heat transfer from this concept and the continuous rating of the machine.

4.5.2 The implications of working fluid on the machine rating

In Section 4.3.2 it was shown that both methanol and propanol are able to maintain a continuous cooling effect on a single pole piece. Each working fluid operates at a different mass flow rate. The higher latent heat of vaporization of methanol causes

lower stresses on the capillary pumping action from the wick. However, the choice of the working fluid and their distinct boiling point influences the continuous heat loss from the power trains investigated in Chapter 3. Figure 4.14 compares the heat transfer from the machine casing at the methanol temperature. Figure 4.15 compares the heat transfer from the machine casing at the propanol temperature.

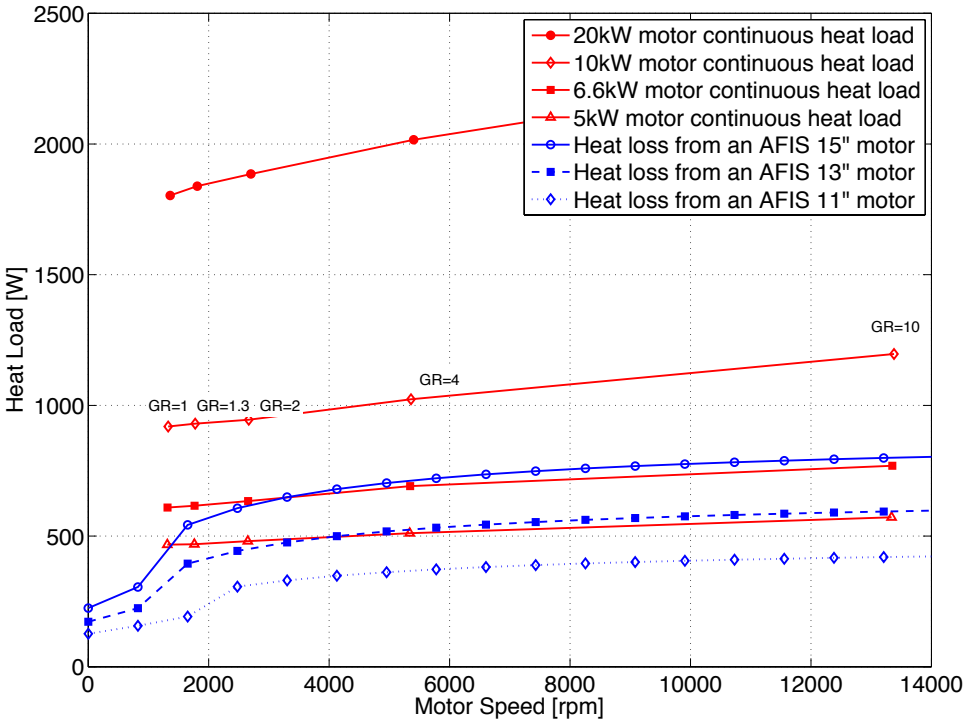


Figure 4.14. Comparison of the stator heat losses with the heat transfer from the casing for methanol

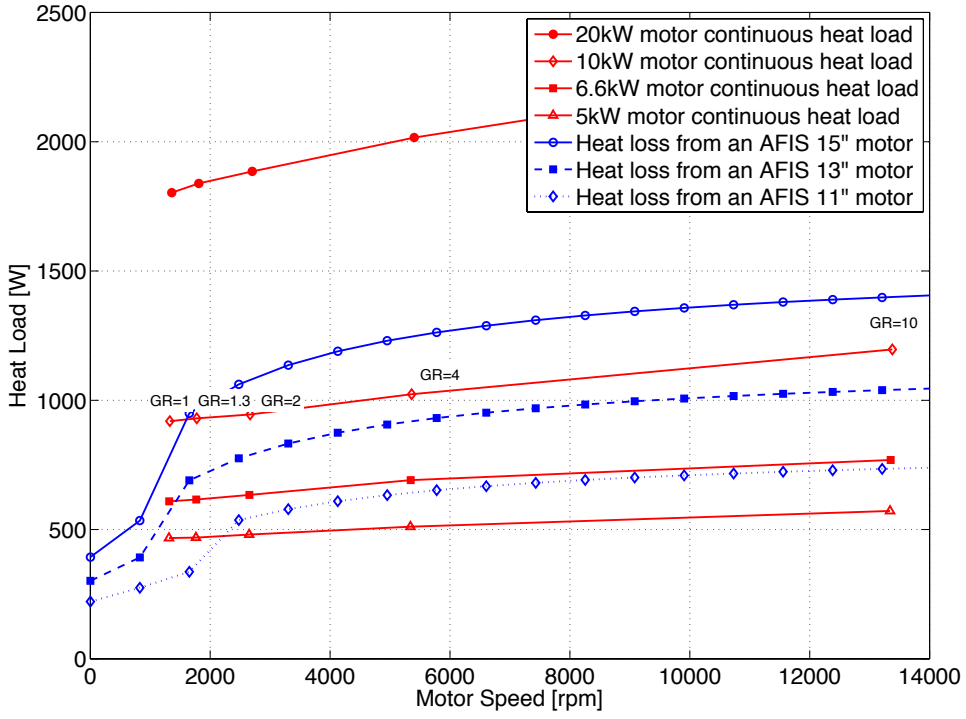


Figure 4.15. Comparison of the stator heat losses with the heat transfer from the casing for propanol

Evaporative cooling mechanism is found to offer a significant improvement in the heat transfer of AFIS machines. The overall thermal resistance of the machine is reduced, as is the dependency of the thermal resistance on the motor speed. When compared to the air-cooled counterpart from Chapter 3, evaporative cooling supports higher machine continuous ratings. Propanol keeps the outer rotor at a higher temperature, allowing it to support machines of up to 10 kW at speeds as low as 2000 rpm. When applied to the context of an in-wheel motor a drive train with a single gear ratio of around 1.3 is required.

4.6 Discussion and Conclusion

This chapter investigated a novel evaporative cooling mechanism to overcome the thermal resistance in the rotor-stator gap. AFIS machines with evaporative cooling are shown to benefit from a significant improvement in heat transfer than their air-cooled counterpart. While both immersion cooling and wick assisted cooling were shown to support continuous operation, it is the author's opinion that wick-assisted cooling is key to the success of this concept. The wick prevents the stator windings from suffering a temperature overshoot and reduces the amount of coolant required in the machine and the drag losses associated with it. However, this concept presents significant challenges to wet the windings. The fluid inside the motor was observed to have different flow regimes at different rotating speeds. At a rotating Reynolds numbers below 13000, the bulk of the working fluid pools at the bottom of the wheel with a thin film of fluid being pulled up the curved surface. Past the critical rotating speed, the fluid quickly transits into a rimming flow. A high-speed machine simplifies the design of the wick as the continuous operation of the machine always falls beyond the critical speed. Hence the wick may be designed to tap into the rimming flow. Heat transfer from the casing was shown to dictate the size of the machine rating and is influenced by the choice of the working fluid. Despite the benefits reported in this research, the introduction of coolant in the rotor presents new construction challenges that require a significant amount of development time. A cost and feasibility study for such a drive train is required. In this research the evaporative cooled motor concept was tested with alcohol as the working fluid. This introduces new safety concerns and the requirement for further development and testing.

5 | Direct Liquid Cooled Electrical Machines

This thesis has so far demonstrated that air-cooled machines suffer from thermal limitations. While the heat transfer in the rotor-stator gap can be improved by introducing evaporative cooling, the thermal path is still restricted by convective heat transfer from the machine casing. This thermal limit does not exist in liquid cooled machines because the heat transfer is augmented by the extended surfaces of an external radiator. Therefore in the context of electric and hybrid vehicles, liquid cooling is applied to high power on-board machines. Liquid cooling is often achieved indirectly by wrapping a cooling jacket around the casing of the machine. However such machines still have the end windings cooled by the airflow over them, which limits the machine performance. Higher current densities are achieved by having the liquid in direct contact with the windings. This is the focus of this chapter.

The effectiveness of direct liquid cooling is influenced by the flow distribution within the stator. This is typically determined through CFD modelling as in Nategh, (2013) and Polikarpova, (2014). However the iterative nature of an electrical machine design requires a lengthy procedure. This chapter therefore presents a fast and accurate thermo-fluid model to determine the flow and temperature distribution in a directly oil cooled segmented stator. This technique can hence be used to investigate geometrical parameters and establish an overall temperature map of the machine with limited use of CFD models. By reducing the dependency on CFD modelling, the machine design process is shortened. Following a description of the cooling system on a YASA machine used as a test case study, this chapter presents the analytical model and a CFD model and validates them against experimental measurements. The analytical model was presented in Paper 4. The same methodology was also applied to heat exchanger design in Paper 5.

5.1. Context to this chapter

Section 2.2 of the literature review highlighted the need for thermal modelling of electrical machines. This is performed either through analytical methods such as Lumped Parameter (LP) methods or numerical techniques such as Finite Element Analysis (FEA) or Computational Fluid Dynamics (CFD). LP models simplify spatial temperature distribution in solids and are fast to solve. However, a number of input parameters such as the heat transfer coefficient (HTC) are required. This is difficult to determine and is obtained from experiments (Howey et al, 2009, Howey et al., 2011, Hettegger et al., 2012), empirical correlations of ideal geometries (Staton and Cavagnino, 2008, Howey et al., 2012,), or CFD simulations (Micallef et al., 2008, Chong et al., 2014, Howey et al., 2011).

In the case of direct liquid cooling, CFD models are also applied to establish the flow distribution within the machine (Nategh, 2013, and Polikarpova, 2014). While CFD models provide detailed information and insight into the fluid behaviour, full machine analysis require significant computational effort and are time consuming (Boglietti et al., 2009). Consequently the use of CFD models is often limited to specific tasks and components, for example to extract the HTC value. This is then introduced into LP models by which the overall machine thermal simulation is performed (Boglietti et al., 2009). The dependence of LP models on HTC input values often implies that improvements to the flow geometry and the thermal path of the machine requires a series of alternating simulations between CFD and LP models. Thus alterations during the design procedure is time consuming and costly. This is especially true for directly cooled machines, whose stator temperature is a function of the flow distribution.

This chapter addresses this problem by coupling together two conventional analytical techniques - the flow network model and the lumped parameter model. The flow network model as applied within the boundaries of a segmented stator direct liquid cooled machine and is used to determine the flow distribution in the stator. The flow distribution is used to estimate HTC values, which acts as an input to a LP model to solve the temperature distribution in the stator. The novelty of coupling a flow network model and a lumped parameter thermal model results in a fast but accurate simulation tool that identifies which of the segmented pole pieces will be at the

highest temperature. During the early design stages of the machine the thermal designer can change the flow geometry to alter the temperature distribution in the stator pole pieces. This allows the thermal designer to investigate a number of 'what if' scenarios in a very short time. The thermal designer can then opt to perform further CFD analysis on a limited number of scenarios. Therefore following a description of the cooling configuration in Section 5.2, a description of the iterative flow network model and its coupling to the lumped parameter thermal model is provided in Section 5.3. The CFD model is described in Section 5.4. An experimental procedure is presented in Sections 5.5 and the results in Section 5.6.

5.2. A Direct Liquid Cooling Configuration

In the introductory chapter electrical machine cooling was categorized into liquid cooling and air-cooling. Liquid cooling is further divided into direct or indirect cooling systems. In his work, Nategh, (2013) shows how direct liquid cooled electrical machines have a shorter thermal path and are hence associated with higher current density machines. This chapter therefore focuses on direct liquid cooling and considers a Yokeless And Segmented Armature (YASA) axial flux machine as a test case study. An example of a direct liquid cooled axial flux machine with segmented windings is shown in Figure 5.1. The research can however be readily adapted to variants of this topology or to direct cooling of radial flux topologies as shown in Figure 5.2.

In the YASA machine for example, the stator is enclosed in a glass fiber casing, allowing liquid coolant to be injected into the stator in direct contact with the windings. Each segmented stator pole piece is made from concentrated windings of square cross section wire. Flow stoppers are used to avoid the flow bypassing around the periphery, dividing the machine into four similar sections. In this respect the liquid flow distribution in the stator is similar to that of a parallel flow liquid cooled heat sink used for cooling high power density electronics. The stator's lack of a physical back plate gives the individual pole pieces a relatively low thermal mass and makes them sensitive to the liquid flow distribution within the stator.

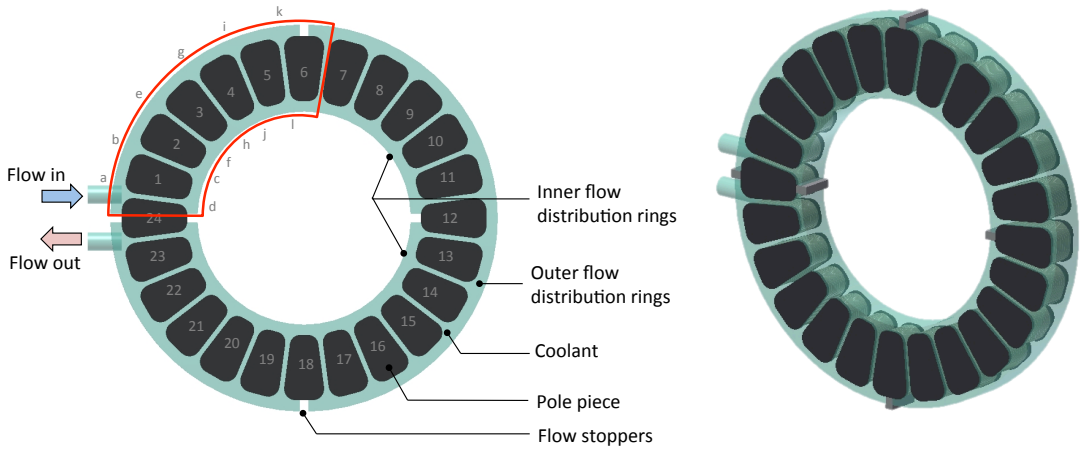


Figure 5.1. Schematic of a direct liquid cooled stator for an axial flux machine. Highlighted: quarter of the stator used for reference at a later section within this chapter

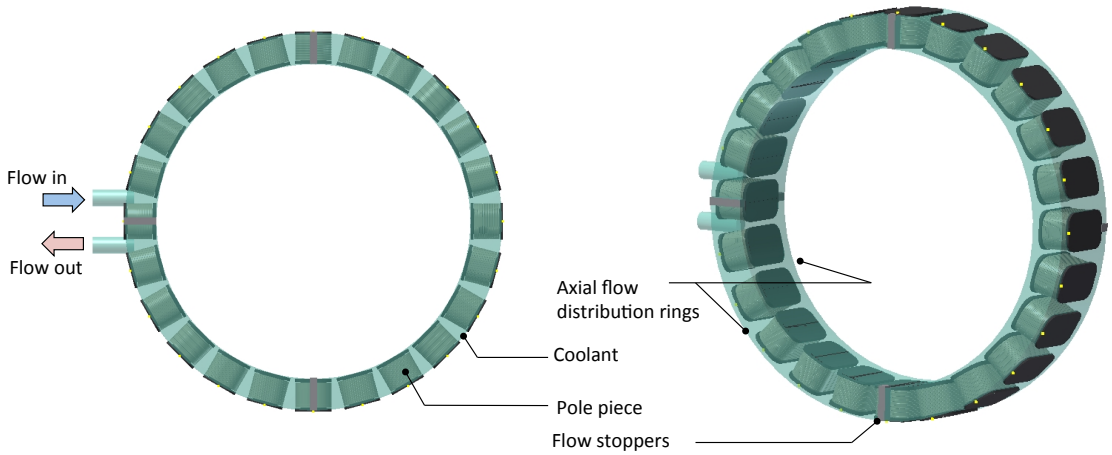


Figure 5.2. Schematic of a direct liquid cooled stator for a radial flux machine

Following a brief introduction of the principles of pipe flow mechanics and flow network models, the following section develops a coupled thermo-fluid flow network model of the YASA stator which is used as a test case scenario. This is followed by CFD modelling and experimental measurements to validate the techniques.

5.3. Thermo-fluid Modelling

5.3.1 Principles of fluid mechanics

The head loss across a pipe h_f varies with flow rate $\dot{Q}$ as described by:

$$h_f = \frac{f l v_f^2}{2 g D_h} = \frac{f l \dot{Q}^2}{2 g D_h A_f^2} \qquad \text{eqn. 5.1}$$

where f is the friction factor, l the pipe length, v_f is the fluid velocity, A_f is the flow area, D_h is the hydraulic diameter and Q the flow rate.

In fully developed laminar flow (Re < 2300), the friction factor is defined by:

$$\mathrm{f} = \frac{64}{\mathrm{Re}} \qquad \text{eqn. 5.2}$$

In fully turbulent flow (Re > 4000) the friction factor becomes a function of the Reynolds number and surface roughness ε, and can be solved iteratively by:

$$\frac{1}{\sqrt{\mathrm{f}}} = -2log_{10}\left(\frac{\varepsilon}{3.7D_{\mathrm{h}}} + \frac{2.51}{Re\sqrt{f}}\right) \qquad \text{eqn. 5.3}$$

where ε is the relative roughness of the pipes. The Reynolds number Re was described in the introduction as a dimensionless property of the flow measuring the ratio of the inertial forces to viscous forces acting in the fluid defined as:

$$\mathrm{Re} = \frac{v_f D_{\mathrm{h}}}{\upsilon} \qquad \text{eqn. 5.4}$$

where v_f is the flow velocity, and υ the kinematic viscosity. The hydraulic diameter D_{h} is defined as:

$$D_{\mathrm{h}} = \frac{4A}{P} \qquad \text{eqn. 5.5}$$

where A is the cross sectional area and P is the wetted perimeter.

Several simplified correlations defining the friction factor at a more restricted Reynolds number range can be found in the literature. The relationship of the friction factor with Reynolds number and surface roughness for a fully developed flow was published by Moody, (1944). Shapiro et al., 1948, show that in laminar flow, the friction factor in the entry region can be up to 10 times larger than the friction factor of the developed flow.

For a fluid flow over a solid, the fluid immediately adjacent to the boundary wall is at rest, while the thin region close to the wall experiences shear stress. The viscosity of the fluid slows down the fluid near the wall. To preserve the continuity of mass, the fluid away from the wall accelerates. The height of the viscous hydrodynamic boundary layer therefore grows downstream, and is defined as the region in which the fluid velocity changes from a value of zero at the solid surface to 99% of its free stream velocity - where the gradient of the velocity in the direction normal to the wall becomes almost constant, (Kays et al., 2004). Figure 5.3 presents a schematic of the boundary layer growth in a pipe.

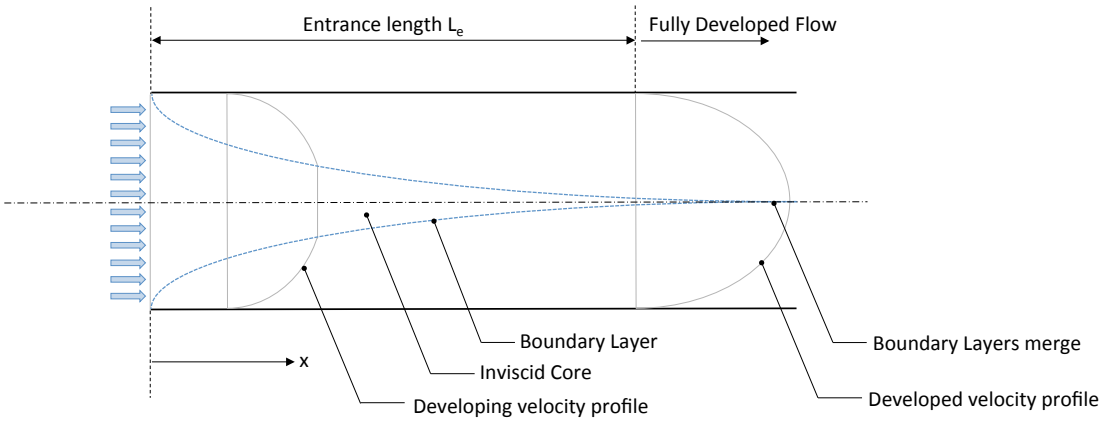


Figure 5.3. Schematic showing the development of the boundary layer

At a finite distance from the entry point the boundary layer around the pipe merges and the velocity profile becomes parabolic; this does not change any further along the length of the pipe. In a laminar flow, the inviscid core disappears and the flow becomes entirely viscous. The distance from the entry to this point is referred to as the developing length L_e and the flow is termed "developing flow". In laminar flow, the entry length is defined in Kays et al., (2004) as:

$$L_e = 0.05\mathrm{Re}.D_h \qquad \text{eqn. 5.6}$$

In the presence of heat exchange between the fluid and a solid surface, the major temperature change is concentrated in the region very close to the surface. Thus the concept of the velocity boundary layer is also extended to the thermal boundary layer (Kays et al., 2004). For a uniform wall temperature with developed hydrodynamic profile, Mills (1999) defines the thermal entry length as:

$$L_{e,\mathrm{thermal}} = 0.017\mathrm{Re}.D_h.\mathrm{Pr} \qquad \text{eqn. 5.7}$$

where Pr was described in the introduction chapter as a non-dimensional ratio between the momentum and the thermal diffusivity.

$$Pr = \frac{\mu c}{k} \qquad \text{eqn. 5.8}$$

where μ is the dynamic viscosity of the fluid, c the heat capacity and k the thermal conductivity of the fluid. If $Pr = 1$, the heat and momentum are diffused at approximately the same rate, and the velocity and temperature profiles develop together. However the oil used for cooling the machine considered here has a $Pr \approx 70$. Therefore the velocity profile develops much faster than the thermal one. The flow within its stator is laminar with $\mathrm{Re} \approx 200$. Hence the entry effects along the

segmented stator pole pieces play an important role and should be taken into consideration. Kays et al., (2004), show that the head loss equation can be modified to take the entrance effects into consideration as follows:

$$h_f = \frac{(4f_{app})L_e {v_f}^2}{2gD_h} = \frac{(4f_{app})L_e \dot{Q}^2}{2gD_h A^2} \qquad \text{eqn. 5.9}$$

The apparent friction factor f_{app} incorporates the combined effects of shear stress at the wall surface and changes the momentum flux associated with changes in velocity profile. A correlation for f_{app} has been developed in Langhaar, (1942):

$$4f_{\text{app}}\left({}^{L_\text{e}}/_{D_\text{h}}\right) = 29.979\left(\frac{{}^{L_\text{e}}/_{D_\text{h}}}{\text{Re}}\right)^{0.6189} \qquad \text{eqn. 5.10}$$

Figure 5.4 compares the head loss along the non-dimensional channel length for a fully developed flow with an assumed parabolic velocity profile, and the developing flow accounting for a changing velocity by eqns. 5.2 and 5.10. The difference in head loss between the developing and developed flows are seen to gradually and asymptotically approach each other as the inlet effects become relatively less significant.

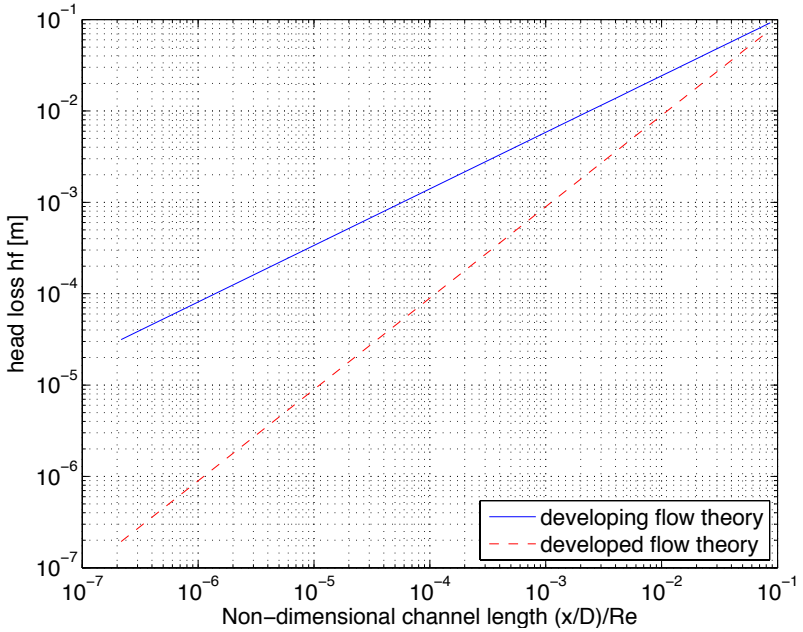


Figure 5.4. Comparison of the theoretical head loss in laminar entry region for a developing and developed flow. Data of the developing flow reproduced from Langhaar, (1942)

Other pipe flow components such as from bends or T-junctions also produce head losses, typically associated with the flow separation from the walls.

These are defined in terms of the velocity head such that:

$$h_{\mathrm{f,i}} = K.\frac{{v_{f_{\mathrm{i}}}}^2}{2g} \qquad \text{eqn. 5.11}$$

where *K* is an empirically defined loss coefficient. Subscript *i* defines the branches of the T-junction. The variation of the loss coefficients with flow and area ratio for each of the branches in a T-junction has been investigated in Miller, (1990). In his work, the author shows that the loss coefficient of T-junctions K takes a different value depending on the direction of the flow with in the junction as shown in Figure 5.5. While such losses are typically considered as a minor source of head loss, in small systems the contribution of combining and dividing manifolds become significant. In the flow model, these were taken into account by adapting a table 'look up and interpolate' function for each of the dividing and combining branches respectively. This selects the correct loss coefficient at each iterative step of the model.

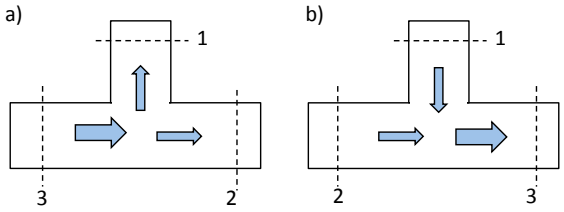


Figure 5.5. Definition of the flow directions in a) a dividing T-junction, b) a combining T-junction

5.3.2. The iterative flow network model

Having determined the sources of head loss, for a known flow rate and flow properties, the pressure drop across a single pipe can be calculated directly using eqn. 5.1. In Section 2.3.1 of the literature review it was shown how this rationale was applied to open circuit (through flow) electrical machines, (Taylor, 1960, Bone, 1978, Staton and Cavagnino, 2008) so that the pressure losses and mass flow rate across the machine could be found. However, in a closed circuit flow network, such as a direct liquid cooled electrical machine stator, the total head loss of the system is equivalent to the sum of the pressure drops along any path connecting the inlet and the outlet, and is the same irrespective of the path. The head loss is dependent on the flow distribution within the system and can only be solved through an iterative procedure.

The iterative technique to determine the flow distribution is based on conservation equations as adapted from Kirchoff's laws for electrical circuits, (Cross, 1936):

- The sum of the current flow I at any junction n is zero.

$$\sum I_n = 0 \qquad \text{eqn. 5.12}$$

In a flow network the sum of the flow rate into and out of any junction is kept zero throughout the analysis by successive correction of the heads around the circuit. This method is hence referred to as the method of balancing heads.

- In the circuit shown, the sum of the voltage at any closed loop m is zero.

$$\sum V_m = 0 \qquad \text{eqn. 5.13}$$

In a flow network the sum of the pressure drop around any closed loop is kept zero throughout the analysis by successive correction of the flows into and out of the junctions. This method is referred to as the method of balancing flows. In this work the method of balancing heads is employed. After the network is divided into flow loops, a conventional flow direction in each loop and an initial flow distribution is decided. Positive and negative head losses are computed depending on the direction of the flows. The total head loss in each loop is algebraically determined from which an incremental correction in the flow is calculated.

Having defined the overall principles of the flow network model, this is now applied to the direct liquid cooled segmented stator. The flow network in the stator shown in Figure 5.1 is converted into a pipe network as shown in Figure 5.6.

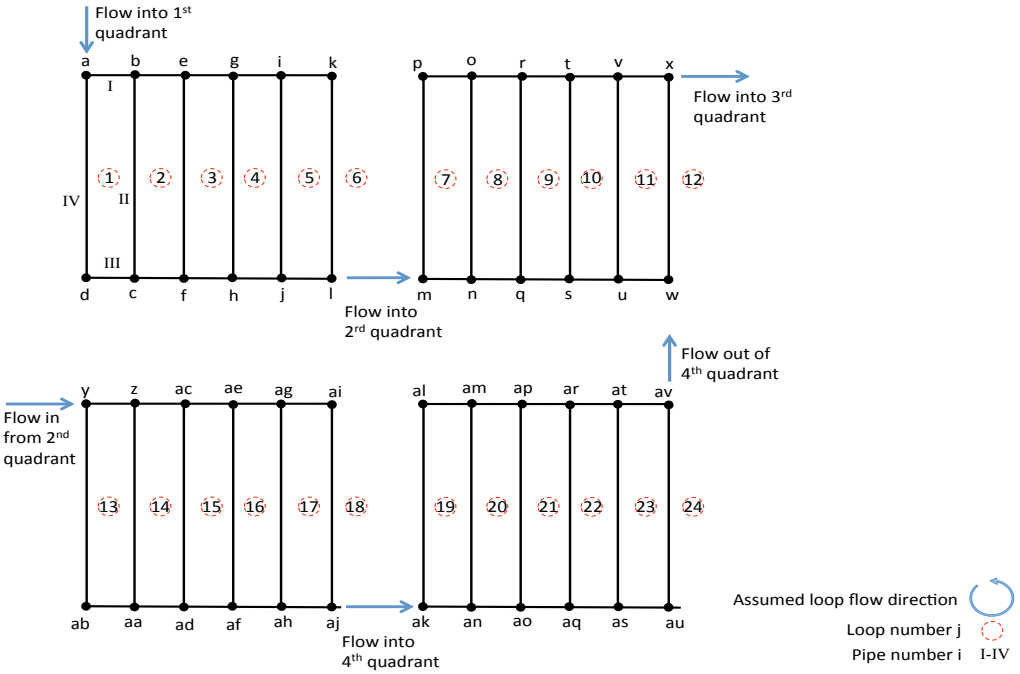


Figure 5.6. Schematic of a simplified flow network for the YASA machine

The first quadrant of Figure 5.6 is used as an example to demonstrate the flow network model. Using an anti-clockwise flow convention, the flow rate in each network loop $\dot{Q}_{\mathrm{j}}$ is made from the flows of each pipe making the loop.

$$\dot{Q} = \begin{bmatrix} \dot{Q}_{\mathrm{j=1}} \\ \dot{Q}_{\mathrm{j=2}} \\ \dot{Q}_{\mathrm{j=3}} \\ \vdots \\ \dot{Q}_{\mathrm{j=6}} \end{bmatrix} \qquad \text{eqn. 5.14}$$

The flows in each loop can be described as vectors:

$$\begin{gathered} \dot{Q}_{\mathrm{j=1}} = [-\dot{Q}_{\mathrm{ab}} \quad -\dot{Q}_{\mathrm{bc}} \quad \dot{Q}_{\mathrm{cd}} \quad \dot{Q}_{\mathrm{da}}] \\ \dot{Q}_{\mathrm{j=2}} = [-\dot{Q}_{\mathrm{be}} \quad -\dot{Q}_{\mathrm{ef}} \quad \dot{Q}_{\mathrm{fc}} \quad \dot{Q}_{\mathrm{cb}}] \\ \vdots \\ Q_{\mathrm{j=6}} = [-\dot{Q}_{\mathrm{ij}} \quad -\dot{Q}_{\mathrm{kl}} \quad \dot{Q}_{\mathrm{lj}} \quad \dot{Q}_{\mathrm{ji}}] \end{gathered} \qquad \text{eqn. 5.15}$$

In the first iteration a uniform flow distribution through the channels is assumed such that:

$$\dot{Q}_{\mathrm{da}} = \dot{Q}_{\mathrm{bc}} = \dot{Q}_{\mathrm{ef}} = \frac{\dot{Q}_{\mathrm{in}}}{N} \qquad \text{eqn. 5.16}$$

where N is the total number of channels between pole pieces in a quadrant. The flow in the peripheral rings is estimated by observing the conservation of mass, therefore:

$$\begin{gathered} \dot{Q}_{\mathrm{ab}} = \dot{Q}_{\mathrm{in}} - \dot{Q}_{\mathrm{ad}} \\ \dot{Q}_{\mathrm{be}} = \dot{Q}_{\mathrm{ab}} - \dot{Q}_{\mathrm{bc}} \\ \dot{Q}_{\mathrm{fc}} = \dot{Q}_{\mathrm{ab}} + \dot{Q}_{\mathrm{dc}} \\ \vdots \\ \dot{Q}_{\mathrm{ik}} = \dot{Q}_{\mathrm{gi}} - \dot{Q}_{ij} \\ \dot{Q}_{\mathrm{jl}} = \dot{Q}_{\mathrm{ij}} + \dot{Q}_{\mathrm{hj}} \end{gathered} \qquad \text{eqn. 5.17}$$

In the following iterations an incremental correction in the flow for each loop $\mathrm{d}Q_{\mathrm{j}}$ is calculated as defined in Cross, (1936):

$$\mathrm{d}\dot{Q}_{\mathrm{j}} = \frac{-h_{\mathrm{f,j}}}{2\Delta_{\mathrm{j}}} \qquad \text{eqn. 5.18}$$

where h_{fj} is head loss in any single loop and is estimated from the vector summation of the head loss in the individual pipes h_{fi}:

$$h_{\mathrm{f,j}} = \sum h_{\mathrm{fi}} \qquad \text{eqn. 5.19}$$

where h_{fi} is dependent on the pipe or component geometry. Details of the values of h_{fi} are given in the following section. Δ_j is head-flow ratio for any loop (Cross, 1936), defined as:

$$\Delta_j = \sum \frac{|h_{f,i}|}{|\dot{Q}_1|} \qquad \text{eqn. 5.20}$$

When pipes are common to more than one loop, an algebraic correction based on the flow convention for each loop is made. The model was solved using MATLAB. Special attention was taken to preserve the flow and head loss vector based on the flow convention taken in each loop. The iterative process set to continue until the maximum change in the branches' flow varied less than 0.1%. The iterative procedure to solve the flow distribution in each sector is shown in Figure 5.7. The simulation for a quadrant is solved in about 60 iterations while that for the whole stator solves in 200 iterations.

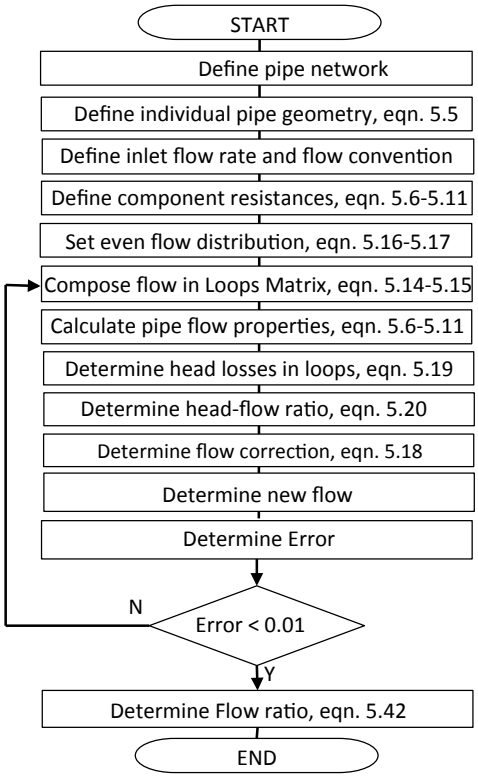


Figure 5.7. Flow chart showing the process to solve the iterative 1D flow model for each stator

The flow network model was validated with measurements of the flow distribution in micro channel heat exchangers available in the literature (Wang et al., 2011). The results of this research were published in the Journal of Applied Thermal Engineering, Nov. 2015, Vol. 90, pp. 551-558, under the paper titled: *"Predicting the flow distribution in compact parallel flow heat exchangers"*. Following validation, the heat exchanger model was used to investigate the effects of the heat exchanger manifold on the flow distribution in compact heat exchangers. Despite similarities between the flow circuit in parallel flow heat exchangers and the flow circuit in the YASA stator,

the design of the heat exchanger is beyond the scope of this thesis and hence the reader is referred to the paper. However, results indicate that:

- An iterative flow network model can accurately simulate the flow in compact heat exchangers.
- The paper investigates the tube to header area ratio (AR) as an indicator for flow mal-distribution in compact heat exchangers.
- The paper demonstrated that as the AR increases, flow mal-distribution becomes sensitive to increasing Reynolds numbers and pipe length.
- While friction dominates flow mal-distribution, as the AR increases inlet losses affect early channels.

In Section 5.8 the same method used to quantify the flow distribution in compact heat exchangers are adopted to quantify the flow distribution in oil cooled electrical machines.

Having demonstrated how the flow distribution across the stator is solved, the influence on the temperature of the segmented stator pole pieces is required. In Section 2.2 of the Literature Review, it was shown how analytical techniques such as Lumped Parameter (LP) models and numerical techniques are often adopted to investigate the thermal behaviour of electrical machines. It was shown how this model suffers from unknown input parameters such as the heat transfer coefficient (HTC). However, after having established the flow distribution alongside each stator, empirical correlations can be used to establish the HTC. This is then input into the LP model to establish a temperature map of the stator. This is described in the following section.

5.3.3. The lumped parameter thermal model

The rate of energy stored in the body $^{dE_{st}}/_{dt}$ can be computed using:

$$\frac{dE_{st}}{dt} = \dot{E}_{in} - \dot{E}_{out} + \dot{E}_g \qquad \text{eqn. 5.21}$$

where $\dot{E}$ is the rate of energy transfer and Subscripts *in*, and *out* define the direction of the energy into or out of the body. Considering that the body has a uniform spatial

temperature distribution and introducing one-dimensional boundary conditions to the pole piece its temperature response with time can be predicted using:

$$\frac{\mathrm{d}T_{\mathrm{p}}}{\mathrm{d}t} = \left(\frac{1}{\rho vc}\right).\left[\frac{(T - T_{\mathrm{f}})}{R_{\mathrm{th}}} + \dot{q}\right] \qquad \text{eqn. 5.22}$$

where $\mathrm{d}T_p/\mathrm{d}t$ is the rate of change of pole piece temperature, ρvc is the thermal capacitance C_{th} for each pole piece while $\dot{q}$ is the total heat losses generated in each of the segmented pole pieces. R_{th} is an unknown convective thermal resistance.

The thermal model considers each of the segmented pole pieces as a lump and is designed to provide an overall temperature distribution of the segmented stator. The thermal resistance is therefore independent of the thermal conductivity of the stator. Hence this has no effect on the simulated results. The assumption that each pole piece has negligible spatial temperature distribution is verified by the Biot number Bi. The Biot number gives a ratio of the heat convected away from the body to the heat conducted within the solid and is defined as:

$$Bi = \frac{hL_c}{k} < 0.1 \qquad \text{eqn. 5.23}$$

where h is the convective heat transfer and k is the thermal conductivity of the solid and L_c the characteristic length defined by:

$$L_c = \frac{V_{body}}{A_{surface}} \qquad \text{eqn. 5.24}$$

The thermal resistance R_{th} is heavily dependent on the flow properties and has been used to couple the fluid model and thermal model. With the flow properties and flow distribution determined, the empirical equation for the Nusselt number Nu for a fluid with Prandtl number > 5 and a developing thermal and fluid boundary layer, Mills (1999) suggests that:

$$\mathrm{Nu} = \mathrm{K}_{\mu,\mathrm{i}}\left[3.66 + \frac{0.0668.\,\mathrm{Pr}.\,\mathrm{Re}_{\mathrm{i}}.\left(\frac{D_{\mathrm{h}}}{L}\right)_{\mathrm{i}}}{1 + 0.04.\left(\mathrm{Pr}.\,\mathrm{Re}_{\mathrm{i}}.\left(\frac{D_{\mathrm{h}}}{L}\right)_{\mathrm{i}}\right)^{0.667}}\right] \qquad \text{eqn. 5.25}$$

The definition of the Nusselt number was defined in Section 1.3.2 as:

$$\mathrm{Nu} = \frac{\mathrm{h}.D_{\mathrm{h}}}{k} \qquad \text{eqn. 5.26}$$

The oil heats up as it flows through the stator, and hence it's properties change along the stator geometry. The factor $\mathrm{K}_{\mu,\mathrm{i}}$ is a corrective factor to take into account the

influence of the temperature dependence of the coolant properties. Kays et al., (2004) defines the corrective factor as:

$$K_\mu = \left(\frac{\mu_w}{\mu_b}\right)^{-0.14} \qquad \text{eqn. 5.31}$$

where μ_w is the viscosity at the wall temperature and μ_b is the viscosity of the bulk fluid at a reference temperature. The variation of fluid properties with temperature are shown in Figure 5.8. The equation of the best fit was used to define the variation of the property with temperature as shown in Table 5.1.

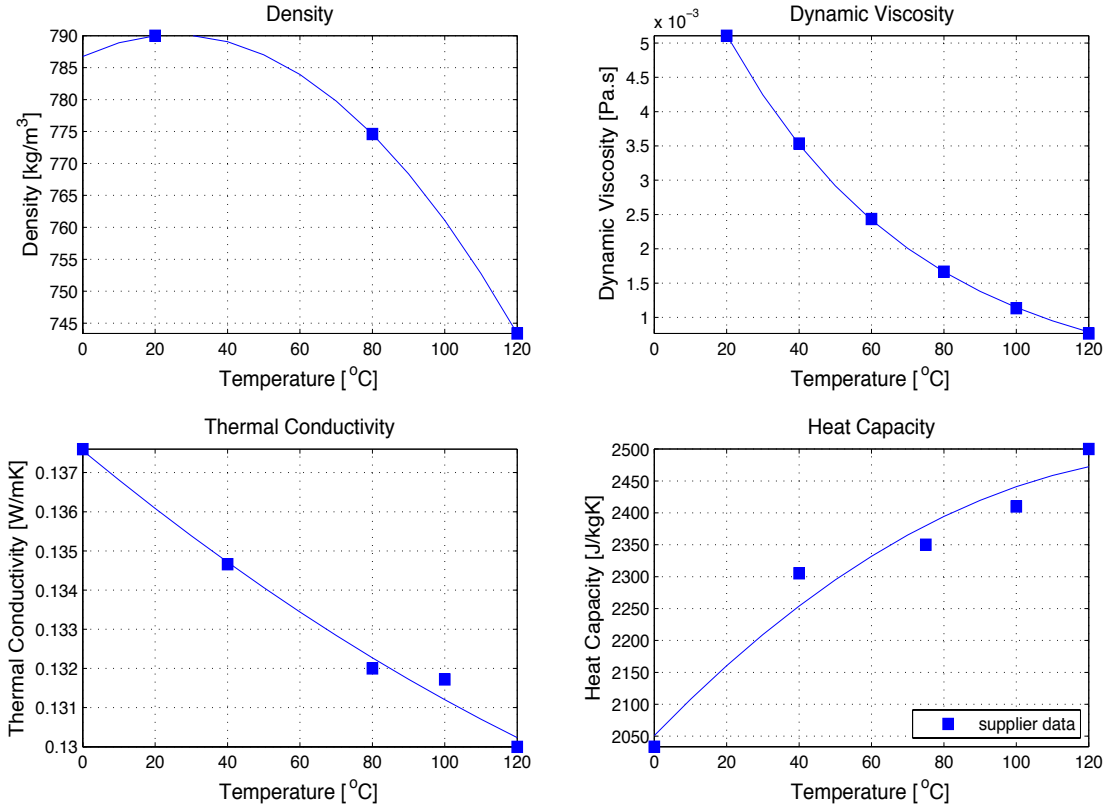


Figure 5.8. Variation of Opticool properties with temperature. Data points from DSI, (2015).

Table 5.1 Variation of Coolant Properties with Temperature T [°C]

Density, ρ [kg/m^3]	$\rho = -0.0052T^2 + 0.2667T + 786.76$	eqn. 5.27
Dynamic viscosity, μ [Pa.s]	$\mu = 0.0079e^{-0.02T}$	eqn. 5.28
Heat Capacity, c [J/kgK]	$c = -0.028T^2 + 6.9105T + 2044.9$	eqn.5.29
Thermal conductivity, k [W/mK]	$k = 1e^{-7}T^2 - 8e^{-5}T + 0.1376$	eqn. 5.30

Due to the flow distribution problem, defining the local fluid temperature is difficult. Therefore in this work the inlet fluid temperature was taken as the reference temperature. The corrective factor K_μ was defined for each flow channel. As during the LP analysis, the solid temperature increases with time, a new K_μ for each channel

is calculated at each time step. In modelling the full stator, a new reference temperature at the inlet of each quadrant is taken. The sensitivity of the model to the variability of the coolant properties with temperature was tested in the model and found to over predict the pole piece temperature by 20%.

The heat transfer coefficient for each of the four sides of the pole piece h_i is determined from eqn. 5.24

$$h_i = \frac{Nu_i . k}{D_h} \qquad \text{eqn. 5.32}$$

where k is the fluid thermal conductivity. The overall heat transfer coefficient U for each pole piece is determined using:

$$U = \sum h_i . A_i \qquad \text{eqn. 5.33}$$

where A_i is the area for each side of the pole piece. Thus the average thermal resistance for each pole piece is determined as:

$$R_{th} = \frac{1}{U} \qquad \text{eqn. 5.34}$$

The properties of the fluid are established at the fluid temperature T_f at the inlet of each quadrant where each pole piece is located. On investigating the whole machine, the fluid properties are therefore adjusted four times, once at every quadrant inlet temperature. The iterative thermal model was solved using the 4th order Runge-Kutta method. The process flow chart for the thermal model is shown in Figure 5.9. The flow and temperature models for the first quadrant are solved in around 60 iterations and takes approx. 4 s. The results of this section are presented in Section 5.6.

Having described an analytical iterative technique for predicting the flow and temperature distribution of the liquid cooled stator, the following section turns its focus to Computational Fluid Dynamics (CFD) as an alternative (numerical) method for predicting the thermo-fluid behaviour within the stator flow field. Following a brief description of the technique, CFD is applied to the same boundary conditions used in experiments so that comparison between the two modelling techniques and experiments can be made.

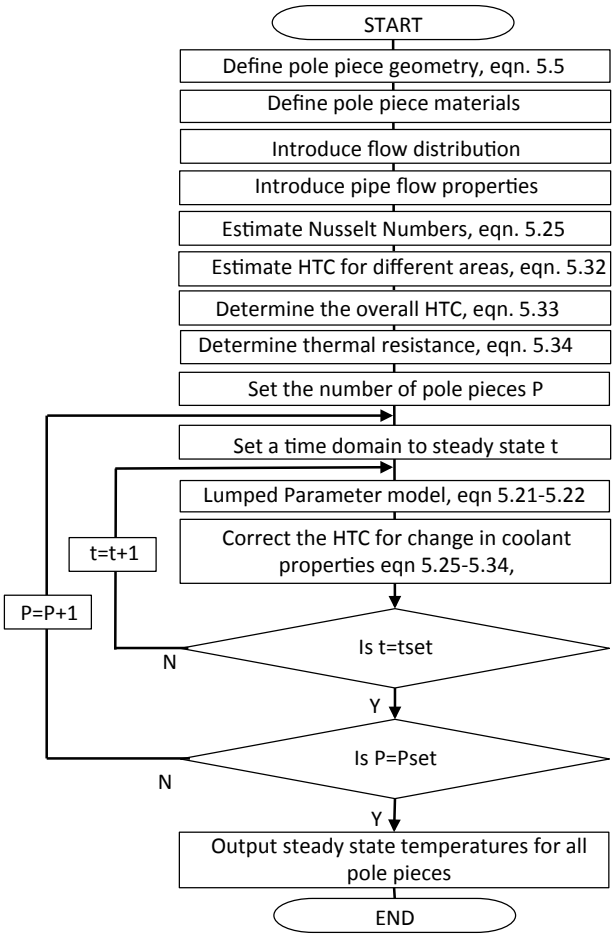


Figure 5.9. Flow chart showing the process to solve the iterative LP thermal model

5.4. Computational Fluid Dynamics

Computational Fluid Dynamics (CFD) is a process of solving the governing equations of the flow field using numerical analysis. In CFD the flow domain is replaced by a grid structure whereby the flow variables are defined at discrete points of the grid. The CFD process is hence made up of a number of steps, which includes: developing the CAD model of the flow field, discretizing the flow field, and applying the correct boundary conditions and governing equations to solve the equations on the discretized points. The results can then be visualized through various post processing techniques. A schematic showing the CFD process is depicted in Figure 5.10. The theory of CFD has been described in many textbooks such as Chung, (2002) and Anderson, (2009). Following a brief description of the governing equations, the focus is turned on the application of the CFD process to the flow geometry within the YASA stator.

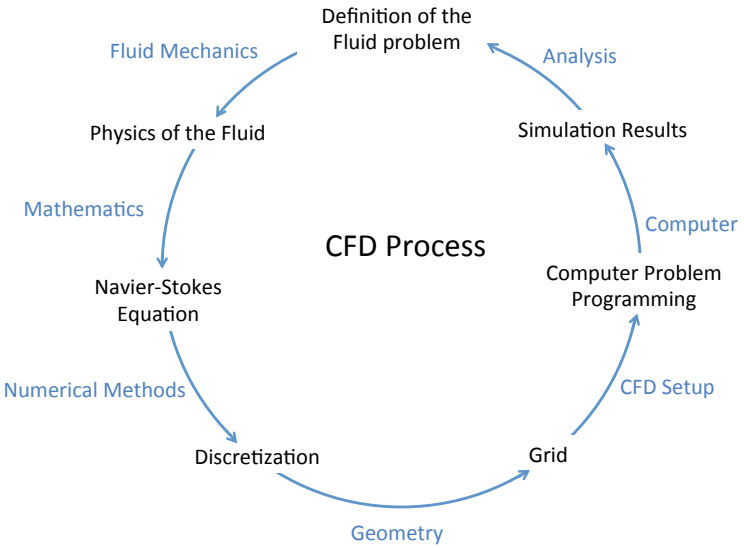


Figure 5.10. Schematic showing the process of CFD

5.4.1. The governing equations for fluid flow and heat transfer

Fluid flow is governed by a set of equations defined as the continuity equation, the momentum equations and the energy equation. The continuity equation describes how the mass of any fluid volume fixed with respect to a reference frame is conserved.

The rate of accumulated mass in a control volume	+	Net flux of mass out of a control surface	=	0

For a differential element in Cartesian coordinate this is defined as:

$$\frac{\partial \rho}{\partial t} + \frac{\partial \rho u}{\partial x} + \frac{\partial \rho v}{\partial y} + \frac{\partial \rho w}{\partial z} = 0 \qquad \text{eqn. 5.35}$$

where ρ is the fluid density, u, v, w are the velocity components in x, y, z Cartesian coordinates respectively, and $^{\partial \rho}/_{\partial t}$ is the increase in fluid storage with time. For a steady flow and constant fluid properties this is reduced to:

$$\frac{\partial u}{\partial x} + \frac{\partial v}{\partial y} + \frac{\partial w}{\partial z} = 0 \qquad \text{eqn. 5.36}$$

The linear momentum through a control volume is described as:

The rate of momentum accumulation in the control volume	+	The momentum flux across the surface area	=	Rate of momentum gain due to body forces	+	Rate of momentum gain due to surface stress

The simplified momentum equations for a steady flow and constant fluid properties is defined in Kays et al, (2004) as:

$$\rho\left(\frac{\partial u}{\partial t}+u\frac{\partial u}{\partial x}+v\frac{\partial u}{\partial y}+w\frac{\partial u}{\partial z}\right)=-\frac{\partial P}{\partial x}+\mu\left(\frac{\partial^2 u}{\partial x^2}+\frac{\partial^2 u}{\partial y^2}+\frac{\partial^2 u}{\partial z^2}\right)+\mathrm{X}_x \qquad \text{eqn. 5.37}$$

$$\rho\left(\frac{\partial v}{\partial t}+u\frac{\partial v}{\partial x}+v\frac{\partial v}{\partial y}+w\frac{\partial v}{\partial z}\right)=-\frac{\partial P}{\partial y}+\mu\left(\frac{\partial^2 v}{\partial x^2}+\frac{\partial^2 v}{\partial y^2}+\frac{\partial^2 v}{\partial z^2}\right)+\mathrm{X}_y \qquad \text{eqn. 5.38}$$

$$\rho\left(\frac{\partial w}{\partial t}+u\frac{\partial w}{\partial x}+v\frac{\partial w}{\partial y}+w\frac{\partial w}{\partial z}\right)=-\frac{\partial P}{\partial z}+\mu\left(\frac{\partial^2 w}{\partial x^2}+\frac{\partial^2 w}{\partial y^2}+\frac{\partial^2 w}{\partial z^2}\right)+\mathrm{X}_z \qquad \text{eqn. 5.39}$$

where X is the body force in the respective cartesian direction.
Likewise, the conservation of energy requires that:

The rate of accumulation of energy in a control volume	+	The net flux of energy across the surface area	=	Rate of gain of energy due to surface forces

In the absence of a mass diffusion term and with a steady flow and constant fluid properties, the energy equation is defined as:

$$\rho\mathrm{c}\left(\frac{\partial T}{\partial t}+u\frac{\partial T}{\partial x}+v\frac{\partial T}{\partial y}+w\frac{\partial T}{\partial z}\right)=\mathrm{k}\left(\frac{\partial^2 T}{\partial x^2}+\frac{\partial^2 T}{\partial y^2}+\frac{\partial^2 T}{\partial z^2}\right)+\mathrm{q}_V \qquad \text{eqn. 5.40}$$

where ρ is the density, c the heat capacity and k the thermal conductivity of the fluid. $\partial T/\partial t$ is the increase in temperature with time and q_V is the energy supplied per unit volume.

Depending on the problem being solved in CFD, the equations above can include coupled, non-linear, second order, partial differential equations. A set of boundary conditions is used to simplify the equations, which are solved numerically. The following section describes some of the techniques used in CFD modelling and the choice adopted for this analysis.

5.4.2. Solving the governing equations numerically

The numerical methods for solving partial differential equations are categorized into three groups: Finite Difference Methods (FDM), Finite Element Methods (FEM) and Finite Volume Methods (FVM). The methods differ in the grid type: structured for

FDM and unstructured for FEM and FVM; in the mathematical schemes which map the various types of partial differential equations in the governing equations onto the grid and also in the strategies that assure stability and convergence. The methods are however analogous in dealing with the physics aspects of fluid flow behaviour. Chung, (2002) shows how appropriate differencing schemes and methods are chosen depending on the particular physics flow problem and presents various methods for deriving the equations for FDM, FEM and FVM and their application to CFD.

Throughout the course of this thesis Autodesk CFD Simulation is used. The FEM software is based on the works of Schnipke, (1986). The successful application of the software to flow and heat transfer problems are documented in the literature (Rice and Schnipke, 1985, Schnipke and Rice, 1985). While the author appreciates the complex mathematics running in the background of any commercial CFD software, the user is often presented with an interface through which a series of key decisions are made. The focus of this section is hence turned on the process of undertaking a CFD study on a section of the YASA stator geometry.

5.4.3. CFD of the stator geometry

The application of CFD to any geometry is defined by the following steps:

1) Defining the geometry of the component under investigation
2) Material selection and setting the boundary conditions
3) Mesh setup
4) Simulation setup and numerical solution
5) Post processing and results analysis

Preliminary calculations of the Reynolds number within the channel show that this is in the range of 50-200. Therefore a laminar flow exists in the channel. The channels between pole pieces have a height to width ratio of 7.5. Hence the flow domain was investigated using a 2D CFD model of a quarter of the stator. While attempts to develop 3D CFD models were also made these was found to require a big mesh (>10M elements), which consumed computer resources. Despite that several strategies to reduce the size of a mesh to a manageable size were applied, very little computational resources for mesh refinement and checks for convergence was left.

The use of 3D CFD simulations in this chapter is hence limited to a few conditions. Still, the author treats the results from 3D CFD in this chapter only as indicative. The following section provides a description of the process CFD modelling.

Defining the stator geometry

2D and 3D CFD modelling require different procedures to develop the CAD geometry. The CAD model for the 2D CFDs simulations consist of a sketch of the quarter section of the stator highlighted in Figure 5.1. This was modelled using Autodesk Inventor® and is shown in Figure 5.11.

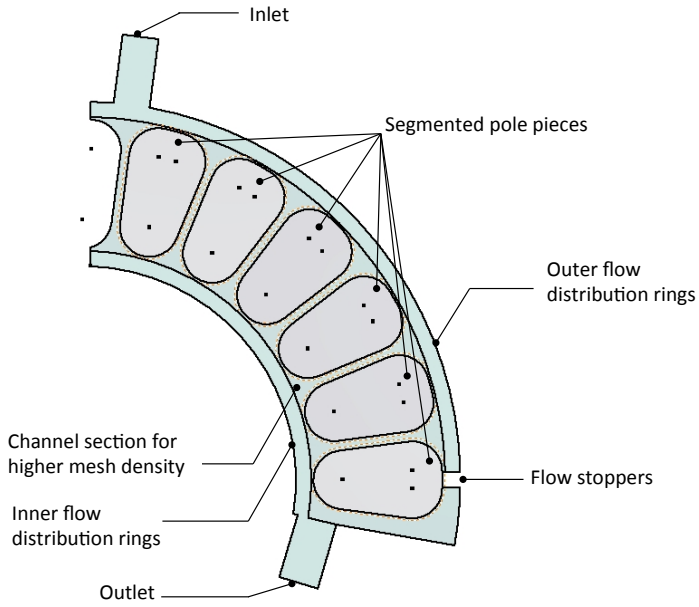


Figure 5.11. Details of the 2D CAD geometry

The CAD model includes the geometry of the flow domain and the geometry of the solid pole pieces. A notch to simulate the flow stopper in the machine is also included. To accurately capture the velocity and temperature gradient in the flow channels between the stator pole pieces it is important that this has a higher mesh density. The CAD modelling and meshing process are often interlinked and thus the user often goes through these processes multiple times to improve the efficiency and accuracy of the simulation. To avoid increasing the mesh density in the entire domain which increases the computational time the flow domain of the 2D model was made from three parts: the outer rim, the channels section and the inner rim.

A 3D CAD model of a quarter of the motor geometry shown in Figure 5.12 was also produced. As the stator has a toroidal shape it is symmetrical on plane perpendicular

to its central axis. Hence to reduce computational effort during the solution stage, only one half of the geometry is modelled. This is run with a symmetrical boundary condition as described in Section 5.4.5. Unlike 2D modelling, sectioning the 3D fluid volume into three components was found to exceed the computer resources and hence the two models adopt different meshing strategies as described in Section 5.4.6. The CAD models have been subsequently exported to Autodesk CFD Simulation® in which the processes of material and boundary definition, meshing and solving are performed. These steps are described in the following sections.

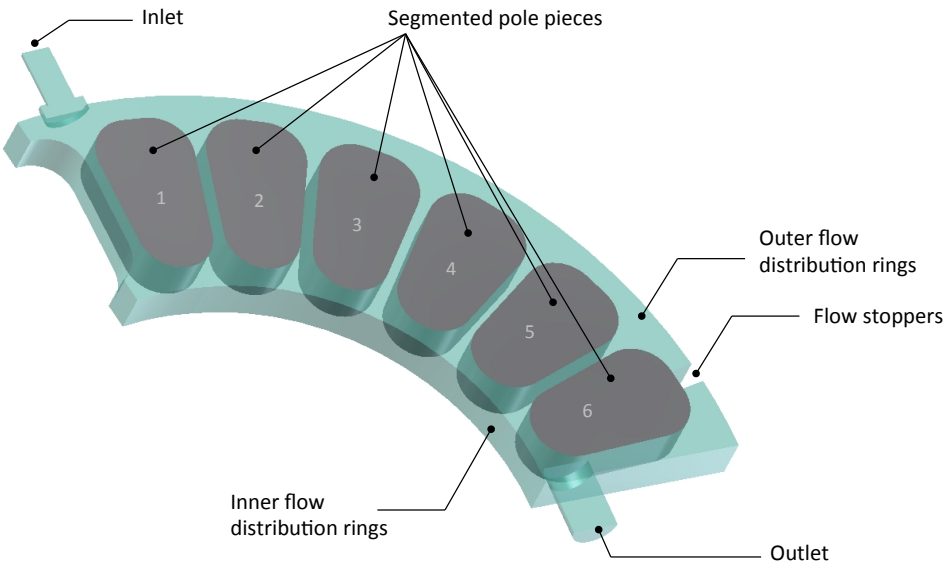


Figure 5.12. Details of the 3D CAD geometry.

Material selection, material properties and boundary conditions

As this simulation will be compared with experiments described later, the pole piece material was set to aluminum while the fluid region was defined as Opticool oil coolant. The properties of oil were defined to vary with temperature as shown in Table 5.1. This was found to have a significant impact on the temperature prediction of pole pieces in scenarios with high heat loads. The sensitivity of the CFD model to the temperature dependent properties was also tested. It was found that in some cases simulations with fixed temperature properties produced a pole piece temperature over predictions of up to 35%.

In the 2D model, a fluid velocity and temperature were set to the inlet edge. An internal heat load density (W/m^3) was set to the pole piece materials. A gauge pressure of 0 Pa was set at the exit edge. Conversely, in 3D modelling the flow rate

and temperature were set to the inlet surface while the pole piece internal heat generation was set to the volume. A gauge pressure of 0 Pa was set at the exit surface. In both 2D and 3D models, the conditions were set to replicate experimental tests, making it easier to validate with experimental results. The experimental conditions are shown in Table 5.3 of Section 5.5.2. The 3D model includes a Slip/Symmetry boundary condition on the middle surface to replicate symmetrical flow and heat transfer. Figure 5.13 and Figure 5.14 show a schematic of the boundary conditions for the 2D and 3D model respectively.

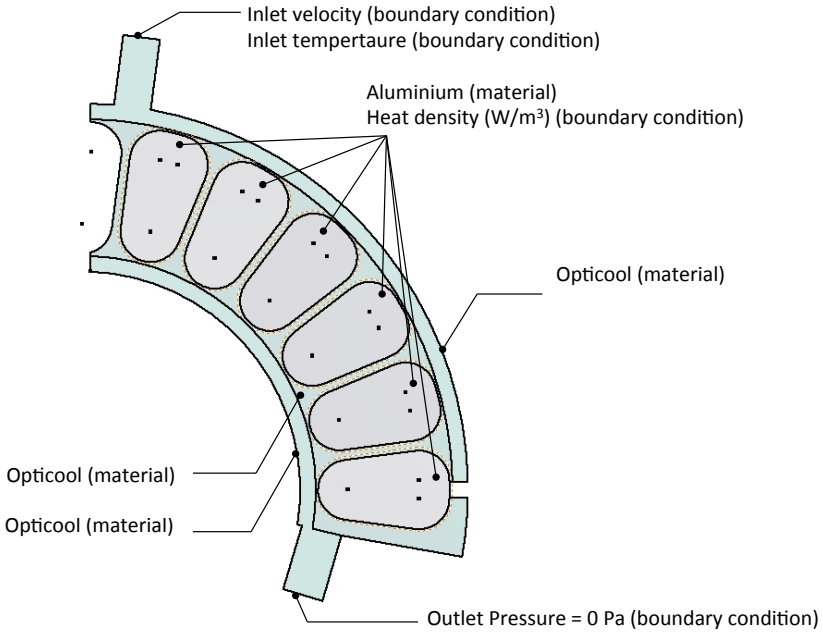


Figure 5.13. Details of the boundary conditions applied to the 2D model

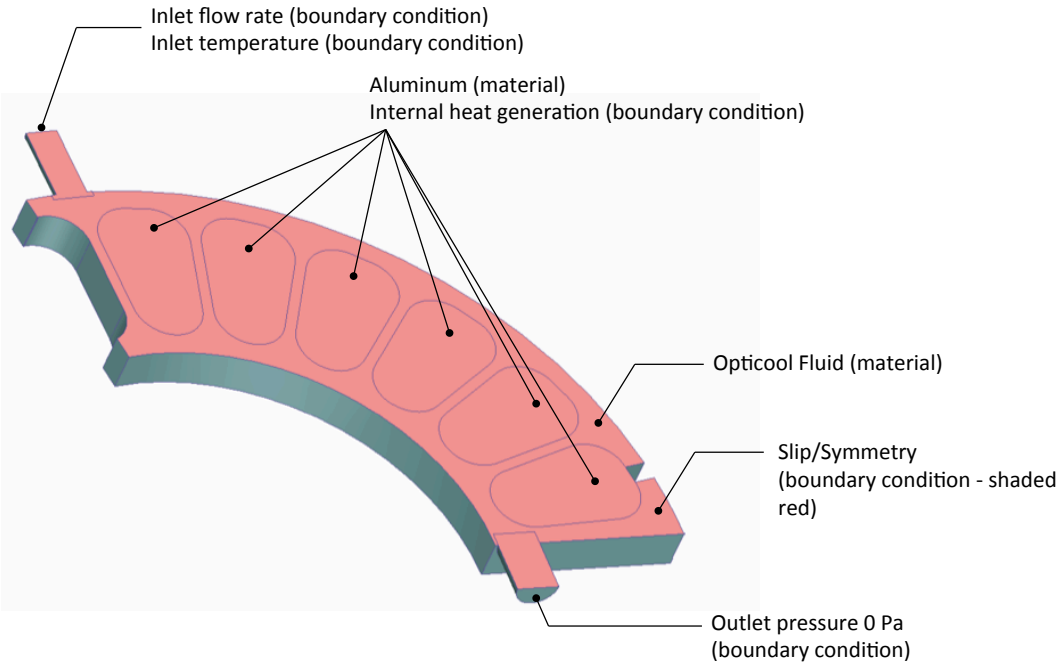


Figure 5.14. Details of the boundary conditions applied to the 3D model

Mesh setup and Enhancement

The meshing procedure in Autodesk CFD Simulation can be setup using manual or automated meshing. Automatic meshing analyzes the CAD geometry and determines the mesh size distribution on the CAD edges, surfaces and volumes. While the automated process simplifies the meshing, the positions of the nodes are visualized giving the user an initial estimate of the mesh size. In this analysis the automatic meshing was adopted. The user is also allowed to customize the mesh size by adjusting the mesh distribution in specific locations of the geometry. Prior to meshing, the software offers a mesh diagnostics in which an algorithm is run to identify potential meshing problems. These are typically related to meshing small edges on which the minimum refinement length of the mesh can be fine-tuned.

In 2D simulations the mesh was formed from triangular elements with the minimum refinement length set to 0.477 on the edges and a maximum size of 0.4 set to the surfaces. With the materials set, the meshing algorithm identifies where the solid-fluid interfaces are and adds a boundary layer mesh along these surfaces. The user is able to enhance the boundary layer mesh by adding layers, define a layer factor to set the boundary layer thickness and layer gradation to set the rate of change in thickness from one layer to the next. In these simulations the boundary layer mesh was enhanced by the setup of 15 layers. The layer factor was set at 1.05 and a gradation of 1.15 was set. The simulation was repeated with tighter mesh settings until the variation in temperature was less than 2% was achieved. This is a key step to establish grid convergence and gaining confidence in the solution. The final mesh size consisted of 0.37M elements, distributed as 0.35M elements within the flow domain and 20k elements within the solid domain. The 2D mesh is shown in Figure 5.15. A solution is found in approximately 3 hrs.

The 3D CFD model adopted tetrahedral elements. The minimum refinement length was set to 0.15 on the edges and a maximum size of 0.3 set to the surfaces. A boundary layer mesh was made from 15 layers with a layer factor of 1.05 and a gradation of 1.15 was set. As the number of meshing elements is computationally limited by the computer RAM, a gap refinement strategy has been adopted, so that the flow channels between the pole pieces contain a minimum of 6 nodes in the free stream region.

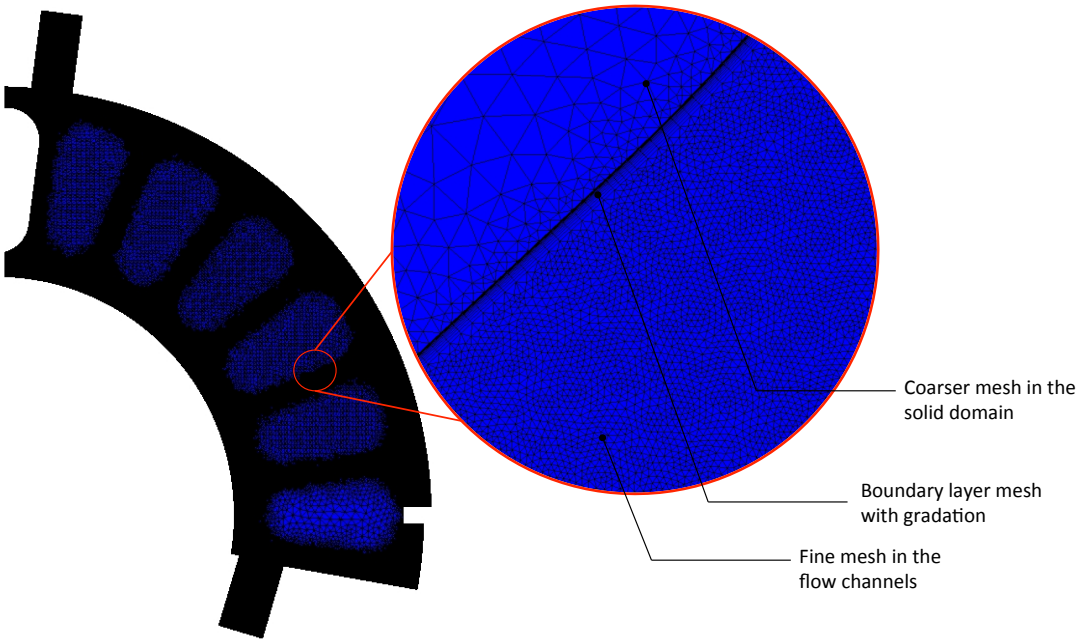


Figure 5.15. Mesh setup for the 2D model with inserts of the uniform mesh in the fluid channels and details of the gradation boundary layer mesh at the solid-fluid boundary

The surface and volume growth rate have been set to 1.20, thus controlling the growth rate of the meshing elements from the finely spaced regions to the sparsely spaced region. The mesh totalled 5.85M elements with 4.51M elements used to model the fluid domain and 1.34M elements to model the solid domain. A solution is found in approximately 4 days. Despite the efforts to reduce the size of the mesh and the computational efforts, the checks for grid convergence were limited by the computer resources.

Simulation setup and numerical solution

Due to the low Reynolds numbers across all the channels, the simulation was run with a Laminar model. In these CFD simulations the author experimented with fixed and temperature dependent coolant properties, conjugate and segregated simulations, and different advection models. The advection models are the numerical mechanisms for transporting quantities such as the velocity and temperature through the solution domain. Five advection schemes are available to Autodesk CFD Simulation. These are described in the Autodesk CFD Simulation Help, (2014). A brief definition is provided in Table 5.2.

Table 5.2 Description and Application of Advection Schemes as from Autodesk, (2016)

ADV 1 (Monotone Streamline Upwind)	Default scheme and starting point for most analysis. Numerically stable and recommended for meshes aligned with flow direction, internal flow with obstructions and extruded meshes.
ADV 2 (Petrov-Galerkin)	Moderate numerical stability and recommended for large domains such as unrestricted external flow, pressure driven flows, compressible flows, energy transport and analysis of rotating regions.
ADV 3 (Flux based scheme)	Numerically unstable for most flows and only suggested for incompressible flows. Tuned for drag or external flow problems.
ADV 4 (Min-Mod scheme – Petrov Galerkin variant)	Moderate numerical stability tuned for flows in long narrow ducts.
ADV 5 (Modified Petrov-Galerkin)	A more stable variation of ADV 2 but produces more conservative results than ADV 2. This Advection scheme has shown improvements in areas of energy balance stability, rotation stability, natural convection stability.

In the choice of the Advections Schemes, ADV 1 and ADV 4 were found to be most accurate with ADV 4 having a slightly better temperature prediction (of around 1%). The simulations were hence run as a conjugate, laminar model with ADV 4 and temperature dependent fluid properties. The simulations were repeated with tightened solution settings to ensure convergence in time.

Post-processing

The post processing section of the CFD software enables the user to visualize pressure, velocity and temperature results amongst others, on selected walls, planes or paths. This provides the user with an insight on the fluid behaviour in the present design, and the foresight on how to improve the design in the next simulation. The post-processing results are presented in Section 5.6 whereby they are validated against experimental measurements and the analytical model.

Having described both analytical and numerical techniques to establish the flow and temperature distribution in the stator, the following section describes the experimental approach required to measure and validate the models. Segmented stators offer the benefit of undertaking thermal analysis on single pole pieces (Wrobel et al, 2011). This significantly speeds up the thermal design of the machine. This approach is taken whereby a quarter of the stator is set up.

5.5. Experimental work

In this section, the process of setting up the experiment, measuring the temperature distribution is presented. Segmented stators offer the benefit of undertaking thermal analysis on single pole pieces rather than the whole machine stator (Wrobel et al, 2011). This significantly simplifies thermal experiments speeding up the thermal design of the machine.

5.5.1. Manufacturing the test piece

In this work, a representative experiment of a quadrant of the stator highlighted in Figure 5.1 was set up. Replicas of the pole piece geometry were machined in aluminium and used to replace the segmented stator pole pieces. Aluminium was chosen due to the high conductivity and ease of manufacturing. The high conductivity will allow the pole piece to be at a homogeneous temperature and eliminate potential temperature measurement errors related to the temperature distribution within each pole piece. This satisfies the scope of this part of the research i.e. to produce a means of validating a numerical model that produces a fast and accurate general temperature overview of the stator. As the flow regime is laminar at a Reynolds number of approximately 200, small differences in the surface finish between actual pole pieces with epoxy and the machined aluminum pieces do not produce significant differences to the heat transfer coefficient. Each aluminum piece was fitted with a 230 V, 150 W cartridge heater of dimensions 10 mm diameter x 50 mm length. The heater simulates the total internal heat generation in each pole piece. Silicone based thermal interface material was applied to improve the heat transfer between the heater and the pole pieces. Each pole piece was drilled with two 1mm holes and fitted with two temperature sensors. The pole pieces were carefully assembled on a plastic base in a test box, recreating the flow channels between them. The plastic base limits the heat transfer to the test box. A schematic of the machine's pole piece with installed cartridge heater is shown in Figure 5.16. The test rig for a quarter of the machine stator is shown in Figure 5.17.

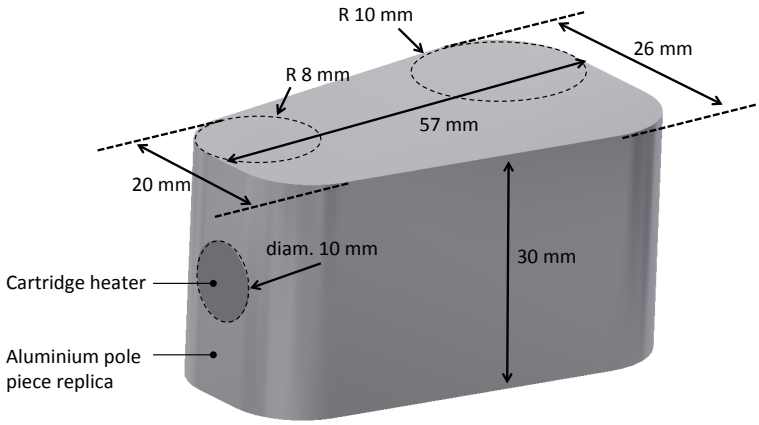


Figure 5.16. Schematic of the machine pole piece with installed heater

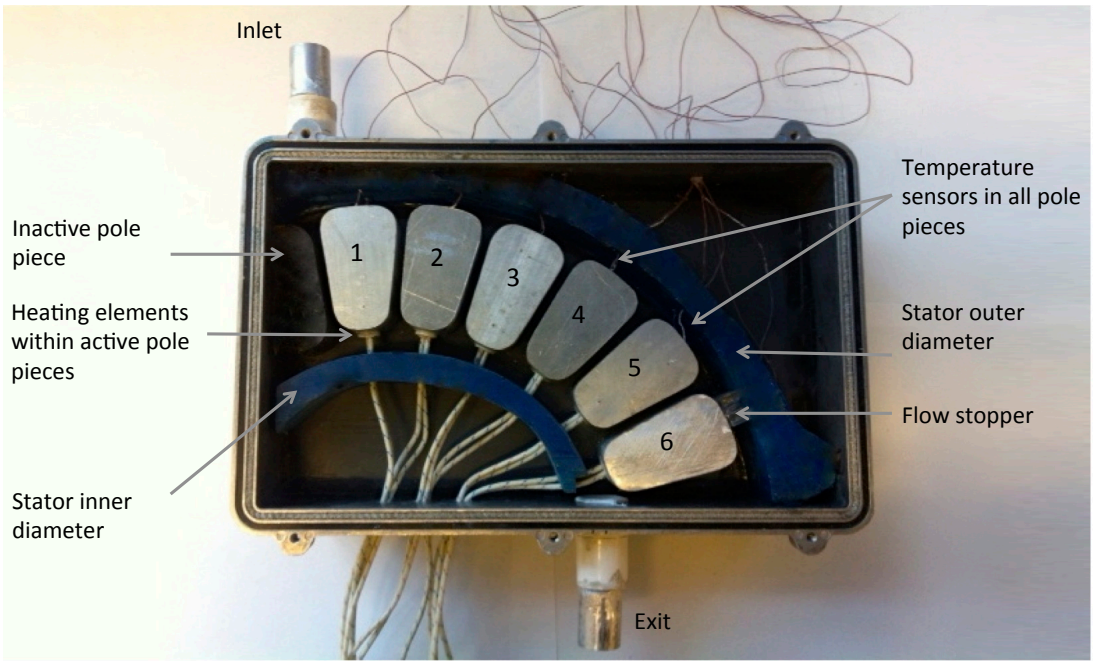


Figure 5.17. Test rig representing the first quarter of the machine stator

5.5.2. Measuring the temperature distribution in the stator

The pole piece heaters were connected to a variable transformer, which was used to regulate the heat input. Current meters and a differential voltage probe were used to measure the current and voltage supplied to the heaters using a PicoScope 3000 series oscilloscope recording at 1 Hz. The heat input P was calculated as:

$$P = I.V \qquad \text{eqn. 5.41}$$

where I and V are the measured dc current and dc voltage supplied to the heaters. Pico data loggers were used to record pole piece temperatures at 1 Hz. The coolant was re-circulated from a reservoir into the test rig and then pumped through a heat exchanger, expelling heat to ambient. The reservoir was also fitted with a heating

element to control the inlet temperature of the fluid into the test section. The power input to the coolant heater was also regulated through a transformer. The flow rate was regulated using a globe valve and measured using a variable area flow meter, as shown in Figure 5.18. Each experiment was run for approximately 3 hours to achieve steady state conditions. The steady state values across the final hour were then averaged to determine the temperature distribution of the pole pieces. The experiment was repeated for various coolant flow rates, inlet temperatures and pole piece heat losses, shown in Table 5.3. The uncertainty analysis for the measurements in this experiment is shown in Appendix 1.

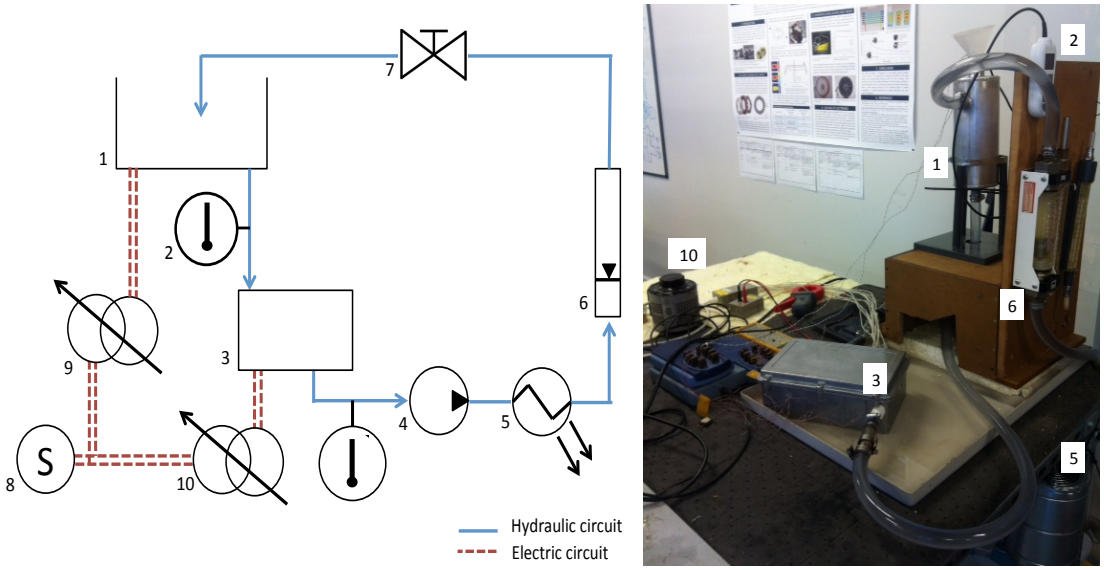


Figure 5.18. Test setup with 1) oil reservoir, 2) temperature sensors, 3) test box, 4) pump, 5) heat exchanger, 6) variable area flow meter, 7) globe valve, 8) ac power supply, 9) variable transformer to power fluid heater, 10) variable transformer to power pole piece heaters

Table 5.3. Experiment Details

Test No.	Coolant inlet temperature [^{o}C]	Flow rate [lpm]	Pole piece heat input [W]
1	24.58	0.96	81.06
2	22.96	0.96	148.14
3	23.57	1.67	81.14
4	24.85	1.77	152.27
5	40.47	1.00	82.02
6	40.83	1.16	148.36
7	40.06	1.76	82.11
8	41.52	1.99	148.89

Following the description of the experimental procedure, the next section presents the results. These are used to validate the analytical model and CFD models and highlight the strengths and weaknesses of each model.

5.6. Test Results and Model Validation

Figure 5.19 and Figure 5.20 compare the measured pole piece temperature to the simulated temperatures from the LP model, 2D CFD model 3D CFD model (with application limited to Test 1, Test 7 and Test 8). The prediction of the flow distribution from the LP and CFD models is shown in Figure 5.21 and Figure 5.22. Pole piece temperature predictions from the LP model are found to be within 6% of the measured pole piece temperatures. Conversely the 2D CFD model matches most measurements to within 5%. However this consistently under predicts the temperature of pole piece 5 by approximately 18%. This has been traced back to small differences in geometry between the CAD model and experimental test rig, which affect the flow and temperature distribution. The 3D CFD model generally over predicts the pole piece temperatures. This model consumes the computer resources and the over prediction is due to a mesh that is not fine enough. While the general shapes of the flow distribution from the LP and CFD models shown in Figure 5.21 and Figure 5.22 follow each other and are generally within 7% of each other. However the worst case scenario stands at channel 2 in Test 6 when the flow rate is very small and the difference between the LP and CFD model is at 21%. The discrepancy is attributed to small differences in geometry. As the flow channels are only 4 mm wide a small difference in the CAD model may have a big impact on the accuracy of the result. The LP model may be more robust and less sensitive to tiny variations.

While the CFD models take longer to solve than LP models, it provides a useful insight into the thermo-fluid behaviour in the flow domain. Figure 5.23 shows an example of the visualization of the velocity map and pressure distribution of the fluid around the stator geometry for boundary conditions shown in Test Case 5. It can be seen how a higher velocity (and thus a higher flow rate) exists in outer ring. The flow takes the path of least resistance bypassing the flow channels and limiting the heat transfer from the pole pieces. Figure 5.24 shows a temperature plot of the stator pole pieces and fluid through the model. The simulation shows an area of hot stagnant

fluid trapped near the exit. This is a property of the test setup and modelling a quarter of the stator. This area would not exist in a full machine stator. It is interesting to note the laminar aspects of the flow in which the hot streaks of fluid in the inner distribution ring with a long mixing length. The extent of the laminar flow is also shown in the segregated viscosity of the fluid, which is affected with temperature of the fluid along the flow domain.

Having compared CFD simulations and the LP model with experimental measurements, the following section simulates the pole piece temperatures for a whole machine stator. While the LP models achieve a quick temperature map of the stator, the insights from CFD are used to develop a strategy that improves the flow distribution in the machine and consequently improving the temperature distribution of the pole pieces. The following section investigates the flow and temperature distribution in the machine stator.

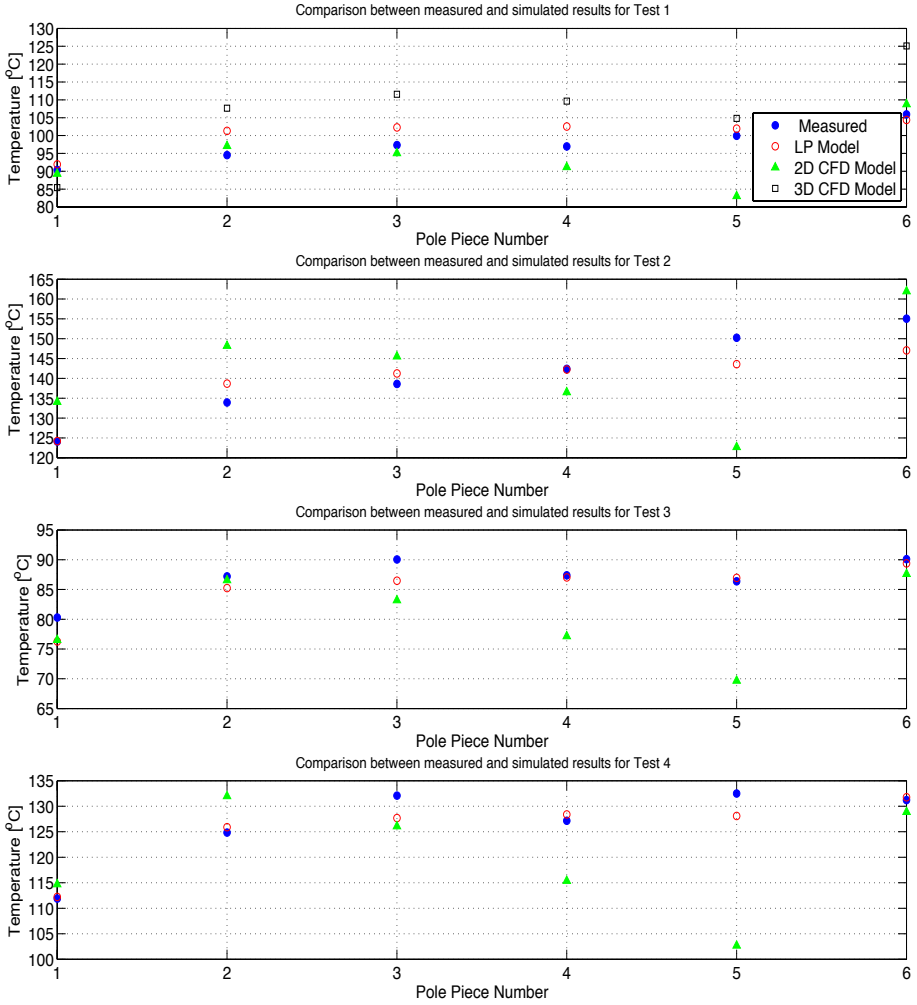


Figure 5.19. Comparison of the measured pole piece temperature with LP model and CFD model for the test conditions 1-4

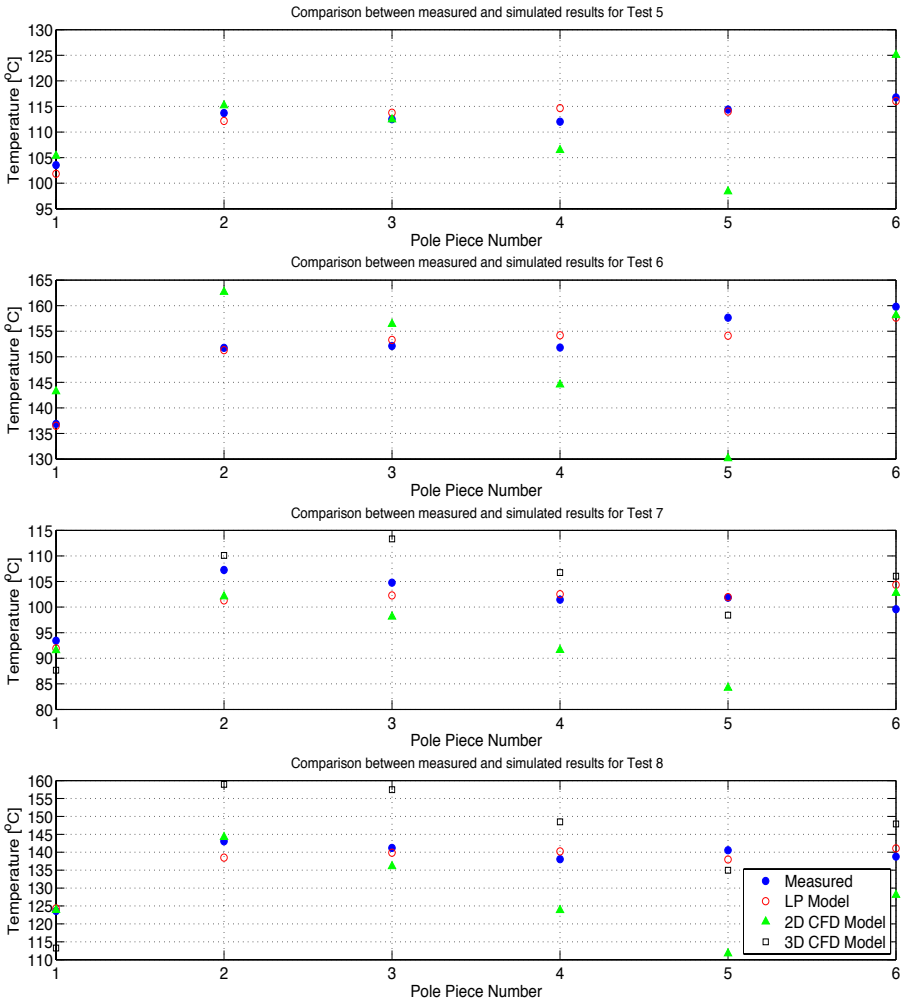


Figure 5.20. Comparison of the measured pole piece temperature with LP model and CFD model for the test conditions 5-8

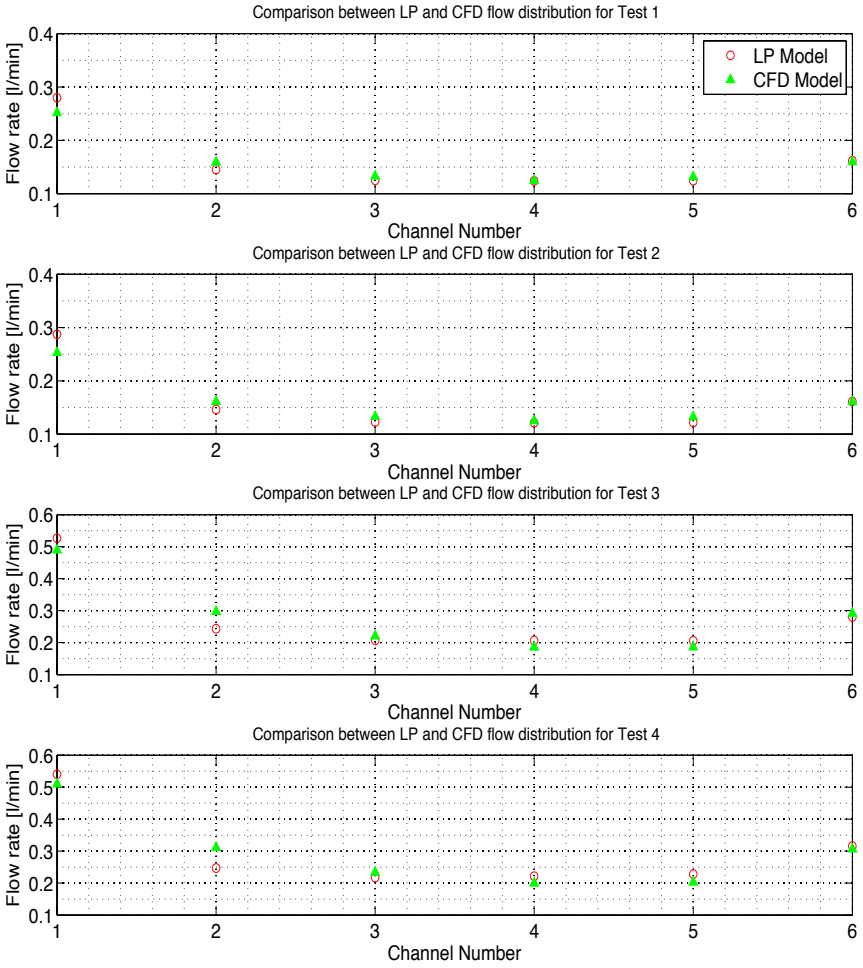


Figure 5.21. Comparison of the flow distribution from the LP model and CFD model for the test conditions 1-4

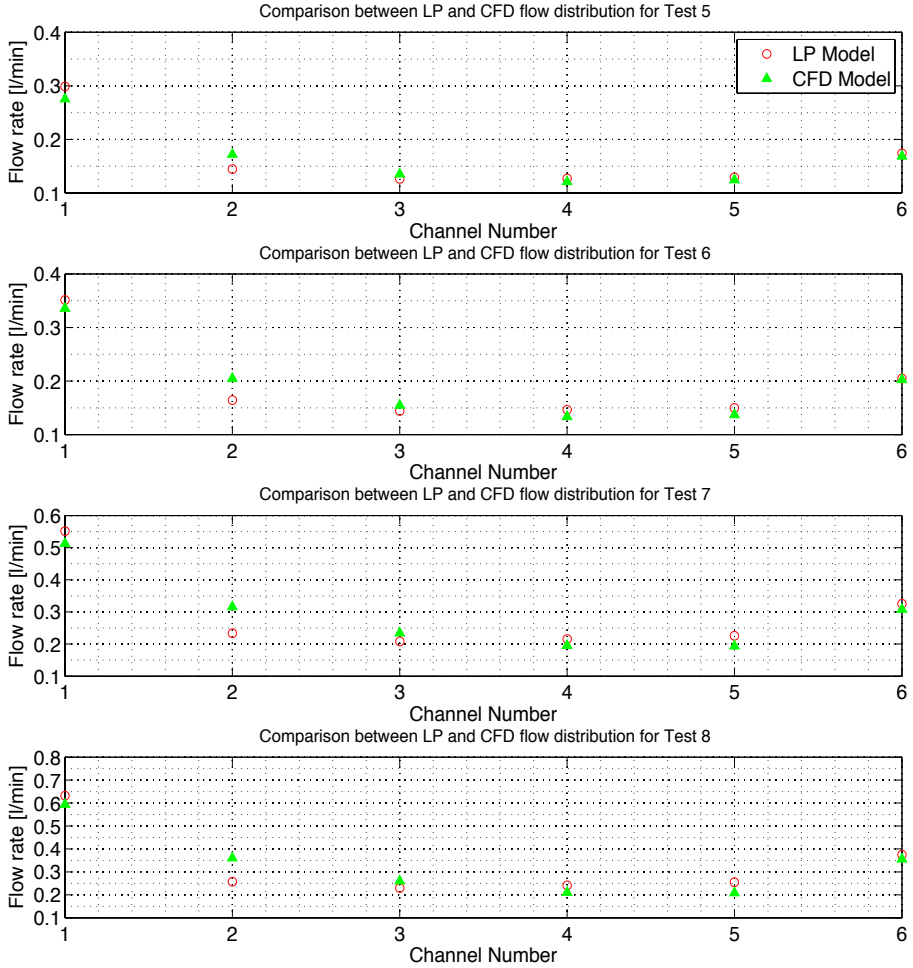


Figure 5.22. Comparison of the flow distribution from the LP model and CFD model for the test conditions 5-10

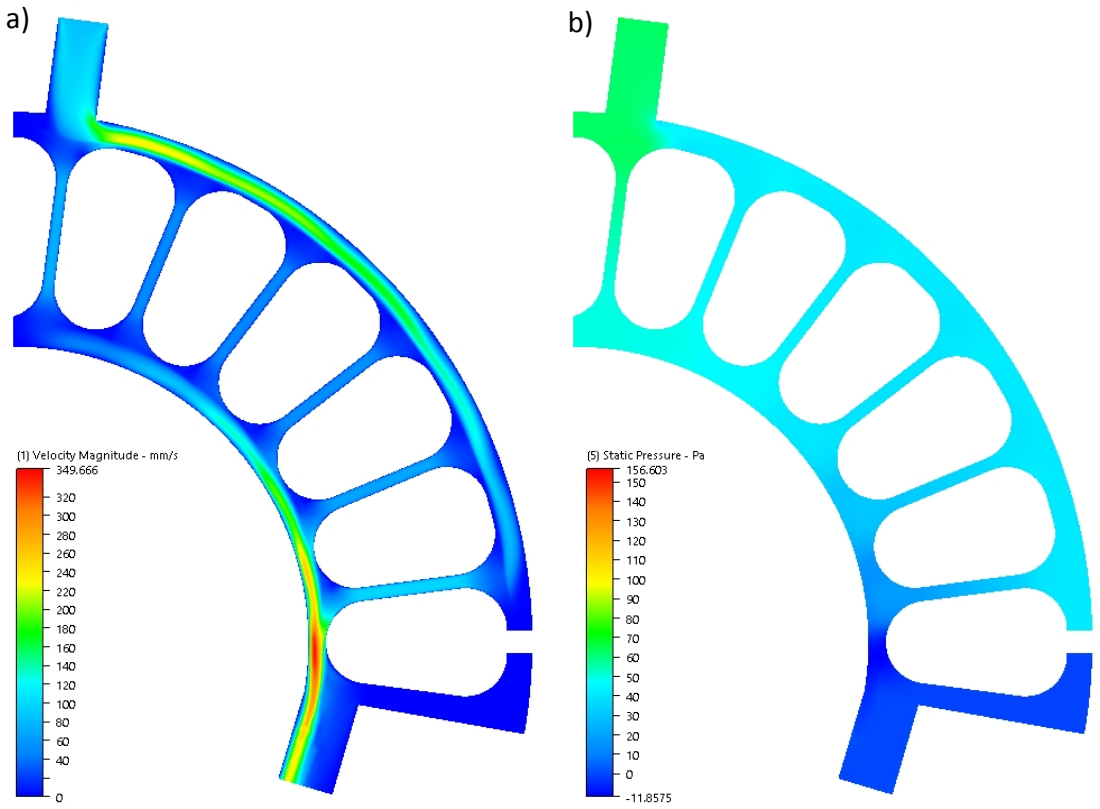


Figure 5.23. a) Example of the fluid velocity map and b) the resulting pressure distribution through the stator flow domain for Test condition 5 from the 2D CFD simulations

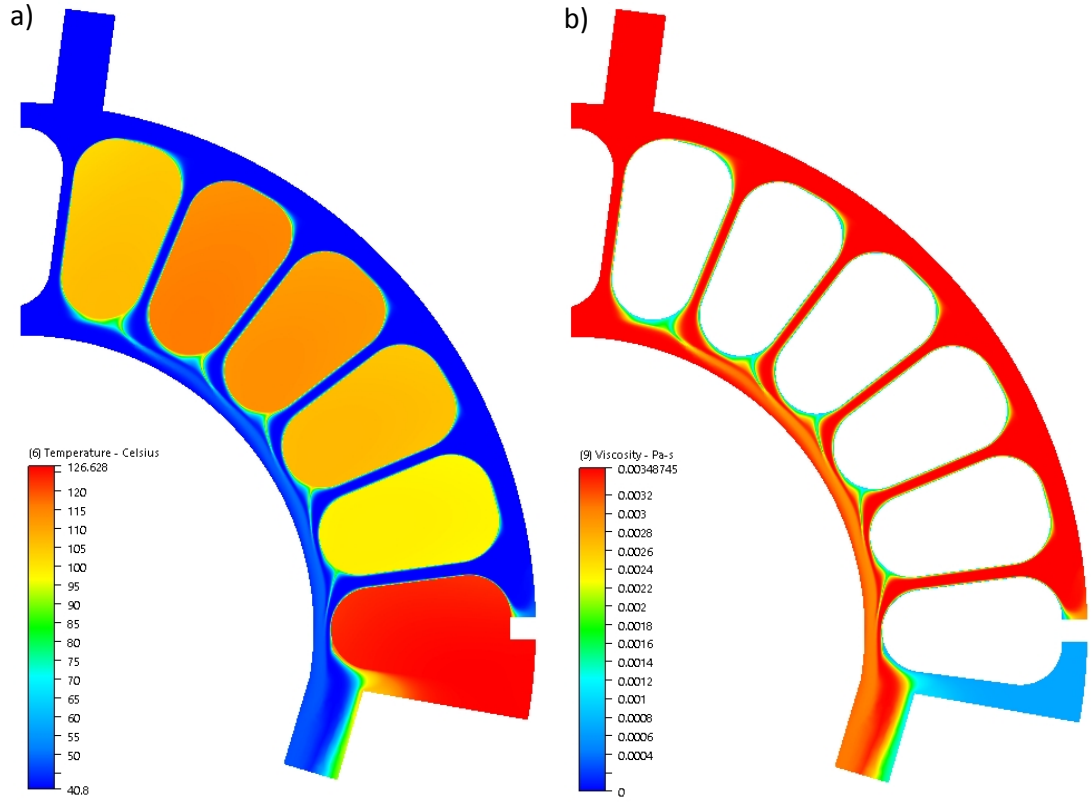


Figure 5.24. a) Example of the Temperature map of the stator and b) the resulting viscosity map in the stator fluid domain for Test condition 5 from the 2D CFD simulations

5.7. Simulation of the Machine Stator

While in Section 5.6 it was shown that both LP and CFD models are able to capture the temperature map of the machine segment, this section scales this up to simulate the temperature distribution of the entire machine stator. Due to its quick and accurate solution, the LP model was used to investigate the full motor geometry. The motor was simulated with a coolant inlet temperature of 80 ^{o}C a nominal inlet coolant flow rate of 6 lpm and various pole piece losses. The resulting temperature map is shown in Figure 5.25.

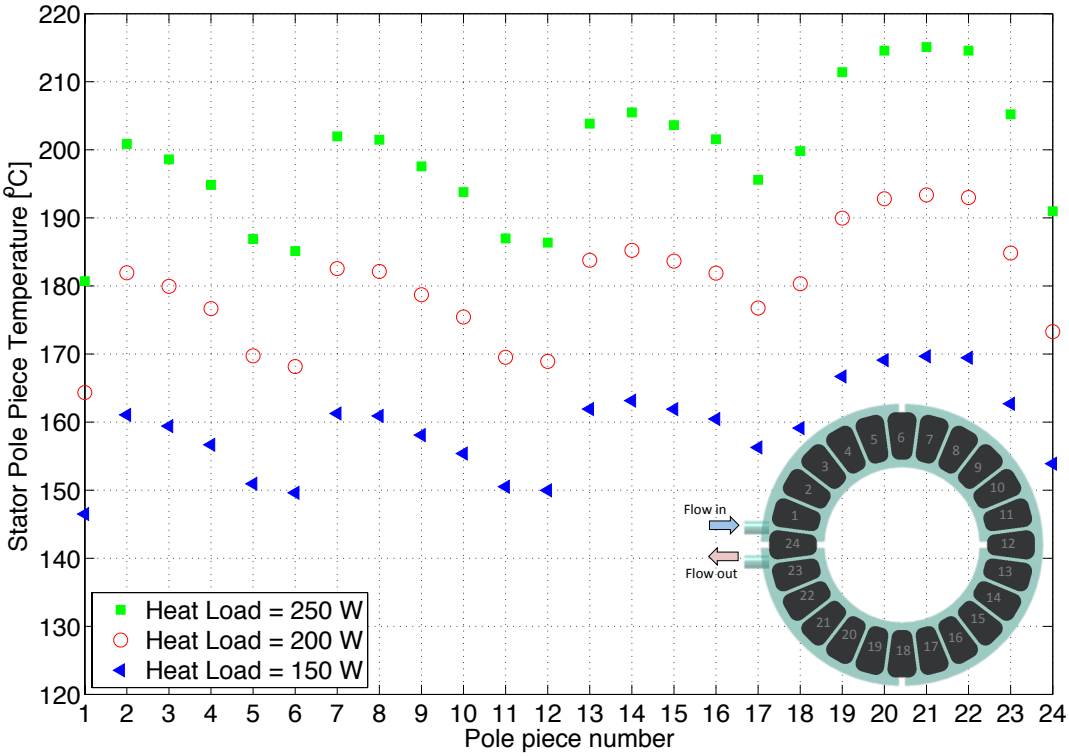


Figure 5.25. Simulation of the machine stator temperature distribution with pole piece heat loads of 250 W, 200 W and 150 W. Insert: schematic of the stator with numbered pole pieces

It can be noted that the pole pieces within each segment suffer from a non-uniform temperature distribution. The temperature pattern is repeated throughout each of the four segments of the stator. As the coolant flows from one segment to the other, the temperature difference between the pole pieces and the coolant gradually deteriorates and hence the coolant looses some of its effectiveness. Hence the pole pieces in each consecutive stator segment suffer from a small increase in temperature. The model was used with different heat loss, inlet flow rate and coolant inlet temperature. The temperature of each pole piece was found to increase with increasing heat loss and inlet temperature and with decreasing coolant flow rate. The temperature range across

the entire motor was also found to increase with increasing heat loss and inlet temperature and with decreasing coolant flow rate.

Having simulated the temperature map of the segmented stator, the following section uses the developed models to improve the design of the stator so that the pole piece temperature is reduced and the current density increased.

5.8. Improvements to the stator temperature distribution

In our pursuit to increase the current density of the machine, the hottest pole piece presents the major limiting factor as the winding insulation on that pole piece will be overstressed. CFD results shown in Figure 5.23 demonstrate insights of the flow being distributed around the inner and outer rings. The lower flow rates between the pole pieces causes some pole pieces to overheat. To promote flow rates in the channels between pole pieces, the effect of the width of the distribution rings on the pole piece temperature was investigated. The results are shown in Figure 5.26.

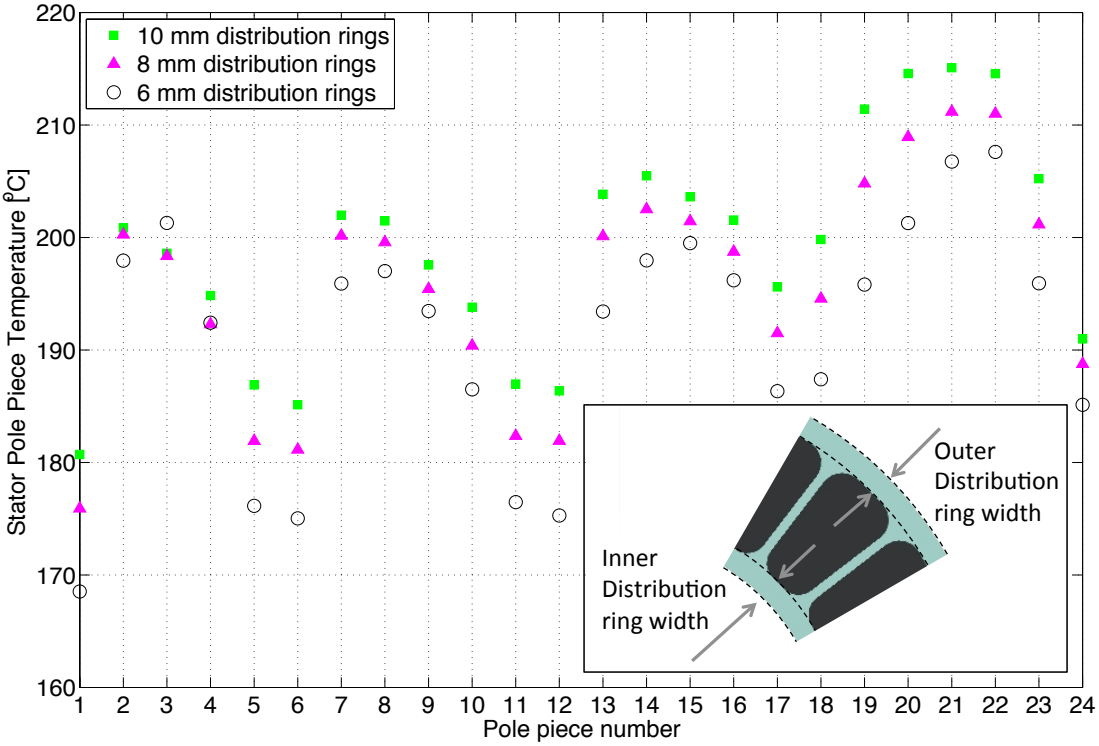


Figure 5.26. Simulation of the machine stator temperatures for a fixed flow rate and constant heat load and distribution rings of 10 mm, 8 mm and 6 mm width. Insert: schematic of the modified dimension

While reducing the width of distribution rings forces higher flow rates through the pole piece channels and was found to lower the temperature of the pole pieces, the temperature non-uniformity increases. Therefore the flow domain was modified further by partially blocking the inner and outer flow distribution rings on several strategic locations. This forces the oil through the pole piece channels in areas where these tend to suffer from higher temperatures. Establishing the best locations of the partial blockages is an iterative process. Hence CFD approach will be time consuming, and unsuitable to apply within a design environment.

The iterative flow network and LP model was again used to investigate the effect of the flow distribution on the pole piece temperature distribution. In a paper on flow distribution in parallel flow heat exchangers, Chiou, (1982) and Wang, (2011) used the concept of standard deviation to define flow non-uniformity ϕ_F.

$$\phi_F = \sqrt{\frac{\sum_{i=1}^{N}\left(\beta_{Fi} - \overline{\beta_F}\right)^2}{N}} \qquad \text{eqn. 5.42}$$

where β_{Fi} is the flow ratio for the ith tube defined as $\beta_{Fi} = {\dot{Q}_i}/{\dot{Q}_{in}}$, and $\sum_{i=1}^{N}|\beta_{Fi}| = 1$. $\overline{\beta_F}$ is the average flow ratio for the total number of tubes defined as $\overline{\beta_F} = {(\sum_{i=1}^{N}\beta_{Fi})}/{N}$. Q_i is the volume flow rate through the ith tube and Q_{in} is the volume flow rate in the machine. The larger the value of ϕ_F the higher the non-uniformity. This concept is also applied to this thesis to quantify the flow non-uniformity along the stator. Furthermore, the concept is adapted to quantify the pole piece temperature non-uniformity ϕ_T. The temperature non-uniformity is defined as:

$$\phi_T = \sqrt{\frac{\sum_{i=1}^{N}(T_i - \bar{T})^2}{N}} \qquad \text{eqn. 5.43}$$

where T_i is the temperature for the ith pole piece for each segment. $\bar{T}$ is the average temperature for the total number of pole pieces in each segment defined as $\bar{T} = {(\sum_{i=1}^{N}T_i)}/{N}$. As with the value of flow non-uniformity ϕ_F, the larger the value of ϕ_T the higher the non-uniformity. Since the primary focus of this investigation is the temperature of the pole pieces, the stator geometry is altered until a low temperature standard deviation for each of the YASA sectors is achieved. It is found that:

1. Decreasing the width of the outer and inner fluid paths increases the head loss from the paths, forcing a larger portion of the flow through the pole piece channels. This increasing the flow velocity and the HTC, reducing the pole piece temperatures. However doing this alone is not enough to produce a uniform pole piece temperature distribution.
2. The flow distribution is determined by the relative head losses of the pipes. By increasing the head losses in the rings, an uneven flow distribution (and temperature distribution) occurs

The flow distribution in the stator is altered by introducing flow-restricting components at specific locations within the inner and outer rings. Figure 5.27 compares the flow ratio in the channels of the stator. Figure 5.28 compares the pole piece temperature in the stator.

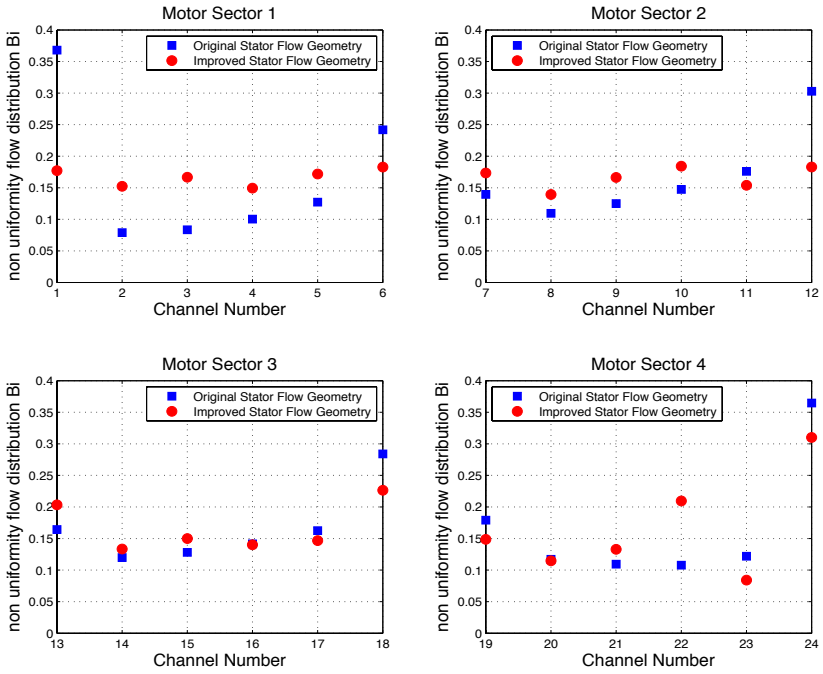


Figure 5.27. Comparison of the flow ratio for the four motor sectors before and after the changes to the stator flow geometry. Simulation with a coolant flow rate of 6 lpm, coolant inlet temperature of 80 ^{o}C, and pole piece losses of 250 W

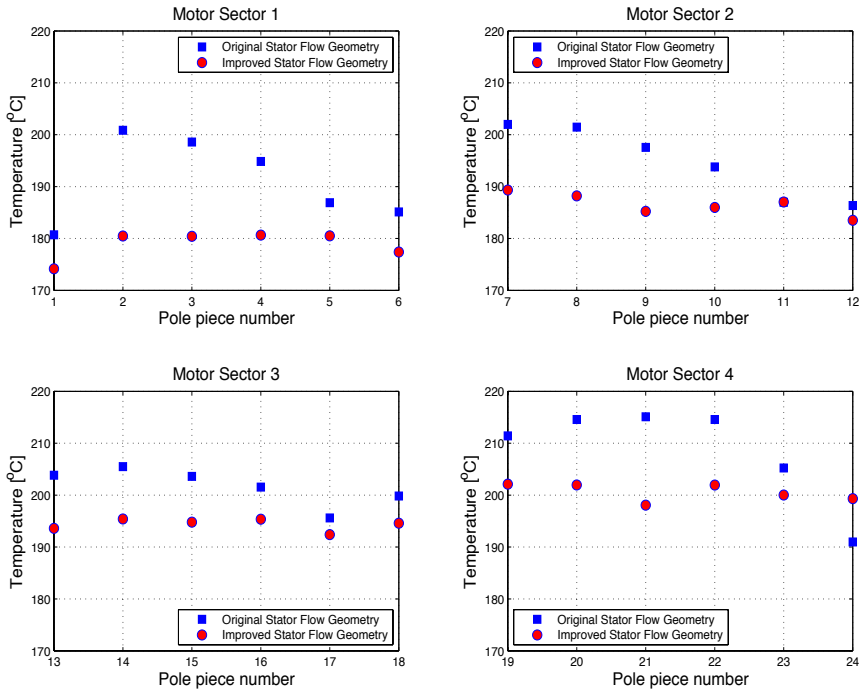


Figure 5.28. Comparison of the predicted stator pole piece temperatures for the original and improved stator flow geometry. Simulation with a coolant flow rate of 6 lpm, coolant inlet temperature of 80 °C, and pole piece losses of 250 W

The flow and temperature non-uniformity before and after the design changes are shown in Table 5.4 and Table 5.5.

Table 5.4 Comparison of the Flow non-uniformity for the Original and Improved stator geometry

Pole piece No.	Flow non-uniformity ϕ_F Original Stator geometry	Flow non-uniformity ϕ_F Improved stator geometry
Sector 1	0.106	0.012
Sector 2	0.064	0.016
Sector 3	0.055	0.035
Sector 4	0.092	0.075

Table 5.5 Comparison of the Temperature Variance for the Original and Improved stator geometry

Pole piece No.	Temperature Variance ϕ_T Original Stator geometry	Temperature Variance ϕ_T Improved stator geometry
Sector 1	7.38	2.42
Sector 2	6.29	1.93
Sector 3	3.25	1.06
Sector 4	8.59	1.54

The flow distribution was seen to have a direct influence on the temperature distribution in the stator. By modifying the flow geometry, the pole piece

temperatures are reduced. The maximum hotspot temperature is reduced by approximately 13 K. The variance for the improved stator geometry is smaller than the variance for the original stator geometry. In some cases the variance in the temperature distribution is reduced by a factor of 3, and in the best case by a factor of 7. The improved stator flow geometry is shown in Figure 5.29.

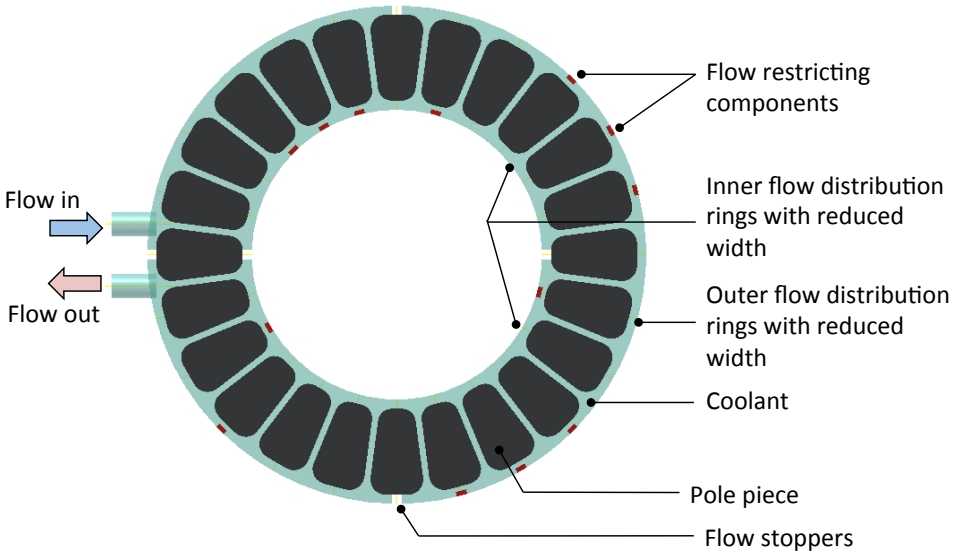


Figure 5.29. The resulting stator flow geometry achieving an improved temperature distribution

5.9. Discussion and Conclusion

This chapter investigated direct liquid cooled electrical machine by addressing an existing gap in the knowledge of flow and temperature distribution in the stator. A fast and accurate numerical simulation tool to predict the flow and temperature distribution of a segmented stator has been developed. The tool has been validated against measurements and compared to CFD modelling for a direct oil-cooled segmented stator that was used as a test case study. While CFD models have been found to provide invaluable insight on the flow behaviour, this process is time consuming and requires a large computational effort. This limits its application to a design environment. The developed LP model provides the thermal designer with an overview of the thermal distribution of the segmented stator at a very early design stage of the machine. The effects of different geometrical and operational conditions on the temperature distribution of the stator can be very quickly investigated, thus limiting the use of CFD and speeding up the development time.

This chapter has shown that by controlling the flow distribution in the stator, the temperature distribution is improved and the hotspot temperature reduced. This can be used to benefit the motor in one of two ways:

1. Increase the lifetime of winding insulation.

In section 1.2 of the introductory chapter it was shown how thermal ageing of insulation is commonly estimated by the Arrhenius reaction rate equation. A 10 K rule of thumb by Montsinger, (1930) is often used a means to measure the reduction of half the life expectancy of the winding insulation. By improving the stator flow geometry of this case study the hot spot temperature has been reduced by 13 K, doubling the lifetime of the stator insulation.

2. Increase the current density of the machine

If the main aim of the machine designer is to achieve a more powerful machine, a higher current can be pushed through the stator windings of the improved stator flow geometry until the same hot spot temperature is reached. In this test case study it was found that the pole piece heat losses in the new stator design are increased by 13% before the same hotspot temperature as the old geometry is reached. Assuming that in a low speed machine the ratio of rotor and iron losses remains constant with a small increase in current, a simultaneous equation in terms of the I^2R losses is formed. Since the resistance will be at the same hotspot temperature, the current in the new stator geometry is described as a factor of the current in the old stator geometry as:

$$I_{new} = 1.066 I_{old} \qquad \text{eqn. 5.44}$$

As a result the new stator design the current density is increased by 6.6%.

After having investigated the flow and temperature distribution in a direct liquid cooled electrical machine, the following chapter is dedicated to the measurement of the heat transfer coefficient on this machine configuration. This is also compared to empirical correlations and CFD models.

6 The Heat Transfer Coefficient in Direct Liquid Cooled Stators

In the previous chapter a flow and temperature distribution of a direct liquid cooled segmented stator was presented using analytical and numerical methods. The analytical method used empirical correlations of the heat transfer coefficient (HTC). This parameter is often unknown, yet the accuracy of thermal models depends on it. Measurements and predictions of the HTC in air-cooled machines have been reported in the literature, (Howey et al., 2010, Airoldi, 2010, Hetteger et al., 2012, Wrobel et al., 2015). However, to the authors' knowledge, no measurements of the HTC in direct oil cooled machines have been reported. Therefore this chapter fills this gap by presenting an experimental investigation of the HTC for a direct oil-cooled segmented stator. The measurements are compared to analytical solutions and CFD predictions. This chapter is based on paper 6.

6.1. The Heat Transfer Coefficient: A definition

The HTC has been described in Section 1.3.2 of the introductory chapter as the parameter dictating the rate of heat flux per unit temperature difference between a solid and fluid. The HTC, h is a complex function of the surface geometry, fluid properties and flow conditions and is often calculated by rearranging Newton's law of convective cooling such that:

$$h = \frac{\dot{q}}{\left(T_{surface} - T_{fluid\ ref}\right)} \qquad \text{eqn. 6.1}$$

where $\dot{q}$ is the heat flux perpendicular to the surface of the body and T is the temperature. The HTC is often defined in terms of a non-dimensional Nusselt number *Nu,* is defined as:

$$Nu = \frac{hD_h}{k} \qquad \text{eqn. 6.2}$$

where D_h is the hydraulic diameter of the flow geometry and k the thermal conductivity of the fluid. The Nusselt number provides a non-dimensional ratio of heat transfer convected away from the surface by the bulk fluid to the heat transfer conducted by the fluid at the stationary point of contact with the surface. Heat transfer correlations are hence often expressed in terms of the Nusselt number. In Section 2.3 of the Literature Review, it was shown how in electrical machine research, thermal designers predict the HTC using existing correlations (Staton, 2008), or by the use of CFD simulations (Howey, 2010, Airoldi, 2010, Wrobel, 2015). The following section examines empirical correlations applicable to direct oil-cooled stator and explores the CFD process for predicting the HTC.

6.2. Predicting the HTC in an Oil Cooled Stator

6.2.1. Empirical Correlations for a Laminar Flow Regime

In Chapter 5, the flow in direct oil cooling was shown to be laminar. This section hence focuses on empirical correlations for this flow range. Mills, (1999) presented a general correlation of Nusselt number on surfaces subjected to laminar flow of fluids with Pr > 5:

$$Nu_{Pr>5} = \left(\frac{\mu_b}{\mu_w}\right)^{0.14} \left[3.66 + \frac{0.0668\, Pr\, Re\, \left(\frac{D_\mathrm{h}}{l}\right)}{1 + 0.04\left(Pr\, Re\, \left(\frac{D_\mathrm{h}}{l}\right)\right)^{0.667}}\right] \text{ for } \mathrm{Pr} > 5 \qquad \text{eqn. 6.3}$$

where Pr is the fluid Prandlt number, Re is the Reynolds number, estimated at the film temperature. D_h is the channel hydraulic diameter. The ratio μ_b/μ_w accounts for the change in viscosity at the hot wall surface and the bulk fluid temperature.

For short pipes with a thermal entrance region the Nu is defined by the Seider Tate equation:

$$Nu_{S-T} = 1.86(Pr\, Re\,)^{0.33} \left(\frac{D_\mathrm{h}}{l}\right)^{0.33} \left(\frac{\mu_b}{\mu_w}\right)^{0.14} \qquad \text{eqn. 6.4}$$

In this chapter, these correlations are used as a reference and compared to CFD simulations and experimental measurements. The process of predicting the HTC using CFD models is discussed in the next section.

6.2.2. CFD Prediction of the HTC in an Oil Cooled Stator

In Chapter 5 it was shown that 3D CFD modelling of a quarter of the stator requires a large mesh and reaches the computing resources available. Hence, to avoid this from happening, the 3D CFD model is reduced to the flow domain of a single channel as shown in Figure 6.1. The 2D CAD geometry developed to simulate the temperature and flow distribution in Chapter 5 is also used to predict the HTC values. The process of developing and solving the 2D CFD model was described in Section 5.6 of Chapter 5 and therefore this section focuses on the modelling of the single channel geometry.

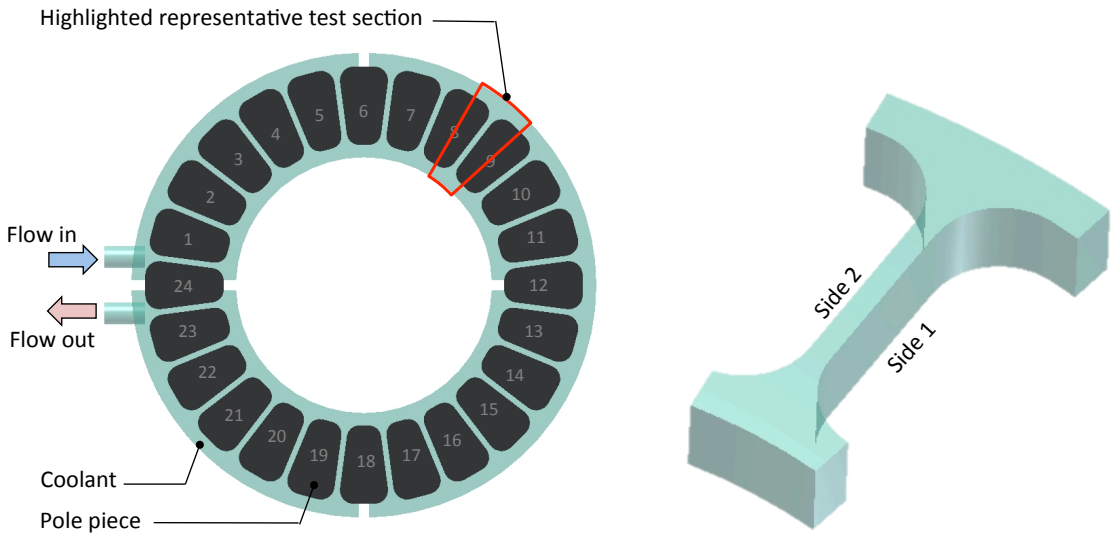


Figure 6.1. (Left) direct liquid cooled stator with highlighted portion of liquid channel (Right) CAD model of the liquid channel

Following the development of the CAD model, it was imported into Autodesk CFD, and the material and boundary conditions were set. The volume was set to Opticool fluid with the properties as described in Table 5.1. An inlet flow rate and fluid temperature were applied on one side of the outer distribution ring while a pressure of 0 Pa was set to the opposite side in the inner distribution ring. These boundary conditions replicate the flow conditions in this portion being modelled. The channel walls were set at a fixed temperature of 90 ^{o}C, thus replicating the pole piece wall temperature. A slip/symmetry boundary condition was applied on the mid-plane to reduce the size of the mesh. A schematic of the boundary conditions is shown in

Figure 6.2. The mesh was formed from tetrahedral elements with a minimum refinement length set to 0.5 and the maximum size of 1.8 set to the surfaces. The boundary layer mesh was made of 15 layers with a layer factor of 0.75 and a gradation of 1.15 was set. The final mesh totalled 4.3M elements and is shown in Figure 6.3.

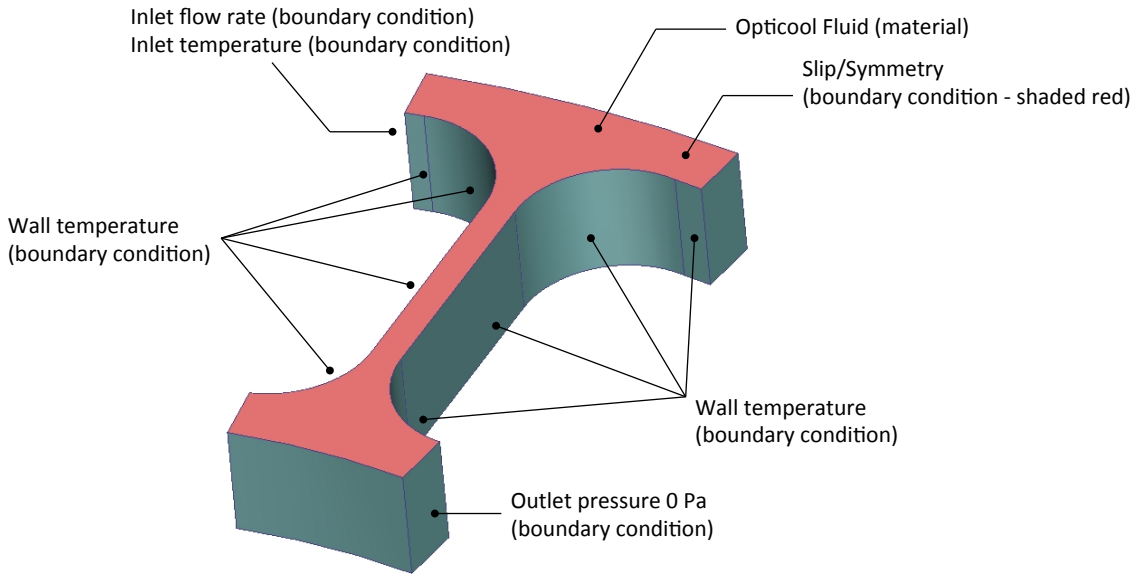


Figure 6.2. Details of the boundary conditions applied to the single channel model

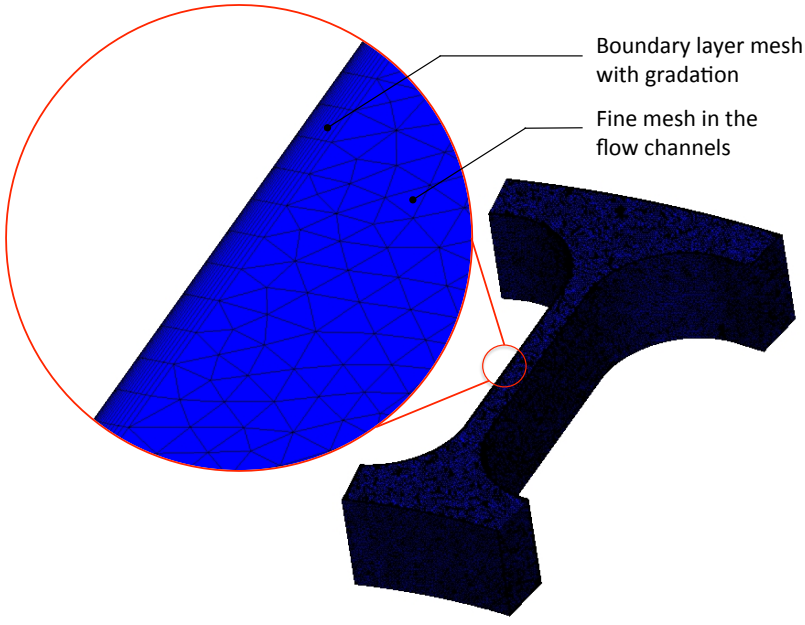


Figure 6.3. Mesh setup for the single channel model

In CFD models the HTC is computed directly from the edges (in 2D CFD) or surfaces (in 3D CFD), once a reference temperature is provided. The fluid reference temperature for computing the HTC should theoretically be the local fluid

temperature above the surface. As this is difficult to measure, the HTC is often defined using an alternative reference fluid temperature. Howey, (2010), and Wrobel et al., (2015), chose the bulk air inlet temperature in the rotor-stator gap as their reference temperature. Airoldi et al., (2008), used the temperature at the centre of the rotor-stator gap. To simplify the experimental validation process, this research adopts the same convention. The oil inlet temperature is hence set as the reference temperature redefining eqn. 6.1 as:

$$h = \frac{\dot{q}}{(T_{surface} - T_{inlet})} \qquad \text{eqn. 6.5}$$

The simulations were run for a number of inlet flow rates, constant oil inlet temperatures and constant pole piece surface temperature, to achieve a plot of HTC with channel Reynolds number. The results of the CFD simulations are compared to experimental measurements in Section 6.5.2.

After having described the modelling techniques, our focus is turned to the experimental work.

6.3. Experimental Work

6.3.1. A Brief Description of the Measurement Techniques

Several techniques to measure the heat flux and the surface temperature were developed and described in the literature (Schultz and Jones, 1973, Astarita et al., 2006). While the adoption of some of the techniques to electrical machine research was reviewed in Section 2.3 of the Literature review, this section focuses on the description of the techniques themselves. These are assessed in the context of oil cooling to select the technique that is most fit for this research.

Heat Flux Gauges consists of thermocouple junctions in series, bonded to both sides of a known thermal barrier. The junctions measure the temperature difference across the material. While one junction on each side is enough, the output signal and sensitivity is dependent on the number of junctions. Therefore multiple pairs of junctions are used in series to amplify the signal and resolution. The heat flux is established through the calculation of Fourier's law of conduction in one dimension, provided that the thermal properties of the barrier material are known. This technique

is perhaps the most commonly used in electrical machines. In the literature review it was shown how this was applied to induction machines by Micallef et al., (2008), and Hetteger et al., (2012), and axial flux machines in Airoldi et al., (2008). The use of this technique requires care as the gauge itself may produce disturbances to the flow and errors in the measurements.

Thin foil heaters make use of a thin metallic foil that is heated by having a current flow through it. The heat energy supplied to the thin foil heater is measured through the product of the voltage and current and the heat flux is determined. As the heater changes in temperature, it's electrical resistivity and electrical resistance changes. For a known temperature coefficient, the surface temperature can be determined and the heat transfer coefficient can be established through an energy balance. The spatial resolution produced by this technique is dependent on the design of the foil heaters, which can be found in a variety of shapes and sizes. Howey et al., (2011) applied this technique to investigate the heat transfer in the rotor-stator gap of an air-cooled electrical machine.

Infra-red (IR) Thermography uses an insulating layer applied onto a thermally conductive, heated test piece. The temperature difference across the insulating material is determined using embedded thermocouples in the metal test piece and an IR camera to measure the surface temperature. The conduction equation across the insulating layer is solved to establish the heat flux normal to the surface. This is used to estimate the HTC. Unlike other techniques, IR thermography does not suffer from lack of spatial resolution. The method however can only be applied to heat transfer research on fluids that are transparent to IR. This is hence unsuitable for measurements of the HTC in oil cooling. The technique requires careful in-situ calibration and optical access, which has limited its application to electrical machines.

Thermochromic Liquid Crystals are substances that have the properties of both liquid and solid crystalline states. In heat transfer research cholesteric liquid crystals are employed. Their optical properties change reversibly with temperature and are hence referred to as thermochromic liquid crystals. A coating of controlled thickness is often applied over a black surface. When a heat flux is applied to the surface, its temperature changes and a transition in surface colour is observed. The technique can

be used for transient measurements with a response time of about 3 ms (Ireland and Jones, 1987). Using an in-situ calibration and a video recording device, the colour is interpreted back into a surface temperature, from which the heat flux and heat transfer coefficient is established. The technique is however very sensitive to light conditions and viewing angles, (Baughn, 1995). While there has been an effort to apply this technique to an air-cooled electrical machine at the Osney Laboratory in Oxford, to the author's knowledge the application of this technique to electrical machines has not been published in the literature.

Thin Film Heat Flux Gauges are a type of thin-film resistance measuring device. The change in electrical resistance R of a sputtered platinum sensor is temperature dependent and can be described by the linear relationship:

$$R = R_o + \alpha.(T - T_o) \qquad \text{eqn. 6.6}$$

where R_o is a known reference resistance at a reference temperature T_o, generally 0 ^{o}C. α is a temperature coefficient of electrical resistance describing the change in film's electrical resistance with temperature. The thickness of thin films is typically up to 300 nm. At this thickness, the temperature coefficient of electrical resistance α deviates from the corresponding bulk values, (Mailly et al., 2001), and is therefore established through a careful calibration process. When measuring the temperature gradient across a substrate of known thermal properties, the heat flux normal to the surface can be determined using Fourier's law of conduction, (Collins, et al., 2015). The multilayer thin film gauge was developed at the University of Oxford (Doorly and Oldfield, 1987) and were found to have a very fast response (100 kHz), making them suitable for transient measurement. Their data reduction is however complex. The basic principles and data reduction for the transient measurement technique has been demonstrated in Schultz and Jones, (1986).

The transient technique has become the preferred measuring method in gas turbine applications, (Jones et al. 1995). Test times are typically 10 μs to 1s, during which a pulse of hot air is passed over the test piece and the change in voltage across the gauge whilst supplied with a constant current, is recorded. The time history of voltage is then used to determine the change in gauge resistance, and hence the surface temperature, with respect to time. The calculation of heat flux history from the

temperature history can be performed in a number of methods, for example the impulse response method documented by Oldfield, (2008). Finally, the convective HTC and adiabatic wall temperature (allowing for compressibility effects) is determined from a linear regression of heat flux and driving temperature. Collins et al., (2015), developed a new technique for fabrication of miniature thin film heat flux gauges, thus improving the accuracy and resolution of the measurement technique.

This research adopts the double-layered thin film heat flux gauge measurement to measure the HTC on the surfaces of a direct oil cooled stator pole piece. This technique has not been applied to electrical machines. It was found to be most adequate for direct oil cooling as it does not depend on the field of vision and has minimal interference with the flow domain. The gauges were found to be compatible with oil coolant by periodical monitoring the resistance of an immersed gauge over a period of one month. No change in gauge resistance over time was observed.

6.3.2. A Steady State HTC Measurement using Thin Film Gauges

While thin film heat flux gauges are known for their use in transient experimentation, (Jones et al., 1995, Collins et al., 2015), the large thermal capacity of the oil cooling system makes the transient impulse response unsuitable. The technique presented here is hence a modification from the transient technique such that rather than passing a pulse of hot fluid over the gauges, the metal substrate is heated until a steady state condition is reached. The metal substrate temperature was measured by two k-type bare-bead thermocouples located on the upper and lower walls. These measurements agreed to within 0.5 ^{o}C, showing that the block was isothermal during testing. A schematic of the gauge used is shown in Figure 6.4.

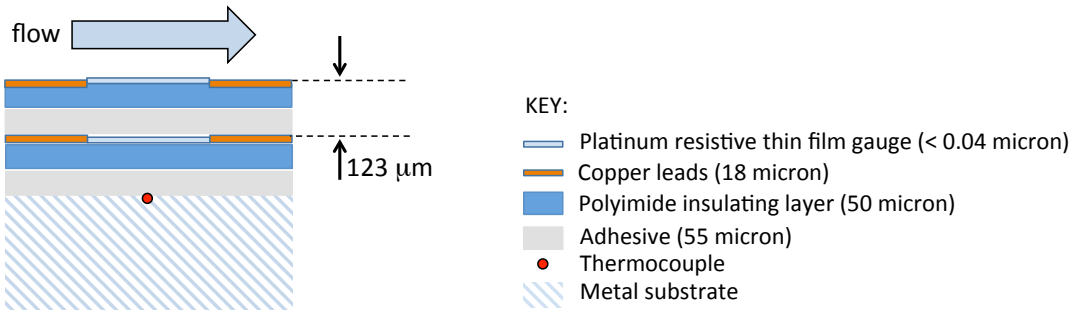


Figure 6.4. Schematic showing a Double sided Direct Heat Flux Gauge

The temperature gradient across the insulating layer and adhesive are measured. For a known thickness and thermal conductivity of the gauge, the steady state heat flux was determined using the one-dimensional Fourier conduction equation across the insulating substrate:

$$\dot{q} = \left(k/x\right)\left(T_{subs_b} - T_{subs_t}\right) \qquad \text{eqn. 6.7}$$

where $\dot{q}$ is the heat flux through the sensor, x is the thickness of the polyimide insulating layer separating the two gauges, k is the thermal conductivity of polyimide, T_{subs_t} and T_{subs_b} are the temperatures at the top and bottom surfaces of the polyimide insulating layer respectively, measured by the thin film gauges. The heat flux is also described in terms of Newton's law of cooling:

$$\dot{q} = h(T_{block} - T_{inlet}) \qquad \text{eqn. 6.8}$$

Tests were conducted over a range of substrate temperatures and a linear regression of heat flux $\dot{q}$ against $(T_{block} - T_{inlet})$, was performed to determine the convective heat transfer coefficient h.

To determine the heat flux, the thermal properties of the heat flux gauges are required. The thermal properties of the polyimide and glue layers used are well documented by the manufacturers. These have similar properties and can be regarded as one material. Piccini et al., (2010) developed a calibration technique to establish the thermal properties of the direct heat flux gauges and substrate. The thermal properties of the substrate between the heat flux gauges are shown in Table 6.1. The values have been provided by Dr Paul Beard from the Osney laboratory at Oxford University, where these gauges have been developed.

Table 6.1. Substrate thermal properties

Thermal conductivity, k (W/m K)	**Thickness, x (μm)**	$\left(k/x\right)$
0.46	105	4380

For a pole piece test area of 1.2 x10^{-3} m^2, the conductive thermal resistance between the pole piece and the fluid was estimated at 0.44 K/W, whereas the thermal resistance between heat flux gauges at 0.19 K/W. The effect of the thermal resistances on the results is discussed further in Section 6.4.2.

The oil inlet temperature is measured by two T-type thermocouples. The temperatures T_{subs_t} and T_{subs_b} are derived from the measured resistances of the thin film gauges on top and bottom of the insulation substrate. It was shown in eqn. 6.4 that calculating each of these temperatures requires the values of R_o and α. These values are found by calibrating the gauges at isothermal conditions for a range of working temperatures. As the gauge parameters, R_o and α, are affected by the manufacturing and mounting process, calibration is performed after the test piece is fully instrumented. Therefore the following section describes the manufacturing and calibration procedures.

6.3.3. Manufacturing and Calibration of the Instrumented Test Piece

The double-layered thin film gauges were manufactured at the fabrication facility of thin film gauges at the Osney Thermo-fluids Laboratory at the University of Oxford. Details of the fabrication process of thin film gauges are found in Collins et al., (2015). A pole piece replica was manufactured in aluminium and instrumented with eight sets of thin film gauges on each side of the oil flow channel, as shown in Figure 6.5. Aluminium was chosen due to its high conductivity and ease of manufacturing. The high conductivity material is important to ensure uniform heating of the segmented pole piece.

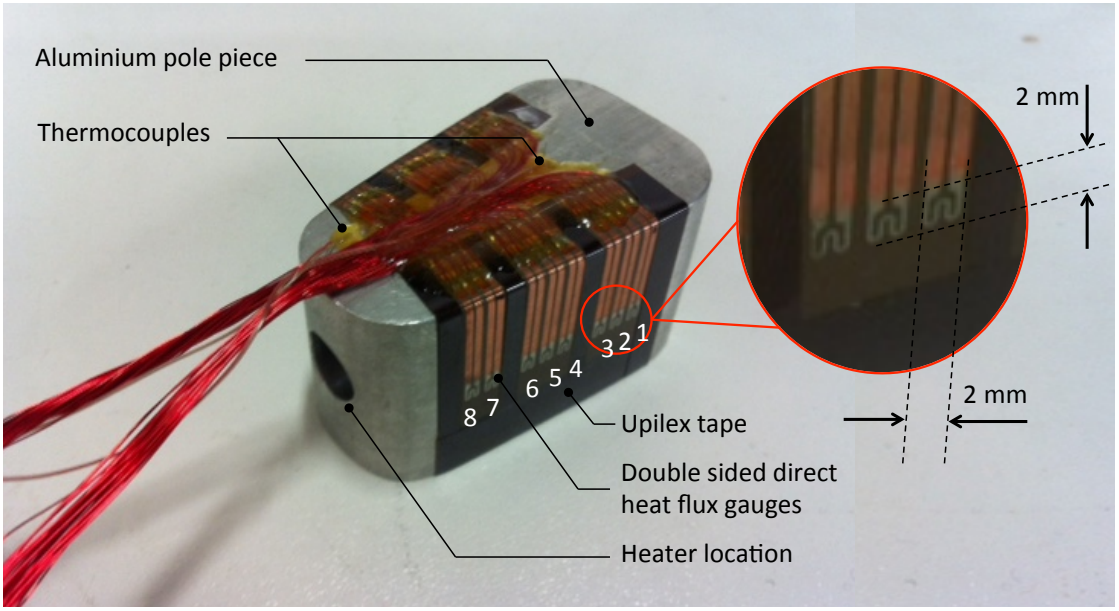


Figure 6.5. Instrumented aluminium pole piece replica (Numbers 1-8 referenced in local HTC results)

The calibration process was performed by Mr Trevor Godfrey using a bespoke calibration facility at the Osney Thermo-Fluids Laboratory. The facility uses a

measurement system based on National Instruments PXI systems with a thermostatically controlled water bath. The water bath temperature is interfaced through a serial interface and a relay switch module is controlled by a Labview script and allows to measure up to 96 resistances simultaneously. During the calibration process, the instrumented test piece was sealed in a plastic bag and placed in a water bath. The linear behaviour of temperature with resistance allow calibration to be made at lower temperatures. Therefore the water bath temperature was increased from 20 ^{o}C to 45 ^{o}C in steps of 5 ^{o}C. The pole piece temperature and water bath temperature were monitored to ensure isothermal conditions. The temperatures and resistances of the thin film gauges were recorded. The resistance of the gauges are expressed as:

$$R_{calib} = R_o + \alpha . T_{calib} \qquad \text{eqn. 6.9}$$

The linear relationship of each gauge resistance was plotted against the known set of temperatures. This allows the extraction of the temperature coefficient α and reference resistance R_o for each gauge. An example of a typical calibration chart for one thin film heat flux gauge is shown in Figure 6.6. The calibration chart of every gauge is shown in Appendix 1.6.

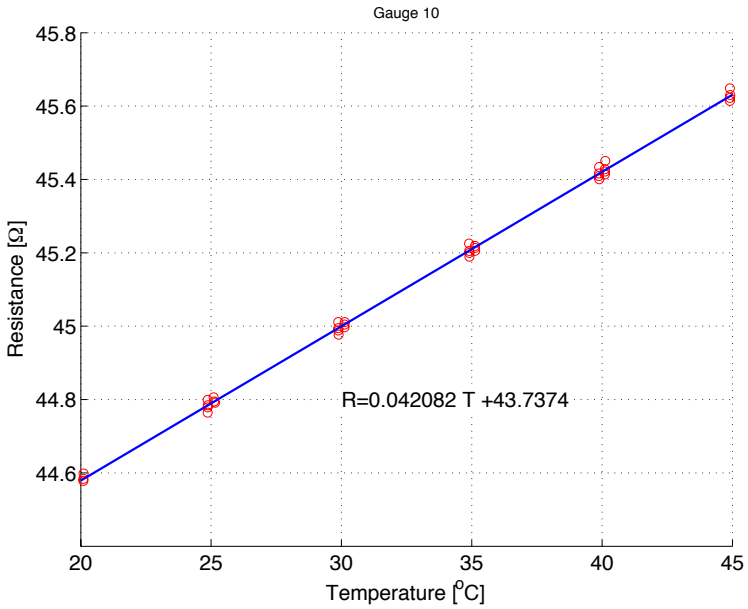


Figure 6.6. Example of a calibration chart for a thin film gauge, from which the values of temperature coefficient α and reference resistance R_o (y-intersect at T=0 ^{o}C) for each gauge is determined

While for platinum, α is found to experience very little variation with temperature and is considered constant; R_o sometimes experiences a drift (Collins et al., 2015). This is mainly experienced in high temperature environments synonymous with aerospace components, and is likely due to induced stresses and relaxation of the gauge

connections. Although the measurements presented in this research are at a low temperature (<100 ^{o}C), steady state experiments take longer to settle and the complete set of tests presented here were performed over a few days. Therefore to counter for any possible drift in R_o during the course of the testing period, an isothermal test was performed at the start of each measured data set. Hence, during the experiment, temperature of the each gauge was determined as a function of the calibration parameter α and measured parameters R, R_{iso} and T_{iso}:

$$T = \left(\frac{R - R_{iso}}{\alpha}\right) + T_{iso} \qquad \text{eqn. 6.10}$$

6.3.4. Assessment of the pole piece heating system

The steady state experiment required the aluminium test piece to be heated. To assess the heating system and the impact on the temperature distribution of the aluminium block, a simulation in Autodesk CFD Simulation was produced. A three-dimensional model of the aluminium block with inserted pencil cartridge heater was designed and meshed. The dimensions of the aluminium block are shown in Figure 5.17. The cartridge heater material was set to stainless steel and the block material to aluminium. An internal heat generation of 80 W was set on the heater volume. A thermal contact resistance of 0.3 K/W was applied on the interface surface between the heater and aluminium block. This represents the thermal contact resistance and the thermal grease. While the value used is an estimate based on experience, simulations with different values would impact the block temperature but not the temperature distribution. An estimated convective heat transfer coefficient of 200 W/m^{2}K was prescribed on the pole piece surfaces in contact with the oil coolant, while the top and bottom surfaces were set to adiabatic to replicate the insulation in the test rig. A schematic of the material and boundary conditions is shown in Figure 6.7. A conduction simulation was solved and the external temperature of the aluminium block is presented in Figure 6.8.

At a surface temperature of 85 ^{o}C, a variation of less then 1 ^{o}C is reached. The models' sensitivity to any additional thermal resistances presented by the polyamide layer in the heat flux gauges was also checked by introducing an additional thermal resistance on the solid-fluid interface. The temperature distribution was found to

remain unchanged. The uniformity of the temperature distribution on the surfaces of interest makes this heating method suitable for steady state experiments.

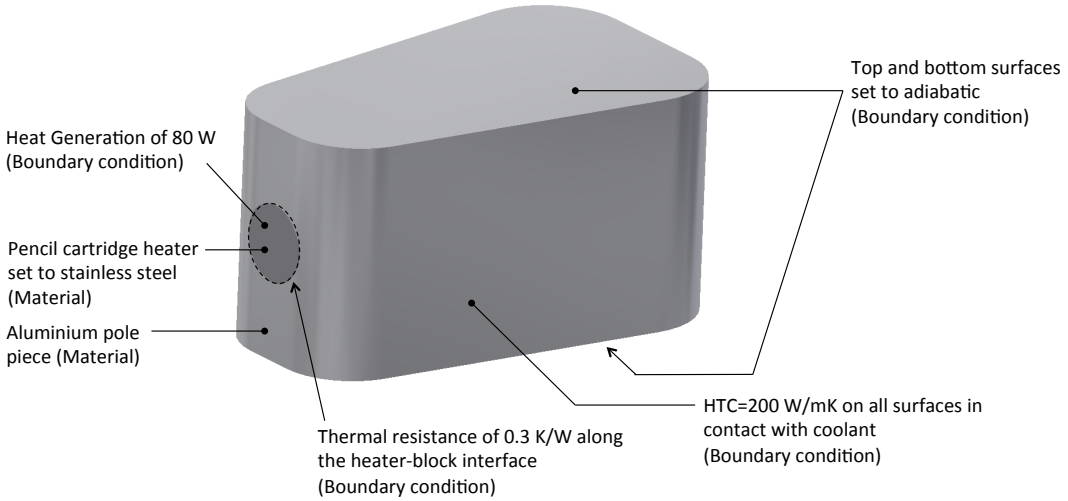


Figure 6.7. Material and boundary conditions to assess the heating system on the aluminium block

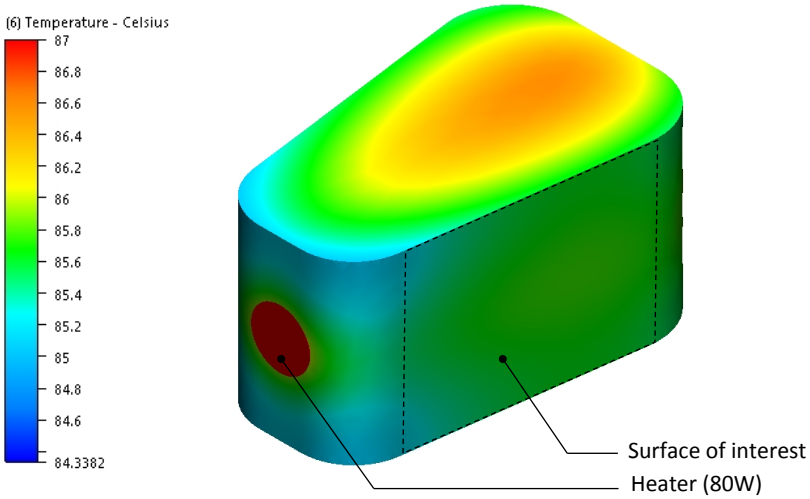


Figure 6.8. Simulation results of the temperature distribution on the aluminium block

Following the description of the various components within this experiment, the following section addresses their integration and the experimental setup.

6.3.5. The Experimental Setup

In this research, the same representative experiment of a quadrant of the stator highlighted presented in Chapter 5 is used here, this time having one pole piece instrumented with heat flux gauges as shown in Figure 6.9. Due to space limitations and to avoid repetition, the reader is kindly directed to the description of the test box in Section 5.5.1. Likewise a description of the test rig has been presented in

Section 5.5.2. A Schematic of the test rig is shown in Figure 5.18 of Section 5.5.2 in Chapter 5. A photograph of the test rig is shown in Figure 6.10. A test matrix was performed for three flow rates between 1 lpm and 6 lpm and three oil inlet temperatures at 25 ^{o}C, 35 ^{o}C and 45 ^{o}C. For each test, the pole piece surface temperature was varied between 30 ^{o}C to 80 ^{o}C, in steps of 10 ^{o}C as shown in Table 6.2. This was required so that the value of heat flux can be plotted against temperature difference to establish the HTC from the gradient.

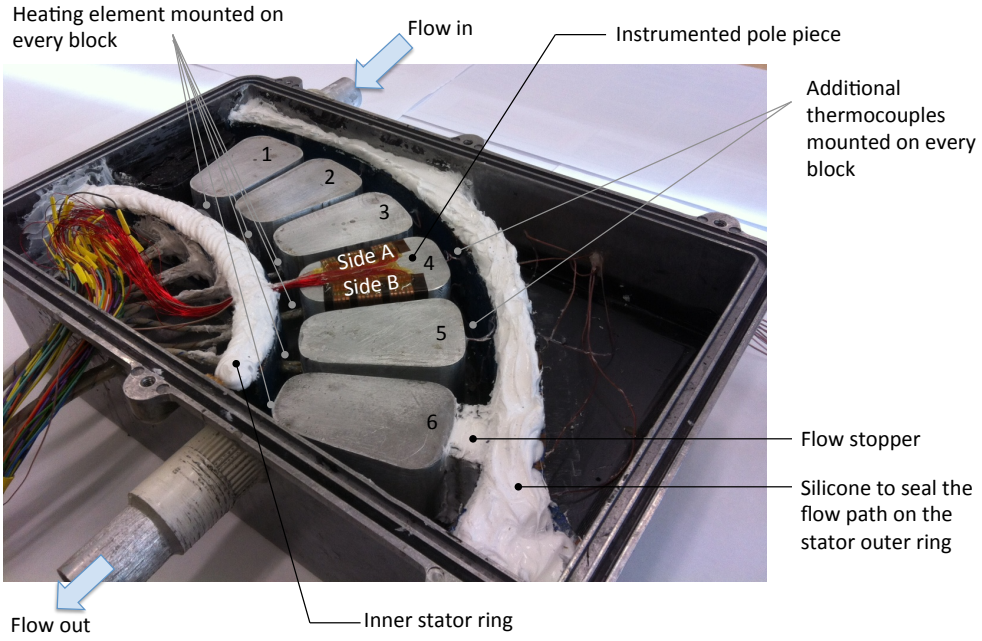


Figure 6.9. Test box showing a section of the stator machine and instrumented pole piece

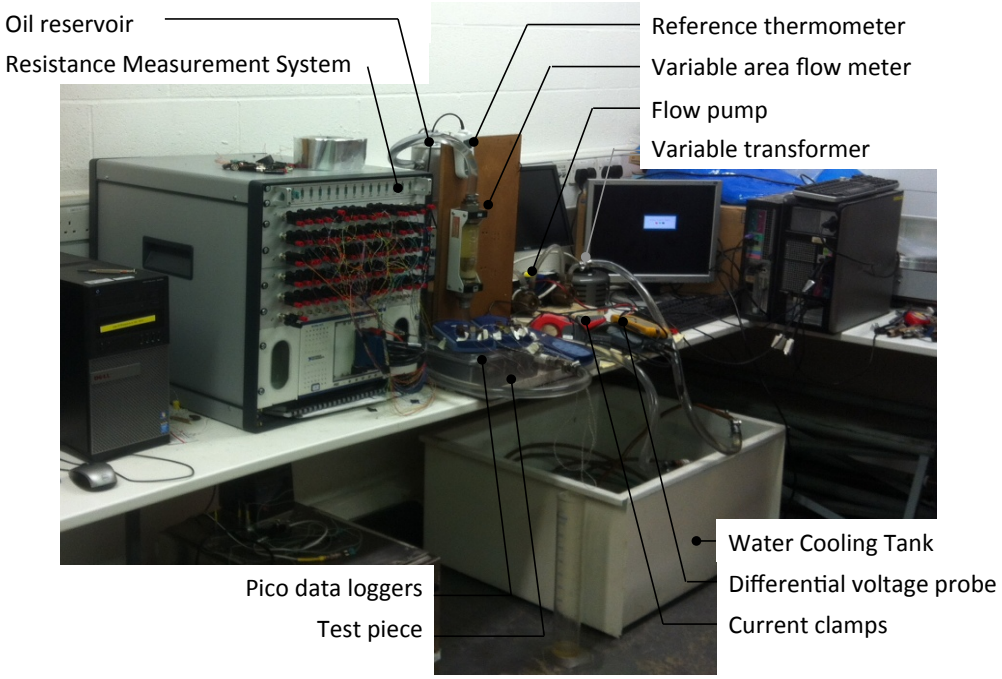


Figure 6.10. Test rig for measuring the HTC

Table 6.2. Test matrix for three oil flow rates of between 1 and 6 lpm

Coolant inlet temperature ^{o}C	**Pole piece temperature ^{o}C**					
25	30	40	50	60	70	80
35		40	50	60	70	80
45			50	60	70	80

Each experiment was run for 1-3 hours to ensure that steady state conditions were achieved. The steady state condition was determined when the pole piece temperatures varied less than 0.2 ^{o}C over a period of about an hour. The steady state values across the final hour were then averaged to determine the oil inlet temperature and the pole piece body temperatures. Thin film heat flux gauge measurements are typically achieved by supplying the gauges with a constant current and measuring an amplified voltage across them. However, due to the small HTC values in this experiment, this method was found to introduce more uncertainties.

Hence in this research the gauge resistances were measured directly using a National Instruments PXI system. The temperature difference across the Upilex substrate causes a difference in resistance between the gauges mounted directly on top of each other. Prior to achieving the gauge temperatures, the test data is processed. This is described in the following section, after which the HTC values are determined and compared to empirical correlations and CFD simulations. The uncertainty analysis for this experiment is shown in Appendix 1.7.

6.4. Results and Discussion

6.4.1. Post Processing the Gauge Measurements

For each flow rate and oil inlet temperature, the gauge resistances are plotted against the pole piece block temperature. This ensures that the thin film gauges behaved as expected with their resistance increasing with temperature. Due to the extensive amount of figures of the full data set only one example is shown in Figure 6.11. The set of charts for the whole experimental regime are shown in Appendix 2.1. A MATLAB script was developed in which eqns. 6.7 - 6.10 are solved. Thus for each gauge location, the individual gauge temperatures was calculated. The temperature difference across the insulation substrate could therefore be calculated for each location, from which the local heat flux is calculated.

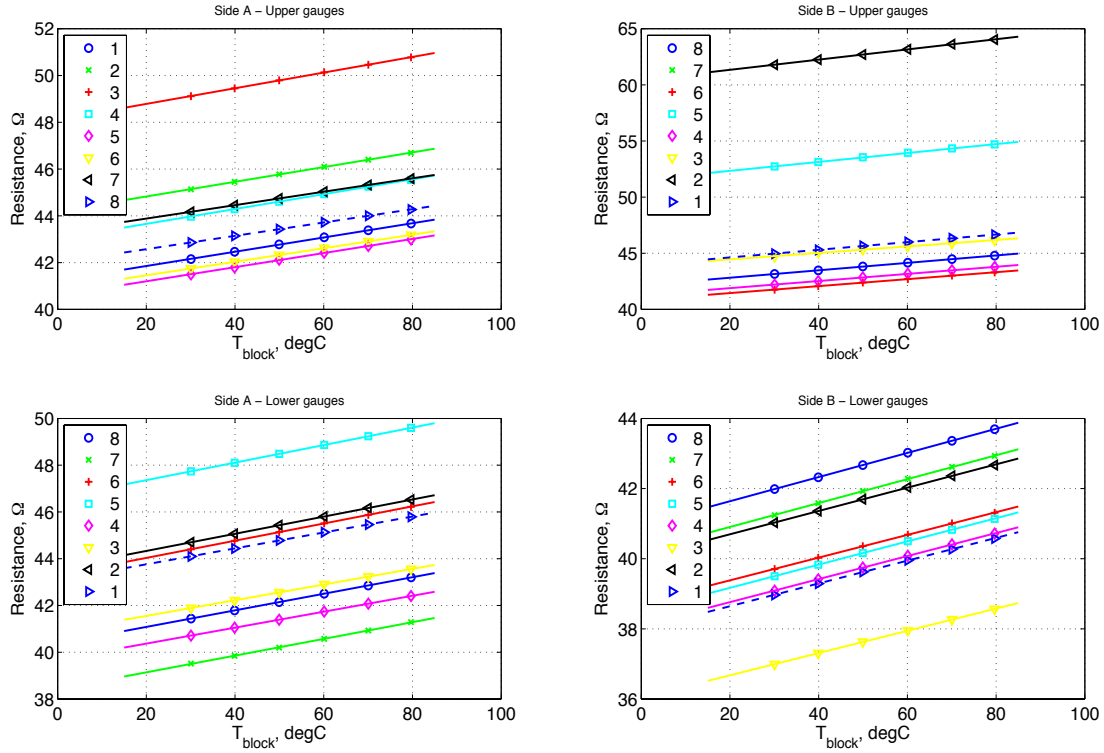


Figure 6.11. Change in gauge resistance with block temperature

The linear relationship of the temperature difference across the insulation substrate against the block temperature, was plotted to check the consistency of the gauges. It was generally noted that at a low temperature difference between the oil and the block temperature the gauge readings do not follow the linear trend. These points were discarded in the calculation of the heat transfer coefficient as they may result in a high uncertainty. An example of this is shown in Figure 6.12. Due to the large data set and space limitations, the set of charts showing the temperature difference for each measured location at each experimental condition are shown in Appendix 2.2.

6.4.2. Predicted and Measured HTC Values

With the local temperature differences across the gauges established, the balance between conductive and convective heat transfer was calculated to establish the local values of the heat transfer coefficient along the sides of the pole piece. An example of the local HTC values on the two instrumented pole piece surfaces is shown in Figure 6.13. The pole piece' sides marked A and B are referenced to Figure 6.9. The gauge numbers are referenced to Figure 6.5. Due to the large data set and space limitations, the set of charts showing the temperature difference for each measured location at each experimental condition are shown in Appendix 2.3.

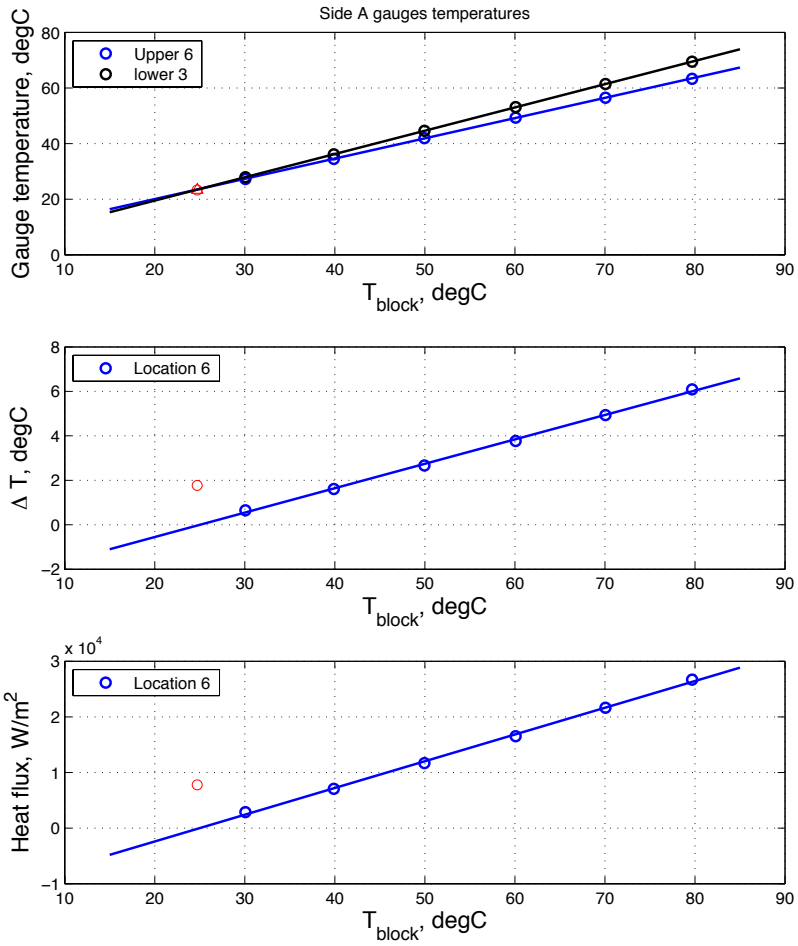


Figure 6.12. Charts mapping (top) The gauge's temperature, (middle) Temperature difference across the insulation substrate, (bottom) Estimated heat flux across the gauges for a specific location instrumented with a set of gauges. The discarded point is shown in red.

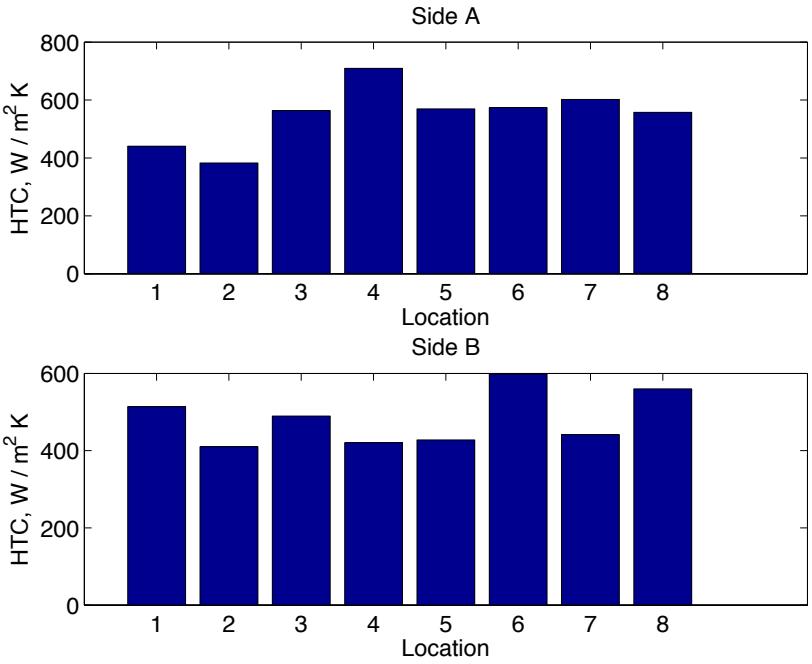


Figure 6.13. Example of the local heat transfer coefficient along the length of the pole piece sides for an inlet flow rate of 2.2 lpm and inlet temperature of 26 ^{o}C

While theoretically the local HTC values should be constant the charts show variability in the local measurements. Further investigation as to why this happened is required. However, the author attributes this to the factors discussed below:

- The local HTC is inferred from the heat flux perpendicular to the film gauges, which is estimated from the conductive equation. The uniformity of the thermal resistance across the stack of heat flux gauges hence is hence important to achieving consistent local HTC values. In Section 6.3.2 it was shown how the thermal resistance is dependent on an equivalent thermal conductivity of the gauges and the thickness of polyamide and adhesive layers. While the thickness of the polyamide is a controlled process, adhesive is put on in a manual operation and its thickness is less controlled. Variation in thickness across the stack of heat flux gauges leads to uncertainty and variability. While this effect may be negligible in high heat flux rates, traditional measured in aerospace applications it may become important in low heat flux values, as measured in this experiment. This hence calls for a tighter control in the thickness of adhesive during the manufacturing process.
- The variability in local measurements may have been influenced by the design of the instrumentation, which includes a step in the surface of approximately 246 μm where the instruments are mounted as shown in Figure 6.5. The individual copper leads of each gauge also introduce a step in surface of 22 μm thickness as shown in and Figure 6.4. While this effect may be negligible in the turbulent regimes at which these gauges are generally applied, it has been documented to enhance the HTC in laminar flows (Kherbeet et al., 2014). This may hence account in part for the variability in local measurements. The influence of the instrumentation can be minimised by designing gauges that wrap around the entire test piece, therefore avoiding any discontinuity on the test surface, and thinning the copper leads on the gauges. The latter solution may however have implications on the gauge electrical resistance, which requires further investigation.
- The uncertainty in HTC measurements can be improved by increasing the temperature gradient across the film gauges. In this experiments, the pole piece temperature was limited to 90 ^{o}C. Beyond this temperature, the adhesive used to stick the gauges to the pole piece softens and starts to loose

its properties. Therefore raising the pole piece to higher temperature requires further investigation into a different adhesive.

While the experiment provides a map of the local heat transfer coefficient along the pole piece sides for various oil inlet flow rates and temperatures, an average value for each side of the pole piece was calculated. The LP flow distribution model presented in Chapter 5 was used to establish the flow distribution along the instrumented pole piece. The Reynolds number for each channel was calculated using the model described in Chapter 5 and plotted against the average HTC, shown in Figure 6.14. The HTC for each side of the pole piece was linearly correlated with the Reynolds number in each channel as shown in the figure. Results from the empirical and CFD predictions are superimposed for comparison.

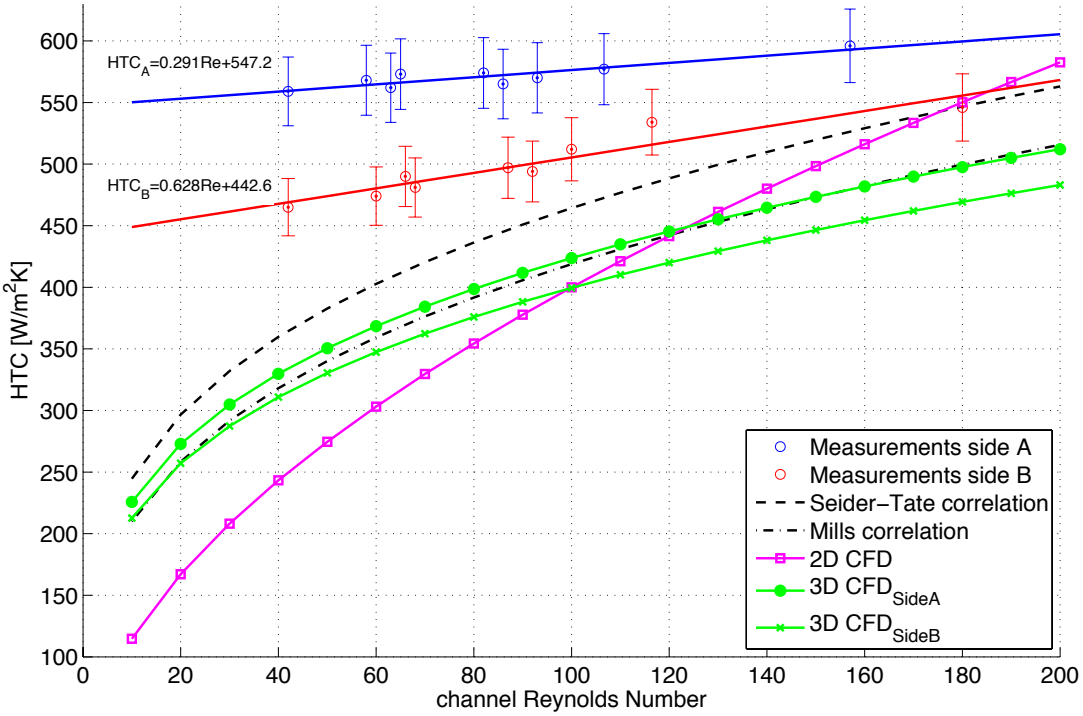


Figure 6.14. Measurement of the average HTC along the length of the pole piece surfaces marked A and B, with superposition of the predicted HTC

The HTC on Side A is noted to experience higher HTC values than that on Side B. This effect is not captured when using analytical correlations. The Seider Tate equation is found to underestimate the HTC by approximately 25% at the channel Reynolds number of 50. This under-prediction tapers off to produce an accurate estimation as the channel Reynolds number increases to 200. The analytical correlation by Mills under-predicts the HTC by 30% at a channel Reynolds number of

50. The under prediction tapers to 10% at a Reynolds number of 200. The 2D CFD model is found to underestimate the HTC by 35% at a low inlet Reynolds numbers. The difference also tapers off to produce an accurate average HTC estimate at a channel Reynolds number of 200. However the gradient of the chart is steeper than those presented from experiments or analytical predictions. This is likely due to the fact that the 2D CFD model is only able to estimate an average HTC value over the entire edge of the pole piece. It is hence unfair to compare this with the surfaces of the channel only. The 3D CFD model requires higher computational resources and solution time but provides a detailed resolution and parameter predictions on the pole piece surfaces. The 3D CFD model captures the difference in HTC value on the sides of the pole piece. The simulations show that this may be due to some degree of impingement of the fluid on surface. The 3D CFD model is found to follow the correlation by Mills, and hence also produces an underestimation of between 10-30% from the measurements.

The author attributes this discrepancy to various factors that are discussed hereunder:

- Despite that the gauges are only 246 μm thick, these have been assembled on the machined pole piece. This was found to reduce the channel flow area by 6% causing to small differences in Re and HTC. This effect was not taken into account in analytical and computational simulations thereby contributing to some of the discrepancies shown in Figure 6.15 and Figure 6.16 respectively.
- The step in surface from the copper leads themselves may lead to enhancement of the HTC as discussed earlier. This effect is not taken into consideration in the analytical solutions, nor replicated in CFD.
- The accuracy in measurement could also be improved if the temperature difference between the heat flux gauges is increased. This can be achieved by increasing the thickness of the Kapton layer between the two thin film gauges, or using a machined thermal insulator such as Perspex. However, to avoid affecting the flow geometry, the instrumented pole piece would need to be machined accordingly so that the final geometrical dimensions remain unchanged. Alternatively the temperature of the pole piece can be increased by doing the changes to the adhesive as discussed earlier.

While the measurements of the HTC were done along the sides of pole piece the CFD models give insight into the distribution of the heat flux along the entire pole piece surface. Figure 6.15 shows that the curved areas experience a higher heat flux and HTC values, particularly the one on Side 1, which is subjected to impingement by the fluid. In hindsight it would have been interesting to include heat flux gauges on the curved surfaces.

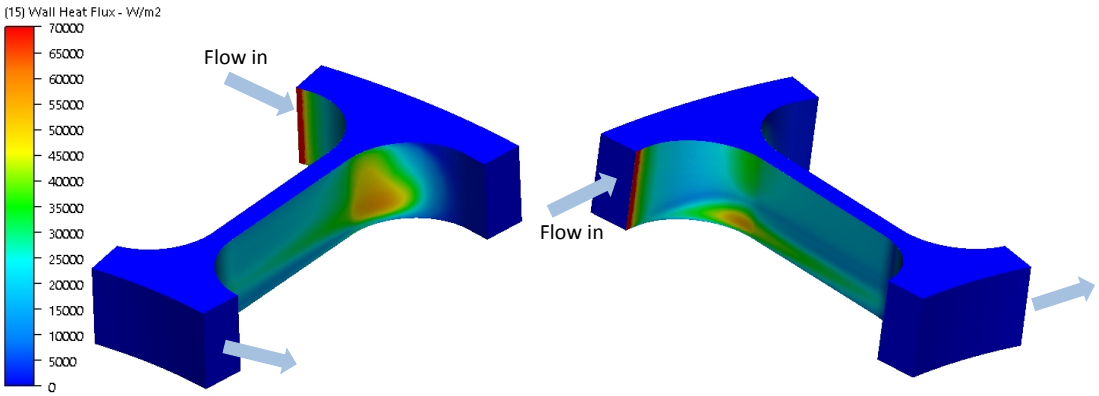


Figure 6.15. Heat flux on the pole piece surfaces (Left) Side 1 (Right) Side 2, at a Re = 150

To establish a non-dimensional comparison all HTC values were converted into Nusselt number *Nu* and plotted against the channel Reynolds number in Figure 6.16. The Nusselt number on each of the pole piece sides was linearly correlated with the channel Reynolds number as shown in the figure. The correlations apply for the range $40 < Re < 180$.

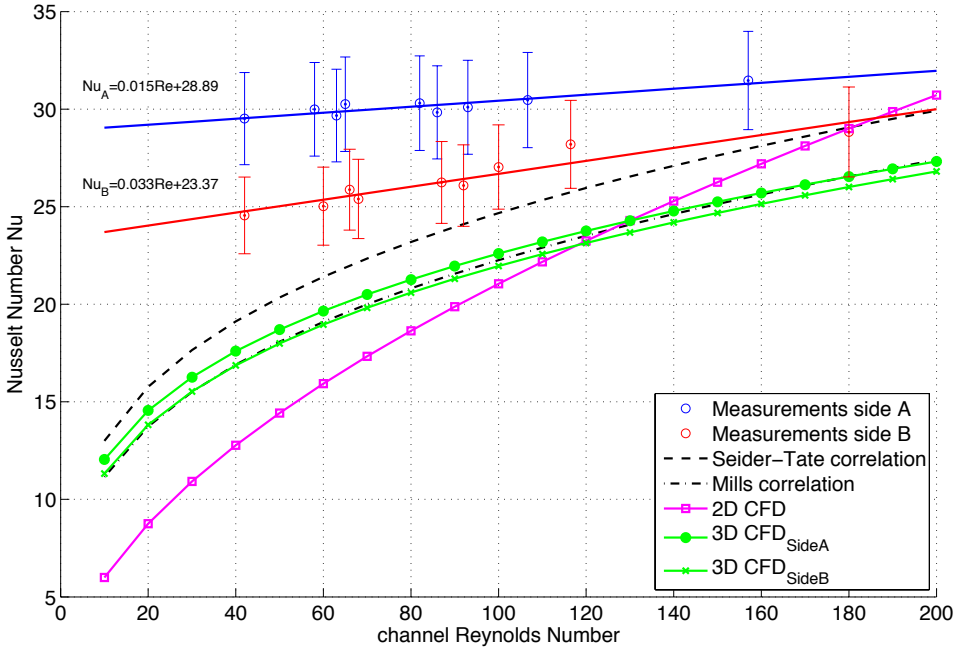


Figure 6.16. Plot of the non-dimensional Nusselt numbers with channel Reynolds numbers

6.5. Conclusion

To the author's knowledge, no HTC measurements of direct oil cooled electrical machines have been reported in the literature. This chapter addresses this gap by measuring the HTC in a directly oil cooled electrical machine with segmented stator using double layer thin film heat flux gauges. The technique, generally used for transient measurement of HTC in turbulent aerospace applications has been adapted for steady state heat flux measurements in laminar oil flow conditions. This was done achieved by heating the pole piece to a set wall temperature. The challenges and procedure with this measurement technique applied to the context of oil cooling have been described. The measurements are compared to existing analytical correlations as well as 2D CFD and 3D CFD predictions. The prediction methods have been shown to under-predict the HTC value on the pole piece surfaces by approximately 10-30%. While empirical correlations of the HTC and non-dimensional Nusselt number with channel Reynolds numbers have been established, the uncertainties associated with this measurement system have also been discussed.

7 | Conductive Heat Transfer in Concentrated Windings

So far this thesis has focused on convective heat transfer. The analysis on the current density with the thermal resistance shown in Sections 1.4.4 showed that both convective and conductive heat transfer play an important role in increasing the current density of stator windings. This chapter turns its attention to the conductive path and uses concentrated windings from a segmented stator as a test case study. This research experimentally investigates the temperature gradient in epoxy infiltrated and non-infiltrated concentrated windings. A thermal model that captures the hot spot temperature in the windings is developed. This chapter is based on paper 6.

7.1. Context to this chapter

Concentrated windings are a composite of materials and typically consist of multiple copper conductors wound around a stator iron tooth (or iron bobbin). Each copper conductor is coated with a two-part insulation consisting of a modified polyester basecoat with a superimposed amide-imide outer coating of approximately 2 microns thickness. The wire cross-section can be circular or square, and the winding configuration open pack or closed pack as shown in Figure 7.1. The wire geometry and winding configuration influences the fill factor and hence the parameters used in modelling the thermal behaviour of the winding. The windings may be sometimes infiltrated with epoxy resin or a process of vacuum pressure impregnation (VPI) to increase mechanical rigidity. Modelling of the windings is hence a complex task. In the literature review several modelling strategies based on lumped parameter (LP) models or finite element analysis (FEA) were shown and the benefits and challenges with each model was described.

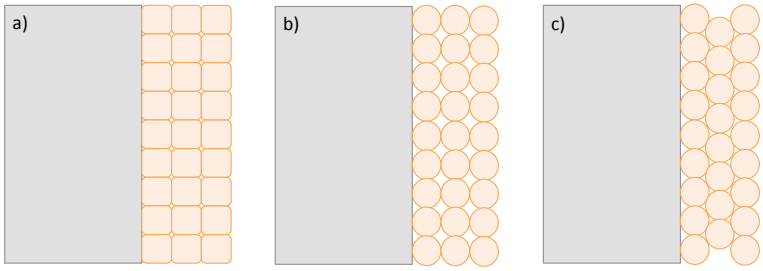


Figure 7.1. Cross section of the windings cross section and fill factor with a) square wire cross section and open pack windings configuration, b) circular wire cross section and open pack winding configuration, and c) circular wire cross section and closed pack winding configuration.

Various researchers have adopted a modelling strategy whereby the heterogeneous windings are converted to a homogeneous material with equivalent thermal properties. To accurately predict the average winding temperature, establishing the equivalent material properties is important. It was hence shown how most of the research has focused on establishing theoretical or experimental techniques for determining equivalent properties. However, it was shown that the equivalent technique method can only compute the average temperature accurately but causes an error in the internal temperature distribution (Driesen et al., 2001, Qi et al., 2014). While layered winding models have been developed for slotted machines, (Staton et al., 2005, Nategh et al., 2012) their application to concentrated windings is still missing in the literature.

This chapter addresses this gap and presents an LP based thermal model for concentrated windings. The LP model has key differences in the definition and placement of the thermal resistances to those presented in the literature. While Staton et al., (2005) and Nategh et al., (2012) attribute the thermal resistance to the conductivity in the epoxy this research considers it as a property of the contact between the winding layers. The author believes that this provides more insight on the behaviour of the windings. Throughout this chapter, a directly oil cooled pole piece with three layers copper windings made from AWG 14 wire of square cross section is used as a test case study.

7.2. A new LP based model for the windings

7.2.1. Description of the model

Prior to defining the equations governing the model, the underlying thermal assumptions and geometrical simplifications are first discussed:

The Heat Flux Assumption

The windings and iron of a pole piece produce internal heat generation which raises their temperature. Heat is transferred against a temperature gradient. In direct liquid cooled machines, the pole piece is surrounded with fluid and hence oil cooled pole pieces experience a heat flux vector in the radial direction. By neglecting axial heat transfer complex multi-layered concentrated windings can be simplified into solid winding layers as shown in Figure 7.2.

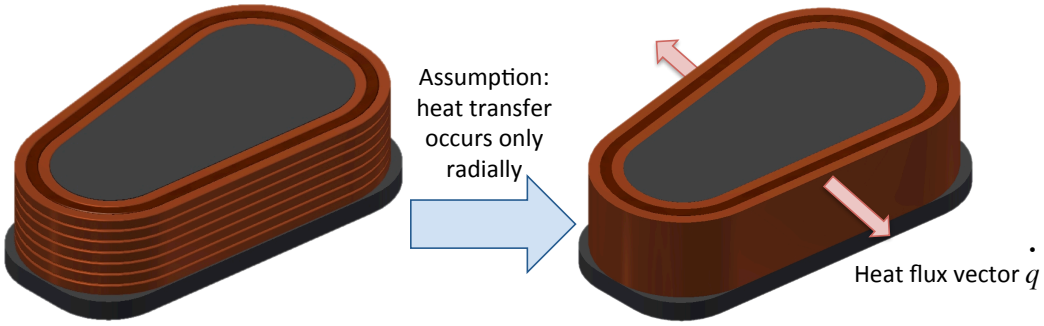


Figure 7.2. Simplification of the winding geometry. Figure showing a cross section of the pole piece for better demonstration purposes

The Temperature Nodes

The heat flux assumption enables a thermal node to be placed on the iron bobbin and the winding layers. In its simplest form with the pole piece subjected to symmetrical boundary conditions, the pole piece can be thermally modelled by four nodes: one on the iron and one on each of the three winding layers as shown in Figure 7.3. Each node within in the model has a uniform thermal capacitance defined by the product of the volume, specific heat capacity and density. Each thermal node is linked with its neighbouring node through a thermal resistance R_{th}.

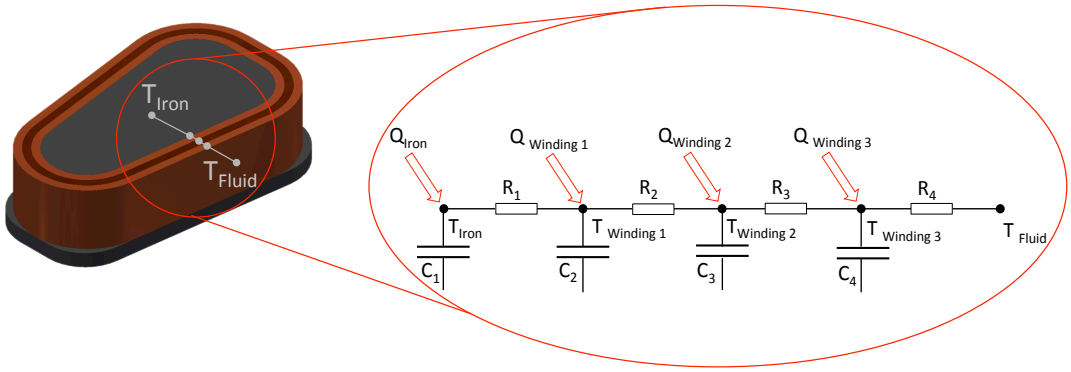


Figure 7.3. LP thermal model with node on each winding layer. (Insert) Thermal resistance network with thermal capacitance and heat generation at each node and thermal resistances between the nodes

In Chapter 5 and Chapter 6 it was shown that directly oil cooled stators suffer from non-uniform flow distribution, which in turn produces an asymmetric boundary condition. Therefore to capture the effect of non-uniform flow distribution on the temperature distribution of the windings, the model can be broken down further to include nodes on either side of the iron as shown in Figure 7.4. The thermal resistance network is shown in Figure 7.5. Both models produce the same result when symmetrical flow conditions are applied.

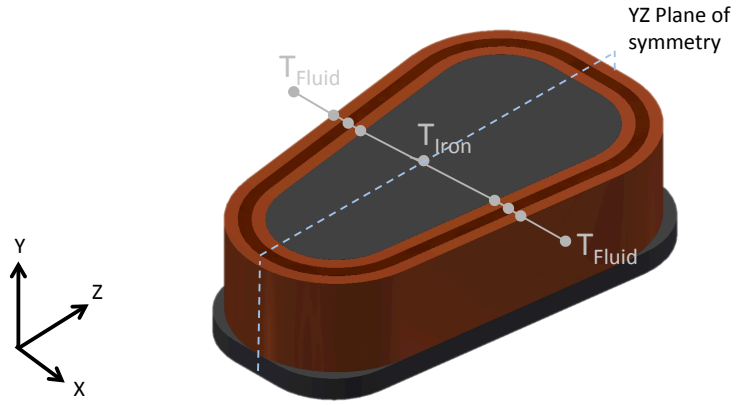


Figure 7.4. LP thermal model with nodes on either sides of the pole piece

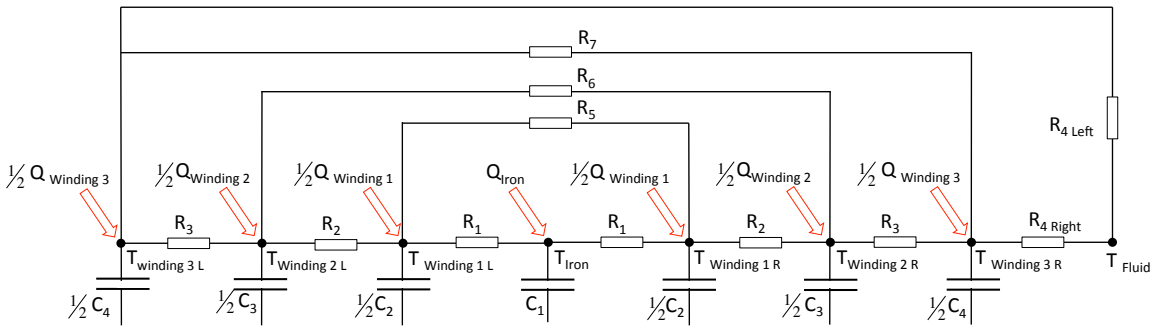


Figure 7.5. Thermal resistance network of the pole piece with left and right temperature resolution

In this case the thermal capacitance of each winding layer is divided between the nodes on the layer. The nodes on each layer are connected together by conductive resistances R_5-R_7. These are defined as:

$$R_{5,6,7} = \frac{l_{nodes}}{kA} \qquad \text{eqn. 7.6}$$

where l_{nodes} is the distance between the left and right nodes along the length of the conductor, k is the thermal conductivity of the copper and A the cross sectional area of the layer.

The governing equations

Having described the underlying assumptions behind the model, the set of equations governing the node temperature for the general model described in Figure 7.3 are presented. In Section 2.1 of the literature review it was shown that every pole piece experiences an internal heat generation $\dot{E}_g$ in the iron bobbin and copper windings. From the first law of thermodynamics, the rate of energy stored in the body $^{dE_{st}}/_{dt}$ can be computed using:

$$\frac{dE_{st}}{dt} = \dot{E}_{in} - \dot{E}_{out} + \dot{E}_g \qquad \text{eqn. 7.1}$$

Where $\dot{E}$ is the rate of energy transfer and subscripts *in*, and *out* define the direction of the energy into or out of the components. When applied to each node, the equations predicting the temperature of the node with time are established and defined hereunder. The iron temperature is defined as:

$$\mathrm{T}_{iron,t+1} = \left(\frac{\mathrm{Q}}{\rho V_b c.}\right)_{iron} - \left[\left(\frac{1}{\rho V_b c.}\right)_{iron}\left(\frac{T_{iron} - T_{Cu1}}{R_{th1}}\right)\right] \qquad \text{eqn. 7.2}$$

The temperature on the node defining the first winding layer is defined as:

$$\mathrm{T}_{Cu1,t+1} = \left(\frac{\mathrm{Q}.\mathrm{R}_{loss}}{\rho V_b c}\right)_{Cu1} - \left\{\left(\frac{1}{\rho V_b c}\right)_{Cu1}\left[\left(\frac{T_{Cu1} - T_{iron}}{R_{th1}}\right) + \left(\frac{T_{Cu1} - T_{Cu2}}{R_{th2}}\right)\right]\right\} \qquad \text{eqn. 7.3}$$

The temperature on the node defining the second winding layer is defined as:

$$\mathrm{T}_{Cu2,t+1} = \left(\frac{\mathrm{Q}.\mathrm{R}_{loss}}{\rho V_b c}\right)_{Cu2} - \left\{\left(\frac{1}{\rho V_b c}\right)_{Cu2}\left[\left(\frac{T_{Cu2} - T_{Cu1}}{R_{th2}}\right) + \left(\frac{T_{Cu2} - T_{Cu3}}{R_{th3}}\right)\right]\right\} \qquad \text{eqn. 7.4}$$

The temperature on the node defining the third winding layer is defined as:

$$\mathrm{T}_{Cu3,t+1} = \left(\frac{\mathrm{Q}.\mathrm{R}_{loss}}{\rho V_b c}\right)_{Cu3} - \left\{\left(\frac{1}{\rho V_b c}\right)_{Cu3}\left[\left(\frac{T_{Cu3} - T_{Cu2}}{R_{th3}}\right) + \left(\frac{T_{Cu3} - T_{oil}}{R_{th4}}\right)\right]\right\} \qquad \text{eqn. 7.5}$$

Where Q_{iron} and Q_{Cu} are the heat loads supplied to the iron and windings nodes respectively. ρ is the density, V_b is the body volume of the iron or winding layers and c the specific heat capacity. R_{loss} is a loss ratio of the windings defined as winding length of the layer to the total copper winding length. The parameters $R_{th1} - R_{th4}$ are thermal resistances between the layers. When the model is split further into its left and right components as defined by Figure 7.4, the body volume for each winding node and the heat input is halved and three more winding equations are added to reflect the left and right nodes of the windings. A MATLAB script was written to solve the differential equations in the LP model using the 4th order Runge Kutta Method.

Having established the governing equation of the model, the following section focuses on defining the material, thermal and electrical properties of the SMC iron and windings.

7.2.2. Defining the material and thermal properties

The material and thermal properties of the SMC iron bobbin and copper windings is essential for the accurate prediction of their temperature. While some parameters such as body volume V_b and density ρ of SMC iron are readily measured, the heat capacity c was achieved through an initial experiment in which the transient heating and cooling of a bobbin was measured. A lumped parameter model with a single node was used to establish its specific heat capacity. The properties of the SMC iron and copper windings are listed in Table 7.1.

Table 7.1. List of thermal and material properties for SMC iron and Copper windings

Material Property	SMC Iron (Somaloy)	Copper Winding
Density [kg/m^3]	7515	8800
Volume [m^3]	2.008E-5	1.632E-5
Thermal conductivity [W/mK]	35	300
Specific heat capacity [J/kgK]	300	400

The thermal model also makes use of thermal parameters such as the thermal resistances between the winding layers. These could only be determined through an initial calibration experiment. The procedure is described in Section 7.3.

The focus of this chapter is now turned on the electrical properties of the windings and SMC iron. These are important for modelling the heat load in the windings and SMC iron. Many LP models found in the literature apply a constant heat load to the windings and iron. However in Section 1.2 of Chapter 1 the electrical resistivity of copper was shown to change with temperature. Hence the electrical resistance and heat load in the windings also vary with temperature. Ignoring this may result in an inaccurate winding temperature prediction. On the other hand the behaviour of the electrical resistance of SMC iron with temperature is not well documented in the literature. Therefore the following section experimentally investigates the variation of the electrical resistance of the copper windings and SMC iron bobbin to establish missing parameters and accurately model this variation.

7.2.3. The electrical properties of copper windings and SMC iron bobbin

In the introduction chapter it was shown that the heat generated by the copper windings Q has been defined in terms of its current I, and electrical resistance R as:

$$\mathrm{Q} = \mathrm{I}^2 R \qquad \text{eqn. 7.7}$$

The electrical resistance R is defined as:

$$R = \frac{\rho_{rT} l}{A_{csa}} \qquad \text{eqn. 7.8}$$

where l is the length of the winding and A_{csa} the cross sectional area of the copper wire. ρ_{T} is a the temperature dependent resistivity defined as:

$$\rho_{rT} = \rho_o[1 + \alpha(T - T_o)] \qquad \text{eqn. 7.9}$$

where ρ_o is a reference resistivity, α is the temperature coefficient of resistivity for copper, T is the winding temperature and T_o is a fixed reference temperature of 20 $^{\mathrm{o}}$C. To establish values of ρ_o and α, a constant dc current was injected into the windings of a pole piece. The dc voltage across the windings and dc current were recorded using the PicoScope 3000 series oscilloscope at a sample rate of 1 Hz. The winding temperature was also recorded using a TC08 Pico Data logger at the same sample rate of 1 Hz. The electrical resistance of the windings was calculated from the voltage and current measurements. As the length of the winding and its cross sectional area are known, the temperature dependent resistivity ρ_{rT} was established. Figure 7.6 plots the temperature dependent resistivity ρ_{rT} with the winding temperature. At a reference

temperature T_o of 20 °C, ρ_o=1.509e-8 Ωm. α was found at 0.0044 K^{-1}. These values are applied in the LP thermal model to estimate the variation in heat load with winding temperature. It is shown that as the winding temperature increases, the resistivity increases and therefore for a constant current supply, (which is the power source used for these experiments), the losses in the windings increase with temperature.

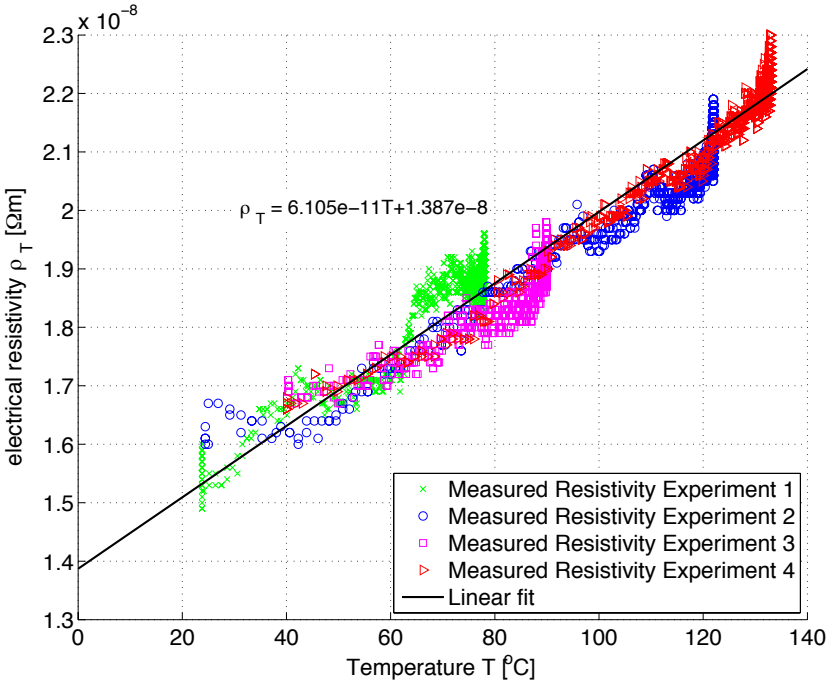


Figure 7.6. The electrical resistivity of copper windings with temperature

The experiment was replicated with an SMC iron bobbin. The bobbin was injected with a dc current and heated through the Joule effect. The dc voltage and dc current across the bobbin were recorded using a PicoScope 3000 series oscilloscope at a sample rate of 1 Hz. The bobbin temperature was recorded using a TC08 Pico Data logger at the same sample rate of 1 Hz. The electrical resistance was calculated from the values of voltage and current. Figure 7.7 shows how the electrical resistance of the SMC iron remains unchanged with temperature. Hence the heat load in the LP model can be assumed constant over the entire test.

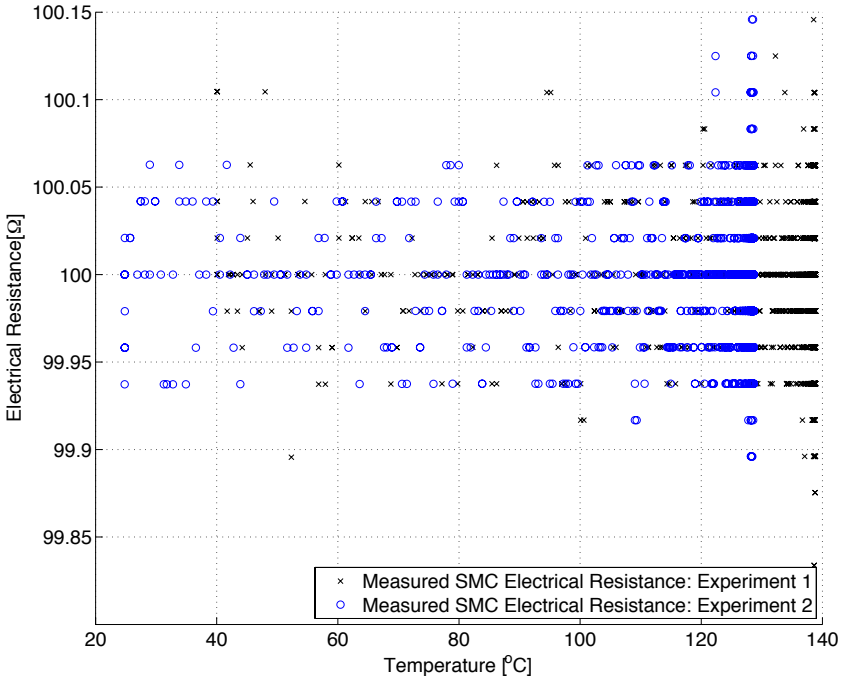


Figure 7.7. Electrical resistance of SMC iron with temperature

7.2.4. Parametric modelling and visualisation

While this chapter makes use of the YASA pole piece as a test case study, a parametric model was developed so that the various shapes of pole pieces for axial or radial machines can be investigated. The geometrical parameters of the pole piece are highlighted in Figure 7.8.

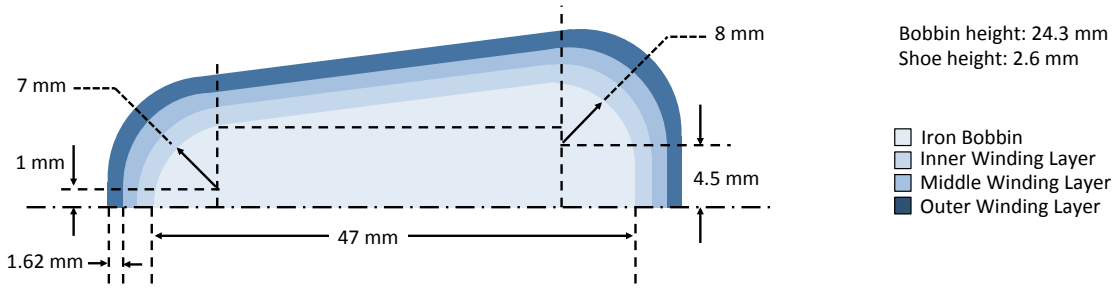


Figure 7.8. Cross sectional area along the XZ plane for half the YASA pole piece

A visualisation tool that allows the thermal designer to analyse the temperature profile across the cross section of the wound pole piece shown in Figure 7.9 was developed. The tool converts the winding temperature into a colour vector and assigns it to winding layer it belongs to.

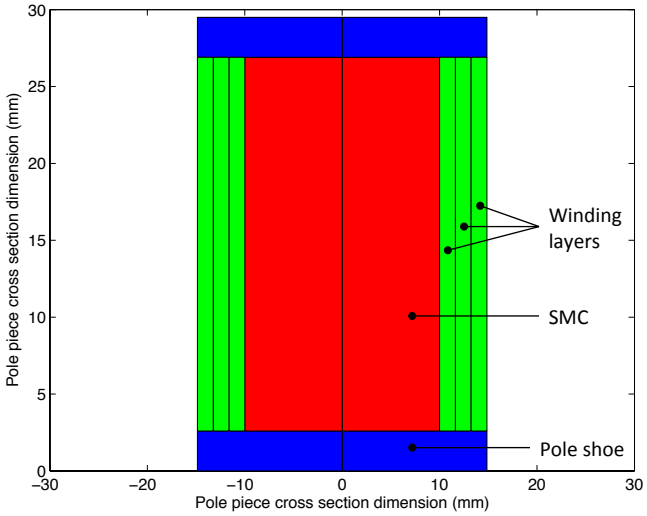


Figure 7.9. Visualisation of the pole piece cross sectional area along the XY plane

Having described all the components of the model, the next section describes the experimental procedure undertaken to validate the model. The experiment also seeks to establish the temperature gradient across concentrated windings.

7.3. Experimental Investigation

This experiment takes advantage of the segmented design of the direct oil cooled YASA machine to produce a detailed temperature map of a concentrated wound pole piece. A control volume for one pole piece shown in Figure 7.10 was replicated in the experimental setup. The setup consists of one active pole piece and the flow channels on either side of the pole piece.

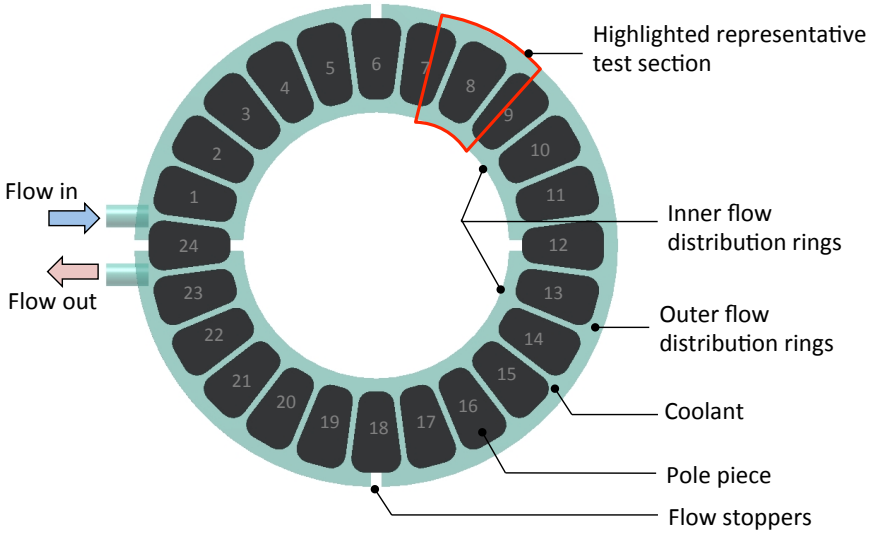


Figure 7.10. Schematic of a directly oil cooled segmented stator. (Highlighted) test Section with one pole piece and respective flow channels

7.3.1. Manufacturing concentrated wound pole pieces

Concentrated wound pole pieces were manufactured at the winding facility at the Department of Physics Winding Lab at the University of Oxford. The winding machine is made of two main components:

a) A lathe machine with controllable speed and modified jaws to grab pole pieces, and

b) A copper reel clamp coupled to fixed speed electric machine via a clutch mechanism with controllable slip.

During the winding process, the copper is subjected to a tension by having an electric motor holding the winding reel and the lathe winding the bobbin rotating in opposite directions. The tension is adjusting by adjusting the slippage on the clutch. Figure 7.11 shows the details of the winding machine. A mould for the bobbin onto which the wire is wound was designed in Autodesk Inventor and 3D printed. This allows the jaws of the lathe to clamp the fragile bobbin without damaging it. The pole piece was wound with a square copper wire of size AWG14 (1.62 mm) with a tension of 100N.

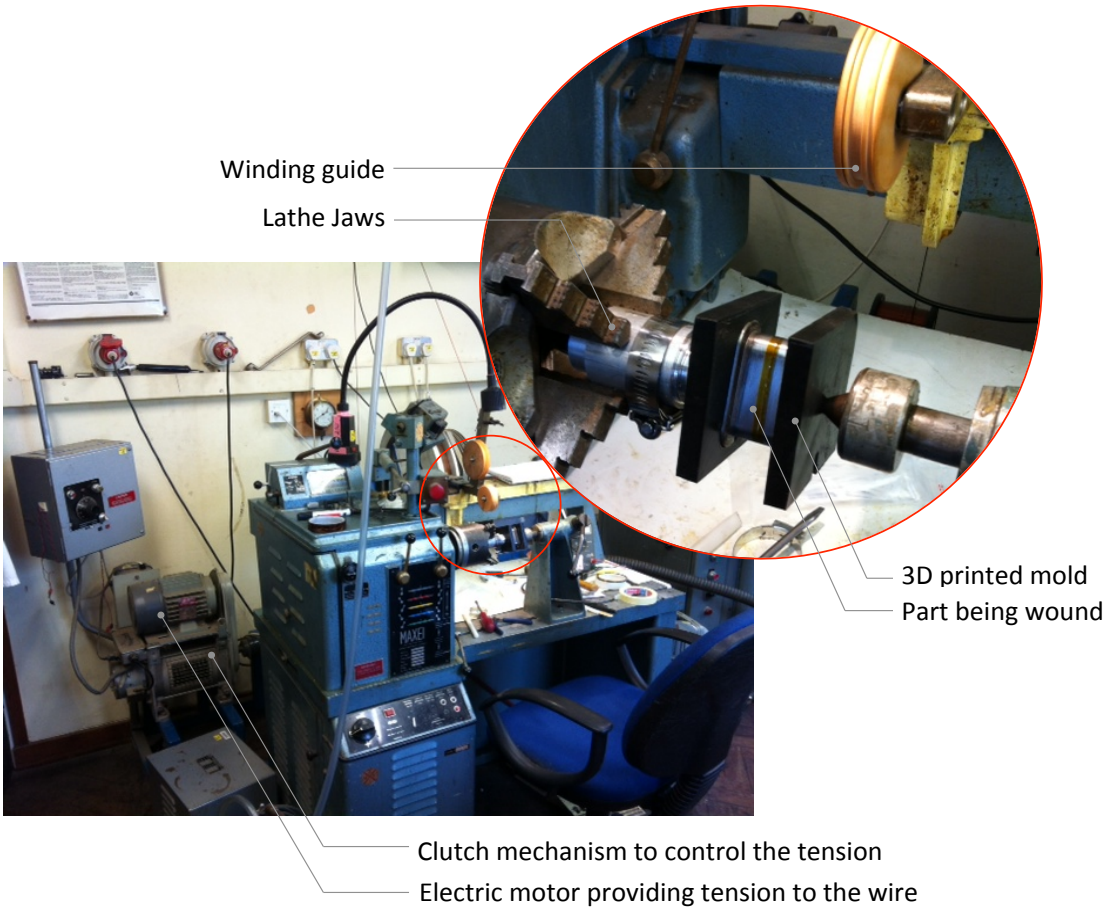


Figure 7.11. Details of the winding machine. (Insert) Details of the clamped part

To improve their mechanical rigidity and improve their ingress protection, pole pieces often undergo a process of epoxy encapsulation. Common techniques include vacuum pressure impregnation (VPI), epoxy infiltration by painting on the windings or coating in varnish or epoxy. VPI requires specialist equipment by which the component is placed in a vacuum chamber and following a vacuum process epoxy is forced into the coil to fill the voids between the windings. On the other hand painting and coating require no specialist equipment. In this research epoxy infiltration by painting is investigated. A viscous layer of filler epoxy resin is painted on each winding layer before the next layer is wound. To investigate any thermal effects from the infiltration process, two pole pieces were wound; one infiltrated with a layer of Stycast epoxy painted between the winding layers and one with no infiltration. The properties of Stycast epoxy are shown in Table 7.2.

Table 7.2. Technical specifications of Stycast Epoxy

Epoxy Name	Stycast 2850 FT
Dielectric Strength [kV/mm]	14.4
Thermal conductivity [W/mK]	1.25
Coefficient of thermal expansion [K^{-1}]	$35x10^{-6}$
Density [kg/m^3]	2350-2450

Thermocouples were mounted on the pole piece during the winding process so that two are mounted on the iron, two between the iron and the first copper layer, two between the first and second copper layers, and two between the second and third copper layers. The mounting of thermocouples is shown in Figure 7.12. Figure 7.13 shows the non-infiltrated pole pieces in a) with the epoxy-infiltrated pole piece in b).

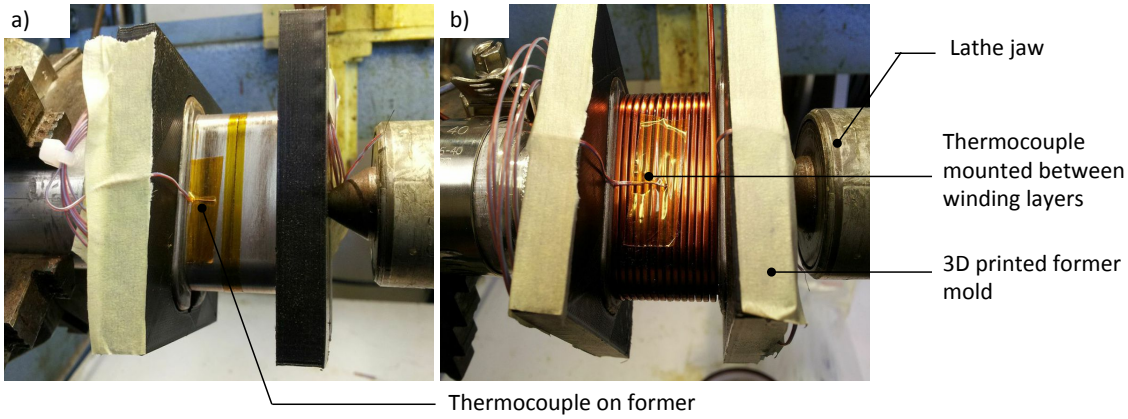


Figure 7.12. Details of the winding process with a) thermocouples mounted on the iron pole, b) thermocouples mount between the winding layers

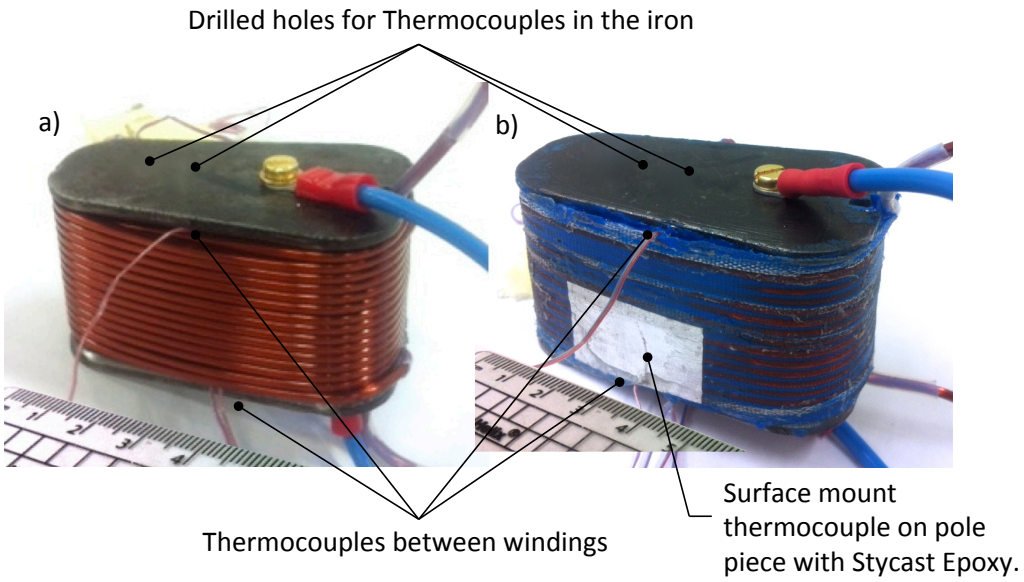


Figure 7.13. a) Concentrated wound pole pieces with no epoxy filler b) Concentrated wound pole piece with Stycast epoxy infiltration

7.3.2. Manufacturing the flow geometry

The instrumented pole piece was mounted on a plastic base and assembled in a test box. The test box was also fitted with two non-energized half poles, one on each side of the test piece to recreate the flow channels between the pole pieces as shown in Figure 7.14.

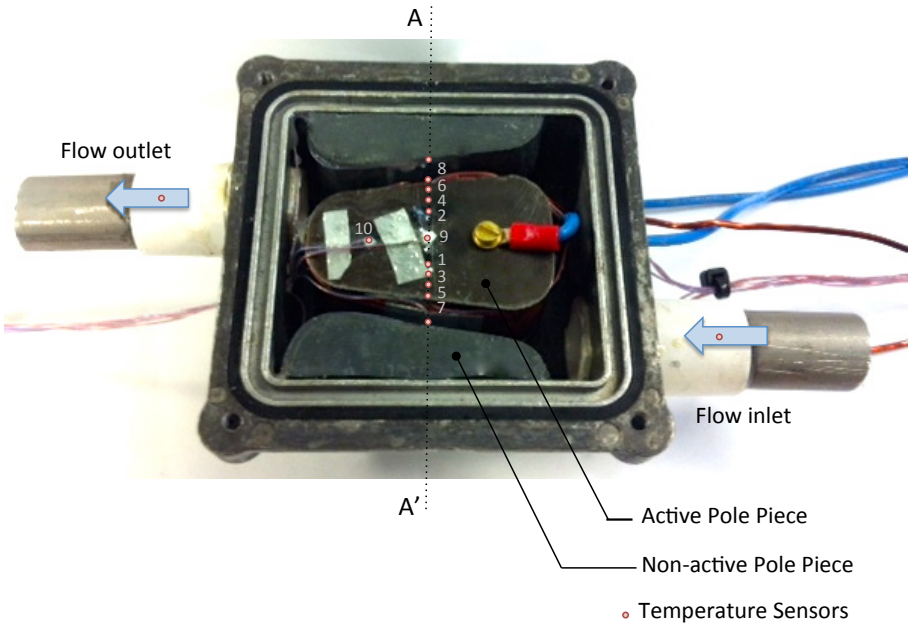


Figure 7.14. Test Section with recreated flow geometry and marked locations of temperature sensors

7.3.3. Measuring the temperature profile across the pole piece

The heat losses in the copper windings and the SMC iron bobbin was simulated by Joule heating. Hence these were each connected to a dc power supply and energized separately. The iron losses were kept at 20% of the total pole piece losses as per manufacturer recommendations. To avoid repetition, the reader is kindly directed to the description of the test rig in Section 5.5.2.

In Section 2.2 of the literature review it was shown that traditionally lumped parameter models require an initial calibration experiment to establish unknown thermal parameters of the model such as the thermal resistances (Boglietti, 2009). This procedure was adopted throughout this research. To do this a set of transient experiments were held. The first experiment was used to fully characterise the pole piece and calibrate the thermal resistances in the model. The remaining experiments were used to validate the calibration parameters of the model at different conditions. During these tests the oil flow was set and run at a fixed flow rate. The heat input to the winding and iron were set. These were energized simultaneously and the increase in temperature of the windings was monitored and recorded. The windings were then de-energized to capture the cooling curve of the pole piece. The heating and cooling portions are important to check the thermal mass of each winding layer. The transient experiments were followed by a series of steady state measurements with the aim to fully capture the temperature gradient across the concentrated windings. Steady state tests were run for approximately two hours to ensure that state conditions were reached. The experimental procedure was repeated for epoxy infiltrated winding and non-infiltrated windings. Details of the transient calibration experiment for epoxy-infiltrated windings are shown in Table 7.3. Those for non-infiltrated windings produced in Table 7.4. Details for steady state experiments for epoxy infiltrated and non-infiltrated windings are shown in Table 7.5 and Table 7.6 respectively.

Table 7.3. Experiment details for the transient characterisation of epoxy-infiltrated windings

Test No.	Coolant inlet temperature [^{o}C]	Flow rate [lpm]	Iron heat input [W]	Copper Winding heat input[1] [W]
1	23.9	3.7	23.13	82.61
2	23.9	3.7	10.87	46.03
3	39.5	4.8	22.99	80.24
4	38.6	4.7	10.19	36.73

Table 7.4. Experiment details for the transient characterisation of non infiltrated windings

Test No.	Coolant inlet temperature [^{o}C]	Flow rate [lpm]	Iron heat input [W]	Copper Winding heat input[1] [W]
1	24.5	3.7	22.85	81.27
2	23.6	3.6	10.8	37.3
3	40.1	4.8	22.87	85.86
4	40.4	4.9	10.18	44.07

Table 7.5. Steady state experiment details for epoxy-infiltrated windings

Test No.	Coolant inlet temperature [^{o}C]	Flow rate [lpm]	Iron heat input [W]	Copper Winding heat input[2] [W]
1	21.0	3.5	10.88	48.37
2	24.8	2.6	10.88	47.39
3	24.6	3.7	24.40	114.90
4	24.8	2.6	24.42	115.83
5	41.1	4.9	10.78	47.48
6	39.9	3.4	10.63	50.58
7	40.4	4.8	24.20	114.59
8	39.9	3.5	24.27	112.36

Table 7.6. Steady state experiment details for non-infiltrated windings

Test No.	Coolant inlet temperature [^{o}C]	Flow rate [lpm]	Iron heat input [W]	Copper Winding heat input[2] [W]
1	22.4	3.6	10.99	47.66
2	23.4	2.5	11.09	44.25
3	22.9	3.9	24.21	111.74
4	24.6	2.5	24.36	117.80
5	40.4	4.9	10.75	49.48
6	39.8	3.4	10.87	51.15
7	39.6	4.8	24.18	119.81
8	40.7	3.5	24.22	123.23

[1] Heat input value for the windings at the time = 0 s

[2] Heat input value for the experiment running at steady state

Having described the experimental procedure the next section presents a comparison between the measured temperature of the windings and the LP model. The test results and model validation of epoxy-infiltrated windings is presented first, followed by the results of non-infiltrated windings.

7.4. Test Results and Model Validation

7.4.1. Epoxy-Infiltrated Windings

The thermal characterisation chart of epoxy-infiltrated windings is shown in Figure 7.15. The thermal resistances between the windings and the thermal capacitances of each winding layer and SMC bobbin are identified by fitting the model to the first experimental data. The model is superimposed on Figure 7.15. The calibrated parameters for epoxy-infiltrated windings are shown in Table 7.7.

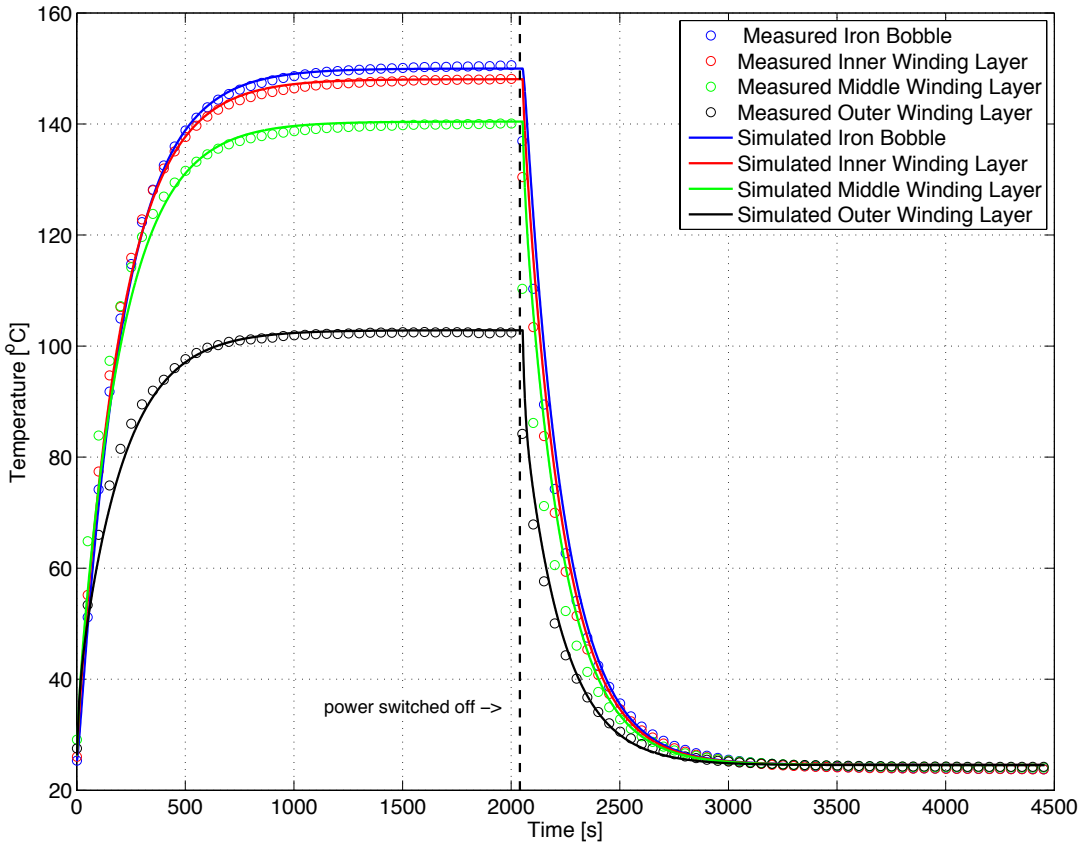


Figure 7.15. Thermal characterisation of the model with three winding layers for a pole piece with epoxy-infiltrated and experiment conditions as shown in Table 7.3, Test No. 1

Table 7.7. Experimental fit of the thermal resistances for epoxy infiltrated windings

Description	Designation with Reference to Figure 7.3	Value
Thermal resistance between the pole piece and the first winding layer [K/W]	R_1	0.12
Thermal resistance between the first and second winding layers [K/W]	R_2	0.18
Thermal resistance between the second and third winding layers [K/W]	R_3	0.45
SMC Iron Specific heat capacity [J/kgK]		300
Copper Specific heat capacity [J/kgK]		400

These parameters were further validated with the other transient experimental conditions. While these charts do not add more value to the results, they are important to confirm the thermal parameters. Hence due to space restrictions the charts for the remaining transient conditions are presented in Appendix 4.1. Having established and confirmed the thermal characteristics of epoxy-infiltrated windings, Figure 7.16. investigates the temperature profile across these windings during steady state conditions. The temperature profile is plotted with reference to temperature sensors mounted along the line AA' shown in Figure 7.14.

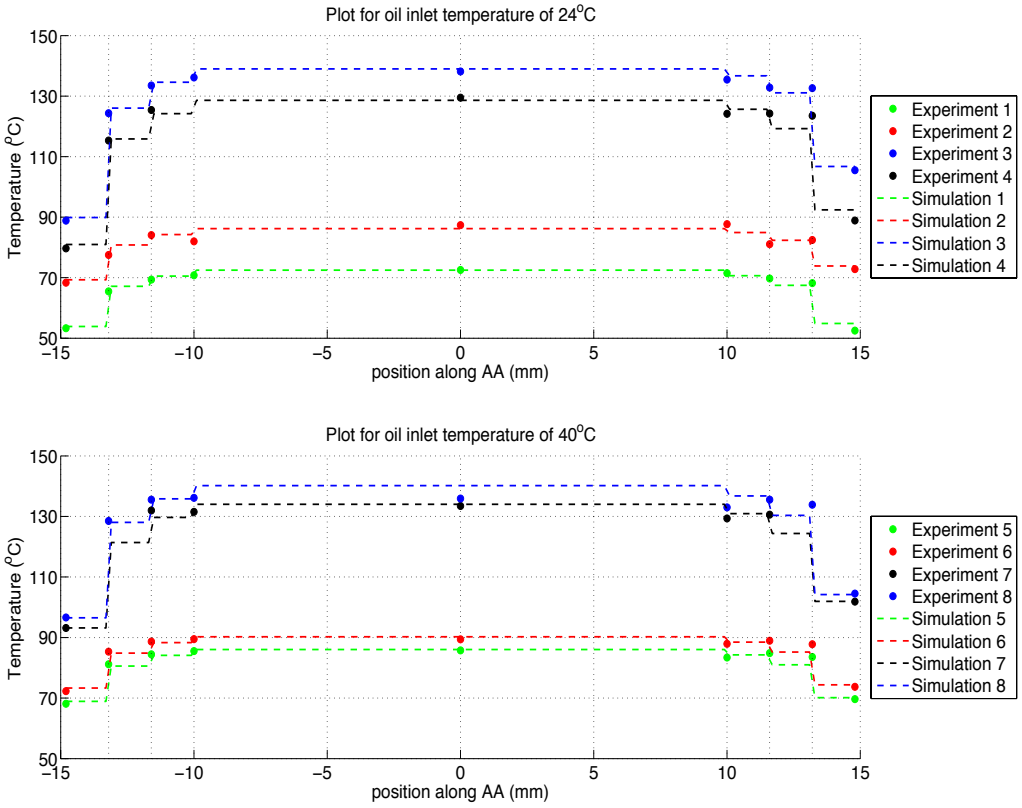


Figure 7.16. The temperature profile for the pole piece with epoxy infiltration under steady state conditions

The calibrated model generally matches the model to within 3% of the measurements.

7.4.2. Non-Infiltrated Windings

The same process was repeated for non-infiltrated windings. However, despite using the same measurement setup it was noted that in non-infiltrated windings no single calibration parameter fits the whole test regime. This is a major difference to epoxy-infiltrated pole pieces. The thermal resistances across the layers were noted to change with heat flux. Hence the thermal resistance across each joint (designated R_1, R_2 and R_3 in Figure 7.3) was correlated with the convective thermal resistance R_4. The relationship is shown in Figure 7.17. . The values of R_1-R_4 are obtained from the best fit of transient thermal behaviour experiments. The implications of this behaviour is important as the commonly applied notion that thermal resistances are only dependent on the manufacturing process may not hold for non-infiltrated windings.

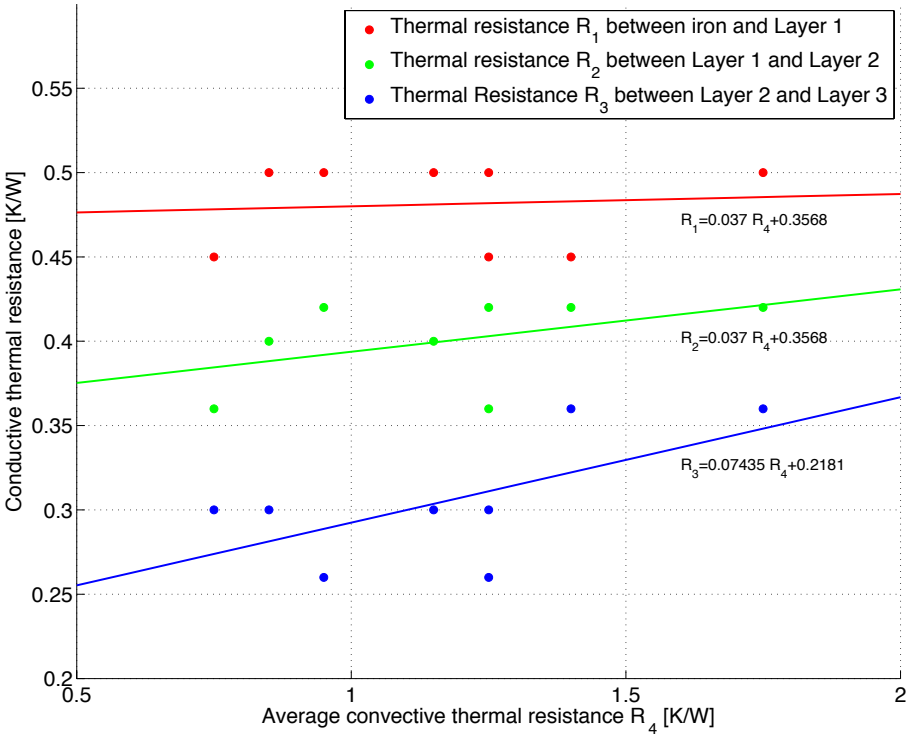


Figure 7.17. Correlation of the thermal resistances across the layers with convective thermal resistance

The transient experiments were used to examine the accuracy of the parameters. An example of the transient behaviour of the windings is shown in Figure 7.18. . Due to space restrictions the charts for the remaining test scenarios are reported in Appendix 4.2. With the thermal characteristics of non-infiltrated windings established the focus is turned to the temperature profile of the pole piece during steady state conditions. Figure 7.19. shows the experimental measurements and simulated results for the

temperature profile across non-infiltrated windings. The temperature profile plotted is referenced to temperature sensors mounted along the line AA' shown in Figure 7.14.

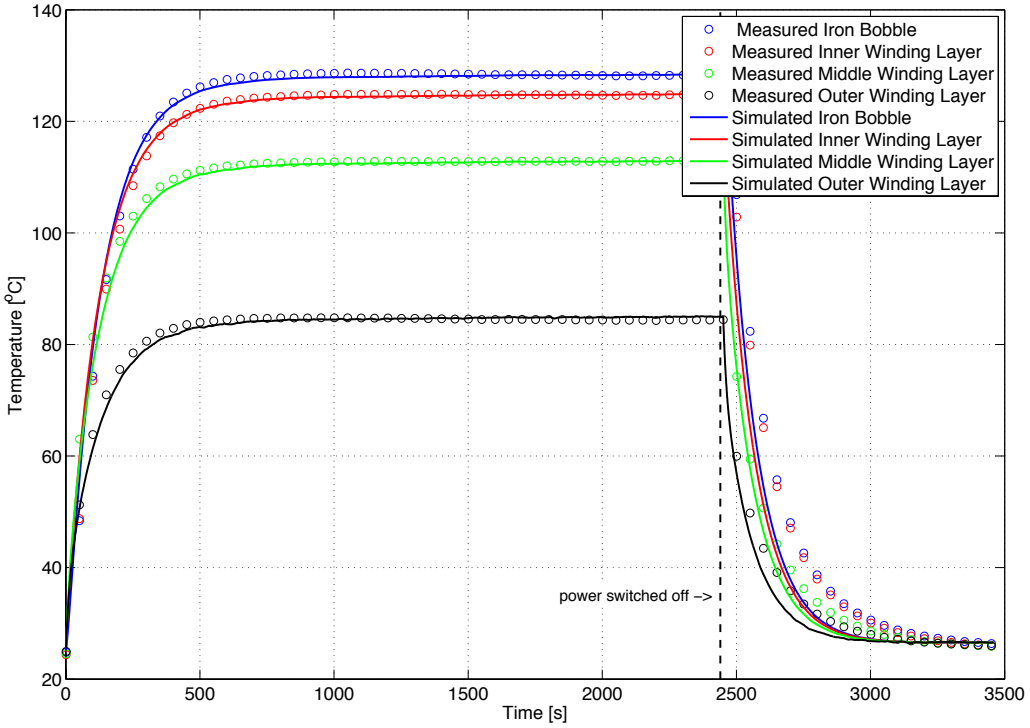


Figure 7.18. Thermal characterisation of non-infiltrated windings for experiment conditions in Test 1

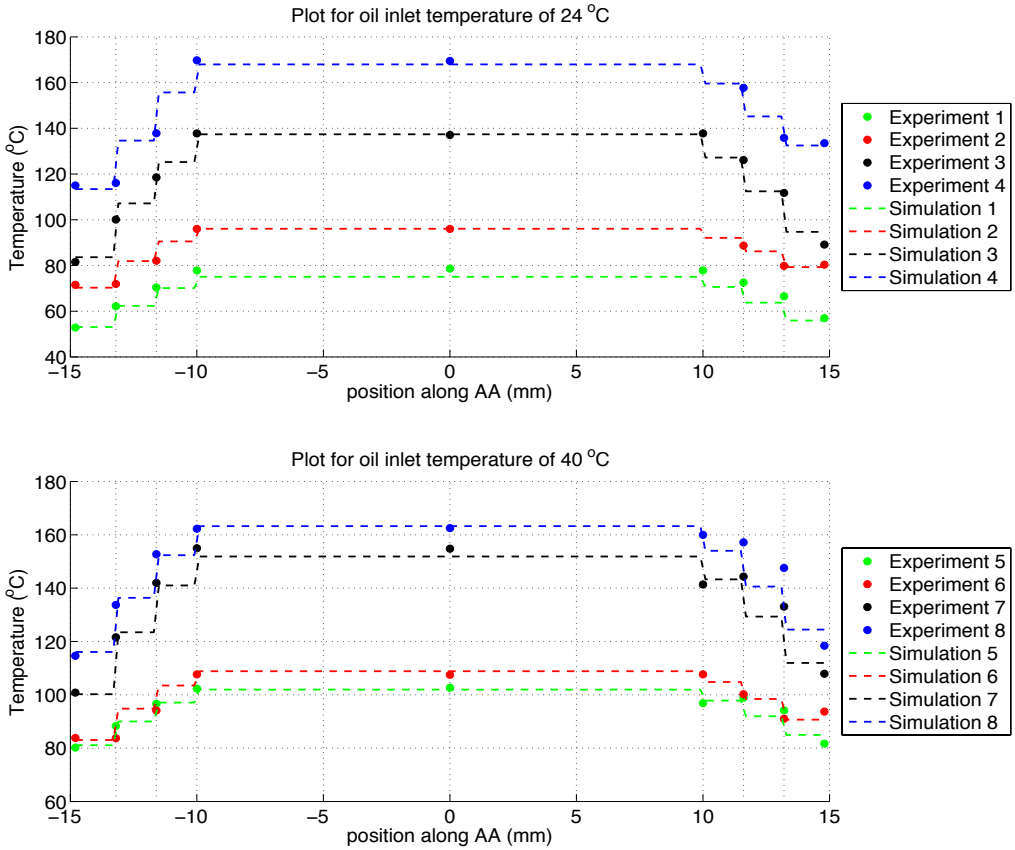


Figure 7.19. Comparison of the temperature profile across the pole piece with no epoxy infiltration

The results presented here raise several points of discussion regarding the contact resistance, the thermal capacitance, and the temperature behaviour of epoxy infiltrated and non-infiltrated windings.

7.5. Discussion

This discussion addresses the observations made from measuring the temperature of the windings.

7.5.1. The Temperature Gradient

The experimental results demonstrate that concentrated windings suffer from a severe temperature gradient across the windings. In the experiments epoxy infiltrated windings experience a maximum temperature gradient of 30 ^{o}C. Non-infiltrated windings experience a maximum temperature gradient of 50 ^{o}C. In direct oil-cooled pole pieces the hot spot temperature is formed on the inner winding layer (experiencing the longest thermal path). Modelling techniques that employ too few nodes to capture the winding temperature may be missing valuable information such as the value and location of the hotspot.

7.5.2. The Thermal Resistances

The model developed in this chapter breaks down the windings into separate layers with a thermal resistance applied between each layer. The interlayer thermal resistance represents three conductive processes: 1) the conductive component across the copper, 2) the conductive component across the electrical insulation and 3) the thermal contact at the interface as shown in in Figure 7.20.

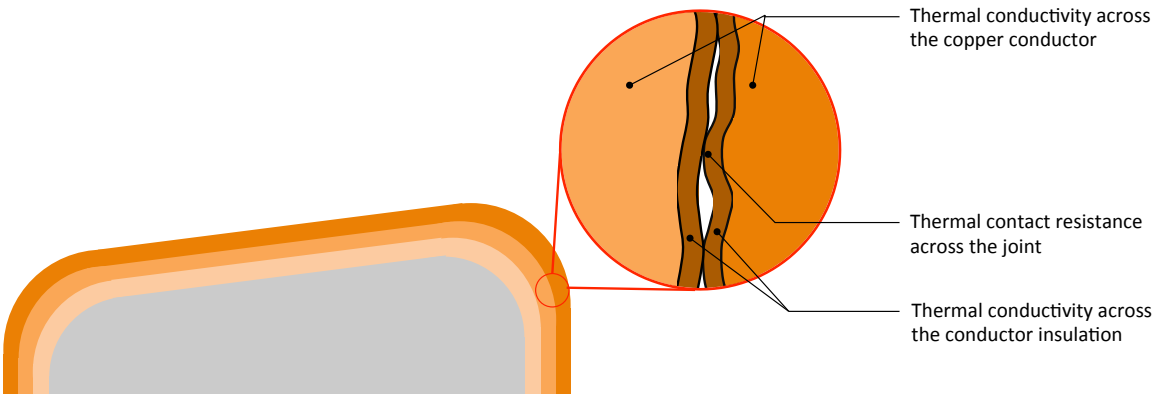


Figure 7.20. Description of the break down of the thermal resistance across non-infiltrated winding layers

The polyamide-imide insulation of copper windings is bonded to the copper substrate and therefore the copper conductor can be assumed to be in perfect thermal contact with the insulation coating. Due to the large copper conductivity and low insulation thickness, the conductive contribution is negligible. Therefore the thermal contact resistance across the winding layers can be seen to dominate the discontinuous conductive process. This research uses an initial experimental calibration to establish the thermal resistance across each of the winding layers. It was noted that each layer has its own thermal resistance value. The inner winding layers tend to have lower thermal resistance values than the outer winding layers. However winding layers are made from the same conductor and therefore variations in the resistance can only arise from variations in thermal contact resistance at the interface. The author theorises that during the winding manufacturing process, the inner windings are subjected to an additional pressure and deformation when subsequent winding layers are wound on top of each other.

In epoxy-infiltrated windings, the thermal resistances have been found to remain constant across the whole test regime. This was not the case with thermal resistances of non-infiltrated windings. The calibration values for non-infiltrated windings demonstrate a peculiar behaviour whereby the thermal resistances were different for every test case study. Hence the notion that thermal resistances are only dependent on the manufacturing process does not hold in non-infiltrated windings. The thermal resistances across the layers were noted to change with heat flux and correlated with the convective thermal resistance. To aid in this discussion and the interpretation of the results the theory for modelling thermal contact resistances (TCR) has been analysed. Due to space restrictions the theory is reported in Appendix 4.

It is shown that the TCR is a function of a few variables namely the contact pressure, material hardness, surface roughness and thermal conductivity. The TCR decreases with an increase in contact pressure and thermal conductivity and with a decrease in surface roughness and material hardness. In flat surfaces these parameters are independent of each other and controllable, (Yovanovich, 2005, Cooper et al, 1969). However, when extending the theory to the contact interface of concentric geometries the temperature difference across the joint causes a differential expansion or contraction. This reinforces or relaxes the contact pressure at the interface, depending

on the direction of the heat flux vector. Therefore the governing contact pressure becomes interrelated with heat flux, (Madhusudana, 1986, Lemczk and Yovanovich, 1987).

In direct cooled electrical machines, the heat flux vector in the windings is radially out, causing a reinforcement of the contact pressure. Therefore with an increase in heat flux, the thermal resistances across the winding layers decrease. The heat flux is dictated by the heat generation and controlled by the convective heat transfer. Therefore the interdependence between the heat transfer across the solids and the fluid domain is very similar to conjugate heat transfer albeit in this case the effect is mainly on the discontinuous conductivity. This effect was only observed in non-infiltrated windings. The author theorises that when epoxy-infiltration is applied, the resin binds the winding layers rigidly together and restricts the movement of the windings. This leads to a constant thermal resistance for epoxy infiltrated windings as observed in the experimental results. To the author's knowledge, this observation of the dependence of thermal resistance of non-infiltrated windings has not been reported in the literature. The author cautions against modelling the transient thermal behaviour of non-infiltrated stator windings with single calibration parameters as this may be an over simplification leading to inaccurate temperature prediction. A degree of variation of the thermal resistances between components with heat flux should first be established.

7.5.3. The Thermal Capacity

The differences in the behaviour of epoxy-infiltrated windings and non-infiltrated windings do not stop with the thermal resistances between the windings. Some peculiarity in the thermal capacity of non-infiltrated windings have also been observed. While the transient behaviour of epoxy-infiltrated windings can be accurately modelled by a fixed thermal mass, non-infiltrated windings seemed to require a larger thermal mass during the cooling process than they had during heating. The thermal mass of the wound pole piece is unchanged and therefore the author theorises that this effect is also related to the slight expanding motion of the winding layers. During heating the coolant oil is also heated up and its viscosity decreases. The thermal expansion experience by non-infiltrated windings may allow the coolant to

infiltrate voids within the windings, acting as an additional thermal mass during cooling. While this effect does not affect the steady state results, it may be important for the investigation of transient modelling of directly oil cooled electrical machines with non-infiltrated windings.

7.5.4. The Effect of Epoxy-Infiltration on the Temperature Profile

To determine if the process of epoxy infiltration has any effects on the temperature profile of concentrated windings, the two validated models were run for a series of equal pole piece losses. The oil inlet temperature and the convective thermal resistance were kept constant. For simplicity a symmetrical convective boundary condition was applied. A comparison of the winding temperatures is shown in Figure 7.21.

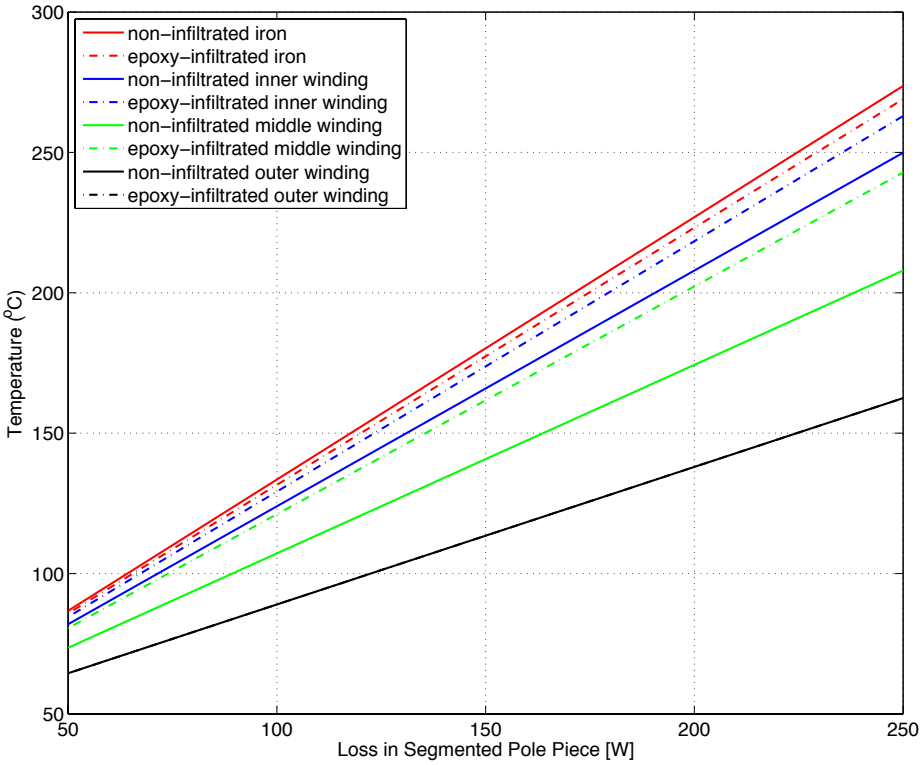


Figure 7.21. Comparison of the temperature profile of: (a) non-infiltrated concentrated windings and (b) epoxy-infiltrated concentrated windings

It can be seen that the temperature distribution in the two constructions is different. Epoxy infiltrated windings offer a benefit in reducing the hot spot temperature. A maximum reduction of 5 ^{o}C is shown at 250 W losses. However, the average temperature in epoxy-infiltrated windings is higher, while in non-infiltrated pole pieces the temperature gradient across its windings is larger. To the authors

knowledge no existing literature on epoxy painting of concentrated windings exists and therefore a comparison of this result is difficult. The existing literature body focuses on vacuum pressure impregnation (VPI) and suggest that when this is applied, the hotspot temperature in induction machines is reduced, (VPI Resins, 2015). Nategh (2014) investigates the effects of increasing the conductivity of epoxy resins from 0.25 W/mK to 3 W/mK on an indirect cooled induction machine. The results show a reduction in hot spot temperature of around 20 ^{o}C. No details of the average winding temperature and temperature gradient have been reported. The author attributes this variation in the benefits achieved to one of two reasons: an unsuitable comparison of the machine geometry or the imperfections in applying epoxy painting process compared to VPI. To examine this further, the focus of this discussion is turned to the process of epoxy infiltration.

When analysing the process of infiltrating the windings with epoxy resin, the filler material between the windings can be represented by one of the scenarios shown in Figure 7.22. . The windings can be a) non-infiltrated, b) perfectly infiltrated in the gap, c) imperfectly (or partially) infiltrated in the gaps, d) overly infiltrated through a process such as painting.

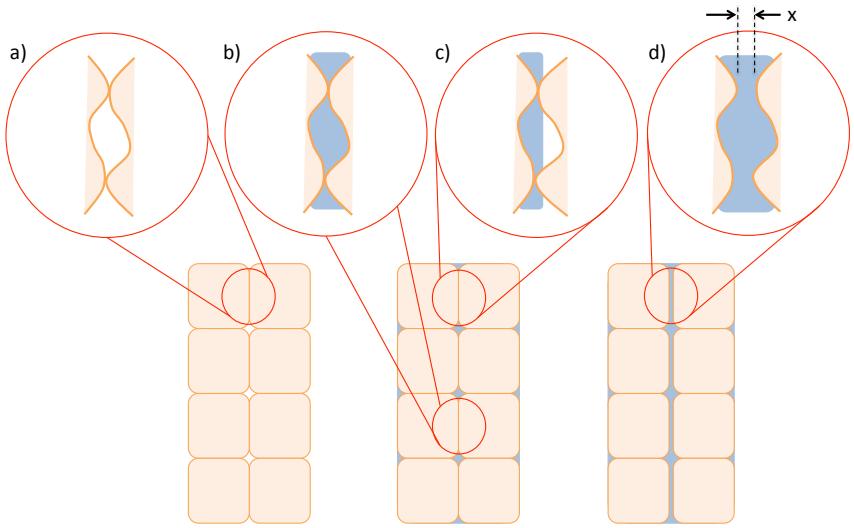


Figure 7.22. Representation of a) non-infiltrated windings, b) perfectly infiltrated in the gaps, c) partial infiltration and d) a thick layer of infiltration material applied between the windings

To discuss these effects, the equations from the thermal contact resistance are analysed. The conductance across a joint h_{jc} is made from two components: the conductance across the surface asperities in contact at the interface h_{cc}, and the conductance across the gaps between the asperities h_{gc}.

$$h_{jc} = h_{cc} + h_{gc} \qquad \text{eqn. 7.12}$$

The conductance h_{cc} is defined as:

$$h_{cc} = \frac{1.25m.k_s}{\sigma}\left(\frac{P_{app}}{H_c}\right)^{0.95} \qquad \text{eqn. 7.13}$$

where m is the mean asperity slope, σ is the RMS surface roughness, k_s is the equivalent conductivity of the two surfaces, P_{app} is the applied pressure and H_c the contact hardness. As the conductivity of the solids decrease, the importance of the component h_{cc} decreases.

When the gap is non-infiltrated as in Figure 7.22. a) h_{gc} can be defined as:

$$h_{gc} = \left(\frac{k_{gap}}{Y + \kappa\xi\Lambda}\right) \qquad \text{eqn. 7.14}$$

where k_{gap} is the conductivity in the gap, Y is the mean separation between the two surfaces and $\kappa, \xi,$ and Λ air constants related as described in Appendix 5.

When the windings are perfectly infiltrated as in Figure 7.22. b), the air in the gap is depleted. This condition can be compared to a perfect VPI process. Yovanovich et al., (1997) show that gap conductance is reduced to:

$$h_{jc} = \left(\frac{k_{gap}}{Y}\right) \qquad \text{eqn. 7.15}$$

If the introduction of the filler material is imperfect as shown in Figure 7.22. c) the joint conductance is reduced to:

$$h_{jc} = h_{cc} + h_{gy} \qquad \text{eqn. 7.16}$$

where h_{gy} is the series resistance of the interstitial filler and air gap, and is defined by:

$$\frac{1}{h_{gy}} = \frac{1}{h_{gc_Y/2}} + \frac{1}{\left({}^{k_{gap}}/_{Y/2}\right)} \qquad \text{eqn. 7.17}$$

This process is compared to an imperfect or partial VPI. In this research it was assumed that only half the mean separation gap is filled. Hence $h_{gc_Y/2}$ is the contact between the winding and the filler. Finally Figure 7.22. d) shows a case in which the interstitial material does not only fill the interstitial gap, but also covers the windings.

This condition resembles epoxy painting. Savija et al., (2003) show that the conductive process is dominated by the additional thickness and the joint conductance is reduced to:

$$h_{jc} = \left(\frac{x}{k_{filler}}\right) \qquad \text{eqn. 7.18}$$

To assess the effect of the four infiltration processes and the conductivity of the filler material, the measurements of the winding surface roughness and winding hardness where made and are also presented in Appendix 4.3. The TCR model was run for the four infiltration cases. Each case was repeated with a varying conductivity of the interstitial filler and a varying contact pressure. The results are shown in Figure 7.23. .

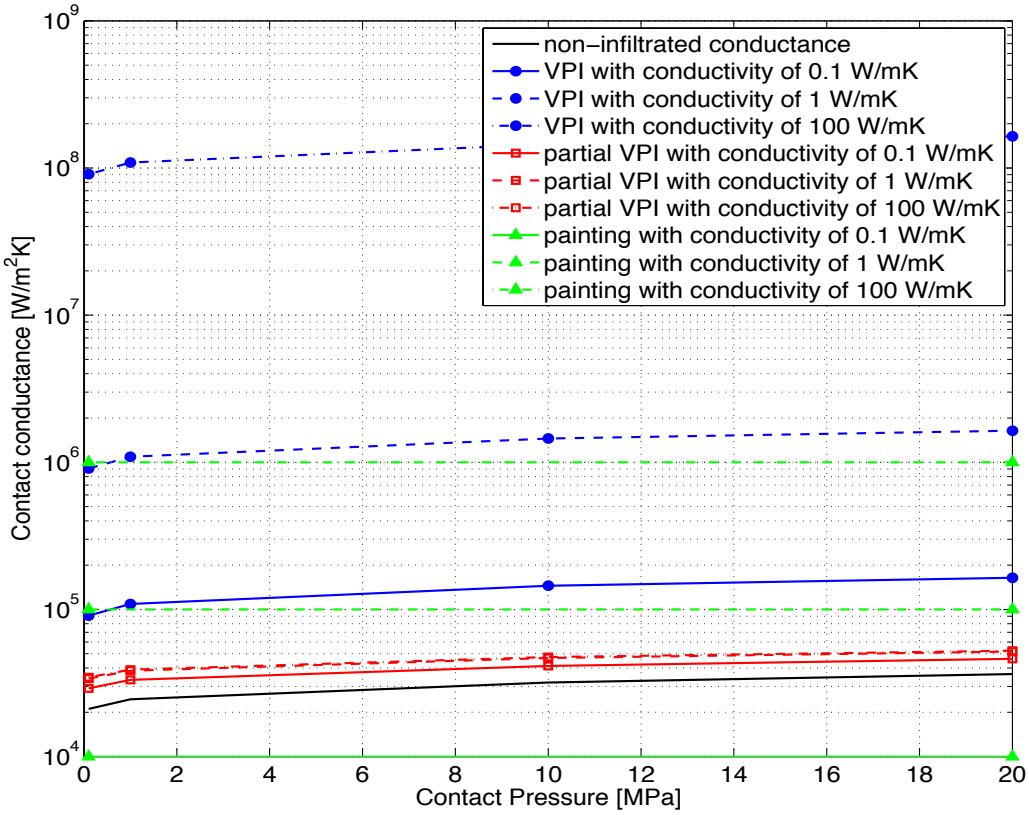


Figure 7.23. Comparison of the joint conductance with different infiltration methods. (Material thickness x for painting assumed at 0.1mm)

The results show that perfectly infiltrated winding offer great potential to improve the conductance across joints when compared the non-infiltrated benchmark. Increasing the conductivity of the filler offers a dramatic improvement in the conductance. However the effectiveness of the filler is significantly reduced when the process is imperfect and air pockets still exist. Any benefit in high conductive filler material is also eroded by the introduction of air gaps. This is important because despite the

recurring research efforts to improve the thermal conductivity of the epoxy fillers, they will not produce the desired improvement in current density unless the process is perfected. On the other hand it can be seen that the painting processes is heavily dependent on the combined conductivity and residual thickness. The painting process is not able to achieve the same benefits offered by VPI. Furthermore with the wrong combination of low conductive materials and a very thick application, the thermal conductance at the joint could be decreased below the non-infiltrated windings.

7.5.5. The Implication on lifetime estimations of the windings

Traditional life estimations of electrical machine windings adopt the Arrhenius equation to predict the life of windings with constant temperature as:

$$L = a'.e^{\left(\frac{-E_a}{k_b T}\right)} \qquad \text{eqn. 7.19}$$

where a' is the Arrhenius equation constant, k_b is the Boltzmann constant, E_a is the activation energy and T is the absolute temperature. However, the life prediction of machine windings during cyclic operation is still unresolved. This is important particularly for applications that are cyclic in their operation, such as electric transportation. Zhurkov, (1965) shows that the life of polymers is also dependent on mechanical stress such that:

$$L = L_o.e^{\left(\frac{U_o-\gamma'\sigma}{k_b T}\right)} \qquad \text{eqn. 7.20}$$

In which L_o, U_o and γ' are material constant coefficients, and σ mechanical stress. The thermal model developed in this chapter may not only establish the hotspot temperature and location, but insights from TCR models by Lemczk and Yovanovich, (1987) give an estimate of the effect of pressure on the windings. Despite that further work in the area of life estimation is required, it is the author's opinion that this research is a step forward in bridging the gap in life prediction of cyclic operation.

So far this chapter has developed a thermal model that captures the temperature gradient across concentrated windings. The model was validated with experiments. In the next section the flexibility of the model to is demonstrated by investigating a number of scenarios during the design of the cooling system of electrical machines. For simplicity, the models assume epoxy-infiltrated windings with experimentally established thermal parameters.

7.6. Demonstration of the model and further development

7.6.1. The effect of cooling the iron bobbin

In high-speed electrical machines, the iron losses are larger than those experienced in slow speed machines. Thermal designers often investigate mechanisms to enhance the cooling on the iron bobbin, for example by introducing liquid channels around the bobbin shoe or within the bobbin iron. An example of the introduction of the cooling channels to the iron is shown in Figure 7.24. To investigate the implication that this has on the temperature profile and hot spot in concentrated windings the LP model is used. The model was modified by linking the iron node to the coolant node through a thermal resistance R_5, as shown in Figure 7.25. The cases presented here assume thermal parameters derived from the epoxy-infiltrated calibration and a symmetric boundary condition on the winding surfaces. The model was run for pole piece losses associated with a typical operating point of 300 Nm and 1500 rpm of the YASA 750 machine, i.e. 175 W winding losses and 43 W iron losses.

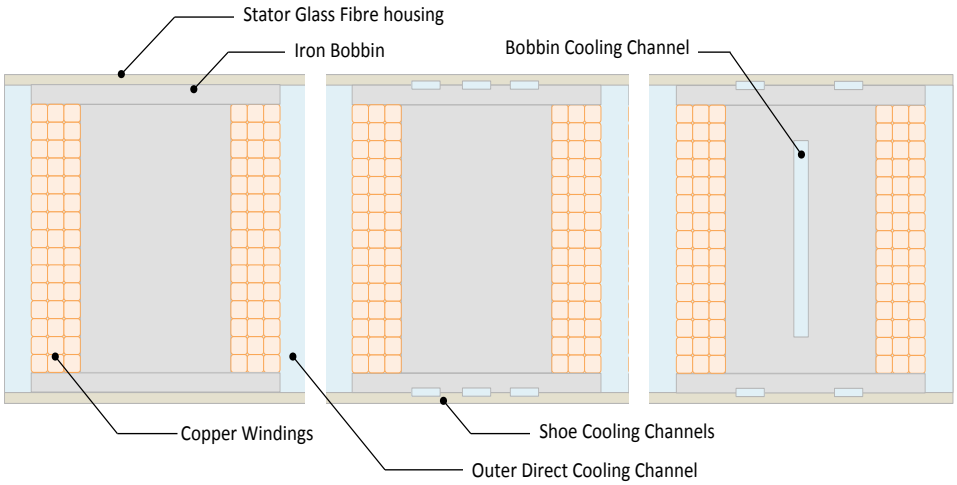


Figure 7.24. Examples of cooling geometries (Left) Traditional direct liquid cooled bobbin, (Centre) Pole piece with cooling channels on the shoe, (Right) Pole piece with cooling channels within the iron and shoe

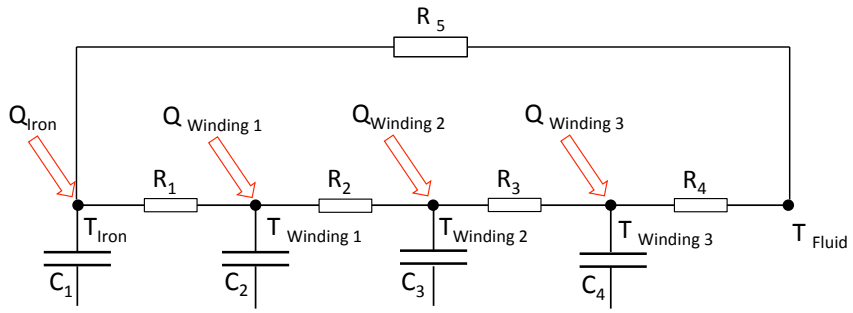


Figure 7.25. Modified LP model to investigate the effect of improving the cooling on the iron bobbin

Figure 7.28 shows how as the ratio between the cooling on the iron (R_5) and cooling on windings (R_4) changes, the hot spot temperature moves along the winding layers. The model is able to capture the location of the hotspot temperature. To accurately define the winding temperature, each analysis is displayed with its own temperature scale (as opposed to one common temperature scale for all analysis).

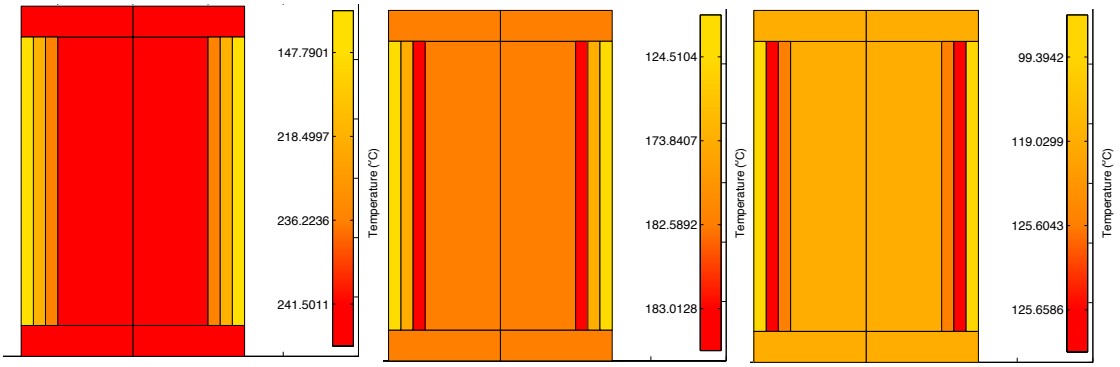


Figure 7.26. Example of how the software captures the temperature profile for a pole piece with: (left) R_5/R_4 >20000, (middle) R_5/R_4 =6.6, (right) R_5/R_4 =1.7

7.6.2. The temperature profile of indirectly cooled concentrated windings

So far this thesis has investigated the temperature profile of concentrated windings applied to direct cooled stator windings. In this section the flexibility of the model are demonstrated by adopting the boundary conditions associate with an indirectly cooled electrical machine. An example of this is the water-cooled machine shown in Figure 7.27. The heat flux in such cooling mechanisms is in the opposite direction to that experienced in direct liquid cooling. Heat flows inwards into the iron bobbin, through stator casing and into the water coolant. To model this scenario, the LP model has been amended to include the path through the stator casing as shown in Figure 7.28.

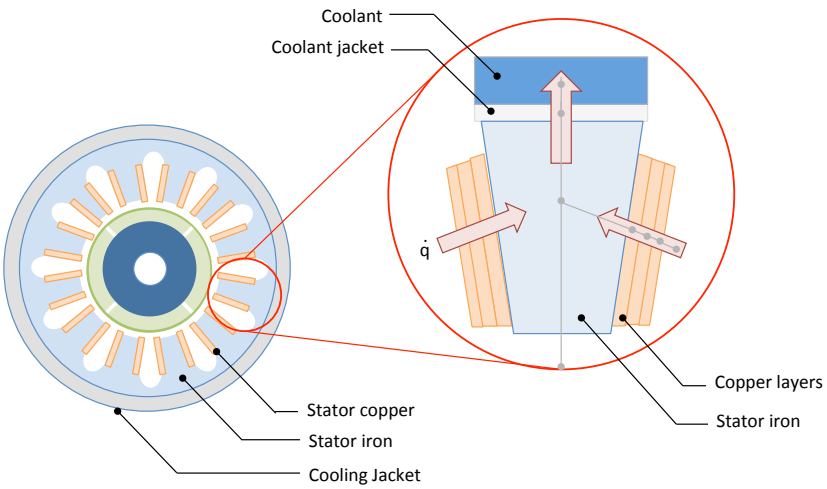


Figure 7.27. Example of an indirect cooled electrical machine using a water cooling jacket. (Insert) Example of a stator tooth with position of nodes

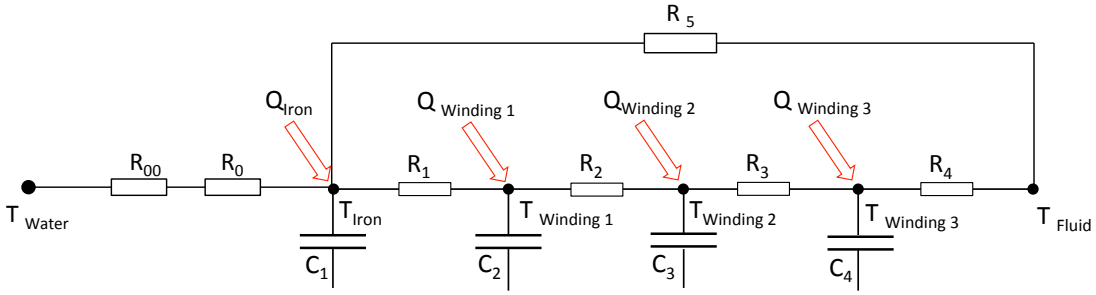


Figure 7.28. LP model to investigate the temperature profile of indirect cooled stator windings

The thermal resistances R_1, R_2, and R_3, from the epoxy-infiltrated calibration have been used. R_4 and R_5 are convective thermal resistance due to air convection from the rotor (Chong, 2014). R_0 is the thermal contact resistances between the stator iron and the cooling jacket and R_{00} is the convective heat transfer from the water coolant. An example of the temperature profile of indirectly cooled pole pieces is shown in Figure 7.29. As expected the hot spot in the winding is formed further away from the coolant.

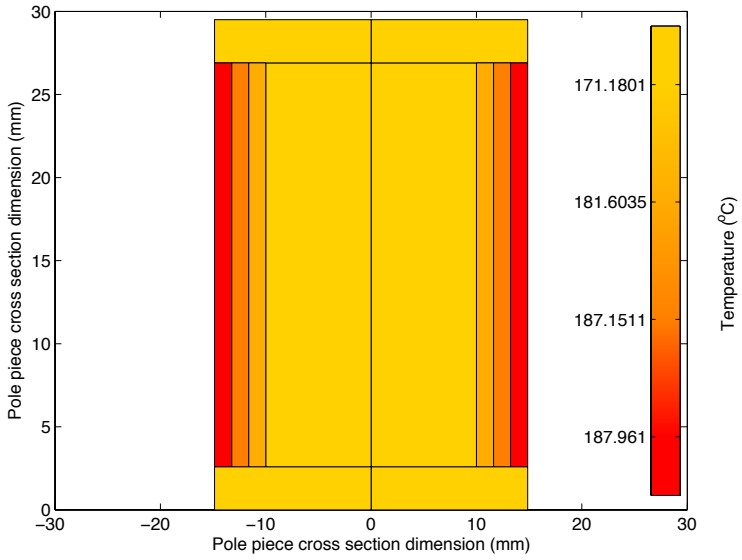


Figure 7.29. Temperature profile for an indirect cooled pole piece

It is interesting to note that the heat flux vector of indirect cooled pole pieces is in the opposite direction of direct cooled pole pieces. Recalling the thermal contact resistance model described in Section 7.5.1, the hotter temperatures on the outer winding layers would cause the outer windings to expand at a larger rate than the inner layers. This causes the contact pressure between the layers to relax, increasing the thermal contact resistance between winding layers.

7.6.3. The effect of axial heat flux

The developed LP thermal model simplifies the winding geometry with winding layers and assumes that the heat flux from concentrated windings is transferred radially outwards. This assumption remains valid as long as no axial heat flux across the windings is present, and the heat load is uniformly distributed in the windings. Recent developments demonstrated in YASA Motors Ltd., (2013), introduce a gap between the iron shoe and the edge of the windings, allowing oil to infiltrate and provide a better cooling. To visualise this effect on the temperature profile of the pole piece, the LP model is modified to model the individual conductors. A schematic of the model is shown in Figure 7.30. (Left). In this model heat flux is enabled to travel both in axial and radial directions by connecting each node on the winding to the four surrounding nodes. Figure 7.30. (Right) shows how the model predicts the variation in winding temperature distribution when heat is transferred in both directions. While the windings experience an axial temperature gradient close to the bobbin shoe, this is limited to the first three conductors due to the combined effects of thermal resistances in the vertical and horizontal directions. Axial thermal effects become more important in short pole pieces. This variant of the model can also be used to assess the effect of ac losses when the heat loads tend to be concentrated on the edges of the windings.

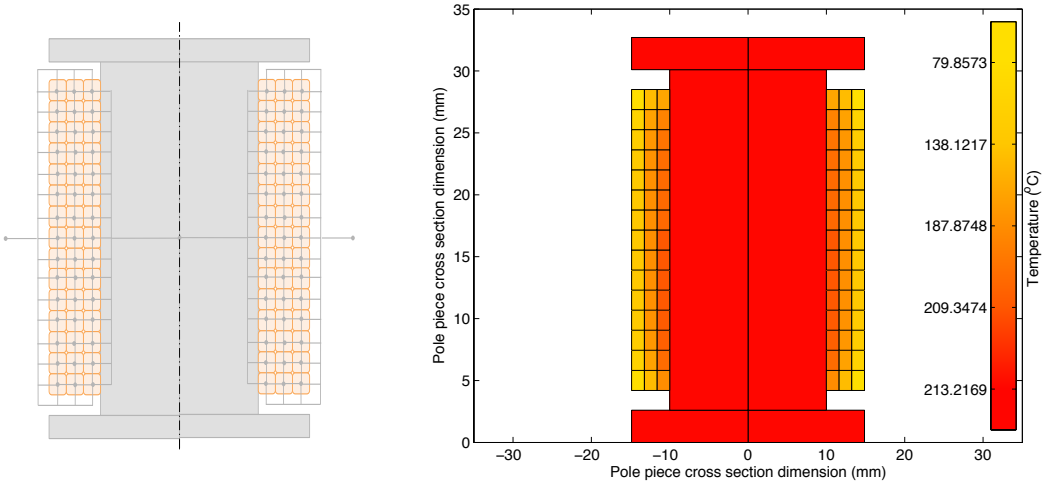


Figure 7.30. (Left) LP thermal model with an individual node on each winding with radial and axial heat flux. (Right) Visualisation of the winding temperature distribution in a pole piece experiencing axial and radial heat flux

7.7. Conclusion

This chapter developed an accurate LP based thermal model that captures the temperature gradient and hotspot temperature within concentrated windings. The

model assumes that the heat generated in concentrated windings is transferred radially towards the coolant and that no axial heat transfer within the windings occur. The individual windings are therefore simplified into winding layers and a thermal node is applied on each layer. Breaking down the windings into winding layers that are connected through thermal resistances is a step away from the traditional analysis of windings, which are often treated as a homogeneous material with an equivalent conductive term. While introducing more nodes results in a larger amount of unknown thermal resistances, a transient calibration experiment has been shown to be enough to establish the unknown values.

The novelty in this simple but effective method enables the thermal designer to determine the hot spot temperature across concentrated windings and examine the effect of the cooling mechanism on the windings. It has been shown that heat generated in the various winding layers is conducted from one consecutive winding layer to the next across a temperature gradient creating a hotspot on the layer faced with the longest thermal path. Knowledge on the formation of the hotspot enables the thermal designer to reduce excessive safety factors thereby increasing the current density of the machine or extend the machines life. Moreover when analysed within existing theories of thermal contact resistance the model presented here provides insights into the relationship between the temperature profile, heat flux and contact pressure. This produces insight into the thermal behaviour of infiltrated and non-infiltrated windings, particularly with different heat flux directions. The flexibility of the model in capturing the hotspot temperature and location within alternative cooling configurations has been demonstrated through numerous case studies.

The intuition gained from this chapter, namely the formation of the hotspot with respect to the thermal path and the role of the thermal contact resistance in the thermal path are the main drivers for the research shown in the next chapter. This develops a new winding construction with a shorter thermal path and consequently a lower hot spot temperature. The thermal contact resistance is also the subject of the final chapter, which extends the relevance of thermal contact resistance to general electrical machines.

8 | Improving the Current Density in Concentrated Windings

In Chapter 7 it has been shown that concentrated windings suffer from a temperature gradient. A hotspot is formed on the layer with the longest thermal path. This chapter proposes two new constructions of concentrated windings with a shorter thermal path. The new constructions operate at lower hot spot temperatures and hence have three distinct advantages:

- A reduction in the winding resistive losses and therefore an increase in efficiency.
- An increase in the winding life time, or provided that the electromagnetic properties of the machine are not saturated, or
- A higher current density for the same temperature.

This chapter is based on patent applications 1 and 2.

8.1. Motivation and introduction to this chapter

In the introductory chapter of this thesis it was shown how integrating heat transfer solutions within the electromagnetic design improves the machine performance. This is clearly seen in direct liquid cooled machines, (YASA, 2010), as opposed to indirect liquid cooling. This chapter adopts this philosophy and applies it to develop two novel concepts for constructing concentrated windings. In the first concept, a heat sink is embedded within the stator windings. The heat sink acts as a shunt, bypassing the thermal resistances between winding layers and thereby shortening the thermal path. The concept is explored through CFD and LP models, validated through a series of experiments. The second concept rethinks the use of flat windings for direct oil cooled machines. Thus the current-carrying conductor acts also as the heat-carrying conductor. While flat windings per se are not novel, their use in electrical machines

has been limited by several manufacturing challenges. This chapter addresses these challenges and their applicability to segmented windings. A thermal model is also developed and used to compare the temperature profile and current density of flat windings with the conventional construction.

8.2. Integrating a heat sink into concentrated windings

8.2.1. Design and Concept formulation

The processes of electro-magnetic design and the thermal management are often kept separate in electrical machine design. The thermal designer often investigates the thermal effects on a 'design ready' machine and establishes the maximum safe rating of the machine. The concept investigated here brings the two design processes closer to each other by interleaving a heat-carrying conductor within the current carrying conductor during the manufacturing stage. In the literature review it was shown that the equivalent thermal conductivity of anisotropic windings with epoxy ranges between 1-3 W/mK, (Wrobel et al., 2014; Simpson et al., 2014; Seising et al., 2014).

The introduction of a heat sink within the winding layers acts as a shunt, bypassing the thermal resistances across the winding layers increasing the equivalent conductivity across the windings. If for example a copper heat sink is used (with a thermal conductivity of 350 W/mK), the heat transfer from the inner windings to the coolant is increased by two orders of magnitude. To achieve this the heat sink requires a good contact with the adjacent winding layers and a means to transport the heat into the coolant. A concept that fulfills these two requirements was developed and is shown in Figure 8.1. The heat sink is designed from sheet metal to provide it with the flexibility to wrap around the winding layers during the manufacturing process. The wrap around design maximizes the contact area between the windings and heat sink. Extended surfaces ensure that the heat can be dissipated into the coolant. A slit in the heat sink body limits the generation of eddy currents when exposed to electromagnetic fields. The integration within the windings is shown in the CAD section in Figure 8.2.

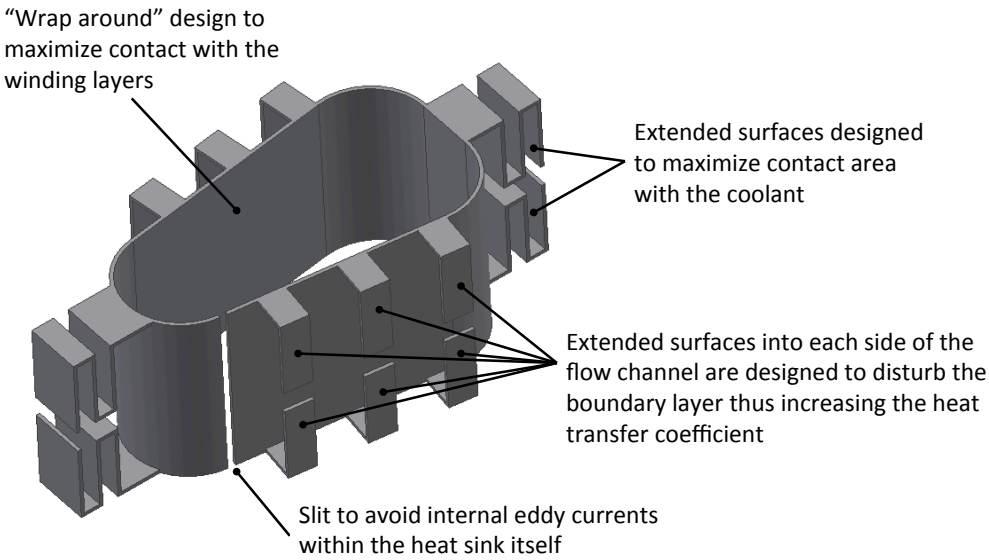


Figure 8.1. CAD model of the heat sink concept

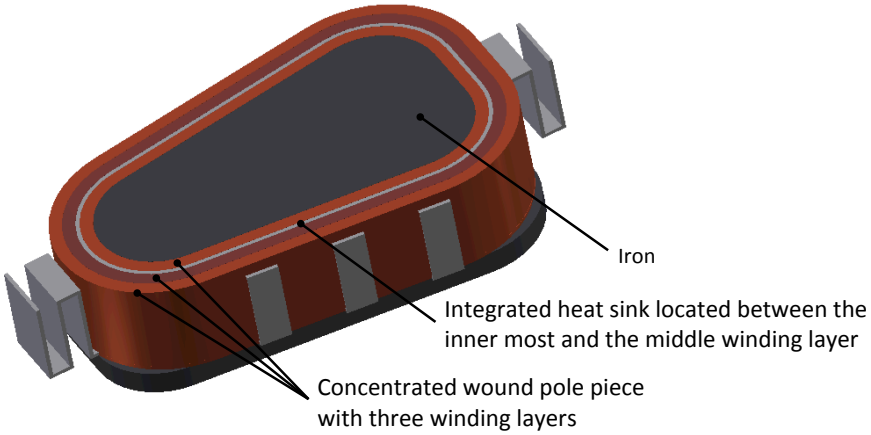


Figure 8.2. CAD model showing cross section of the pole piece with integrated heat sink

To assess the effectiveness of the new winding construction with integrated heat sink both CFD models and LP models are used. The CFD model was developed to gather an insight on the effects that the heat sink, compare the new construction with the traditional construction, and establish the location of the heat sink for maximum effectiveness. This was followed by the development of a LP model for the new construction and an experiment to validate the models. This is discussed in the following section.

8.2.2. CFD Modelling of the new construction with integrated heat sink

The process of CFD modelling has been described in Section 5.4. As the heat sink has a complex geometry, a 3D CFD model was produced.

Defining the CAD model

The 3D CAD geometry for a single pole piece with the surrounding flow domain was modelled using Autodesk Inventor®. In Section 2.5 of the literature review it was shown that many researchers model the windings as a homogeneous material with an equivalent conductivity. This approach would not provide any information about the effectiveness of the heat sink. However, it was also shown that modelling discrete windings would amount to a very large differences in the mesh and therefore require a big computational effort. Therefore the discrete windings were once again simplified into winding layers and a thermal contact resistance was applied between the winding layers. The symmetrical CAD model along the X-Z plane was developed to allow a symmetrical boundary condition that lowers the computational efforts. CAD models for a traditional construction and new construction are shown in Figure 8.3

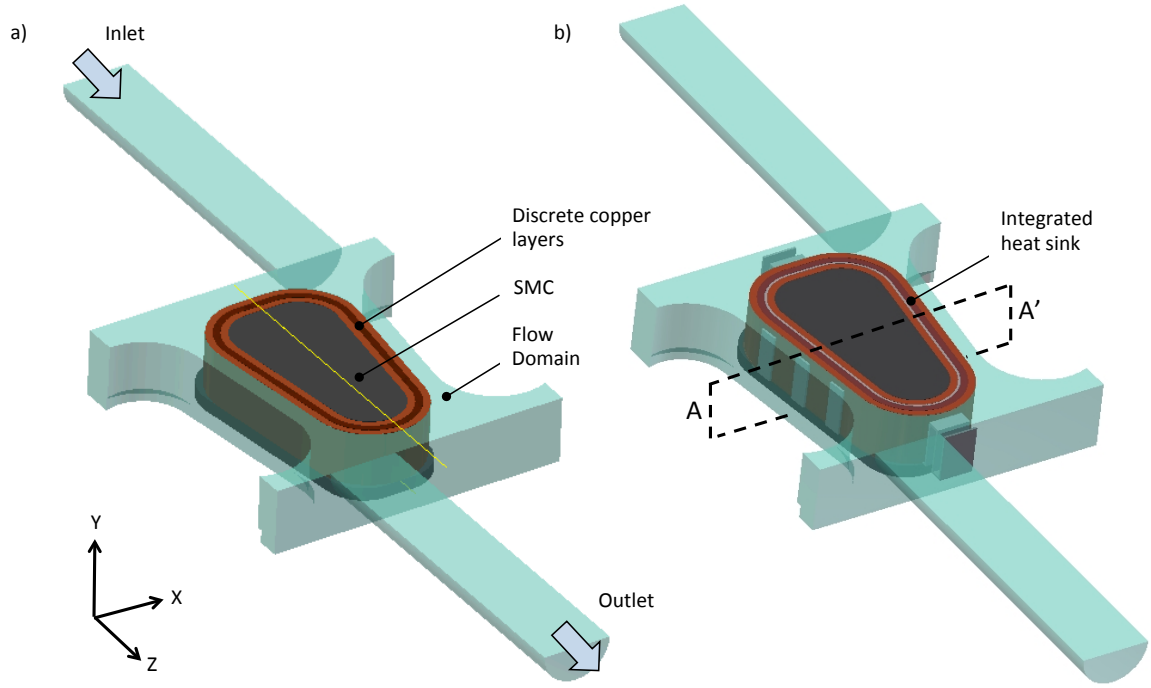


Figure 8.3. Details of the CAD geometry. a) A traditional pole piece with windings modelled as layers, b) The new construction with windings modelled as layers and integrated heat sink

The mounting position of the heat sink was tested in two positions: directly on the SMC iron and integrated between the first and second winding layers. While high-speed machines may have higher iron losses, low speed high torque machines may suffer from higher copper losses. Therefore investigating the performance of the heat sink in these two locations is important. The CAD models were exported to Autodesk CFD Simulation, in which the next modelling steps are applied.

Material selection and boundary conditions

The material of the winding layers was set to copper, and the bobbin was set to iron. In the new construction the heat sink material was also set to copper. The fluid region was defined as Opticool fluid with temperature dependent properties as shown in Table 5.1. To allow a validation of the model with existing test results, the boundary conditions of the model were matched to Test 2 of the experiment conditions shown in Table 7.5. The copper heat load was evenly distributed among the winding layers. The contact resistances identified in Table 7.7 were applied on the interfaces between the winding interfaces. A Slip/Symmetry boundary condition was set on the X-Z plane. A schematic showing the material and boundary conditions is shown in Figure 8.4.

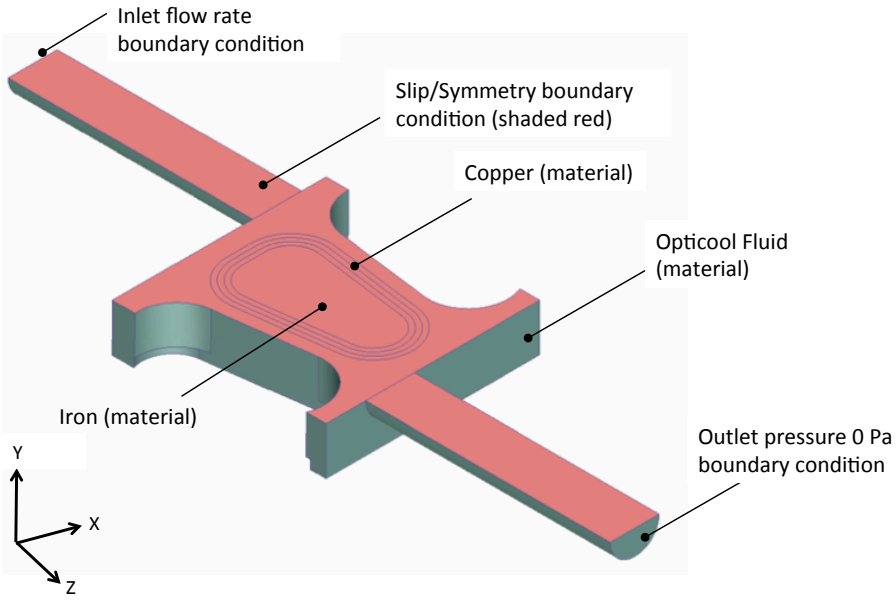


Figure 8.4. Schematic showing material and boundary conditions

Mesh Setup

The meshing process for a 3D model is described in Section 5.4.3. The same technique using a gap refinement mesh of 8 nodes was used. The mesh included a boundary layer mesh enhancement of 15 layers with a layer factor of 1.02 and a layer gradation of 1.05. The volume growth rate was set to 1.20, and the gap refinement length was set to 8. The final mesh had a total of 3.58M elements with 2.55M elements used to model the fluid domain and 1.03M elements to model the solid domain. Figure 8.5 shows the details of the mesh.

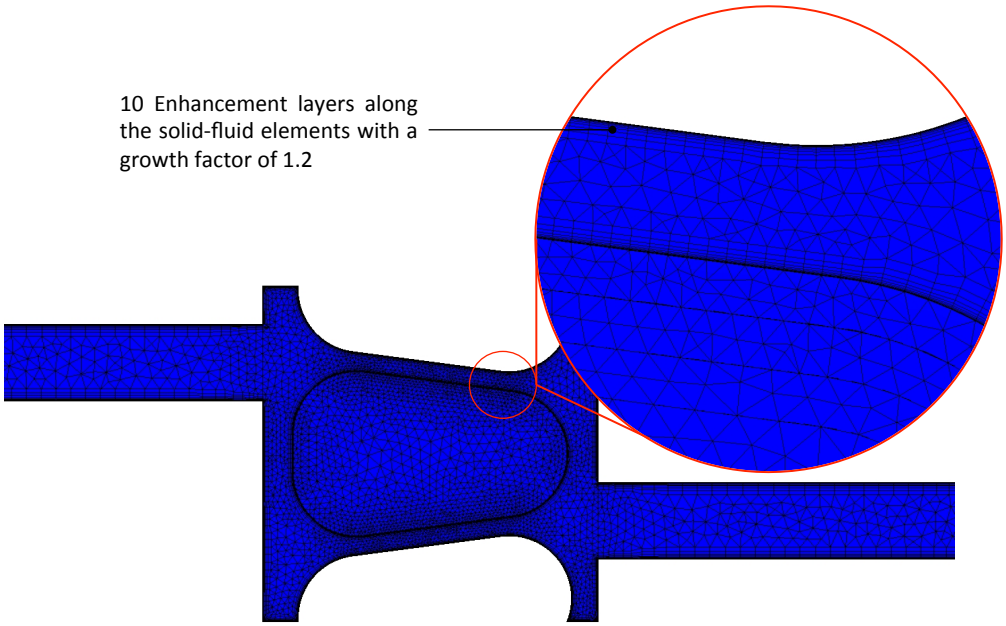


Figure 8.5. Mesh setup with insert showing the details at the solid-fluid boundary.

Simulation setup and solution

The simulations were run with a conjugate, laminar solver with ADV 4 and temperature dependent fluid properties. The justification for each of these decisions has been provided in Section 5.4.3. The simulation was repeated with tightened convergence criteria to ensure time convergence.

Sensitivity on the thermal contact resistance between the heat sink and windings

To investigate the effects of the contact resistance between the heat sink and the adjacent windings, the CFD solution was repeated for increasing values of thermal resistances within a range of 0-2 K/W. However this was found to offer little effect on the overall benefit offered by the heat sink.

Post processing

The CFD model was used to establish an early assessment of the concept. Therefore unlike the earlier chapters which compared the post processed results to experimental measurements, in this chapter these are used as an early indication of the feasibility of the concept. Figure 8.6 compares the winding temperatures for the conventional construction to the new construction with heat sink mounted on the iron and on the first winding layer.

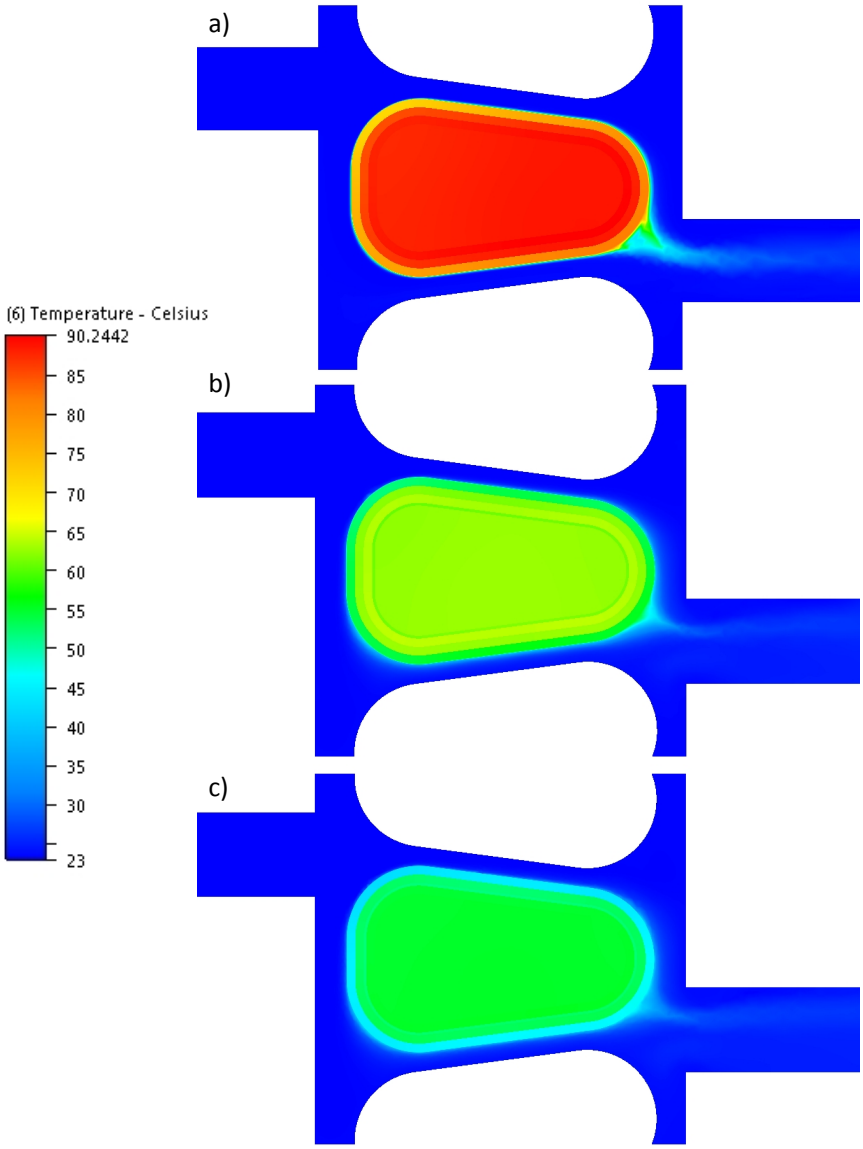


Figure 8.6. Temperature profile of the windings for a) conventional construction, b) new construction with heat sink mounted on the SMC, c) new construction with heat sink mounted between the 1st and 2nd layers

For the conditions simulated, the new construction shows a drop in winding temperature of approximately 25 ^{o}C when the heat sink is mounted directly on the SMC bobbin (Figure 8.6 b), and a reduction of 35 ^{o}C when integrating the heat sink between the first and second winding layers (Figure 8.6 c). The mounting position of the heat sink can be decided based on the machine type (high speed or low speed) and the impact that the machine designer needs to achieve. Throughout the rest of this chapter, a reduction in winding temperature is targeted and therefore the models and experimental validation will contain a heat sink mounted between the first and second winding layers. Figure 8.7 shows how the heat sink also affects the velocity profile of the oil around the windings. The results are referenced to plane AA' in Figure 8.3.

Case b) makes use of an integrated heat sink experiences a velocity profile that is uniformly distributed throughout the flow channel. The differences in velocity profile is likely due to the disturbances caused by the fins shown in Figure 8.8 and the reduced flow area. The higher velocity however comes at a penalty of increased pressure losses. This however can be adjusted for by careful selection of the coolant circulation pump. It can be noted that both simulations exhibit a difference in left and right velocity due to flow distribution.

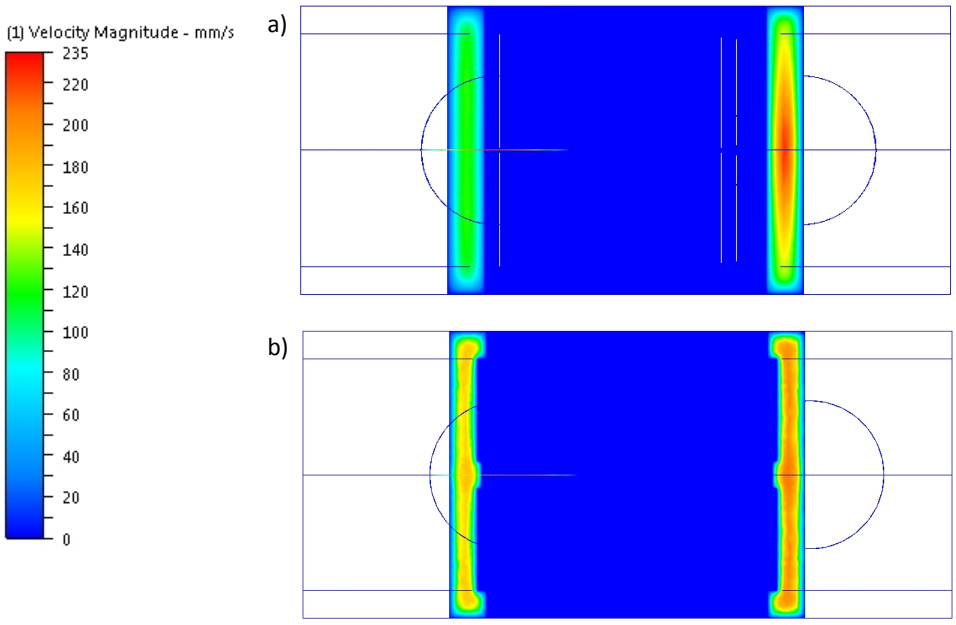


Figure 8.7. Velocity profiles on plane AA' for a) traditional construction, and b) new construction

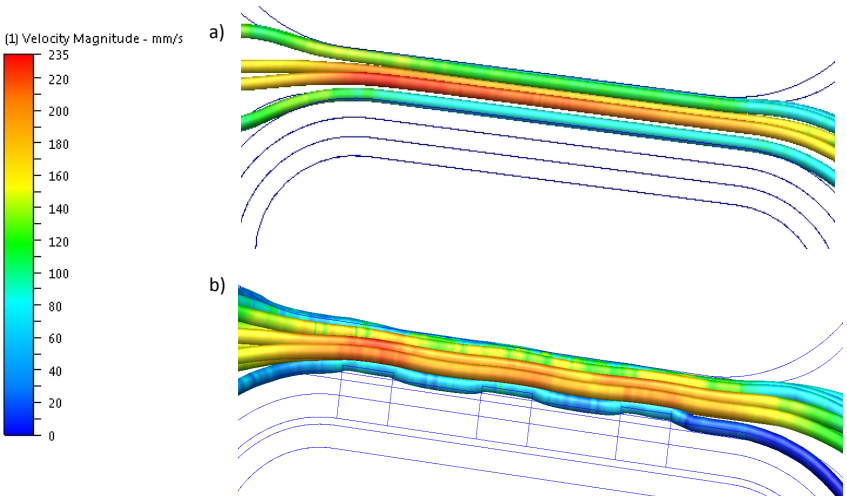


Figure 8.8. Schematic showing velocity traces a) windings with no heat sink, b) windings with heat sink

Having established the potential of the new construction and the mounting position for the heat sink, the focus is turned to extend the LP model developed in Chapter 7 to this construction. The fast solution produced by the LP model allows an investigation

on several scenarios that would otherwise require too much time and computational effort by CFD. Following a validation process, the benefits of the new construction will hence be evaluated further using the LP model.

8.2.3. LP Modelling of the new construction with integrated heat sink

Figure 8.9 shows a general schematic of the LP model for the new construction. As with the previous chapter, the model of the windings can be further broken down into its left and right components to capture the effect of non-uniform flow distribution. A schematic is shown in Figure 8.10. The heat sink is connected to the fluid temperature through a thermal resistances R_{Fin} representing the conductive path through the heat sink and convective resistance through the heat sink fin. To fully characterise the values of the thermal resistances, an initial calibration procedure similar to that shown in Chapter 7 is performed.

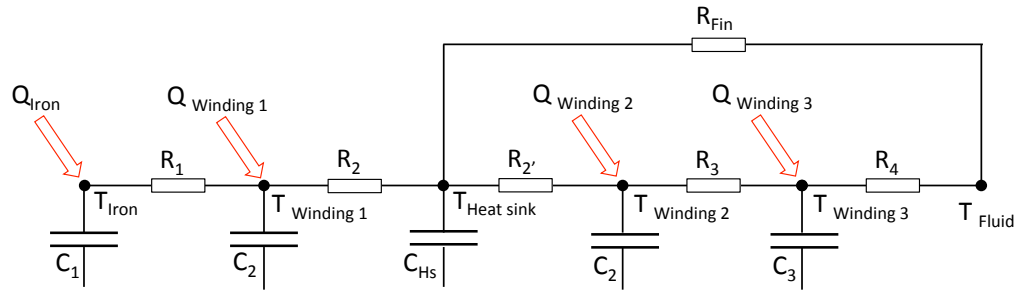


Figure 8.9. Schematic of the LP model of the new pole piece construction with integrated heat sink between the windings

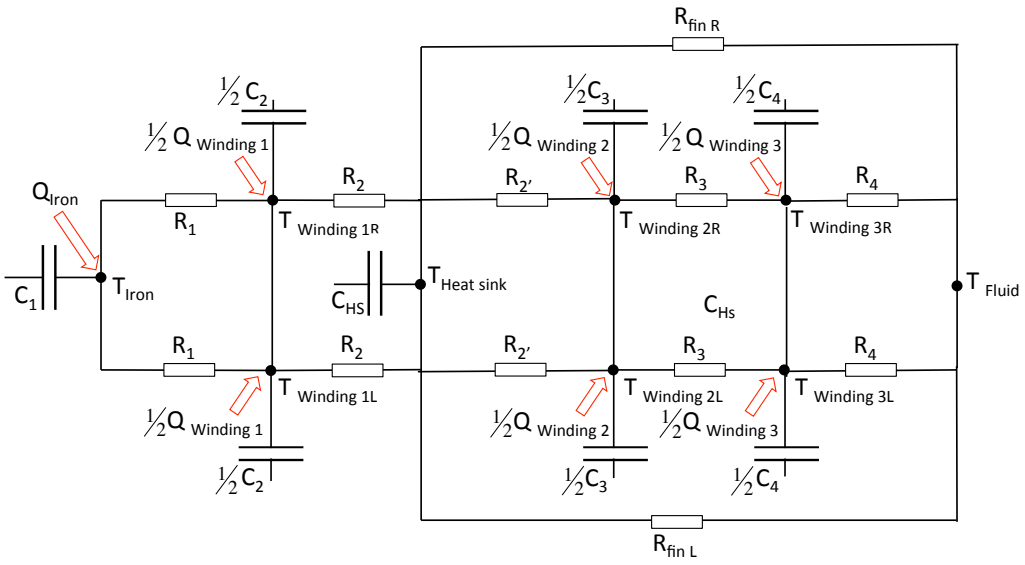


Figure 8.10. Schematic of the LP model broken down into the left and right components

To produce the experimental measurements, the same control volume having one active pole piece and the flow channels on either side of the pole piece as shown in Section 7.3 of Chapter 7 was used. The following section demonstrates the manufacturing process of a prototype of the new winding construction and a description of the experimental procedure.

8.2.4. Experimental Investigation of the Concept

Manufacturing a prototype with an integrated heat sink

The design of the heat sink for integration within a concentrated wound pole pieces takes into consideration various parameters including the material conductivity, thickness and contact with the adjacent windings and with coolant. Copper was chosen as the heat sink material due to its excellent thermal conductive properties and malleability making it easy to form the fins. Various copper thicknesses were trialled. While increasing the thickness improves the conductive heat transfer, stiffer fins were found to be less resilient to bending processes required during manufacturing. A thickness of 0.3 mm thick was found to be malleable enough and satisfy the manufacturing requirements. The new manufacturing procedure was developed so that an inner layer of the winding is first wound onto the core. The flat state metal heat sink is then positioned on the winding and heat exchange fins are folded away so that subsequent layers of the windings are wound on top of it, as shown in Figure 8.11.

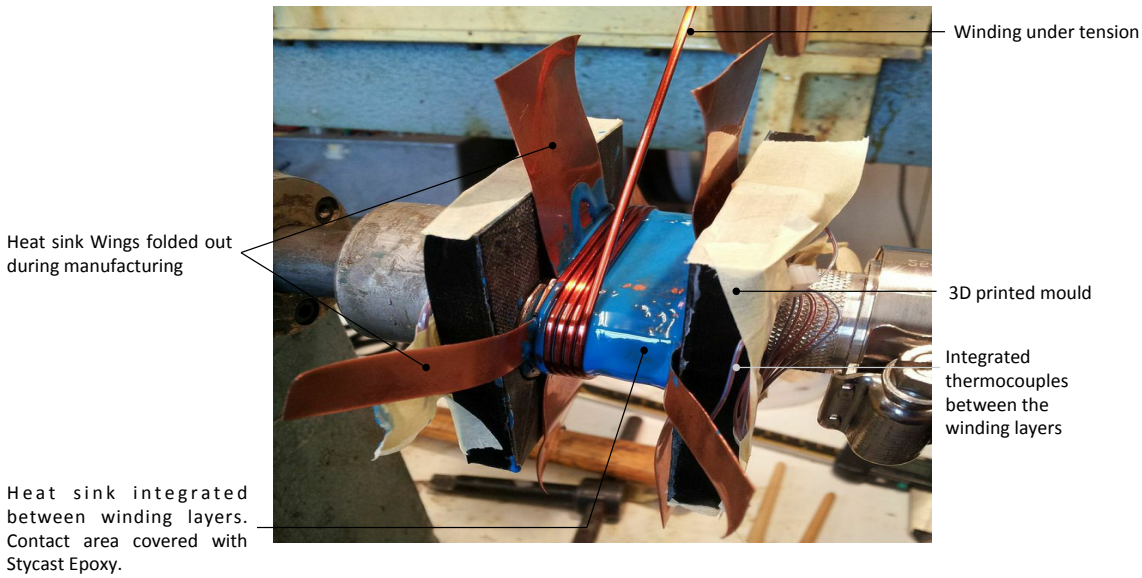


Figure 8.11. Manufacturing of the pole piece with integrated heat sink and epoxy resin infiltration

The fins are finally folded into shape just before assembly of the segmented piece in the machine stator. Stycast epoxy resin was painted between the winding layers for its ability to keep the construction rigid after curing. The windings were wound with a wire tension of 100 N. As in the previous set of experiments shown in Section 7.3, a total of eight thermocouples were mounted on the pole piece, two on the iron, two between the iron and the first copper layer, and the rest in between each winding layer. A finished prototype of a concentrated wound pole piece with integrated heat sink is shown in Figure 8.12.

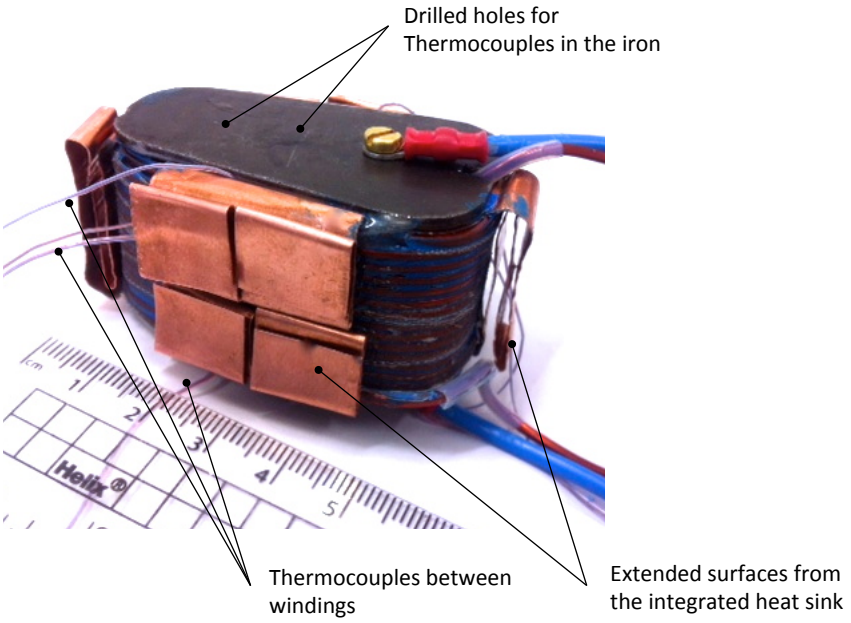


Figure 8.12. Prototype of a concentrated wound pole piece with integrated heat sink and epoxy on the windings, instrumented with temperature sensors

The same experimental setup and process described in section 7.3.3 was used to test the new construction. As with the experiments described in Chapter 7, a set of transient experiments is first performed. The first experiment is used to characterise the pole piece and calibrate the model. The remaining transient experiments are used to verify the calibration parameters. The transient experiments are followed by a set of steady state experiments from which the temperature profile across the pole piece is measured. The calibrated model is used to simulate this profile.

Measuring the transient characteristics of the pole piece

The oil flow rate was set and the windings and iron were energized simultaneously. The increase in temperature of the windings with time was monitored and recorded. The windings were then de-energized thus capturing the cool down curve of the pole

piece. The experiment was repeated for various flow rates, coolant inlet temperature and pole piece heat losses as shown in Table 8.1.

Table 8.1. Experiment details for the transient characterisation of the new construction

Test No.	Coolant inlet temperature [^{o}C]	Flow rate [lpm]	Iron heat input [W]	Copper Winding heat input* [W]
1	23.9	3.7	21.86	110.03
2	24.6	3.7	10.20	72.80
3	24.0	2.5	22.06	108.6
4	24.3	2.5	10.16	71.16
5	41.5	5.0	22.17	113.79
6	41.6	5.0	10.22	72.65
7	39.7	3.4	22.12	113.58
8	41.9	3.6	10.20	71.27

*Heat input value for the windings at the coolant inlet temperature

Measuring the temperature profile across the pole piece

The steady state temperature profiles for the windings in the new construction with integrated heat sink were measured. The measurements will be used to validate the LP model for the new construction, allowing a comparison between the new construction and the conventional construction. The experiment was repeated for various flow rates, coolant inlet temperature and pole piece heat losses as shown in Table 8.2.

Table 8.2. Experiment details for the steady state temperature profile of the new construction

Test No.	Coolant inlet temperature [^{o}C]	Flow rate [lpm]	Iron heat input [W]	Copper Winding heat input^{+} [W]
1	24.3	3.7	9.68	48.88
2	23.9	2.5	10.18	51.8
3	25.0	3.8	21.66	108.4
4	25.1	2.6	22.16	74.62
5	39.9	4.8	10.18	53.15
6	39.6	3.4	10.21	53.54
7	40.5	4.9	21.82	112.44
8	41.6	3.6	22.28	79.86

$^{+}$ Heat input value for the experiment running at steady state

8.2.5. Test Results and Discussion

Transient thermal behaviour of the new construction

The following section investigates the behaviour of the new construction under a transient heating and cooling condition. The first experiment, shown in Figure 8.13 has been used to calibrate the thermal parameters of the model, which is also shown in the figure. The calibrated parameters for the new construction are shown in Table 8.3.

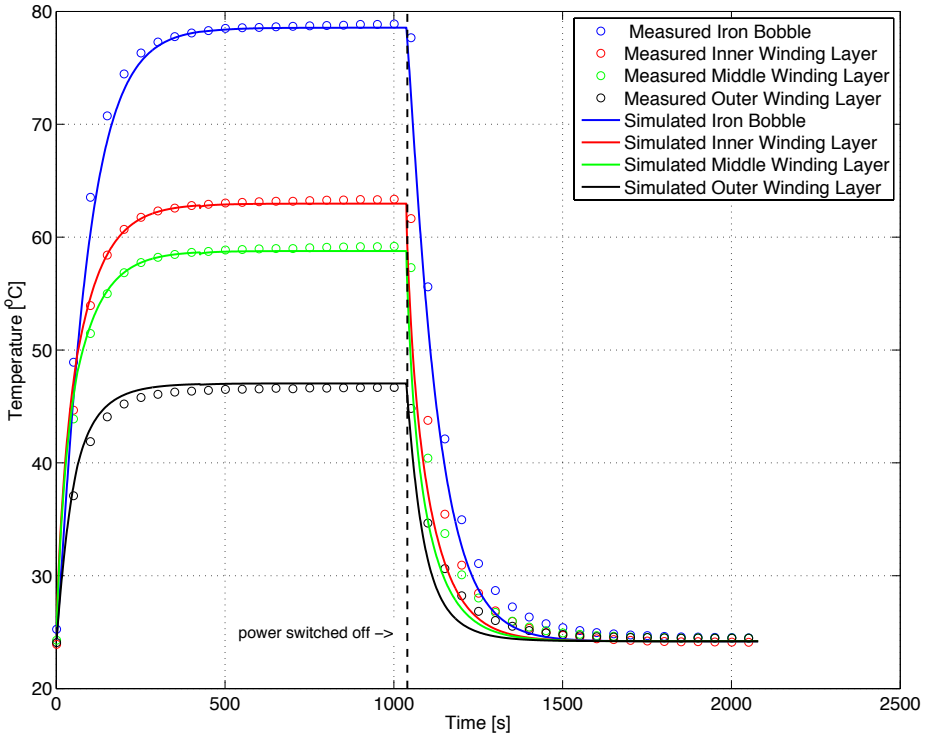


Figure 8.13. Thermal characterisation of the model for the new construction with infiltrated pole piece and experiment conditions shown in Test 1

Table 8.3. Calibrated thermal parameters for the new construction

Description	Designation with Reference to Figure 8.9	Value
Thermal resistance between the pole piece and the first winding layer [K/W]	R_1	0.8
Thermal resistance between the first winding layer and the heat sink [K/W]	R_2	0.14
Thermal resistance between the second winding layer and the heat sink [K/W]	R_3	0.15
Thermal resistance between the second winding layer and the third winding layer [K/W]	R_4	0.12
SMC Iron Specific heat capacity [J/kgK]		300
Copper Specific heat capacity [J/kgK]		400

In coherence with the observations on the epoxy painted pole piece tested earlier in Chapter 7, the calibration parameters extracted here have also been unchanged with heat flux. The other transient experiments have been used to verify the thermal parameters. Due to space restrictions these are shown in Appendix 3.3. While these charts do not add more value to the results, they are important to confirm the thermal parameters. Having characterised the thermal resistances across the windings, the focus is turned to the temperature profile across the windings. This is plotted in Figure 8.14. The location of the temperature sensors is referenced along the line AA' shown in Figure 7.13.

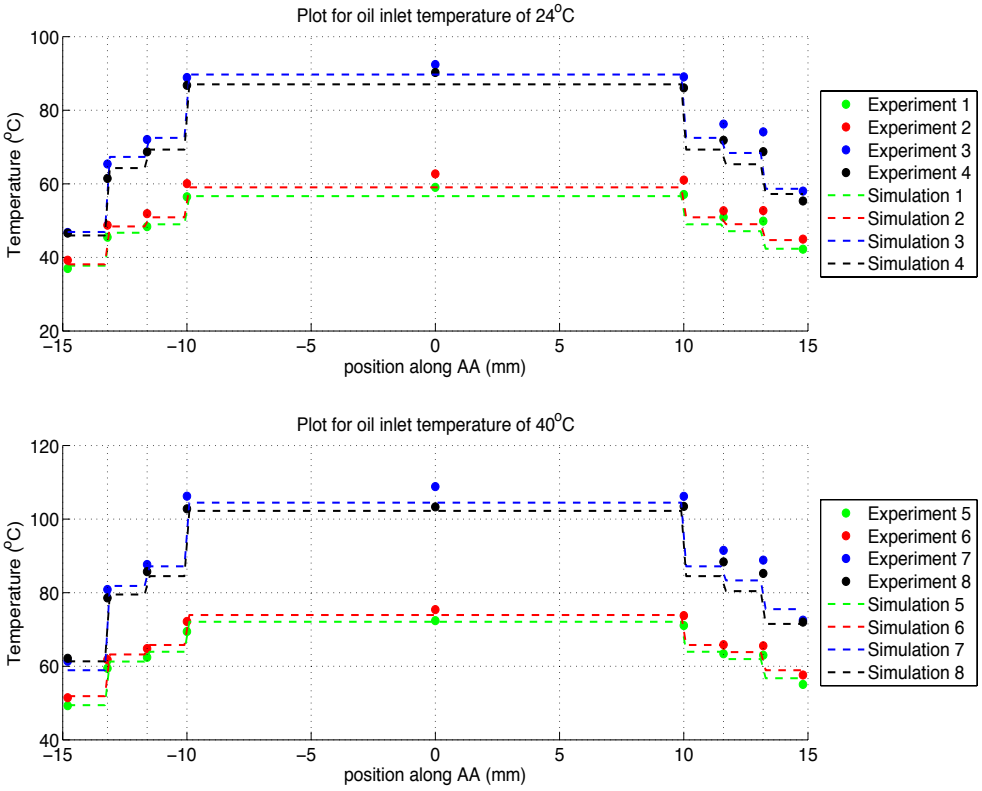


Figure 8.14. The temperature profile for the new construction under steady state conditions

Both transient and steady state charts show how the temperature of the windings in contact with the heat sink are drawn closer together. It is also noted that modelling the heat sink with one node lead to slight inaccuracies when flow mal-distribution occurs. This is likely because while the windings have been split into the left and right components, the heat sink is not and is represented by a single temperature node. A better approach would be that depending on the extent of flow mal-distribution, separate convective heat transfer resistances are applied on the fins of the left and right heat sink components. From the temperature profiles we can note that although

the introduction of the heat sink does not eliminate the temperature gradient cross the pole piece windings, the hot spot temperature is reduced by about 55 ^{o}C when compared to conventional constructions. This will be further analysed in Section 8.4, in which the various pole piece models will be used to establish the benefits of this design.

The focus of this chapter is now turned to investigate a second concept in which the current carrying conductor acts also as the heat-carrying conductor.

8.3. Rethinking Flat copper windings

8.3.1. Design and Concept formulation

The application of flat windings is not a novel concept in the manufacturing of electrical machines (Tong, 1990). Flat windings are stacked on top of each other axially rather than onto each other radially. The recent focus on improving the current density of electrical machines have led machine designers to rethink this winding configuration as a means for increasing the fill factor, (Popescu et a., 2016). Figure 8.15 shows an example of stacked winding and a cross section through the winding construction.

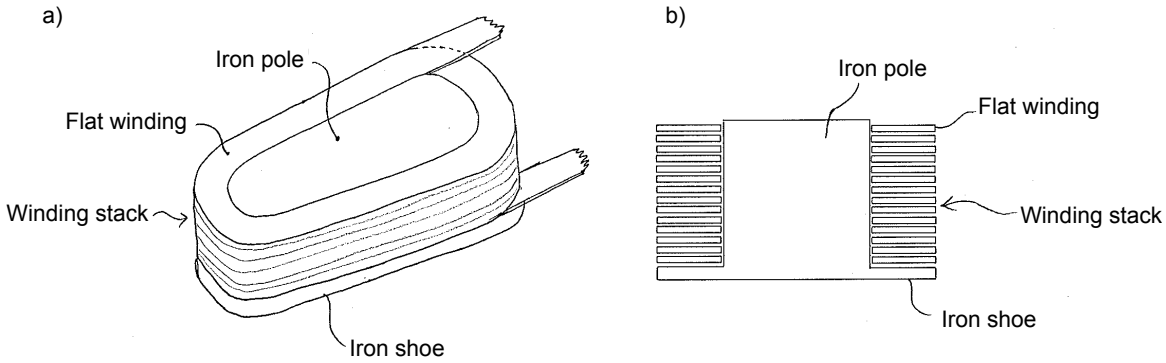


Figure 8.15. Concept of stacking flat windings

However, the flat windings eliminate winding layers in the radial direction, and hence the dependency on the thermal resistances between the winding layers is removed. This would provide a distinct advantage in thermal management. Yet, the application of flat-stacked windings to electrical machines offers manufacturing challenges. Flat windings are manufactured by punching the shape of the preformed tooth, one turn at a time. The stack is then built by joining each winding turn with the next by soldering

or mechanical crimping. This process not only makes the manufacturing technique costly but also introduces a new electrical resistance at the joint of the windings, increasing the I^2R losses.

This section explores a solution that simplifies the manufacturing process of flat windings. This may in turn contribute to the uptake of flat windings and reap the thermal benefits associated with the removal of winding layers. Taking inspiration from origami folding techniques, a method for manufacturing the entire winding stack from a single piece of copper was developed. Figure 8.16 a) shows a pre-stamped winding from a single piece of copper. The folding lines are marked. Figure 8.16 b) shows the windings following the folding process while Figure 8.17 shows an example of the windings assembled onto an SMC bobbin.

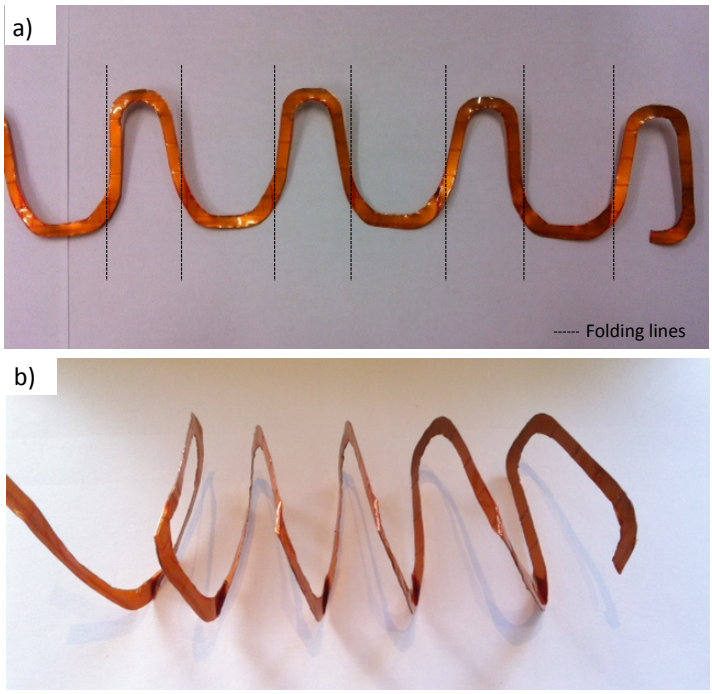


Figure 8.16. Manufacturing a prototype of the winding with: a) flat windings from a single sheet and, b) folded sample of the windings



Figure 8.17. Side view (left) and Top view (right) of a flat winding assembled on half a bobbin

As this manufacturing process does not involve a wire tensioning process, the copper conductor may lack the contact pressure with the iron bobbin. The design and stamping process should hence be precise to avoid air gaps at this interface, which would limit the thermal performance. VPI may also be applied.

While this folding technique solves the manufacturing issues traditionally linked with flat windings new challenges arise. An example of this is the folded section which is twice the thickness of the current carrying conductor. This limits the number of windings that can be stacked axially and therefore reducing the fill factor of the pole piece. This challenge can be solved by a number of options such as:

1) Adopting a running fold,
2) Thinning the overlap conductor by etching or rolling, or
3) Taking the fold outside the winding area.

When applied to direct liquid cooled electrical machines, extending the folds outside the winding area and into the coolant will further enhance the thermal performance as these will therefore act as heat exchangers as shown in Figure 8.18. In the context of direct liquid cooled machines, the heat exchanger protrusions can be used to control the flow distribution within the machine as discussed earlier in Section 5.9.

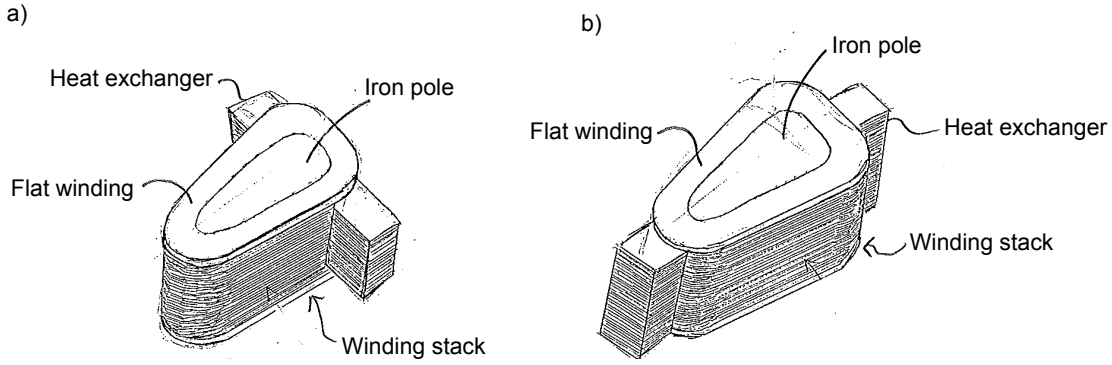


Figure 8.18. Example of the folds outside the winding area to act as heat exchangers

When applied to high frequency alternating current applications, electrical conductors suffer from eddy currents and skin effects. Skin effect is the tendency of the current flow to become distributed closer to the edges of the conductor. While flat windings offer an improvement over AWG14 wire used in this investigation, the uniformity of the current flow can be further improved by introducing slits along the length of the flat conductor. Figure 8.19 shows the overlapping area when the flat winding is

folded, and the introduction of the slit at the fold. The process of manufacturing the windings from a single sheet of finite dimensions was also taken into consideration so that less wastage is produced. Figure 8.20 shows how by inverting one of the conductors and shifting it along, the meandering paths of two conductor patterns intermesh better, reducing wastage of the raw material. Depending on the shape of the bobbin, tessellation can be allowed, therefore producing more conductors from a single sheet.

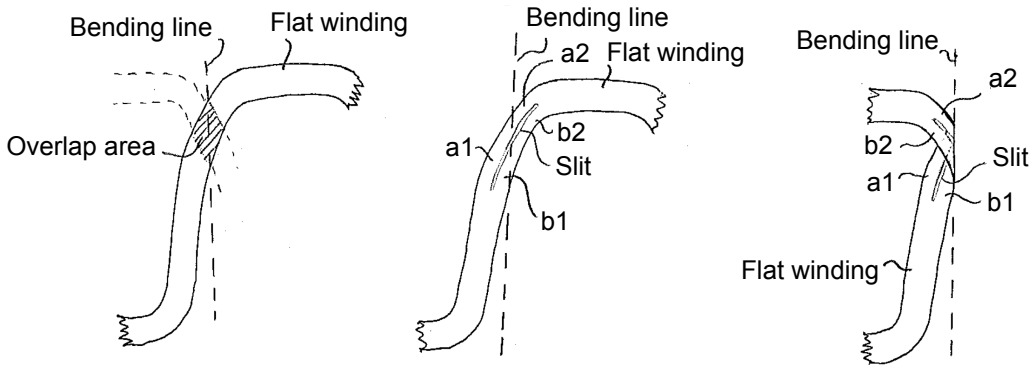


Figure 8.19. Schematic of the flat winding showing (Left) the overlapping area at the fold, (Middle) the introduction of the slit at the fold and (Right) the folded slit

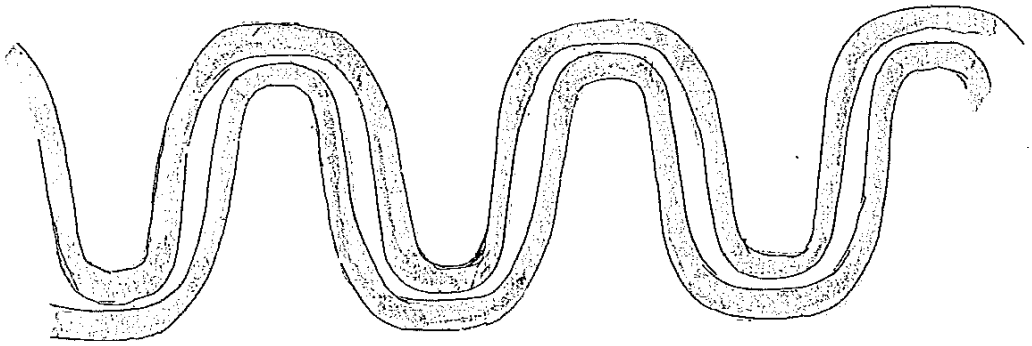


Figure 8.20. Intermesh of the windings to reduce wastage

Having explored the initial challenges of this concept, its thermal effectiveness is assessed through a LP thermal model. This process is described in the following section.

8.3.2. LP Modelling of Flat Windings

The LP model is once again used to assess the effectiveness of this concept. Once again the heat transfer is assumed to take place only along the radial direction. The model can is hence simplified to include one node for the SMC iron and one node for the flat windings as shown in Figure 8.21.

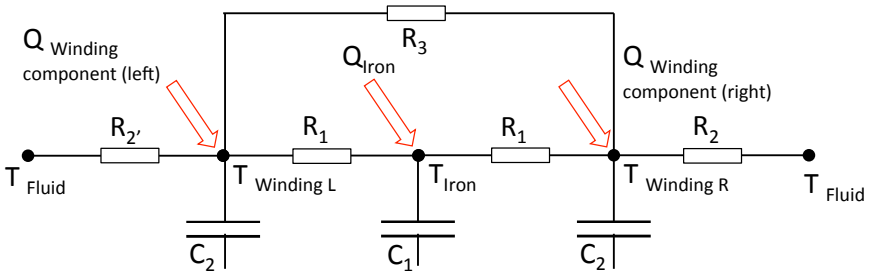


Figure 8.21. Schematic of the LP model of the new pole piece construction with flat windings

R_1 is the contact resistance between the windings and the iron, R_2 and $R_{2'}$ are convective resistances and R_3 is the conductive resistance linking the left and right components of the windings. To test the model's sensitivity to R_1, this was run with values of 0.5 K/W, 1 K/W and 2 K/W respectively for a constant value of R_2. The results are shown in Figure 8.22. It can be seen how while the HTC value fixes the winding temperature, the hot spot temperature on the SMC iron increases with R_1. Based on previous experience with experimental measurements on epoxy-infiltrated windings, the thermal resistance R_1 was set to 1 W/K.

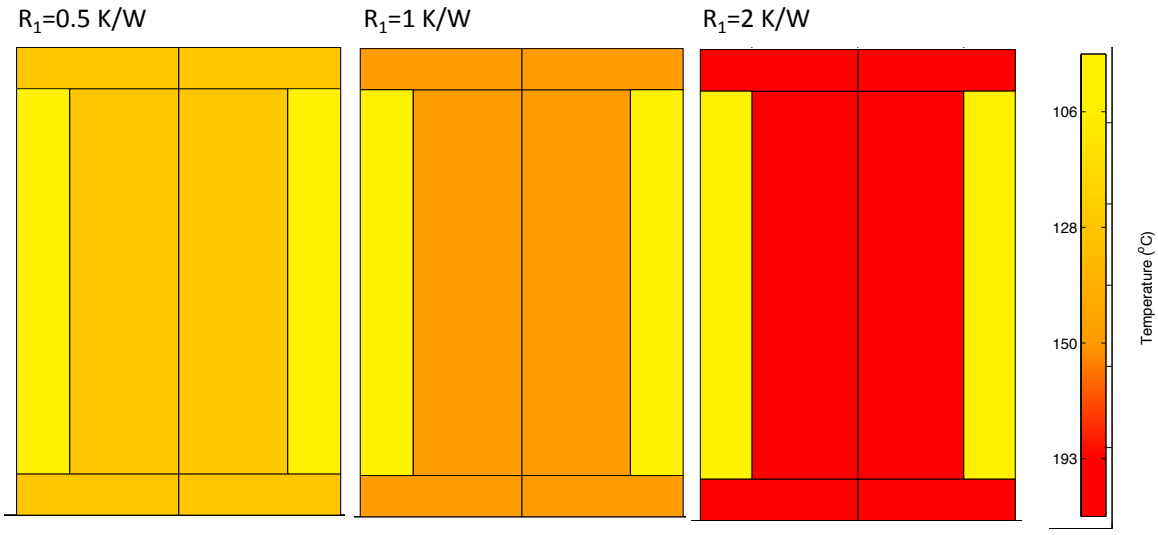


Figure 8.22. Sensitivity analysis of the model with variation in thermal resistance R_1 and a constant value of convective resistance R_2

Having explored the two alternative constructions and established the thermal models to predict the temperature in concentrated windings, the following section uses the models to quantify the effect of reducing the hotspot on increasing in current density.

8.4. The Current Density of the New Constructions

Having established the thermal characteristics of various pole piece constructions, the LP model is used to compare the temperature profile of the new constructions with the conventional ones. The modes were run with a range of winding losses at a fixed convective resistance and varying inlet temperatures. Figure 8.23 shows an example of the steady state temperature profiles for a case scenario with 175 W copper losses and 43 W iron losses. To accurately define the winding temperature for each analysis temperature scale is defined next to each analysis (as opposed to displaying one common scale).

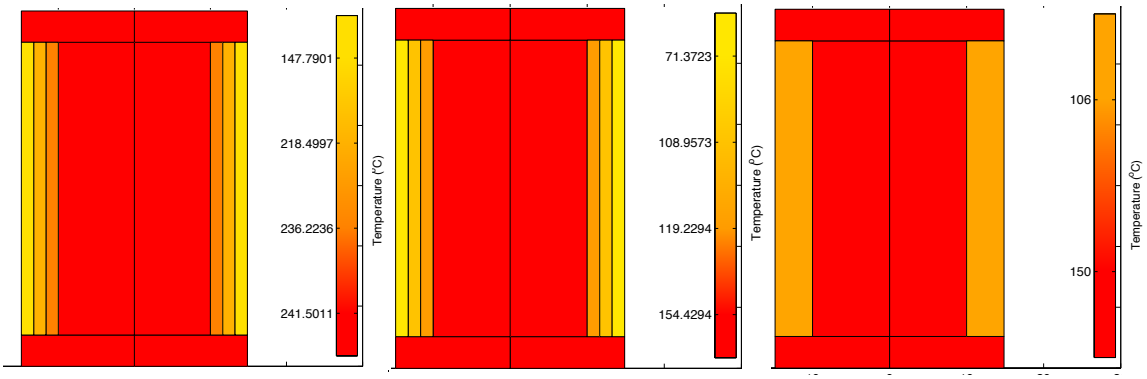


Figure 8.23. Comparison of the steady state temperature profile for (left) conventional construction with epoxy-infiltrated concentrated windings used as a reference, (middle) new construction with integrated heat sink and epoxy infiltration, and (right) flat windings. Note that the non-linear temperature scale

The new construction with integrated heat sink provides a reduction in hot spot temperature of 87 ^{o}C. The flat windings reduce the hotspot temperature by 91 ^{o}C. Reducing the winding and hotspot temperature benefits the machine from an increase in lifetime, an increase in efficiency or an increase in current density. The latter is particularly sought after in automotive applications as the current density is directly related with the torque produced. The comparison of the windings transient behaviour in shown in Figure 8.24.

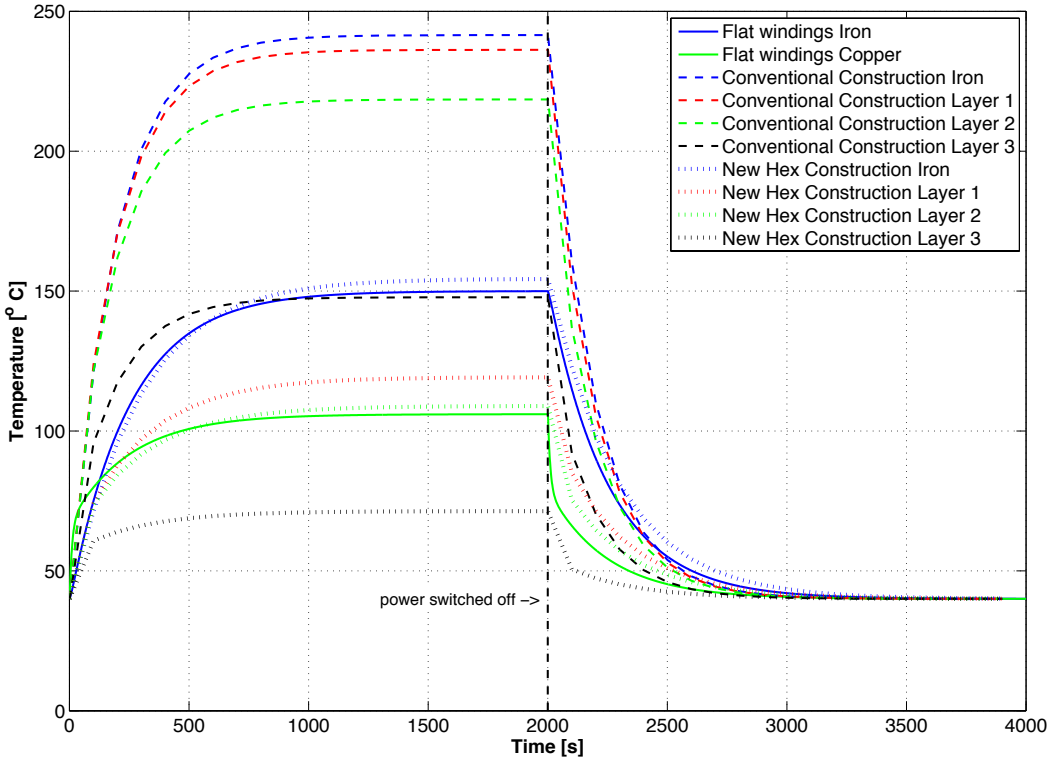


Figure 8.24. Comparison of the transient temperature profile for a) conventional construction with epoxy-infiltrated concentrated windings, b) new construction with integrated heat sink and epoxy infiltration, and c) flat windings

To quantify the potential of increasing the current density with the new winding constructions, the electromagnetic properties of the pole pieces are assumed unsaturated and the heat load in the windings and the iron core were proportionally increased until the hotspot temperature of the conventional construction was reached. The resulting temperature profiles of the new construction with integrated heat sink and flat windings are shown in Figure 8.25.

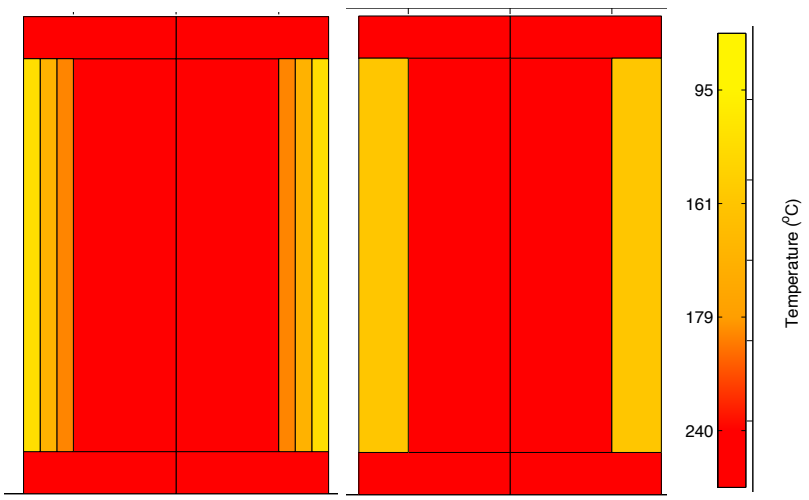


Figure 8.25. Temperature profile for the new construction with integrated heat sink (left) and new construction with flat windings (right)

For each construction a simultaneous equation in terms of the I^2R losses is formed

$$I_{old}^2 R = Q_{old} \quad \text{eqn.8.1}$$

$$I_{new}^2 R = Q_{new} \quad \text{eqn.8.2}$$

Assuming constant electrical resistances for the windings in different constructions, the current of the new construction is described as a factor of the conventional one.

$$I_{new} = \sqrt{\frac{Q_{new}}{Q_{old}}}.I_{old} \quad \text{eqn.8.3}$$

The new construction with integrated heat sink the pole piece losses could be increased by 75% before the same hotspot temperature of the conventional construction is reached. This results in a 32% increase in current density. Conversely the new construction with flat windings the pole piece losses could be increased by 80%, producing a 35% increase in current density. It should be noted that while this analysis is limited to matching the hot spot temperature, the winding temperatures in both new constructions are still kept cooler than those in the conventional construction. This gives space for further improvement in current density from the new constructions.

8.5. Discussion and Conclusion

This chapter proposed two new methods for constructing concentrated windings. The new constructions encourage a deeper integration between the thermal aspects and electromechanical aspects of the design of the stator windings. In the first construction a heat sink has been embedded within the windings while the second proposal revisits flat windings and proposes solutions to some of the manufacturing difficulties faced with these windings.

An LP based thermal model has been developed for each new construction and used to compare their temperature profile with the conventional construction. This chapter has demonstrated that the new construction methods offer a reduction in hotspot temperature by approximately 90 ^{o}C. In the YASA machine used as a test case study for this research, the new constructions offer an increased current density of 33-35%.

However, the new constructions are not limited to the YASA machine and can be applied various machine topologies with concentrated wound pole pieces. For example Switched Reluctance machines are of great interest to the automotive sector as these are highly fault tolerant and cost effective as they do not make use permanent magnets. However SR machines suffer from a torque density that is about 50% lower to that achieved by PM machines, (Gao and McCulloch, 2012). The new winding constructions may hence be adapted to bridge this gap.

However the author recognizes the fact that this study focused on the thermal behaviour of the windings. Adopting the constructions to different machine topologies may require a comprehensive investigation. Flat windings for example may exhibit a different electrical behaviour with greater AC losses. Therefore adoption of the new constructions requires further investigation.

9 The Relevance of Thermal Contact Resistance in Electrical Machines

The investigation on the temperature gradient across concentrated windings held in Chapter 7 identified the thermal resistance between the winding layers as the main limitation in the conductive path. This chapter broadens the investigation and discussion of thermal contact resistance to a wider audience by researching the interface between the stator iron and the casing of indirect cooled machines. The aim here is to bring some of the complexities of thermal contact resistance to the reader's attention. This chapter is based on paper 7.

9.1. Motivation behind this chapter

Driesen et al., (2001) highlights how thermal contact resistances (TCRs) are found in several locations within electrical machine geometry. A schematic of this is shown in Figure 9.1.

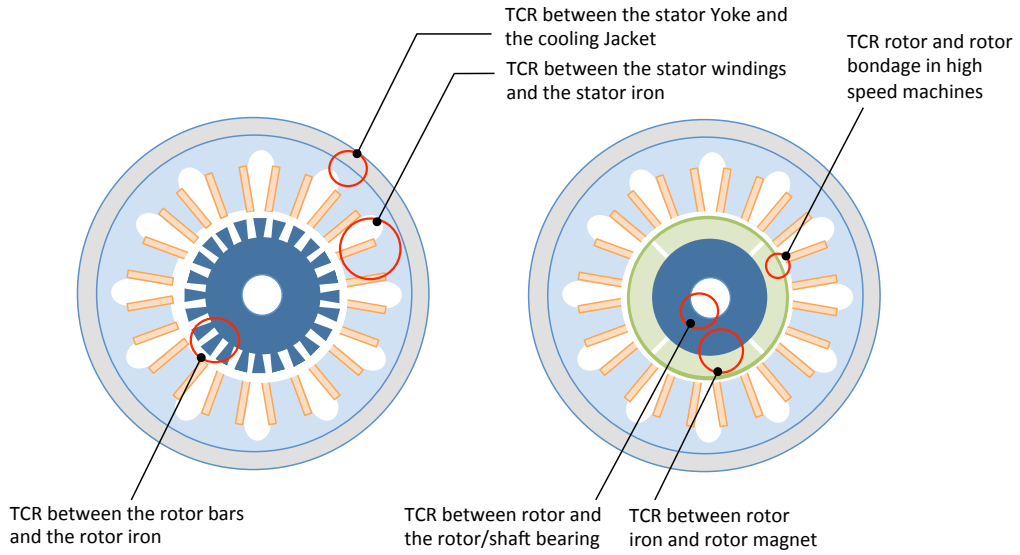


Figure 9.1. Highlights of TCR within (left) an induction machines and (right) a permanent magnet machines

TCRs are often on the main thermal path of electrical machines and therefore play an important role in their thermal analysis. The difficulties in determining the TCR in electrical machines have been highlighted in Staton et al., (2012). TCR between solid boundaries of electrical machine components is modelled by introducing a small effective interface air gap, whose thickness is defined through an initial experimental calibration (Staton et al., 2001, 2005, Boglietti et al, 2008). The general assumption by thermal designers is that the TCR is a constant which depends on the shrink fit pressure and the manufacturing process. The variability in the manufacturing process has always led to the assumption that establishing empirical correlations for the TCR is difficult. However, in Section 2.5 of the literature review the data was categorized according to the material interface and correlations of the gap thickness with machine power were presented.

Furthermore, the TCR model for concentric cylinders preseted in Lemczk et al, (1987), and discussed in Section 7.5 demonstrates a complex interaction between heat flux, contact pressure, surface roughness and material hardness. As the cylinders are heated, they gradually expand. Depending on the direction of the heat flux vector, the contact pressure at the interface joint is reinforced or relaxed. Thus the TCR changes with heat flux. To the author's knowledge the awareness of such a complex interaction is missing in the literature of electrical machine thermal modelling. The current modelling practice using a constant is an oversimplification. The relevance of this interplay becomes important in examining the transient thermal behaviour of electrical machines, for example in applications such as automotive or wind generation.

This chapter focuses on the TCR at the interface between the stator lamination and machine housing. This value is important as it is on the main heat removal path of the electrical machine affecting the accuracy of the predicted stator temperatures. Despite this, very little work has been dedicated to investigate this parameter. Moreover, the few existing studies, (Kulkarni et al., 2012) fail to establish correlations or provide important parameters such as material properties that allow results to be replicated. This research fills this gap by experimentally demonstrating the behaviour of TCR with pressure and heat flux, and establishes empirical correlations.

9.2. Design of the Experiment

In this research the machine geometry is simplified to two concentric cylinders. The outer aluminium cylinder representing the machine casing is shrunk over an inner cylinder made from carbon steel representing the stator iron. The dependence of the thermal conductivity of electrical steel with silicon content has been long noted, (Gotter, 1954, Roberts, 1969, Banks, 1961, Schumichen, 1966). A correlation of the variation of the thermal conductivity is shown in Figure 9.2. Despite the variation in conductivity between silicon steels and carbon steel, the latter was still used due to its ease of manufacturing and availability.

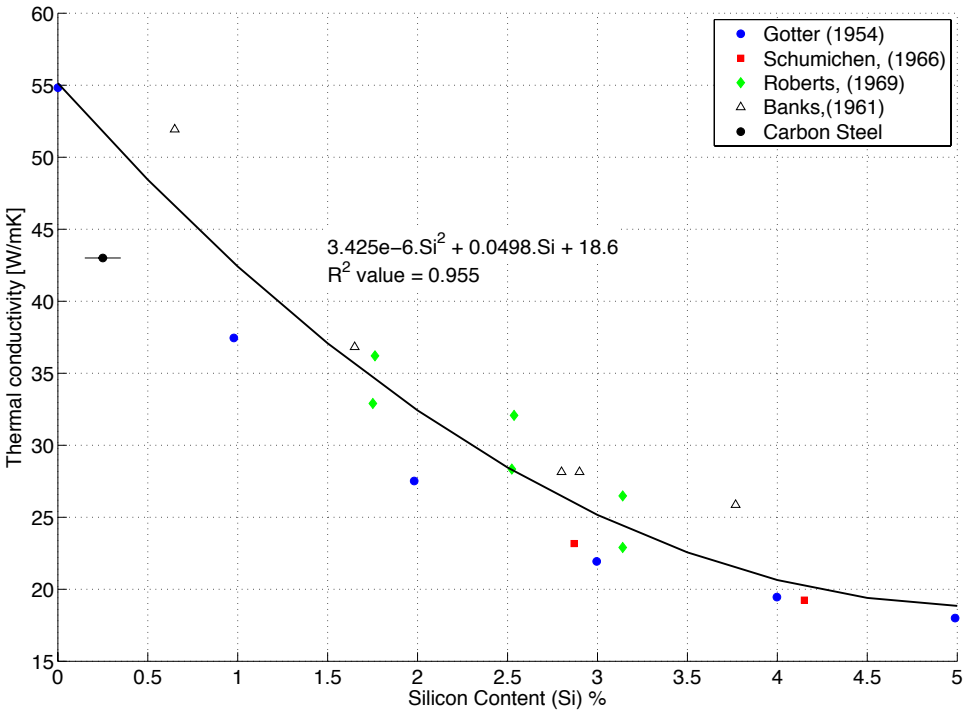


Figure 9.2. Variation of thermal conductivity with Silicon content. Data from (Gotter, 1954, Roberts, 1969, Banks, 1961, Schumichen, 1966)

The thermal resistance R_{th} between two bodies at different temperatures in contact at a common interface and subjected to a heat transfer Q at the interface can be calculated using:

$$R_{th} = \frac{(T_i - T_o)}{Q} \qquad \text{eqn. 9.1}$$

where in T_i is the temperature of the inner cylinder, T_o is the temperature of the inner cylinder. Therefore to replicate this condition, in this experiment, the inner cylinder is heated using a cartridge heater. The heating power and steady state temperature of each cylinder is measured. The test setup is shown in Figure 9.3.

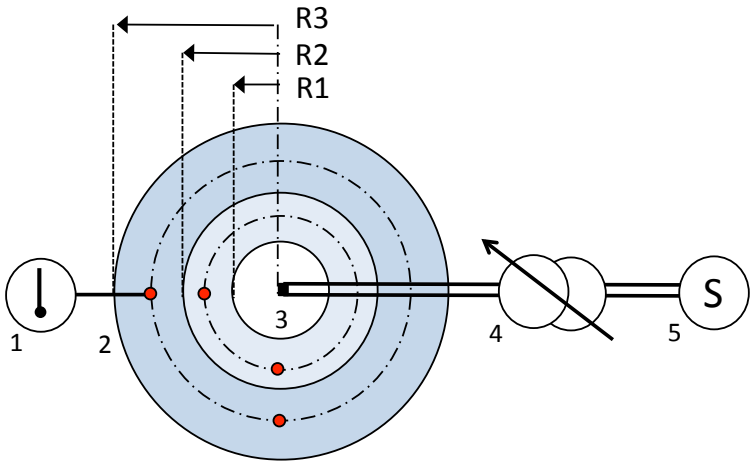


Figure 9.3. Test setup with 1) temperature sensors (locations marked with a red dot), 2) concentric assembly with 3) internal cartridge heater, 4) variable transformer, 5) ac power supply

To eliminate the effect of the thermal conductivity across each cylinder, and account only for the contact conductance at the joint, the thermal resistance was defined as follows:

$$R_{th} = \frac{\ln\left(\frac{2r_2}{r_1 + r_2}\right)}{2\pi k_i L} + \frac{1}{2\pi r_2 L h_j} + \frac{\ln\left(\frac{r_3 + r_2}{2r_2}\right)}{2\pi k_o L} \qquad \text{eqn. 9.2}$$

where r is the radius of the cylinders, L the height of the cylinder, k the thermal conductivity and h_j the conductance at the joint. h_j is calculated by reorganizing the formula as follows:

$$h_j = \frac{1}{2\pi r_2 L\left[\frac{(T_i - T_o)}{Q} - \frac{\ln\left(\frac{2r_2}{r_1 + r_1}\right)}{2\pi k_i L} - \frac{\ln\left(\frac{r_3 + r_2}{2r_2}\right)}{2\pi k_o L}\right]} \qquad \text{eqn. 9.3}$$

While in TCR models it was shown that surface properties and material hardness play an important role, these are often overlooked by electrical machine thermal designers. Consequently they are often missing from electrical machine papers leaving the thermal designer unable to replicate results. In this research these have been measured and reported. The following section describes the manufacturing process of the test samples, the measurement of the material properties, the experimental setup and test procedure.

9.4. Experimental Work

9.4.1. Manufacturing the Test Samples

Four pairs of concentric cylinders were manufactured on a lathe. The materials were chosen so as to replicate the interaction between the shrink-fit aluminium outer housing onto an internal steel stator. Each pair was machined so that it contains an interference fit, thus enabling to test a range of shrink fit pressures. The cylinder height/thickness ratio was kept to an approximate value of ten so that the heat transfer in the axial direction can be neglected and only heat transfer in the radial direction is considered.

9.4.2. The Surface Roughness

The surface finish of a material is dependent on the material and the process used for machining the component. The outer aluminium cylinders were machined using a precision reaming tool while the interface surface of the inner mild steel cylinders was machined on the lathe using a carbide-tip tool. Surface finish charts from (Engineer's Handbook, Surface roughness tables, 2013) were used to establish typical surface roughness values. These were verified using an Alicona Infinite Focus Digital Profilometer. The measured RMS roughness values were determined by taking an N number of equally spaced samples along a trace and establish its vertical distance y from the mean line to the data point, such that:

$$\sigma = \sqrt{\frac{1}{N}\sum_{i=1}^{N} y_i^2} \qquad \text{eqn. 9.4}$$

Table 9.1 compares the measured RMS roughness with suggested values found in the literature.

Table 9.1. Comparison between measured and reference surface properties

Description	Measured RMS roughness [μm]	Suggested RMS roughness [μm]*
Mild Steel surface machined with a Carbide-tip lathe tool	1.83	0.4-6.3
Aluminium surface machined with a Reaming tool	3.27	0.8-3.2 [1]

* values obtained from Engineer's Handbook, (2013)

9.4.3. Material Bulk and Micro Hardness

The average material hardness was established by measuring six samples of each material using a Vickers Armstrong indenter. With the machine loaded an indent was applied on the curved surfaces of both the inner and outer cylinders. This ensures that the effect of work hardening during machining was accounted for. Loads were varied between 20 kg and 40 kg. The diagonal lengths of the indent were measured. The hardness was determined using the correlation by Yovanovich, (2006):

$$H[GPa] = \frac{18187.74F}{d^2} \qquad \text{eqn. 9.5}$$

Indents whose diagonal lengths varied by more than 10% from each other were discarded so as to avoid skewed deformations. The mean and standard deviation of the measured hardness values for the two materials is shown in Table 9.2 The procedure was repeated using a micro hardness machine to achieve the values c_1' and c_2' required for establishing the non-dimensional contact pressure shown in eqn. 9.14. The relationship of indent diameter with micro hardness for the Carbon Steel inner cylinder and Aluminium Outer cylinder are shown in Figure 9.4. The coefficients c_1' and c_2' are found to compare well with those presented by (Hegazy, 1985) as shown in Table 9.2.

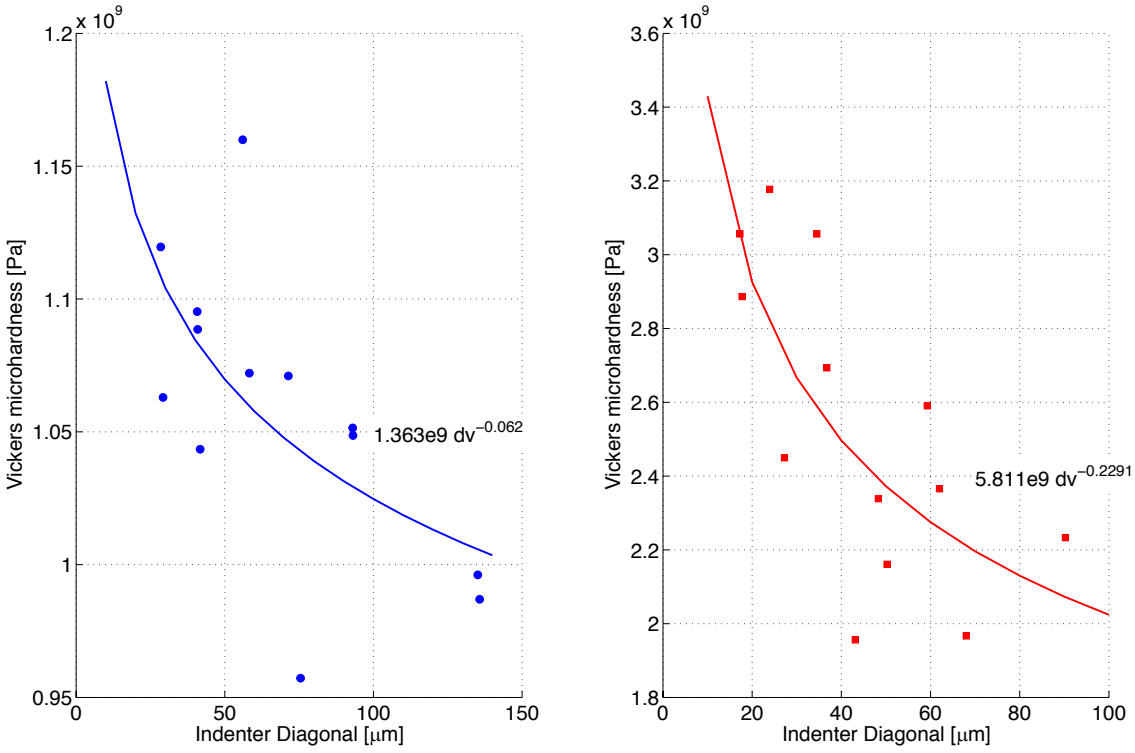


Figure 9.4. Micro hardnessp for (Left) Aluminium outer cylinder (Right) inner Carbon Steel cylinder

Table 9.2. Bulk Hardness values for the inner and outer cylinders and comparison of the micro hardness coefficients c_1' and c_2'

Material	Vickers Bulk Hardness [GPa]	c_1' [GPa]	c_2'
Mild Steel Inner Cylinder	1.920 ± 0.074	5.811	-0.2291
Stainless Steel (Hegazy, 1985)		6.27	-0.229
Aluminium Outer Cylinder	1.099 ± 0.023	1.363	-0.062
Alclad (Hegazy, 1985)		1.11	-0.00487

Having described the surface and material properties of the test section, the assemblies were shrink fit. The procedure is described in the section below.

9.4.4. Shrink Fit Assemblies

Following machining, the interface diameters of all inner outer cylinders were surveyed at 45^o intervals, at various cylinder heights. This ensured that the cylinders are paired with the correct interference fit and that the desired range of shrink fit pressure is achieved. Traditionally, thermal interface material (TIM) is not applied between the stator iron and the machine casing, and therefore TIM was not applied in these tests either. The cylinders analysed in this test were assembled by a shrink fit procedure in which the inner steel cylinder was subjected to a thermal contraction at a temperature of -5 ^{o}C while the aluminium outer cylinder was placed in a Carbolite oven and subjected to a thermal expansion at a temperature of 300 ^{o}C. The change in diameter for each cylinder due to temperature difference was calculated using:

$$\Delta D = \alpha D\left(T_{e,c} - T_{\infty}\right) \qquad \text{eqn. 9.6}$$

The resulting contact pressure at the interface of each assembly was determined by solving Lame's equations (Hearn, 1997):

$$\sigma_R = A - \frac{B}{r^2} \qquad \text{eqn. 9.7}$$

$$\sigma_H = A + \frac{B}{r^2} \qquad \text{eqn. 9.8}$$

The geometrical dimensions and the resulting contact pressures at the interface are listed in Table 9.3. An example of a final shrink fit assembly is shown in Figure 9.5.

Table 9.3. Dimensions of test geometry

Cylindrical Position	Material	Inner diameter [mm]	Outer diameter [mm]	Interference [mm]	Shrink fit contact pressure [MPa]
Inner	Mild steel	10 ± 0.005	19.024 ± 0.005	-0.0033	0
Outer	Aluminium	19.027 ± 0.005	32 ± 0.005		
Inner	Mild steel	10 ± 0.005	19.032 ± 0.005	0.0120	35.2
Outer	Aluminium	19.020 ± 0.005	32 ± 0.005		
Inner	Mild steel	10 ± 0.005	19.048 ± 0.005	0.0313	91.7
Outer	Aluminium	19.017 ± 0.005	32 ± 0.005		
Inner	Mild steel	10 ± 0.005	19.065 ± 0.005	0.0495	145.0
Outer	Aluminium	19.015 ± 0.005	32 ± 0.005		

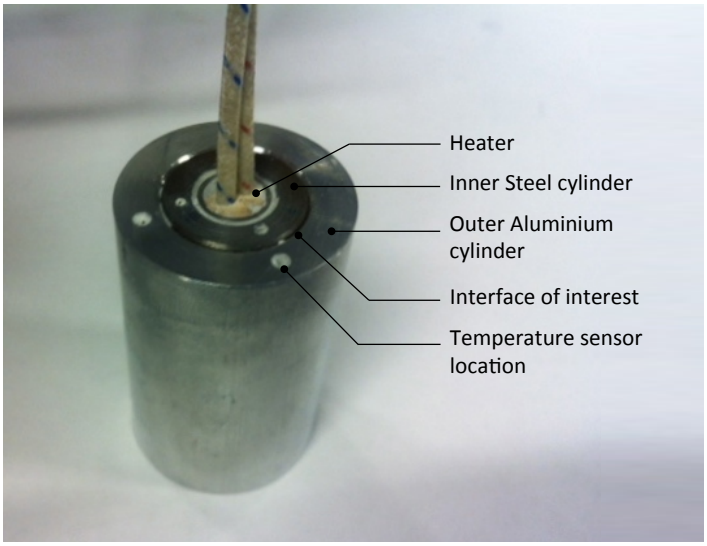


Figure 9.5. Example of a shrink fit assembly

Following the description of the test specimen, the following section describes the test procedure for measuring the TCR.

9.4.5. Measuring the Thermal Contact Resistance

To estimate the thermal contact resistance, a heat flux and a temperature difference across the cylindrical joint is required. To control the heat flux, it was decided that the inner cylinder was heated by a measureable source while the outer cylinder was cooled by natural convection. A 230 V, 150 W cartridge heater was mounted inside the inner cylinder. Silicon based thermal interface material was applied to improve the heat transfer between the heater and the inner cylinder. T-type thermocouples were mounted in machined holes within each of the two cylinders. Temperature sensor holes were also

filled with thermal interface material to ensure a good contact between the sensor and the component. Temperature sensors were recorded using TC-08 Pico data loggers. A controlled ambient temperature was also monitored. The heater was connected to a transformer so that the heat input could be regulated. A current meter and a differential probe were connected to PicoScope 3000 series and were recorded at 1s intervals. The heat input was calculated as:

$$Q = I.V \qquad \text{eqn. 9.9}$$

The assembly was placed between thick polystyrene blocks to reduce thermal losses from the end surfaces. The variable transformer was used to regulate the voltage to the heating element and the test was repeated for a number of heat fluxes. For each heat flux, the experiment was left to run for approximately 6 hours until a steady state condition was reached, and a further 2 hours during steady state.

9.5. Test Results

The variation of thermal contact conductance with heat flux and contact pressure are shown in Figure 9.6.

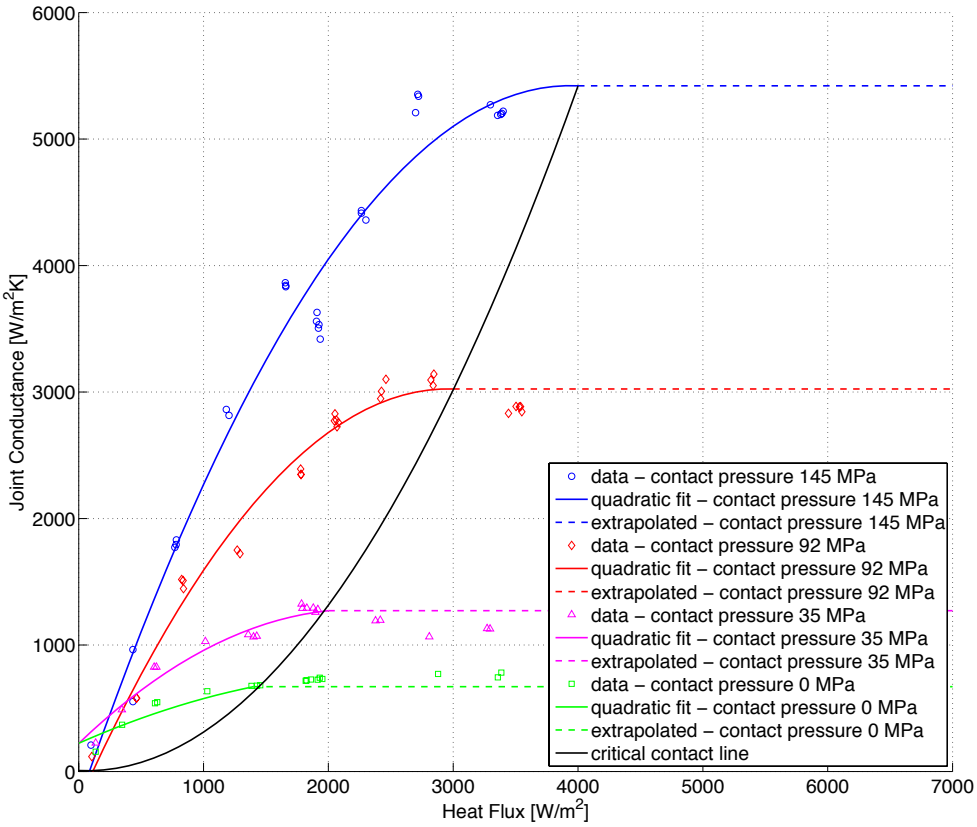


Figure 9.6. Variation of thermal contact conductance with heat flux and shrink fit pressure

The thermal contact conductance increases as the shrink fit pressure increases. This behaviour is generally assumed in the thermal modelling of electrical machines. However, it is interesting to note that at a constant shrink fit pressure the thermal contact conductance increases with heat flux. Each setup was found to reach a critical heat flux value, after which the thermal contact conductance flattens out. It has also been noted how with larger the shrink fit pressures takes a higher heat flux before the thermal contact conductance flattens out. To the author's knowledge the relevance of this observation to electrical machine modelling has not been reported in the literature. For any particular shrink fit pressure, the critical heat flux has been correlated to a quadratic equation as:

$$critical\ hc = 3.497e^{-4}\dot{q}^2 - 0.04574\dot{q} + 7.283 \qquad \text{eqn. 9.10}$$

A set of quadratic correlations of conductance with heat flux for various shrink fit pressures are listed in Table 9.4.

Table 9.4. correlations of conductance with heat flux

Shrink fit contact pressure [MPa]	Quadratic correlation		Measure of degree of fit R^2
145	$h_j = -3.65e^{-4}\dot{q}^2 + 2.877\dot{q} - 243.1$	eqn. 9.11	0.9837
92	$h_j = -3.72e^{-4}\dot{q}^2 + 2.207\dot{q} - 243.7$	eqn. 9.12	0.9899
35	$h_j = -2.11e^{-4}\dot{q}^2 + 0.9461\dot{q} - 222.1$	eqn. 9.13	0.9613
0	$h_j = -8.378e^{-5}\dot{q}^2 + 0.4367\dot{q} - 223.3$	eqn. 9.14	0.9562

By correlating the coefficients with the shrink fit contact pressure, a general correlation in terms of the shrink fit pressure P_{sh} and heat flux at the joint $\dot{q}$ can be deduced as:

$$h_j = (-2e^{-6}P_{sh} - 1e^{-4})\dot{q}^2 + (1.75{-}2e^{-2}P_{sh} + 0.428)\dot{q} - (0.1708P_{sh} + 221.19) \qquad \text{eqn. 9.15}$$

9.6. Discussion and Conclusion

To investigate how this experimental data compare with thermal conductance values in the literature a survey of electrical machines has been carried out. The published values of the effective air gap thickness used to represent the discontinuous conductivity were converted back into a conductance value by equating:

$$h_j = \frac{Q}{A.\Delta T} = \frac{k_{air}}{x} \qquad \text{eqn. 9.17}$$

Despite the radial geometry of the machines, the linear conductivity equation had to be used for consistency with the literature. A heat flux across the stator and machine casing is required. Therefore the heat load Q is estimated using the machine power rating P and efficiency η such that:

$$Q = (1 - \eta).P \qquad \text{eqn. 9.18}$$

The machine efficiencies and dimensions have been obtained from the manufacturer data (Fimet Motori e Riduttori, 2014) so that the heat flux of the machine $\dot{q}$ can be computed. The steady state heat flux was estimated by assuming a machine loss distributed at 80% stator and 20% rotor. The machine data is shown in Table 9.5. A comparison of the machine joint conductance with experimental correlations is shown in Figure 9.7

Table 9.5. Details of the machines used to compare the thermal contact conductances. Data from Boglietti et al., (2008), Staton et al., (2005) and Mellor, (1995).

Reference	Machine Description	Efficiency η	Heat flux $\dot{q}$ [W/m2]	Effective air gap x [mm]	Joint conductance h_j [W/m2K]
Boglietti et al., (2008)	1.5 kW TEFC			0.027	
Boglietti et al., (2008)	2.2 kW TEFC			0.049	
Boglietti et al., (2008)	3 kW TEFC			0.03	
Staton et al., (2005)	4 kW TEFC IM MA112M4	85%	3670.16	0.042	611.90
Staton et al., (2005)	7.5 kW TEFC IM MA132M4	88%	5704.48	0.0762	337.27
Staton et al., (2005)	15 kW TEFC IM MA160L4	90%	4708.43	0.077	333.77
Staton et al., (2005)	30 kW TEFC IM MA200L4	91%	4957.10	0.016	1606.25
Staton et al., (2005)	55 kW TEFC IM M250M4	93%	4799.97	0.037	694.59
Mellor, (1995)	5.5 kW TEFC IM 132S	85%	4168.34	-	288.20
Mellor, (1995)	5.5 kW TEFC IM 132S	85%	4168.34	-	1310
Mellor, (1995)	75 kW TEFC IM 250M	93%	6545.42	-	2722

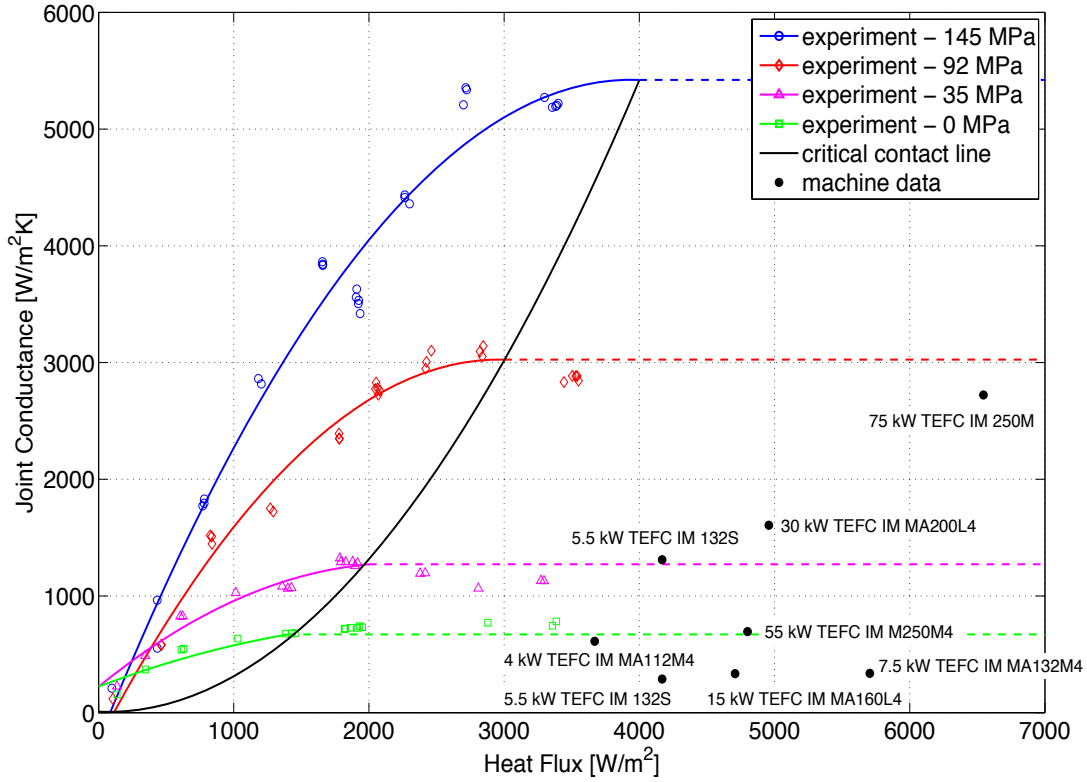


Figure 9.7. Variation of temperature with heat flux for all shrink fit assemblies

While the lack of information on the shrink fit pressure and surface properties in the literature makes definite deductions difficult to make, the following remarks can be made:

- The conductance values from electrical machine data found in the literature do not fit the experimental patterns. This may be largely due to different values of surface roughness, material hardness, or completely different materials altogether. The lack of material information in machine literature may cause a classical example of comparing ‘apples to oranges’. However the author still makes this comparison to bring stress about the importance of material data and bring the issue to the attention of the thermal designer.
- Despite the lack of machine data it can be noted that all machine data points fall beyond the critical heat flux line. The experimental evidence on a simple model presented here shows that the thermal contact resistance varies with contact pressure, heat flux and the resultant component temperature. Only at sufficiently large heat flux values, can the TCR be assumed constant. The machine data corresponds to the steady state conductance values for a continuous rating and therefore the heat flux through the stator-casing interface is expected to be constant and beyond the critical heat flux line.

- It is noted that some points fall below the 0 MPa line. While this could be attributed to different material or surface properties, it could also be due to different manufacturing processes such as when a light press fit is adopted rather than a shrink fit. In the case of a press fit the thermal designer should be aware that defects in the surface finish would be extruded along the whole length of the casing, which would make thermal modelling challenging.

The experiment demonstrates that the common notion that the thermal contact resistances is a single value, set during the machine assembly and used for thermal modelling across the whole operation range of the machine is an oversimplification. It is advised that the thermal designer establishes the critical heat flux first to assess this assumption. When modelling transient thermal behaviour the TCR must be set as a function of heat flux. Empirical correlations of the variation of TCR with contact pressure and heat flux have been developed. However, machine designers are cautioned to take into account the surface effects material hardness properties in their design before blindly applying the correlations presented.

10 | Conclusions and Further Work

The aim of this research is to increase the current density of electrical machines by addressing key parameters limiting convective and conductive heat transfer. In the introductory chapter of this thesis the current density of electrical machines is shown to be interdependent on temperature and parameters governing heat transfer. The interdependencies are replicated in Figure 10.1. The current density J is shown to improve dramatically with an increase in heat transfer coefficient h and equivalent conductivity k_{eq}.

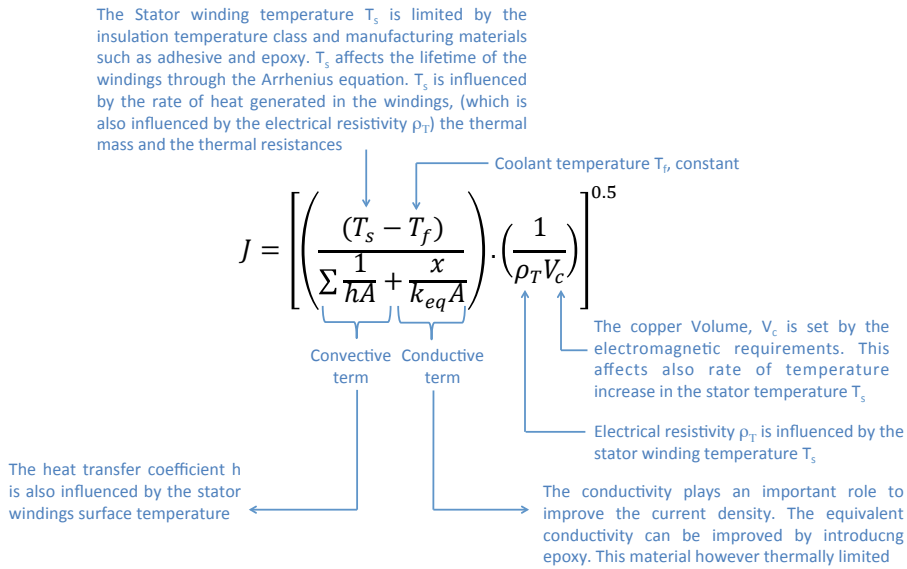


Figure 10.1. Interdependency of current density with thermal parameters

In Section 1.6 a set of research questions on the topics of convective and conductive heat transfer was posed. The answers to these questions are found within the chapters of this thesis. This chapter shows how each of the set targets have been achieved and directs the reader to where each of these can be found within this thesis. This chapter provides also the concluding remarks on the topics investigated. While this research has strived to find an answer to the research questions, often the answers open up more interesting questions. This leaves space for further work that could not be undertaken during the course of this

DPhil. Hence this chapter also discusses limitations of this research and provides insights where further work could be produced.

The research starts by investigating the questions: “What is the thermal limit of air cooled electrical machines?” and “What role will they play in electric or hybrid vehicles?” These were addressed in Chapter 3. It was shown that in the context of urban mobility, the machine topology affects the convective thermal limit. The propulsive power is required to be distributed amongst the wheels, confining the use of air-cooled electrical machines to smaller in-wheel motors. In axial flux internal rotor (AFIR) machines the thermal limitation was shown to be from convective heat transfer in the motor casing. The heat transfer in AFIR machines improves with extended fins and can be applied to machines of up to 10 kW. The machine was shown to be mostly suitable for rotor speeds below 8000 rpm. Such machines can be designed for direct drive or subjected to a single gear with a gear ratio smaller than 6. Conversely, axial flux internal stator (AFIS) machines were found to suffer from convective heat transfer limitations in the rotor-stator gap. The heat transfer in AFIR machines improves with rotor speed but not with added extended surfaces to the machine outer rotor. The machine power is hence confined to approximately 5 kW, operated at speeds beyond 8000 rpm and gear ratios larger than 4. The use of a gear box introduces a higher level of complexity, weight and inefficiency. Hence the author is of the opinion that AFIR topologies may be better suited at supporting urban mobility vehicles with in-wheel motors as they offer higher torque. However the selection of drivetrain components often requires an in depth study on cost and weight. Low speed machines may require a larger amount of permanent magnets at higher costs.

The analysis presented in this chapter assumed that the heat losses of the machine lie primarily within the stator windings. The author is aware that rotor losses increase with machine speeds, and recognises that this is a limit of this research. Hence it would be interesting to investigate how changing the machine loss distribution would affect thermal limits and the implications on the vehicle. The estimations made throughout this chapter were mostly based on empirical correlations from ideal geometries. However electrical machines often have particular geometries such as protruding surface that may impact these correlations. The design of air-cooled machines is also focused for the application of in-wheel motors. These will experience secondary aerodynamic effects, which in this thesis have not been investigated.

To address the thermal limitations in the rotor stator gap of AFIS machines, a novel evaporative cooling mechanism for an outer rotor machine was experimentally investigated in Chapter 4. This research finds that wick assisted cooling may prevent the windings from overheating and offers significant benefits at reducing the thermal resistance than its air-cooled counterpart investigated in Chapter 3. An evaporative cooling in AFIS machines supports a continuous power of up to 10 kW at speeds as low as 2000 rpm. The machines can be applied as in wheel motors with a single speed gear and a gear ratio of about 1.3. However this cooling mechanism comes with significant challenges as the liquid was observed to pool at the bottom at low speeds and rim on the outer edges at high speeds. It hence requires an intricate wick, designed to keep the windings wet at any operating condition. The author is of the opinion that at sufficiently high speeds the continuous operation of the machine would be above the critical Reynolds number. The design requirements on the wick can hence be reduced to tap into the rimming flow. The research on evaporative cooling requires further development. Developing a full working prototype would further assess the potential of this cooling mechanism and provide interesting insights into its operation. This would therefore be an interesting area for further work.

The convective thermal limit from the machine casing does not exist in liquid cooled electrical machines as the heat transfer is augmented by the extended surfaces of an external radiator. Therefore the attention was turned to direct liquid cooling in Chapter 5. One way of shortening the thermal path is to inject the coolant in direct contact with the stator windings. This chapter addresses the question: “What challenges are still linked with direct liquid cooling?” It was shown that directly cooled machines are faced with a flow distribution problem, leading to an uneven temperature distribution in the stator. The current density is then limited by the hottest pole piece. This chapter addresses this problem by developing a fast and accurate thermo-fluid model to establish the flow distribution and an overall stator temperature map. The analytical model was compared to computational fluid dynamics (CFD) models and validated to within 6% of experimental measurements. Despite the fact that CFD models were found to be computationally intensive, they provide an insight into the thermo-fluid behaviour of the coolant and stator pole pieces. It was shown that the coolant tends to flow around the path of least resistance – which is the inner and outer distribution rings. The thermo-fluid model was used to investigate the effects of changing geometrical parameters on the flow and temperature

distribution. It was shown that by carefully directing the flow in the channels between pole pieces the temperature distribution is improved and the hot spot temperature reduced by 13 K. This doubles the insulation lifetime or for the same hot spot increases the current density by 7%. Despite that this arrangement increases the pressure in the flow, this can be readily solved by upsizing the circulation pump. This analysis has not been made and the author understands that there is a point with very large circulation pumps where the system experiences a drop in efficiency. The experimental part of this research is limited by the fact that the flow distribution is only derived from the temperature distribution of the pole pieces. A more accurate way is to measure the flow distribution, for example by using a hot wire anemometer. However due to the small dimensions of the flow channels, care must be taken so that the instrumentation do not affect the results. It will be an interesting exercise to extend the thermo-fluid model to the various machine types using direct liquid cooling and investigate the effect of flow and temperature uniformity on their current density.

The research on directly oil cooled segmented stator continued by measuring the heat transfer coefficients (HTC) on the sides of the pole pieces in Chapter 6. This chapter adopts double-sided thin film gauges to measure the steady state HTC on oil cooled pole pieces. The chapter presents experimentally derived correlations and compares them to a CFD model and empirical analytical calculations such as the Seider-Tate equation and Mills equation for laminar flows. The measurements showed two different HTC values for each side of the pole piece. This effect may be likened to the pressure and suction sides of turbine blades. This effect is not captured when using analytical correlations but is shown in 3D CFD simulations. The Seider-Tate equation is found to underestimate the HTC by approximately 25% at a channel Reynolds number of 50. This under-prediction tapers off to produce an accurate estimation as the channel Reynolds number increases to 200. The analytical correlation by Mills under-predicts the HTC by 30% at a channel Reynolds number of 50. The under-prediction tapers off to 10% at a channel Reynolds number of 200. The 2D CFD models are found to underestimate the HTC by 35% at a low inlet Reynolds numbers. The difference also tapers off to produce an accurate average HTC estimate at a channel Reynolds number of 200. However the gradient of the chart than those from other predictions or measurements. This is likely because the 2D CFD model is only able to produce an average HTC value on the entire edge of the pole piece and therefore the it is not a ‘like with like’ comparison. The 3D CFD model requires

higher computational resources and solution time but provides a detailed resolution on the pole piece surfaces. The 3D CFD model was found to follow the Mills correlation, but produce an underestimation of between 10-30% from the measurements. In hindsight, the measurement process could have been simplified by using thin film temperature sensors. The application of different heat transfer measurement techniques to different electrical machine topologies is an interesting topic of further research.

The focus is turned on conductive heat transfer in Chapter 7. Stator windings are often defined by a single temperature node or treated as homogeneous windings with an equivalent thermal conductivity. This chapter addresses the question: “How do we model the temperature profile of concentrated windings?” This chapter experimentally demonstrates that concentrated windings suffer from a severe temperature gradient and develops a lumped parameter (LP) thermal model that captures the temperature gradient across concentrated winding layers. The heat generated in the winding layers is conducted from one consecutive winding layer to the next across creating a hotspot on the layer faced with the longest thermal path. The thermal path was dominated by the thermal contact between adjacent winding layers. While the new LP model introduces more nodes resulting in a larger amount of unknown thermal resistances, a transient experimental calibration establishes the unknown values in a similar fashion to traditional calibration of LP models. Knowledge on the formation of the hotspot enables the thermal designer to reduce excessive safety factors thereby increasing the current density of the machine or extend the machines life.

Moreover the experiments provide insight into the behaviour of infiltrated and non-infiltrated windings. The research showed that each interface at the winding layers requires its own thermal resistance value. While in epoxy-infiltrated windings this value remains constant for various heat loads, the thermal resistances in non-infiltrated windings change with heat flux. The theory for modelling the thermal contact resistance in a solid-solid interface was found useful to interpret the behaviour of the windings. It was shown how this TCR model provides the mechanical pressure acting on the interface. While this theory was used to assess the potential to improve the conductive heat transfer with different impregnation methods, further work can also lead to the life estimation of windings in cyclic operation.

One shortcoming with this research is that the heat load on the windings and iron has been assumed uniformly distributed. However often pole pieces experience higher heat losses at the tips due to eddy currents. As the general model ignores axial effects, it does not have nodes along the axial length to distribute the heat load. However, in Section 7.6.5 it was shown that the model is readily modified to contain axial nodes. These can be used to input heat loads as required and assess the axial temperature distribution. This research was produced within the geometrical boundary conditions of AWG14 square windings (1.62 mm thickness). While the model is readily adopted to thicker windings, defining the winding layers in smaller winding thicknesses such as litz wire may be challenging. One idea for modelling litz wire is to consider a group of windings as the winding layer. Further work is therefore required to extend the use of the winding model to different winding geometries and test new modelling hypothesis.

The insights about the formation of the hotspot with respect to the thermal path and the role of the thermal contact resistance in the thermal path were the basis for the investigation in Chapter 8. This chapter addresses the question: "How do we manufacture windings so that the thermal path is improved, and thereby improving their current density?" This chapter develops a new winding construction by introducing a heat sink interleaved between the winding layers. This offers the inner windings with a means to bypass the thermal resistances, thus reducing the hotspot temperature by approximately 65 ^{o}C – 70 ^{o}C. It was shown that for the same hot spot temperature as a conventional construction, the new construction allows an increase in current density by 30%. While the concept of integrating a heat sink into the windings may be applied to any cooling mechanism, in a directly cooled stator, the heat sink's fins can be used to control the flow distribution as shown in Chapter 5. The manufacturing challenges associated with flat windings was also revisited. A folding technique is proposed to reduce the amount of soldering joints, which are traditionally required at each turn. The folded windings can also be redesigned to contain a portion emerging into the flow. This acts as an additional heat sink and a means to control the flow distribution in direct liquid cooled machines. This research was limited to the thermal investigation of an integrated heat sink and flat windings. The electrical impact of these concepts was not investigated. Some areas requiring further investigation include the effectiveness of the slot to limit eddy currents being generated within the heat sink, and the effect of electrical resistance in flat windings. This research was also limited to assessing the temperature profile and

improvement in current density from a single pole piece. However, it would also be interesting to design, develop, construct and characterise an electrical machine whose stator is entirely made of these alternative winding constructions.

The findings on the behaviour of thermal contact resistance (TCR) in the windings motivated the author to broaden the research to general electrical machines. Therefore Chapter 9 investigates the role and relevance of the TCR in the design, manufacturing and operation of electrical machines. This value is important as it is often on the main thermal path of the machine. TCR between solid boundaries of electrical machine components is currently modelled by introducing a small effective interface air gap, whose thickness is defined through an initial experimental calibration. The general assumption by electrical machine thermal designers is that the TCR at the solid-solid interface is a constant which depends on the shrink fit pressure and the manufacturing process. This chapter experimentally demonstrates that the TCR of concentric cylinders is also sensitive to the heat flux vector and the operating temperature. Therefore the current modelling technique may be an oversimplification, particularly when investigating the transient operation of electrical machines. This chapter provides empirical correlations for two concentric cylinders representing the machine casing shrunk over the stator iron. However it is important to point out that steel laminations have different material and surface properties and therefore further tests to characterize the effect of the laminations on the empirical correlations are required. The lack of machine data in the literature limits the analysis of the findings from this chapter. It would be useful for this experimental procedure to be scaled up to several materials and machine geometries.

In view of the findings presented in this thesis, the author concludes that segmented stators with concentrated windings offer the highest potential to cool the windings effectively and increase the current density of electrical machines. The segmented stator design allows direct liquid cooling which shortens the thermal path. Due to their low dielectric constant, oil is traditionally the coolant of choice for direct cooled machines. However oil offers a higher viscosity and produces low Reynolds numbers and low heat transfer coefficients. In oil-cooled machines, the coolant temperature may be kept at a level to provide the best compromise between a raised viscosity and a sufficient temperature difference. However, the author is of the opinion that the migration towards a coolant that produces turbulent flow will present further benefits. In this respect

unconventional coolants may be explored. To the author's knowledge some OEM's have researched direct water-cooling of electrical machines with additional protection on the windings due to the high dielectric constant of water. Establishing low viscosity liquids with low dielectric constants is challenging as these become flammable. Flow control is important to assure that no single pole piece will over heat and impose a limit to the current density. The heat transfer from smooth surfaces is often lower than that from rough surfaces. The surfaces of epoxy-infiltrated windings can be roughened to improve the HTC.

The segmented pole pieces can be manufactured using the new construction. By interleaving a heat sink into the layers of concentrated windings a shorter thermal path is achieved and the hot spot temperature is reduced. Moreover, using a current carrying conductor with the highest insulation temperature rating, a higher current density can be pushed through the stator windings. The heat sink portion extending into the coolant not only increases the heat exchange from the windings, but it ties the winding construction with aspects of flow control in the stator. With the cooling on the stator windings improved, the thermal limit may shift on the rotor and hence research effort on rotor cooling may become increasingly important. This research shows that closed R-S air-gaps suffer from thermal limitations. One solution is to make use of open-rotors, which draws in fresh ambient air. However, this reduces the ingress protection, which is often desired in automotive applications. As the current density of electrical machines keep increasing machine designers may seek innovative way to introduce liquid cooling to the rotors.

References

ABG First Drive: 2010 Honda Insight, http://www.autoblog.com/2009/01/11/abg-first-drive-2009-honda-insight-63-4-mpg/, accessed on July 2014.

Airoldi. G., *Numerical Investigations of Air Flow and Heat Transfer in Axial Flux Permanent Magnet Electrical Machines,* PhD. Thesis, Durham University, 2010.

Airoldi, G., Ingram G.L., Mahkamov, K., Bumby, J.R., Dominy, R.G., Brown, N.L., Mebarki, A., Shanel, M., *Computations on Heat Transfer in Axial Flux Permanent Magnet Machines*, Proc. of the 2008 Int. Conf. on Electr. Machines, ICEM2008, 6-9 Sept. 2008, Vilamoura, Portugal.

Amoros, J.G Andrada, P., Blanque, B., *An analytical approach to the thermal design of a double sided linear switched reluctance motor*, XIX Int. Conf. on Electrical Machines (ICEM) 2010, 6-8 Sept. 2010, Rome, Italy, pp. 1-4.

Anderson J.D., *Chapter 2: Governing Equations of Fluid Dynamics in Computational Fluid Dynamics*, Wendt J.F. Eds., Springer-Verlag Berlin Heidelberg, 2009, pp. 15-51.

Antonetti, V.W. and Yovanovich, M.M., *Thermal Contact Resistance in Microelectronic Equipment*, Thermal Management Concepts in Microelectronic Packaging from Component to System, ISHM Technical Monograph Series 6984-003, 1984, pp.135-151.

Antonetti, V.W. and Yovanovich, M.M., *Enhancement of thermal contact conductance by metallic coatings: Theory and experiment,* Journal of Heat Transfer, Vol. 107, 1985, pp. 513-519.

Antonetti, V.W., Whittle, T.D., Simons, R.E., *An Approximate Thermal Contact Conductance Correlation*, Experimental and Numerical Heat Transfer in Combustion and Phase Change, Vol. 170, 1991, pp. 35-42.

Apex Drive, http://www.apexdrivelabs.com/pdf/Apex_Motors_and_Generators_Oct_2008.pdf, accessed on 23rd August, 2010.

Astarita, T., Cardone, G., Calomagno, G.M., *Infrared thermography: An optical method in heat transfer and fluid flow visualization*, Optics and Lasers in Engineering, Vol. 44, 2006, pp. 261-281.

aus der Wische, S., *Heat transfer in a rotating disk in parallel air crossflow,* Int. J. Thermal Sciences, Vol. 46, 2006, pp. 745-754.

Aydin, M., Huang, S., Lipo, T.A., *Axial Flux Permanent Magnet Disc Machines: A Review*, Symp. Power Electronics, Electrical Drives, Automation, and Motion (SPEEDAM) 2004, Capri, Italy, June 16-18, 2004.

Banks, P.J., *Thermal conductivity of sheet steel laminations*, AEI Manchester Report No. TP/R/1, 188, 1961.

Baughn, J.W., Liquid crystal methods for studying turbulent heat transfer, Int. J. Heat and Fluid Flow, Vol. 16, 1995, pp. 365-375.

Bell, S., Measurement Good Practice Guide No. 11. Iss. 2: *A Beginner's Guide to Uncertainty of Measurement*, March 2001, National Physical Laboratory, UK.

Boglietti, A., Cavagnino, A., Lazzari, M., Pastorelli, M., *A Simplified thermal model for variable speed self cooled industrial induction motor*, IEEE Trans. Ind. Appl., Vol. 39, No. 4, pp. 945-952, Jul./Aug. 2002.

Boglietti, A., *Guest Editorial,* IEEE Trans. Ind. Electron., Vol. 55, 2008, pp. 3498-3499.

Boglietti, A., Cavagnino, A., Staton, D., *Determination of Critical Prameters in Electrical Machine Thermal Models*, IEEE Trans. on Ind. Appl., Vol. 44, No. 4, July-Aug 2008, pp. 1150-1159.

Boglietti, A., Cavagnino, A., Staton, D., Shanel, M., Mueller, M., Mejuto, C., *Evolution and Modern Approaches of Thermal Analysis of Electrical Machines*, IEEE. Trans. on Ind. Electron., Vol. 56, No. 3, Mar. 2009, pp. 871-882.

Boiling Point, Fluids and Gasses, http://www.engineeringtoolbox.com/boiling-points-fluids-gases-d_155.html, accessed on: April, 2013.

Borges, S.S., Cezario, C.A., Kunz, T.T., *Design of Water Cooled Electric Motors Using CFD and Thermography Techniques,* 18th Int. Conf. on Electr. Machines, ICEM2008, 6-9 Sept., 2008, Vilamoura, Portugal.

Borroni-Bird, C.E., *Personal urban mobility for the twenty first century*, in Energy, Transport and the Environment: Addressing the Sustainable Mobility Paradigm, Interwildi O.R., and King, D.A. Eds., New York: Springer Energy Series, Springer Scientific, 2012, pp. 313-334.

Bruetsch, R., Tari, M., Froehlich, K., Weiers, t., and Vogelsang, R., *Insulation Failure Mechanisms of Power Generators*, IEEE Electrical Insulation Magazine, Vol. 24, pp. 17-25, 2008.

Burton Simile, C., *Critical Evaluation of Wicking in Performance Fabrics,* MSc Thesis, School of Polymer, Textile, and Fiber Engineering, Georgia Inst. of Technology, Atlanta, Georgia, USA 2004.

Calin M.D., Helerea, E., *Temperature influence on magnetic characteristics of NdFeB permanent magnets*, 7th Int. Symp. On Adv. Topics in Electr. Engineering (ATEE), 12-14 May, 2011, Bucharest.

Caricchi, F. Crescimbino, F., Honorati, O., Di Napoli, A. and Santini, E., *Compact Wheel Direct Drive for EV,* IEEE Industry Applications Magazine, Vol. 2, pp. 25-32, 1996.

Childs, P.R.N., Rotating Flow. Oxford: Elsevier, 2011.

Chiou, J.P., *The effect of non-uniform fluid flow distribution on the thermal performance of solar collector*, Solar Energy Vol. 29, 1982, pp. 487-502.

Chong, Y.C., Echenique Subiabre, E.J., Mueller, M.A., Chick, J., Staton, D.A., McDonald, A.S., *The Ventialtion Effect on Stator Convective Heat Transfer of an Axial-Flux Permanent Magnet Machine,* IEEE Trans. Ind. Appl., Vol. 61, No. 8, 2014, pp. 4392-4403.

Chung, T.J., Computational Fluid Dynamics, Cambridge University Press, 2002.

Cirani, M., Sadarangani, C. Thelin, P., Analysis of an innovative design for an axial flux Torus machine, accessed from http://www.jaewoo.com/product/software/doc, on 11/5/2011.

Cobb, E.C. and Saunder, O.A., *Heat transfer from a rotating disk*, Proceedings of the Royal Society, London, Vol. 236, 1956, pp. 343-351.

Collins, M., Chana, K., Povey, T., *Improved Methodologies for the Time Resolved Heat Transfer*

Measurements, Demonstrated in an Unshrouded Transonic Turbine Casing, Proceedings of ASME Turbo Expo 2015: Turbine Technical Conf. and Exposition GT2015, June 15-19, Montreal, Canada.

Collins, M., Chana, K., Povey, T., *New technique for the fabrication of miniature thin film heat flux gauges*, Meas. Sci. Technol., Vol. 26, 2015, pp. 1-10.

Connor, P.H., Pickering S.J, Gerada, C., Eastwick, C.N., Micallef, C., Tighe C., *Computational fluid dunamics modelling of an entire synchronous generator for improved thermal management*, IET Electr. Power Appl., 2013, Vol. 7, Iss. 3, pp. 231-236.

Convective heat transfer coefficient Tables, http://www.engineersedge.com/heat_transfer/convective heat_transfer_coefficients__13378.htm, accessed on 21/09/2015.

Cooper, M., Mikic, B.B. and Yovanovich, M.M., *Thermal Contact Conductance,* Journal of Heat and Mass Transfer, Vol. 12, 1969, pp. 279-300.

Cros, J., Viarouge, P., *Synthesis of High Performance PM Motors with Concentrated Windings*, IEEE Trans. on Energy Conv., Vol. 17, No. 2, June 2002, pp. 248-253.

Cryogenic properties of Copper, http://www.copper.org/resources/properties/cryogenic/, accessed on 23/07/2015.

Culham, J.R., Muzychka, Y.S., *Optimization of Plate Fin Heat Sinks Using Entropy Generation Minimization*, IEEE Trans. Component and Packaging Tech., Vol. 24, No. 2., June 2001, pp. 159-165.

Daily, J.W., and Nece. R.E., *Chamber dimension effects on induced flow and frictional resistance of enclosed rotating disks.* Journal of Basic Engineering Vol. 82, 1960, pp. 217-232.

Dajaku, G., Gerling, D., *Low Costs and High-Efficiency Electric Machines*, 2nd Int. Electric Drives Production Conference, (EDPC 2012), 15-18 Oct. 2012, Nuremberg.

Dielectric Constants for some common Liquids, http://www.engineeringtoolbox.com/liquid-dielectric-constants-d_1263.html, accessed on: April, 2013.

Dorfman, L.A., *Hydrodynamic resistance and the heat loss of rotating solids,* Oliver and Boyd, Edinburgh, 1963.

Doorly, J. E., and M. L. G. Oldfield, *The theory of advanced multi-layer thin film heat transfer gauges*, Int. J. of Heat and Mass Transfer Vol. 30 Iss. 6, 1987 pp. 1159-1168.

Driesen, J., Belmans, R.J.M., Hameyer, K., *Finite Element Modelling of Thermal Contact Resistances and Insulation Layers in Electrical Machines*, IEEE Trans. Ind. Appl., Vol. 37, No. 1, Jan./Feb. 2001, pp.15-20.

DSI, Opticool Fluid, http://dsiventures.com/electronics-cooling/opticool-fluid/, accessed: 6, Mar. 2015.

Du-Bar, C., *Design of an axial flux machine for an in-wheel motor application*, MSc. Thesis, Chalmers University of Technology, Goteborg, Sweden, 2011.

Dunn, P. D., and Reay, D. A., Heat Pipes. Elsevier Science Ltd, Oxford, UK, 1994.

Engineer's Handbook, Reference Tables – Surface Roughness Table, http://www.engineershandbook.com/Tables/surfacero ughness.htm , accessed on: November, 26, 2013.

Fedoseyev, L and Pearce, E.M., Rotor assembly with heat pipe cooling system, US Patent Application 2014/0368064 A1, issued 2014.

Fei, W., Luk, P.C.K., Jinupun, K., *Design and Analysis of a High-Speed Air Coreless Axial Flux Permanent Magnet Generator with Circular Magnets and Coils,* Electric Power Applications, Vol. 4, Iss. 9, Nov. 2010, pp. 738-747.

Fimet Motori e Riduttori, Fimet Motor Catalogs, http://www.fimetmotori.com/download-catalogs/, accessed on: 29/01, 2014.

Fluids – Latent Heat of Evaporation, http://www.engineeringtoolbox.com/fluids-evaporation-latent-heat-d_147.html, accessed on: April, 2013.

Galindo Lopez, C. H., *Evaluating new ways of conducting convective heat dissipation experiments with ventilated brake discs*, PhD Thesis. Cranfield University, Bedfordshire, UK, 2001.

Gao, Y., McCulloch, M.D., *A Review of High Power Density Switched Reluctance Machines Suitable for Automotive Applications*, International Conference on Electrical Machine, ICEM2012, 2-5, Sept. 2012, Marseille, France, pp. 2610-2614.

General Motors. *GM EN-V,* http://media.gm.com/content/autoshows/Shanghai/2010/public/cn/en/env/news.detail.html/content/Pages/news/cn/en/2010/March/env01.html, accessed on: 6/16, 2012.

Gieras, J.F., Wang, R.J. and Kamper, M.J. *Axial Flux Permanent Magnet Brushless Machines*. Springer Science, 2008.

Gotter, G., Heating and cooling of electrical machines, 1954, Springer-Verlag, Berlin.

Guo, S.M., Lai, C.C., Jones, T.V., Oldfied, M.L.G., Lock, G.D., Rawlinson, A.J., *The application of thin-film technology to measure turbine-vane heat transfer and effectiveness in a film-cooled, engine-simulated environment*, Int. J. of Heat and Fluid Flow, Vol. 19, 1998, pp.594-600.

Hashin, Z., *Theory of Fiber Reinforced Materials*, NASA Washington, DC, USA, NASA Contractor Rep., 1972.

Hegazy, A.A., *Thermal Joint Conductance of Conforming Rough Surfaces,* PhD thesis, University of Waterloo, Canada, 1985.

Heiles, F., *Design and Arrangement of Cooling Fins*, Elecktrotecknik and Masghinenbay, Vol. 69, No. 14, July, 1952.

Hettegger, M., Streibl, B., Biro, O., Neudorfer, H., *Measurements and Simulations of the Convective Heat Transfer Coefficients on the End Windings of an Electrical Machine*, IEEE Trans. Ind. Electron., Vol. 59, No. 5, pp. 2299 – 2308, May 2012.

Hey, J., Howey, D.A., Martinez-Botas, R. and Lamperth, M., *Transient Thermal Modelling of an Axial Flux Permanent Magnet (AFPM) Machine Using a Hybrid Thermal Model,* World Academy of Science, Engineering and Technology, Vol. 71, 2010, pp. 912-921.

Hoffman, K.A., Chiang, S.T., *Computation Fluid Dynamics – Volume 1*, Fourth Ed., Engineering Education System, Wichita, USA, 2000.

Holman, J.P., Heat Transfer, McGraw Hill, 1997.

Howey. D.A., *Thermal Design of Air-Cooled Axial Flux Permanent Magnet Machines,* PhD. Thesis,

Imperial College London, 2010.

Howey, D.A., Holmes, A.S., Pullen, K.R., *Measurement of stator heat transfer in air-cooled axial flux permanent magnet machines,* 35th Annual Conf. of IEEE Trans. Ind. Electron., IECON'09, 3-5 November, 2009, Porto, Portugal, 2009, pp. 1197-1202.

Howey, D.A., Holmes, A.S., Pullen, K.R., *Radially resolved measurement of the stator heat transfer in a rotor-stator disc system*, Int. J. Heat Mass Transf., Vol. 53, No. 1-3, pp. 491-501, Jan. 2010.

Howey, D.A., Holmes, A.S., Pullen, K.R., *Measurement and CFD Prediction of Heat Transfer in Air-Cooled Disc-Type Electrical Machines,* IEEE Trans. Ind. Appl., Vol. 47, No. 4, 2011, pp. 1716-1723.

Howey, D.A., Childs, P.R.N., Holmes, A.S., *Air-gap convection in rotating electrical machines,* IEEE Trans. Ind. Electron., Vol. 59, No. 3, 2012, pp. 1367-1375.

Hsu T.R. and Tam, W.K., *On Thermal Contact Resistance in Compound Cylinders*, AIAA Paper No. 79-1069, AIAA 14th Thermophysics Conference, June 4-6, 1979, Orlando, Florida.

Huang, S., Aydin, M., Lipo, T.A., *A Direct Approach to Electrical Machine Performance Evaluation: Torque Density Assessment and Sizing Optimization, Proc. of Int. Conf. on Elect. Machines, ICEM'02, 26-28 Aug., 2002, Bruges, Belgium.*

Huang, Z., Marquez, F., Alakula, M., Yuan, J., *Characterization and application of forced cooling channels for traction motors in HEVs*, XXth Int. Conf. on Electrical Machines, ICEM2012, pp. 1212-1218, 2-5 Sept., 2012, Marseille, France.

Ireland, P.T., and Jones, V., *The response time of a surface thermometer employing encapsulated thermochromic liquid crystals, J. Phys. E: Sci. Instrum.* Vol. 20, 1987, pp. 1195–9.

Janna, W.S., *Engineering Heat Transfer*, Van Nostrand, Reinhold, 1988.

Jain, M., and Williamson, S.S., *Suitability analysis of in-wheel motor direct drives for electric and hybrid electric vehicles, in* IEEE Electrical Power & Energy Conference EPEC'09, 2009.

Jones, T. V., 1995, *The thin film heat transfer gauges – a history and new developments,* Invited lecture, 4th national UK heat transfer conference, IMechE conference transaction, Manchester p. 1-12.

Jungreuthmayer, C., Bauml, T., Winter, O., Ganchev, M., Kapeller, H., Haumer, A., Kral, C., *A Detailed Heat and Fluid Flow Analysis of an Internal Permanent Magnet Synchronous Machine by Means of Computational Fluid Dynamics,* IEEE Trans. Ind. Appl., Vol. 59, No. 12, 2012, pp. 4568-4578.

Kanzaki, H., Sato, K., Kumugai, M., *A Study of an Estimated Method for Predicting the Equivalent Thermal Conductivity of an Electric Coil*, Heat Transfer Research Japan, Vol. 21, Iss. 2, 1992, pp.123-138.

Karapetoff, V., *Experimental Electrical Engineering*, 2nd Ed., Vol. 2, pp. 69-74

Kays, W., Crawford, M., and Weigand, B., *Chapter 7: Laminar internal flows: Momentum transfer*, in Convective Heat & Mass Transfer, 4th ed. New York: McGraw Hill Education, 2004, pp. 74-76, 330.

Kennelly, A.E., *The Thermal Time Constant of Dynamo-Electric Machines*, Transactions A.I.E.E., 1925, pp. 137-154.

Kherbeet, A.S., Mohammed, H.A., Munisamy, K.M., Salman, B.H., *The effect of step height of microscale backward-facing step on mixed onvection nanofluid flow and heat transfer characteristics*, Int. J. Heat and Mass Transfer, Vol. 68, Jan. 2014, pp. 554-566.

Kostikov, O. N., Malykhin, E., Fedyushkin, A. M., Yakovlev, A., and Yakovlev, Y. V., *Electric Machine*, Russian Patent SU741377 A1 19800615, issued May 10, 1980.

Kraus, A. D., and Bar-Cohen, A. B., *Design and Analysis of Heat Sinks*, New York: John Wiley & Sons Inc., 1995.

Kreith, F., *Convection heat transfer in rotating systems,* Adv. Heat Transfer, Vol. 5, 1968, pp. 129-251.

Kulkarni, D.P., Rupertus, G., Chen, E., *Experimental Investigation of Contact Resistance for Water Cooled Jacket for Electrical Motors and Generators*, IEEE Trans. of Energy Conv., Vol. 27, 2012, pp. 204-210.

Laing. N., *Rotating Electrical Machine with Evaporation Cooling*, US Patent 3838947, Oct. 1, 1974.

Langhaar, H. L., *Steady Flow in the Transition of a Straight Tube,* Journal of App. Mech., Vol. 64, 1942, pp. A55-A58.

Lamperth, M., Beaudet, A. And Jaensch, M., *Disc motors for automotive applications, in* Hybrid and Eco-Friendly Vehicle Conference. IET HEVC2008, 8-9 Dec, 2008, Coventry, UK, pp. 1-5.

Lark, W.J., *City Car: Optimizing vehicle and urban efficiencies through a shared adaptive platform*, MSc. Thesis, MIT 2005.

Latour, B., Bouvier, P., and Harmand, S., *Convective heat transfer on a rotating finned cylinder with transverse airflow,* Int. J. Heat and Mass Transfer, Vol. 54, 2011, pp. 4710-4718.

Launder, B., Poncet, S., Serre, E., *Laminar, Transitional and Turbulent flows in Rotor-Stator Cavities*, Ann. Rev. Fluid Mech., Vol. 42, 2010, pp. 229-248.

Lee, S., *Optimum Design and Selection of Heat Sinks*, IEEE Trans On Components, Packaging & Manufacturing Technology-Part A, Vol 18, No 4, Dec. 1995, pp. 812-817.

LeFevre E.J. and Ede, A.J. *Laminar free convection from the outer surface of a vertical circular cylinder, in* Proc. 9th Int. Congr. Appl. Mech. Brussels, Belgium, 1956, pp. 175-183.

Lemczk, T.F. and Yovanovich, M.M., *New models and methodology for predicting thermal contact resistance in compound cylinders and fin-tubes*, Thermal/Mechanical Heat Exchanger Design – Karl Gardner Memorial Session, 1987, pp. 59-70.

Limpert, R., *Cooling Analysis of Vented Brake Rotors,* SAE Technical Paper 751014, 1975.

Lohner-Porsche-Mixte-Voiturette, http://www.ultimatecarpage.com/car/3456/Lohner-Porsche-Mixte-Voiturette.html, accessed on: 02/08, 2011.

Lovatt, H.C., Ramsden, V. S., and Mecrow, B.C., *Design of an in-wheel motor for a solar-powered electric vehicle*, *Proc. Inst. Electr. Eng. Electr. Power Appl.,* Vol. 145, No. 5, Sep. 1998, pp. 402-408.

Madhusudana, C.V, *On Heat Flow across Cylindrical Joints*, Heat Transfer 1986, Proceedings of the 8th Int. Heat Transfer Conference, pp.651-658.

Madhusudana, C.V., *Thermal conductance of cylindrical joints*, Int. J. Heat and Mass Transfer, Vol. 42, 1999, pp. 1273-1287.

Mailly, F.; Giani, A.; Bonnot, R.; Temple-Boyer, P.; Pascal-Delannoy, F.; Foucaran, A.; Boyer, A. *Anemometer with hot platinum thin film*. Sens. Actuat. A, 2001, Vol. 94, pp. 32-38.

Mantelli, M.B.H. and Yovanovich, M.M., *Chapter 16: Thermal Contact Resistance*, Spacecraft Thermal Control Handbook, Volume I: Fundamental Technologies, 2nd Ed., 2002, Ed: Gilmore, D.G., The Aerospace Press, El Segundo, CA.

Mellor, P.H., Roberts, D., Turner, D.R., *Lumped parameter thermal model for electrical machines of TEFC design*, IEE Proceedings-B, Vol. 138, No. 5, Sept. 1991, pp. 205-218.

Mejuto, C., Mueller, M., Shanel, M., Mebarki, A., Reekie, M., Staton, D.A. *Improved synchronous machine thermal modelling*,18th Int. Conf. Elect. Machines (ICEM2008), 6-9 Sept. 2008, Vilamoura, Portugal pp. 1-6.

MetaFoam. *Metal Foam Manufacturer,* http://metafoam.com/home.htm, accessed on: 7/9, 2013.

Micallef, C., Pickering, S.J., Simmons, K.A., and Bradley, K.J., *Improved cooling in the end region of a strip-wound totally enclosed fan-cooled induction electric machine*, IEEE Trans. Ind. Electron., Vol. 55, no. 10, Oct. 2008, pp. 3517–3524.

Mitchell, W.J., Borroni-Bird, C.E., Burns, L.D., *Reinventing the Automobile: Personal Urban Mobility for the 21st Century*, MIT Press, 2010.

Mills, A.F., *Heat Transfer*, 2nd ed. Prentice Hall, New Jersey, 1999.

Mohanty, A. K., Tawfek, A. A., and Prasad, B.V.S.S.S., *Heat Transfer from a Rotating Cylinder in Crossflow,*Experimental Thermal and Fluid Science, Vol. 10, 1995, pp. 54-61.

MotorCAD, http://www.motor-design.com/motorcad.php, accessed on 16 Mar. 2015.

Montsinger, V.M., *Loading Transformers by Temperature*, AIEE Trans., Part1 (Communications and Electronics),Vol. 49, 1930, pp. 776-792.

Nategh, S., *Thermal Analysis and Management of High Performance Electrical Machines*, 2013, PhD Thesis, KTH School of Electrical Engineering, Stockholm, Sweden.

Nategh, S., Wallmark, O., Leksell, M. Zhao, S., *Thermal Analysis of a PMaSRM Using Partial FEA and Lumped Parameter Modelling*, IEEE Trans. on Energy Conv., Vol. 27, No. 2, June 2012, pp. 477-488.

Nategh, S., Huang, Z., Krings, A., Wallmark, O., Leksell, M., *Thermal Modelling of Directly Cooled Electric Machines Using Lumped Parameter and Limited CFD Analysis*, IEEE Trans. on Energy Conv., Vol. 28, No. 4, Dec. 2013, pp. 979-990.

Nategh, S., Krings, S., Wallmark, O., Leksell, M., *Evaluation of Impregnation Materials for Thermal Management of Liquid Cooled Electric Machines*, IEEE Trans. Ind. Electron., Vol. 61, No. 11, Nov. 2014, pp. 5956-5965.

Negus, K.J., and Yovanovich, M.M., *Correlation of Gap Conductance Integral for Conforming Rough Surfaces*, Journal of Thermophysics and Heat Transfer, Vol. 2, No. X, March 1988, pp. 279-281.

NGNR, http://ngnr.blogspot.com/2012/01/typhoon-update.html, accessed on 6 Mar. 2015.

Nilssen, R., Skaar, S. E., Lund, R., Skjellnes, T., Øvrebø, S., and Løvli, E., "*Design of a permanent magnet synchronous motor integrated in the wheel rim on wheelchairs*", Proceedings of the 11th Power Electronics and Application Conference, EPE 2005, 11-14 September 2005, Dresden, Germany.

Oldfield, M. L. G., *Impulse response processing of transient heat transfer gauge signals*, ASME J. Turbomach., Vol. 130, Iss.2, 2008, pp. 210-223.

Owen, J.M., *The Reynolds Analogy Applied to Flow Between a Rotating and a Stationary Disc, Int*. J. Heat and Mass Transfer, Vol. 14, 1971, pp. 460-472.

Owen, J., Haynes, C., Bayley, F., *Heat Transfer from and Air Cooled Rotating Disk*, Proceedings of the Royal Society of London, Series A, Mathematical and Physical Sciences, (1934-1990), Vol. 336, No. 1607, pp. 453-473, 1974.

Parviainen, A., *Design of axial flux permanent magnet low speed machines and performance comparison between radial flux and axial flux machines*, PhD Thesis, Lappeenranta University of Technology, Lappeenranta, Finland, 2005.

Parviainen, A., Niemela, M., Pryhonen, J., Mantere, J., *Performance comparison between low-speed axial flux and radial flux permanent magnet machines including mechanical constraints*, IEEE Int. Conf. on Electric Machines and Drives ICEM2005, 15-17 May 2005, San Antonio, TX, pp. 1695-1702.

Pechanek, R. and Bouzek, L., *Analyzing Two Types of Water Cooling for Electric Motors Using Computational Fluid Dynamics*, 15th Int. Conf. Power Electron and Motion Control, EPE-PEMC2012, 4-6 Sept., Novi Sad, Serbia.

Perez, I.J. and Kassakian, J.G., *A stationary thermal model for smooth air-gap rotating electric machines*, Electric Machines and Power Systems, Vol. 3, No. 3-4, 1979, pp. 285-303.

Peterson, G.P., *Heat Pipes: Modelling, Testing and Applications*. John Wiley & Sons Inc., New York, USA, 1994.

Piccini, E., Guo, S.M., Jones, T.V., *The development of a new direct heat flux gauge for heat transfer facility*, Meas. Sci. Techno. Vol. 11, 2000, pp. 342-349.

Popescu, M., Staton, D., Boglietti, A., Cavagnino, A., Hawkins, D., Goss, J., *Modern Heat Extraction Systems for Power Traction Machine – A Review*, Trans. on Ind. Appl., 2016, (in press).

Potgieter, J., Kamper, M.J., *Evaluation, Application and Comparison of a Double-Rotor Toothed Toroidal Wining Wind Generator Over a Wide Power Range*, International Conference on Electrical Machine, ICEM2014, 2-5, Sept. 2014, Berlin, Germany, pp.1158-1164.

Polikarpova, M., *Liquid Cooling Solutions for Rotating Permanent Magnet Synchronous Machines*, 2014, PhD Thesis, Lappeenranta University of Technology, Finland.

Ponomarev, P., Polikarpova, M., Pyrhonen, J., *Thermal modelling of directly oil cooled permanent magnet synchronous machine*, XXth Int. Conf, in Electr. Mach., ICEM2012, pp. 1882-1887, 2-5 Sept., 2012, Marseille, France.

Powell, D.J., *Modelling of high power density electrical machines for aerospace*, PhD. Dissertation, University of Sheffield, Sheffield, UK, May, 2003.

Qi, F., Schenk, M., De Doncker, R.W., *Discussing details of lumped parameter thermal modelling in*

electrical machines, 7th IET Int. Conf. on Power Electronics, Machines and Drives (PEMD 2014), 8-10 Apr., Manchester, UK.

Qi, F., Stippich, A, Guettler, M., Neubert, M., De Doncker, R.W., *Methodical Considerations for Setting Up Space Resolved Lumped Parameter Thermal Models for Electrical Machines*, 17th Int. Conf. on Electr. Machines and Systems, (ICEMS2014) 22-25 Oct., 2014, Hangzhou, China.

Rahman, Z., *Evaluating Radial, Axial and Transverse Flux Topologies for 'In-Wheel' Motors,* Power Electronics in Transportation, 2004, pp. 75-81.

Rasekh, A., Sergeant, P., Vierendels, J., *Convective heat transfer prediction in disk-type electrical machines*, Appl. Thermal. Eng., Vol. 91, 2015, pp. 778-790.

Renault. *Renault TWIZY URBAN,* http://www.renault-ze.com/en-gb/z.e.-range/twizy/twizy-urban-1949.html, accessed on: 6/16, 2012.

Reay, D.A., and Kew, P., *Heat Pipes: Theory, Design and Applications*, Elsevier Science Ltd, Oxford, UK, 2006.

Rice, J.G., and Schnipke, R.J., *An equal-order Velocity-Pressure formulation that does not inhibit spurious pressure modes*, Computer Methods in Applied Mechanics and Engineering, Vol. 58, 1986, pp. 135-149.

Roberts, T.J., *Determination f the thermal constants of heat flow equations of electrical machines*, Proc. IME, 1969-1970, Vol. 184, Part 3E, pp. 84-92.

Romanazzi, P., Howey, D.A., *Air-Gap Convection in a Switched Reluctance Machine*, 2015 Tenth Int. Conf. on Ecological Vehcles and Renewable Energies (EVER), Mar. 31 – Apr. 2, 2015, Monte Carlo.

Ross A.M. and Stoute, R.L., *Heat transfer coefficient between UO2 and zircaloy-2,* Tech. Rep. AECL-1552, 1962.

Sahin, F., *Design and Development of a High-Speed Axial-Flux Permanent-Magnet Machine*, PhD. Dissertation Eindhoven University of Technology, Netherlands, 2001.

Savija, I., Culham, J.R., Yovanovich, M.M., *Review of Thermal Conductance Modles for Joints Incorporating Enhancement Materials*, J. Thermophysics and Heat Transfer, Vol. 17. No. 1, Jan-March, 2003, pp. 43-52.

Scowby, S.T., Dobson, R.T., and Kamper, M.J., *Thermal Modelling of an axial flux permanent magnet machine,* Applied Thermal Engineering, Vol. 24, 2004, pp. 193-207.

Schnipke, R.J. and Rice, J.G., *Examination of a new finite element method applied to convection heat transfer, Finite Elements in Analysis and Design*, May 1985, pp. 227-239.

Schnipke, R.J., *A Streamline Upwind Finite Element Method for Laminar and Turbulent Flow*, PhD Dissertation, University of Virginia, May 1986.

Schultz, D.L. and Jones, T.V., *Heat Transfer Measurements in Short-Duration Hypersonic Facilities*, AGARD-AG-165, 1973, Advisory Group for Aerospace Research & Development (AGARD).

Schumichen, M., *Longitudinal and transverse thermal conductivity of laminated transformer sheets*, Electrie, Vol. 20, Iss. 12, 1966.

Shapiro, A.H., Smith, R.D., and NACA. *Friction Coefficients in the Inlet Length of Smooth Round Tubes*, 1948.

Shlykov, Y.P. and Ganin, Y.A., *Thermal resistance of metalic contacts,* Int. J. Heat and Mass Transfer, Vol. 7, 1964, pp. 921-929.

Shishoo, R., *An overview of the recent developments in materials for sportswear, in* Textile Bioengineering and Informatics Symposium, 11th August, Ueda, Japan, 2012.

Siesing, L., Reinap, A., Andersson, M., *Thermal properties on high fill factor electrical windings: Infiltrated vs non infiltrated*, 2014 Int. Conf. Electrical Machines (ICEM), 2014, 2-5 Sept. 2014, Berlin, Germany, pp. 2218-2223.

Silverstein, C.C., Design and Technology of Heat Pipes for Cooling and Heat Exchange. Taylor and Francis Ltd., London, UK, 1992.

Simons, R.E. and Schmidt, R.R., *A Simple Method to Estimate Heat Sink Air Flow By-pass*, Electronics Cooling, Vol. 3, No. 2, 1997, pp. 36-37.

Simpson, N., Wrobel, R., Mellor, P.H., *Estimation of Equivalent Thermal Parameters of Impregnated Electrical Windings*, IEEE Trans. on Industr. Appl., Vol. 49, No. 6, Nov./Dec. 2013, pp. 2505-2515.

Sitapati, K., Krishnan, K., *Performance Comparison of Radial and Axial Field, Permanent Magnet, Brushless Machines*, IEEE Trans. on Ind. Appl., Vol. 37, No. 5, Sept./Oct. 2001, pp. 228-234.

Sisson, A.E., *Thermal Analysis of Vented Brake Rotors,* SAE Technical Paper 780352, 1978.

Szabo, L., Ruba, M., *Segmental Stator Switched Reluctance Machine for Safety-Critical Applications*, IEEE Trans. Ind. Appl., Vol. 48, No. 6, Nov/Dec 2012, pp. 2223-2229.

Song, S., and Yovanovich, M.M., *Relative Contact Pressure: Dependence on Surface Roughness and Vickers Hardness*, AIAA Journal of Thermophysics 2, Vol. 1, Jan. 1988, pp. 43-47.

Sridhar, M.R. and Yovanovich, M.M., *Review of Elastic and Plastic Contact Conductance Models: Comparison with Experiment*, Journal of Thermophysics and Heat Transfer Vol. 8, No. 4, Oct.-Dec. 1994, pp. 633-640.

Staton, D.A., Pickerng, S., Lampard, D., *Recent advancement in the thermal design of electric motors*, SMMA 2001 Conference on Emerging Technologies for Electric Motion Industry, Durham, North Carolina, USA, 2001, pp. 1-11.

Staton, D., Boglietti, A., Cavagnino, A., *Solving the More Difficult Aspects of Electric Motor Thermal Analysis in Small and Medium Size Industrial Induction Motors*, IEEE Trans. on Energy Conv., Vol. 20, No. 3, Sept. 2005, pp. 620-628.

Staton, D.A., and Cavagnino, A., *Convection Heat Transfer and Flow Calculations Suitable for Electric Machine Thermal Models*, IEEE Trans. Ind. Electron., Vol. 55, No. 10, 2008, pp. 3509-3516.

Stasiek, J.A., Kowalewski, T.A., *Thermochromic liquid crystals applied for heat transfer research,* Opto-Electronics Review, Vol. 10, No.1, 2002, pp. 1-10.

Steven, R.E., *Electrical Machines and Power Electronics*, New York: Van Nostrand-Reinhold, 1983.

Sumislawska, M., Gyftakis, K.N., Kavanagh, D.F., McCulloch, M., Burnham, K.J., Howey, D.A., *The*

Impact of Thermal Degradation on Electrical Machine Winding Insulation, in IEEE SDEMPED 2015, Sept. 1-4, 2015, Guarda, Portugal.

Taylor, J.L., *Calculating airflow through electrical machines*, Electrical Times, 21st July, 1960.

Teertstra, P., Yovanovich, M.M., Culham, J.R., Lemczyk, T., *Analytical Forced Convection Modelling of Plate Fin Heat Sinks*, Proc. of 15th IEEE Semiconductor Thermal Measurement and Management, 9-11 March 1999, San Diego, USA, pp. 34-41.

Thoolen te Horn, F. J. M., *System for cooling the rotor of an electric machine*, Netherlands Patent NL9401710 A 19960603, issued 1996.

Thoroddsen, S.T., and Mahadevan, L., *Experimental study of coating flows in a partially-filled horizontal rotating cylinder,* Experiments in Fluids, Vol. 23, 1997, pp. 1-13.

Tong, A.K., *Flat Stator Winding for Alternator Starter*, US Patent. No. 4,916,345, Apr. 10, 1990.

Torok, V., *Electric Machine*, US Patent 7411152-7, issued March 5, 1976.

TOYOTA. *Toyota i-REAL,* http://www.toyota-global.com/innovation/personal_mobility/i-real.html, accessed: 16/6, 2012.

Van De Pol, D.W., and Tierney, J.K., *Free Convection Nusselt Number for Vertical U-Shaped Channels*, Trans. ASME Nov. 1973.

Vansompel, H., Sergeant, P., Dupre, L., Van den Bossche, A., *Performance of Axial Flux PM Machines with Concentrated Windings*, IEEE Trans. Energy Conv. Vol. 27, No. 2, June 2012, pp. 403-410.

Vacuum Pressure Impregnation Resins, Selection Chart, http://www.dolphs.com/pdfs/Dol_VPI_Chart.pdf, accessed on 21/12, 2015.

Versèle, C., De Grève, Z., Vallée, F., Hanuise, R., Deblecker, O., Delhaye, M., Lobry, J., *Analytical Design of an Axial Flux Permanent Magnet In-Wheel Synchronous Motor for Electric Vehicle*, 13th European Conference on Power Electronics and Applications, EPE '09, 8-10 Sept 2009, Barcelona, Spain, pp. 1-9.

Veziroglu, T.N., *Correlation of Thermal contact Conductance Experimental Results*, Prog. Astron. Aero, Vol. 20, 1967, pp. 879-907.

Vilar, Z.W., Patterson, D., Dougal, R. A., *Thermal Analysis of a Single Sided Axial Flux Permanent Magnet Motor*, 31st Annual Conference of the Industrial Electronics Society, IECON 2005, 6-10 Nov, 2005, Sheraton Capital Center Raleigh, NC, USA.

Vun, S.T., McCulloch, M.D., and Leong, C.Y., *The development of an electromagnetic analytical design tool for megawatt-scale YASA generators,* The 2011 IET Renewable Power Generation Conference, 20-21 June 2011, Glasgow, UK.

Vun, S.T., McCulloch, M.D., 2015, *Optimal Design Method for Large-Scale YASA Machines,* IEEE Trans. of Energy Conversion, Vol. PP., Iss. 99, April 2015, pp. 1-8.

Wallis, L., Leonardi, E., Milton, B., and Joseph, P., *Air Flow and Heat Transfer in Ventilated Disc Brake Rotors with Diamond and Tear-drop Pillars,* Numerical Heat Transfer, PartA: Applications, Vol. 41, pp. 643-655, 2002.

Wang, C.C., Yang, K.S., Tsai, J.S., Chen, I.Y., *Characteristics of flow distribution in compact parallel flow heat exchangers, Part I: Typical inlet header*, Applied Thermal Engineering, Vol. 31, 2011, pp. 3226-3235.

Wang, C.C., Yang, K.S., Tsai, J.S., Chen, I.Y., *Characteristics of flow distribution in compact parallel flow heat exchangers, Part II: Modified inlet header*, Appl. Thermal Eng., Vol. 31, 2011, pp. 3235-3242.

Watel, B., Harmand, S., and Desmet, B., *Influence of fin spacings and rotational speed on the convective heat exchanges from a rotating finned tube,* Int. J. Heat and Fluid Flow, Vol. 21, 2000, pp. 221-227.

Woolmer, T.J., and McCulloch, M.D., *Axial Flux Permanent Magnet Machines; A new topology for high performance applications*. Hybrid Vehicle Conference, IET'06, 12-13 Dec., 2006, Coventry, UK, pp.27-42.

Woolmer, T.J., and McCulloch, M.D., *Analysis of a Yokeless and Segmented Armature machine*, IEEE International Electric Machines and Drives Conference, IEMDC'07, 3-5 May, 2007, Antalya, Turkey, pp.704-708.

Woolmer, T.J., *The Yokeless And Segmented Armature Machine Developed For The LIFECar*, PhD. Thesis, University of Oxford, UK, 2009.

Woolmer, T.J., *Electric Machine – Evaporative Cooled*, UK Patent 2469562, issued: 10 Oct. 2010.

Wrobel, R., McNeill, N., Mellor, P.H., *Performance Analysis and Thermal Modelling of a High Energy Density Prebiased Inductor*, IEEE Trans. on Industr. Electron., Vol. 57, No. 1, Jan. 2010.

Wrobel, R., Mellor, P.H., Holliday, D., *Thermal Modelling of a Segmented Stator Winding Design*, IEEE, Trans. on Industr. Appl., Vol. 47, No. 5, Sept./Oct. 2011, pp. 2023-2030.

Wrobel, R. and Mellor, P.H., *A General Cuboidal Element for Three-Dimensional Thermal Modelling*, IEEE Trans. on Magnetics, Vol. 46, No. 8m Aug. 2010, pp. 3197-3200.

Wrobel, R. and Mellor, P.H., *Thermal Design of High Energy Density Wound Components*, IEEE, Trans. on Industr. Electron., Vol. 58, No. 9, Sept. 2011, pp. 4096-4104.

Wrobel, R., Vainel, G., Copeland, C., Duda, t., Staton, D., Mellor, P., *Investigation of Mechanical Loss Components and Heat Transfer in an Axial-Flux PM Machine*, 2015, (accepted for publication in IEEE Transactions on Industry Applications).

Xu, W., Zhu, J., Guo, Y., Wang, S., Wang, Y., Shi, Z., *Survey on Electrical Machines in Electrical Vehicles*, Int. Conf. on Appl. Superconductivity and Electromagnetic Devices, 2009, ASEMD2009, 25-27 Sept. 2009, Chengdu, China, pp. 167-170.

YASA Motors, http://www.yasamotors.com/technology/products/, accessed on 5 Nov. 2010.

YASA Motors Ltd., *Pole Shoe Cooling*, Filed Patent Application EP 2 763 288 A2, 2013.

Yang, K.T., *Laminar Forced Convection of Liquids in Tubes with Variable Viscosity,* Heat Transfer, Vol. 84, pp. 353-362, Nov. 1962.

Yeadon, W.H., Frustaglio, B.M., *Current Density*, SMMA Fall Conference, 9-11 Nov. 2010, St. Louis.

Yovanovich, M.M., *New Contact and Gap Conductance Correlations for Conforming Rough Surfaces*, AIAA Paper No. 81-1164, AIAA 16th Thermophysics Conf., June 23-25, 1981, Palo Alto, CA, USA.

Yovanovich, M.M., *Thermal Contact Correlations*, Spacecraft Radiative Transfer and Temperature Control, Astronautics and Aeronautics, Vol. 83, 1982, pp. 83-95.

Yovanovich, M.M., Hegazy, A.A., and DeVaal, J., *Surface Hardness Distribution Effects Upon Contact, Gap and Joint Conductances*, AIAA 82-0887, AIAA/ASME 3rd Joint Thermophysics, Fluids, Plasma and Heat Transfer Conference, June 7-11, 1982, St. Louis, Missouri, USA.

Yovanovich, M.M., DeVaal, J., and Hegazy, A.A., *A Statistical Model to Predict Thermal Gap Conductance Between Conforming Rough Surfaces*, AIAA 82-0888, AIAA/ASME 3rd Joint Thermophysics, Fluids, Plasma and Heat Transfer Conf., June 7-11, 1982, St. Louis, Missouri, USA.

Yovanovich, M.M., Culham, J.R., Teertstra, P., *Calculating Interface Resistance*, Electronics Cooling, Vol. 3, No. 2., May 1997, pp. 24-29.

Yovanovich, M.M., *Four Decades of Research in Thermal Contact, Gap, and Joint Resistance in Microelectronics*, IEEE Trans. on Components and Packaging Tech., Vol. 28, 2005, pp. 182-206.

Yovanovich, M.M., *Micro and Macro Hardness Measurements, Correlations, and Contact Models*, 44th AIAA Aerospace Sciences Meeting and Exhibit., 9-12 Jan. 2006, Reno, Nevada, USA, pp.1-28.

Zienkiewicz, O.C., and Cheungm Y.K., *Finite elements in the solution of field problems*, The Engineer, 1965, pp.507-510.

Zhang, .S., Xu, J., Junak, J., Fiederling, D., Sawczuk, G., Koch, M., Schalja, A., Podack, M., Baumgartner, J., *Permanent Magnet Technology for Electric Motors in Automotive Applications*, 2012 2nd Int. Electric Drives Production Conf. (EDPC), 15-18 Oct. 2012, Nuremberg, Germany, pp. 1-11.

Zhang, Z., Profumo, F., Tenconi, A., *Axial flux versus radial flux permanent magnet motors*, Electromotion, Vol. 3, 1996, pp. 134-140.

Zhurkov, S.N., *Kinetic Concept of the Strength of Solids*, Int. J. Fracture Mechanics, Vol. 1, No. 4, Dec. 1965, pp. 311-322.

Appendix

A1: Calibration and Uncertainty

The experiments produced in this thesis involved oil flowing through a test piece, which was subjected to a heat source and temperature measurements using T-type thermocouples or thin film gauges. The experimental procedures were described in Section 5.4, Section 6.4, Section 7.3. This section goes through each instrument used for measurement and describes the calibration process it required, and the uncertainty of measurement associated with it.

A1.1. T-type Thermocouples: Calibration

This thesis produced experiments in which the temperature of various components was measured using T-Type thermocouples. Such experiments were demonstrated in Section 5.4 of Chapter 5, Section 6.4 of Chapter 6 and Section 7.3 of Chapter 7. All T-type thermocouples were calibrated in an accurate temperature controlled Carbolite oven for temperatures between 20 ^{o}C - 150 ^{o}C. The thermocouples and Pico data logging system were calibrated against a PT100 temperature probe with an accuracy of $\pm$ 0.05 K. The oven hysteresis was measured at 0.1 K while the thermocouple offset was measured at 0.33 K.

A1.2. T-Type thermocouples: Uncertainty of Measurement

The standard deviation σ_T of the steady state temperature measurements logged over an hour at a rate of 1 Hz was 0.18 K and the random uncertainty of steady state temperature measurements as defined in Bell (2011) was estimated at 0.006 K

The systematic uncertainty of a temperature measurement is defined in terms of the uncertainty in the thermocouple offset $u(T_{\mathrm{TC}})$, the reference temperature accuracy to which the thermocouples are calibrated $u(T_{\mathrm{RT}})$, and the oven temperature hysteresis $u(T_{\mathrm{OH}})$ during calibration. The temperature systematic uncertainty $\mathrm{u(T)}_{sys}$was therefore calculated as:

$$\mathrm{u(T)}_{sys} = \sqrt{[u(T_{\mathrm{TC}})]^2 + [u(T_{\mathrm{RT}})]^2 + [u(T_{\mathrm{OH}})]^2} \qquad \text{eqn. A4}$$

The temperature systematic uncertainty was calculated as 0.35 K. The overall uncertainty in temperature measurement is hence expressed as:

$$u(T) = \sqrt{u(T)_{rand}^2 + u(T)_{sys}^2} \qquad \text{eqn. A5}$$

The overall uncertainty of temperature measurements are calculated at 0.35 K.

A 1.3. The Variable Area Flow Meter: Calibration

Variable area flow meters were used to measure the flow rate of oil coolant through the test piece. Variable area flow meters are calibrated by the manufacturer for water flow rate at a temperature of 20 ^{o}C. To account for the oil flow through the meter, and the variation in the properties of Opticool fluid with temperature a recalibration process of the flow meters at various inlet temperatures was performed. The calibration of variable flow meters is classified by weight or by volume in Standards APTI435 and ISA-RP16.6-1961. In this thesis the two procedures were followed. The calibration setup is shown in Figure A.1. The flow pump was started with the 3-way valve (6) positioned to allow the oil to recirculate. The valve is shifted to the measuring cylinder and with the position of the flow meter noted, the mass and volume of the fluid collected were measured and timed.

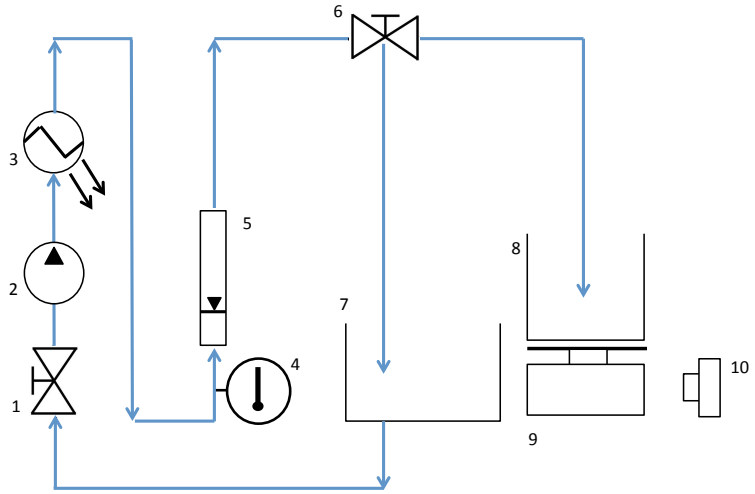


Figure A.1. Schematic showing flow meter calibration by mass using 1) gate valve, 2) pump, 3) heat exchanger, 4) thermometer, 5) flow meter, 6) 3-way valve, 7) reservoir, 8) collecting beaker, 9) scales, 10) video camera

The calibration process was repeated for two flow meters designated ‘A’ and ‘B’ respectively. Flow meter ‘A’ had original water flow rate ranging between 0.2-2 lpm, while flow meter ‘B’ had original water flow rate ranging between 2-22 lpm. For each

flow meter the calibration curves were for three different oil temperatures were established. An excel sheet to interpolate the flow rate at any temperature and float position was developed for each of the flow meters. Figure A.2 shows the calibration chart for a flow meter designated 'A' with original water flow rate range between 0.2 – 2 lpm. Figure A.2. shows the calibration chart for a flow meter designated 'B' with original water flow rate range between 2 – 22 lpm.

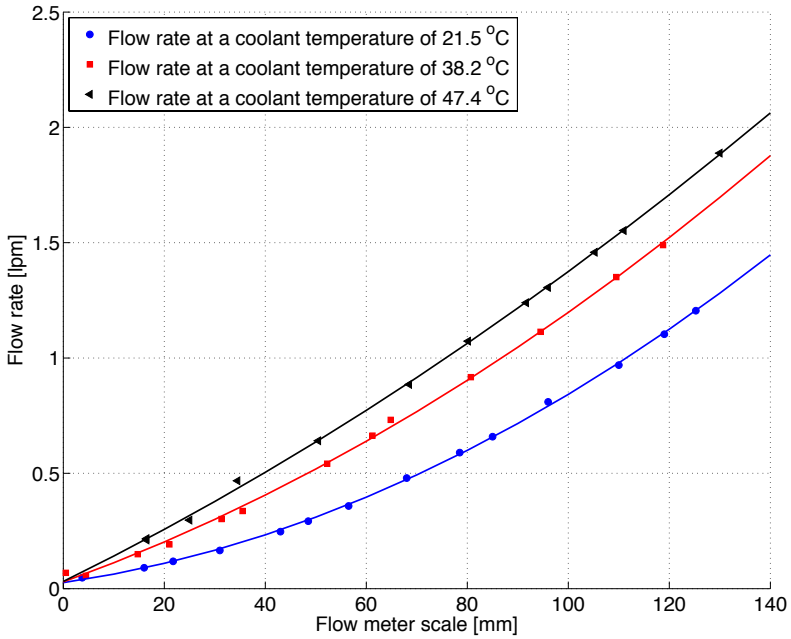


Figure A.2. Calibration chart for flow meter A (originally calibrated for a water flow rate range between 0.2-2 lpm at 20 °C).

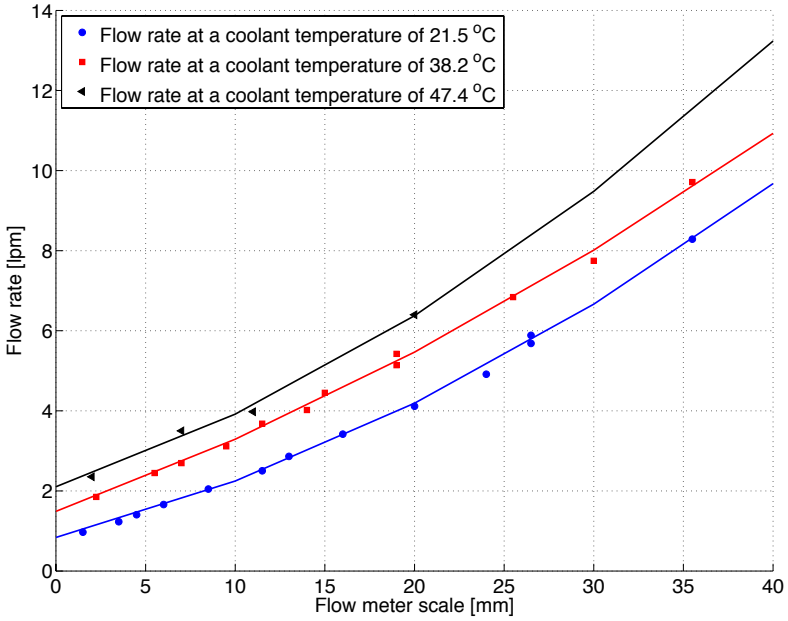


Figure A.3. Calibration chart for flow meter B (originally calibrated for a water flow rate range between 2-22 lpm at 20 °C).

A1.4. Variable Area Flow Meter: Uncertainty of Measurement

As the flow rate curves vary with temperature, the maximum uncertainty in measurement is reported. The uncertainty in measurement of the flow meter *u(Q)* was calculated using:

$$u(Q) = \sqrt{[u(V).t]^2 + [u(t).V]^2 + \left[u(Q_{fm})\right]^2} \qquad \text{eqn. A6}$$

u(V) is the uncertainty of the readings from the volume beaker. The reading error is estimated ±5 mL. V is the measured volume, set to 900 mL. *u(t)* is the uncertainty in the time measurement. This was done using a stopwatch with a reading error of ±1 s. (Note: to measure the uncertainty time is required in minutes to keep units consistent with flow rate measured in litres/min). *t* is the time taken to calibrate each point. This was kept at 1 min. The uncertainty in the flow meter $u(Q_{fm})$ was ±0.1 l/min. The systematic uncertainty of the measured flow rate was therefore computed to ±0.1 l/min.

A1.5. Cartridge Heat Sources: Uncertainty of Measurement

In the experiments demonstrated in Sections 5.4 of Chapter 5 and Section 6.4 of Chapter 6, cartridge heaters were used to simulate the internal heat generation of pole pieces and raise their temperature. Off the shelf components were used and no further calibration was required. The heating power injected into each pole piece was calculated by the multiplication of the measured current I and voltage V. The systematic uncertainty for the power injected in the pole pieces is defined as:

$$\mathrm{u(P)} = \sqrt{[u(V).I]^2 + [u(I).V]^2} \qquad \text{eqn. A7}$$

The uncertainty in the voltage meter $u(V)$ was measured at $\pm 0.2\,V$ while the uncertainty in the current meter $u(I)$ was $\pm 0.01\,mA$. The uncertainty of heat input was found to range between 4 mW at a low heat input and 33 mW at a high heat input.

A1.6. Thin Film Heat Flux Gauges: Calibration

In Section 6.4.2 of Chapter 6, the calibration process was described. During the calibration process, the instrumented test piece was sealed in a plastic bag and placed in a water bath. The water bath temperature was increased from 20 ^{o}C to 45 ^{o}C in steps of 5 ^{o}C. The pole piece temperature and water bath temperature were monitored

to ensure isothermal conditions. The temperatures and resistances of the thin film gauges were recorded. The resistance of the gauges was expressed as:

$$R_{calib} = R_o + \alpha . T_{calib} \qquad \text{eqn. A8}$$

The linear relationship of each gauge resistance was plotted against the known set of temperatures. The temperature coefficient α and reference resistance R_o for each gauge is extracted. An example of a typical calibration chart for one thin film heat flux gauge was shown in Section 6.4.2, this section shows the calibration charts for every gauge. The instrumentation consists of eight pairs of thin film gauges (on top and below the insulating substrate), on each side of the pole pieces. Gauges 23 and 28 were found defective and therefore this section shows 30 calibration charts, one for each of the remaining gauges.

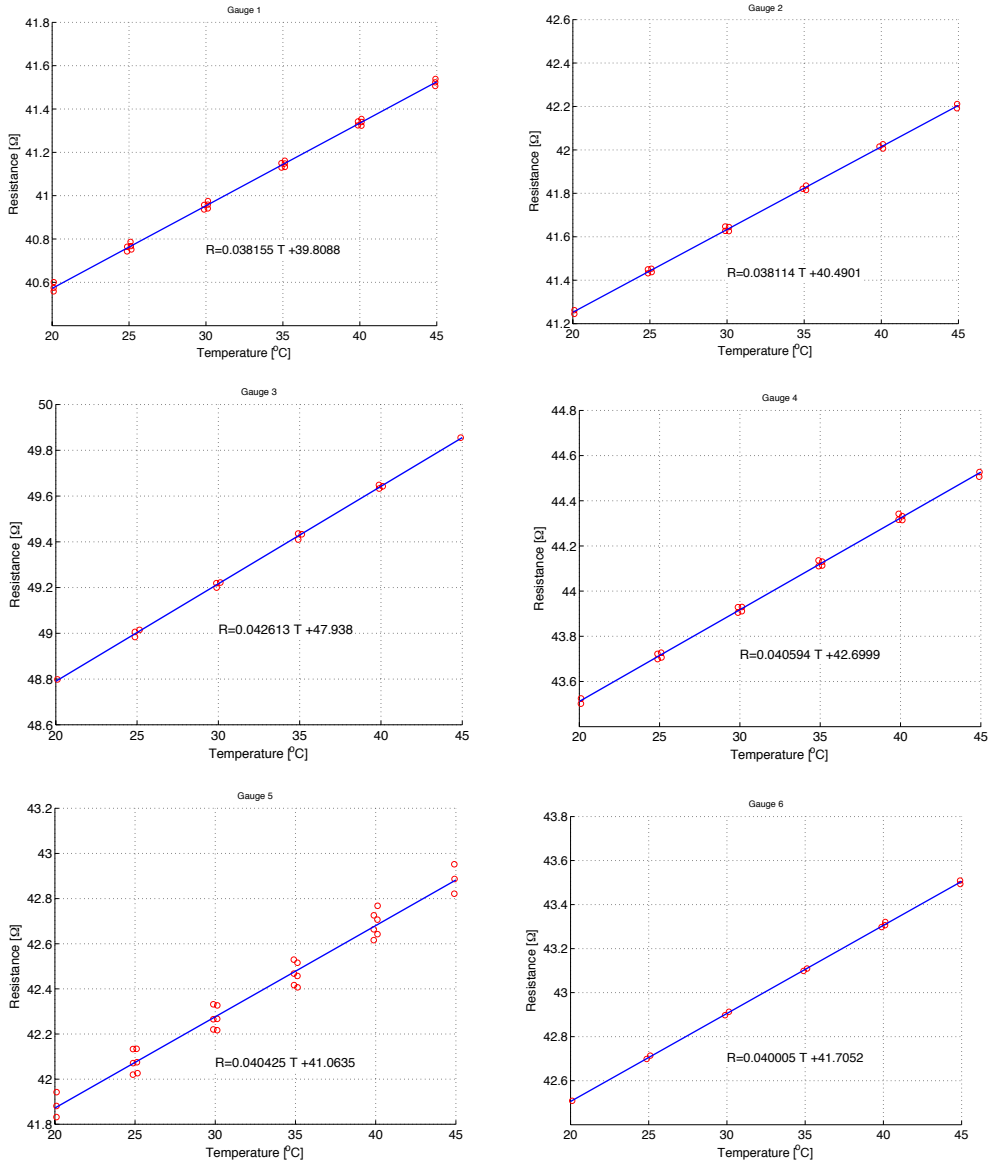


Figure A.4. Calibration charts for a thin film gauges 1-6

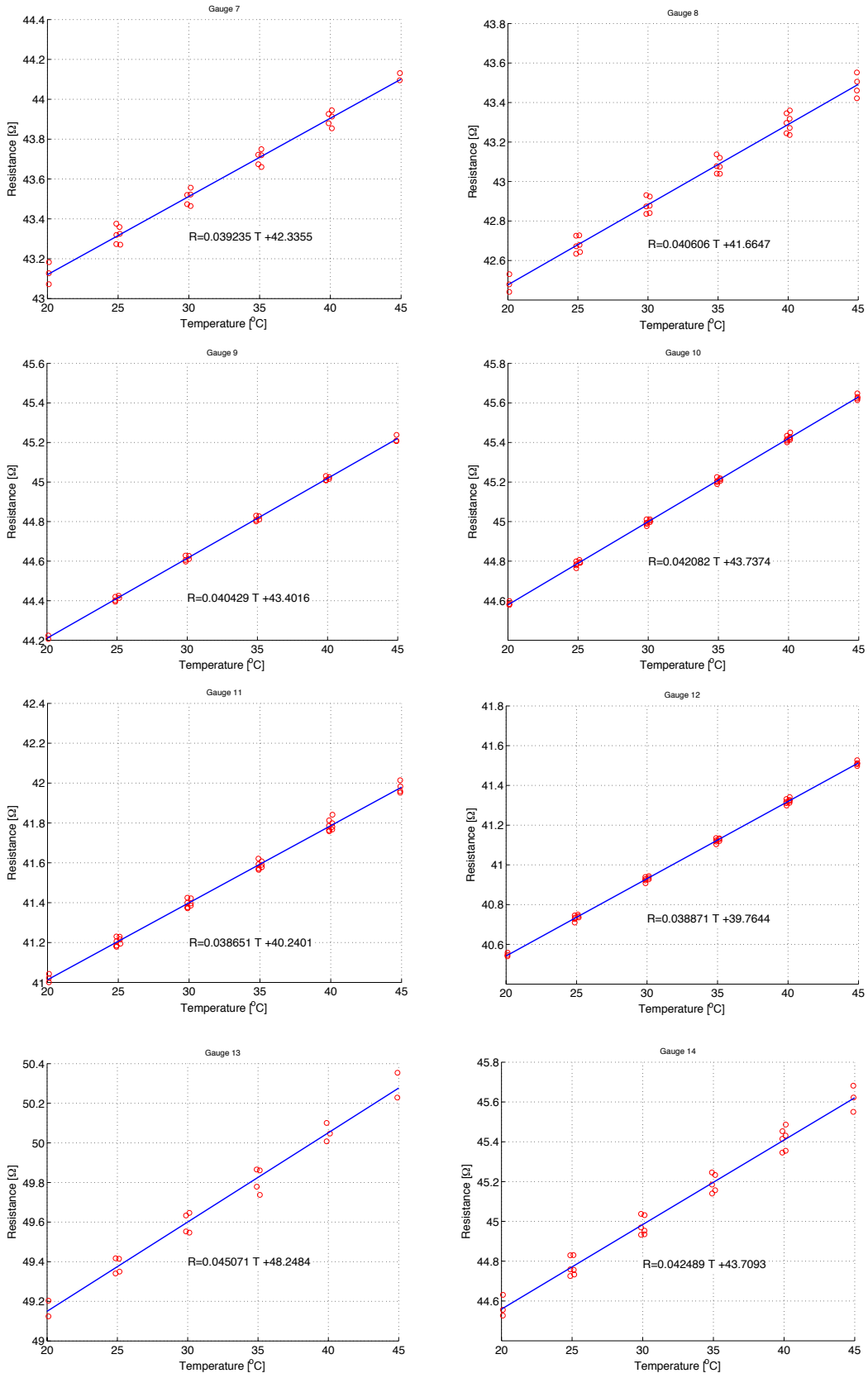


Figure A.5. Calibration charts for a thin film gauges 7-14

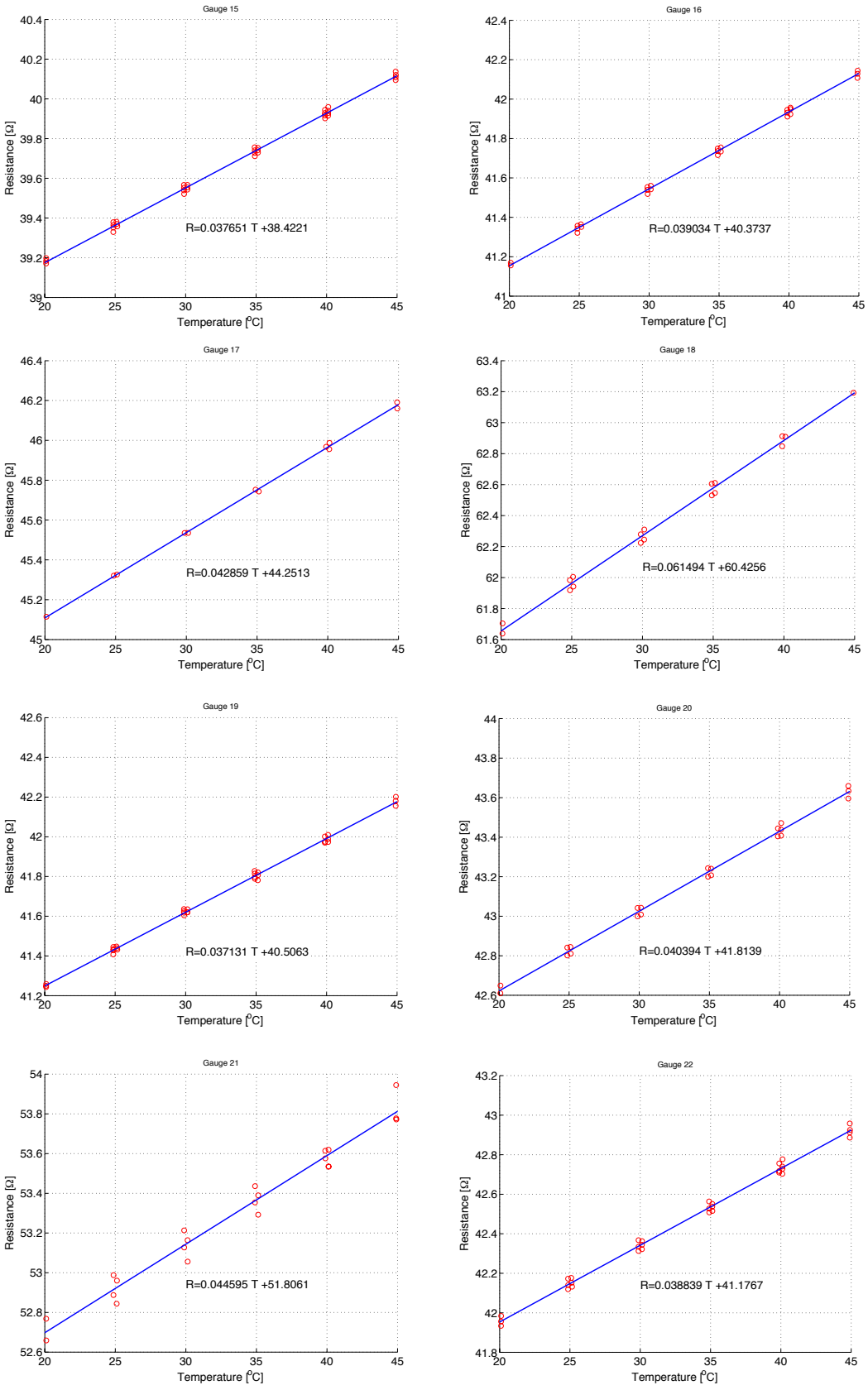


Figure A.6. Calibration charts for a thin film gauges 15-22

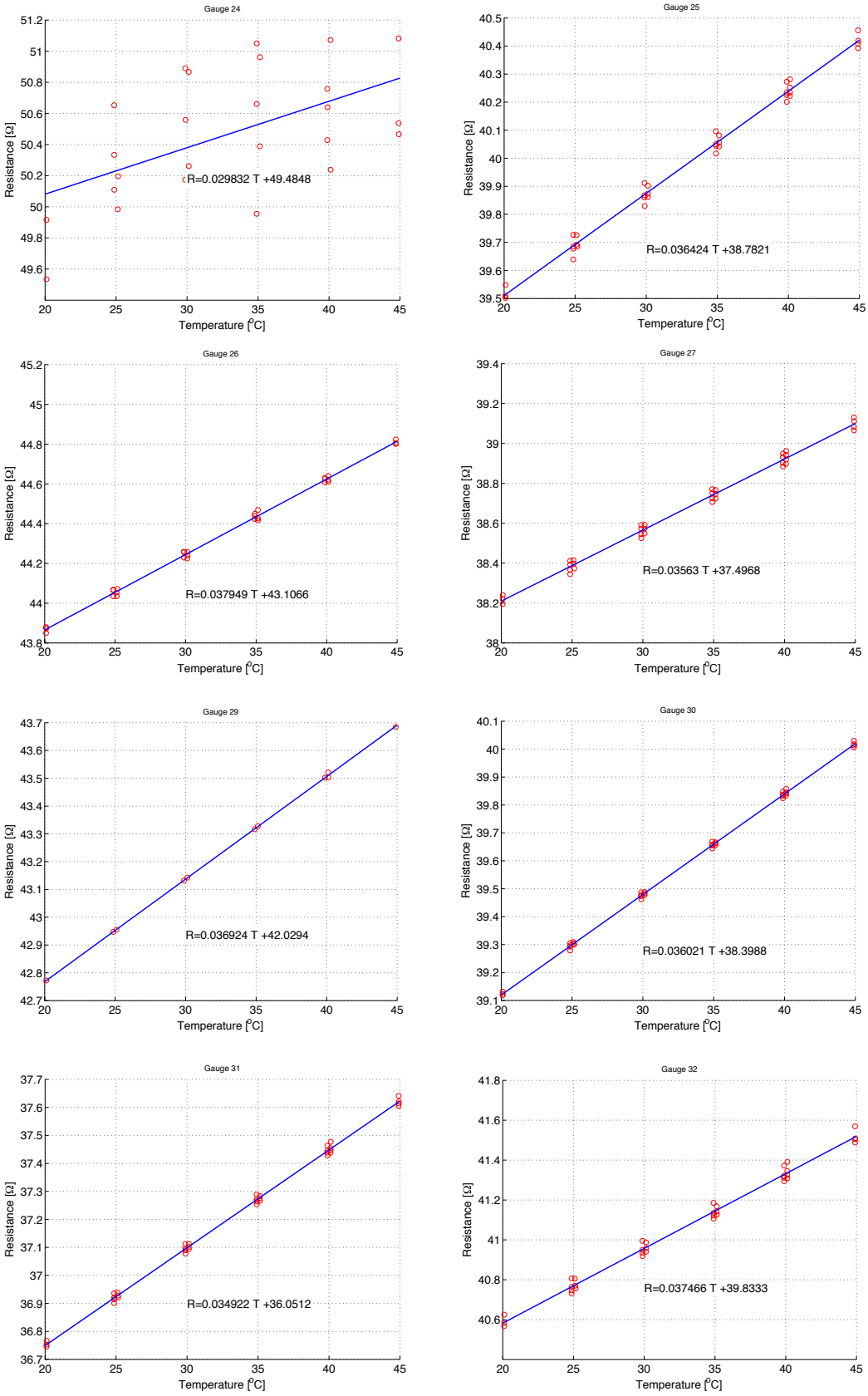


Figure A.7. Calibration charts for a thin film gauges 24-27, 29-32

A1.7. Thin Film Heat Flux Gauges: Uncertainty

In his work, Collins, (2015) estimates that the uncertainty of R_o is 3%. The regression analysis is estimated to have an uncertainty of 2-5%. Hence the estimation of the Nusselt number in this work has an uncertainty range of 5-8%.

A2: Post Processing TFHFG Data

In Section 6.5.1, it was shown that the data measured by the thin film heat flux gauges (TFHG) required significant post processing to check the accurate operation and derive the heat flux. Due to the vast amount of charts, only one example was demonstrated in the main text. Therefore this section presents the data processing involved. Section A2.1 presents the gauge resistance with block temperature. Section A2.2 maps the temperature difference across the insulation substrate from which the heat flux is calculated. Finally Section A2.3 shows the local heat transfer coefficient on the pole piece surfaces along the flow channel, at different flow rates and inlet temperatures.

A2.1 TFHFG – Gauge Electrical Resistance with Temperature

In Section 6.5.1 it was discussed how for each experimental setup, the gauge resistance was plotted with block temperature. This ensured that the gauges behaved as expected. While an example of this was given within the text in Figure 6.7, the full data set is presented in this section.

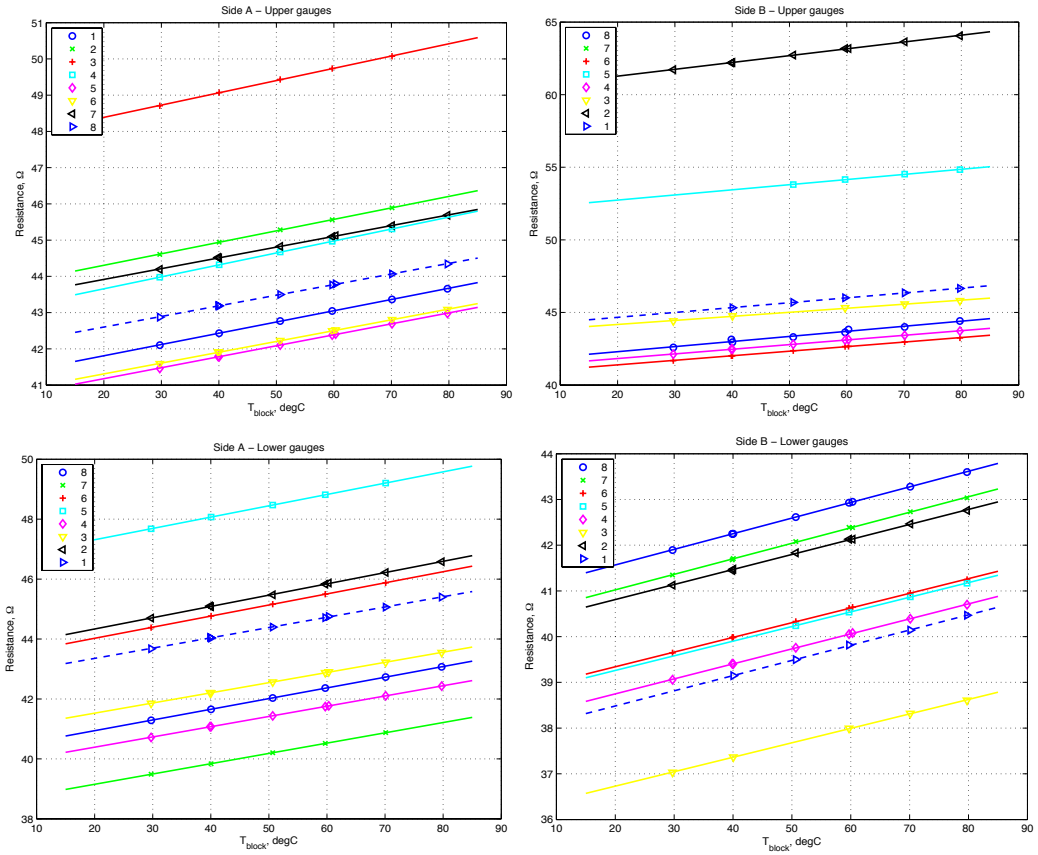


Figure A.8. Resistance with temperature for a flow rate of 2.2 lpm and inlet temperature of 26 ^{o}C

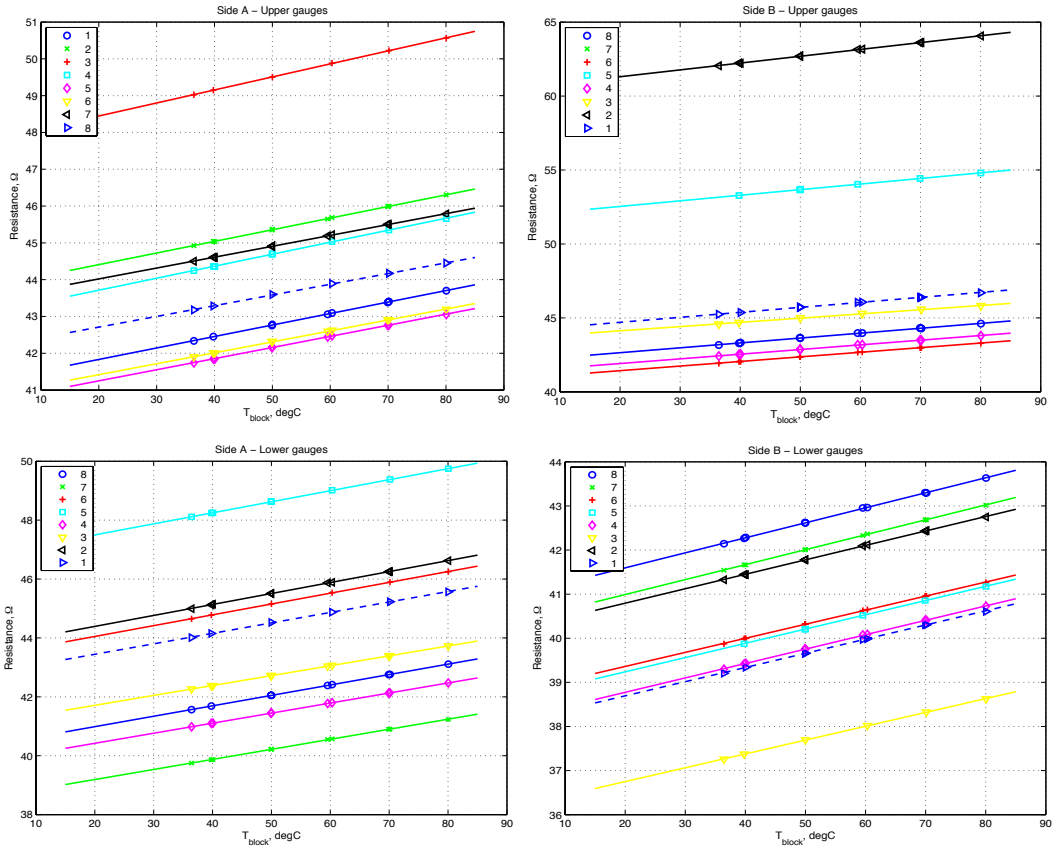


Figure A.9. Resistance with temperature for a flow rate of 2.6 lpm and inlet temperature of 38 ^{o}C

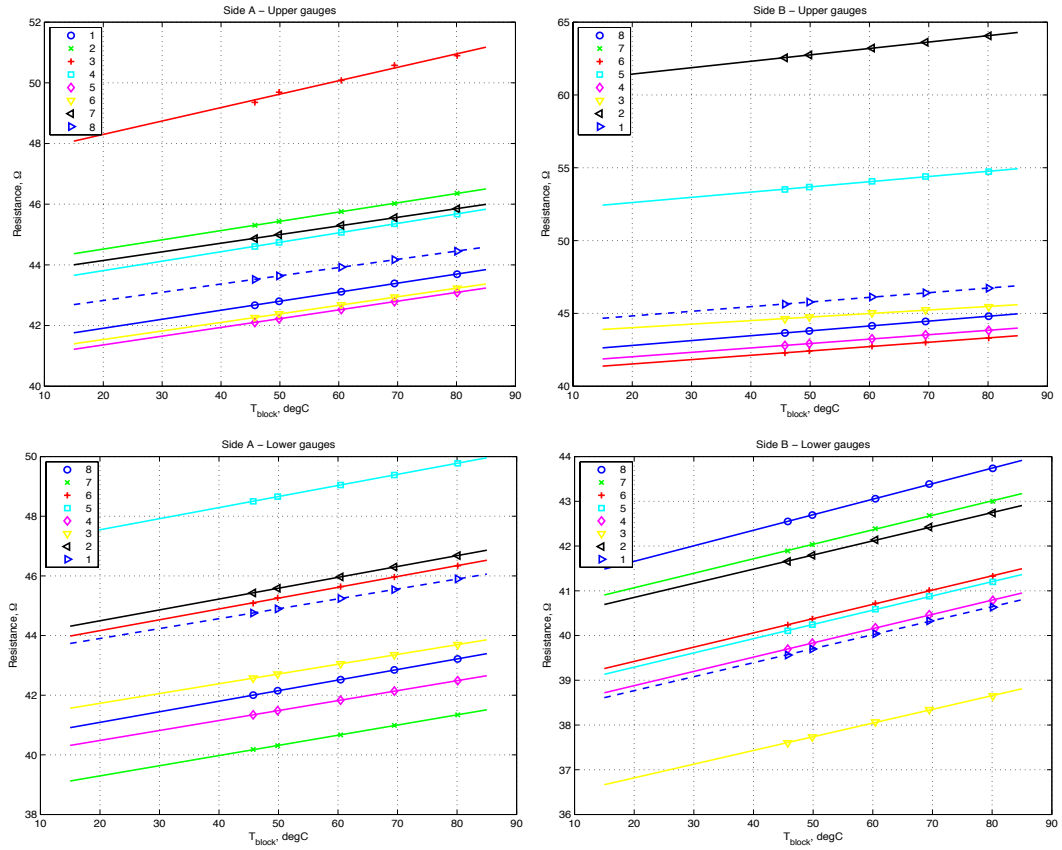


Figure A.10. Resistance with temperature for a flow rate of 2.4 lpm and inlet temperature of 41.1 ^{o}C

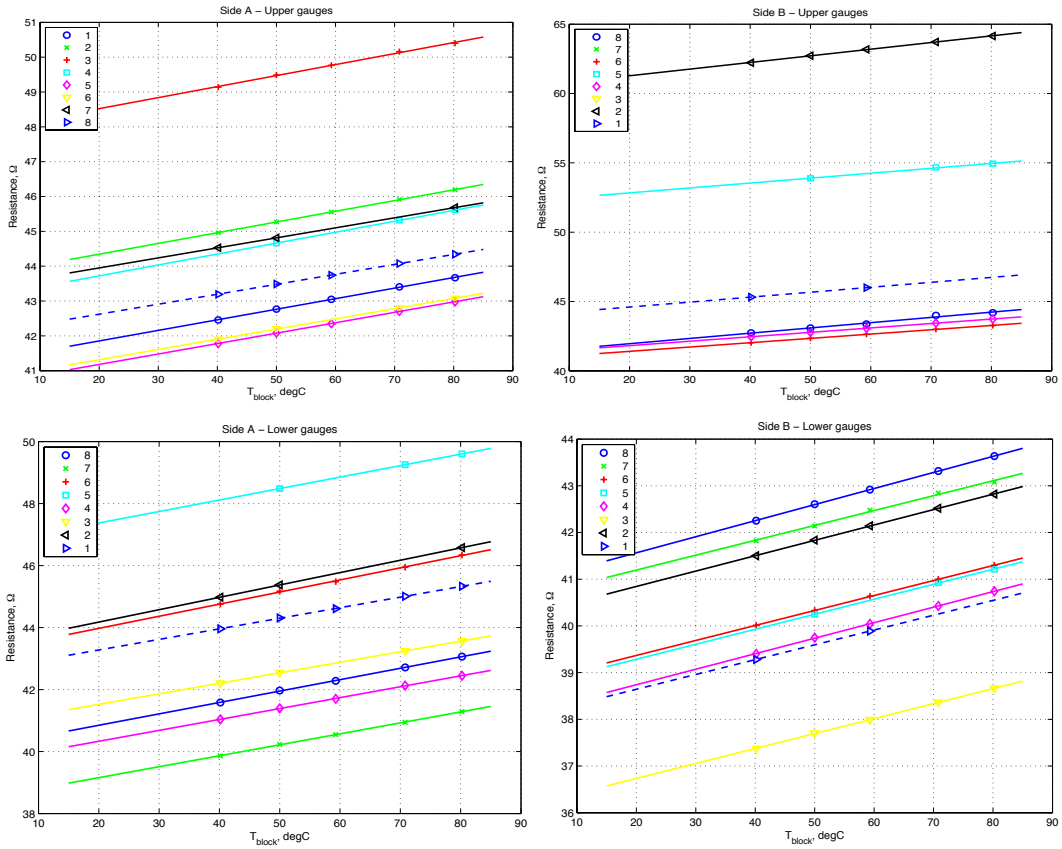


Figure A.11. Resistance with temperature for a flow rate of 3.5 lpm and inlet temperature of 26.5 ^{o}C

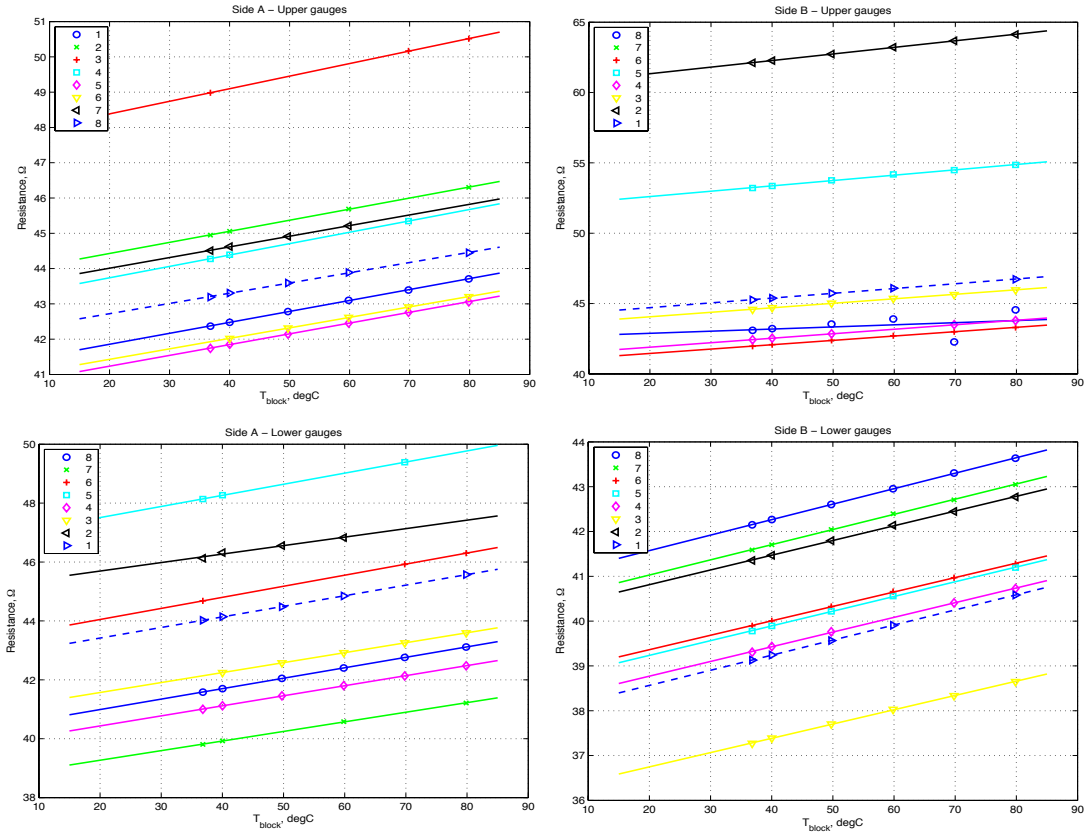


Figure A.12. Resistance with temperature for a flow rate of 3.8 lpm and inlet temperature of 37.7 ^{o}C

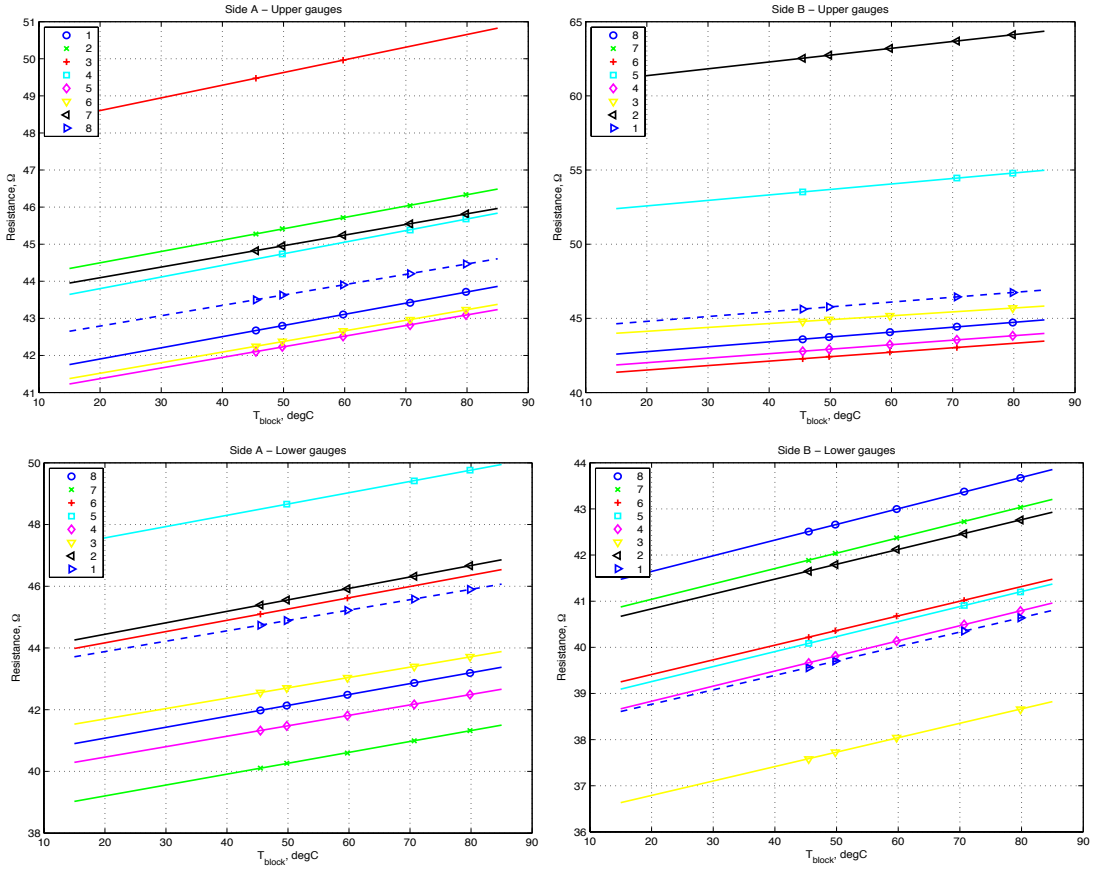


Figure A.13. Resistance with temperature for a flow rate of 3.6 lpm and inlet temperature of 42.6 ^{o}C

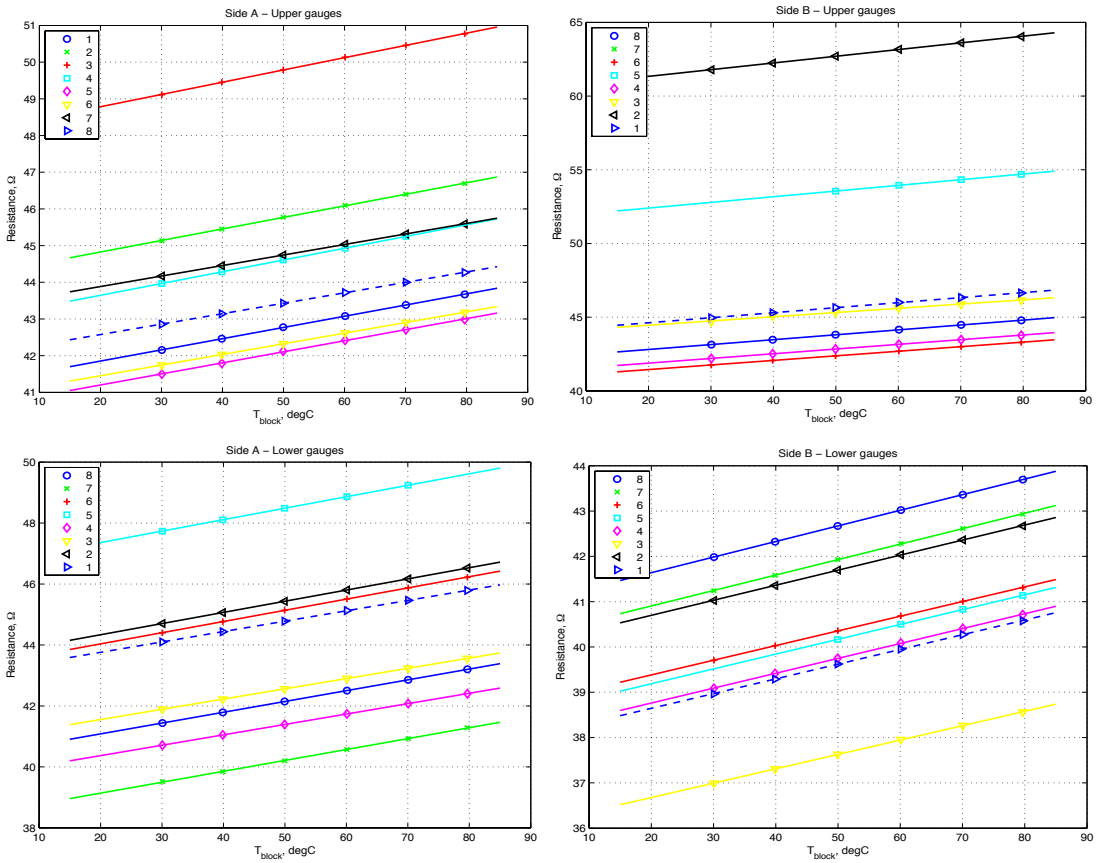


Figure A.14. Resistance with temperature for a flow rate of 4.7 lpm and inlet temperature of 28.3 ^{o}C

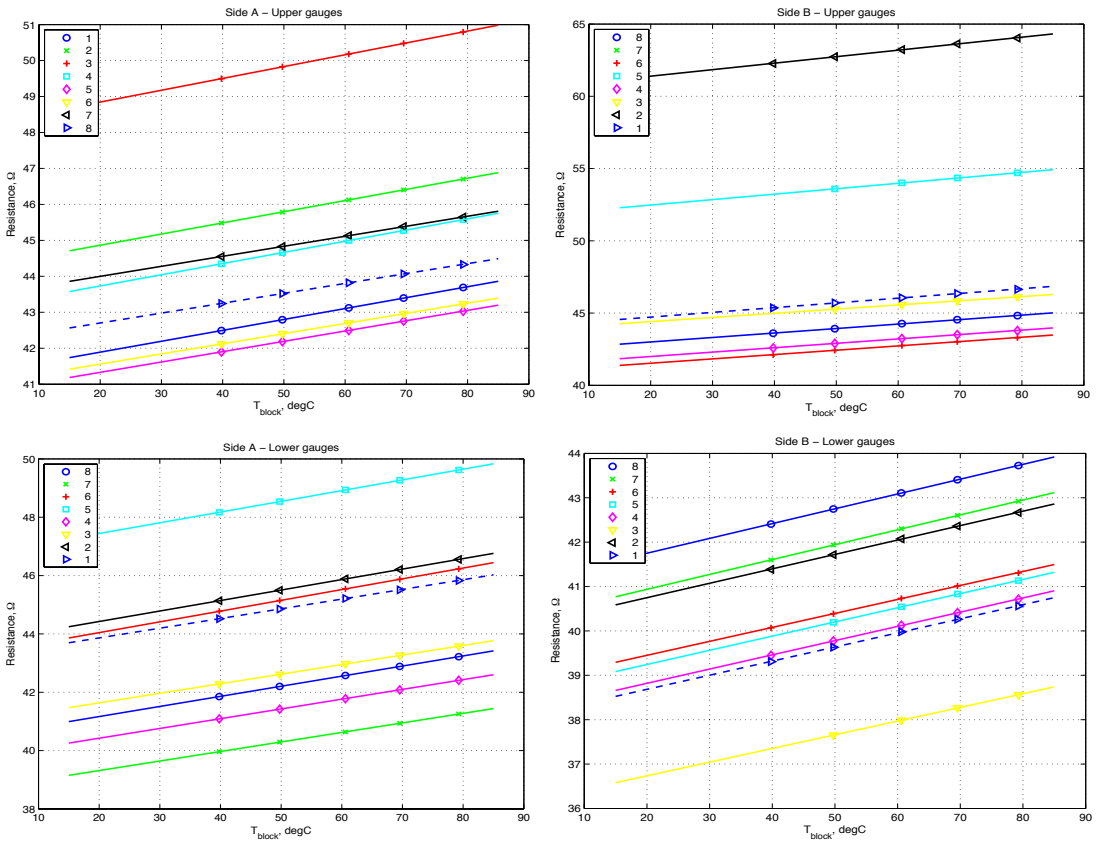


Figure A.15. Resistance with temperature for a flow rate of 5 lpm and inlet temperature of 35.5 ^{o}C

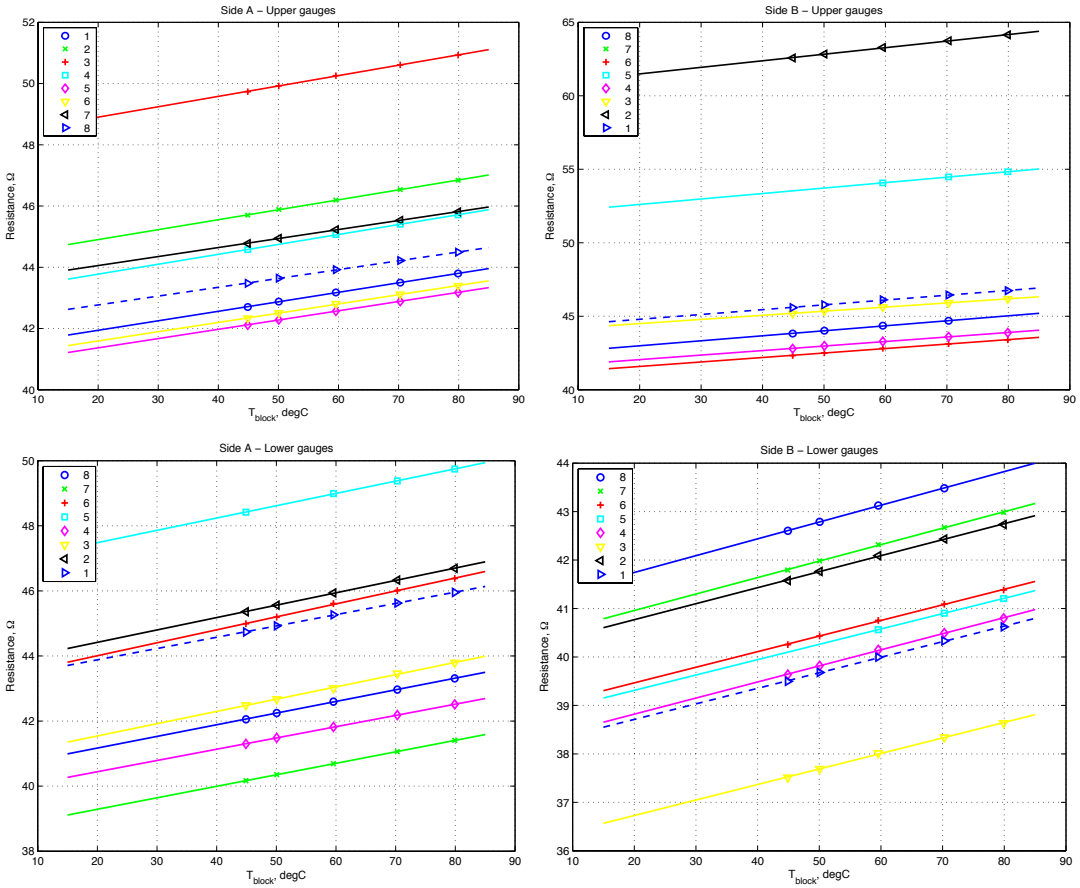


Figure A.16. Resistance with temperature for a flow rate of 6.6 lpm and inlet temperature of 45 ^{o}C

A2.2 TFHFG – Δ*T* across upper and lower gauges and heat flux

In section 6.5.1 it was shown that the temperature difference across the upilex film is derived and the heat flux for each location estimated. An example of this process for one set (upper and lower) film gauges mounted on one side at a particular experiment condition was given in Figure 6.8. The Figures below show the whole data set for each of the 8 sets of film gauges fixed on each side of the pole piece, at every experimental condition.

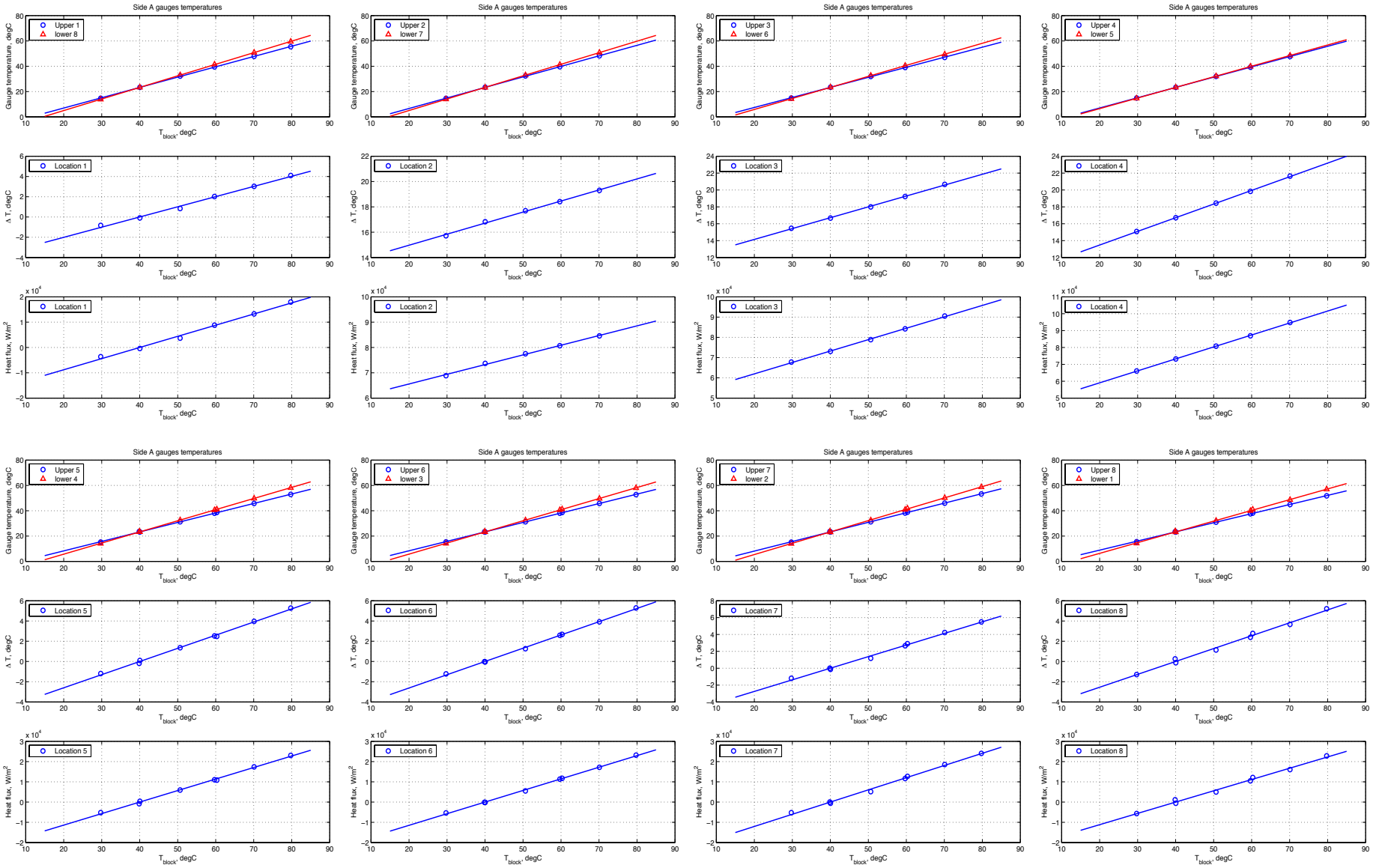


Figure A.17. Temperature difference and heat flux across the sensors mounted on side A for a flow rate of 2.2 lpm and inlet temperature of 26 ^{o}C

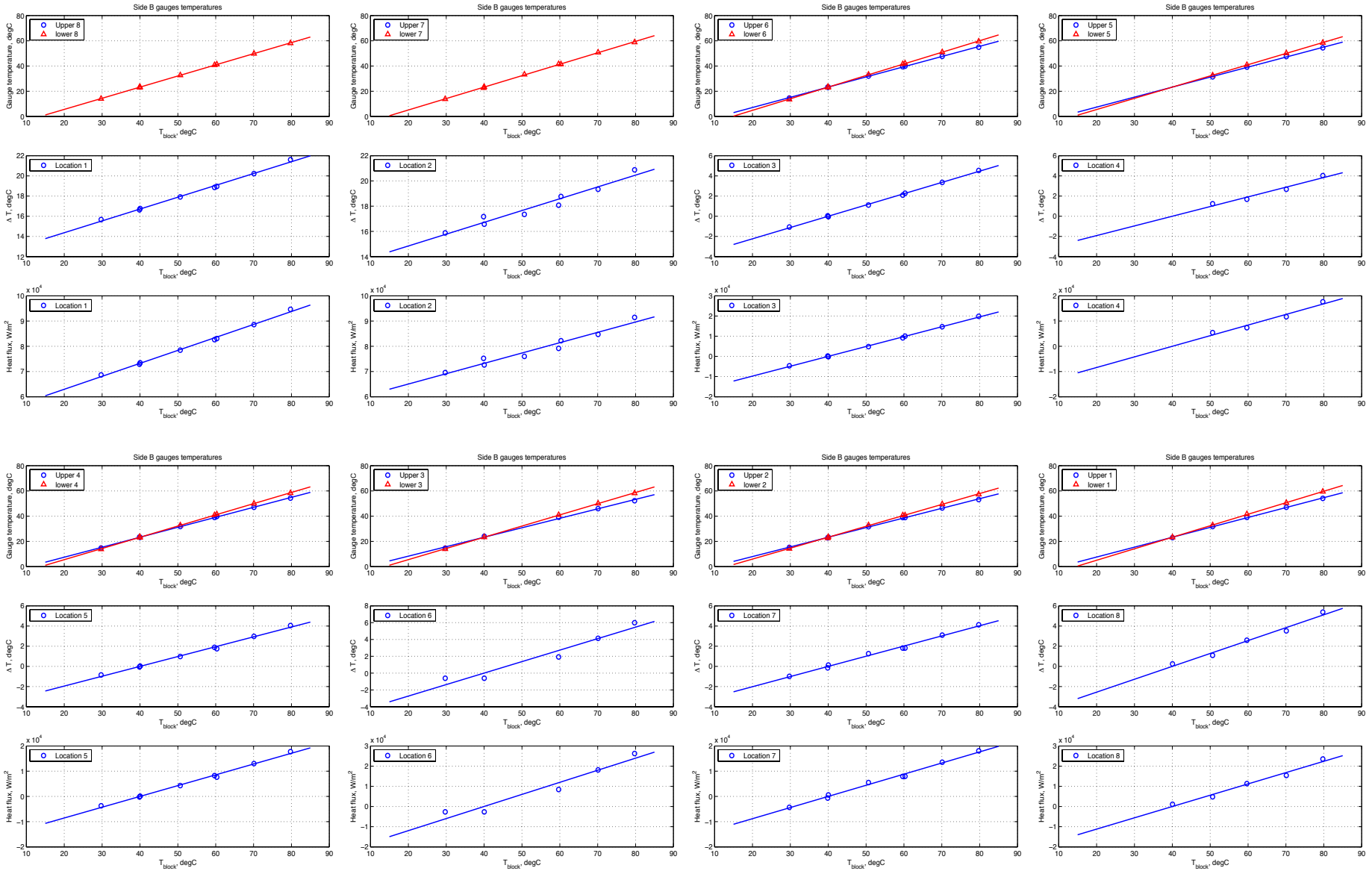


Figure A.18. Temperature difference and heat flux across the sensors mounted on side B for a flow rate of 2.2 lpm and inlet temperature of 26 ^{o}C

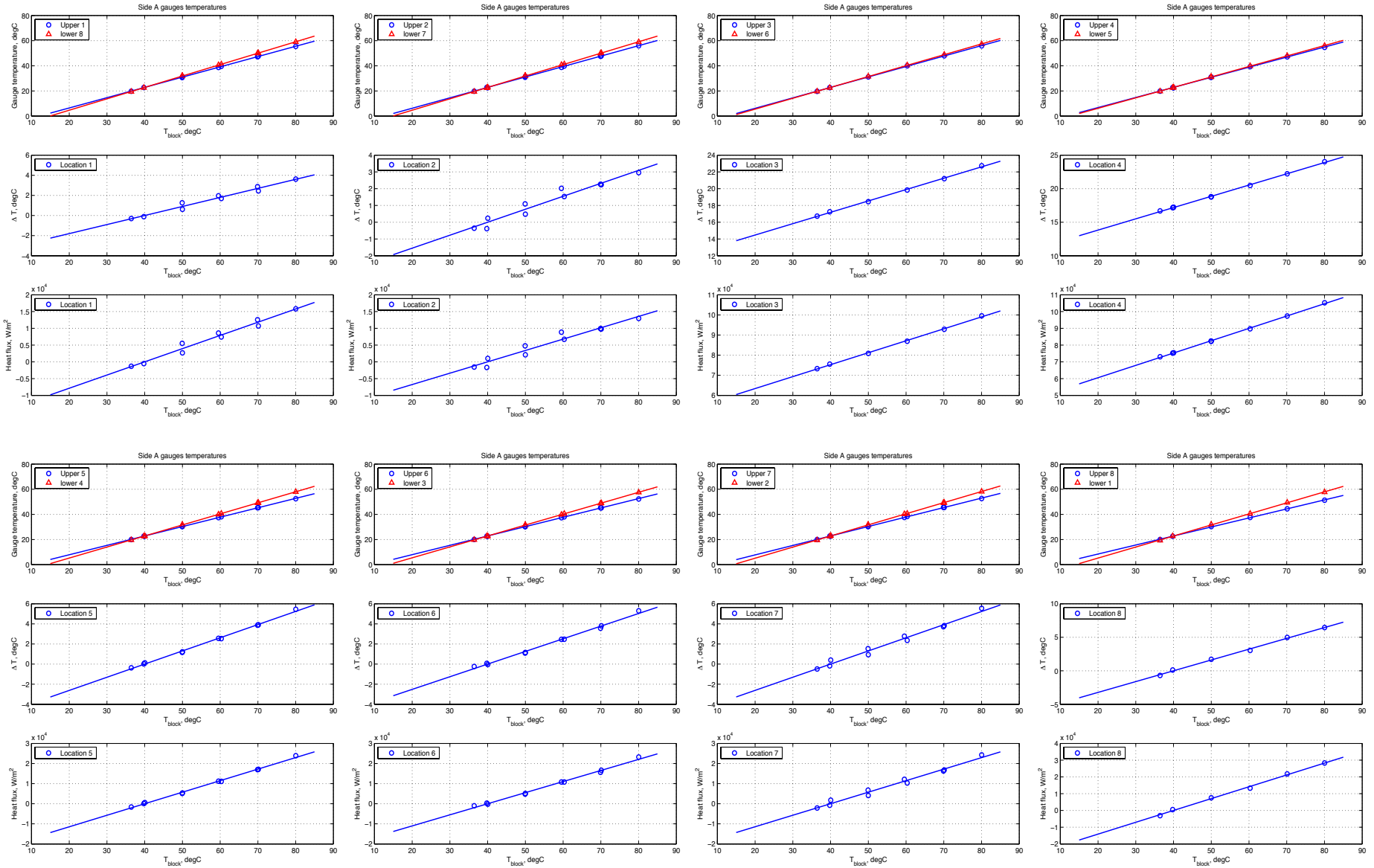


Figure A.19. Temperature difference and heat flux across the sensors mounted on side A for a flow rate of 2.6 lpm and inlet temperature of 38 ^{o}C

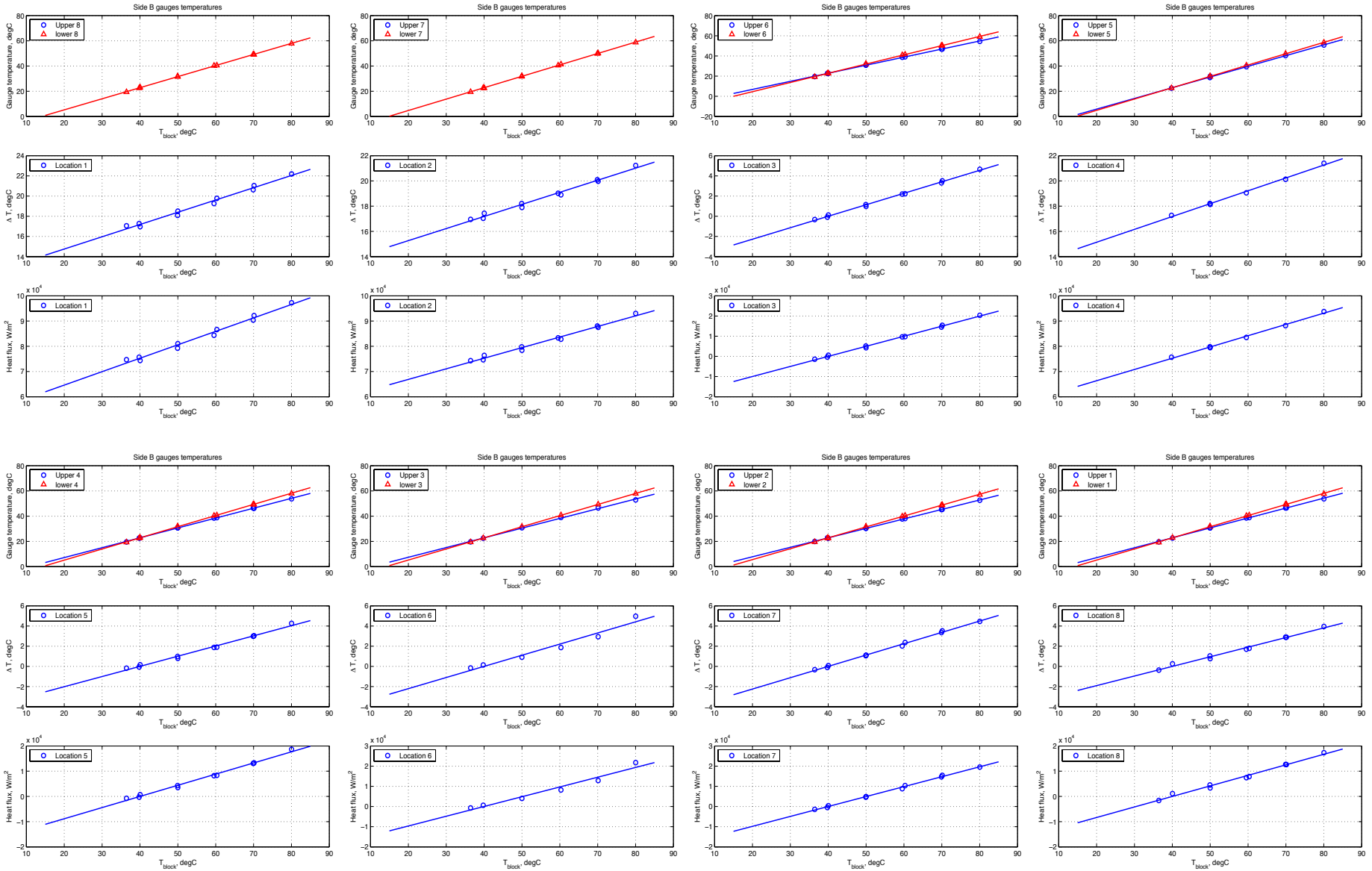


Figure A.20. Temperature difference and heat flux across the sensors mounted on side B for a flow rate of 2.6 lpm and inlet temperature of 38 ^{o}C

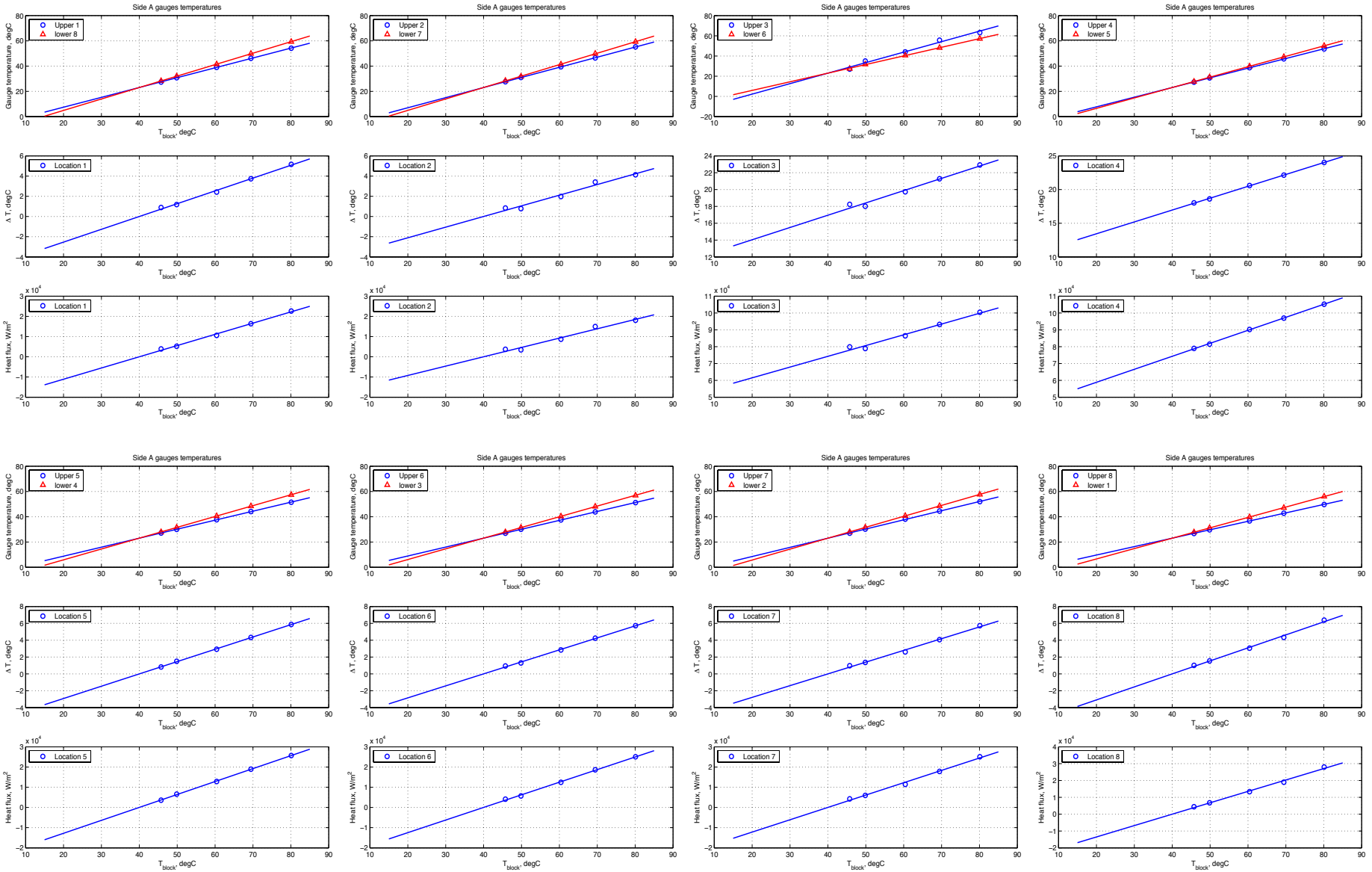


Figure A.21. Temperature difference and heat flux across the sensors mounted on side A for a flow rate of 2.4 lpm and inlet temperature of 41.1 ^{o}C

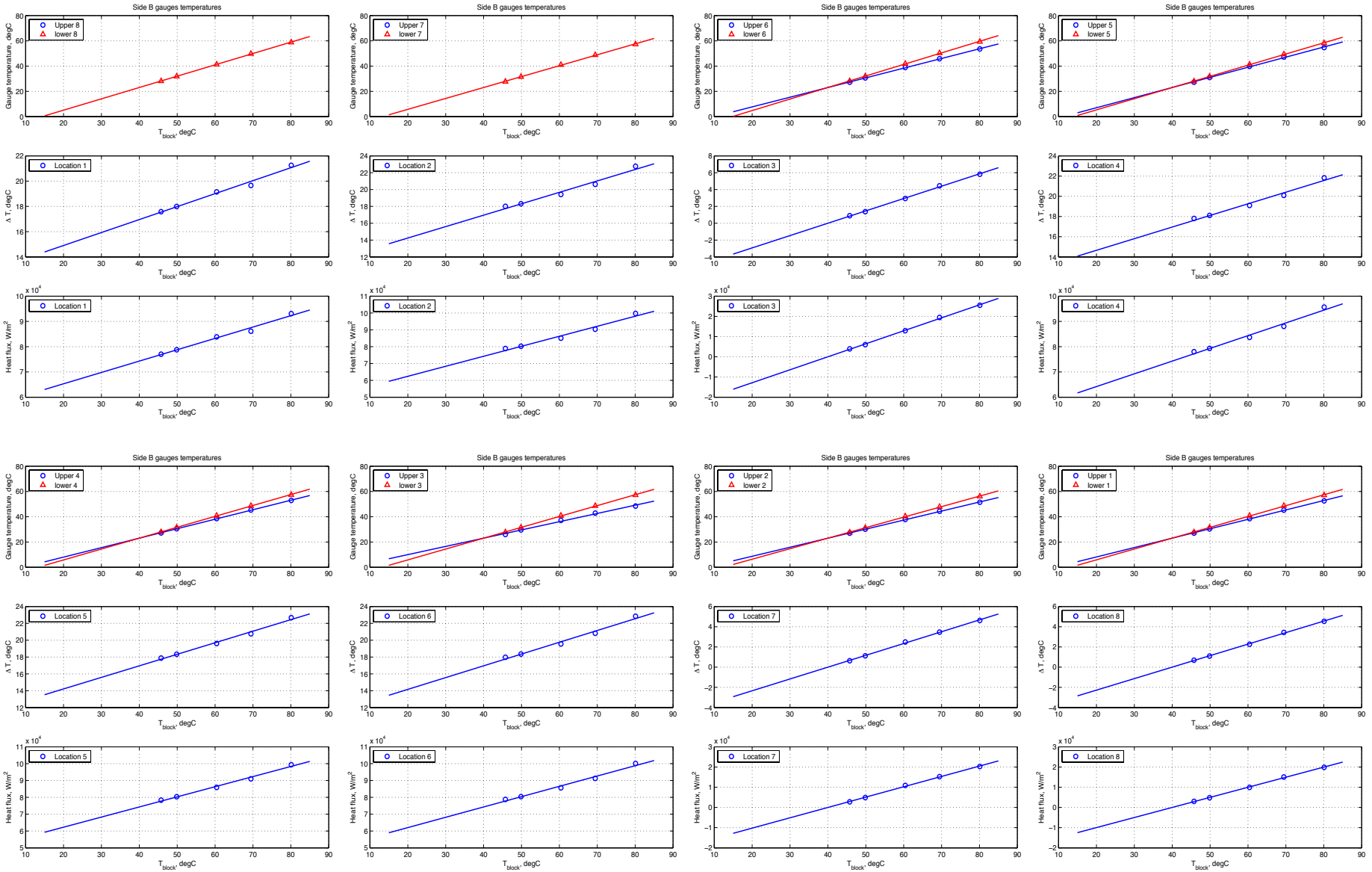


Figure A.22. Temperature difference and heat flux across the sensors mounted on side B for a flow rate of 2.4 lpm and inlet temperature of 41.1 ^{o}C

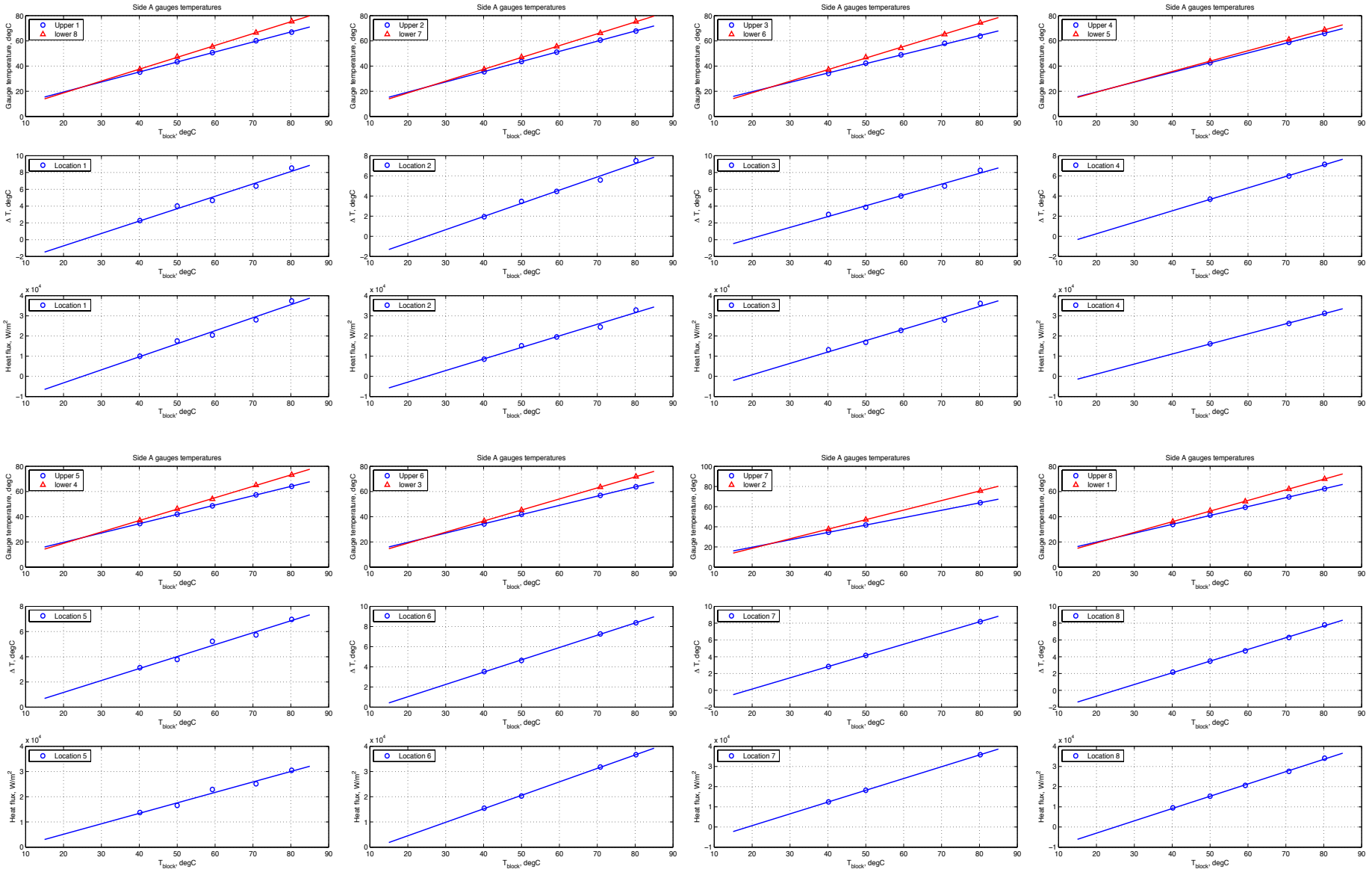


Figure A.23. Temperature difference and heat flux across the sensors mounted on side A for a flow rate of 3.5 lpm and inlet temperature of 26.5 ^{o}C

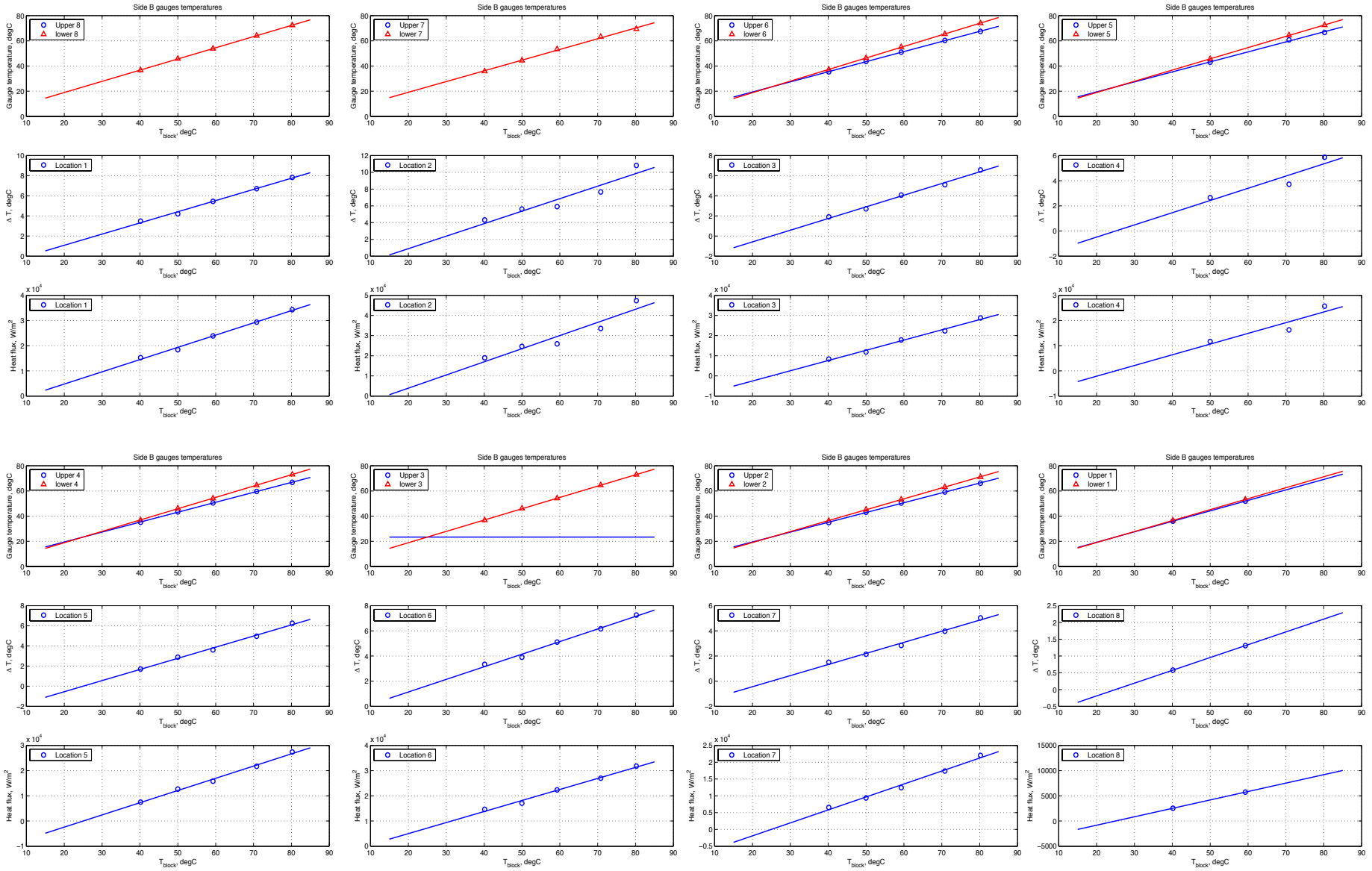


Figure A.24. Temperature difference and heat flux across the sensors mounted on side B for a flow rate of 3.5 lpm and inlet temperature of 26.5 ^{o}C

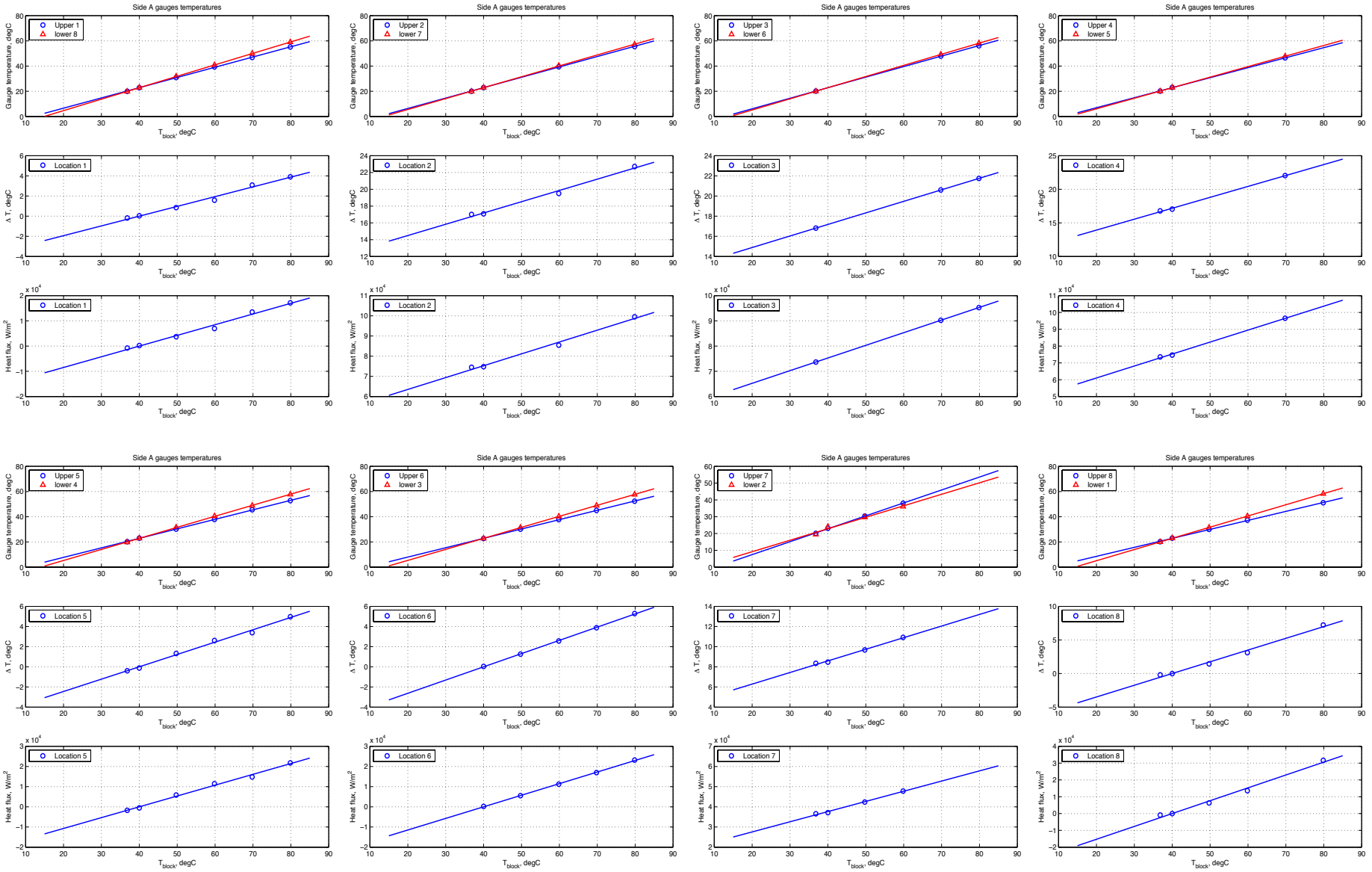


Figure A.25. Temperature difference and heat flux across the sensors mounted on side A for a flow rate of 3.8 lpm and inlet temperature of 37.7 ^{o}C

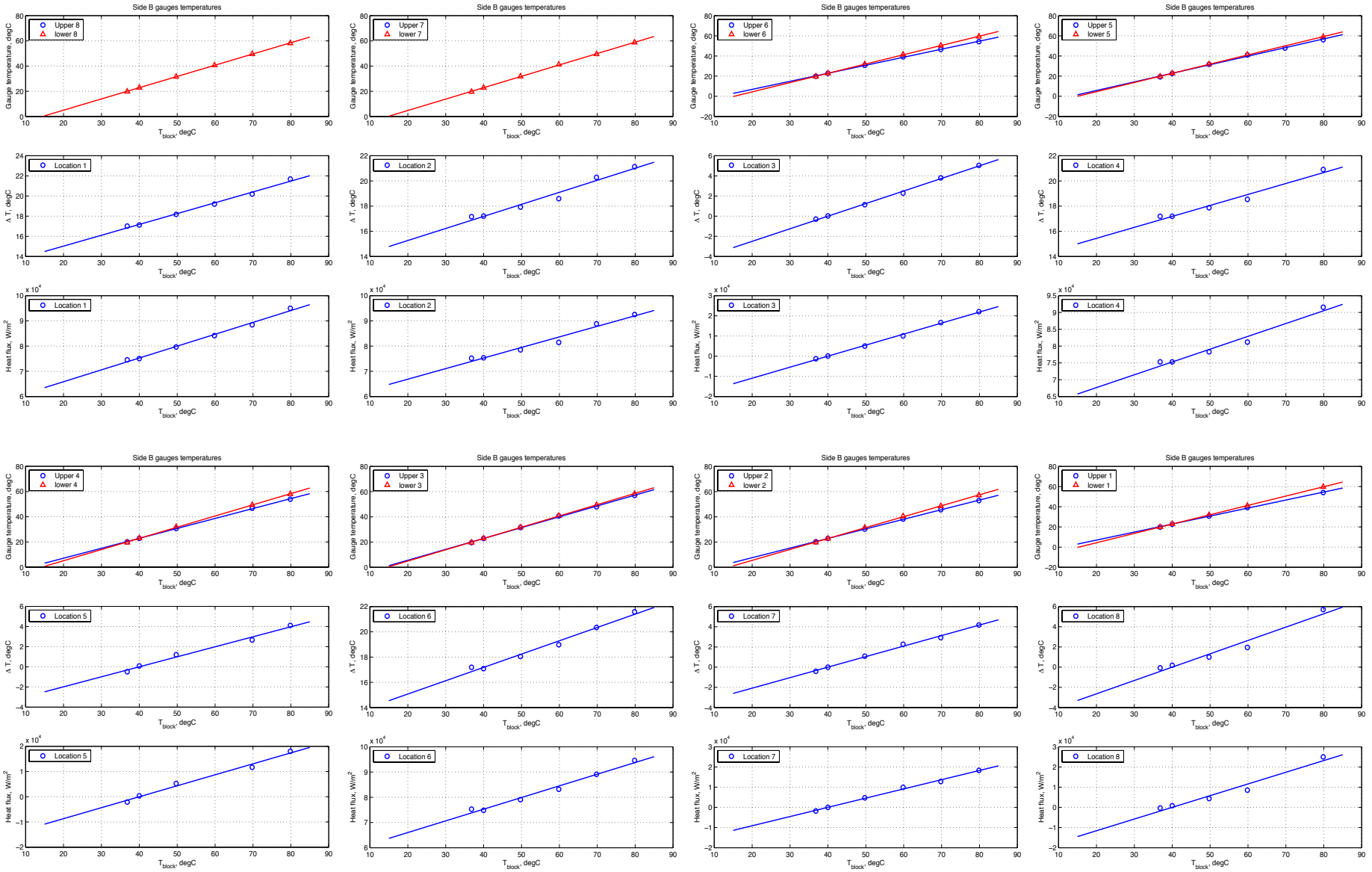


Figure A.26. Temperature difference and heat flux across the sensors mounted on side B for a flow rate of 3.8 lpm and inlet temperature of 37.7 ^{o}C

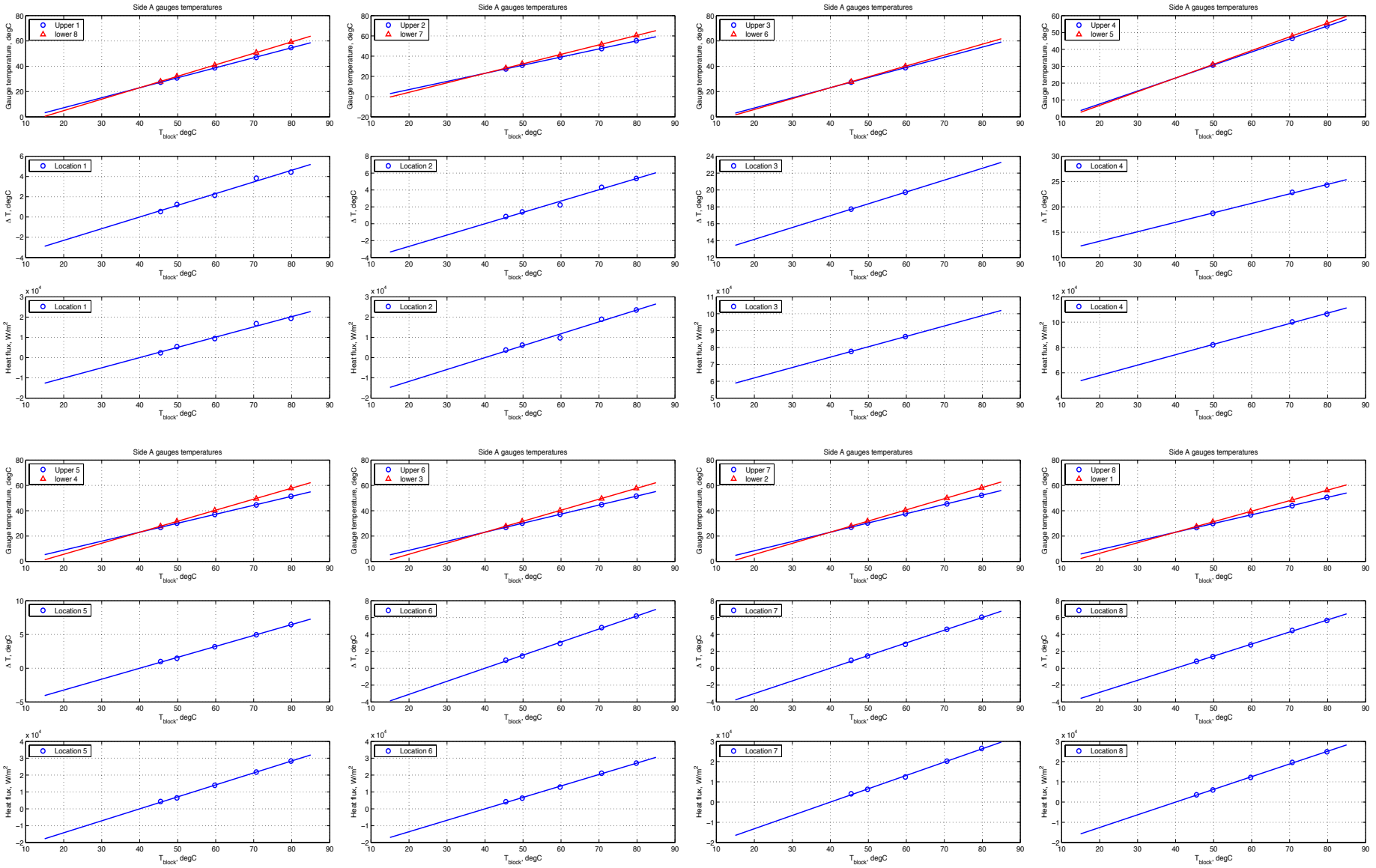


Figure A.27. Temperature difference and heat flux across the sensors mounted on side A for a flow rate of 3.6 lpm and inlet temperature of 42.6 ^{o}C

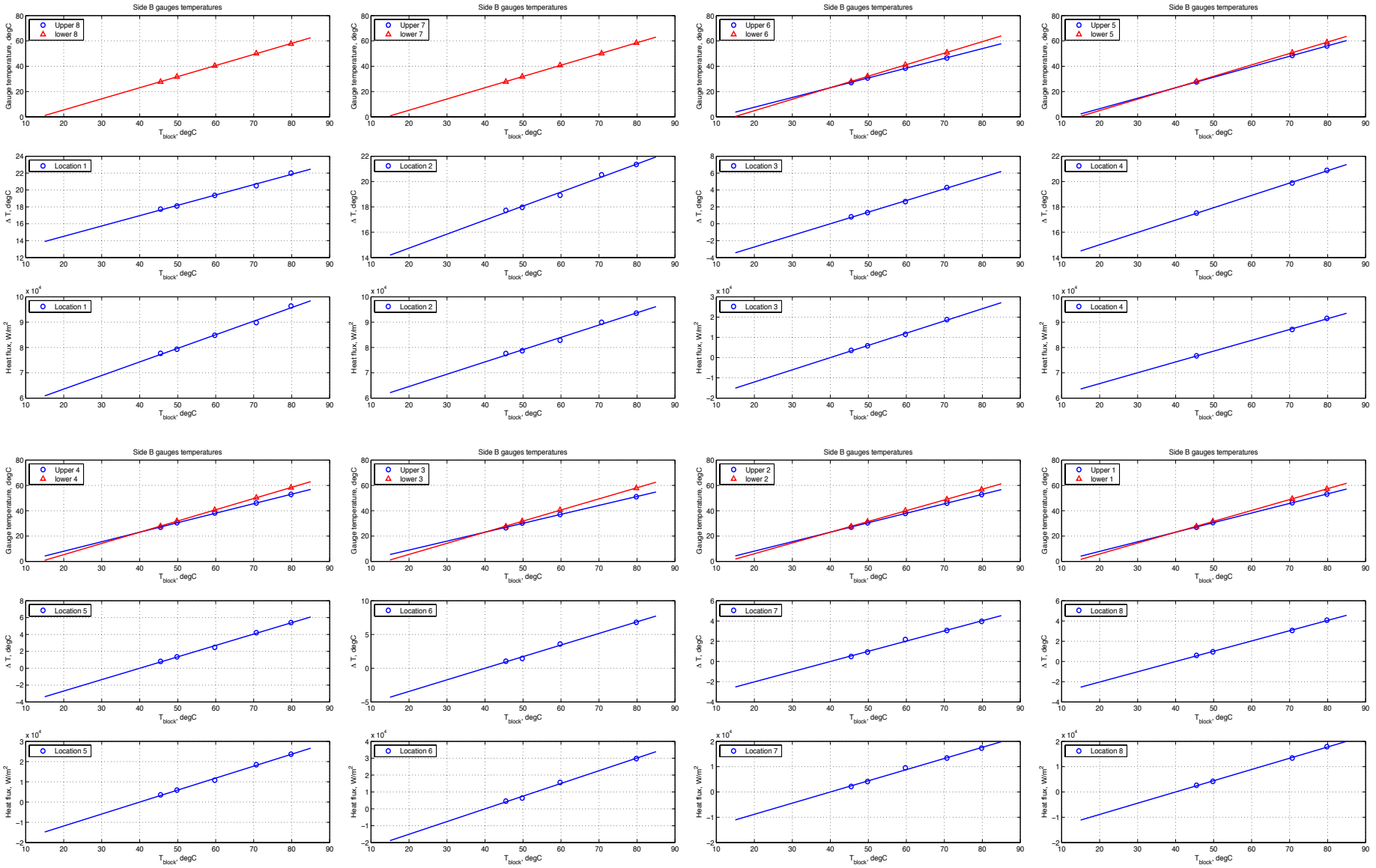


Figure A.28. Temperature difference and heat flux across the sensors mounted on side B for a flow rate of 3.6 lpm and inlet temperature of 42.6 ^{o}C

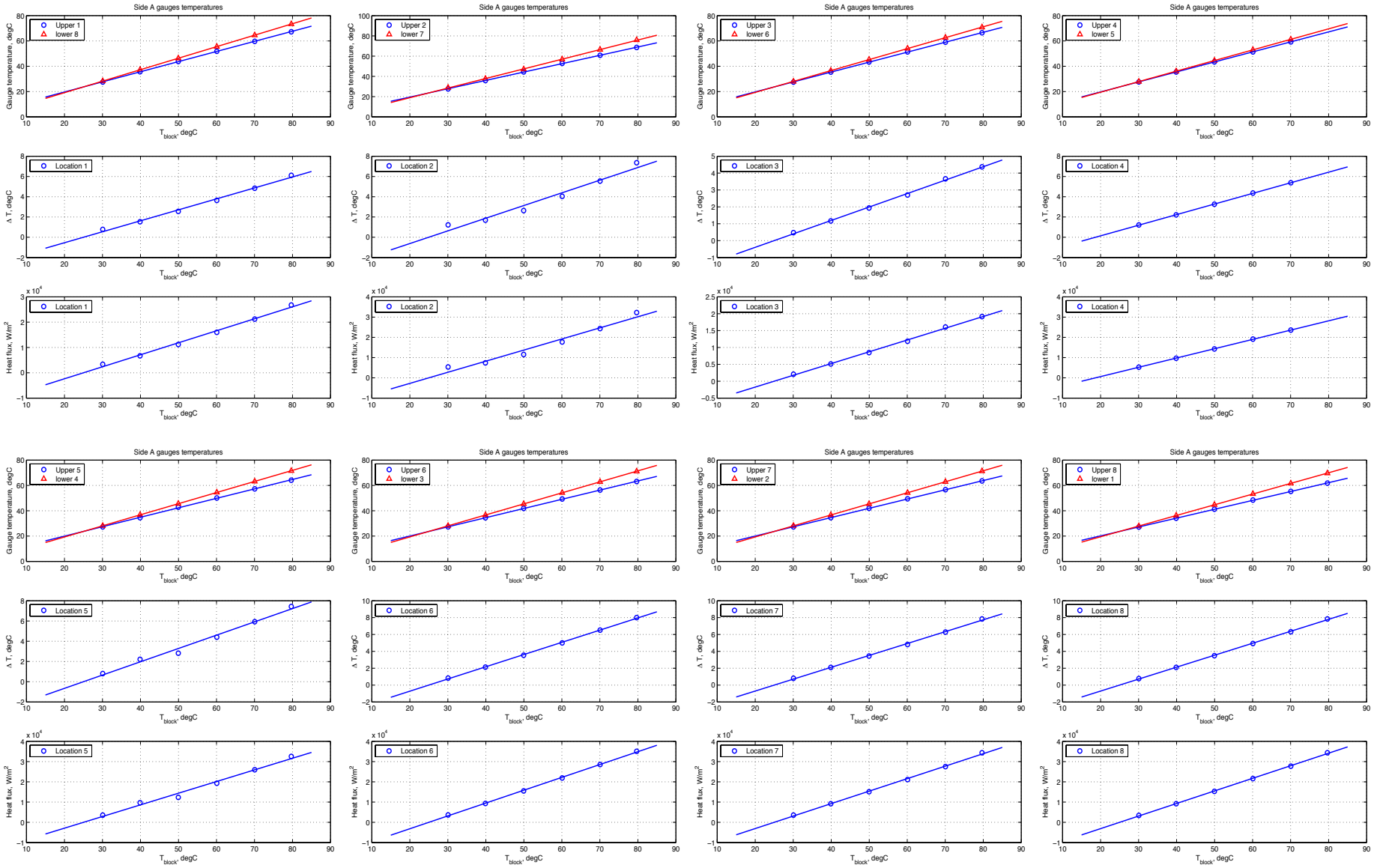


Figure A.29. Temperature difference and heat flux across the sensors mounted on side A for a flow rate of 4.7 lpm and inlet temperature of 28.3 ^{o}C

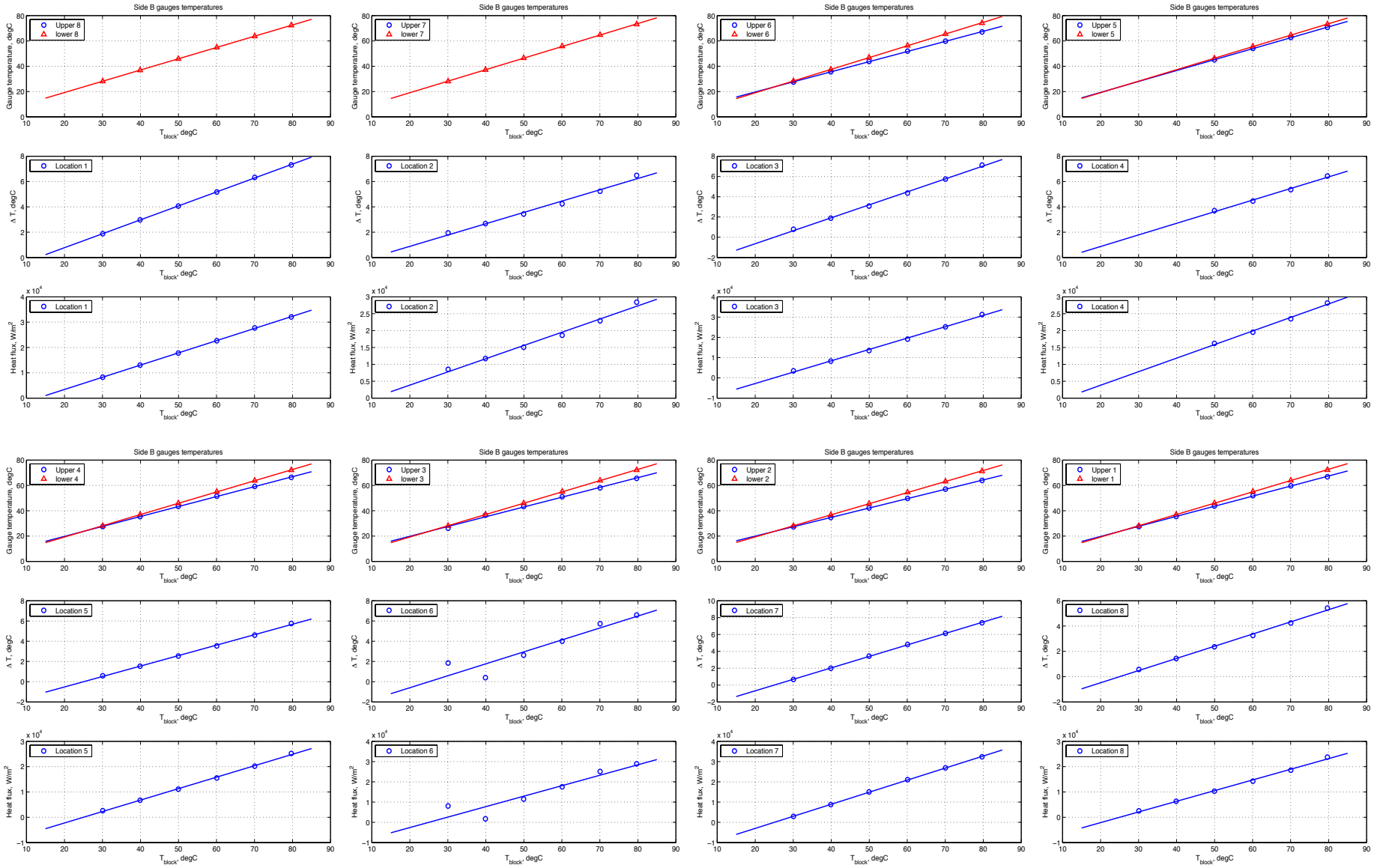


Figure A.30. Temperature difference and heat flux across the sensors mounted on side B for a flow rate of 4.7 lpm and inlet temperature of 28.3 ^{o}C

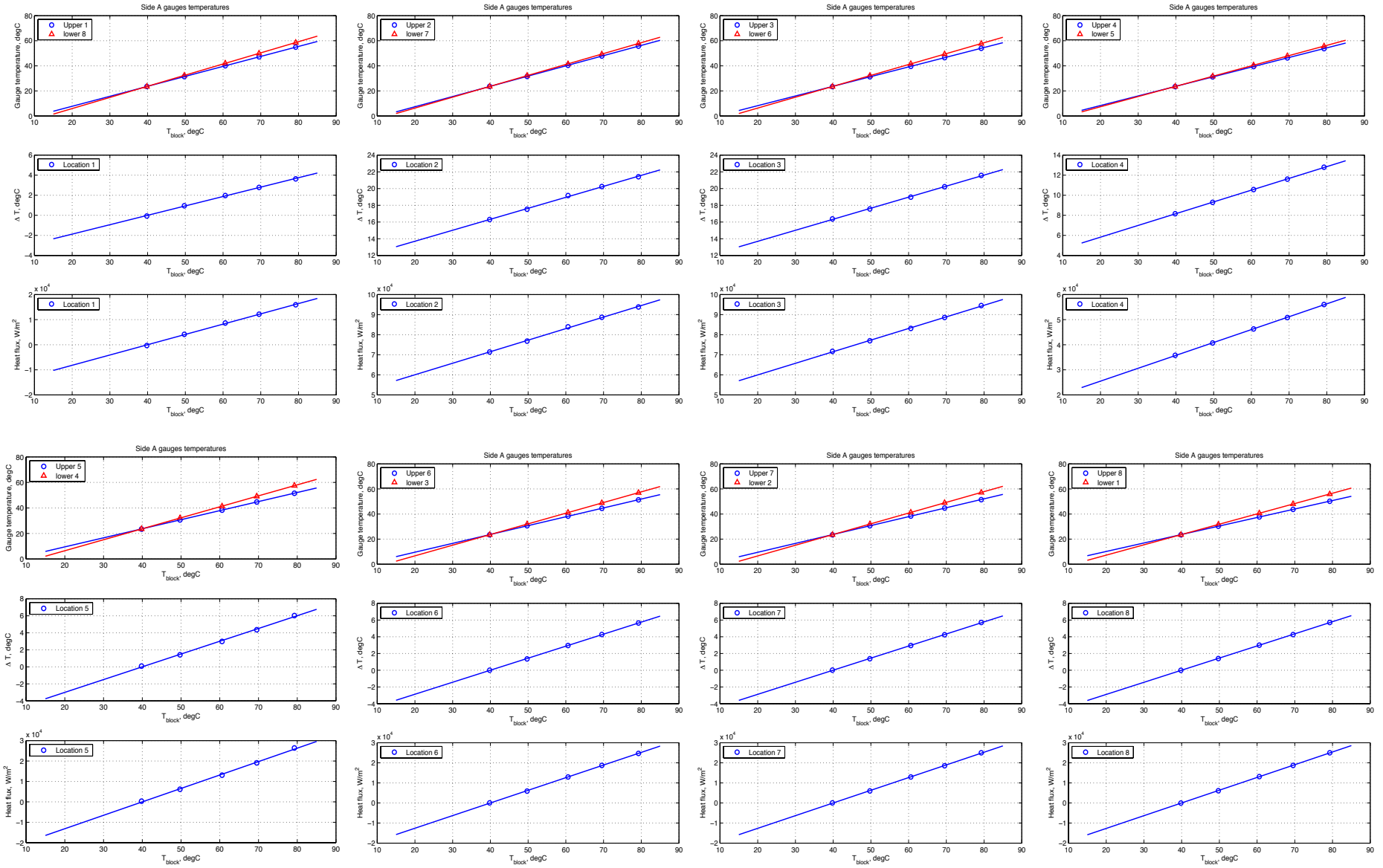


Figure A.31. Temperature difference and heat flux across the sensors mounted on side A for a flow rate of 5 lpm and inlet temperature of 35.5 ^{o}C

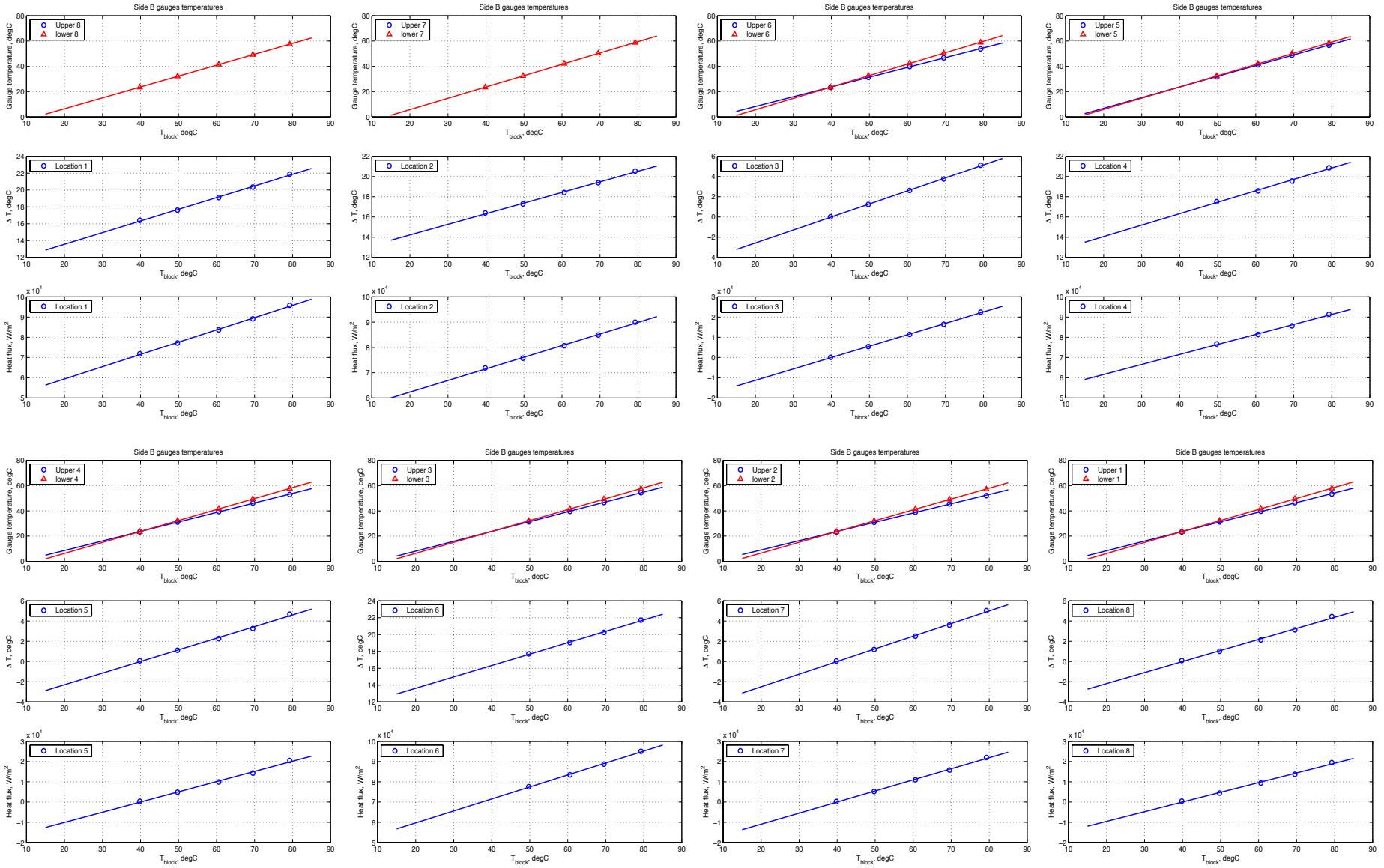


Figure A.32. Temperature difference and heat flux across the sensors mounted on side B for a flow rate of 5 lpm and inlet temperature of 35.5 ^{o}C

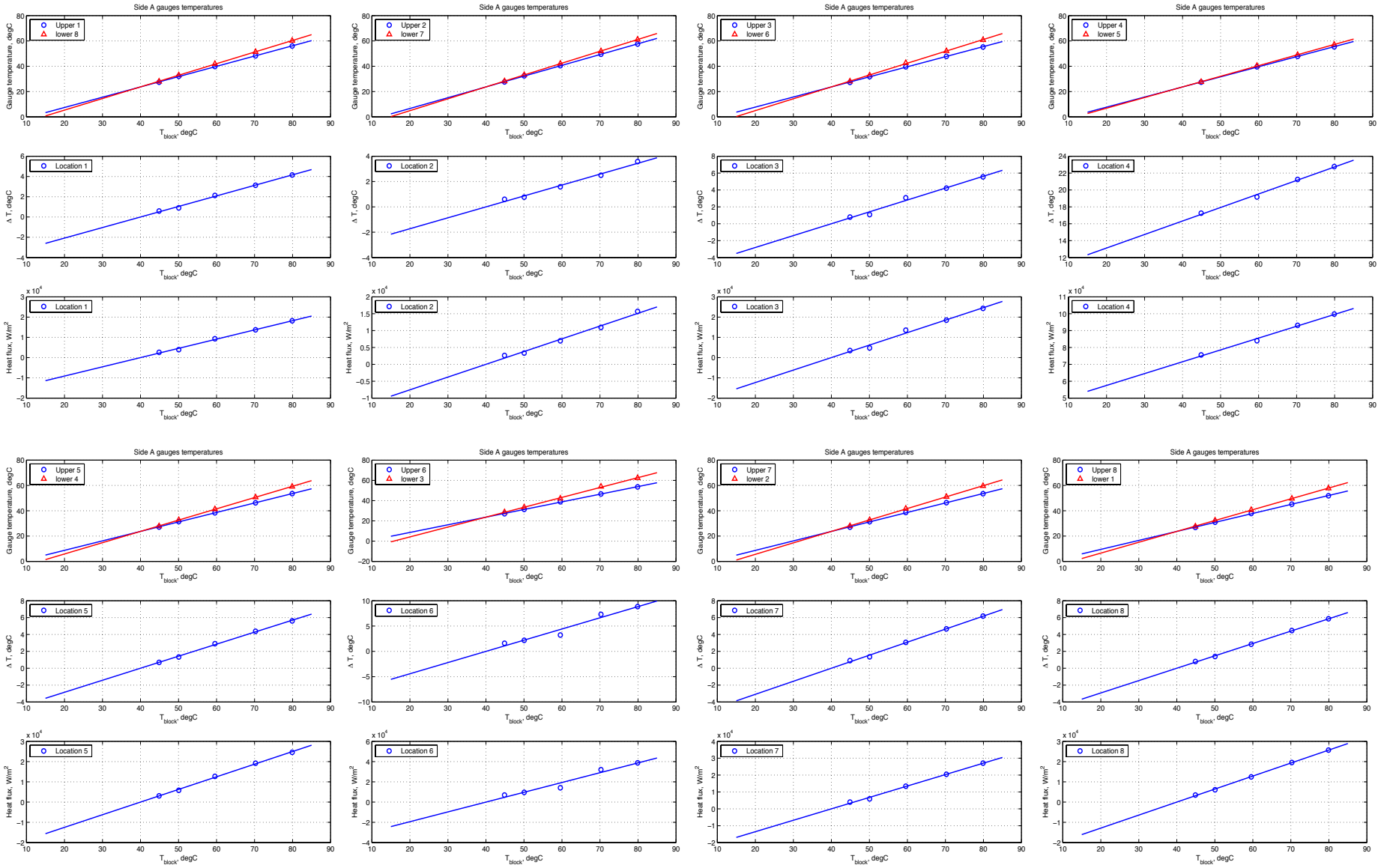


Figure A.33. Temperature difference and heat flux across the sensors mounted on side A for a flow rate of 6.6 lpm and inlet temperature of 45 ^{o}C

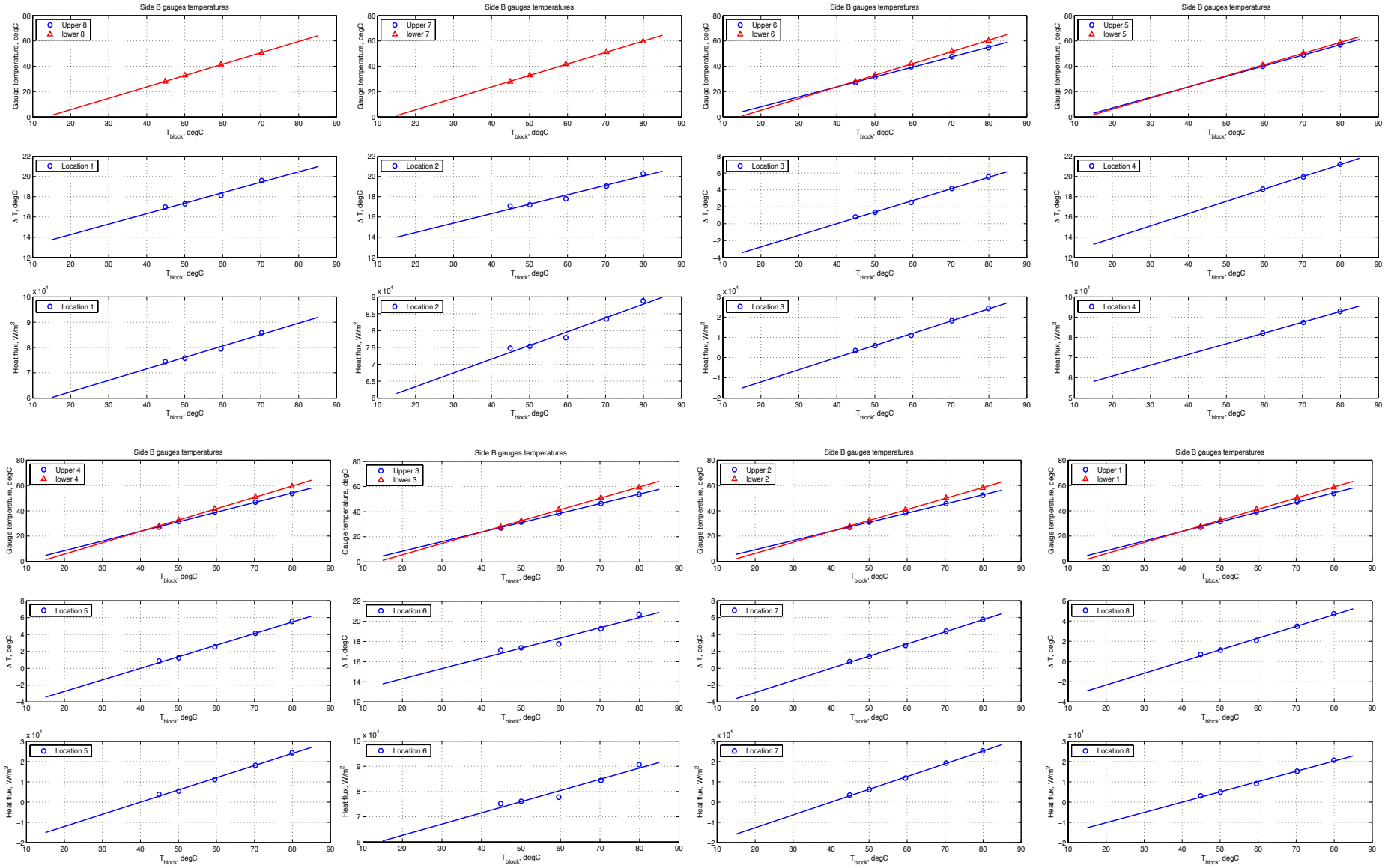


Figure A.34. Temperature difference and heat flux across the sensors mounted on side B for a flow rate of 6.6 lpm and inlet temperature of 45 ^{o}C

A2.3. Local heat transfer coefficient

This section presents the local heat transfer coefficient for each side of the pole piece and the test matrix presented in Section 6.4.4, Table 6.2.

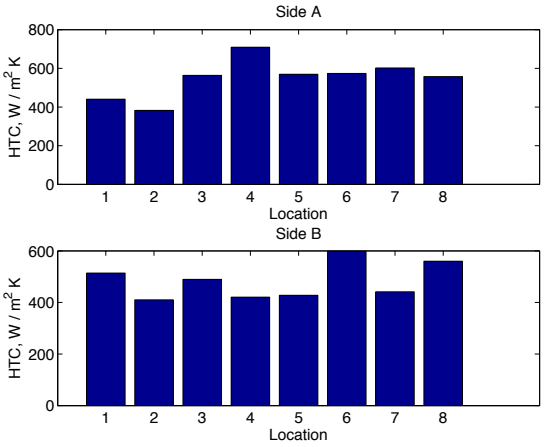


Figure A.35. Local heat transfer coefficients for a flow rate of 2.2 lpm and inlet temperature of 26 °C

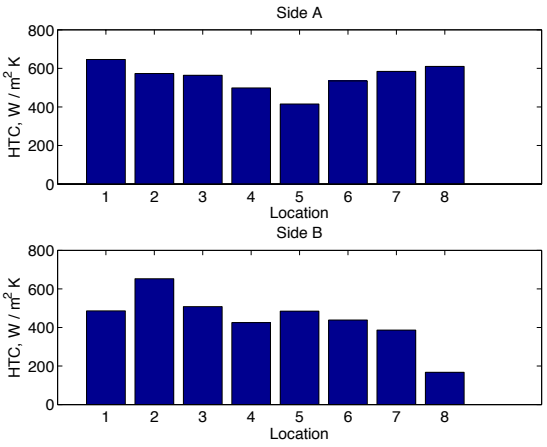


Figure A.38. Local heat transfer coefficients for a flow rate of 3.5 lpm and inlet temperature of 26.5 °C

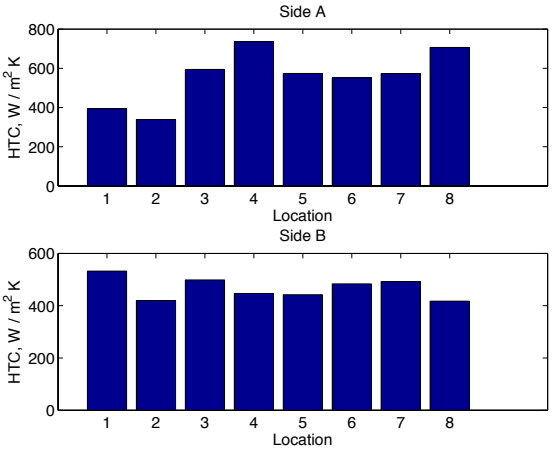


Figure A.36. Local heat transfer coefficients for a flow rate of 2.6 lpm and inlet temperature of 38 °C

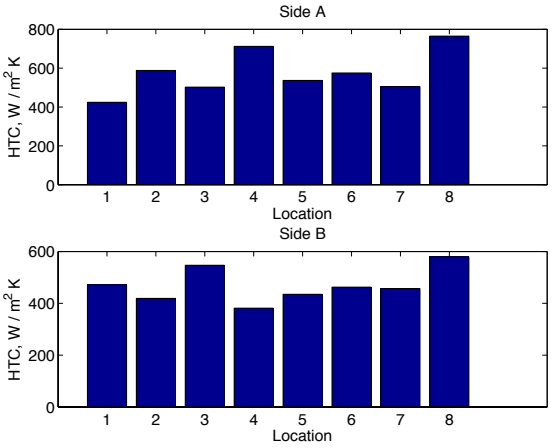


Figure A.39. Local heat transfer coefficients for a flow rate of 3.8 lpm and inlet temperature of 37.7 °C

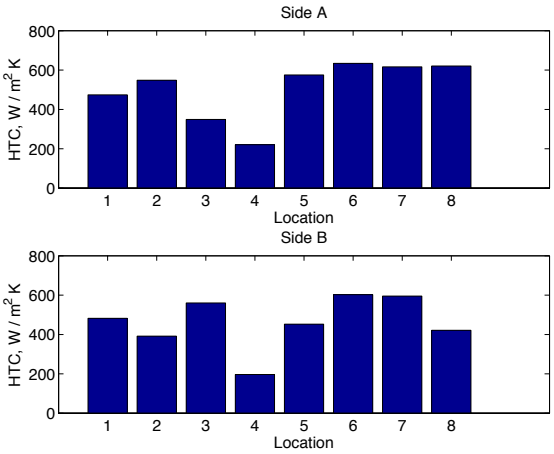


Figure A.37. Local heat transfer coefficients for a flow rate of 2.4 lpm and inlet temperature of 41.1 °C

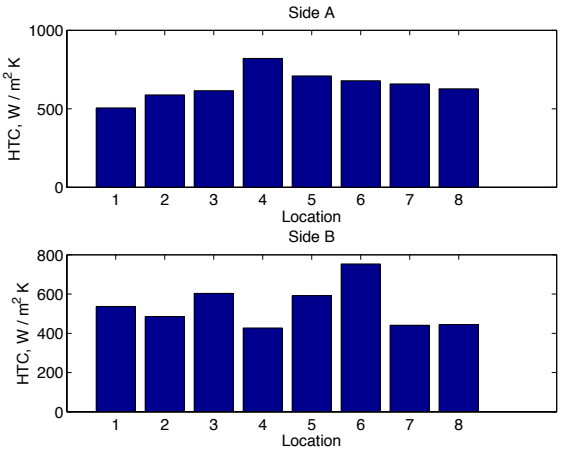


Figure A.40. Local heat transfer coefficients for a flow rate of 3.6 lpm and inlet temperature of 42.6 °C

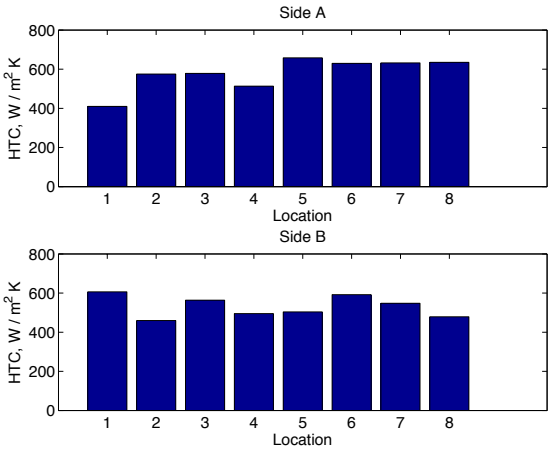


Figure A.41. Local heat transfer coefficients for a flow rate of 4.7 lpm and inlet temperature of 28.3 ^{o}C

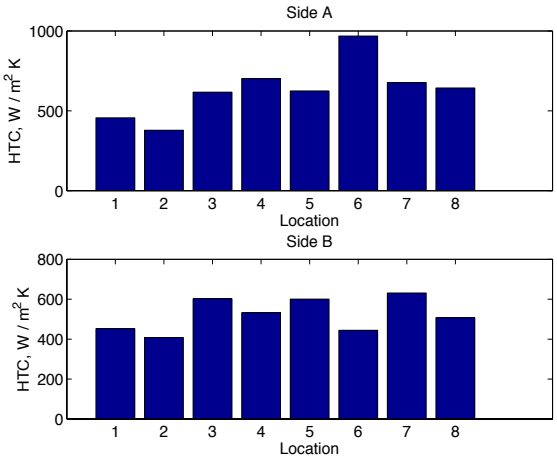


Figure A.43. Local heat transfer coefficients for a flow rate of 6.6 lpm and inlet temperature of 45 ^{o}C

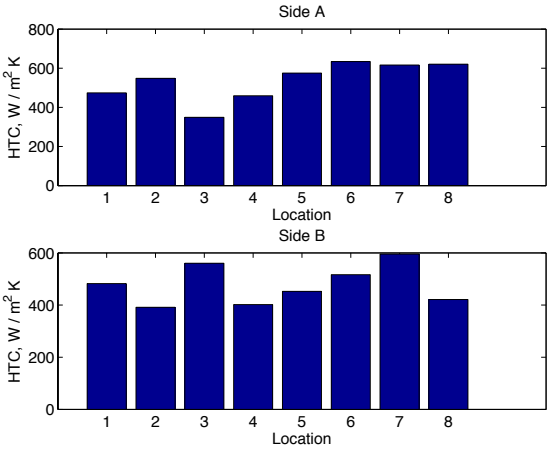


Figure A.42. Local heat transfer coefficients for a flow rate of 5 lpm and inlet temperature of 35.5 ^{o}C

A3: Transient temperature charts

In Section 7.3 and Section 8.2.5 a series of transient experiments were reported. The first experiment is used to derive initial calibration parameters while the remaining experiments are used to confirm the parameters. While the chart of the first experiment is shown in the main text the remaining charts for epoxy infiltrated windings are shown in A3.1, for non-infiltrated windings in A3.2 and for the new construction in A.3.2.

A3.1. Transient charts for epoxy infiltrated windings, Section 7.3

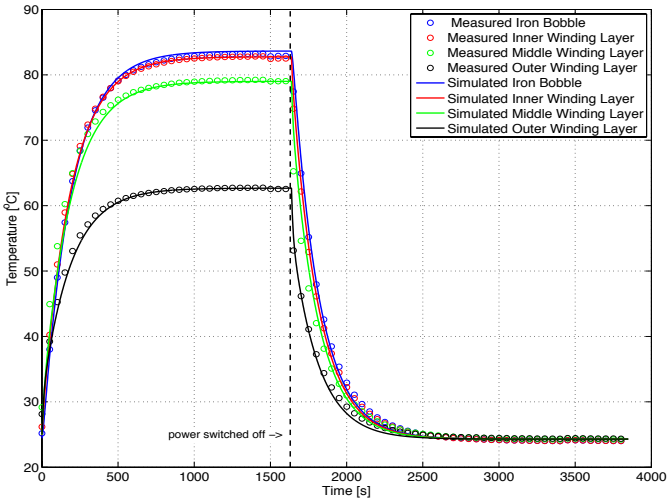


Figure A.44. Comparison of modelled and measured transient thermal behaviour for a pole piece infiltrated with epoxy resin and experiment conditions shown in Test 2.

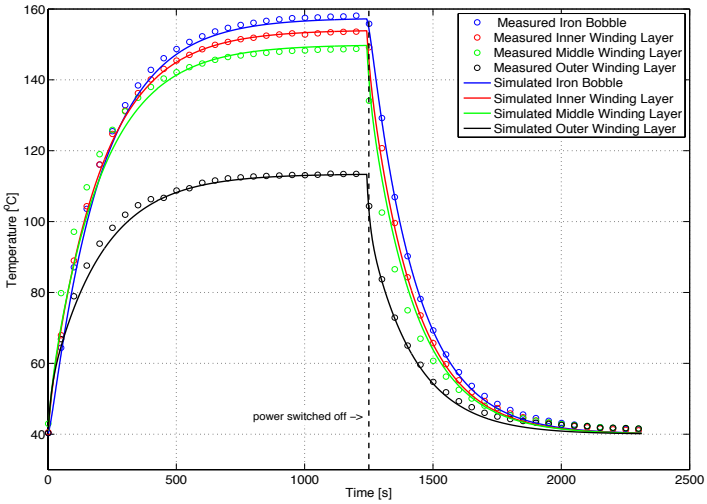


Figure A.45. Comparison of modelled and measured transient thermal behaviour for a pole piece infiltrated with epoxy resin and experimental details of Test 3.

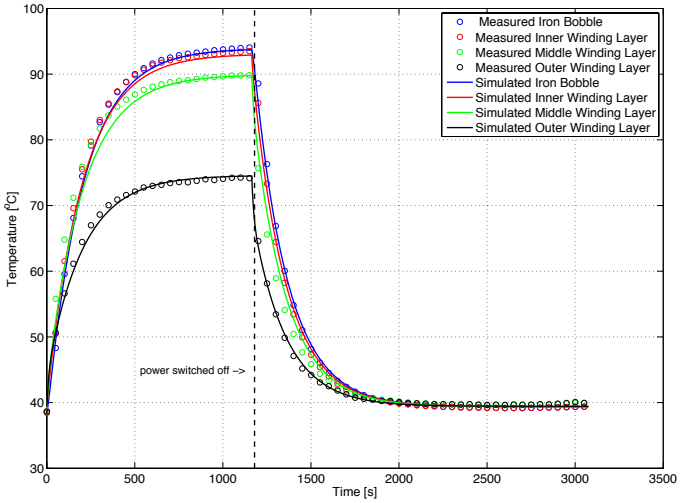


Figure A.46. Comparison of modelled and measured transient thermal behaviour for a pole piece infiltrated with epoxy resin and experimental details of Test 4.

A3.2. Transient charts for non-infiltrated windings, Section 7.3

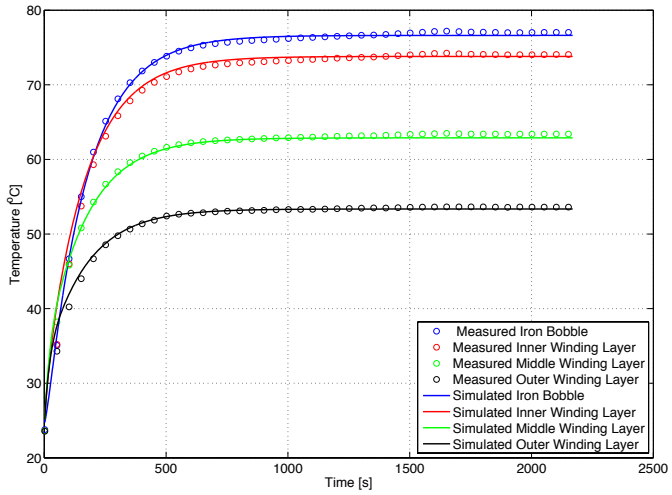


Figure A.47. Comparison of modelled and measured transient thermal behaviour of a non-infiltrated windings for experimental details of Test 2

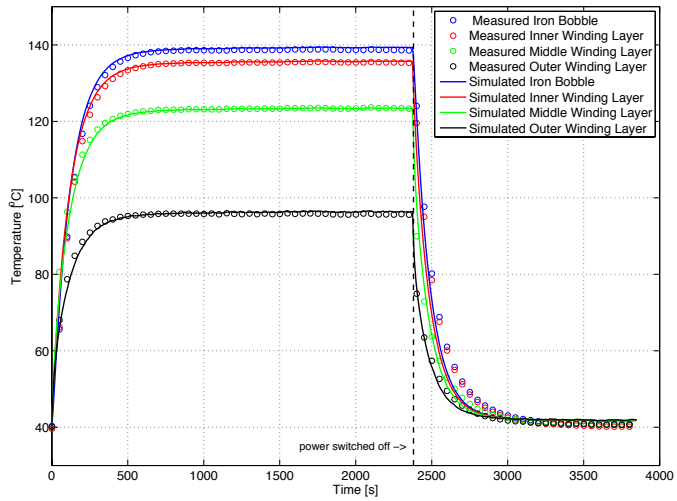


Figure A.48. Comparison of modelled and measured transient thermal behaviour of a non-infiltrated windings for experimental details of Test 3

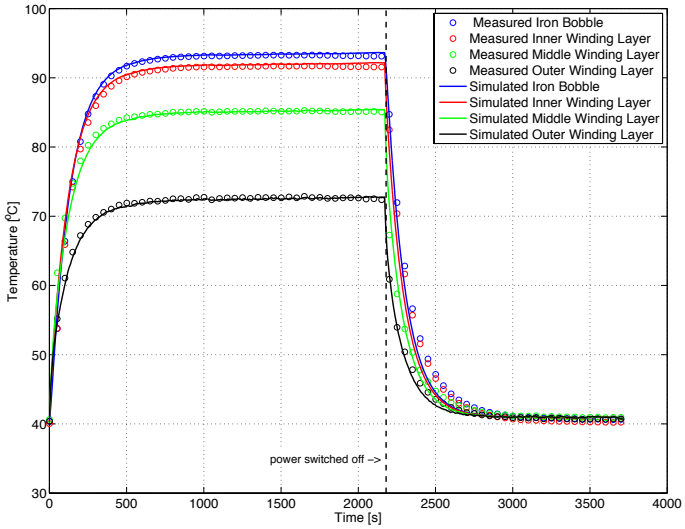


Figure A.49. Comparison of modelled and measured transient thermal behaviour of a non-infiltrated windings for experimental details of Test 4

A3.3 Transient charts for the new construction, Section 8.2.5

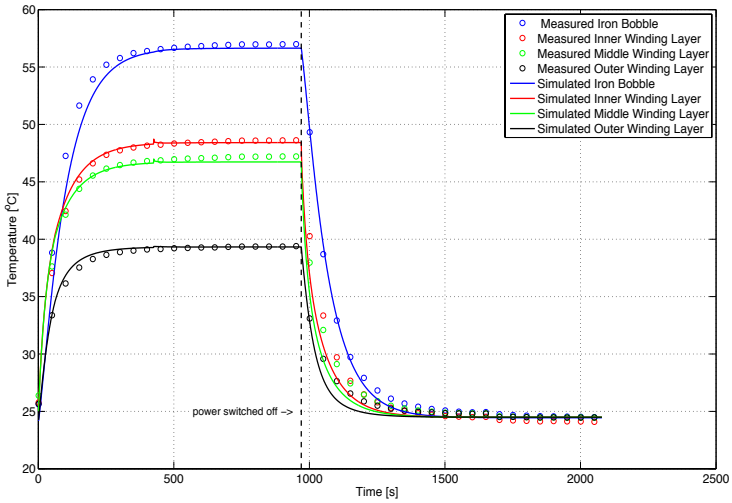


Figure A.50. Comparison between modelled and measured transient thermal behaviour for the new construction with infiltrated pole piece and experiment conditions shown in Test 2.

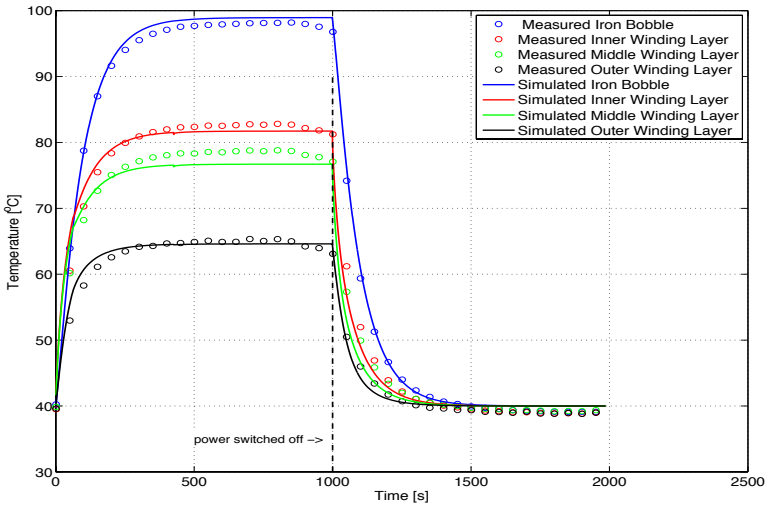


Figure A.51. Comparison between modelled and measured transient thermal behaviour for the new construction with infiltrated pole piece and experiment conditions shown in Test 5.

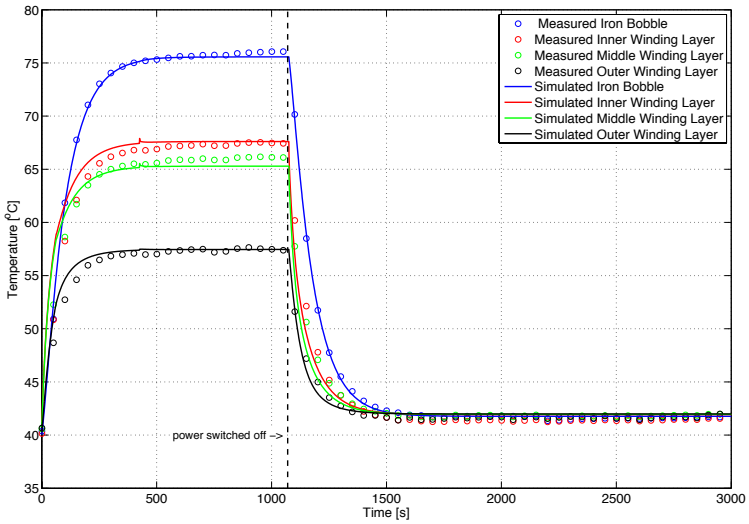


Figure A.52. Comparison between modelled and measured transient thermal behaviour for the new construction with infiltrated pole piece and experiment conditions shown in Test 6.

A4: Thermal Contact Resistance Models

A4.1. The CMY model for flat surfaces

While there have been many attempts to accurately model TCR in flat joints, (Ross and Stoute, 1962, Shlykov and Ganin, 1964, Verzigolu, 1967, Cooper et al, 1969), Yovanovich, (2005) demonstrates that the model developed by Cooper et al, (1969) is the most accurate as this takes into account the force exerted at the contact interface. This model is hence used in this research. When two surfaces are in contact to form a contact joint, intimate solid-solid contact only occurs between the peaks of the asperities at the surface of the material. This contact area is usually less than 2% of the nominal contact area, (Mantelli and Yovanovich, 2002). The remaining area consists of the voids between the asperities as shown in Figure A.55.

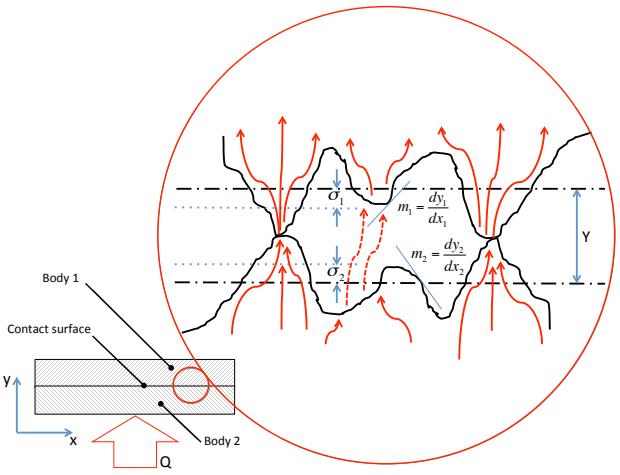


Figure A.53. Schematic of the conductive heat transfer across a joint. σ is the RMS surface roughness of the surface, m is the asperity slope and Y the mean plane separation.

For a joint with apparent area A_a and a temperature difference across it ΔT_{jt} the heat transfer across the joint Q_{jt} has been defined by Mantelli and Yovanovich, (2002) through a conductance equation:

$$Q_{jc} = h_{jc} A_{app} \Delta T_{jc} \qquad \text{eqn. A9}$$

h_{jc} is the joint conductance and can be broken down to the three modes of heat transfer:

$$h_{jc} = h_{cc} + h_{gc} + h_{rad} \qquad \text{eqn. A10}$$

h_{cc} is the conductance through the contact of micro asperities and h_{gc} is the conductance through gas that fills the voids. As the voids are too small, convective

heat transfer is unlikely to occur (Song, 1988). h_{rad} is the radiative conductance from within the air gaps. For temperatures below 600 ^{o}C, Song, (1988) showed that the radiation component can be neglected leaving the joint conductance as the sum of the contact and gap conductance.

$$h_{jc} = h_{cc} + h_{gc} \qquad \text{eqn. A11}$$

The following sections give an overall description of the contact and gap conductance.

A4.1.1 The contact conductance

Cooper et al, (1969) showed that the process of heat transfer across a joint is very complex as the contact conductance is influenced by thermal, geometric, material and mechanical parameters. The authors develop a heat constriction model to define the contact conductance h_{cc}. The authors simplify the asperities in contact by a number of tubes in contact through which the heat flux occurs. The real contact area between two flat surfaces is hence approximated by a number of tubes of contact radius *r*, spread across the surface by a Gaussian distribution. The contact radius is difficult to calculate as this varies with contact pressure and material hardness. These variables dictate the mean plane separation Y and govern how much the materials asperities get crushed into each other and deformed. Several approximations of the mean separation plane have been proposed as shown in Table A6.

Table A.1. Approximations of the mean plane separation

Reference	Correlation*	
Yovanovich, (1981)	$Y = 1.184\sigma\left[-\ln\left(3.132\left(\frac{P_{app}}{H_c}\right)\right)\right]^{0.547}$	eqn. A.21
Song and Yovanovich, (1988)	$Y = 1.363\sigma\left[-ln\left(5.589\left(\frac{P_{app}}{H_c}\right)\right)\right]^{0.5}$	eqn. A.22
Antonetti, (1984)	$Y = 1.53\sigma\left(\frac{P_{app}}{H_c}\right)^{-0.097}$	eqn. A.23

* correlations valid for a range of $2 \leq {}^{Y}/_{\sigma} \leq 4.75$ and $10^{-6} \leq {}^{P}/_{H_c} \leq 2.3\text{x}10^{-2}$

where P is the contact pressure, H_c is the micro contact hardness at the point of contact and σ the RMS surface roughness. Yovanovich, (1981), produced a simplified correlation within 1.5% of the theory in which $h_{cc}$is modelled as:

$$h_{cc} = \frac{1.25m.k_{eq}}{\sigma}\left(\frac{P_{app}}{H_c}\right)^{0.95} \qquad \text{eqn. A12}$$

k_{eq} is the effective thermal conductivity defined as:

$$k_{eq} = \frac{2k_1k_2}{k_1 + k_2} \qquad \text{eqn. A13}$$

σ is the RMS surface roughness $\sigma = \sqrt{{\sigma_1}^2 + {\sigma_2}^2}$ and m is the mean asperity slopes defined as $m = \sqrt{{m_1}^2 + {m_2}^2}$. The surface asperity slope is often unknown. Therefore Antonetti et al., (1991) established a correlation to determine the asperity slope from the RMS surface roughness:

$$ms = 0.125(\sigma.10^6)^{0.402} \qquad \text{eqn. A14}$$

For a surface roughness range between $0.216\ \mu m \leq \sigma < 9.6\ \mu m$.

Hegazy, (1985), observed that the micro contact hardness H_c is not equivalent to the bulk hardness of the material. As the material surfaces press on each other the surface of the material work hardens. Song and Yovanovich, (1988), propose a correlation to establish the non-dimensional contact hardness.

$$\frac{P}{H_c} = \left[\frac{P}{c'_1\left(1.62\ \sigma/m\right)^{c'_2}}\right]^{1/(1+0.071c'_2)} \qquad \text{eqn. A15}$$

Sridhar and Yovanovich, (1994), show how the coefficients c'_1 and c'_2 can be predicted by correlating the Vickers microhardness to the indent diameter as:

$$H_V = c'_1 {d_v}^{c'_2} \qquad \text{eqn. A16}$$

A4.1.2 The gap conductance

Heat transfer across the gap is very difficult to analyze, due to the complexity of the gap geometry. Hence an overall model for heat transfer across the gap has been developed (Yovanovich et al., 1988). Assuming that the heat transfer through the air gap is by conduction, the gap conductance was reduced to:

$$h_{gc} = \frac{k_{gap}}{Y + \kappa\xi\Lambda} \qquad \text{eqn. A17}$$

where κ is an accommodation coefficient determined empirically. ξ is a property of the fluid filling the gap defined as:

$$\xi = \frac{2\gamma}{(\gamma + 1)Pr} \qquad \text{eqn. A18}$$

where γ is the ratio of specific heats and Pr the Prandtl number. Λ is the molecular mean free path defined as:

$$\Lambda = \Lambda_o \left(\frac{T}{\mathrm{T}_o}\right)\left(\frac{\mathrm{P}_o}{P}\right) \qquad \text{eqn. A19}$$

Values of $\kappa, \xi, \Lambda_o, k_g, T/\mathrm{T}_o, \mathrm{P}_o/P$ have been reported by Yovanovich, (1981), and are shown in Table A2.

Table A.2. Variation of air Parameters with Temperature T [K]

Parameter	Empirical Correlations
κ	-0.001T+2.6212
ξ	1.62
Λ_o	6.4e-8
k_g [W/mK]	-0.0003T+0.1331
T/T_o	0.0035T-0.0031
P_{go}/P_g	1

A4.3. Surface and material measurements for windings

Despite that the TCR model was developed to investigate metallic contacts, the CMY theory can be tuned to model different materials by changing the effective micro hardness of the layer-substrate combination, (Antonetti and Yovanovich, 1985). Therefore this section reports the surface and material measurements used to model the effectiveness of various infiltration processes in Section 7.5.4. The RMS roughness or an AWG 14 wire coated with polyimide-amide insulation was measured at 0.3 μm.

To establish the non-dimensional contact hardness shown in eqn A.22, the parameters c_1' and c_2' are required. Therefore the relationship between micro hardness and diagonal length of the indent as described by eqn A.23 is required. The Vickers micro hardness of an AWG 14 wire was measured at different loads. The relationship between the micro hardness and indenter diameter is shown in Figure A.56.

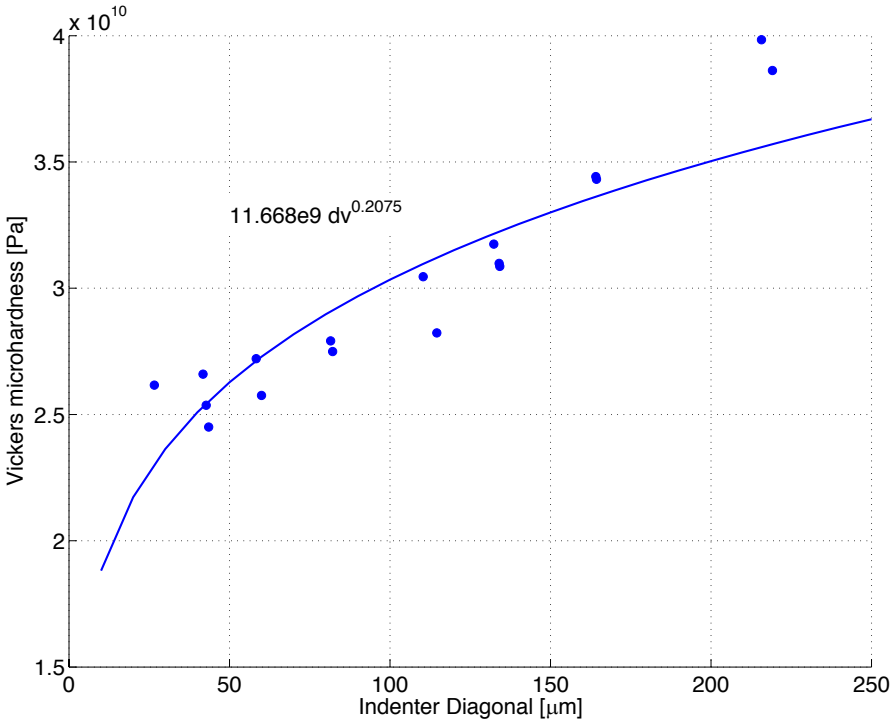


Figure A.54. The micro hardness relationship for AWG 14 copper winding.